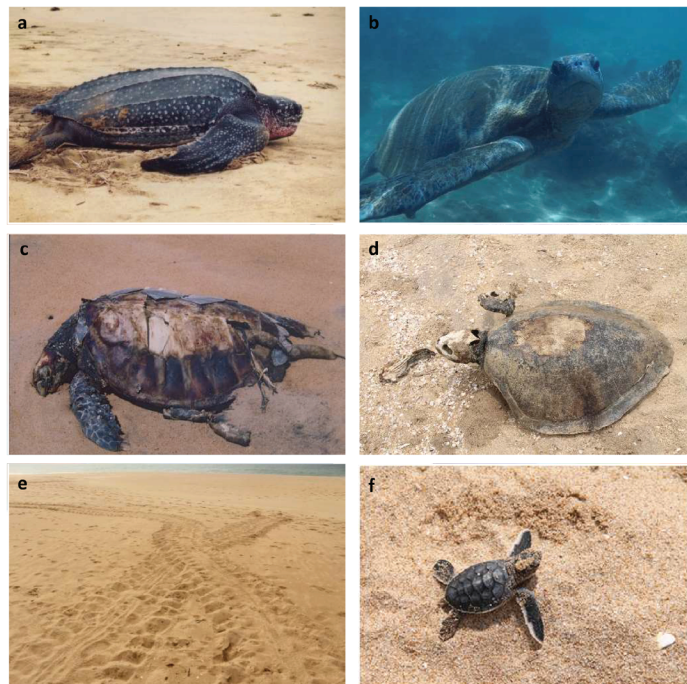


Journal of the

National Science Foundation of Sri Lanka



**JOURNAL OF THE
NATIONAL SCIENCE FOUNDATION
OF SRI LANKA**

Volume 50 Number 4

December 2022

C O N T E N T S

EDITORIAL

- 723 **Empiricism and non-empirical research**
Ajit Abeysekera
-

RESEARCH ARTICLES

- 725 **Investigation of oil level and type of solid insulator on creeping discharges propagating under an AC electric field**
S Ediriweera, PB Jayarathna, R Samarasinghe and R Lucas
- 733 **Poly- β -hydroxybutyrate (PHB) production potential of naturally existing cyanobacterial blooms**
RS Wijerathne, PM Manage and FS Idroos
- 745 **Influence of different bone meal particle size induced calcium specific appetite on performance and egg quality parameters of layer chickens**
TS Gamage, RK Mutucumarana and MS Andrew
- 755 **Assessment of marine turtle nesting habitats from Tangalle to the Kumbukkan Oya estuary in south-eastern Sri Lanka**
SJ Perera, WPN Perera, S de A Goonatilake, K Ekaratne, D Wijesinghe, LV Perera, D Chandranimal and A Ediriweera
- 771 **A new multivariate transmuted family of distributions: theory and application for modelling of daily world COVID-19 cases**
JA Darwish, LI Al-Turk and MQ Shahbaz
- 785 **Synthesis of polyethylene glycol-grafted graphite and effect of its loading on properties of natural rubber composites**
WDM Sampath, CAN Fernando and DG Edirisinghe
- 799 **Analysis of instantaneous, daily and monthly statistics 2017-2021 of rooftop solar energy**
JR Lucas
- 813 **Assessment of wave climate change and its impact on littoral drift along the Kalutara and Kalpitiya beaches in Sri Lanka**
RSM Samarasekara, MM Sahthy, AHMS Siriwardana and HPAM Siriwardana
- 827 **M-polynomial and topological indices for the anti-tuberculosis drugs**
TP Jude, P Elango and M. Koneswaran

- 839 **Developing a model to predict the propagation of sulphide stress corrosion of steel used for petroleum pipelines**
A Manimendra, I De Silva and R Jayasundara
- 851 **Anomalous propagation pathway of the Sri Lanka Dome in summer 2014**
G Pathirana, G Chen, D Wang, MK Abeyratne and T Priyadarshana
- 863 **Simulation of coloured particles radiation spectra from black holes**
CNT Wijewardhana and KAILW Gamalath
- 881 **Designing a closed-loop information flow model in bridging the market information gap among agriculture stakeholders in Sri Lanka**
TB Mallikaarachchi, G Samaraweera, A Walisadeera, L De Silva and S Munasinghe

-
- 897 **List of Referees**
- I **Author Index**
- XI **Subject Index**
-

Guidelines for Contributors



Cover: Leatherback (a), green (b - adult & f - hatchling), hawksbill (c) and olive ridley (d) turtles who nest in Sri Lankan beaches, green turtle crawl marks (e) and by-catch of sea turtles in fisheries (c & d).

Photo credits: SJ Perera (a & c), WPN Perera (b & e), K Ekaratne (d & f)

See *J.Natn.Sci. Foundation Sri Lanka* 2022 50(4): 755 - 769

EDITORIAL

Empiricism and non-empirical research

Empiricism, the doctrine that knowledge is derived from experience, is a dominant feature of the natural sciences which primarily seeks to understand natural phenomena occurring in the world we live in. In contrast, formal sciences (of which mathematics is the foremost example) deals with abstract structures which may or may not be applicable to real world phenomena.

There has always been a close connection between mathematics and natural science. Galileo Galilei (1564–1642) expressed the view that nature is written in a mathematical language. The development of computers was historically connected with the attempt to carry out mathematical calculations using a machine rather than the human brain. Modern developments in computer science and technology have resulted in the development

of powerful tools such as machine learning (a field within artificial intelligence), which are beginning to be applied to complex problems, particularly those involving vast amounts of data, in many fields of natural science.

A key issue in machine learning models is generalizability. Problems with regard to application of machine learning models in health care have been highlighted recently in the literature. It is reported that many models are unreliable when applied to data from outside the training data set. The JNSF, in keeping with its focus on natural science have introduced with the current issue new guidelines for authors submitting papers on computing and related areas such as artificial intelligence and machine learning, which emphasize the need for empirical evaluation of research findings.

Ajit Abeysekera

RESEARCH ARTICLE

High voltage engineering

Investigation of oil level and type of solid insulator on creeping discharges propagating under an AC electric field

S Ediriweera^{1*}, PB Jayarathna², R Samarasinghe² and R Lucas³

¹ Department of Electrotechnology, Faculty of Technology, Wayamba University of Sri Lanka, Kuliyapitiya, Sri Lanka.

² Department of Electrical Engineering, Faculty of Engineering, University of Moratuwa, Moratuwa, Sri Lanka.

³ Department of Electrical, Electronic & Telecommunication Engineering, General Sir John Kotelawala Defence University, Ratmalana, Sri Lanka.

Submitted: 8 August 2021; Revised: 8 March 2022; Accepted: 25 March 2022

Abstract: This paper presents a study on the use of different solid insulators and oil volumes inside oil-filled high voltage equipment to minimize the effect of damage that occurs due to creeping discharge activity. A point-plane electrode arrangement-based test apparatus, energized by a high voltage supply, is used for analyzing the propagation of creeping discharges over solid/coconut oil interfaces using visual observation. In particular, the effect of oil level and the effect of the kind of solid insulators, such as glass and acrylic, are analyzed incorporating the discharge length associated with pattern propagation. The result shows that the glass and acrylic insulators do not have a significant effect on the discharge length when they are immersed in coconut oil even if the breakdown voltage of acrylic is higher than that of glass by 28%. The results also show that when the oil level inside the test cell increases, the amount of ramification and propagation of streamers decreases, reducing the discharge length. The fall of the coconut oil level under electric field-generated electrodynamic motion inside the oil-filled high voltage equipment can create an opposition force on the discharge propagation. However, such a phenomenon can initiate discharge propagation at low voltage values.

Keywords: Coconut oil, discharge length, electric field, electrodynamic motion, propagation, Oil Height,

INTRODUCTION

An efficient and reliable electrical power supply plays an important role in the quality of electricity. Failure of high voltage equipment leads to catastrophic events, resulting

in economic losses and injury to humans. Therefore, power utilities are putting their maximum effort to maintain high voltage assets with a reliable operation (Beroual & Boubakeur, 1991; Kebbabi & Beroual, 2006; Ediriweera *et al.*, 2018). Solid/liquid or solid/gas interfaces can be seen in oil or gas-filled high voltage equipment such as power transformers, capacitors, bushings, and circuit breakers. These composite insulation systems are subjected to different stresses and when the tangential electric field at the interface exceeds a threshold value, discharges can be initiated and propagated over the interface (Douar *et al.*, 2015). These discharges are commonly called creeping discharges. Due to the frequent occurrence of creeping discharges, the insulation system can undergo irrecoverable damage, and finally, this may lead to flashover (Douar *et al.*, 2015).

Conventionally, petroleum-based mineral oil has been used inside oil-filled high voltage apparatus due to its better electrical and thermal properties. However, recently attention has been paid to the useability of natural ester oils such as coconut oil, soybean oil, and sunflower oil, due to several disadvantages associated with mineral oil such as future scarcity and poor biodegradability. Past research has concluded that treated ester oils can be used as an alternative oil, with improved dielectric properties (Abey Bandara *et al.*, 2001; Lucas *et al.*, 2002). Coconut oil is a commercially available vegetable oil, used for

* Corresponding author (ediriweera.sampath@gmail.com;  <https://orcid.org/0000-0002-5937-7932>)



This article is published under the Creative Commons CC-BY-ND License (<http://creativecommons.org/licenses/by-nd/4.0/>). This license permits use, distribution and reproduction, commercial and non-commercial, provided that the original work is properly cited and is not changed in anyway.

cooking purposes in countries such as Sri Lanka, India, and Malaysia. Studies have shown that the physical, chemical, thermal, and dielectric properties of the oil have acceptable levels for it to be used as a dielectric liquid. Compared to other natural esters, coconut oil is rich in saturated fatty acids (around 90%), which increases its melting point and conductivity levels (Matharage *et al.*, 2013). A lot of work has recently been devoted to the creeping discharges propagating on solid insulators immersed in mineral oil and different kinds of esters (Kebbabi & Beroual, 2006; Sitorus *et al.*, 2015; Zhou *et al.*, 2016;). Therefore, it is worthwhile to study creeping discharge formation on insulators immersed in coconut oil.

On the other hand, engineers have carried out many studies to understand the creeping discharge propagation mechanism to reduce the likelihood of a breakdown. Most of the work has focused on the formation of streamers which are low-density conductive gaseous channels that are formed in the liquid closer to the interface (FitzPatrick *et al.*, 1990; Lesaint *et al.*, 1988; Gournay & Lesaint, 1994). In our previous studies, the effect of the pressure generated by the mass of the coconut oil on the gaseous streamers and the fractal dimension of the creeping discharges have been analyzed (Ediriweera *et al.*, 2019). The electrohydrodynamic motion of the coconut oil has limited the discharge propagation reducing the possibility of flashover. Thus, the effect of oil levels on the variation of discharge length should be studied to reduce the effect on the creeping discharge formation.

The main objective of this paper is to analyse

experimental creeping discharges propagating over glass and acrylic insulating materials immersed in coconut oil, using a test apparatus. The experiential model, which is based on a point-plane electrode system, is used to carry out the experimental tests. The effect of the kind of dielectric material on the discharge propagation, while incorporating the structure and discharge length of the patterns and the effect of oil level on creeping discharge propagation, incorporating the discharge length, are analysed.

MATERIALS AND METHODS

Experimental test setup

Figure 1 shows the schematic view of the test setup, similar to what has been used in previous studies (Ediriweera *et al.*, 2020). The test cell basically consists of a cylindrical core made of clear acrylic and has a point-plane electrode arrangement inside it. The gap between the point electrode and the plane electrode can be varied and thin flat insulating material samples can be inserted for testing purposes. The samples are immersed in insulating liquid by filling the test cell with coconut oil. A CCD camera, with a high frame rate connected to a high-performance video card, is mounted over the test cell and the integrated images taken by it are used for the optical observation of the discharge. The plane electrode is grounded and the point electrode is energized by a partial discharge (PD) free HVAC test transformer. If the flashover or the complete dielectric breakdown is observed, the test cell is refilled with new oil to maintain the condition of the oil.

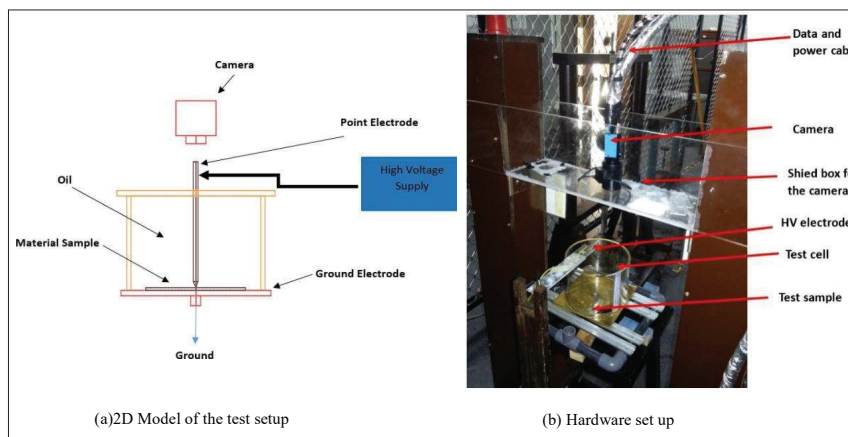


Figure 1: Experimental test setup

Experimental procedure

Flat square-shaped solid material samples of a side length of 9 cm and a thickness of 3 mm are used for the study. Two kinds of pre-prepared solid materials, namely glass and acrylic are used to analyze the creeping discharge propagation over the solid/coconut oil interface. In particular, the effect of kind of the solid dielectric and oil level on the solid material sample on discharge propagation are analysed using the test setup. Commercially available copra type coconut oil is selected as the liquid dielectric medium. More details on the extraction method and chemical composition of copra-type coconut oil can be found in earlier research (Matharage *et al.*, 2013). Table 1 shows the dielectric breakdown voltage and dielectric constant of material samples. The parallel plate method is used to measure the relative permittivity of the solid material samples at 100 Hz using an LCR meter as in previous studies (Mandric *et al.*, 2018; Karunarathna *et al.*, 2019). The breakdown voltages of the solid samples and coconut oil were found according to the ASTM D-149 standard and IEC 60156 standard, respectively.

The influence of hydrostatic pressure on creeping discharges has been studied (Kebbabi & Beroual, 2003; Beroual & Kebbabi, 2008; Matharage *et al.*, 2013; Beroual & Khaled, 2018), and according to these findings, low-density gaseous channels are affected by the hydrostatic pressure. In the current study, the level of copra-type coconut oil inside the test cell is changed in order to analyse the effect of the oil level over the solid sample on creeping discharge propagation, and glass material samples are used. The heights of the oil levels inside the test cell, and the corresponding calculated volumes are listed in Table 2.

Table 1: Dielectric properties of material samples

	Acrylic	Glass	Coconut oil
Breakdown voltage (kV/mm)	41	32	15
Dielectric constant	4.5	5	2.9

Table 2: Considered oil levels

	Level 1	Level 2	Level 3	Level 4
Oil height (mm)	10	20	35	50
Oil volume (mL)	154	307	548	769

Discharge length

Creeping discharges may have several mainstreamers starting from their starting point, and there may be side branches starting from mainstreamers. Discharge morphology depends on different factors such as electric field distribution. As an example, with mineral oils, negative streamers tend to propagate radially while positive streamers are more concentrated around their initiation point with more ramified branches having different discharge lengths (Kebbabi & Beroual, 2006). Therefore, each streamer may have different total discharge lengths. In this paper, two terms, final discharge length and radial discharge length, are defined for the purpose of analysis of the creeping discharges. What is defined as the final discharge length in this paper is the maximum discharge length of a particular streamer out of all the streamers that the pattern has, and it assesses the voltage required to get a discharge of a particular length. The other term is the radial discharge length which measures the maximum radial extension the pattern makes from its initiating point.

RESULTS AND DISCUSSION

Type of solid dielectric material

Creeping discharges under an alternating voltage do not always propagate radially with this point plane arrangement. An electric field distorted by space charges on the insulators is considered to be the main reason for such an orientation (Beroual *et al.*, 2011). Creeping discharge characteristics such as light intensity, number of mainstreamers and branches, and amount of ramification depend on the type of solid material. Figure 2 and Figure 3 show the development of discharge patterns propagating over acrylic and glass samples respectively. The size of the discharge patterns increases when the applied voltage is increased. The thickness and the brightness of the channels reduce along with the streamers.

The shape of the discharges on the glass/oil interface is different from what was observed on the acrylic/oil interface. It accounts for luminosity, the number of mainstreamers, the amount of ramification, and shape. On this material, it is noted that the patterns have more ramified branches and luminous points. Previous studies have shown that negative discharges propagating under vegetable oils have the same characteristics as what was observed on the glass/coconut oil interface (Dang *et al.*, 2012). Therefore, patterns propagating over a

glass/oil interface show the characteristics of negative streamers rather than positive ones. On the other hand, the brightness of the streamers has no high dependency on the applied voltage, compared to that on the acrylic/oil interface.

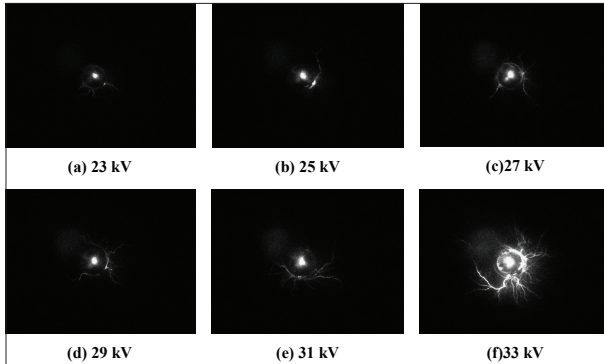


Figure 2: Development of creeping discharges on acrylic material samples

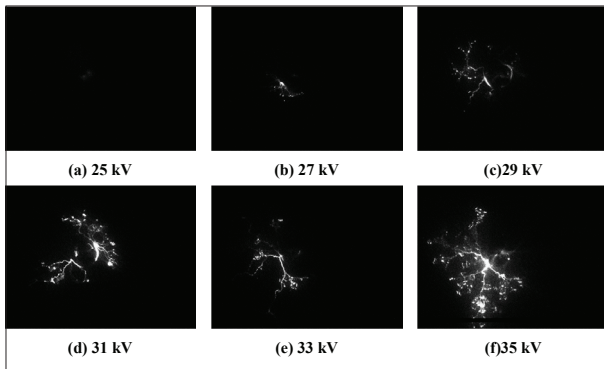


Figure 3: Development of creeping discharges on glass material samples

As the voltage increases, the brightness of the streamers propagating on both interfaces increases. The luminous points on the glass surface make the streamers less prominent so that they cannot be identified separately or defined very well just by the naked eye. Other than that, discharge patterns propagating over the glass surface tend to propagate radially compared to that on the acrylic surface, where curved streamers can be observed, as a result of the electro-hydrodynamic motion of oil in the vicinity of the point electrode. Therefore, streamers try to follow these contours. Even though the light emitted by the patterns propagating over the acrylic/oil interface is not intense at the initial stage of development compared

to that of glass/oil, the amount of ionization on the glass interface increases as the voltage increases. The contours closer to the tip of the point electrode have caused the space charges to concentrate more around it, resulting in a more intensive glow around the tip of the point electrode.

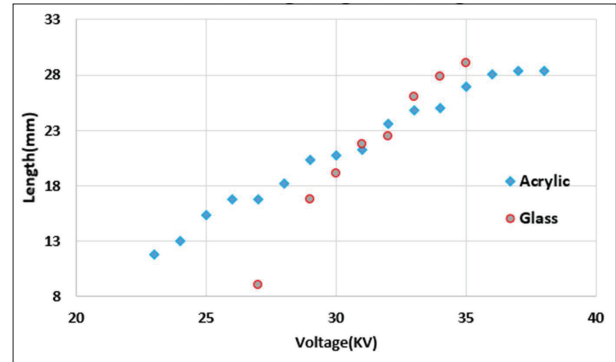


Figure 4: Variation of the final discharge length of the creeping discharges propagating over the different solid samples with the applied AC voltage

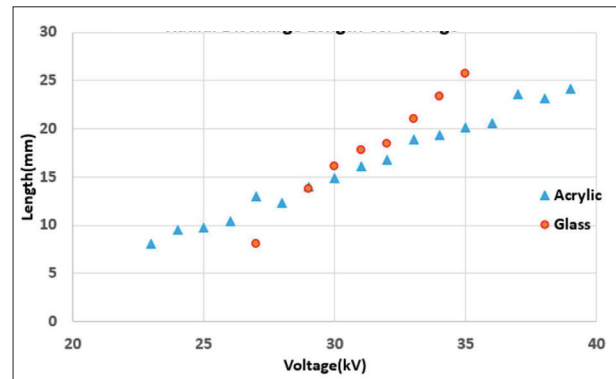


Figure 5: Variation of the radial discharge length of the creeping discharges

The final discharge length and radial discharge length increase quasi-linearly with the voltage, as shown in Figure 4 and Figure 5, respectively. It is to be noted that all the discharge length values listed in the paper are the average of four experiments conducted under the same conditions. With a high-speed CCD camera, it is possible to take the discharge patterns at their maximum extension. Even if at low voltage values, the lengths corresponding to the acrylic/oil interface is slightly higher than that of the glass/oil interface, when the voltage increases, the discharge length of patterns on glass/oil exceed that

on the acrylic/oil interface. However, the discharge length cannot exactly define which interface promotes more discharges. Further, the capacitive effect of the slightly different permittivity values of the solid material samples, as shown in Table 1, on discharge prorogation, is also negligible.

Effect of oil level

Figures 6–8 show the development of creeping discharge patterns on the glass surface at applied voltages of 18 kV, 23 kV, and 26 kV respectively, for the different oil levels shown in Table 2.

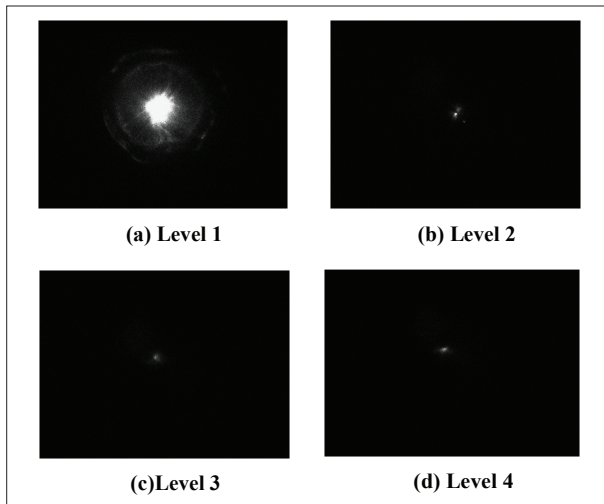


Figure 6: Oil level on creeping discharge development under 18 kV

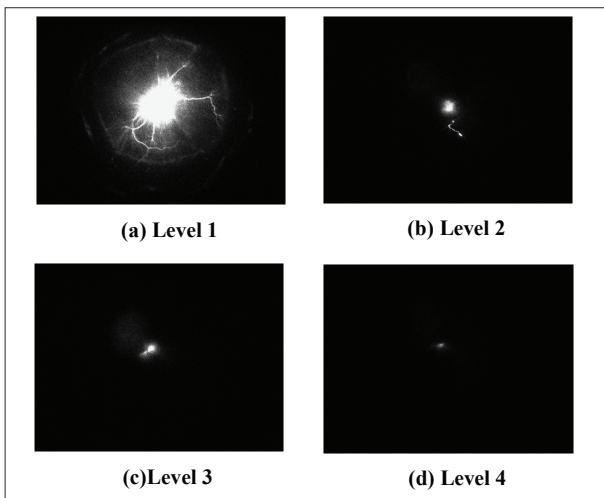


Figure 7: Oil level on creeping discharge development under 23 kV

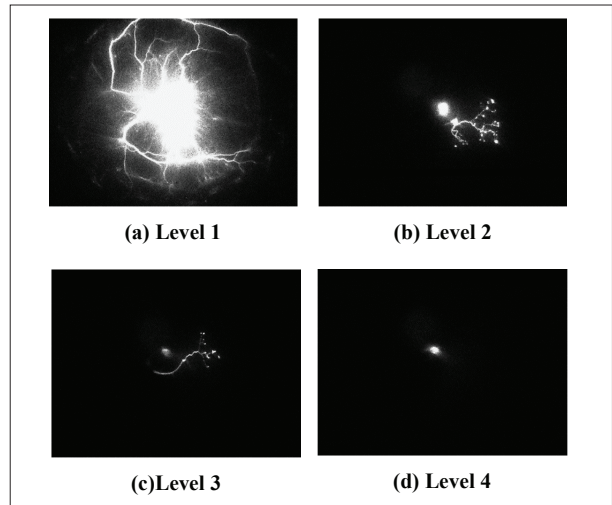


Figure 8: Oil level on creeping discharge development under 26 kV

When the oil level increases, the size of the pattern, the number of branches, and emitted light decrease due to the reduction in the tangential electric field at the tip of the point electrode. At low coconut oil levels, electrodynamic motion becomes more prominent and affects the pattern prorogation and its characteristics. More details on the electrodynamic motion associated with coconut oil and the effect of the tangential electric field at the tip of the point electrode on the pattern propagation can be found in Ediriweera *et al.* (2019).

When the oil level is increased, the final and radial discharge lengths of creeping discharges are reduced, as shown in Figure 9 and Figure 10 respectively, and the discharge length curves show a quasi-linear behaviour with the applied voltage irrespective of the oil level when the solid samples are immersed in copra-type coconut oil. Such a variation on the discharge length was observed for different hydrostatic pressure values by Beroual *et al.* in 2002, 2003, and in 2008 under AC, DC, and impulse voltages with solid samples immersed in petroleum-based mineral oil (Kebbabi & Beroual, 2003; Beroual & Kebbabi, 2008; Beroual & Khaled, 2018).

The slopes of discharge length curves and the associated R-square values, considering the quasi-linearity of discharge length curves, are listed in Tables 3 and 4. With the R square value of each curve close to 1, their quasi-linearity is confirmed. The rate of rise of discharge length with applied voltage depends on the coconut oil level. The rate of rise of each curve becomes weaker as the oil level increases, except the curve

corresponding to level 1. The rate of rise of the curves corresponding to level 1 is lower than that corresponding to level 2, because the fall of the oil level at low oil levels due to electric field generated electrodynamic motion opposes the pattern propagation, and it had become more prominent at oil level 1.

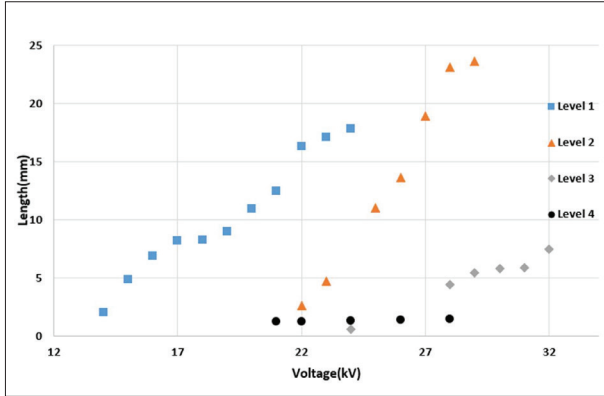


Figure 9: Variation of the final discharge length of the creeping discharges propagating over the solid samples versus the applied AC voltage for different oil levels.

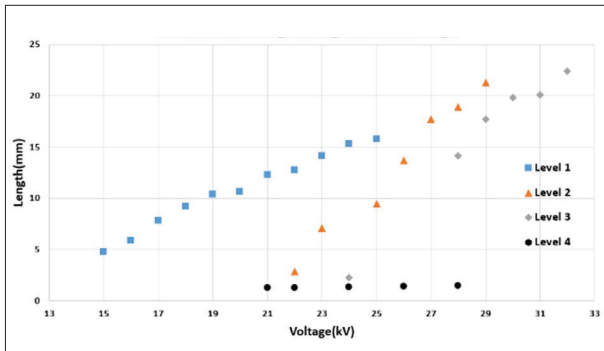


Figure 10: Variation of the radial discharge length of the creeping discharges propagating over the solid samples versus the applied AC voltage for different oil levels.

Table 3: Information of final discharge length curves

	Final discharge length with oil level			
	Level 1	Level 2	Level 3	Level 4
Slope	1.523	3.25	0.8098	0.033
R square value	0.9653	0.9825	0.9653	0.9717

Table 4: Information of radial discharge length curves

	Radial Discharge Length with oil level			
	Level 1	Level 2	Level 3	Level 4
Slope	1.1021	2.6196	2.5475	0.033
R square value	0.9856	0.9771	0.9679	0.9717

CONCLUSION

This paper presented a study of creeping discharge propagation over solid/coconut oil insulation interfaces. Experiments were carried out with a point plane electrode arrangement and a high-speed image recorder in order to investigate creeping discharges along surfaces of glass and acrylic samples immersed in coconut oil with varying oil levels under an AC divergent field. Pattern propagating on the glass surface can be more characterized by luminous, ramified streamers. Glass and acrylic material samples do not have a significant effect on the discharge length when they are immersed in coconut oil even though the breakdown voltage of acrylic is higher than that of glass by 28%. The study has shown that the final discharge length and radial discharge length increase quasi-linearly with the applied voltage even on materials immersed in coconut oil. It has been observed that size, brightness, and discharge length reduce as the oil level increases. The rate of change of the discharge length with the applied voltage decreases when the oil height over the solid dielectric increases. Electrodynamic motion has been shown to be a key factor in deciding the characteristics of discharge propagation along with the tangential electric field. Decrease in oil level due to the electric field generated electrodynamic motion can create an opposing force on the discharge propagation, reducing the possibility of flashover as the discharges try to follow the contours created by the oil. However, discharges can get initiated at low voltage values with low oil levels. In industrial applications, the insulation systems are normally subjected to high stress levels. Thus, it can be concluded that the volume or the height of oil inside coconut oil filled high voltage equipment should be maintained to minimize the discharge initiation.

Conflict of interest

The authors declare that they have no known competing financial interests or personal relationships that could have appeared to influence the work reported in this paper.

REFERENCES

- Abeyundara D., Weerakoon C., Lucas R., Gunatunga K. & Obadage K. (2001). Coconut oil as an alternative to transformer oil. *Proceedings of the 7th Symposium (ERU) on Research for Industry*, November 2001, Moratuwa, Sri Lanka, pp. A12–A22.
- Beroual A. & Boubakeur A. (1991). Influence of barriers on the lightning and switching impulse strength of mean air gaps in point/plane arrangements. *IEEE Transactions on Electrical Insulation* **26**(6): 1130–1139.
DOI: <https://doi.org/10.1109/14.108150>
- Beroual A., Coulibaly M., Aitken O. & Girodet A. (2011). Investigation on creeping discharges propagating over epoxy resin and glass insulators in the presence of different gases and mixtures. *The European Physical Journal - Applied Physics* **56**(3): 30802.
DOI: <https://doi.org/10.1051/ep-jap/2011110122>
- Beroual A. & Kebbabi L. (2008). Influence of hydrostatic pressure on morphology and final length of creeping discharges over solid/liquid interfaces under impulse voltages. *Proceedings of the 2008 IEEE International Conference on Dielectric Liquids*, 30 June - 03 July, Chasseneuil, France, pp. 1–4.
DOI: <https://doi.org/10.1109/ICDL.2008.4622472>
- Beroual A. & Khaled U. (2018). Influence of hydrostatic pressure on creeping discharge characteristics over solid/liquid insulating interfaces under ac and dc voltages. *IET Generation, Transmission and Distribution* **12**(2): 267–271.
DOI: <https://doi.org/10.1049/iet-gtd.2017.0622>
- Dang V.-H., Beroual A., Coulibaly M.-L. & Perrier C. (2012). Investigation on creeping discharges propagating over pressboard immersed in mineral and vegetable oils submitted to AC and DC voltages. *Proceedings of the 2012 International Conference on High Voltage Engineering and Application*, 17-20 September. Shanghai, China, pp. 215–218.
DOI: <https://doi.org/10.1109/ICHVE.2012.6357024>
- Douar M.A., Beroual A. & Souche X. (2015). Propagation of creeping discharges in air depending on the electric field direction and insulator materials under lightning impulse voltage. *Proceedings of the 2015 IEEE Conference on Electrical Insulation and Dielectric Phenomena (CEIDP)*, 18–21, October 2015. Ann Arbor, USA, pp. 880–883.
DOI: <https://doi.org/10.1109/CEIDP.2015.7352036>
- Ediriweera S., Jayarathna P., Lucas R. & Samarasinghe R. (2019). Fractal analysis of creeping discharges propagating over solid/liquid interfaces-influence of oil level. *Proceedings of the 9th International Conference on Power and Energy Systems (ICPES)*, 10–12 December. Perth, Australia, pp. 1–6.
DOI: <https://doi.org/10.1109/ICPES47639.2019.9105611>
- Ediriweera S., Jayarathna P., Samarasinghe R. & Lucas R. (2020). Effect of the shape of the cross-section of the solid insulators immersed in coconut oil on the area and the dimension of creeping discharge propagation. *Proceedings of the 2020 IEEE International Conference on Power Systems Technology (POWERCON)*, 14-16 September. Bangalore, India, pp. 1–5.
DOI: <https://doi.org/10.1109/POWERCON48463.2020.9230573>
- Ediriweera W.E.P.S., Jayarathna K.L.I.M.P.B., Lucas J.R. & Samarasinghe R. (2018). Effect of the shape of the insulator on fractal characteristics of creeping discharges. *Proceedings of the 2018 Moratuwa Engineering Research Conference (MERCon)*, 30 May - 01 June. Moratuwa, Sri Lanka, pp. 506–510.
DOI: <https://doi.org/10.1109/MERCon.2018.8421974>
- FitzPatrick G.J., McKenny P.J. & Forster E.O. (1990). The effect of pressure on streamer inception and propagation in liquid hydrocarbons. *IEEE Transactions on Electrical Insulation* **25**(4): 672–682.
DOI: <https://doi.org/10.1109/14.570879>
- Gournay P. & Lesaint O. (1994). On the gaseous nature of positive filamentary streamers in hydrocarbon liquids. II: Propagation, growth, and collapse of gaseous filaments in pentane. *Journal of Physics D: Applied Physics* **27**(10): 2117.
- Karunarathna P., Chithradewa K., Kumara S., Weerasekara C., Sanarasinghe R. & Rathnayake T. (2019). Study on dielectric properties of epoxy resin nanocomposites. *Proceedings of the 2019 International Symposium on Advanced Electrical and Communication Technologies (ISAECT)*, 27–29 November. Rome, Italy, pp. 1–5.
DOI: <https://doi.org/10.1109/ISAECT47714.2019.9069694>
- Kebbabi L. & Beroual A. (2003). Influence of the properties of materials and the hydrostatic pressure on creepage discharge characteristics over solid/liquid interfaces. *Proceedings of the 2003 Annual Report Conference on Electrical Insulation and Dielectric Phenomena*, 19–22 October. Albuquerque, USA, pp. 293–296.
DOI: <https://doi.org/10.1109/CEIDP.2003.1254851>
- Kebbabi L. & Beroual A. (2006). Optical and electrical characterization of creeping discharges over solid/liquid interfaces under lightning impulse voltage. *IEEE Transactions on Dielectrics and Electrical Insulation* **13**(3): 565–571.
DOI: <https://doi.org/10.1109/TDEI.2006.1657969>
- Lesaint O., Kattan R. & Denat A. (1988). Generation and growth of gaseous bubbles in hydrocarbon liquids under high divergent field. *1988 Annual Report, Conference on Electrical Insulation and Dielectric Phenomena*, 16–20 October. Ottawa, Canada, pp. 269–274.
DOI: <https://doi.org/10.1109/CEIDP.1988.26344>
- Lucas R., Abeyundara D., Weerakoon C., Perera M., Obadage K. & Gunatunga K. (2002). Coconut oil insulated distribution transformer. *Proceedings of the Annual Conference of IEE Sri Lanka*, Colombo, Sri Lanka, pp. 1–5.
- Mandric V., Rupcic S., Srnovic M. & Benšic G. (2018). Measuring the dielectric constant of paper using a parallel plate capacitor. *International Journal of Electrical and*

- Computer Engineering Systems* **9**: 1–10.
DOI: <https://doi.org/10.32985/ijeces.9.1.1>
- Matharage B.S.H.M.S.Y., Fernando M.A.R.M., Bandara M.A.A.P., Jayantha G.A. & Kalpage C.S. (2013). Performance of coconut oil as an alternative transformer liquid insulation. *IEEE Transactions on Dielectrics and Electrical Insulation* **20** (3): 887–898.
DOI: <https://doi.org/10.1109/TDEI.2013.6518958>
- Sitorus H.B., Beroual A., Setiabudy R. & Bismo S. (2015). Creeping discharges over pressboard immersed in *Jatropha curcas* methyl ester and mineral oils. *Proceedings of the*

- IEEE 11th International Conference on The Properties and Applications of Dielectric Materials (ICPADM)*, 19–22 July 2015. Sydney, Australia, pp. 152–155.
DOI: <https://doi.org/10.1109/ICPADM.2015.7295231>
- Zhou X., Shi H., Kuhnke M., Werle P., Gockenbach E. & Borsi H. (2016). Evolution and discharge pattern of creeping discharge at aged oil/pressboard interface. *Proceedings of the 2016 IEEE Conference on Electrical Insulation and Dielectric Phenomena (CEIDP)*, 16–19 October, Toronto, Canada, pp. 1053–1056.
DOI: <https://doi.org/10.1109/CEIDP.2016.7785568>

RESEARCH ARTICLE

Environmental biotechnology

Poly-β-hydroxybutyrate (PHB) production potential of naturally existing cyanobacterial blooms

RS Wijerathne¹, PM Manage^{1,2} and FS Idroos^{1*}

¹ Center for Water Quality and Algae Research, Department of Zoology, Faculty of Applied Science, University of Sri Jayewardenepura, Sri Lanka.
² Faculty of Graduate Studies, University of Sri Jayewardenepura, Sri Lanka.

Submitted: 19 August 2021: Revised: 12 May 2022: Accepted: 27 May 2022

Abstract: Detrimental effects imposed by petrochemical plastics on the environment are among the most often discussed concerns in the current era. Although the scientific community has discovered numerous eco-friendly alternatives, the cost of manufacture has restricted the usage of such material. The present study focused on the direct utilization of naturally existing cyanobacterial blooms to extract biodegradable poly-β-hydroxybutyrate (PHB) aiming to minimize the cost of production by eliminating the need for growing of cyanobacterial monocultures. This attempt provides remedies for plastic pollution and hazardous cyanobacterial blooms simultaneously. Fresh cyanobacterial bloom samples were collected from the hypereutrophic Beira Lake, Colombo. They were maintained under *in vitro* conditions for 7 days, provided with a 12/12 hours light/dark cycle, and deprived of an external supply of nutrients. PHB production was optimized for Nitrogen, Phosphate, and Carbon sources: glucose, sucrose, and lactose. The extracted PHB was quantified by spectrophotometric analysis. Structure confirmation was carried out using FTIR and Raman spectroscopy. The mean percentage weight of PHB yield was $7.13 \pm 0.12\%$ w/w. Optimization studies showed that nitrate deficiency and the presence of glucose as an exogenous carbon source imposed a stimulatory effect for PHB accumulation by cyanobacteria. The maximum amount of PHB (9.6% w/w) was found to be accumulated by cyanobacteria on the fourth day following the bloom sample collection. Hence, the present study proposes a sustainable utilization method of cyanobacterial blooms as a promising source for PHB production.

Keywords: Beira Lake, biodegradable plastics, cyanobacteria, poly-β-hydroxybutyrate (PHB), polyhydroxyalkanoates (PHAs).

INTRODUCTION

In the modern era of technology, plastics have become some of the most widely used and indispensable materials worldwide. Plastics are incorporated with home appliances, components of automobiles, computer equipment, packaging, medical tools and devices, and many such essential items that are regularly used (Rahimi & Garcia, 2017). Due to their light weight, stability, durability, and economic feasibility, plastics have replaced wood, glass, and metal components in domestic and industrial applications. Conventional petrochemical plastics are the most extensively used and are generally inexpensive (Geyer *et al.*, 2017). Nonetheless, such synthetically produced polymers cause serious environmental problems due to their persistent nature (Chen & Patel, 2012; Mohammadi *et al.*, 2015).

These non-biodegradable plastics take a very long time to degenerate and therefore accumulate in the environment creating a large spectrum of environmental impacts (Welden, 2020) as well as animal and human health impacts (Halden *et al.*, 2010, Awuchi & Awuchi, 2019). Severe environmental concerns like safe disposal,

* Corresponding author (sumaiyaidroos@sci.sjp.ac.lk;  <https://orcid.org/0000-0003-4872-836X>)



This article is published under the Creative Commons CC-BY-ND License (<http://creativecommons.org/licenses/by-nd/4.0/>). This license permits use, distribution and reproduction, commercial and non-commercial, provided that the original work is properly cited and is not changed in anyway.

solid waste management, and plastic waste incineration justify the production of materials like green polymers, biodegradable plastics, or bioplastics utilizing renewable resources (Singh *et al.*, 2017).

Biodegradable plastics are a class of bioplastics produced from biobased materials and biodegradable into elemental and simple substances (Carpine *et al.*, 2015). PHAs are polymers that are entirely of microbial origin and are composed of various hydroxyalkanoic acids as their monomer units (Muhammadi *et al.*, 2015). PHA biopolymers are predominantly linear, head-to-tail thermoplastics with hydroxyalkanoic acid as monomer units. The carboxyl group of one monomeric unit forms an ester bond with the hydroxyl group of the adjacent monomeric unit. They are described by the common structural formula as shown in Figure 1. Each PHA monomeric unit possesses a side chain R group which can differ from a hydrogen to a methyl to a tridecyl group (Muhammadi *et al.*, 2015).

PHA bioplastics can be subdivided into three groups; short-chain-length-PHAs (SCL-PHAs), medium-chain-length-PHAs (MCL-PHAs), and long-chain length-PHA (LCL-PHAs). Among SCL-PHAs, polyhydroxybutyrate (PHB) is the most widespread in various bacterial and cyanobacterial species. The chemical structure of PHB is illustrated in Figure 2. PHB has gained the scientific community's interest due to its properties such as thermoplastic processability, hydrophobicity, complete biodegradability, biocompatibility, optical purity and piezoelectricity (Singh *et al.*, 2017).

Many microorganisms are known to produce PHB as an intracellular energy and carbon storage product (Ansari & Fatma, 2016; Troschl *et al.*, 2017). The biosynthesis of this type of polymers is limited to prokaryotic organisms and usually formed as intracellular inclusions under stressed growth conditions; that is, in the presence of an excess of a carbon source and a limited nutrient supply, particularly nitrate and phosphate (Balaji *et al.*, 2013; Muhammadi *et al.*, 2015). As a result of these unbalanced growth conditions, reduction equivalents created by metabolic oxidation processes are stored in a water-insoluble, chemically and osmotically inert form, which is PHB or any other kind of PHA (Chong *et al.*, 2021).

The worldwide progression of the PHB thermoplastic market is powered by its variety of uses in different arenas and the ever-increasing interest in eco-friendly alternatives. Commercial PHB production is based on the pure cultures of natural PHB producing heterotrophic bacteria: *Ralstonia eutropha*, *Alcaligenes* sp.,

Azotobacter sp., *Bacillus* sp., *Nocardia* sp., *Pseudomonas* sp. and *Rhizobium* sp. (Chandani *et al.*, 2014).

Successful and viable synthesis of PHB requires the optimal incorporation of technological innovations with economic feasibility for their commercial production and marketing. Therefore presently, to overcome such limitations, advanced and intensified research on the exploitation of photoautotrophic hosts (plant systems and cyanobacteria) is receiving much attention over the heterotrophic bacterial systems with an ultimate aim to produce cost-effective PHB (Sakthiselvan & Madhumathi, 2019).

Cyanobacterial production of PHA thermoplastics was described for the first time in a nitrogen fixing cyanobacterium, *Chlorogloea fritschii*, grown with acetate supplementation (Singh *et al.*, 2017). To date, the occurrence of PHB has been reported in many cyanobacterial species, including *Spirulina* sp., *Aphanothea* sp., *Microcystis* sp., *Nostoc* sp., and *Synechocystis* sp. (Balaji *et al.*, 2013). The main advantages of using cyanobacteria for the production of PHB instead of using conventional heterotrophic bacteria and plant sources are, (a) cyanobacteria do not compete for resources with the agro-food market; (b) the contribution of cyanobacteria for the carbon sequestration decreases the burden of the greenhouse gas released to the atmosphere; and (c) the nutrient requirement of cyanobacteria is minimal (Gopi *et al.*, 2014; Carpine *et al.*, 2015).

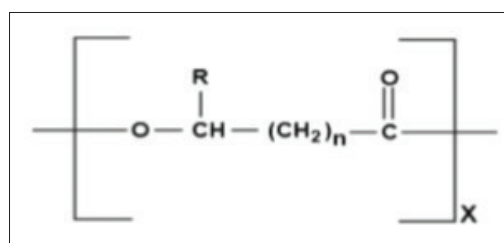


Figure 1: Structure of PHAs (Brandl *et al.*, 1990)

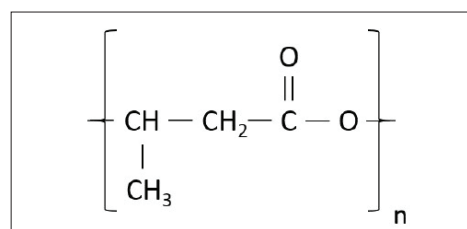


Figure 2: Structure of PHB

Although the cyanobacterial PHB has been the subject of research for many years, it has not reached the market (Kamravamanesh *et al.*, 2018). Cyanobacterial monocultures are yet an expensive alternative correlated to the low yield they provide compared to heterotrophic bacteria. Thus, the present study aimed to develop a method to extract PHB from naturally occurring cyanobacterial blooms, which will reduce the cost of culturing the microbes for PHB production and concurrently provides a novel use of problematic algal blooms.

In Sri Lanka, most of the eutrophicated freshwater bodies are conquered by the cyanobacterial genus *Microcystis*. Beira Lake is a hypereutrophic lake situated in Colombo city, where the cyanobacterial species *Microcystis aeruginosa* and *Spirulina* sp. are abundant throughout the year (Idroos & Manage, 2014). Both these genera have been recorded as PHB synthesizers in variable amounts (Balaji *et al.*, 2013; Ansari & Fatma, 2016). Thus, the Beira Lake was selected to collect cyanobacteria bloom samples for PHB extraction in the present study.

MATERIALS AND METHODS

Sample collection

Before collecting the bloom samples, the temperature, pH, and electrical conductivity (EC) of the surface water were recorded at the site (GPS location - 6°55'02" N 79°51'16" E). Approximately 15 litres of bloom samples were collected into plastic containers and transported to the laboratory. The concentrations of total phosphate and nitrate of the samples were determined using standard methods (Silva *et al.*, 1996).

Identification of cyanobacteria

The morphological features of colonies and solitary species in the sample were identified following the standard phytoplankton and cyanobacteria identification keys (Manage, 2012).

Microscopic visualization of PHB

PHB accumulated in cyanobacteria was visualized microscopically using the Sudan Black B staining method (0.3% Sudan Black B in 70% ethanol), following the heat fixed procedure (Wei *et al.*, 2011). The slides were immersed in xylene for 5-10 minutes for complete decolorization and then the smear was counterstained with safranin solution (0.5% in water) for 10 seconds followed by gentle rinsing with running tap water. The

slides were allowed to dry and then observed under oil immersion using a light microscope (at a magnification of 10×100), and the images were captured by Microscopic Image Projection System (MIPS).

Extraction of PHB

The cyanobacteria bloom samples were stored at room temperature for 7 days under laboratory conditions. Subsequently, the samples were freeze-dried and stored at 4°C. PHB was extracted using a modification of the method described by Yellore and Desai (1998). A weight of 100 mg of dry biomass was added into an Erlenmeyer flask with 100 mL of analytical grade methanol, followed by sonication for 15 minutes in ice, and stored overnight at 4°C to remove pigment (Ansari & Fatma, 2016). Subsequently, the samples were centrifuged at 8000 rpm for 20 minutes, and the resulting pellet was dried at 60°C for 20 minutes to complete the removal of methanol. The polymer was extracted by boiling with chloroform and precipitated with cold diethyl ether. The precipitate was separated by centrifuging at 9000 rpm for 30 minutes and the pellet obtained was washed with acetone and dissolved in hot chloroform, followed by evaporation at 4°C to obtain the crude extract of PHB.

Determination of the optimum day for yield of PHB

The biosynthesis and utilization of PHB are affected by the intensity of the nutrient stress. Therefore, bloom samples were maintained at a 12/12 light/dark cycle in the laboratory for 7 days without providing any nutrient supplements. Then the production of PHB was determined following the method described. Equal volumes (500 mL each) of bloom samples were stored in 7 similar glass jars, and 100 mL of sub-sample was collected and freeze-dried from one jar per day. PHB was extracted from known weights of dried biomass, and the yield was calculated each day.

Optimization of an exogenous carbon source

PHB production was optimized by changing carbon sources as given in (Table 1).

Nutrient optimization

Optimization was carried out to study the effect of nitrate and phosphate concentrations on PHB yield. The samples were provided with 1 mg/L and 2 mg/L of nitrate (potassium nitrate) and phosphate (anhydrous potassium phosphate), respectively, in excess of their initial concentrations recorded in the field. The samples were maintained in the laboratory for 3 days and the yields of PHB in each sample were quantified.

Table 1: Optimization for the exogenous carbon sources

Jar number	The volume of the algae sample (mL)	Supplement added	The volume of supplement added (mL)
1 (L)	800	Lactose (1g)	200
2 (S)	800	Sucrose (1g)	200
3 (G)	800	Glucose (1g)	200
4 (C)	800	Distilled water	200

Spectrophotometric analysis

Both qualitative and quantitative analyses were performed with Thermo Scientific GENESYS 10S Series UV-Vis spectrophotometer.

The conventional protocol for the determination of PHB is based on the conversion of PHB into crotonic acid (2-butenic acid) when heated in conc. H_2SO_4 and measuring its absorbance at 235 nm (Ansari & Fatma, 2016). Initially, the UV spectrum was obtained for crotonic acid derived from standard PHB, and the wavelength which gives the highest absorbance (λ_{max})

was confirmed. Then a standard curve was prepared using absorbance measurements for a series of known concentrations.

PHB extracted from 100 mg of dry microalgal biomass was taken into a boiling tube. Subsequently, 10 mL of conc. H_2SO_4 acid was added and heated at $100^\circ C$ for 20 minutes. The absorbance was measured at the λ_{max} obtained from the scanning spectrum of PHB. The PHB concentration of the sample was determined using the standard curve. The average weight percentage yield of PHB was calculated using the following equation.

$$\text{average weight \% yield of PHB} = \frac{\text{Mean weight of PHB extracted}}{\text{Weight of dry algal biomass}} \times 100$$

Raman spectroscopy analysis

Raman spectra were obtained for the standard PHB and the crude extract using a DXR2 Smart Raman instrument, and overview spectra were acquired in the range of $60\text{--}3300\text{ cm}^{-1}$.

Statistical analysis

All the tests were conducted in triplicate, and the calculations of statistical mean, standard deviation, standard error and pair-wise comparison of quantitative data were performed using MINITAB 14 software.

RESULTS AND DISCUSSION

Cyanobacterial blooms are a widespread nuisance, abundantly found in eutrophic surface waters worldwide. The mass development of planktonic cyanobacteria forming dense and occasionally toxic blooms in

freshwater, brackish, and marine environments threatens ecosystem functioning and human health by causing the water quality for recreation, drinking, and fisheries to deteriorate (Idroos *et al.*, 2017). The present study focused on directly utilizing existing cyanobacterial blooms to extract biodegradable PHB, simultaneously providing a considerable remedy to hazardous cyanobacterial blooms availability of other organisms such as heterotrophic bacteria, protozoans, and zooplankton as predators in the ambient environment.

Many species of cyanobacteria are known to perform both autotrophic and heterotrophic production of PHB under illuminated and non-illuminated conditions, respectively. Under non-illuminated environments, both *Microcystis* sp. and *Spirulina* sp. can utilize organic carbon sources available in the environment for their metabolism (Chen *et al.*, 1996). The bloom samples were provided with a 12/12-hour light/dark cycle in the present study. Since solar energy is unavailable during non-illuminated hours, it can be assumed that heterotrophic

production of PHB is carried out mostly within the dark 12 hours. Sharma and Mallick (2005) stated that dark periods are required for PHB accumulation in photoautotrophic cultures. A 12/12-hour light/dark cycle has been recognized as the optimum light condition for PHB production in cyanobacterial monocultures (Sharma & Mallick, 2005).

Identification of PHB producing cyanobacteria

Microscopic analysis of the collected bloom samples showed the presence of three species namely *Microcystis incerta*, *Microcystis aeruginosa*, and *Spirulina platensis*. Of these, *M. aeruginosa* was the most dominant and *Spirulina platensis* was observed occasionally.

Microscopic visualization of PHB

PHB is a lipid-like compound that accumulates in granules in the cytoplasm of cyanobacterial cells, which can be visualized under the light microscope by staining with Sudan black B. Sudan black B is a lipophilic stain that stains lipid-rich environments. Since cyanobacteria are visible under the light microscope, owing to the presence of pigments chlorophyll and phycobilin, counterstaining with Safranin is not mandatory. Intracellular vesicles containing PHB were visible in black colour after being stained with Sudan Black B. It was noticeable that the intracellular vesicles containing PHB in *Microcystis* spp. were more numerous on day three than on day one. PHB granules were not observed in *Spirulina* on day one.

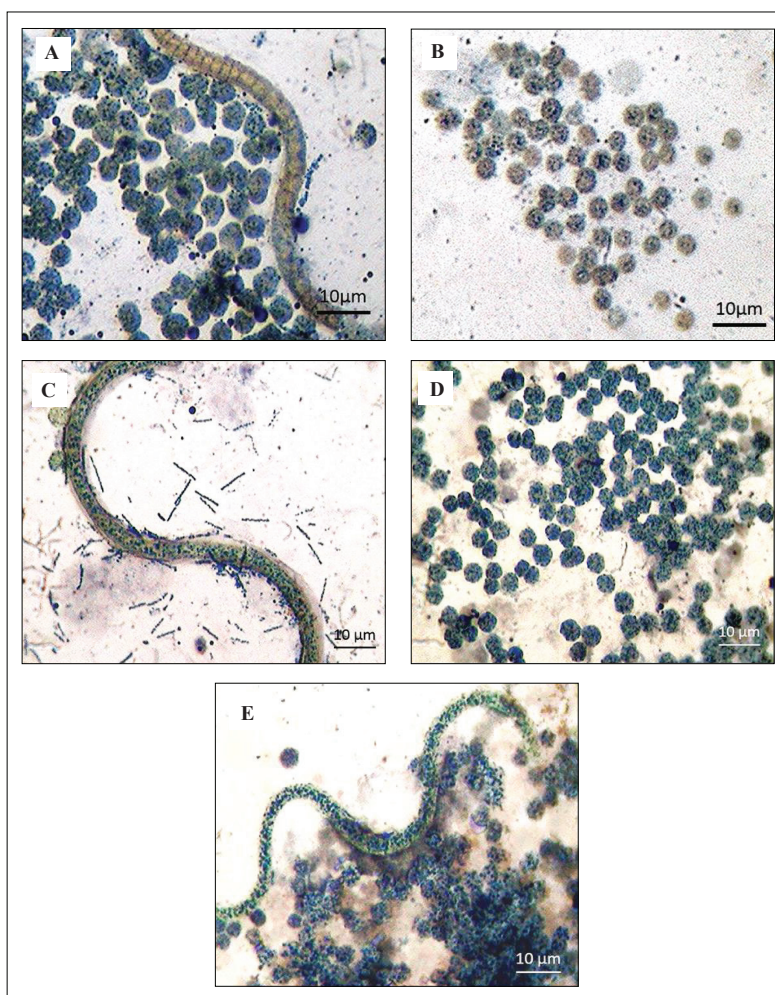


Figure 3: Visualization of PHB by Sudan black B staining. (a) *Spirulina* and *Microcystis* day 1, (b) *Microcystis* day 1, (c) *Spirulina* day 3, (d) *Microcystis* day 3, (e) *Spirulina* and *Microcystis* day 3 at the magnification of 10×100.

Microscopic visualization of bloom samples fixed and stained after one and three days of storing under *in vitro* conditions provides pictorial evidence that synthesis of PHB granules in *Microcystis* spp. commences earlier than in *Spirulina platensis* (Figure 3).

Extraction of PHB

The recovery of PHB requires rupturing of cyanobacterial cells and elimination of the protein layer that wraps PHB granules. Subsequently, PHB has to be selectively dissolved in a suitable solvent. Solvent extraction, used in the present study, was the most extensively adopted procedure to extract PHB from cellular biomass, due to its simplicity and efficiency (Kunasundari & Sudesh, 2011). This method also eliminates endotoxins, causes negligible polymer deterioration and provides high purity (Jacquel *et al.*, 2008). Despite the above advantages, the solvent extraction method is not suitable for large-scale recovery of PHB due to the consumption of large amounts of toxic and volatile solvents that pose threats to the environment. Hence, enzymatic digestion methods are well established as alternative recovery methods in the large scale recovery of PHB (Kunasundari & Sudesh, 2011). While solvent extraction methods involve solubilization of PHB, enzymatic digestion involves solubilization of cellular structures surrounding PHB.

Cyanobacterial biomass was pretreated with methanol to remove pigments and cyanotoxins before the extraction. Subsequently, methanol should be removed from the biomass by centrifuging followed by heating at 65°C for nearly 20-30 minutes since the presence of methanol inhibits solubilization of PHB in chloroform (Carpine *et al.*, 2015). Subsequently, PHB was extracted into hot chloroform and precipitated with diethyl ether. Precipitation of the polymer with diethyl ether and washing the precipitate with acetone assists in the removal of contaminating lipids (Sharma & Mallick, 2005). Chloroform was evaporated at a temperature of 4°C to obtain the final crude extract. This allows gradual precipitation of PHB, enabling crystallization. Evaporation of chloroform at the end of the organic extraction procedure resulted in an off-white coloured crude extract in amorphous form.

Determination of the optimum day for yield of PHB

Under laboratory conditions a continuous supply of nutrients was not provided for the microalgal samples. Henceforth, the growing cyanobacterial community consumes the available nutrients, thus causing progressive nutrient stress. The collected scum samples

were maintained in the laboratory for seven days, and the amount of PHB accumulated in the cyanobacteria was measured on each day. The mean PHB yield gradually increased up to day four. The maximum PHB yield, 9.6 % w/w of PHB, was obtained on the fourth day (Figure 4).

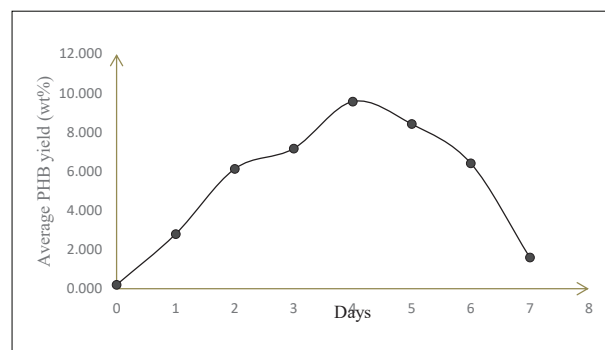


Figure 4: Variation of % yield of PHB yield along with the number of days of maintaining the samples under *in vitro* conditions

In related studies, the results obtained for the optimum day vary within a wide range. This aspect could depend on many variables including the initial concentration of nutrients, the species of cyanobacteria, cell density in the sample, availability of other organisms that consume the same nutrient sources, and bioavailability of nutrients in the solution.

A remarkable reduction in PHB yield was recorded after the 4th day of the sample maintenance. Hence, it could be suggested that produced PHB might be an alternative energy and carbon reserve for cyanobacteria. PHB might have been degraded to be utilized as an energy source to maintain cell viability. Moreover, studies done by Ansari and Fatma (2016) have further confirmed the uptake of accumulated PHB by cyanobacteria.

Optimization of an exogenous carbon source

Carbon dioxide is the major inorganic carbon source used for the synthesis of PHB by cyanobacteria (Wang *et al.*, 2013). However, they can also utilize various exogenous organic carbon sources for the heterotrophic accumulation of PHB under dark conditions simultaneously (Francisco *et al.*, 2014). In the present study, cyanobacteria bloom samples were provided with glucose, sucrose, and lactose as exogenous carbon sources at a similar concentration (1 g/L).

The percentage mean yields obtained for different carbon sources and the control showed a statistically significant difference ($p = 0$, One Way ANOVA). The

average PHB yield given by glucose supplementation was significantly higher than that of the control and other carbon sources (Table 2). Although the average PHB yield obtained from the bloom samples provided with sucrose and lactose expressed a higher and a lower value, respectively, than that of the control, the differences were not statistically significant. The samples supplemented with glucose resulted in the highest yield (11.585% w/w) of PHB.

Table 2: Yield of PHB for different exogenous carbon sources

Carbon source	Mean yield (% w/w)
Control*	7.1287 ^{BC}
Lactose	6.6263 ^C
Glucose	11.585 ^A
Sucrose	8.366 ^B

* No added carbon source. Means followed by the same superscript letter do not differ significantly (Tukey’s test)

According to Sharma and Mallick (2005) and Lee *et al.* (1995), higher intracellular concentrations of NADPH and higher ratios of NADPH/NADP stimulate biosynthesis of PHB since NADPH is a prerequisite for the activity of the enzyme acetoacetyl-CoA reductase involved in the PHB biosynthetic pathway. Glucose utilization in cyanobacteria takes place through the pentose phosphate pathway that produces the reduced cofactor NADPH (Lee *et al.*,1995). The enhanced accumulation of PHB in glucose-supplemented samples could be due to high amounts of NADPH generated in the glucose utilization pathway. A similar explanation could be valid for

sucrose-supplemented samples (Ansari & Fatma, 2016). The bloom samples supplemented with lactose showed a lower PHB yield compared to the control.

Optimization of nutrients

Nitrogen (as NO₃⁻) and phosphorus are the mandatory primary nutrients that are required for cyanobacterial growth and metabolism (Idroos & Manage, 2012; Gunasekara *et al.*, 2019). The initial nitrate and phosphate concentrations in the scum samples were 0.011 mg/L and 0.156 mg/L respectively. Nitrate optimization was performed by maintaining scum samples at 0.011 mg/L (initial), 1.011 mg/L, and 2.011 mg/L concentrations. For the optimization of phosphate concentration, samples were provided with 0.156 mg/L (initial), 1.156 mg/L and 2.156 mg/L phosphate concentrations.

The samples treated with three different concentrations of nitrates presented statistically significant differences in PHB yields (p = 0.002, One-way ANOVA). The highest average yield of 6.87% w/w was obtained from the cyanobacterial scum treated with the lowest concentration of nitrate. The yield diminishes with the increasing nitrate concentration in the medium. The PHB yields given by scum samples treated with different phosphate concentrations do not show a statistically significant difference (p = 0.088, One-way ANOVA) (Figure 5).

The limitation of nitrate appeared to be a suitable stimulant to enhance cyanobacterial PHB production. This corroborates with the findings of Carpine *et al.* (2015), where PHB production was enhanced under nitrogen starvation conditions of cyanobacterial monocultures.

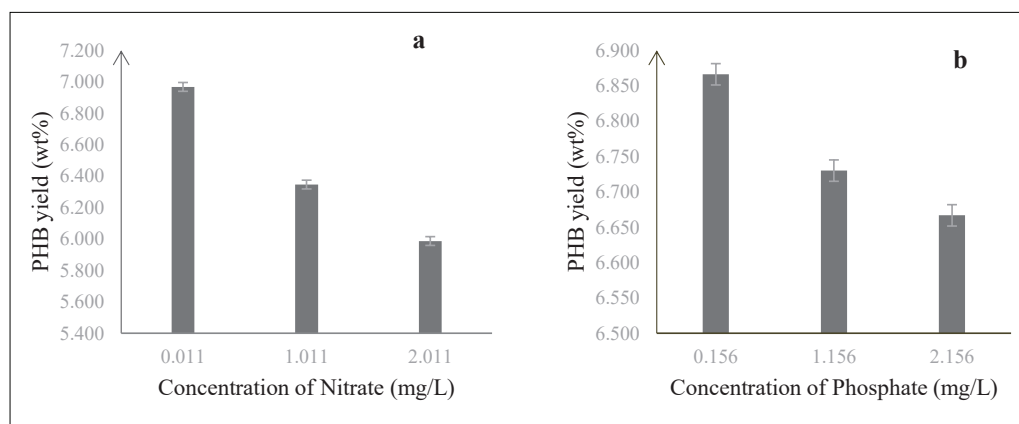


Figure 5: Yields of PHB as percentages in different concentrations of Nitrate (a) and Phosphate (b)

Spectrophotometric analysis

The quantification of PHB was performed by spectrophotometric analysis of acid digested PHB. Under acidic conditions together with high temperatures,

PHB is monomerized into crotonic acid (Panda *et al.*, 2008). The UV spectrum of the crotonic acid derived from the commercial standard PHB gave the maximum absorbance wavelength (λ_{\max}) as 235 nm, corresponding with the literature (Figure 6).

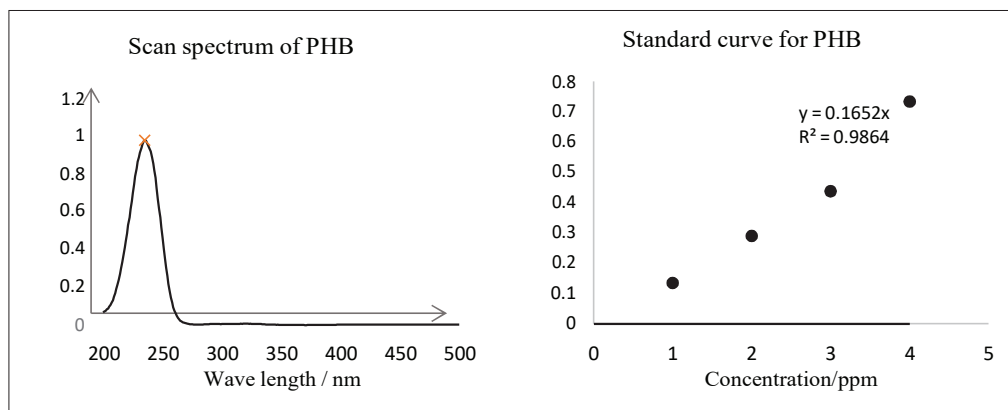


Figure 6: Scanned spectrum and the standard curve for commercial PHB

Raman spectroscopy

Raman spectroscopy has already been proven as a powerful tool for the characterization of PHB as it only requires small quantities of the sample and minimal sample preparation (Hermann *et al.*, 2020). Analyses of Raman spectra are precise and less time-consuming.

The Raman spectrum of crude PHB extract conspicuously showed the presence of peaks that are distinctively present in the spectrum of commercial standard PHB (Figure 7). The most prominent bands in the spectrum of standard PHB are located at 433 cm^{-1} , 839 cm^{-1} , and 1725 cm^{-1} and can be assigned to $\delta(\text{CC})$ skeletal deformations, $\nu(\text{CC})$ skeletal stretches and $\nu(\text{C}=\text{O})$ stretching vibrations respectively. The regions from 1040 cm^{-1} to 1140 cm^{-1} and from 1250 cm^{-1} to 1460 cm^{-1} show bands caused by $\nu(\text{CC})$ skeletal stretches and $\delta(\text{CH})$, $\delta(\text{CH}_2)$, and $\delta(\text{CH}_3)$ deformations, respectively (De Gelder *et al.*, 2008). When recording the spectrum of the crude sample, all Raman-active biomolecules contribute to the resulting range, and their signals overlap. The spectrum of the crude sample shows several Raman peaks provided by PHB (837, 1455, and 1736 cm^{-1}). Among them, the emission line at 1736 cm^{-1} can be considered as the most useful candidate because the vibrations of the other components of crude extract do not considerably interfere with this emission line.

The band positions of PHB in the spectrum may differ several wave numbers from the reference spectrum due to differences in crystallinity (De Gelder *et al.*, 2008). The dissimilar regions result from the superimposition of signals of PHB and Raman active contaminants.

Although accumulation of PHB in *Spirulina* monocultures has been studied extensively (Costa *et al.*, 2018; Da Silva *et al.*, 2018; Duangsri *et al.*, 2020), the kinetics of biosynthesis of PHB in *Microcystis* sp. has not been widely investigated. This could be due to the relatively low yield given by *Microcystis* sp. in comparison to other cyanobacterial genera such as *Synechocystis*, *Nostoc*, and *Spirulina*. This study is the first record of the potential utilization of *Microcystis* sp. dominated, naturally existing, cyanobacteria blooms for PHB extraction. Since *Microcystis* is one of the most widely prevalent cyanobacterial genera that occur as massive natural blooms in eutrophic waters, the present study has proposed a sustainable application of these blooms in PHB extraction.

Nevertheless, for low PHB yield, the results of the present study are promising with respect to the data reported in the literature. Therefore, the current study can be regarded as a preliminary effort to establish the concept of green innovation via the effective utilization of naturally occurring cyanobacterial blooms as a source for PHB extraction.

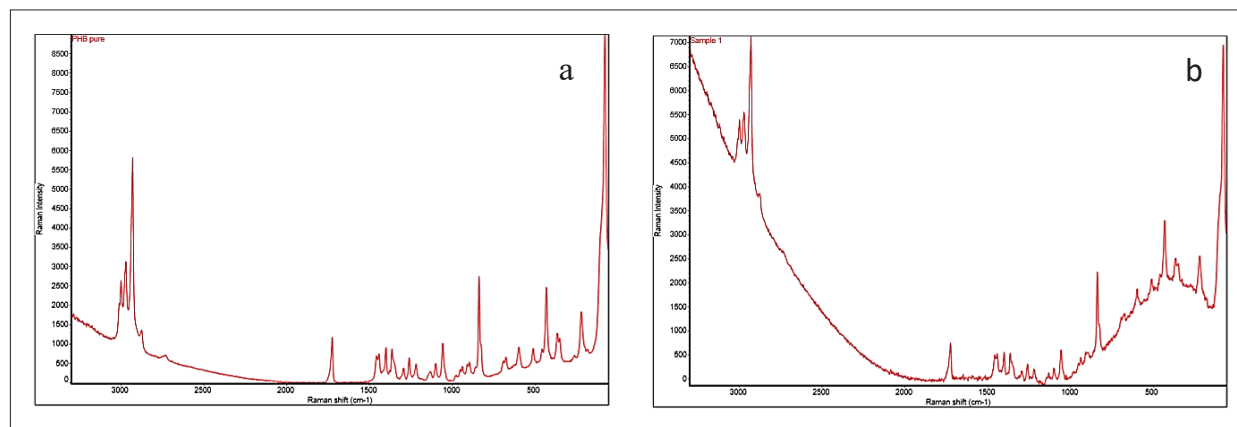


Figure 7: Raman spectrum for commercial standard PHB (a), and the crude extract (b)

CONCLUSION

Plastic pollution has struck the world's oceans and land environment. Hence, explorations on biodegradable plastics are in the limelight. PHB is an intracellular energy and carbon storage product. PHB thermoplastic has conquered the world market mainly due to its variety of uses in different arenas and the ever-increasing interest in eco-friendly alternatives, as a biodegradable plastic material. The current study concludes that naturally occurring cyanobacterial blooms carry a considerable potential to accumulate PHB. The PHB yield can be enhanced by supplementing the bloom sample with exogenous organic carbon sources, mainly glucose. Low nitrate concentration has a significant effect on improving the PHB yield. The mean percentage weight of PHB yield was 7.13 ± 0.12 % w/w. Optimization studies showed that nitrate deficiency and the presence of glucose as an exogenous carbon source imposed a stimulatory effect for PHB accumulation by cyanobacteria. The maximum amount of PHB (9.6% w/w) was found to be accumulated by cyanobacteria on the fourth day following the bloom sample collection. Hence, *in vitro* maintained cyanobacterial blooms could be used as a promising candidate to extract high concentrations of PHBs.

Acknowledgement

The authors would like to thank the Instrument Centre of the Faculty of Applied Sciences, University of Sri Jayewardenepura, for providing instrument facilities. Further, we are grateful to the Centre for Water Quality and Algae Research of the University of Sri Jayewardenepura.

REFERENCES

- Ansari S. & Fatma T. (2016). Cyanobacterial polyhydroxybutyrate (PHB): screening, optimization and characterization. *PLoS One* **11**(6): 526–546.
DOI: <https://doi.org/10.1371/journal.pone.0158168>
- Awuchi C.G. & Awuchi C.G. (2019). Impacts of plastic pollution on the sustainability of seafood value chain and human health. *International Journal of Advanced Academic Research* **5**(11): 46–138.
- Balaji S., Gopi K. & Muthuvelan B. (2013). A review on production of poly β hydroxybutyrates from cyanobacteria for the production of bio plastics. *Algal Research* **2**(3): 278–285.
DOI : <https://doi.org/10.1016/j.algal.2013.03.002>
- Brandl H., Gross R.A., Lenz R.W. & Fuller R.C. (1990). Plastics from bacteria and for bacteria: poly (β -hydroxyalkanoates) as natural, biocompatible, and biodegradable polyesters. *Microbial Bioproducts* **21**(2): 77–93.
DOI: <https://doi.org/10.1007/BFb0010232>
- Carpine R., Olivieri G., Hellingwerf K., Pollio A. & Marzocchella A. (2015). The cyanobacterial route to produce poly- β -hydroxybutyrate. *Chemical Engineering Transactions* **43**: 289–294.
- Chandani N., Mazumder P.B. & Bhattacharjee A. (2014). Production of polyhydroxybutyrate (biopolymer) by *Bacillus tequilensis* NCS-3 isolated from municipal waste areas of Silchar, Assam. *International Journal of Sciences* **3**(12): 198–203.
- Chen F., Zhang Y. & Guo S. (1996). Growth and phycocyanin formation of *Spirulina platensis* in photoheterotrophic culture. *Biotechnology Letters* **18**(5): 603–608.
DOI: <https://doi.org/10.1007/BF00140211>
- Chen G.Q. & Patel M.K. (2012). Plastics derived from biological sources: present and future: a technical and environmental review. *Chemical Reviews* **112**(4): 2082–2099.
DOI: <https://doi.org/10.1021/cr200162d>

- Chong J.W.R., Tan X., Khoo K.X., Ng H.S., Jonglertunya W., Yew G.Y. & Show P.L. (2021). Microalgae-based bioplastics: Future solution towards mitigation of plastic wastes. *Environmental Research* **206**:112620
DOI: <https://doi.org/10.1016/j.envres.2021.112620>
- Costa J.A.V., Moreira J.B., Lucas B.F., Braga V.D.S., Cassuriaga A.P.A. & Morais M.G.D. (2018). Recent advances and future perspectives of PHB production by cyanobacteria. *Industrial Biotechnology* **14**(5): 249–256.
DOI: <https://doi.org/10.1089/ind.2018.0017>
- Da Silva C.K., Costa J.A.V. & de Morais M.G. (2018). Polyhydroxybutyrate (PHB) synthesis by *Spirulina* sp. LEB 18 using biopolymer extraction waste. *Applied Biochemistry and Biotechnology* **185**(3): 822–833.
DOI: <https://doi.org/10.1007/s12010-017-2687-x>
- De Gelder J., Willems-Erix D., Scholtes M.J., Sanchez J.I., Maquelin K., Vandenaabeele P., De Boever P., Puppels G.J., Moens L. & De Vos P. (2008). Monitoring poly (3-hydroxybutyrate) production in *Cupriavidus necator* DSM 428 (H16) with Raman spectroscopy. *Analytical Chemistry* **80**(6): 2155–2160.
DOI: <https://doi.org/10.1021/ac702185d>
- Duang斯里 C., Mudtham N.A., Incharoensakdi A. & Raksajit W. (2020). Enhanced polyhydroxybutyrate (PHB) accumulation in heterotrophically grown *Arthrospira platensis* under nitrogen deprivation. *Journal of Applied Phycology* **32**(6): 3645–3654.
DOI: <https://doi.org/10.1007/s10811-020-02272-4>
- Francisco É.C., Franco T.T., Wagner R. & Jacob-Lopes E. (2014). Assessment of different carbohydrates as exogenous carbon source in cultivation of cyanobacteria. *Bioprocess and Biosystems Engineering* **37**(8): 1497–1505.
DOI: <https://doi.org/10.1007/s00449-013-1121-1>
- Getachew A. & Woldesenbet F. (2016). Production of biodegradable plastic by polyhydroxybutyrate (PHB) accumulating bacteria using low cost agricultural waste material. *BMC Research Note* **9**(1): 1–9.
DOI: <https://doi.org/10.1186/s13104-016-2321-y>
- Geyer R., Jambeck J.R. & Law K.L. (2017). Production, use, and fate of all plastics ever made. *Science Advances* **3**(7): 17–34.
DOI: <https://doi.org/10.1126/sciadv.1700782>
- Gopi K., Balaji S. & Muthuvelan B. (2014). Isolation purification and screening of biodegradable polymer PHB producing cyanobacteria from marine and fresh water resources. *Iranian Journal of Energy and Environment* **5**(9): 94–100.
DOI: <https://doi.org/10.5829/idosi.ijee.2014.05.01.14>
- Gunasekara N.D., Idroos F.S. & Pathmalal M.M. (2019). Microbial degradation of nitrate: put microbes to work. *Environment and Natural Resources Journal* **17**(2): 30–40.
DOI: <https://doi.org/10.32526/enrj.17.2.2019.10>
- Halden R.U. (2010). Plastics and health risks. *Annual Review of Public Health* **31**: 179–194.
DOI: <https://doi.org/10.1146/annurev.publhealth.012809.103714>
- Hermann D.R., Lilek D., Daffert C., Fritz I., Weinberger S., Rumpler V., Herbinger B. & Prohaska K. (2020). *In situ* based surface-enhanced Raman spectroscopy (SERS) for the fast and reproducible identification of PHB producers in cyanobacterial cultures. *Analyst* **145**(15): 5242–5251.
DOI: <https://doi.org/10.1039/D0AN00969E>
- Idroos F.S. & Manage P.M. (2012). Aquatic life health quality assessment of the Bolgoda canal and Waga stream with respect to selected physico-chemical parameters and bioindicators. *Journal of Tropical Forestry and Environment* **2**(2): 13–26.
DOI: <https://doi.org/10.31357/jtfe.v2i2.590>
- Idroos F.S., De Silva B. & Manage P.M. (2017). Biodegradation of microcystin analogues by *Stenotrophomonas maltophilia* isolated from Beira Lake Sri Lanka. *Journal of the National Science Foundation of Sri Lanka* **45** (2): 91.
DOI: <https://doi.org/10.4038/jnsfsr.v45i2.8175>
- Idroos S.F. & Manage P.M. (2014). Seasonal occurrence of Microcystin-LR with respect to physico-chemical aspects of Beira lake water. *International Journal of Multidisciplinary Studies* **1**(2): 27–37.
DOI: <https://doi.org/10.4038/ijms.v1i2.49>
- Jacquel N., Lo C.W., Wei Y.H., Wu H.S. & Wang S.S. (2008). Isolation and purification of bacterial poly (3-hydroxyalkanoates). *Biochemical Engineering Journal* **39**(1): 15–27.
DOI: <https://doi.org/10.1016/j.bej.2007.11.029>
- Kamravamanesh D., Lackner M. & Herwig C. (2018). Bioprocess engineering aspects of sustainable polyhydroxyalkanoate production in cyanobacteria. *Bioengineering* **5**(4): 111.
DOI: <https://doi.org/10.3390/bioengineering5040111>
- Kumalaningsih S., Hidayat N. & Aini N. (2011). Optimization of polyhydroxyalkanoates (PHA) production from liquid bean curd waste by *Alcaligenes latus* bacteria. *Journal of Agriculture and Food Technology* **1**(6): 63–67.
- Kunasundari B. & Sudesh K. (2011). Isolation and recovery of microbial polyhydroxyalkanoates. *Express Polymer Letters* **5**(7): 620–634
DOI: <https://doi.org/10.3144/expresspolymlett.2011.60>
- Lee I.Y., Kim M.K., Chang H.N. & Park Y.H. (1995). Regulation of poly-β-hydroxybutyrate biosynthesis by nicotinamide nucleotide in *Alcaligenes eutrophus*. *FEMS Microbiology Letters* **131**(1): 35–39.
DOI: [https://doi.org/10.1016/0378-1097\(95\)00231-S](https://doi.org/10.1016/0378-1097(95)00231-S)
- Manage P.M. (2012). *Training Modules and Guide for Field and Laboratory Studies of Cyanobacteria and Cytotoxins*
- Muhammadi S., Afzal M. & Hameed S. (2015). Bacterial polyhydroxyalkanoates-eco-friendly next generation plastic: production, biocompatibility, biodegradation, physical properties and applications. *Green Chemistry Letters and Reviews* **8**(3-4): 56–77.
DOI: <https://doi.org/10.1080/17518253.2015.1109715>
- Panda B., Sharma L., Singh A.K. & Mallick N. (2008). Thin layer chromatographic detection of poly-β-hydroxybutyrate (PHB) and poly-β-hydroxyvalerate (PHV) in cyanobacteria. *Indian Journal of Biotechnology* **7**(2): 230–234.

- Rahimi A. & García J.M. (2017). Chemical recycling of waste plastics for new materials production. *Nature Reviews Chemistry* **1**(6): 1–11.
DOI: <https://doi.org/10.1038/s41570-017-0046>
- Sakthiselvan P. & Madhumathi R. (2019). Optimization on microbial production of polyhydroxybutyrate (PHB): a review. *International Journal of Research and Analytical Reviews* **6**(1): 243–251.
- Sharma L. & Mallick N. (2005). Accumulation of poly- β -hydroxybutyrate in *Nostoc muscorum*: regulation by pH, light-dark cycles, N and P status and carbon sources. *Bioresource Technology* **96**(11): 1304–1310.
DOI: <https://doi.org/10.1016/j.biortech.2004.10.009>
- Silva E.I.L., Namarathne S.Y., Weerasooriya S.V.R. & Munaweera L. (1996). *Water Analysis User Friendly Field /Laboratory Manual*. AJ prints , Dehiwala, Sri lanaka.
- Singh A.K., Sharma L., Mallick N. & Mala J. (2017). Progress and challenges in producing polyhydroxyalkanoate biopolymers from cyanobacteria. *Journal of Applied Phycology* **29**(3): 1213–1232.
DOI: <https://doi.org/10.1007/s10811-016-1006-1>
- Solaiman D.K., Ashby R.D. & Foglia T.A. (2000). Rapid and specific identification of medium-chain-length polyhydroxyalkanoate synthase gene by polymerase chain reaction. *Applied Microbiology and Biotechnology* **53**(6): 690–694.
DOI: <https://doi.org/10.1007/s002530000332>
- Troschl C., Meixner K. & Drosig B. (2017). Cyanobacterial PHA production-Review of recent advances and a summary of three years' working experience running a pilot plant. *Bioengineering* **4**(2): 26.
DOI: <https://doi.org/10.3390/bioengineering4020026>
- Wang B., Pugh S., Nielsen D.R., Zhang W. & Meldrum D.R. (2013). Engineering cyanobacteria for photosynthetic production of 3-hydroxybutyrate directly from CO₂. *Metabolic Engineering* **16**: 68–77.
DOI: <https://doi.org/10.1016/j.ymben.2013.01.001>
- Wei Y.H., Chen W.C., Huang C.K., Wu H.S., Sun Y.M., Lo C.W. & Janarthanan O.M. (2011). Screening and evaluation of polyhydroxybutyrate-producing strains from indigenous isolate *Cupriavidus taiwanensis* strains. *International Journal of Molecular Sciences* **12**(1): 252–265.
DOI: <https://doi.org/10.3390/ijms12010252>
- Welden N.A. (2020). The environmental impacts of plastic pollution. In: *Plastic Waste and Recycling*, pp 195–222. Academic Press, USA.
DOI: <https://doi.org/10.1016/B978-0-12-817880-5.00008-6>
- Yellore V. & Desai A. (1998). Production of poly-3-hydroxybutyrate from lactose and whey by *Methylobacterium* sp. ZP24. *Letters in Applied Microbiology* **26**(6): 391–394.
DOI: <https://doi.org/10.1046/j.1472-765X.1998.00362.x>

RESEARCH ARTICLE

Poultry science

Influence of different bone meal particle size induced calcium specific appetite on performance and egg quality parameters of layer chickens[†]

TS Gamage¹, RK Mutucumarana^{1*} and MS Andrew²

¹ Department of Livestock Production, Faculty of Agricultural Sciences, Sabaragamuwa University of Sri Lanka, P.O. Box 02, Belihuloya, Sri Lanka.

² Maxies and Company (Pvt.) Ltd., Wennappuwa, Sri Lanka.

Submitted: 23 August 2021; Revised: 01 April 2022; Accepted: 05 April 2022

Abstract: The effects of free choice feeding of bone meal (BM) of different particle sizes on performance and egg quality traits of layer chickens were assessed. A total of 128 Hy-line White layers (56 wks old, BW \pm SD: 1500 \pm 18 g) were assigned randomly into 16 cages of 8 birds each. Four dietary treatments based on BM particle sizes (Layer Diet/Control; Layer diet + 1–2 mm BM; Layer diet + 2–3 mm BM; Layer diet + 3–4 mm BM) were choice fed for five weeks. Dry matter (DM), calcium (Ca), total phosphorus (TP), ash content, particle size distribution and *in vitro* solubility of BM were tested. The birds' performance and external and internal egg quality traits were examined over a 5 wk period. The DM, Ca, TP and ash content of BM were 893, 79, 44 and 476 g/kg, respectively. The geometric mean diameter (GMD) and the geometric standard deviation (GSD) of BM were 1.7 and 1.6 mm, respectively. *In vitro* solubility of 1–2 mm, 2–3 mm and 3–4 mm BM particles were 56.3, 47.5 and 39.8%, respectively. Bone meal, when choice fed, increased BM intake, Ca intake, and laying percentage, and reduced damaged egg percentage. Birds fed with BM having 2–3 mm particles performed best in improving the performance and egg quality. Bone meal significantly ($p < 0.05$) improved the egg shell thickness with maximum thickness recorded from birds fed with BM of 2–3 mm particle size. BM with 2–3 and 3–4 mm particles improved ($p < 0.05$) shell ratio and unit surface shell weight. The present study concluded that feeding with BM with 2–3 mm particle size is the best to improve the overall performance and egg quality traits of layer chickens.

Keywords: Bone meal, calcium, egg shell, egg quality, free choice, particle size.

INTRODUCTION

Calcium (Ca) is the most copious mineral in an animal's body. In poultry, Ca serves as the major element of skeletal structure. Its role in the regulation of acid-base balance and blood clotting is also well known (McDonald *et al.*, 2002). Ca is the major mineral of the egg shell. A chicken egg has 2.2 g of Ca, that exists mainly in the form of CaCO₃ in its eggshell (Pelicia *et al.*, 2009).

The recommended Ca intake of white egg layers is 3.25 g/hen/day (NRC, 1994). However, many researchers have shown that the daily Ca intake in layer chickens should be above this recommended value (Zhang *et al.*, 2017). The dietary recommendation of Ca for Hy-line layers ranges between 4.00 and 4.65 g per hen per day (Hy-line, 2016) or 4.0–4.6% of the total feed volume (Bradbury *et al.*, 2014; Wilkinson *et al.*, 2014b). Layers have high demand for Ca, especially during peak egg production period (Saunders-Blades *et al.*, 2009). This high demand for Ca is largely met by the use of Ca supplements or grits in layer diets. Commercially available layer rations are mostly formulated to contain

* Corresponding author (ruvinim@agri.sab.ac.lk;  <https://orcid.org/0000-0002-4860-8205>)

[†] Presented in part in Abstracts of 7th International Conference of Sabaragamuwa University of Sri Lanka, Sabaragamuwa University of Sri Lanka, Belihuloya, Sri Lanka, 14–15 November 2019.



grains and their by-products, which have very low Ca content (Peixoto & Rutz, 1988), and the most of the layer rations available in the local market do not contain the recommended dietary Ca levels of 4.0-4.6%. Therefore the use of an external Ca source is recommended to avoid serious shell quality issues. It has been estimated that about 6–8% of the total eggs laid worldwide are either cracked or broken before reaching the hands of consumers (Englmaierová *et al.*, 2017). However, with the resulting profit loss and health risks associated with cracked shells, eggshell quality remains one of the major concerns of the global poultry industry.

In the commercial poultry industry, supplementation of layer feed with external Ca sources is related in a straightforward manner to the grit feeding practices. Feed manufacturers have used oysters shell as a source of Ca for more than 100 years (Roland & Bryant, 1999; Saunders-Blades *et al.*, 2009). However, limestone has become the major supplemental Ca source used in layer rations due to its abundance, low price and easy application (Çath *et al.*, 2012). Oyster shells and limestone provide Ca in the form of CaCO₃, and each contains about 38% Ca (Saunders-Blades *et al.*, 2009). Bone meal (BM) is an excellent dietary source of Ca and phosphorus (P) (Orban & Roland, 1992). Bone meal contains considerable levels of Ca ranging from 354 to 362 g/kg, depending on the species used (Orban & Roland, 1992). Studies that investigated the potential of BM as a Ca supplement to feed free choice in commercial layers are highly limited and the study by Rathnayaka *et al.* (2020) concluded that use of BM when choice fed, improves the shell thickness in layers, compared to those who were fed oyster shells and lime stone.

The best particle size of Ca supplements for layer chickens has been a controversial topic for almost a century (Saki *et al.*, 2019). The particle size of Ca sources used in rations may have an influence on its availability to the laying hens. According to Zhang and Coon (1997), large limestone particle sizes (> 0.8 mm) with low *in vitro* solubilities (30–50%), were retained for a prolonged time in the gizzard, increasing *in vivo* solubility to higher than 94%. Eggshell is known to be synthesized during the night, when layers are off feed. Therefore, using larger particle sizes slows passage through the gastrointestinal tract (Tunç & Cufadar, 2015). This allows dietary Ca to be available for eggshell formation, with lower mobilization of bone Ca by the layer chickens (Saki *et al.*, 2019). A number of research projects have been conducted to assess the effect of limestone, oyster shells, and egg shells as sources of Ca in layer diets and the effect of their particle sizes on egg

shell quality (Saunders-Blades *et al.*, 2009; Olgun *et al.*, 2015; Tunç & Cufadar, 2015). However, no literature is available on the optimal particle size of BM to improve the egg shell quality parameters of layers.

As for other nutrients like lysine, methionine and selenium, poultry exhibit a special appetite for Ca (Wilkinson *et al.*, 2014a). The existence of a special appetite in broilers (Wilkinson *et al.*, 2013; 2014a) and layers (Bradbury *et al.*, 2014) for Ca has been therefore widely tested by much research. This research used limestone as the primary Ca source. Therefore, the objective of the present study was to investigate the effect of free choice feeding of three different BM particle sizes on improving performance and egg quality characters of layer chickens.

MATERIALS AND METHODS

The experiment was reviewed and approved (ERC/A/04/2019/03) by the Institutional Animal Care and Use Committee of Animal and Research Ethics, Sabaragamuwa University of Sri Lanka. All birds were reared and cared for under the guidelines of the Hy-line layer management guide (Hy-line, 2016)

Experimental site

The study was conducted for a period of 5 weeks in a large-scale commercial layer farm in the Wennappuwa region (geographical coordinates: 7° 20' 48" N, 79° 50' 12" E), located in the North Western Province of Sri Lanka.

Birds

Fifty-six weeks old Hy-line white layers were individually weighed (1500 ± 18 g), and a total of 128 birds with uniform weight were assigned to 16 cages of 8 birds each so that the weight variation among cages was minimum. Each of four dietary treatments was randomly assigned to 4 cages. Each bird was provided 550 cm² cage space. The cages were housed in an environmentally controlled room (21 ± 1°C) and a 20L:4D lighting schedule was provided. According to the Hy-line Management Guide (Hy-line, 2016), the layer feed (except the Ca supplements) was provided and water was available all the time.

Processing bone meal

Broiler thigh bones were separated and boiled to remove the meat parts. Bones were washed and were sterilized at 120°C for one hour using an autoclave (VARIO

3028, Dixons Surgical Instruments Ltd, Wickford, UK). Sterilized bones were oven dried (180°C) for 3 h. On completion of drying, the bones were ground into small pieces.

Particle size distribution of bone meal samples

Representative BM samples were tested in duplicates to determine the particle size distribution. A set of sieves sized 1.00, 2.00, 3.00, 4.00 mm and the particles were separated into different fractions through shaking for 10 min. The amounts of particles retained on each sieve was weighed and the Geometric Mean Diameter (GMD) and Geometric Standard Deviation (GSD) were calculated (Baker & Herman, 2002). The calculations were based on the assumption that the weight distributions of the BM samples were logarithmically normal (Martin, 1985).

$$d_i = (d_u \times d_0)^{1/2} \quad \dots(1)$$

$$\text{GMD} = \log^{-1} [\sum (W_i \log d_i) / \sum W_i] \quad \dots(2)$$

$$\text{GSD} = \log^{-1} [\sum W_i (\log d_i - \log \text{GMD})^2 / \sum W_i]^{1/2} \quad \dots(3)$$

where,

d_i = Geometric mean diameter of particles on i^{th} sieve in the sieve stack,

d_u = Diameter of sieve openings of the i^{th} sieve,

d_0 = Diameter of openings in next larger i^{th} sieve in set,

W_i = Weight fraction on i^{th} sieve in the stack.

Dietary treatments

A commercially available formulated layer feed was used as the basal diet. Bone meal having three different particle size ranges (*i.e.*, 1–2 mm, 2–3 mm and 3–4 mm particle sizes) were used as the test ingredients. Thigh bones from a commercial meat processing plant were processed into BM. Bone meal was separated into three fractions and the particles retained on 1.00, 2.00 and 3.00 mm sieves set was considered as the test ingredients. Bone meal separated based on three particle size ranges was introduced to its respective treatment in separate feeders, and offered *ad libitum* in accordance with the classical choice feeding method. The treatment fed only the layer feed with no supplemental BM served as the control.

Chemical analysis

The layer diet was analyzed in duplicate for its proximate composition (AOAC International, 2005). Bone meal

was analysed in duplicates for moisture and ash contents (AOAC International, 2005). Dry matter (DM) contents of the layer diet and BM were analyzed by drying samples at 105°C overnight in a pre-weighed dried crucible in a convection oven (Model No: YCO – 010, Gemmy Industrial Corp, Taipei, Taiwan). Ash content in the layer diet and BM was determined by igniting the sample in a muffle furnace (FH- 12, Daihan Scientific Co. Ltd, Gangwon-do, Korea.) at 600 °C for 6 hours. Nitrogen was determined by the Kjeldahl method. Ether extract (EE) was determined by Soxhlet extraction. Calcium in layer diet and BM were determined by Inductively Coupled Plasma Mass Spectroscopy (Agilent ICP-MS 7900, Agilent, USA) following to microwave digestion with undiluted nitric acid (Fleischer *et al.*, 2014). Total P in layer diet and BM were determined colorimetrically (UV-Vis-1900 Shimadzu Corp., Kyoto, Japan) (AOAC International, 2005). The gross energy (GE) content of feed samples was measured using bomb calorimetry (Model No: IKA C 200, IKA Werke GmbH & Co. KG, Staufen, Germany). Three different particle sizes of BM were analysed in duplicate for their *in vitro* solubility by weight loss method (Cheng & Coon, 1990; Anwar *et al.*, 2016).

Performance parameters

Daily Ca intake, body weight gain (BWG), feed conversion ratio (FCR), weekly egg production, and weekly damaged egg percentage (%) were recorded over 5 weeks. Daily Ca intake of birds were derived from summing up both the dietary and BM Ca intakes from each respective treatment. Feed conversion ratio was calculated as the amount of feed (kg) required to produce 12 eggs. Mortality was recorded over the experimental period.

Egg quality parameters

A total of 80 eggs (5 eggs per replicate) were collected on every 4th day of the week for analysis. Damaged eggs were identified through visual observation and candling. The eggs that had gross cracks or hair-line cracks were considered damaged eggs. The egg weights were measured with an electronic balance (Model No: AS III R2, Radwag Elektroniczne, Poland) to the nearest 0.01 g. A digital caliper was used to measure egg length and width to the nearest 0.01 mm. Eggs were broken individually on a white flat tile in order to measure the yolk height, yolk diameter, albumen length, albumen height and the yolk colour. The yolk was separated from egg albumen and the weight was measured. Egg shells were washed gently to remove the retained albumen. Egg shells were air dried for 24 hours and the shell weight was

measured. The shell thickness was measured from three points. Calculations to determine external and internal egg quality parameters were done using the formulae given below, described by Kul and Seker (2004) and Duman *et al.* (2016).

$$\text{Shape Index (\%)} = \frac{\text{Width (cm)}}{\text{Length (cm)}} \times 100$$

$$\text{Shell Ratio (\%)} = \frac{\text{Shell weight (g)}}{\text{Egg weight (g)}} \times 100$$

$$\text{Egg Surface Area (S)} = 3.9782 W^{0.7056}$$

Where;

S = Egg surface area (cm^2)

W = Egg weight (mg)

$$\text{Unit Surface Shell Weight } \left(\frac{\text{mg}}{\text{cm}^2}\right) = \frac{\text{Shell weight (mg)}}{\text{Egg surface area (cm}^2\text{)}}$$

Albumen Index (%) =

$$\frac{\text{Albumen height (mm)}}{[\text{Albumen length (mm)} + \text{Albumen width (mm)}] / 2} \times 100$$

$$\text{Albumen Ratio (\%)} = \frac{\text{Albumen weight (g)}}{\text{Egg weight (g)}} \times 100$$

$$\text{Hauh Unit (HU)} = 100 \log (H + 7.57 - 1.7W^{0.37})$$

Where;

H = Albumen height (mm)

W = Egg weight (g)

$$\text{Yolk Index (\%)} = \frac{\text{Yolk height (mm)}}{\text{Yolk diameter (mm)}} \times 100$$

Statistical analysis

Data were subjected to one-way ANOVA in a Completely Randomized Design and were analyzed using the GLM procedure of SAS (SAS, 2002). Differences between

means were separated using Duncan's Multiple Range Test at a significant level of 0.05.

RESULTS AND DISCUSSION

Particle size distribution

The Geometric Mean Diameter (GMD) and Geometric Standard Deviation (GSD) of BM were 1.70 mm and 1.63 mm, respectively (Figure 1). Bone meal particles that passed through the 4.00 mm sieve and were retained on the 2.00 mm sieve were considered coarse. The particles that passed through the 2.00 mm sieve were considered as fine particles. The relative proportion (59.6%) of fine particles (0–2 mm) was higher than the proportion of coarse particles (40.4%).

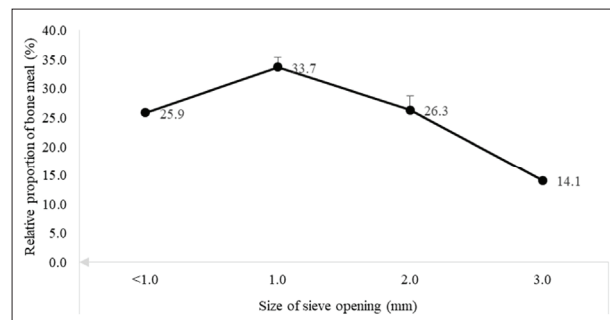


Figure 1: Particle size distribution of raw bone meal used in the experiment

Analysed composition of the layer feed and bone meal

According to NRC (1994) and Hy Line (2016), Crude Protein (CP) levels for layer rations could range from 155 to 170 g/kg (Table 1). The analysed CP content of the layer feed is 183.2 g/kg (Table 1). Layer diets are formulated to contain 40–46 g/kg Ca (Bradbury *et al.*, 2014; Wilkinson *et al.*, 2014b). The analysed Ca content in the diet (31 g/kg) was lower than that of the recommended dietary Ca level for layer chickens (Table 1).

Table 1: The analyzed composition of the layer feed (as received basis)

Item	Dry matter (g/kg)	Ash (g/kg)	Crude protein (g/kg)	Crude fat (g/kg)	Calcium (g/kg)	Total phosphorus (g/kg)	Gross energy (kJ/kg)
Layer feed	908.9	118.0	183.2	144.0	31.0	7.5	4040.3
Bone meal	892.8	476.0	-	-	79.0	44.0	-

According to NRC (1994), BM is supposed to contain 298 g/kg of Ca and 125 g/kg of total P. The analysed Ca (79 g/kg) and P (44 g/kg) content in BM used in the present study were much lower than those of reported in NRC (1994). Differences in Ca and P contents of BM have been reported. The calcium content of BM was found to range from 193 to 370 g/kg (Orban & Roland, 1992; Field, 2000; Phiraphinyo *et al.*, 2006; Khalil *et al.*, 2017). Phosphorus in BM ranged from 17.7 to 193.3 g/kg (Orban & Roland, 1992; Khalil *et al.*, 2017). However, Ca and P contents of bones are known to be affected by the species, age, nutrition and sampling site (Orban & Roland, 1992; McDonald *et al.*, 2002; Phiraphinyo *et al.*, 2006; Khalil *et al.*, 2017). However, the Ca and P contents of BM produced from thigh bones in the present study are lower than those reported by Rathnayaka *et al.* (2020) for BM (Ca 101.6 g/kg and P 59.8 g/kg) of thigh bone origin.

***In vitro* solubility test results**

According to Rao & Roland (1989), Ca supplements with larger particle sizes had a higher *in vivo* solubility but they were less soluble under *in vitro* conditions. In the present study, fine particle sizes (1–2 mm) recorded the highest solubility (56.25%) (Table 2). Some researchers have found no relationship between Ca solubility *in vitro* and Ca solubility *in vivo* when two Ca sources of the same particle sizes were compared (Rao & Roland, 1990). Orban and Roland (1992) revealed that the *in vitro* solubility of coarse (3.3 mm), granular (2.2 mm) and fine (0.8 mm) chicken BM were 13, 53 and 32%, respectively.

Table 2: *In vitro* solubility of bone meal (BM) samples used in the experiment

Particle size (mm)	<i>In vitro</i> solubility (%) ± SE ¹
1.0–2.0	56.25 ± 0.45
2.0–3.0	47.45 ± 0.32
3.0–4.0	39.80 ± 0.30

¹ Standard error

The particle size of an ingredient may be a factor influencing digestibility of Ca and P. Larger feed particles are digested over a longer time in the gizzard than fine feed particles, making Ca more available during the period of shell formation throughout the night (Scott *et al.*, 1971). According to Hyline (2016) feeding layers over 63-weeks of age with 65% of the coarse limestone

(2 and 4 mm in diameter) effectively maintains egg quality. Pizzolante *et al.* (2009) revealed that feeding coarse limestone to the layers produced fewer cracked eggs.

Performance parameters

No mortality was detected during the entire experimental period. Bone meal intake, Ca intake, damaged egg percentage and laying percentage were affected significantly ($p < 0.05$) by particle sizes of the BM. However, FCR and weight gain of layers were not affected ($p > 0.05$) by the particle size of BM (Table 3).

Bone meal intake and Ca intake

The highest daily BM intake (37.39 g/b/day) ($p < 0.05$) was observed in the birds fed with BM having 2–3 mm particle size (Table 3). The lowest BM intake (21.85 g/b/day) was observed in birds fed with BM having 1–2 mm particle size. The birds fed with BM having 2–3 mm particle size showed the highest ($p < 0.05$) daily Ca intake (5.74 g/b/day) (Table 3). The birds fed with the control diet showed the lowest Ca intake (2.79 g/b/day). It is noteworthy that all three BM diets were able to fulfil the recommended daily dietary Ca requirement of layers. This could be due to the layers' ability to select Ca when BM was fed in separate feeders. This Ca-specific appetite has been previously reported by Wilkinson *et al.* (2014a) for broilers when choice-fed with limestone.

Damaged egg percentage

The highest damaged egg percentage (9.34%) was reported from the group fed with the control diet (Table 3). Feeding BM to the layers significantly ($p < 0.05$) reduced the damaged egg percentage (1.28–1.57%). However, feeding BM with different particle sizes had no effect ($p > 0.05$) on the damaged egg percentage. The finding of this study is comparable to that reported by Rathnayaka *et al.* (2020) who found that free-choice feeding of BM reduced the damaged egg percentage (1.01%) in layers as compared to those fed with a control diet alone, limestone, and oyster shells. This effect of BM supplementation to reduce damaged egg percentage may be due to (i) the birds' ability to meet their daily Ca requirement through BM intakes and (ii) the availability of BM Ca to the birds for shell formation.

Feed conversion ratio (FCR)

Choice feeding of BM has no effect on FCR ($p > 0.05$) (Table 3). According to Auttawong *et al.* (2013), coarse

feed improved FCR when birds were fed *ad libitum*. However, when feeding time was limited or restrictedly, the coarse feed effect disappeared. Throughout this experiment the birds were fed based on Hy-line nutrition guidelines (Hy-line, 2016) with *ad libitum* water. This can be the reason for the insignificant effect among the treatments for FCR.

Laying percentage

The laying percentage was highest ($p < 0.05$) in birds fed with BM having 2–3 mm particle size (90.07%) (Table 3). Feeding with the control diet reduced ($p < 0.05$) the laying percentage. However, Rathnayaka *et al.* (2020) found that feeding BM to the commercial layers has no effect on laying percentage and the laying percentages

observed during their study were not affected by the source of Ca. In contrast, Ahmed *et al.* (2013) found that the laying percentage increased when fed with limestone.

Weight gain

The weight gain of birds was similar ($p > 0.05$) among treatments (Table 3). The non-significant effect of Ca on weight gain of layers has been previously reported (Pelicia *et al.*, 2009; Rathnayaka *et al.*, 2020).

External egg quality parameters

The effect of feeding three different particle sizes of BM on external egg quality parameters in commercial layers is presented in Table 4. No BM particle size effect was

Table 3: Effect of different treatments on layer performance¹

	Bone meal intake per bird per day (g)	Ca intake per bird per day (g)	Egg damage (%)	FCR (kg feed/12 egg)	Laying percentage (%)	Weight gain (g/bird/day)
Control	0.0 ^d	2.79 ^d	9.34 ^a	1.29 ^a	68.44 ^c	40.0 ^a
1–2 mm	21.85 ^c	4.52 ^c	1.57 ^b	1.28 ^a	85.00 ^b	42.0 ^a
2–3 mm	37.39 ^a	5.74 ^a	1.28 ^b	1.32 ^a	90.07 ^a	38.0 ^a
3–4 mm	36.68 ^b	5.69 ^b	1.35 ^b	1.29 ^a	84.99 ^b	40.0 ^a
SEM ²	0.14	0.01	0.76	19.35	1.29	11.92
Probability	***	***	***	NS	***	NS

NS = not significant; * $p < 0.05$; ** $p < 0.01$; *** $p < 0.001$.

¹ Each value represents the mean of four replicates (8 birds/replicate).

² Pooled standard error mean.

^{a-d} Means in a column not sharing a common superscript are significantly different at $p < 0.05$.

Table 4: Effect of three different particle sizes of bone meal on external egg quality characteristics commercial layers¹

	Egg weight (g)	Shape index (%)	Shell ratio (%)	Unit surface shell weight (mg/cm ²)	Shell thickness (mm)
Control	65.04 ^a	73.72 ^a	12.03 ^b	86.02 ^b	0.412 ^c
1–2 mm	66.54 ^a	74.49 ^a	11.90 ^b	86.37 ^b	0.434 ^b
2–3 mm	66.58 ^a	72.44 ^b	12.34 ^a	88.43 ^a	0.47 ^a
3–4 mm	66.26 ^a	73.64 ^a	12.51 ^a	89.55 ^a	0.435 ^b
SEM ²	0.534	0.350	0.136	0.890	0.006
Probability	NS	***	**	*	***

NS = not significant; * $p < 0.05$; ** $p < 0.01$; *** $p < 0.001$.

¹ Each value represents the mean of four replicates (8 birds/replicate).

² Pooled standard error mean.

^{a-c} Means in a column not sharing a common superscript are significantly different at $p < 0.05$.

found for egg weight ($p < 0.05$). Shape index, shell ratio, unit surface shell weight (USSW), and shell thickness were affected significantly ($p < 0.05$) by different BM particle sizes.

Egg weight

Egg weights of birds among treatments were similar ($p > 0.05$) (Table 4). According to Amornthewaphat *et al.* (2007), the particle size of the corn feed did not influence the egg weight. Guinotte and Nys (1991) demonstrated that the layers fed with coarser limestone particles produced heavier eggs as compared to those consuming pulverized limestone.

Shape index

The egg shape index of birds was affected significantly ($p < 0.05$) by the different particle sizes of BM. A significant reduction ($p < 0.05$) of the shape index was observed when the birds were fed with 2–3 mm particle size (72.4%), as compared to 1–2 mm (74.5%) or 3–4 mm (73.64%) particle sizes of BM and the control diet (73.7%). As defined by Duman *et al.* (2016), all the eggs produced during the present experiment can be considered oval (72–76%). According to Alkan *et al.* (2010), a significant negative correlation exists between the egg shape index and shell thickness. Similarly, the birds fed with BM having 2–3 mm particle size reported the lowest shape index and the highest shell thickness (0.477 mm).

Shell ratio and unit surface shell weight (USSW)

The birds fed with BM having 2–3 mm and 3–4 mm particle sizes recorded the highest shell ratio (12.3% and 12.5%, respectively). According to Ozcelik (2002), the shell ratio depends on egg weight, shell weight, and shell thickness. However, it is evident that no proportional increase exists between egg weight and shell weight, and therefore the shell ratio (Kul & Seker, 2004). This may be a reason for observed differences in shell ratios in the present study although the egg weights were similar.

Feeding with BM having 2–3 mm and 3–4 mm particle sizes resulted the highest ($p < 0.05$) unit surface shell weight (USSW). As shown by Zhang *et al.* (2017), USSW was significantly increased with higher Ca levels and lower limestone solubility. According to these researchers, the highest USSW was obtained at 4–5 g/day Ca intakes and 30.1–39.8% limestone solubilities. The

birds fed with BM having 2–3 mm and 3–4 mm particle sizes in the present study reported the highest Ca intake per day while exhibiting comparatively lower *in vitro* solubilities of the BM. Higher retention time in gizzards due to lower *in vitro* solubilities may be the reason for the highest USSW reported in birds fed BM supplements having 2–3 mm and 3–4 mm particle sizes.

Egg shell thickness

Egg shell thickness of birds differed significantly ($p < 0.05$) among treatments. The highest egg shell thickness (0.477 mm) was reported for the birds fed with BM having 2–3 mm particle size. The lowest egg shell thickness (0.411 mm) was recorded in birds fed with the control diet. Dietary Ca level is known to have an effect on the egg shell thickness. The layer diet used for the present experiment contained 31 g/kg Ca. The birds fed the control diet received Ca solely from the layer diet. This may be the reason for having the lowest egg shell thickness in birds fed with the control diet.

According to Scott *et al.* (1971), Ca supplements with large particle size are expected to be retained for a prolonged period in the gizzard making Ca more available during the period of shell formation. This may be a reason for the highest shell thickness recorded in the birds fed with BM having 2–3 mm particle size .

Internal egg quality parameters

The effect of feeding three different particle sizes of BM on internal egg quality parameters in commercial layers is presented in Table 5.

All the internal egg quality parameters tested were not affected ($p > 0.05$) by the particle sizes of BM. The result of the present study for internal egg quality parameters are in agreement with the findings of Rathnayaka *et al.* (2020), who found that feeding layers with either limestone, oyster shells or BM did not improve internal quality traits of chicken eggs. Moreover, the Haugh unit was not altered when Hy-Line Brown layers were fed with diets ground by roller and hammer mill to different particle sizes (Pérez-Bonilla *et al.*, 2014). The present study also confirmed that different particle sizes had no effect on the Haugh unit. According to Wang *et al.* (2014) particle sizes of Ca sources have no effect on the egg yolk colour of Longyan ducks, which is in agreement with the results of the present study.

Table 5: The effect of feeding three different particle sizes of bone meal on internal egg quality characteristics of commercial layers¹

	Albumen index (%)	Albumen ratio (%)	Haugh unit	Yolk colour	Yolk index (%)	Yolk ratio (%)
Control	5.50 ^a	60.08 ^a	59.78 ^a	12.04 ^a	42.61 ^a	27.59 ^a
1–2mm	5.54 ^a	60.76 ^a	60.11 ^a	12.09 ^a	42.53 ^a	27.21 ^a
2–3mm	5.69 ^a	60.42 ^a	59.99 ^a	12.01 ^a	42.69 ^a	27.22 ^a
3–4mm	5.69 ^a	60.35 ^a	60.28 ^a	12.02 ^a	42.41 ^a	27.16 ^a
SEM ²	0.07	0.33	0.50	0.05	0.10	0.23
Probability	NS	NS	NS	NS	NS	NS

NS = not significant.

¹ Each value represents the mean of four replicates (8 birds/replicate).

² Pooled standard error means.

^{a-b} Means in a column not sharing a common superscript are significantly different at $p < 0.05$.

CONCLUSION

The present study demonstrated that free-choice feeding of BM improves the egg shell thickness and reduces damaged egg percentage in commercial layers. Bone meal containing 2–3 mm particles improves BM intake, Ca intake, laying percentage and shell thickness more than other sized particles. Neither BM nor its particle sizes have positive effects on feed conversion ratio, weight gain, egg weight, or internal egg quality parameters tested. The present study concludes that BM particle size influences the Ca specific appetite of layer chickens and feeding BM having 2–3 mm particle size is the best in improving overall performance and egg quality parameters.

Conflict of interest

The authors disclose that they have no conflicts of interest concerning this article.

Acknowledgement

The authors acknowledge the assistance of the technical staff of Maxies and Company (Pvt.) Ltd, Wennappuwa, Sri Lanka and the technical staff of the Department of Livestock Production, Faculty of Agricultural Sciences, Sabaragamuwa University, Belihuloya, Sri Lanka.

REFERENCES

Ahmed N.M., Atti A.K.A., Elamin K.M., Dafalla K.Y., Malik H.E.E. & Dousa B.M. (2013). Effect of dietary calcium

- sources on laying hens performance and egg quality. *Journal of Animal Production Advances* **3**(07): 226–231.
DOI: <https://doi.org/10.5455/japa.20130718034818>
- Alkan S., Karabağ K., Galiç A., Karsli T. & Balcioglu M.S. (2010). Effects of selection for body weight and egg production on egg quality traits in Japanese quails (*Coturnix coturnix japonica*) of different lines and relationships between these traits. *Kafkas Universitesi Veteriner Fakültesi Dergisi* **16**(02): 239–244.
DOI: <https://doi.org/10.9775/kvfd.2009.633>
- Amornthewaphat N., Attamangkune S., Songserm O., Ruangpanit Y. & Thomawong P. (2007). Effects of corn particle size in layer diet on laying performance and uniformity of egg quality under high stocking density. *Proceedings of the 16th European Symposium on Poultry Nutrition*, Strasbourg, France. 26 – 30 August 2007, World's Poultry Science Association (WPSA) Beekbergen, Netherlands. pp. 479–482.
- Anwar M.N., Ravindran V., Morel C.H., Ravindran G. & Cowieson A.J. (2016). Apparent ileal digestibility of calcium in limestone for broiler chickens. *Animal Feed Science and Technology* **213**: 142–147.
DOI: <https://doi.org/10.1016/j.anifeedsci.2016.01.014>
- AOAC International. (2005). *Official Methods of Analysis*, 18th edition. AOAC International, Washington, DC.
- Auttawong S., Brake J., Stark C. & Yahav S. (2013). Time-limited feeding of grower feed negates the effects of corn particle size, dietary energy level, and post-pellet liquid fat application on broiler live performance from 14 to 28 days of age. *Poultry Science* **92**: 32.
- Baker S. & Herrman T. (2002). *Evaluating Particle Size. MF-2051 Feed Manufacturing*, pp. 5. Department of Grain Science Industry, Kansas State University, Manhattan, USA.
- Bradbury E., Wilkinson S., Cronin G., Bedford M. & Cowieson A. (2014). Exploring the calcium appetite of layers with choice feeding. 25th Australian Poultry Science Symposium.

- Available at <https://en.engormix.com/poultry-industry/articles/exploring-calcium-appetite-layers-t36174.htm>, Accessed 22 July 2020.
DOI: <https://doi.org/10.3382/ps.2013-03537>
- Çath A.U., Bozkurt M., Küçükyılmaz K., Çinar M., Bintaş E., Çöven F. & Atik H. (2012). Performance and egg quality of aged laying hens fed diets supplemented with meat and bone meal or oyster shell meal. *South African Journal of Animal Science* **42**(01): 74–82.
DOI: <http://dx.doi.org/10.4314/sajas.v42i1.9>
- Cheng T.K. & Coon C.N. (1990). Effect of calcium source, particle size, limestone solubility *in vitro*, and calcium intake level on layer bone status and performance. *Poultry Science* **69**(12): 2214–2219.
DOI: <https://doi.org/10.3382/ps.0692214>
- Duman M., Şekeroğlu A., Yıldırım A., Eleroğlu H. & Camcı Ö. (2016). Relation between egg shape index and egg quality characteristics. *European Poultry Science* **80**: 1–9
DOI: <https://doi.org/10.1399/eps.2016.117>
- Englmaierová M., Skřivan M., Skřivanová E. & Čermák L. (2017). Limestone particle size and *Aspergillus niger* phytase in the diet of older hens, *Italian Journal of Animal Science* **16**(04): 608–615.
DOI: <https://doi.org/10.1080/1828051X.2017.1309258>
- Field R.A. (2000). Ash and calcium as measures of bone in meat and bone mixture. *Meat Science* **55**: 255–264.
DOI: [https://doi.org/10.1016/S0309-1740\(99\)00147-3](https://doi.org/10.1016/S0309-1740(99)00147-3)
- Fleischer H., Vorberg E., Thurow K., Warkentin M. & Behrend D. (2014). Determination of calcium and phosphorus in bones using microwave digestion and ICP-MS: Comparison of manual and automated methods using ICP-MS. *5th IMEKO TC 19 Symposium on Environmental Instrumentation and Measurements*. Available at <https://www.imeko.info/publications/tc19-2014/IMEKO-TC19-2014-020.pdf>, Accessed 23 July 2020.
- Guinotte F. & Nys Y. (1991). Effects of particle size and origin of calcium sources on eggshell quality and bone mineralization in egg laying hens. *Poultry Science* **70**: 583–592.
DOI: <https://doi.org/10.3382/ps.0700583>
- Hy-Line (2016). Hy-line W-36 Interactive Management Guide. Hy-Line International, USA. Available at <https://www.hyline.com/>, Accessed 8 October 2019.
- Khalil R., Ferawati Y.F.K. & Agustin F. (2017). Studies on physical characteristics, mineral composition and nutritive value of bone meal and bone char produced from inedible cow bones. *Pakistan Journal of Nutrition* **16**: 426–434.
DOI: <https://doi.org/10.3923/pjn.2017.426.434>
- Kul S. & Seker I. (2004). Phenotypic correlations between some external and internal egg quality traits in the Japanese quail (*Coturnix coturnix japonica*). *International Journal of Poultry Science* **3**: 400–405.
DOI: <https://doi.org/10.3923/ijps.2004.400.405>
- Martin S.A. (1985). Comparison of hammer mill and roller mill grinding and the effect of grain particle size on mixing and pelleting. *MSc Thesis*, Kansas State University, Manhattan, KS, USA.
- McDonald P., Edwards R.A., Greenhalgh J.F.D. & Morgan C.A. (2002). *Animal Nutrition*. 6th edition. Pearson Education LTD. Harlow, Essex, UK.
- NRC (1994). *National Research Council, Nutrient Requirements of Poultry*, 09th revised edition. National Academy Press, Washington DC, USA.
- Olgun O., Yildiz A.Ö. & Cufadar Y. (2015). The effects of eggshell and oyster shell supplemental as calcium sources on performance, eggshell quality and mineral excretion in laying hens. *Indian Journal of Animal Research* **49**(2): 205–209.
DOI: <https://doi.org/10.5958/0976-0555.2015.00056.4>
- Orban J. & Roland D. (1992). The effect of varying bone meal sources on phosphorus utilization by 3-week old broilers. *Journal of Applied Poultry Research* **11**: 75–83.
DOI: <https://doi.org/10.1093/japr/1.1.75>
- Ozcelik M. (2002). The phenotypic correlations among some external and internal quality characteristics in Japanese quail eggs. *Veterinary Journal of Ankara University (Turkey)* **49**: 67–72.
- Peixoto R.R. & Rutz F. (1988). Fontes de cálcio para poedeiras comerciais. I. Calcários “Matarazzo”, “Trevo Filler” and “Trevo Dolomítico”. *Revista Brasileira de Zootecnia* **1**: 17–29.
- Pelicia K., Garcia E.A., Faitarone A.B.G., Silva A.P., Berto D.A., Molin A.B. & Vercese F. (2009). Calcium and available phosphorus levels for laying hens in second production cycle, *Brazilian Journal of Poultry Science* **11**(1): 39–49.
DOI: <https://doi.org/10.1590/s1516-635x2009000100007>
- Pérez-Bonilla A., Frikha M., L’Azaro R.P. & Mateos G.G. (2014). Type of grinding of the main cereal of the diet affects production of brown egg-laying hens. *Animal Feed Science and Technology* **194**: 121–130.
DOI: <https://doi.org/10.1016/j.anifeeds.2014.05.012>
- Phiraphinyo P., Taepakpurenat S., Lakkatanaporn P., Suntornsuk W. & Suntornsuk L. (2006). Physical and chemical properties of fish and chicken bones as calcium source for mineral supplements. *Songklanakarinn Journal of Science and Technology* **28**(02): 327–335.
- Pizzolante C.C., Saldanha E.S.P.B., Laganá C., Kakimoto S.K. & Togashi C.K. (2009). Effects of calcium levels and limestone particle size on the egg quality of semi heavy layers in their second production cycle. *Brazilian Journal of Poultry Science* **11**(02): 79–86.
DOI: <https://doi.org/10.1590/s1516-635x2009000200002>
- Rao K.S. & Roland Sr, D.A. (1989). Influence of dietary calcium level and particle size of calcium source on *in vivo* calcium solubilization by commercial Leghorns. *Poultry Science* **68**(11): 1499–1505.
DOI: <https://doi.org/10.3382/ps.0681499>
- Rao K.S. & Roland Sr, D.A. (1990). *In vivo* limestone solubilization in commercial Leghorns: role of dietary calcium level, limestone particle size, *in vitro* limestone solubility rate, and the calcium status of the hen. *Poultry Science* **69**(12): 2170–2176.
DOI: <https://doi.org/10.3382/ps.0692170>
- Rathnayaka R.M.D.B., Mutucumarana R.K. & Andrew M.S. (2020). Free-choice feeding of three different dietary

- calcium sources and their influence on egg quality parameters of commercial layers. *Journal of Agricultural Sciences-Sri Lanka* **15**(01): 50–62.
DOI: <http://doi.org/10.4038/jas.v15i1.8671>
- Roland D.A. & Sr, Bryant M. (1999). Optimal shell quality possible without oyster shell. *Feedstuffs* **71**: 18–19.
- Saki A., Rahmani A. & Yousef A. (2019). Calcium particle size and feeding time influence egg shell quality in laying hens. *Acta Scientiarum*. Available at <https://periodicos.uem.br/ojs/index.php/ActaSciAnimSci/article/view/42926/pdf> , Accessed on 26 March 2022.
- SAS Institute (2002). SAS/Stat 9.0. SAS Institute Inc., *User's Guide*. Cary, NC, USA.
- Saunders-Blades J.L., MacIsaac J.L., Korver D.R. & Anderson D.M. (2009). The effect of calcium source and particle size on the production performance and bone quality of laying hens. *Poultry Science* **88**: 338–353.
DOI: <https://doi.org/10.3382/ps.2008-00278>
- Scott M.L., Hull S.J. & Mullenhoff P.A. (1971). The calcium requirement of laying hens and effects of dietary oyster shells upon eggshell quality. *Poultry Science* **50**: 1055–1063.
DOI: <https://doi.org/10.3382/ps.0501055>
- Tunç A.E. & Cufadar Y. (2015). Effect of calcium sources and particle size on performance and eggshell quality in laying hens. *Turkish Journal of Agriculture - Food Science and Technology* **3**(04): 205–209.
DOI: <https://doi.org/10.24925/turjaf.v3i4.205-209.262>
- Wang S., Chen W., Zhang H.X., Ruan D. & Lin Y.C. (2014). Influence of particle size and calcium source on production performance, egg quality, and bone parameters in laying ducks. *Poultry Science* **93**: 2560–2566.
DOI: <http://dx.doi.org/10.3382/ps.2014-03962>
- Wilkinson S.J., Bradbury E.J., Bedford M.R. & Cowieson A.J. (2014a). Effect of dietary nonphytate phosphorus and calcium concentration on calcium appetite of broiler chicks. *Poultry Science* **93**(07): 1695–703.
DOI: <https://doi.org/10.3382/ps.2013-03537>
- Wilkinson S.J., Selle P.H., Bedford M.R. & Cowieson A.J. (2013). Separate feeding of calcium improves performance and ileal nutrient digestibility in broiler chicks. *Animal Production Science* **54**: 172–178.
DOI: <https://doi.org/10.1071/an12432>
- Wilkinson S., Cowieson A. & Bradbury E. (2014b). Optimizing calcium, phosphorus and phytase formulation in layer diets. Available at <https://en.engormix.com/poultry-industry/articles/optimizing-calcium-phosphorus-phytase-t36325.htm>, Accessed on 8 October 2019.
- Zhang B. & Coon C.N. (1997). The relationship of calcium intake, source, size, solubility *in vitro* and *in vivo*, and gizzard limestone retention in laying hens. *Poultry Science* **76**: 1702–1706.
DOI: <https://doi.org/10.1093/ps/76.12.1702>
- Zhang B., Caldas J.V. & Coon C.N. (2017). Effect of dietary calcium intake and limestone solubility on egg shell quality and bone parameters for aged laying hens. *International Journal of Poultry Science* **16**(04): 132–138.
DOI: <https://doi.org/10.3923/ijps.2017.132.138>

RESEARCH ARTICLE

Turtle conservation

Assessment of marine turtle nesting habitats from Tangalle to the Kumbukkan Oya estuary in south-eastern Sri Lanka

SJ Perera^{1*}, WPN Perera², S de A Goonatilake², K Ekaratne², D Wijesinghe², LV Perera¹, D Chandranimal³ and A Ediriweera⁴

¹ Department of Natural Resources, Sabaragamuwa University, P.O. Box. 02, Belihuloya 70140, Sri Lanka.

² IUCN - International Union for Conservation of Nature, Sri Lanka Country Office, Colombo, Sri Lanka.

³ 32/3, Central Road, Thalpitiya North, Wadduwa, Sri Lanka.

⁴ Anantara Peace Haven Tangalle Resort, Sri Lanka.

Submitted: 06 September 2021; Revised: 29 December 2021; Accepted: 27 May 2022

Abstract: This study assessed marine turtle nesting habitats along the south-eastern coastline of Sri Lanka, with the specific objectives of (i) reporting the quality of turtle nesting habitats, turtle nesting abundance, and threats to nesting turtles; (ii) comparing the current results with the results of a study conducted in 2004 and (iii) recommending conservation actions. The current study was carried out from August 2017 to May 2018 to assess the three parameters given in objective (i) above, along a 133 km coastal belt in 531 transects of 250 m each. Direct visual observations were supplemented with data collected from local people and validated using habitat suitability modelling using MaxEnt software. The study demarcated seven turtle nesting hotspots and recommends priority areas for nine turtle conservation activities. Those include the declaration of the Palatupana beach that connects the existing Nimalawa Sanctuary and Yala National Park including its shallow sea as a sanctuary. Its management is recommended through public-private partnerships ensuring healthy nesting turtle populations and their monitoring, while promoting turtle-based tourism under strict guidelines. Factors contributing adversely for nesting turtles such as coastal constructions and clearance of beach vegetation should be considered in management actions for the conservation of these globally threatened reptiles. The need for future research is also identified.

Keywords: Habitat suitability, marine turtles, MaxEnt, nesting habitats, southern Sri Lanka, turtle nesting hotspots.

INTRODUCTION

In general, the abundance of marine vertebrates has declined by about 22% during the past four decades, and marine turtles have the highest percentage of threatened species among these groups (WWF 2012 – Living Planet Report cited by McCauley *et al.*, 2015). Anthropogenic threats, such as destruction of feeding and nesting habitats, poaching and predation of eggs, illegal harvesting for meat, and by-catch in fisheries are driving this loss (Wallace *et al.*, 2011). As a consequence of these threats, six out of seven species of marine turtles are listed as globally threatened with the risk of extinction. Of these six species, leatherback (*Dermochelys coriacea*, Vandelli, 1761), loggerhead (*Caretta caretta*, Linnaeus, 1758) and olive ridley (*Lepidochelys olivacea*, Eschscholtz, 1829) are listed as Vulnerable (Wallace *et al.*, 2013; Casale & Thicker, 2017; Abreu-Grobois & Plotkin, 2008, respectively), green turtle (*Chelonia mydas*, Linnaeus, 1758) as Endangered (Seminoff, 2004) and Kemp's ridley (*Lepidochelys kempii*, Garman, 1880) and hawksbill (*Eretmochelys imbricata*, Linnaeus, 1766) as Critically Endangered (Wibbels & Bevan, 2019; Mortimer & Donnelly, 2008, respectively). Flatback

* Corresponding author (sandun.perera@appsc.sab.ac.lk;  <https://orcid.org/0000-0002-4241-0062>)



This article is published under the Creative Commons CC-BY-ND License (<http://creativecommons.org/licenses/by-nd/4.0/>). This license permits use, distribution and reproduction, commercial and non-commercial, provided that the original work is properly cited and is not changed in any way.

(*Natator depressus*, Garman, 1880) remains in the Data Deficient category (RLS & PS, 1996). Destruction of nesting habitats is a major threat for these species that exhibit nesting site fidelity (Mazaris *et al.*, 2009). Although egg and meat poaching has decreased in some parts of the world due to increased conservation efforts, coastal development and associated infrastructure, as well as coastal armouring, are contributing to shrink the turtle nesting habitats (Lopez *et al.*, 2015; Fuentes *et al.*, 2016).

Sri Lanka is a continental island located at the southern tip of the Indian subcontinent between the northern latitudes 5° 54' & 9° 52' and the eastern longitudes 79° 39' & 81° 53'. Its coastline is approximately 1,620 km including the shoreline of bays and inlets excluding lagoons (Government of Sri Lanka, 2018). The coastal zone is rich in biotic and abiotic resources, including a diverse array of ecosystems (MoMDE, 2016). The ocean around the island is part of the northern Indian Ocean global marine biodiversity hotspot (Roberts *et al.*, 2002). Of the seven species of marine turtles, five nest in South Asian shores, including those of Sri Lanka. The species that nest in Sri Lanka are the green, hawksbill, leatherback, loggerhead, and olive ridley turtles (IUCN, 2005; Perera *et al.*, 2005; Rajakaruna *et al.*, 2018). All these species are protected under the Fauna and Flora Protection Ordinance No. 2 of 1937, as amended by Act No. 22 of 2009. International trade of these species is prohibited under the Convention on International Trade in Endangered Species of Wild Fauna and Flora (CITES) (CITES, 2021) and in Appendices I and II of the Convention on the Conservation of Migratory Species of Wild Animals (CMS) (CMS, 2020). Despite their conservation value and the importance of Sri Lankan beaches for their sustained survival, little progress has been made on scientific research on marine turtle nesting habitats along the shores of the island. Research is restricted to a few populations at beaches identified as turtle hotspots in southern Sri Lanka, such as Kosgoda (Ekanayake *et al.*, 2010), Rekawa (Kapurusinghe, 1998; Ekanayake *et al.*, 2001), Godawaya (Ekanayake *et al.*, 2002), Kalametiya (Kapurusinghe, 2006), Bundala National Park (NP) (Kapurusinghe, 2006), Yala NP (Kapurusinghe, 2006), Kumana NP, Panama and Komari (Ellepola *et al.*, 2014). As noted by Perera *et al.* (2005), most of these studies focused on the biology of each species but paid little attention to the ecological conditions of turtle nesting habitats.

In 2004, prior to the Indian Ocean Tsunami, turtle nesting habitats from Tangalle fishery harbour to Menik Ganga estuary in Pilinnawa in the Yala NP had been

assessed (Figure 1; Perera *et al.*, 2005). The current study builds upon the above research, with the specific objectives of (i) assessing the quality of turtle nesting habitats, (ii) assessing the turtle nesting abundance, (iii) assessing threats to nesting turtles, (iv) comparing the results with the 2004 study and (v) making recommendations for conservation.

MATERIALS AND METHODS

Study area and duration of study

The current study, conducted from 25 August 2017 to 8 May 2018, extended along approximately 133 km of the south-eastern coastal belt (specifically, the littoral zone) of Sri Lanka, from the Anantara Resort at Goyambokka beach, Tangalle (N 6° 0'35.61"; E 80°46'52.04") to the Kumbukkan Oya estuary (N 6°30'8.69"; E 81°42'17.52") in the Yala NP (Figure 1). For data collection and analyses, the study coastline was divided into 531 transects each extending to 250 m. These transects were further grouped into 21 major beach stretches, each comprising 15-50 transects following a landscape approach of longer beach stretches with less heterogeneity.

Field data collection

This study used the same methodology of Perera *et al.* (2005), which adapted the method used by Shanker *et al.* (2003a; b) and Choudhary *et al.* (2003). This replication facilitated the temporal comparison of results. However, technological advancement of using GPS (*etrex 30*) for field navigation allowed more accurate demarcation of beach transects (250 m) during the present survey.

A separate field data recording form was filled for each transect, for three major sets of parameters, i.e., habitat quality, turtle nesting abundance and threats to nesting turtles. The full length of the littoral zone from Anantara Tangalle Resort to Kumbukkan Oya Estuary was walked. Each transect was navigated using a GPS navigator loaded with a Google Earth® KML file of the 531 pre-determined transects to collect their data.

During a single data collection day, a 5–6 km stretch of the beach was surveyed for nearly six hours. Hence, approximately a 30 km beach stretch was covered within a six-day sampling session, with the entire survey consisting of four sessions. Two random nocturnal beach surveys of about 2–3 km were also conducted within the same 30 km beach stretch during each sampling session to supplement data on turtle nesting, human

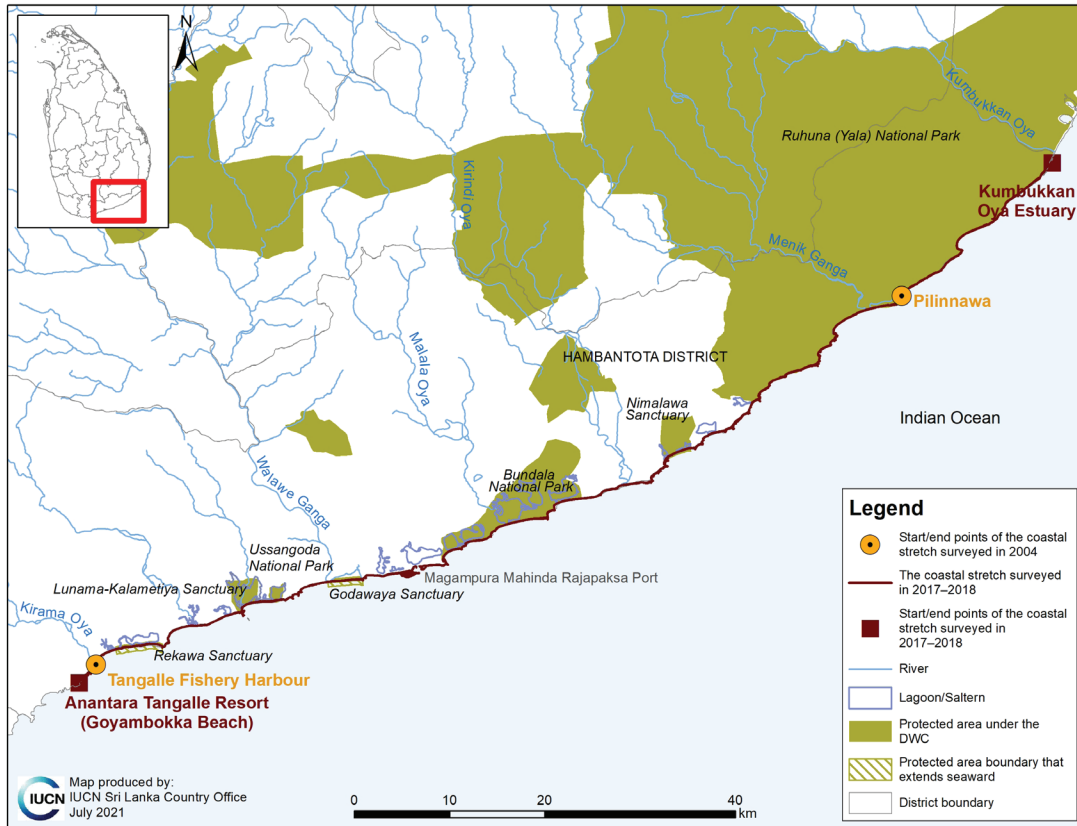


Figure 1: The coastal stretches surveyed in 2004 and 2017–2018 along the south-eastern coast of Sri Lanka

traffic, illumination in the night, egg poaching and turtle egg predation by feral dogs and wild animals. These nocturnal observations were used to augment the data collected during transect walks.

Secondary information was also collected from literature and by interviewing locals such as fishermen, hoteliers and other people engaged in tourism-related activities in beach stretches, villagers including suspected egg poachers, officers representing government organisations including the Department of Wildlife Conservation (DWC) and personnel from non-governmental organizations. Maximum of five individuals were interviewed from each category.

These data were validated by modelling the habitat suitability for marine turtle nesting, described under the section on data analyses.

Marine turtle nesting habitat quality

The following five parameters were recorded to assess the quality of marine turtle nesting habitat: (i) the general nature of the substrate, i.e., sandy shore (coarse/fine), shell deposit, or rocky shore, etc.; (ii) average width and slope of the beach; (iii) general beach habitat with a detailed habitat profile (based on Perera *et al.*, 2005) using the ecosystem classification of MoMD&E (2016); (iv) backshore and foredune backing the beach or their replacement habitats such as sand dunes, scrublands, coconut plantations, human habitation, etc., and (v) naturalness and human activities as measures of the quality of the beach and backshore/foredune habitats, which were scored on a scale of 1 to 4 (low = 1; moderate = 2; high = 3; very high = 4) based on the consensus of field ecologists ensuring that the same ecologists contributed to the scoring for all beach transects.

Since the current survey was conducted using a rapid assessment methodology for a very long stretch of coastline, all the seasonal changes have not been captured. Of the five parameters measured, only the average width and slope of the beach are affected by coastal dynamics driven by the south-westerly Asian monsoon that blows over May through September. However, this period falls outside the general nesting season for many turtle species and hence avoided during this study. Further, the average width and slope have been measured at a minimum of three points and recorded as an average for the entire transect. Parameters such as the substrate, vegetation, naturalness and human activity are not subjected to marked seasonal changes. While calculations were performed based on data for 250 m transects, analyses were conducted and recommendations on broader conservation applications have been made for longer beach stretches using these rapid assessment data.

Marine turtle nesting abundance

The number of (i) fresh nesting crawls, (ii) old nesting crawls, (iii) non-nesting (false) crawls, (iv) fresh nests (with/without eggs), (v) old nests, (vi) damaged/predated nests, and (vii) nests washed by the wave action were recorded for each beach transect following Perera *et al.* (2005).

As the present survey neither extended over an entire year nor investigated all possible species-specific nesting seasons for all beach stretches, the field data were supplemented by (a) information collected on nesting turtles and their signs during the nocturnal surveys, (b) secondary information gathered from the fishermen, general community, hoteliers and DWC officers, and (c) recently published information. Data compiled through all above sources were used to determine the turtle hotspots in the area. These nesting abundance data were further validated by habitat suitability modelling for nesting turtles. Since the survey avoided the monsoonal rough sea conditions, some of the nesting signs could be found on the beach for weeks after the nesting events. Therefore, although the data were collected once for a given transect, it was ensured that a value close to the real marine turtle nesting abundance was obtained for each transect.

Threats to nesting marine turtles

To assess the threats to nesting marine turtle populations, the severity of the following parameters was quantified on a score of 0 to 5 (0 = nil; 1 = very low; 2 = low; 3 = moderate; 4 = high; 5 = very high), based on the observations made and consensus reached by the field

ecologists for each 250 m transect. These were also substantiated from interviews with the local community and the DWC representatives. Status of five direct threats to nesting turtles and their eggs were recorded: (i) poaching of eggs, (ii) turtle meat consumption and turtle shell industry, (iii) by-catch in fishing gear, (iv) egg predation by wild animals (for example, wild boar and jackals), and (v) by feral animals (domestic dogs and pigs) (Perera *et al.*, 2005). The status of thirteen indirect threats to nesting turtles were also recorded for each transect: (i) sand mining, (ii) erosion prevention measures (beach armouring), (iii) signs of beach pollution, (iv) signs of marine pollution, (v) beach seine fisheries, (vi) human traffic (for example, tourism and fisheries-related activities), (vii) infrastructure (for example, houses, hotels and roads), (viii) ports, fishing harbours and jetties, (ix) clearance of beach vegetation, (x) coral mining, (xi) plantations of exotic flora (e.g. *Casuarina*), (xii) spread of invasive alien species (e.g. *Opuntia*), and (xiii) artificial illumination (Perera *et al.*, 2005).

Data analyses

Data collected from each transect ($n = 531$) were analysed to obtain a composite score for the three major parameters from which the importance of each transect was assessed for the conservation of marine turtles. Composite scores were calculated as detailed below, tabulated and mapped. The scoring protocol was kept consistent with the 2004 survey for comparison.

Marine turtle nesting habitat quality

The equation (1) (adapted from Perera *et al.*, 2005) given below describes the calculation of the composite score of the nesting habitat quality as a percentage rounded up to the closest integer.

The field data form for each transect had two scores: (i) for the beach, and (ii) for the backshore/foredune. Each score comprised two components: (i) naturalness, and (ii) human disturbance (both these were scored on a scale of 1- 4, with 1 = low and 4 = very high). The naturalness score ranged from 4 (very high level of naturalness) to 0 (completely transformed beach habitats such as beach armouring). The human disturbance value for the calculation was taken as the highest possible score of 4 minus the score of the observation ($4 - \text{the observed score}$), i.e., if the observed score for human disturbance was 4, the value is taken as 0 ($4 - 4 = 0$).

The percentage of the overall composite score of the habitat quality of a given transect was then calculated

with a weightage of 75% of the score for nesting beach habitat quality and 25% of the score for the backshore/foredune. The composite score was calculated as follows:

$$\text{Composite score of the nesting habitat quality (\%)} = \frac{[\text{NB} + (4 - \text{HAB})/8] \times 75}{[\text{NBF} + (4 - \text{HABF})/8] \times 25} \dots(1)$$

Where

NB = Naturalness score for nesting beach habitat
 HAB = Human activity score for nesting beach habitat
 NBF = Naturalness score for backshore and foredune
 HABF = Human activity score for backshore and foredune

The above percentage composite score was then converted to one of four categorical scores as 1 = Low: 0–35%; 2 = Moderate: 36–55%; 3 = High: 56–80% and 4 = Very high: 81–100%.

Marine turtle nesting abundance and hotspots

The composite score for the abundance of nesting turtles was calculated based on three indices listed under the section on Field Data Collection. Primary field observations – the number of crawls and/or nests (whichever was higher) was counted for each transect as an index of abundance. All identifiable crawls and/or nests were counted within each transect, irrespective of how old they were. The second index was based on the secondary data collected from villagers, fishermen and DWC officers on the maximum number of turtles they had recorded from the given transect per night within the last three years. The third index was from reviewed literature (published from 2014 to 2018) on turtle nesting abundance in the beach stretch to which the transect belonged. The above counts were then converted to one of four categorical scores. 1 = Rare: 0 crawls/nest; 2 = Uncommon: 1 crawl/nest; 3 = Common: 2 crawls/nests; and 4 = Very common: ≥ 3 crawls/nests. While the primary data of crawls/nests were always a count, the secondary and published data were assigned to one of the categorical scores. The highest among the (a) primary count score (0–4); (b) secondary score (0–4); and (c) literature score (0–4) was assigned to each transect as its final score for nesting turtle abundance. Turtle nesting hotspots were identified based on this final score for the nesting turtle abundance.

Threats to nesting marine turtles

The composite score for the threats was calculated by obtaining the cumulative score of all threats ($n = 18$ as listed above) recorded for each transect. Each identified threat in a particular transect was given a score from 0 = none to 5 = very high. After scoring a given transect for all 18 threats, the composite score of threats to nesting turtles was calculated as a percentage of the total possible value of all threats, rounded up to the closest integer, using the following formula (adapted from Perera *et al.*, 2005):

$$\text{Composite score of threats to nesting turtles (\%)} = \frac{\sum T}{(5 \times 18)} \times 100 \dots(2)$$

Where

T = composite score of threats

The above % score was then converted to one of four categories of overall threat value per given transect as 1 = Low: 0–10%; 2 = Moderate: 11–20%; 3 = High: 21–30%; and 4 = Very High: 31–100%.

Preparation of maps

The final scores of the three parameters assessed were used for the preparation of maps for visualization. These maps were prepared using the ArcGIS 10.2.2 software (ESRI, 2012) based on the Google Earth® for the 21 beach stretches. Maps were prepared to compare the same stretches of beach between the 2004 study and the current one. However, the number of transects in each stretch did not completely match, given that transects of approximately 250–300 m in length were estimated by foot in the 2004 survey, in contrast to the accurate GPS-based 250 m transects of the current survey.

Identification of priority areas for marine turtle conservation activities

The priorities for turtle conservation activities were determined based on a comparative analysis on the average habitat quality, abundance of nesting turtles and threat scores for the 21 beach stretches, following the criteria given by Perera *et al.* (2005): (i) High nesting frequency - high habitat quality - low threats: declare as a protected area for turtles, *in situ* conservation and research programmes; (ii) High nesting frequency - high habitat quality - high human threats: carry out

awareness programmes and *ex situ* turtle nest protection programmes with the participation of local communities; (iii) High nesting frequency - high habitat quality - high natural threats: declare as a protected area for turtles, *in situ* conservation programmes with nest protection measures, supplemented by *ex situ* conservation programmes (for example, concrete cylinders or hume pipes have been proven to be a good defence against wild boar predation), together with associated research and tourism development; (iv) Moderate nesting frequency - high threats - irrespective of habitat quality: strengthen law enforcement with regular night patrolling by the DWC; (v) High nesting frequency - low habitat quality - irrespective of threats: engage in habitat enrichment programmes.

Validation of marine turtle nesting abundance data

Each of the 531 transects could only be surveyed once during the survey period, irrespective of the seasonality of turtle nesting and the weather. Although more comprehensive repetitive and year-round surveying of each transect extending across nesting seasons for all species would likely have provided information of the actual abundance of nesting turtles, this study was constrained by a time limit. Therefore, the survey may have missed the peak nesting seasons of some species for some transects. However, the methodology was designed to minimise the impact of this constraint by developing and using scores for the abundance of nesting turtles based on indices (not only based on actual counts), derived as described above. In addition, our analyses were conducted at broader, landscape-scale beach stretches rather than on individual transects, allowing our data to be more useful for conservation decisions. In addition, although we collected species-based data for transects, our analyses were based on nesting turtle abundance regardless of the species.

Habitat suitability modelling for marine turtle nesting habitat suitability

To validate qualitative results of nesting turtle abundance based on the rapid assessment, they were compared with quantitative results from two separate predictions of habitat suitability for nesting turtles using the following method. Maximum entropy (MaxEnt) distribution modelling, recommended as the best approach among similar methods for species distribution modelling, was used because of its high performance (Phillips *et al.*, 2006; Ortega-Huerta & Peterson, 2008; Elith *et al.*, 2011), ease of interpretation (Phillips *et al.*, 2004) and the use of presence-only data (Phillips *et al.*, 2004; 2006).

MaxEnt is a presence-only, machine learning approach for modelling habitat suitability that uses maximum entropy as a proxy for the occupation of the habitat by the species of concern (Phillips *et al.*, 2006). It identifies areas with the highest probability of finding the species of concern by maximising entropy, based on constraints derived from climatic and habitat variables (Phillips *et al.*, 2006; 2017).

Habitat suitability for marine turtle nesting (irrespective of the species) was predicted using the MaxEnt algorithm (version 3.4.1.a), based on data for the confirmed presence of nesting sites (Phillips *et al.*, 2017). Two separate habitat suitability models were run for two separate datasets of environmental variables available at contrastingly different resolutions—the first continuous and the second categorical—to avoid any confounding effects of combining the two.

Continuous bioclimatic variables ($n = 19$) for the current period were obtained with a resolution of 30 arc-seconds ($\sim 1 \text{ km}^2$) from the online database WorldClim (Version 2) (Hijmans *et al.*, 2005; Fick & Hijmans, 2017) for the first model. Data layers of BIOCLIM variables were clipped into our study area to produce a set of raster maps for the MaxEnt model.

For the second model, values of the categorical habitat variables ($n = 18$) collected at each of 531 beach transects were used. All categorical values assigned for each transect were used to produce a raster map for each habitat variable, using the data interpolation tool in ArcGIS 10.2.2 (ESRI, 2012), and the layers obtained were used as the measured categorical variables.

Occurrence points of turtle nests were collected from published literature and field observations and checked for accuracy. Sixty-four locations were used as presence only data for marine turtle nesting. All spatial data were processed using ArcGIS 10.2.2 and were projected to WGS 1984 UTM Zone 44N, which is the transverse Mercator projection parameter for Sri Lanka.

The MaxEnt model was run using the default software settings (Phillips & Dudík, 2008) and each model was run for 1,000 iterations with linear, quadratic, product, and hinge features (Elith *et al.*, 2011), with a majority of aforementioned turtle nesting presence data as training data to fit the model, keeping the rest to test the model, in order to maintain cross-validation, while the regularization was set at 0.1 to avoid over-fitting of test data (Phillips *et al.*, 2004). A maximum number of 10,000 background points were used and a convergence

threshold value was set at 0.00001. A 10-fold cross-validation method was used to estimate model error and predictive performance (Rodriguez *et al.*, 2010; Pascoe *et al.*, 2019). The model performance and the model structure were evaluated using the highest mean area under the receiver operator characteristic curve (AUC) value. AUC values assess the predictive accuracy of the model, with 0.5 indicating that the model is no better than random at predicting habitat suitability and 1 indicating a perfect ability of the model to estimate species presence

(Phillips *et al.*, 2006). The relevance and the contribution of each environmental variable for the model prediction were determined by the percent contribution from the heuristic test for each variable in the MaxEnt output, supported by the Jackknife variable contribution test or the regularised training gain (Phillips *et al.*, 2006). The more important a variable is in modelling habitat suitability, the higher its values of regularised training gain. Final outputs of model predictions were exported to ArcGIS 10.2.2 for further analysis.

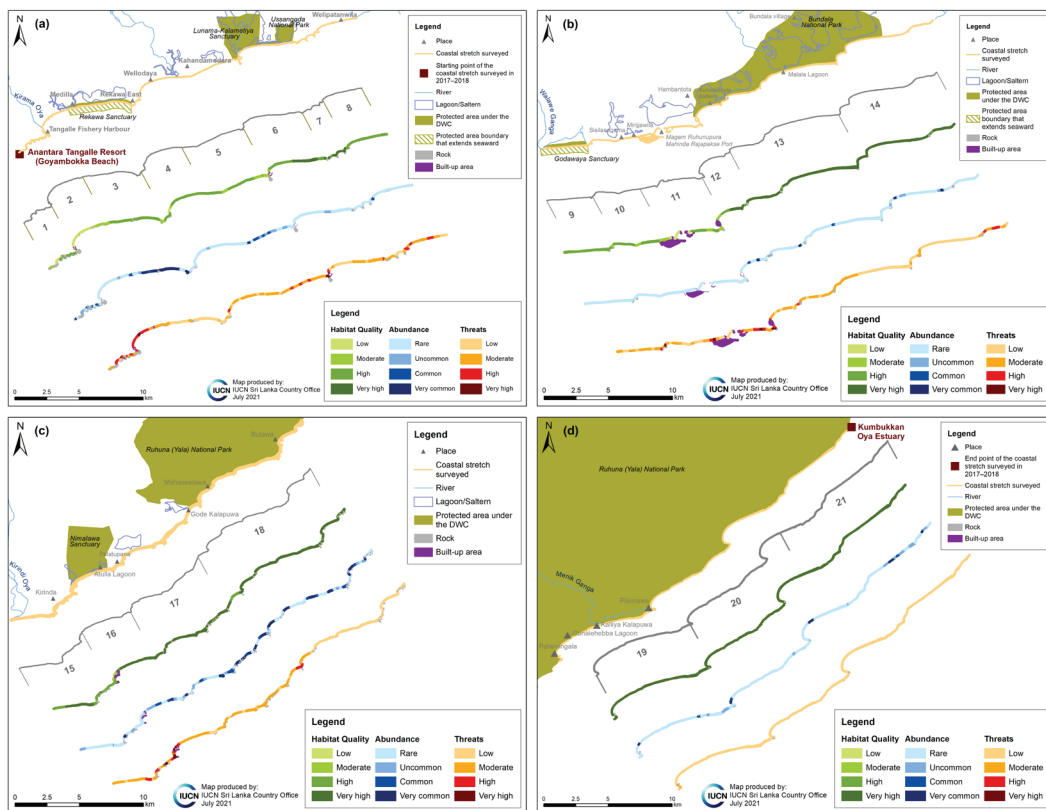


Figure 2: Summary of results of the marine turtle nesting habitat assessment; nesting habitat quality (green tones), nesting turtle abundance (blue tones) and threats to nesting turtles (red tones) along the 133 km coastal belt from Tangalle to the Kumbukkan Oya estuary in 21 beach stretches and 531 transects
(a) 1 - Tangalle (4 km; transects 001–016), 2 - Tangalle-Medilla (3.5 km; 017–030), 3 - Rekawa Sanctuary (5 km; 031–050), 4 - Rekawa East-Wellodaya (3 km; 051–067), 5 - Kahandamodara (5 km; 068–088), 6 - Lunama-Kalameitiya Sanctuary (5 km; 089–109), 7 - Ussangoda National Park (NP) (2 km; 110–118), and 8 - Welipatanwila (3.5 km; 119–131); **(b)** 9 - Godawaya Sanctuary (4 km; 132–146), 10 - Sisilasagama-Mirijjawila (4 km; 147–162), 11 - Magam Ruhunupura port (5 km; 163–183), 12 - Hambantota (4 km; 184–199), 13 - Koholankala-Malala in Bundala NP (9.5 km; 200–237), and 14 - Bundala in Bundala NP (9 km; 238–274); **(c)** 15 - Bundala village-Kirinda (7 km; 275–301), 16 - Nimalawa Sanctuary (4 km; 302–318), 17 - Palatupana (7.5 km; 319–348), and 18 - Gode Kalapuwa-Mahaseelawa-Butawa-Patanangala in Yala NP (12.5 km; 349–399); and **(d)** 19 - Patanangala-Pilinnawa in Yala NP (9.5 km; 400–439), 20 - Pilinnawa-Mihirawa in Yala NP (11.5 km; 440–485), and 21 - Mihirawa-Kumbukkan Oya in Yala NP (11.5 km; 486–531).

RESULTS AND DISCUSSION

Marine turtle nesting habitat quality

Of the 21 beach stretches, 57% had high levels of habitat quality (38% = very high; and 19% = high); while 24% of the beaches were moderate, and 19% were of low quality. Importantly, the protected beaches of the Lunama-Kalameiya Sanctuary, Ussangoda NP and Godawaya Sanctuary as well as the continuous and mostly protected 82 km stretch of beach from Koholankala and Malala in Bundala NP up to the Kumbukkan Oya estuary in Yala NP were reported with higher habitat quality, while Rekawa Sanctuary was recorded as moderate (Figure 2); See supplementary Figure 1 (a-u) for detailed maps of 531 transects in 21 beach stretches.).

Supplementary Table 1 summarizes the scores given for the quality of marine turtle nesting habitats within each beach stretch surveyed along the study area.

The current study identified beach stretches of the Bundala NP, Nimalawa Sanctuary, Palatupana and Yala NP as having a very high overall nesting habitat quality – almost in their natural state. Even with a certain degree of human disturbance, the nesting habitat quality of the beach stretches of Rekawa Sanctuary, Kahandamodara, Welipatanwila, Sisilasagama-Mirijjawila and Hambantota remain moderate, where the beach habitats are better than the backshore/foredune.

The quality of the beach stretches from Tangalle to Medilla, Rekawa East and Wellodaya, as well as Magam Ruhunupura Port and the adjacent coastline is poor because many of these beaches are subjected to heavy anthropogenic disturbances. In addition to the port itself, threats from fishery harbours and other fisheries-related activities were observed in these areas.

Changes in turtle nesting habitat quality since 2004

In most areas, habitat degradation from 2004 to 2017–2018 has been considerable, except in Bundala and Yala NPs and Nimalawa Sanctuary. A reduction of habitat quality from high to moderate/low was observed in beach stretches in Rekawa Sanctuary and Sisilasagama-Mirijjawila, largely because of coastal constructions in backshore/foredune habitats – many of which are illegal and directly affecting nesting turtles. The quality of the nesting habitats in the Bundala village-Kirinda stretch has dropped from very high to high. In addition, the moderate habitat quality observed in 2004 for nesting turtles in the stretch of Magam Ruhunupura Port and

adjacent coastline has dropped to low. The nesting habitat quality along the studied coastline did not appear to have a significant long-term impact from the 2004 Indian Ocean tsunami [see Bambaradeniya *et al.* (2006) and references therein, and Perera *et al.* (2006) and for more details].

Marine turtle nesting abundance

Around 33% of the 21 beach stretches had very high nesting abundance (19% = very common and 14% = common). This included a 24 km stretch of continuous and mostly protected beach from Nimalawa Sanctuary, Gode Kalapuwa-Mahaseelawa-Butawa to Patanangala in Yala NP, as well as Tangalle (4 km), Rekawa Sanctuary (5 km) and Kahandamodera (5 km) (Figure 2; supplementary Figure 1). Twenty-nine percent (29%) of beach stretches had low nesting turtle abundance, while 38% were visited rarely by nesting turtles. These results suggest that only a fraction of good quality nesting beach habitats are actually being used by nesting turtles.

The current assessment revealed that the beach stretches of Rekawa East-Wellodaya, Lunama-Kalameiya Sanctuary, Ussangoda NP, Welipatanwila, Godawaya Sanctuary, Sisilasagama-Mirijjawila, Magam Ruhunupura port, as well as Koholankala and Malala in Bundala NP are visited only rarely by nesting turtles. Except for the above, all other beaches from Anantara Tangalle Resort at Goyambokka beach to the Kumbukkan Oya estuary in Yala National Park are important for marine turtles as nesting grounds (Figure 2; Supplementary Figure 1).

Supplementary Table 2 provides turtle nesting scores calculated from the number of nests and crawls recorded during this study, as well as scores calculated from secondary information and published data for each transect. In addition, it provides a comparison of nesting turtle abundance for each beach stretch between 2004 and 2017–2018, as well as the nesting habitat suitability supported by predictive modelling (Figure 3; see supplementary Figure 2 (a-u) for detailed habitat suitability maps of the 21 beach stretches.). Beach stretches with the highest model-predicted habitat suitability, over 0.6 for both models (habitat suitability modelled using BIOCLIM variables as well as with measured variables), are listed here as congruent hotspots from MaxEnt models. Beach stretches identified as turtle nesting hotspots by both the nesting abundance results and MaxEnt models are highlighted as the current marine turtle nesting hotspots along the study coastline. Figure 4 provides a map of turtle nesting hotspots found in this study, as well as those identified by Perera *et al.* (2005).

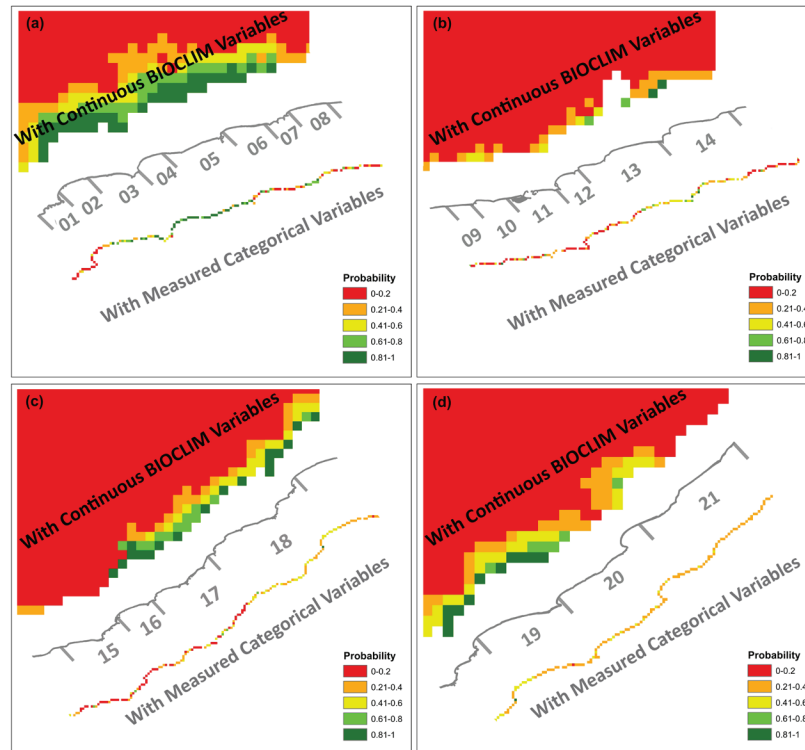


Figure 3: Habitat suitability distribution for marine turtle nesting modelled using BIOCLIM continuous variables (above) and measured categorical variables (below), along the sampled beach stretches (a) 1–8; (b) 9–14; (c) 15–18; and (d) 19–21.

Marine turtle nesting hotspots along the surveyed coastal belt

Seven beach stretches with abundance scores of 4–5 were considered initially as turtle nesting abundance hotspots: Tangalle (4 km), Rekawa Sanctuary (5 km), Kahandamodara (5 km), Nimalawa Sanctuary (4 km), Palatupana (7.5 km), Gode Kalapuwa-Mahaseelawa-Butawa-Patanangala in Yala NP (12.5 km), and Mihirawa-Kumbukkan Oya in Yala NP (11.5 km) (Supplementary Table 2; Figure 4). It is important to note that both the starting and ending beach stretches of the study coastal line have been identified as turtle nesting hotspots, suggesting that the study area needs to be expanded both westward from Tangalle, and north-eastward from the Kumbukkan Oya estuary to obtain a complete picture of marine turtle nesting grounds in south-eastern Sri Lanka.

The AUC of the habitat suitability model using measured categorical variables was 0.827, indicating that this model is useful in drawing conclusions; while the same for the model using BIOCLIM continuous

variables was 0.988, indicating an excellent model prediction (Swets, 1988; Elith, 2002). The relevance and the contribution of each environmental variable for the model prediction is given by the results of the heuristic test, *i.e.*, percent contribution of each variable (Supplementary Table 3 and 4, respectively, for the models fitted using BIOCLIM variables and measured variables), supported by the Jackknife variable contribution test (Supplementary Figure 3 a-d). Those variables with the highest contribution for both models are similar in both tests (Supplementary Figure 4). The test revealed that among the BIOCLIM variables used for the model development, the annual range of temperature (bio-7) and the precipitation of the wettest month (bio-13) were the most significant contributors to the habitat suitability for nesting marine turtles. Similarly, among the measured variables, the most significant contributors for the model prediction were coastal construction (cn) and clearance of vegetation (cv). Response curves of marine turtle nesting to each environmental variable are provided in Supplementary Figures 5a & 5b, respectively for continuous and categorical variables.

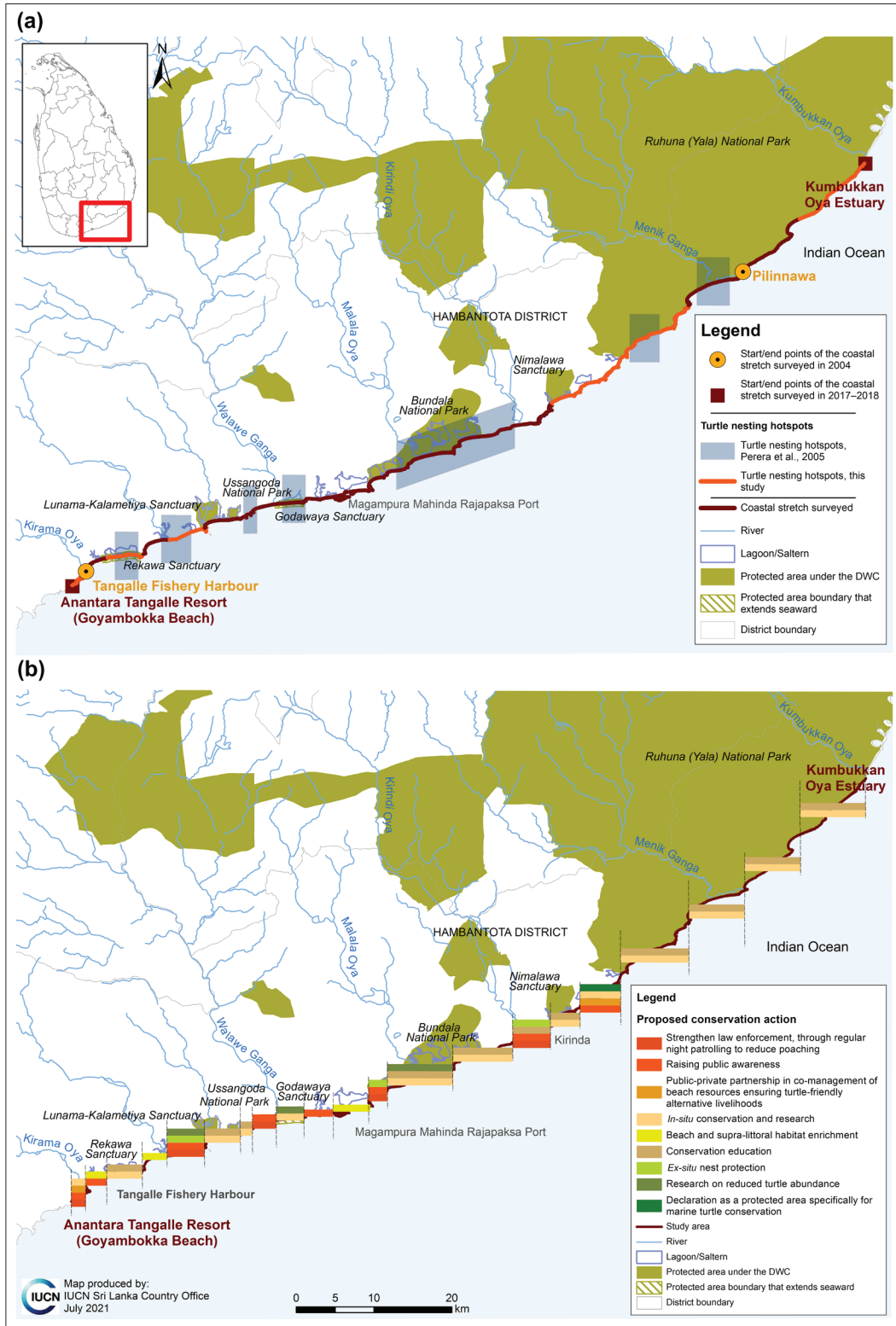


Figure 4: (a) Turtle nesting hotspots identified in Perera *et al.* 2005 and this study, and (b) marine turtle nesting habitat conservation recommendations based on results of this study.

Two additional nesting habitat suitability hotspots reported with high nesting turtle abundance in the 2004 survey indicated a lowered nesting score during the current study. These are Bundala and Koholankala-Malala beaches in Bundala NP. These have also been identified as suitable nesting habitats by MaxEnt models because historical records identify these locations as turtle nesting areas. However, even with historical turtle nesting presence in the MaxEnt dataset, the Godawaya Sanctuary has not been predicted for high suitability for turtle nesting, while the observed turtle nesting abundance in the present survey has indicated a marked reduction of nesting turtles in the Godawaya beach, indicating a need for further investigation of the underlying causes. Similarly, highly reduced turtle nesting identified in Bundala and Koholankala-Malala beaches in Bundala NP may be due to increased levels of human-induced threats.

Two other MaxEnt habitat suitability congruent hotspots are not supported by the current nesting turtle abundance nor from the 2004 survey. These are Rekawa East-Wellodaya, and Lunama-Kalameitiya Sanctuary. This could be explained by sub-tidal habitat conditions that may prevent nesting turtles from coming ashore, indicating that turtles do not use all beaches with high predicted suitability based on the habitat variables used here. This may be due to other unknown variables, especially in adjacent sub-tidal habitats, including ocean currents and availability of daytime feeding grounds.

Changes in turtle hotspots since 2004

The study reveals an overall decline in the marine turtle nesting abundance in the south-eastern coastline of Sri Lanka (Supplementary Table 2). Many beaches with “uncommon” or even “common” turtle abundance in 2004 have now declined to “rare” occurrences. The result of declining turtle abundance indicated by the derived index of abundance remains important for conservation planning. Hence, a confirmation of the declines in absolute numbers using a systematic year-round survey—focusing on turtle nesting abundance and the causes for such declines—is recommended.

A comparison of turtle nesting hotspots identified in the 2004 and 2017–2018 surveys provide important insights into changes that have occurred during that period in turtle nesting preferences. In both surveys, three coastal stretches have recurred as turtle nesting hotspots. These are Rekawa Sanctuary, Kahandamodara and the stretch from Gode Kalapuwa, Mahaseelawa-Butawa to Patanangala in Yala NP, which confirms their excellent

status of nesting habitats (Figure 4). In addition, four new turtle nesting hotspots have been documented in Tangalle from Anantara Resort at Goyambokka beach to the Tangalle headland, Nimalawa Sanctuary, Palatupana, and the stretch from Mihirawa to Kumbukkan Oya estuary in Yala NP (Figure 4). In this study, the extension of the study area has resulted in identifying two new turtle nesting hotspots.

Nevertheless, four turtle nesting hotspots recorded during the 2004 survey were not identified in this study. These hotspots are Ussangoda to Welipatanwila, Godawaya, Koholankala to Kirindi Oya estuary in Bundala NP, and Patanangala to Pilinnawa, especially Gonalehebbu to Kalliya Kalapuwa section in Yala NP (Figure 4). This also suggests that further studies are needed to ascertain the cause of such decline, as well as to identify remedial actions.

Threats to nesting marine turtles in each coastal stretch

Of the 18 threats stated in the Materials and Methods section, the main threats were poaching of eggs, egg predation by feral and wild animals, human traffic, beach pollution, illegal constructions on the beach, clearance of beach vegetation, and artificial beach illumination during the night. Two of the above, i.e., illegal constructions on the beach and clearance of beach vegetation, were confirmed also by Jackknife values for turtle nesting habitat suitability modelling.

Poaching of eggs was commonly seen in areas with human settlements, especially around permanent fishing villages or temporary fishing huts. Most of these poached egg holes also showed signs of predation of any remaining eggs by feral dogs. The results of this study revealed that wild boar is the main egg predator in natural areas such as Bundala NP, Nimalawa Sanctuary, forested areas in Palatupana, and within the Yala NP. However, inside Nimalawa Sanctuary and Yala NP, the threat of egg predation by wild boar is less because their population is controlled by leopards (Kittle *et al.*, 2017). In Bundala NP, which lacks leopards (Bambaradeniya *et al.*, 2002), the wild boar population may have increased and their predation on turtle eggs is, therefore, higher. Threats due to other animals such as water monitors, crocodiles, and birds of prey were also occasionally recorded.

Coastal armouring has been known to disturb the nesting habitats of marine turtles (Choi & Eckert, 2009; Witherton *et al.*, 2011; Lopez *et al.*, 2015). The only coastal armour found within the study area was

revetments, observed in the beach stretches such as Tangalle, Medilla, Kahandamodara, Hambantota, and from Bundala village to Kirinda. However, beach armouring is unlikely to have a significant impact on nesting turtles along the south-eastern coast of Sri Lanka.

Beach pollution was high and was observed in most stretches and this could deter turtles from visiting these areas for nesting. This pollution is mainly caused by fishing-related garbage in the Tangalle and Kirinda fishery harbours, household garbage in the west bank of the Walawe estuary and the beach bordering Hambantota town, and accumulated plastic waste washed ashore by marine pollution in the Attulla Lagoon mouth area of the Nimalawa Sanctuary (transect 311 to 313) and the eastern end of Gode Kalapuwa (transect 351 to 352).

Light disturbance was also very high in Tangalle due to hotels and guest houses bordering the coastline and fishery harbour, and also in the beach bordering Hambantota town and the Kirinda fishery harbour.

Spread of invasive alien species on nesting beaches has also been identified as a threat to nesting sea turtles (Pagad *et al.*, 2013). *Opuntia dillenii* was observed spreading widely at the Walawe estuary, Godawaya Sanctuary, the beach bordering the Hambantota saltern, Koholankala Lagoon and the Malala fish landing site.

The intensity of incidental by-catch of marine turtles in fishing gear is severely underestimated in this survey, as the estimation is based purely on information collected on the beach and the assessment periods may not have coincided with peak fishing activities. Most of the by-catch of marine turtles in fishing gear were recorded from the areas where there are major fishery harbours (*e.g.*, Tangalle, Kalametiya and Welipatanwila).

The overall threat to nesting turtles is high in the beach stretches in Tangalle from Anantara Resort at Goyambokka beach to Tangalle fishery harbour, Tangalle to Medilla, Hambantota, and the beach stretch from Bundala village to Kirinda (Figure 2; supplementary Figure 1).

Changes of threats to nesting turtles since 2004

Increased levels of threats were observed to marine turtles, especially in areas outside the protected areas further emphasizing the need to declare and maintain protected areas. Night patrolling by DWC officers is necessary in beach stretches where considerable nesting

abundance coincided with higher levels of threat. These beach stretches are Tangalle, Tangalle to Medilla, Kahandamodara, Hambantota, Bundala in Bundala NP, Bundala village to Kirinda, Nimalawa Sanctuary and Palatupana (Figure 2; supplementary Figure 1).

Among the specific threats to marine turtle nesting habitat that have reduced markedly during the period from 2004 to 2017–2018 are coral and sand mining for building construction. This may be due to effective law enforcement and increased levels of awareness during the recent past.

Summary of comparison between the 2004 and 2017–2018 studies

Supplementary Table 5 summarizes the changes in nesting habitat quality, nesting abundance, and the threats faced by marine turtles in each beach stretch studied in 2004 and 2017–2018. Comparative results suggest an overall decrease of the nesting habitat quality and nesting turtle abundance. Specific beach stretches where there are conspicuous changes have been highlighted in grey, together with turtle conservation actions recommended for each beach stretch (see Figure 4b).

CONCLUSIONS

Perera *et al.* (2005) identified two important stretches of beaches that needed immediate protection to ensure the retention of a high abundance of nesting turtles. These two stretches were Rekawa, mainly for the olive ridley and green turtles, and Godawaya, mainly for leatherback turtles. Their results and recommendations led to the establishment of two sanctuaries, *i.e.*, Rekawa and Godawaya, for nesting turtle conservation, under the jurisdiction of the DWC (Government of Sri Lanka, 2006). In 2004, Rekawa recorded decreasing nesting turtle abundance, but has now achieved a relative stability. This must be attributed to the protection of the area and active law enforcement by the DWC. In addition, there have been successful community-based turtle conservation and tourism activities in the area. However, in the Godawaya Sanctuary, the stable nesting turtle population dominated by giant leatherback turtles in 2004, has now markedly decreased. This needs further investigation.

Recommendations from the current study

Revisitation of the turtle nesting habitats in the south-eastern coastline of Sri Lanka after 13 years from

the previous study provides data-driven recommendations to sustain the marine turtle nesting in the area. This study showed that the south-eastern coastal belt is still home to seven turtle nesting hotspots for all five species that visit Sri Lanka. Among these, habitat suitability models validated four beach stretches as the most important turtle nesting hotspots. Three of these are within DWC protected areas. The exception is Palatupana beach, which needs formal protection as a sanctuary under the DWC like Rekawa and Godawaya. However, it is recommended that this sanctuary incorporates public-private and inter-agency collaboration, ensuring eco-friendly hotel development. This is especially important, due to increased turtle nesting abundance in this beach. It is the only unprotected beach stretch among the four most important turtle nesting hotspots identified in this study.

Significantly increased levels of threats to these animals, together with decreasing quality of nesting habitats, were recorded in this study. It is essential, therefore, that the nine recommendations for conservation actions made herein for specific coastal stretches be considered by the DWC and incorporated into their management plans. In addition, significant threats identified for habitat suitability for nesting turtles such as coastal construction and clearance of beach vegetation should also be mitigated. Further the identified research gaps should also be addressed.

Acknowledgements

The study was funded by Anantara Peace Haven Tangalle Resort through the project entitled “Conservation of marine turtles and coastal habitats around Anantara Peace Haven Tangalle Resort” and we thank Dilan Bandara (former Resident Manager) and Ross Saunders (former General Manager) for the support extended. Ananda Mallawatantri (former Country Representative) and Shamen Vidanage (former Programme Coordinator) of the Sri Lanka Country Office of IUCN are acknowledged for their guidance. Permission to carry out this study was granted by the DWC through their research permit number WL/3/2/53/17. We thank the following staff of the DWC for the support extended during the survey: N.C.G. Sooriyabandara, (Director General), Manjula Amerarathne (Director Operations), Lukshman Peiris (former Deputy Director, Research and Training), D.P. Siyasinghe (former Park Warden, Yala National Park), R.G.R.S. Ranatunga (former Park Warden, Bundala National Park), Uthpala Adaranga (former Range Officer, Kalamatiya Range), Wijaya Kumara (Range Officer, Hambantota Range) and Asitha Sanjaya

Gunadasa (Range Officer, Nimalawa Range) and the staff who joined the field surveys. Field support for 2017/2018 study by Sanjaya Karunaratne and Sampath Bandara and for the 2004 study by Roshan K. Rodrigo, M.D.C. Asela, V.A. Prasanna Samarawickrema and Kaushalya Wijayaweera as well as the guidance of Channa N.B. Bambaradeniya during the initial assessment are greatly acknowledged. We also thank Sriyanie Miththapala for providing insightful comments on an earlier version of this manuscript.

Conflict of interest statement

The authors disclose that they have no conflicts of interest concerning this article.

REFERENCES

- Abreu-Grobois A & Plotkin P. (2008). *Lepidochelys olivacea*. *The IUCN Red List of Threatened Species 2008*: e.T11534A3292503.
DOI: <https://dx.doi.org/10.2305/IUCN.UK.2008.RLTS.T11534A3292503.en>
- Bambaradeniya C.B.N., Ekanayake S.P., Fernando R.H.S.S., Perera W.P.N. & Somaweera R. (2002). A biodiversity status profile of Bundala National Park- A Ramsar wetland in Sri Lanka. *Occasional Papers of IUCN Sri Lanka*, pp. 37. International Union for Conservation of Nature, Colombo, Sri Lanka. available at <https://www.iucn.org/content/a-biodiversity-status-profile-bundala-national-park-a-ramsar-national-wetland-sri-lanka>, Accessed 14 June 2021.
- Bambaradeniya C.N.B., Perera S. & Samarawickrema P. (2006). A rapid assessment of post-tsunami environmental dynamics in relation to coastal zone rehabilitation and development activities in the Hambantota District of Southern Sri Lanka. *Occasional Papers of IUCN Sri Lanka 10*, pp. iv+27. International Union for Conservation of Nature, Colombo, Sri Lanka.
- Casale P. & Tucker A.D. (2017). *Caretta caretta* (amended version of 2015 assessment). *The IUCN Red List of Threatened Species 2017*: e.T3897A119333622.
DOI: <https://dx.doi.org/10.2305/IUCN.UK.2017-2.RLTS.T3897A119333622.en>
- Choi G-Y. & Eckert K.L. (2009). *Manual of Best Practices for Safeguarding Sea Turtle Nesting Beaches*. WIDECAS Technical Report No. 9. pp 86. Wider Caribbean Sea Turtle Conservation Network, Ballwin, Missouri, USA. Available at https://www.caribbeanhotelandtourism.com/downloads/CAST_TurtleNestingBeaches.pdf, Accessed 12 June 2021.
- Choudhary B.C., Pandav B., Tripathy B. & Andrews H.V. (2003). *Sea Turtle Manual*. Centre for Herpetology/Madras Crocodile Bank Trust, Tamil Nadu, India.
- Convention on International Trade in Endangered Species of Wild Fauna and Flora (CITES) (2021). *Appendices I, II and III*. Available at <https://cites.org/eng/app/appendices.php>,

- Accessed 22 May 2021.
- Convention on the Conservation of Migratory Species of Wild Animals (CMS) (2020). *Appendices I and II of the Convention on the Conservation of Migratory Species of Wild Animals (CMS)*. Available at https://www.cms.int/sites/default/files/basic_page_documents/appendices_cop13_e_0.pdf, Accessed 22 May 2021.
- Ekanayake E.M.L., Ranawana K.B. & Kapurusinghe T. (2001). Estimation of the average number of nests for green turtles on the Rekawa beach in Southern Sri Lanka: Three year study from September 1996 to September 1999. *Proceedings of the Twenty First Annual Symposium on Marine Turtle Biology and Conservation*, Philadelphia, USA.
- Ekanayake E.M.L., Rajakaruna R.S., Kapurusinghe T., Saman M.M., Rathnakumara D.S., Samaraweera P. & Ranawana K.B. (2010). Nesting behavior of the Green Turtle at Kosgoda Rookery, Sri Lanka. *Ceylon Journal of Science (Biological Sciences)* **39**(2): 109–120.
- Ekanayake E.M.L., Kapurusinghe T., Saman M.M. & Premakumara M.G.C. (2002). Estimation of the number of leatherback (*Dermochelys coriacea*) nesting at the Godawaya turtle rookery in Southern Sri Lanka during the nesting season in the year 2001. *Kachhapa. A Newsletter for the Indian Ocean on Sea Turtle Conservation and Management* **6**: 11–12.
- Elith J. (2002). Quantitative methods for modeling species habitat: comparative performance and an application to Australian plants. In: *Quantitative Methods for Conservation Biology* (eds. S. Ferson & M. Burgman), pp. 39–58. Springer-Verlag, New York.
DOI: <https://doi.org/10.1007/b97704>
- Elith J., Phillips S. J., Hastie T., Dudík M., Chee Y. En & Yates C. J. (2011). Statistical explanation of MaxEnt for ecologists. *Diversity and Distributions* **17**(1):43–57.
DOI: <https://doi.org/10.1111/j.1472-4642.2010.00725.x>
- Ellepola G., Harischandra S. & Dhanushka M.G.G. (2014). *In-situ* Sea Turtle Nest Protection Program in Panama - Okanda Coastal Stretch in the East. *Wildlanka* **2**: 163–170.
- ESRI (2012). ArcGIS Desktop Software. Release 10. Environmental Systems Research Institute, Inc. Redlands, CA.
- Fick S.E. & Hijmans R.J. (2017). WorldClim 2: new 1km spatial resolution climate surfaces for global land areas. *International Journal of Climatology* **37**(12): 4302–4315.
- Fuentes M.M.P.B. et al. (12 authors) (2016). Conservation hotspots for marine turtle nesting in the United States based on coastal development. *Ecological Applications* **26**(8): 2708–2719.
DOI: <https://doi.org/10.1002/eap.1386>
- Government of Sri Lanka (2018). Sri Lanka Coastal Zone and Coastal Resource Management Plan – 2018. Gazette Extraordinary No. 2072/58, 2018.05.25.
- Government of Sri Lanka (2006). The Fauna and Flora Protection Ordinance (Chapter 469) Order under Sub-section (4) of Section 2. Gazette Extraordinary No. 1446/27 2006.05.25.
- Hijmans R.J., Cameron S. & Parra J. (2005). WorldClim—Global Climate Data, available at <http://www.worldclim.org/>
- IUCN Sri Lanka (2005). *Marine Turtle Conservation Strategy and Action Plan for Sri Lanka*. pp. 80. Department of Wildlife Conservation, Colombo, Sri Lanka.
- Kapurusinghe T. (1998). Destructive exploitation of natural resources and the decline of the nesting marine turtle population in Rekawa, Sri Lanka. 1993–1996. In: *Biology and Conservation of the Amphibians, Reptiles and their habitats in South Asia. Proceedings of the international Conference on the Biology and Conservation of the Amphibians and Reptiles of South Asia*, Sri Lanka, 1–5 August, 1996, pp. 189–193.
- Kapurusinghe T. (2006). Status of leatherback turtles in Sri Lanka, Indian Ocean – South-East Asian Leatherback Turtle Assessment, IOSEA Marine Turtle MoU – 2006. pp. 131–139.
- Kittle A.M., Watson A.C. & Fernando T.S.P. (2017). The ecology and behaviour of a protected area Sri Lankan leopard (*Panthera pardus kotiya*) population. *Tropical Ecology* **58**(1): 71 – 86.
- Lopez G.G., Salies E. de C., Lara P.H., Tognin F., Marcovaldi M.A. & Serafini T.Z. (2015). Coastal development at sea turtles nesting ground: Efforts to establish a tool for supporting conservation and coastal management in northeastern Brazil. *Ocean & Coastal Management* **116**: 270–276.
DOI: <http://dx.doi.org/10.1016/j.ocecoaman.2015.07.027>
- McCaughey D.J., Pinsky M.L., Palumbi S.R., Estes J.A., Joyce F.H. & Warner R.R. (2015). Marine defaunation: Animal loss in the global ocean. *Science* **347**: 6219.
DOI: <http://dx.doi.org/10.1126/science.1255641>
- Mazaris A.D., Matsinos G. & Pantis J.D. (2009). Evaluating the impacts of coastal squeeze on sea turtle nesting. *Ocean & Coastal Management* **52**:139–145.
- MoMD&E (2016). *National Biodiversity Strategy and Action Plan 2016-2022*, pp. 284. Biodiversity Secretariat, Ministry of Mahaweli Development and Environment, Colombo, Sri Lanka.
- Mortimer J.A & Donnelly M. (2008). *Eretmochelys imbricata*. The IUCN Red List of Threatened Species 2008: e.T8005A12881238.
DOI: <https://dx.doi.org/10.2305/IUCN.UK.2008.RLTS.T8005A12881238.en>
- Ortega-Huerta M.A. & Peterson A.T. (2008). Modeling ecological niches and predicting geographic distributions: A test of six presence-only methods. *Revista Mexicana De Biodiversidad* **79**: 205 – 216.
- Pagad S., Genovesi P. & Scalera R. (2013). *Review of the Impact of Invasive Alien Species on Species Protected under the Convention on Migratory Species (CMS)*. Report for the Convention on the Conservation of Migratory Species of Wild Animals (CMS), United Nations Premises, Bonn, Germany. Available at https://www.cms.int/sites/default/files/document/Inf_10_11_1_Invasive_Alien_Species_full_Report_Eonly.pdf, Accessed 12 June 21.

- Pascoe E.L., Marcantonio M., Caminade C. & Foley J.E. (2019). Modeling potential habitat for *Amblyomma* tick species in California. *Insects* **10**(7): 201.
- Perera M.S.J., Rodrigo R.K., Wijayaweera K., Samarawickrema V.A.P., Asela M.D.C. & Bambaradeniya C.N.B. (2005). *Assessment of Turtle Nesting Habitats from Tangalle to Pilinnawa, together with Rapid Surveys on Sub-Tidal Habitats and Socioeconomic Status of Coastal Communities*. IUCN, Colombo, Sri Lanka, pp.57.
- Perera M.S.J., Bambaradeniya C.N.B., Perera P.G.D.R. & Samarawickrema V.A.M.P.K. (2006). Post-tsunami natural regeneration of coastal vegetation in the Hambantota District in south-eastern Sri Lanka. In: *11th International Forestry and Environment Symposium*. 22–23 December 2006, Kalutara, Sri Lanka, pp. 60.
- Phillips S.J., Dudík M. & Schapire R.E. (2004). A maximum entropy approach to species distribution modeling. In: *Proceedings of the 21st International Conference on Machine Learning*; ACM Press: New York, USA, pp. 655–662.
- Phillips S.J., Anderson R.P. & Schapire R.E. (2006). Maximum entropy modeling of species geographic distributions. *Ecological Modelling* **190**(3–4): 231–259.
- Phillips S.J. & Dudík M. (2008). Modeling of species distributions with Maxent: new extensions and a comprehensive evaluation. *Ecography* **31**: 161–175.
- Phillips S.J., Anderson R.P., Dudík M., Schapire R.E. & Blair M. E. (2017). Opening the black box: an open-source release of Maxent. *Ecography* **40**(7): 887–893.
DOI: <https://doi.org/10.1111/ecog.03049>
- Rajakaruna R.S., Ekanayake E.M.L. & Suraweera P.A.C.N.B. (2018). Sri Lanka. In: *Sea Turtles in the Middle East and South Asia Region: MTSG Annual Regional Report 2018* (eds. A.D. Phillott & A.F. Rees). Draft Report of the IUCN-SSC Marine Turtle Specialist Group, 2018.
- Red List Standards & Petitions Subcommittee (RLS&PS) (1996). *Natator Depressus*. The IUCN Red List of Threatened Species 1996: e.T14363A4435952.
DOI: <https://dx.doi.org/10.2305/IUCN.UK.1996.RLTS.T14363A4435952.en>
- Roberts C.M., McClean C.J., Veron J.E., Hawkins J.P., Allen G.R., McAllister D.E., Mittermeier C.G., Schueler F.W., Spalding M., Wells F. & Vynne C. (2002). Marine biodiversity hotspots and conservation priorities for tropical reefs. *Science* **295**(5558): 1280–1284.
- Rodriguez M., Rodriguez A., Bayer J., Vilaseca F., Girones J. & Mutje P. (2010). Determination of corn stalk fibers' strength through modeling of the mechanical properties of its composites. *BioResources* **5**(4): 2535–2546.
- Seminoff J.A. (2004). *Chelonia mydas*. The IUCN Red List of Threatened Species 2004: e.T4615A11037468.
DOI: <https://dx.doi.org/10.2305/IUCN.UK.2004.RLTS.T4615A11037468.en>
- Shanker K., Choudhary B.C. & Andrews H.V. (2003a). Sea Turtle Conservation: Beach Management and Hatchery Programmes. A GOI-UNDP Project Manual. Centre for Herpetology/Madras Crocodile Bank Trust, Mamallapuram, Tamil Nadu, India.
- Shanker K., Pandav B. & Choudhary B.C. (2003b). Sea Turtle Conservation: Population Census and Monitoring. A GOI-UNDP Project Manual. Centre for Herpetology/Madras Crocodile Bank Trust, Mamallapuram, Tamil Nadu, India.
- Swets J.A. (1988). Measuring the Accuracy of Diagnostic Systems. *Science* **240**(4857): 1285–1293.
DOI: <https://dx.doi.org/10.1126/science.3287615>.
- Wallace B.P., Tiwari M. & Girondot M. (2013). *Dermochelys coriacea*. The IUCN Red List of Threatened Species 2013: e.T6494A43526147.
DOI: <https://dx.doi.org/10.2305/IUCN.UK.2013-2.RLTS.T6494A43526147.en>
- Wallace, B.P. *et al* (32 authors) (2011). Global conservation priorities for marine turtles. *PLoS ONE* **6**(9): e24510. DOI: <https://dx.doi.org/10.1371/journal.pone.0024510>
- Wibbels T. & Bevan E. (2019). *Lepidochelys kempii* (errata version published in 2019). The IUCN Red List of Threatened Species 2019: e.T11533A155057916.
DOI: <https://dx.doi.org/10.2305/IUCN.UK.2019-2.RLTS.T11533A155057916.en>
- Witherington B., Hiram S. & Mosier A. (2011). Sea turtle responses to barriers on their nesting beach. *Journal of Experimental Marine Biology and Ecology* **401**(1–2): 1–6

RESEARCH ARTICLE

Statistics: distribution theory

A new multivariate transmuted family of distributions: theory and application for modelling of daily world COVID-19 cases

JA Darwish¹, LI Al-Turk² and MQ Shahbaz^{2*}

¹ Department of Statistics, College of Science, University of Jeddah, Jeddah, Saudi Arabia.

² Department of Statistics, College of Science, King Abdulaziz University, Jeddah, Saudi Arabia.

Submitted: 19 July 2021; Revised: 14 March 2022; Accepted: 27 May 2022

Abstract: Multivariate distributions are helpful in the simultaneous modeling of several dependent random variables. The development of a unique multivariate distribution has been a difficult task and different multivariate versions of the same distribution are available. The need is, therefore, to suggest a method of obtaining a multivariate distribution from the univariate marginals. In this paper, we have proposed a new method of generating the multivariate families of distributions when information on univariate marginals is available. Specifically, we have proposed a multivariate family of distributions which provides a univariate transmuted family of distributions as marginal. The proposed family is a re-parameterization of the Cambanis (1977) family. Some properties of the proposed family of distributions have been studied. These properties include marginal and joint marginal distributions, conditional distributions, and marginal and conditional moments. We have also obtained the dependence measures alongside the maximum likelihood estimation of the parameters. The proposed multivariate family of distributions is studied for the Weibull baseline distributions giving rise to the multivariate transmuted Weibull (MTW) distribution. Real data application of the proposed *MTW* distribution is given in the context of modeling the daily COVID-19 cases of the World. It is observed that the proposed *MTW* distribution is a suitable fit for the joint modeling of the COVID-19 data.

Keywords: Dependence functions, maximum likelihood estimation, multivariate $T-X$ family of distributions, transmuted distributions, Weibull distribution.

INTRODUCTION


Probability distributions have been widely used in several areas of life. Certain situations arise where

the standard probability models are not capable of capturing complex behaviour of the data and hence some extensions are required. Numerous methods are available in the literature to extend any baseline distribution. One such method of extending the univariate distribution is the transmuted family of distributions proposed by Shaw and Buckley (2007). The cumulative distribution function (cdf) of the transmuted family of distributions is

$$F(x) = G(x)[1 + \lambda - \lambda G(x)]; -1 \leq \lambda \leq 1$$

where $G(x)$ is the *cdf* of any baseline distribution and λ is the transmutation parameter. The transmuted family of distributions is useful to obtain the transmuted version of any baseline distribution such that the resulting distribution has much wider applicability as compared with the baseline distribution. More details about the transmuted distributions can be found in Rahman *et al.* (2020).

The transmuted family of distribution can be obtained as a member of the $T-X$ family of distributions proposed by Alzaatreh *et al.* (2013). The transmuted family of distributions has been studied by several authors for different baseline distributions. Some examples include the transmuted-G family of distributions by Nofal *et al.* (2016), the Kumaraswamy transmuted-G family of distributions by Afify *et al.* (2016), the beta transmuted-H family by Afify *et al.* (2017) and the T-transmuted X family of distributions by Jayakumar and Babu (2017). A comprehensive review of developments in transmuted distributions has been given in Rahman *et al.* (2020).

* Corresponding author (qshahbaz@gmail.com;  <https://orcid.org/0000-0002-0695-1216>)



The development in the area of bivariate and multivariate families of distributions is relatively challenging and not many methods are available to obtain the bivariate or multivariate distribution from the given marginals. A classical method to obtain the bivariate distribution, from the given univariate marginals, has been proposed by Gumbel (1960) as is known as the Gumbel bivariate distribution. The joint *cdf* of the Gumbel bivariate distribution is

$$F(x, y) = G(x)G(y)[1 + \gamma\{1 - G(x)\}\{1 - G(y)\}] ;$$

$$0 \leq \gamma \leq 1$$

where $G(x)$ and $G(y)$ are any marginal *cdf*'s and γ is an association parameter. This family has been studied by various authors. For example, the bivariate Kumaraswamy distribution has been studied by Barreto-Souza and Lemonte (2013) and the bivariate Pareto distributions by Sankaran *et al.* (2014) among others. Recently, Sarabia *et al.* (2014) have extended the *Beta - G* family of distributions to the bivariate case by using bivariate beta distribution as baseline distribution. Darwish *et al.* (2021) have used the bivariate *T-X* family of distributions to propose a new bivariate transmuted family of distributions. The proposed family can be used with any baseline distribution. This family has opened the door for development of new bivariate distributions by using any baseline distributions.

Various complex situations arise where the joint modeling of several variables is required and in such cases the multivariate distributions are required. The multivariate families of distributions have not been investigated. Some common multivariate distributions include generalization of the power exponential family of distributions, by Gomez *et al.* (1998) and family of multivariate generalized *t* distributions by Arslan (2004). The main aim of this study is to propose a new family of distributions which generate a multivariate distribution from the given marginals. The proposed family will be named as the *multivariate transmuted family of distributions*. This new family will be suitable for any baseline distributions and will be useful in modelling joint and complex phenomena.

MATERIALS AND METHODS

The methodology in this paper is primarily based upon the transmuted distributions and the *T-X* family of distributions. The transmuted distributions are briefly discussed in the introduction. The *T-X* family of distributions has been proposed by Alzaatreh *et al.* (2013). The *cdf* of the proposed family is

$$F_{T-X}(x) = \int_a^{W[G(x)]} r(t) dt = R[W\{G(x)\}], x \in \mathfrak{R},$$

..(1)

where $r(t)$ is any probability distribution defined over $[a, b]$, $W[G(x)]$ is any differentiable function of $G(x)$ such that $W(0) \rightarrow a$ and $W(1) \rightarrow b$. The probability density function (*pdf*) corresponding to (1) is

$$f_{T-X}(x) = \left[\frac{d}{dx} W\{G(x)\} \right] r[W\{G(x)\}], x \in \mathfrak{R}.$$

The *T-X* family of distributions can be used to propose a new distribution by using a suitable $r(t)$.

The transmuted family of distributions, proposed by Shaw and Buckley (2007), can be obtained from the *T-X* family of distributions by using a suitable $r(t)$ with support on $[0, 1]$ in (1) and $W[G(x)] = G(x)$. Alizadeh *et al.* (2017) have shown that the transmuted family of distribution can be obtained by using $r(t) = 1 + \lambda - 2\lambda t$ in (1).

In this paper, we focus on extending the transmuted family of distributions to the multivariate case. It is, therefore, suitable to present the bivariate *T-X* family of distributions and then extend it to propose a new multivariate transmuted family of distributions. The *cdf* of the bivariate *T-X* family of distributions is

$$F_{X_1, X_2}(x_1, x_2) = \int_{a_2}^{W[G_2(x_2)]} \int_{a_1}^{W[G_1(x_1)]} r(u_1, u_2) du_1 du_2,$$

... (2)

with the usual properties of $W[G(x_1)]$, and $W[G(x_2)]$ and $r(u_1, u_2)$ is any bivariate distribution with suitable support for random variables U_1 and U_2 .

The multivariate extension of (2) is immediately written as

$$F_{\mathbf{x}}(\mathbf{x}) = \int_{a_p}^{W[G_p(x_p)]} \dots \int_{a_1}^{W[G_1(x_1)]} r(u_1, u_2, \dots, u_p) du_1 \dots du_p,$$

... (3)

where $\mathbf{x} = (X_1, X_2, \dots, X_p)$ is a p -vector of random variables and $r(u_1, u_2, \dots, u_p)$ is any p -variate density function with support over $[a_1, b_1] \times \dots \times [a_p, b_p]$.

A simpler version of (3) is obtained when the random vector $\mathbf{u} = (u_1, u_2, \dots, u_p)$ has support over $[0, 1]^p$ and is given as

$$F_{\mathbf{x}}(\mathbf{x}) = \int_0^{G_p^{\phi_p}(x_p)} \dots \int_0^{G_1^{\phi_1}(x_1)} r(u_1, u_2, \dots, u_p) du_1 \dots du_p, \quad \dots(4)$$

where $(\phi_1, \phi_2, \dots, \phi_p) > 0$.

RESULTS AND DISCUSSION

In this section, a new multivariate family of distributions has been proposed which provides the univariate transmuted family of distributions as marginals. The properties of the proposed families are studied. The new multivariate family of distributions is proposed in the following sub-section.

A new multivariate family of distributions

In this subsection, a new multivariate family of distributions has been proposed. This multivariate family has been proposed by using (4) with a suitable choice of $r(u_1, u_2, \dots, u_p)$. The *cdf* of the multivariate transmuted family of distributions can be obtained by using

$$r(u_1, u_2, \dots, u_p) = 1 + \sum_{i=1}^p \lambda_i (1 - 2u_i) + \lambda_{p+1} \left(p - 2 \sum_{i=1}^p u_i \right),$$

and $\phi_1 = \phi_2 = \dots = \phi_p = 1$ in (4) and is given as

$$F_{\mathbf{x}}(\mathbf{x}) = \int_0^{G_p(x_p)} \dots \int_0^{G_1(x_1)} \left[1 + \sum_{i=1}^p \lambda_i (1 - 2u_i) + \lambda_{p+1} \left(p - 2 \sum_{i=1}^p u_i \right) \right] du_1 \dots du_p.$$

Solving the above multiple integral, the *cdf* of multivariate family of distributions is

$$F_{\mathbf{x}}(\mathbf{x}) = \left\{ \prod_{i=1}^p G_i(x_i) \right\} \left[1 + \sum_{i=1}^p (\lambda_i + \lambda_{p+1}) \{1 - G_i(x_i)\} \right]; \quad \mathbf{x} \in \mathfrak{R}^p, \quad \dots(5)$$

where $G_i(x_i)$ is the marginal *cdf* of the *i*th random variable X_i , and $(\lambda_1, \lambda_2, \dots, \lambda_p, \lambda_{p+1})$ are transmutation parameters such that $(\lambda_i + \lambda_{p+1}) \in [-1, 1]$ for $i = 1, 2, \dots, p$ and $-1 \leq \sum_{i=1}^p \lambda_i + p\lambda_{p+1} \leq 1$. The proposed family will be named as the multivariate transmuted family of distributions and is a re-parameterization of the Cambanis (1977) family.

The density function corresponding to (5) is

$$f_{\mathbf{x}}(\mathbf{x}) = \left\{ \prod_{i=1}^p g_i(x_i) \right\} \left[1 + \sum_{i=1}^p (\lambda_i + \lambda_{p+1}) \{1 - 2G_i(x_i)\} \right]; \quad \mathbf{x} \in \mathfrak{R}^p, \quad \dots(6)$$

where $g_i(x_i)$ is density function corresponding to $G_i(x_i)$. It is to be noted that the transmuted family of distributions, proposed by Shaw and Buckley (2007), turns out to be a special case of (5) for $p = 1$ and $\lambda_{p+1} = 0$. The bivariate transmuted family of distributions, proposed by Darwish *et al.* (2021), appears as special case of (5) for $p = 2$.

The proposed multivariate transmuted family of distributions can be used to obtain multivariate distributions from the univariate marginals. In the following section, we will give some properties of the new proposed multivariate transmuted family of distributions.

Properties of the multivariate transmuted family of distributions

This sub-section contains some important properties of the proposed multivariate family of distributions. These include the marginal distributions, conditional distributions, conditional moments and multivariate dependence measures. We will also give an estimation of the unknown model parameters.

The marginal distributions

In this subsection, we will obtain the univariate marginal distribution of a single variable, the bivariate marginal distributions of two random variables and the joint marginal distribution of a subset. The marginal distribution function of *i*th variable is obtained as

$$F_{X_i}(x_i) = G_i(x_i) \left[1 + (\lambda_i + \lambda_{p+1}) \{1 - G_i(x_i)\} \right]; \quad x_i \in \mathfrak{R}, \quad \dots(7)$$

which is a transmuted family of distribution with transmutation parameter $\lambda_i + \lambda_{p+1}$. The marginal density function of *i*th random variable is immediately written as

$$f_{X_i}(x_i) = g_i(x_i) \left[1 + (\lambda_i + \lambda_{p+1}) \{1 - 2G_i(x_i)\} \right]; \quad x_i \in \mathfrak{R}, \quad \dots(8)$$

where $g_i(x_i)$ is the density function of i th random variable. The joint marginal distribution of two random variables (X_i, X_m) is obtained by using $G_j(x_j) = 1$, for $j = 1, 2, \dots, p; j \neq (i, m)$ in (5) and is given as

$$F_{X_i, X_m}(x_i, x_m) = G_i(x_i)G_m(x_m) \left[1 + (\lambda_i + \lambda_{p+1}) \{1 - G_i(x_i)\} + (\lambda_m + \lambda_{p+1}) \{1 - G_m(x_m)\} \right], \quad \dots(9)$$

for $(x_i, x_m) \in \mathbb{R}^2$ with $G_i(x_i)$ and $G_m(x_m)$ being the *cdf*s of i th and m th random variables. The joint *cdf*, given in (9) is same as given in Darwish et al. (2021). The joint bivariate density function of two random variables is

$$f_{X_i, X_m}(x_i, x_m) = g_i(x_i)g_m(x_m) \left[1 + (\lambda_i + \lambda_{p+1}) \{1 - 2G_i(x_i)\} + (\lambda_m + \lambda_{p+1}) \{1 - 2G_m(x_m)\} \right] \quad \dots(10)$$

The joint marginal distribution of a subset of variables, say $\mathbf{x}_1 = (X_1, X_2, \dots, X_t)$, is given as

$$f_{\mathbf{x}_1}(\mathbf{x}_1) = \left\{ \prod_{i=1}^t g_i(x_i) \right\} \left[1 + \sum_{i=1}^t (\lambda_i + \lambda_{p+1}) \{1 - 2G_i(x_i)\} \right]; \mathbf{x}_1 \in \mathfrak{R}^t, \quad \dots(11)$$

which is also a multivariate transmuted family of distribution.

Conditional distributions

We can study several conditional distributions in case of a multivariate distribution and in the following we have obtained some conditional distributions for the multivariate transmuted family of distributions. The conditional density function of a single variable for given information of the other variables is defined as

$$f(x_i | \mathbf{x}_{(i)}) = \frac{f(x_i, \mathbf{x}_{(i)})}{f(\mathbf{x}_{(i)})},$$

where $\mathbf{x}_{(i)} = (X_1, \dots, X_{i-1}, X_{i+1}, \dots, X_p)$. The conditional distribution of X_i given the information of all other variables for the multivariate transmuted distribution is

$$f(x_i | \mathbf{x}_{(i)}) = \frac{g_i(x_i)}{\Delta_i(\mathbf{x}_{(i)})} \left[1 + \sum_{i=1}^p (\lambda_i + \lambda_{p+1}) \{1 - 2G_i(x_i)\} \right]; x_i \in \mathfrak{R}; \mathbf{x}_{(i)} \in \mathfrak{R}^{p-1}, \quad \dots(12)$$

$$\text{where } \Delta_i(\mathbf{x}_{(i)}) = \left[1 + \sum_{j \neq i=1}^p (\lambda_j + \lambda_{p+1}) \{1 - 2G_j(x_j)\} \right].$$

The joint conditional distribution of two random variables X_i and X_m given the information of other variables is obtained by using

$$f(x_i, x_m | \mathbf{x}_{(i,m)}) = \frac{f(x_i, x_m, \mathbf{x}_{(i,m)})}{f(\mathbf{x}_{(i,m)})},$$

where $\mathbf{x}_{(i,m)} = (X_1, \dots, X_{i-1}, X_{i+1}, \dots, X_{m-1}, X_{m+1}, \dots, X_p)$. The joint conditional distribution of two random variables for a multivariate transmuted family of distributions is

$$f(x_i, x_m | \mathbf{x}_{(i,m)}) = \frac{g_i(x_i)g_m(x_m)}{\Delta_{i,m}(\mathbf{x}_{(i,m)})} \left[1 + \sum_{i=1}^p (\lambda_i + \lambda_{p+1}) \{1 - 2G_i(x_i)\} \right], \quad \dots(13)$$

where $(x_i, x_m) \in \mathfrak{R}^2, \mathbf{x}_{(i,m)} \in \mathfrak{R}^{p-2}$ and

$$\Delta_{i,m}(\mathbf{x}_{(i,m)}) = \left[1 + \sum_{j \neq (i,m)=1}^p (\lambda_j + \lambda_{p+1}) \{1 - 2G_j(x_j)\} \right].$$

Proceeding in a similar way, it is easy to show that the conditional density function of an one subset of variables, say \mathbf{x}_1 , given the information of an other set of variables, say \mathbf{x}_2 , in multivariate transmuted family of distribution is given as

$$f(\mathbf{x}_1 | \mathbf{x}_2) = \frac{1}{\Delta_t(\mathbf{x}_2)} \prod_{i=1}^t g_i(x_i) \left[1 + \sum_{i=1}^p (\lambda_i + \lambda_{p+1}) \{1 - 2G_i(x_i)\} \right]; \mathbf{x}_1 \in \mathfrak{R}^t; \mathbf{x}_2 \in \mathfrak{R}^{p-t} \quad \dots(14)$$

$$\text{where } \Delta_t(\mathbf{x}_2) = \left[1 + \sum_{j=t+1}^p (\lambda_j + \lambda_{p+1}) \{1 - 2G_j(x_j)\} \right].$$

The conditional distributions can be studied for any baseline distributions and can be used to compute the conditional moments which are given in the following subsection.

Conditional moments

The single and product moments for univariate and bivariate transmuted family of distributions can be found on the lines given in Darwish et al. (2021). We can also obtain various conditional moments by using the multivariate transmuted family of distributions. The r th conditional moment of X_i given the information of other variables for multivariate transmuted family of distributions is obtained by using

$$\mu_{X_i | \mathbf{x}_{(i)}}^r = \int_{-\infty}^{\infty} x_i^r f(x_i | \mathbf{x}_{(i)}) dx_i,$$

which for the conditional distribution in (12) is

$$\mu_{X_i|\mathbf{x}_{(i)}}^r = \frac{1}{\Delta_i(\mathbf{x}_{(i)})} \int_{-\infty}^{\infty} x_i^r g_i(x_i) \left[1 + \sum_{j=1}^p (\lambda_j + \lambda_{p+1}) \right.$$

$$\left. \{1 - 2G_j(x_i)\} \right] dx_i,$$

and on simplification we have

$$\mu_{X_i|\mathbf{x}_{(i)}}^r = \frac{1}{\Delta_i(\mathbf{x}_{(i)})} \left[\beta \mu_{x_i}^r - 2 \mu_{x_i}^r \sum_{j \neq i=1}^p (\lambda_j + \lambda_{p+1}) G_j(x_j) - (\lambda_i + \lambda_{p+1}) \mu_{x_i(2;2)}^r \right], \quad \dots(15)$$

where $\beta = 1 + \sum_{i=1}^p \lambda_i + p\lambda_{p+1}$, $\mu_{x_i}^r$ is r th raw moment of X_i and $\mu_{x_i(2;2)}^r$ is r th moment of larger observation in a sample of size 2 from $G_i(x_i)$.

The joint conditional moment of X_i and X_m given the information of other variables is obtained by using

$$\mu_{X_i, X_m|\mathbf{x}_{(i,m)}}^{r,s} = \int_{-\infty}^{\infty} \int_{-\infty}^{\infty} x_i^r x_m^s f(x_i, x_m | \mathbf{x}_{(i,m)}) dx_i dx_m.$$

Using the joint conditional distribution of X_i and X_m from (13), we have

$$\mu_{X_i, X_m|\mathbf{x}_{(i,m)}}^{r,s} = \frac{1}{\Delta_{i,m}(\mathbf{x}_{(i,m)})} \int_{-\infty}^{\infty} \int_{-\infty}^{\infty} x_i^r x_m^s g_i(x_i) g_m(x_m)$$

$\left[1 + \sum_{i=1}^p (\lambda_i + \lambda_{p+1}) \{1 - 2G_i(x_i)\} \right] dx_i dx_m$. the above integral, the joint conditional moment of X_i and X_m given the information of other variables is

$$\begin{aligned} \mu_{X_i, X_m|\mathbf{x}_{(i,m)}}^{r,s} &= \frac{1}{\Delta_{i,m}(\mathbf{x}_{(i,m)})} \left[\beta \mu_{x_i}^r \mu_{x_m}^s - 2 \mu_{x_i}^r \mu_{x_m}^s \sum_{j \neq (i,m)=1}^p (\lambda_j + \lambda_{p+1}) G_j(x_j) - (\lambda_i + \lambda_{p+1}) \right. \\ &\quad \left. \times \mu_{x_i(2;2)}^r \mu_{x_m}^s - (\lambda_m + \lambda_{p+1}) \mu_{x_i}^r \mu_{x_m(2;2)}^s \right], \quad \dots(16) \end{aligned}$$

where $\Delta_{i,m}(\mathbf{x}_{(i,m)})$ and β are defined above. The conditional mean vector and conditional covariance matrix can be obtained from (15) and (16).

Multivariate dependence measures

The dependence among random variables is an important measure to study the relationship between the variables. In this subsection, we will obtain three important dependence measures for the multivariate transmuted family of distributions. These dependence measures include Kendall's multivariate coefficient of concordance, the multivariate local dependence function, and the multivariate version of Spearman's Rho. The results for the dependence measures are derived below.

The multivariate Kendall's Tau coefficient for joint continuous random variables, defined by Taylor (2016), is computed by using

$$\begin{aligned} \tau_p &= \frac{2^p}{2^{p-1} - 1} \int_{-\infty}^{\infty} \dots \int_{-\infty}^{\infty} F_{\mathbf{x}}(\mathbf{x}) f_{\mathbf{x}}(\mathbf{x}) dx_1 \dots dx_p - \frac{1}{2^{p-1} - 1} \\ &= \frac{2^p}{2^{p-1} - 1} I_K - \frac{1}{2^{p-1} - 1}, \quad \dots(17) \end{aligned}$$

where

$$I_K = \int_{-\infty}^{\infty} \dots \int_{-\infty}^{\infty} F_{\mathbf{x}}(\mathbf{x}) f_{\mathbf{x}}(\mathbf{x}) dx_1 \dots dx_p.$$

Now, using (5) and (6) in above equation, we have

$$\begin{aligned} I_K &= \int_{-\infty}^{\infty} \dots \int_{-\infty}^{\infty} \left\{ \prod_{i=1}^p G_i(x_i) \right\} \left[1 + \sum_{i=1}^p (\lambda_i + \lambda_{p+1}) \{1 - G_i(x_i)\} \right] \\ &\quad \times \left\{ \prod_{i=1}^p g_i(x_i) \right\} \left[1 + \sum_{i=1}^p (\lambda_i + \lambda_{p+1}) \{1 - 2G_i(x_i)\} \right] dx_1 \dots dx_p. \end{aligned}$$

Writing $\delta_i = \lambda_i + \lambda_{p+1}$, and making the transformation $G_i(x_i) = u_i$, we have

$$\begin{aligned} I_K &= \int_0^1 \dots \int_0^1 \left(\prod_{i=1}^p u_i \right) \left[1 + \sum_{i=1}^p \delta_i (1 - u_i) \right] \\ &\quad \left[1 + \sum_{i=1}^p \delta_i (1 - 2u_i) \right] du_1 \dots du_p. \end{aligned}$$

Solving the multiple integral, we have

$$\begin{aligned} I_K &= \frac{1}{2^p} \left(1 - \frac{2}{9} \sum_{i=1}^p \sum_{k=i+1}^p \delta_i \delta_k \right) \\ &= \frac{1}{2^p} \left[1 - \frac{2}{9} \sum_{i=1}^p \sum_{k=i+1}^p (\lambda_i + \lambda_{p+1}) (\lambda_k + \lambda_{p+1}) \right]. \end{aligned}$$

Using the value of I_K in (17) Kendall's multivariate coefficient of association for a multivariate transmuted family of distributions is

$$\tau_p = -\frac{2}{9(2^{p-1} - 1)} \sum_{i=1}^p \sum_{k>i}^p (\lambda_i + \lambda_{p+1})(\lambda_k + \lambda_{p+1}). \dots(18)$$

It can be seen that, for $p = 2$, (18) reduces to the Kendall's coefficient of association for bivariate transmuted family of distribution given by Darwish *et al.* (2021).

Again, the Spearman Rho for a multivariate distribution is defined by Schmid and Schmidt (2007) as

$$\rho_p = \frac{2^p(p+1)}{2^p - (p+1)} \int_{-\infty}^{\infty} \dots \int_{-\infty}^{\infty} F_{\mathbf{x}}(\mathbf{x}) \prod_{i=1}^p f_i(x_i) dx_1 \dots dx_p - \frac{(p+1)}{2^p - (p+1)} = \frac{2^p(p+1)}{2^p - (p+1)} I_S - \frac{(p+1)}{2^p - (p+1)}, \dots(19)$$

where $I_S = \int_{-\infty}^{\infty} \dots \int_{-\infty}^{\infty} F_{\mathbf{x}}(\mathbf{x}) \prod_{i=1}^p f_i(x_i) dx_1 \dots dx_p$.

Now using the joint density function of multivariate transmuted family of distributions, from (5), and marginal density function of a single random variable, from (8), in above equation we have

$$I_S = \int_{-\infty}^{\infty} \dots \int_{-\infty}^{\infty} \left\{ \prod_{i=1}^p G_i(x_i) \right\} \left[1 + \sum_{i=1}^p (\lambda_i + \lambda_{p+1}) \{1 - G_i(x_i)\} \right] \times \prod_{i=1}^p [g_i(x_i) \{1 + (\lambda_i + \lambda_{p+1}) [1 - 2G_i(x_i)]\}] dx_1 \dots dx_p.$$

Writing $\delta_i = \lambda_i + \lambda_{p+1}$, and making the transformation $G_i(x_i) = u_i$, we have

$$I_S = \int_0^1 \dots \int_0^1 \left(\prod_{i=1}^p u_i \right) \left[1 + \sum_{i=1}^p \delta_i (1 - u_i) \right] \left[\prod_{i=1}^p \{1 + \delta_i (1 - 2u_i)\} \right] du_1 \dots du_p.$$

Solving the multiple integral, we have

$$I_S = \frac{1}{6^p} \left[\prod_{i=1}^p (3 - \delta_i) + \sum_{i=1}^p \left\{ \delta_i \prod_{j \neq i}^p (3 - \delta_j) \right\} \right] = \frac{1}{6^p} \left[\prod_{i=1}^p (3 - \lambda_i - \lambda_{p+1}) + \sum_{i=1}^p \left\{ (\lambda_i + \lambda_{p+1}) \prod_{j \neq i}^p (3 - \lambda_j - \lambda_{p+1}) \right\} \right].$$

Using this value in (19), we have

$$\rho_p = \frac{(p+1)}{3^p [2^p - (p+1)]} \left[\prod_{i=1}^p (3 - \lambda_i - \lambda_{p+1}) \left\{ 1 + \sum_{i=1}^p \frac{(\lambda_i + \lambda_{p+1})}{(3 - \lambda_i - \lambda_{p+1})} \right\} - 3^p \right] \dots(20)$$

It is easy to see that, for $p = 2$, (20) reduces to the Spearman's coefficient of association for a bivariate transmuted family of distribution given by Darwish *et al.* (2021).

A local dependence function for two absolutely continuous random variables has been defined by Holland and Wang (1987) as

$$\gamma(x_1, x_2) = \frac{\partial^2}{\partial x_1 \partial x_2} \ln f(x_1, x_2).$$

The multivariate extension the above dependence function is immediately written as

$$\gamma(x_1, x_2, \dots, x_p) = \frac{\partial^p}{\partial x_1 \partial x_2 \dots \partial x_p} \ln f(x_1, x_2, \dots, x_p),$$

where $f(x_1, x_2, \dots, x_p)$ is the multivariate density function. The multivariate local dependence function for the multivariate transmuted family of distribution is

$$\gamma(x_1, x_2, \dots, x_p) = -\frac{2^p(p-1)! \prod_{i=1}^p (\lambda_i + \lambda_{p+1}) g_i(x_i)}{\left[1 + \sum_{i=1}^p (\lambda_i + \lambda_p) \{1 - 2G_i(x_i)\} \right]^p} \dots(21)$$

We can see that Kendall’s coefficient of association and Spearman’s Rho remains the same irrespective of the baseline distribution but the multivariate local dependence function involves the density and distribution function of the baseline distribution.

Estimation of parameters

In the following, we will discuss the maximum likelihood estimation of the parameters of multivariate transmuted family of distributions assuming that all the parameters of $G_i(x_i)$ are known for $i = 1, 2, \dots, p$. First, suppose that $\mathbf{x}_1, \mathbf{x}_2, \dots, \mathbf{x}_n$ is a random sample of n vector observations from the multivariate transmuted density function, given in (6). The likelihood function is therefore

$$L = \prod_{j=1}^n \left\{ \prod_{i=1}^p g_i(x_{ij}) \right\} \left[1 + \sum_{i=1}^p (\lambda_i + \lambda_{p+1}) \{1 - 2G_i(x_{ij})\} \right].$$

The log-likelihood function is

$$\ell = \sum_{j=1}^n \sum_{i=1}^p \ln [g_i(x_{ij})] + \sum_{j=1}^n \ln \left[1 + \sum_{i=1}^p (\lambda_i + \lambda_{p+1}) \{1 - 2G_i(x_{ij})\} \right]. \quad \dots(22)$$

The derivatives of log-likelihood function with respect to $\lambda_i ; i = 1, 2, \dots, p+1$ are

$$\frac{\partial \ell}{\partial \lambda_i} = \sum_{j=1}^n \left[\frac{1 - 2G_i(x_{ij})}{1 + \sum_{i=1}^p (\lambda_i + \lambda_{p+1}) \{1 - 2G_i(x_{ij})\}} \right]; i = 1, 2, \dots, p$$

$$\text{and } \frac{\partial \ell}{\partial \lambda_{p+1}} = \sum_{j=1}^n \left[\frac{2 \left[1 - \sum_{i=1}^p G_i(x_{ij}) \right]}{\left[1 + \sum_{i=1}^p (\lambda_i + \lambda_{p+1}) \{1 - 2G_i(x_{ij})\} \right]} \right].$$

The maximum likelihood estimators of $\lambda_i ; i = 1, 2, \dots, p+1$ can be obtained by equating the above derivatives to zero and numerically solving the resulting equations.

The proposed multivariate transmuted family of distributions can be explored for any baseline distributions. In the following section, we will study the multivariate transmuted family of distributions for the baseline Weibull distribution and the resulting distribution is named as multivariate transmuted Weibull distribution.

The multivariate transmuted Weibull distribution

In this sub-section, we have proposed the multivariate transmuted Weibull (MTW) distribution by using the

following density and distribution functions of the Weibull distribution

$$g_i(x_i) = \frac{\alpha_i}{\theta_i^{\alpha_i}} x_i^{\alpha_i-1} e^{-(x_i/\theta_i)^{\alpha_i}} \text{ and } G_i(x_i) = 1 - e^{-(x_i/\theta_i)^{\alpha_i}} ;$$

$$x_i, \theta_i, \alpha_i > 0 \quad \dots(23)$$

in (5). The *cdf* of the proposed *MTW* distribution is

$$F_x(\mathbf{x}) = \left[\prod_{i=1}^p \left\{ 1 - e^{-(x_i/\theta_i)^{\alpha_i}} \right\} \right] \left[1 + \sum_{i=1}^p (\lambda_i + \lambda_{p+1}) e^{-(x_i/\theta_i)^{\alpha_i}} \right]; \mathbf{x}, \alpha, \theta > 0, \quad \dots(24)$$

where

$\mathbf{x} = [X_1 \ X_2 \ \dots \ X_p]^t ; \boldsymbol{\alpha} = [\alpha_1 \ \alpha_2 \ \dots \ \alpha_p]^t$, $\boldsymbol{\theta} = [\theta_1 \ \theta_2 \ \dots \ \theta_p]^t$ and λ_i are transmutation parameters such that $(\lambda_i + \lambda_{p+1}) \in [-1, 1]$ for $i = 1, 2, \dots, p$ and $-1 \leq \sum_{i=1}^p \lambda_i + p\lambda_{p+1} \leq 1$. The density function corresponding to (24) is

$$f_x(\mathbf{x}) = \left[\prod_{i=1}^p \left\{ \frac{\alpha_i}{\theta_i^{\alpha_i}} x_i^{\alpha_i-1} e^{-(x_i/\theta_i)^{\alpha_i}} \right\} \right] \left[1 + \sum_{i=1}^p (\lambda_i + \lambda_{p+1}) \left\{ 2e^{-(x_i/\theta_i)^{\alpha_i}} - 1 \right\} \right]; \mathbf{x}, \alpha, \theta > 0. \quad \dots(25)$$

Some properties of the proposed *MTW* distribution will be studied in the following section.

Properties of multivariate transmuted Weibull distribution

In this sub-section, we will discuss some important properties of the proposed *MTW* distribution. These properties include marginal and conditional distributions and the conditional moments.

The marginal distributions

We have seen above that the marginal distribution of any random variable of multivariate transmuted family of distributions is a transmuted distribution. We have

also seen that the joint marginal distribution of a pair of random variables is a bivariate transmuted distribution, proposed by Darwish *et al.* (2021). Using these results we can readily say that the marginal distribution of any variable X_i in an *MTW* distribution is a transmuted Weibull distribution, proposed by Khan *et al.* (2017), with density

$$f_{X_i}(x_i) = \left[\frac{\alpha_i}{\theta_i^{\alpha_i}} x_i^{\alpha_i-1} e^{-(x_i/\theta_i)^{\alpha_i}} \right] \left[1 + (\lambda_i + \lambda_{p+1}) \left\{ 2e^{-(x_i/\theta_i)^{\alpha_i}} - 1 \right\} \right]; x_i, \theta_i, \alpha_i > 0.$$

The joint marginal distribution of any pair of random variables in an *MTW* distribution is a bivariate transmuted Weibull distribution, proposed by Darwish *et al.* (2021), with joint density function

$$f_{X_i, X_m}(x_i, x_m) = \left[\frac{\alpha_i}{\theta_i^{\alpha_i}} x_i^{\alpha_i-1} e^{-(x_i/\theta_i)^{\alpha_i}} \right] \left[\frac{\alpha_m}{\theta_m^{\alpha_m}} x_m^{\alpha_m-1} e^{-(x_m/\theta_m)^{\alpha_m}} \right] \times \left[1 + (\lambda_i + \lambda_{p+1}) \left\{ 2e^{-(x_i/\theta_i)^{\alpha_i}} - 1 \right\} + (\lambda_m + \lambda_{p+1}) \left\{ 2e^{-(x_m/\theta_m)^{\alpha_m}} - 1 \right\} \right]; x_i, x_m > 0.$$

The marginal distribution of any subset of variables, say $\mathbf{x}_1 = [X_1 \ X_2 \ \dots \ X_t]$, in an *MTW* distribution is again *MTW* with density and distribution functions given as

$$f_{\mathbf{x}_1}(\mathbf{x}_1) = \left[\prod_{i=1}^t \left\{ \frac{\alpha_i}{\theta_i^{\alpha_i}} x_i^{\alpha_i-1} e^{-(x_i/\theta_i)^{\alpha_i}} \right\} \right] \left[1 + \sum_{i=1}^t (\lambda_i + \lambda_{p+1}) \left\{ 2e^{-(x_i/\theta_i)^{\alpha_i}} - 1 \right\} \right]; \mathbf{x}_1, \alpha, \theta > 0, \dots(26)$$

and

$$F_{\mathbf{x}_1}(\mathbf{x}_1) = \left[\prod_{i=1}^t \left\{ 1 - e^{-(x_i/\theta_i)^{\alpha_i}} \right\} \right] \left[1 + \sum_{i=1}^t (\lambda_i + \lambda_{p+1}) e^{-(x_i/\theta_i)^{\alpha_i}} \right]; \mathbf{x}_1, \alpha, \theta > 0. \dots(27)$$

The conditional distributions

The conditional distributions in the case of a multivariate transmuted family of distributions are discussed above. In the following, we will discuss the conditional distributions for the *MTW* distribution.

The conditional distribution of any variable X_i given the information of other variables for a multivariate transmuted family of distributions is given in (12). Now, using the density and distribution functions of the Weibull distribution, the conditional density function of X_i given the other variables is

$$f(x_i | \mathbf{x}_{(i)}) = \frac{1}{\Delta_i(\mathbf{x}_{(i)})} \left[\frac{\alpha_i}{\theta_i^{\alpha_i}} x_i^{\alpha_i-1} e^{-(x_i/\theta_i)^{\alpha_i}} \right], \left[1 + \sum_{i=1}^p (\lambda_i + \lambda_{p+1}) \left\{ 2e^{-(x_i/\theta_i)^{\alpha_i}} - 1 \right\} \right]; x_i > 0 \dots(28)$$

where

$$\Delta_i(\mathbf{x}_{(i)}) = \left[1 + \sum_{j \neq i=1}^p (\lambda_j + \lambda_{p+1}) \left\{ 2e^{-(x_j/\theta_j)^{\alpha_j}} - 1 \right\} \right].$$

The joint conditional distribution of any pair of random variables given the information of other variables for a multivariate transmuted family of distributions is given in (13) which, for the case of the *MTW* distribution, is

$$f(x_i, x_m | \mathbf{x}_{(i,m)}) = \frac{1}{\Delta_{i,m}(\mathbf{x}_{(i,m)})} \left[\frac{\alpha_i}{\theta_i^{\alpha_i}} x_i^{\alpha_i-1} e^{-(x_i/\theta_i)^{\alpha_i}} \right] \left[\frac{\alpha_m}{\theta_m^{\alpha_m}} x_m^{\alpha_m-1} e^{-(x_m/\theta_m)^{\alpha_m}} \right] \times \left[1 + \sum_{i=1}^p (\lambda_i + \lambda_{p+1}) \left\{ 2e^{-(x_i/\theta_i)^{\alpha_i}} - 1 \right\} \right]; (x_i, x_m) > 0, \dots(29)$$

where

$$\Delta_{i,m}(\mathbf{x}_{(i,m)}) = \left[1 + \sum_{j \neq (i,m)=1}^p (\lambda_j + \lambda_{p+1}) \left\{ 2e^{-(x_j/\theta_j)^{\alpha_j}} - 1 \right\} \right].$$

The conditional distribution of one subset of variables given the information of other subset of variables in the case of *MTW* distribution can be obtained by using the density and distribution functions of Weibull random variables in (14) and is given as

$$f(\mathbf{x}_1 | \mathbf{x}_2) = \frac{1}{\Delta_t(\mathbf{x}_2)} \left[\prod_{i=1}^t \left\{ \frac{\alpha_i}{\theta_i^{\alpha_i}} x_i^{\alpha_i-1} e^{-(x_i/\theta_i)^{\alpha_i}} \right\} \right],$$

$$\left[1 + \sum_{i=1}^p (\lambda_i + \lambda_{p+1}) \left\{ 2e^{-(x_i/\theta_i)^{\alpha_i}} - 1 \right\} \right]; x_1 > 0$$

where

$$\Delta_t(\mathbf{x}_2) = \left[1 + \sum_{j=t+1}^p (\lambda_j + \lambda_{p+1}) \left\{ 2e^{-(x_j/\theta_j)^{\alpha_j}} - 1 \right\} \right].$$

In the following subsection we will discuss the marginal and conditional moments for the *MTW* distribution.

The marginal and conditional moments

The moments of a distribution are useful in studying the properties of the distribution. The marginal and joint marginal moments in case of the *MTW* distribution can be easily obtained by using the marginal distribution of a single random variable and the joint marginal distribution of two random variables. The joint moments in case of two random variables are discussed by Darwish *et al.* (2020). In the following, we will obtain the single and joint conditional moments for the parent *MTW* distribution.

The *r*th conditional moment of a single random variable given the information of other random variables is given in (15). We can see that the conditional moment for a multivariate transmuted family of distributions is based upon the raw moments of the parent distribution and the raw moments of the larger observation in a sample of size 2 from the parent distribution $G_i(x_i)$. Now to compute the conditional moment for the *MTW* distribution we first see that the *r*th raw moment and *r*th moment of the larger observation in a sample of size 2 from the Weibull distribution, given in (23), are

$$\mu_x^r = \theta^r \Gamma\left(\frac{r}{\alpha} + 1\right) \text{ and } \mu_{X(2;2)}^r = 2\theta^r \Gamma\left(\frac{r}{\alpha} + 1\right) \left(1 - 2^{-(r/\alpha+1)}\right).$$

Now, using these in (15), the *r*th conditional moment of X_i given the information of other random variables for *MTW* distribution is

$$\mu_{X_i|\mathbf{x}_{(i)}}^r = \frac{\theta_i^{\alpha_i}}{\Delta_i(\mathbf{x}_{(i)})} \Gamma\left(\frac{r}{\alpha_i} + 1\right) \left[\beta - 2 \sum_{j \neq i=1}^p (\lambda_j + \lambda_{p+1}) \left\{ 1 - e^{-(x_j/\theta_j)^{\alpha_j}} \right\} - 2(\lambda_i + \lambda_{p+1}) \left(1 - 2^{-(r/\alpha_i+1)}\right) \right] \dots(30)$$

where

$$\beta = 1 + \sum_{i=1}^p \lambda_i + p\lambda_{p+1} \text{ and}$$

$$\Delta_i(\mathbf{x}_{(i)}) = \left[1 + \sum_{j \neq i=1}^p (\lambda_j + \lambda_{p+1}) \left\{ 2e^{-(x_j/\theta_j)^{\alpha_j}} - 1 \right\} \right].$$

The joint conditional moment for two random variables given the information of other random variables for a multivariate transmuted family of distributions is given in (16). Now, the same for *MTW* distribution is given as

$$\mu_{X_i, X_m | \mathbf{x}_{(i,m)}}^r = \frac{1}{\Delta_{i,m}(\mathbf{x}_{(i,m)})} \left[\beta \mu_{x_i}^r \mu_{x_m}^s - 2 \mu_{x_i}^r \mu_{x_m}^s \sum_{j \neq (i,m)=1}^p (\lambda_j + \lambda_{p+1}) G_j(x_j) - (\lambda_i + \lambda_{p+1}) \mu_{x_i(2;2)}^r \mu_{x_m}^s - (\lambda_k + \lambda_{p+1}) \mu_{x_i}^r \mu_{x_m(2;2)}^s \right],$$

$$\mu_{X_i, X_m | \mathbf{x}_{(i,m)}}^{r,s} = \frac{\theta_i^r \theta_m^s}{\Delta_{i,m}(\mathbf{x}_{(i,m)})} \Gamma\left(\frac{r}{\alpha_i} + 1\right) \Gamma\left(\frac{s}{\alpha_m} + 1\right) \left[\beta - 2 \sum_{j \neq (i,m)=1}^p (\lambda_j + \lambda_{p+1}) \left\{ 1 - e^{-(x_j/\theta_j)^{\alpha_j}} \right\} - 2(\lambda_i + \lambda_{p+1}) \left(1 - 2^{-(r/\alpha_i+1)}\right) - 2(\lambda_m + \lambda_{p+1}) \left(1 - 2^{-(s/\alpha_m+1)}\right) \right], \dots(31)$$

where β and $\Delta_{i,m}(\mathbf{x}_{(i,m)})$ are defined above. The conditional moments are useful in computing conditional means, conditional variances and conditional covariances for *MTW* distribution.

Parameter estimation for multivariate transmuted Weibull distribution

In this sub-section, we will discuss the maximum likelihood estimation for parameters of the *MTW* distribution. For this suppose $\mathbf{x}_1, \mathbf{x}_2, \dots, \mathbf{x}_n$ is a random sample of *n* vector observations from the *MTW* distribution. The likelihood function for the given sample is

$$L = \prod_{j=1}^n \left[\left\{ \prod_{i=1}^p \left(\frac{\alpha_i}{\theta_i^{\alpha_i}} x_{ij}^{\alpha_i-1} e^{-(x_{ij}/\theta_i)^{\alpha_i}} \right) \right\} \left\{ 1 + \sum_{i=1}^p (\lambda_i + \lambda_{p+1}) \left(2e^{-(x_{ij}/\theta_i)^{\alpha_i}} - 1 \right) \right\} \right],$$

which has $(3p+1)$ unknown parameters. The log-likelihood function is

$$\begin{aligned} \ell = \sum_{i=1}^p & \left[n \ln \alpha_i - n \alpha_i \ln \theta_i + (\alpha_i - 1) \sum_{j=1}^n \ln x_{ij} \right. \\ & \left. - \sum_{j=1}^n \left(x_{ij} / \theta_i \right)^{\alpha_i} \right] \\ & + \sum_{j=1}^n \ln \left[1 + \sum_{i=1}^p (\lambda_i + \lambda_{p+1}) \left\{ 2e^{-(x_{ij} / \theta_i)^{\alpha_i}} - 1 \right\} \right]. \end{aligned} \tag{32}$$

The derivatives of the log-likelihood function with respect to unknown parameters are

$$\begin{aligned} \frac{\partial \ell}{\partial \theta_i} = & -\frac{n \alpha_i}{\theta_i} + \frac{\alpha_i}{\theta_i^2} \sum_{j=1}^n \left\{ x_{ij} \left(x_{ij} / \theta_i \right)^{\alpha_i - 1} \right\} + \frac{2 \alpha_i}{\theta_i^2} (\lambda_i + \lambda_{p+1}) \\ & \sum_{j=1}^n \frac{x_{ij} \left(x_{ij} / \theta_i \right)^{\alpha_i - 1} e^{-(x_{ij} / \theta_i)^{\alpha_i}}}{1 + \sum_{i=1}^p (\lambda_i + \lambda_{p+1}) \left\{ 2e^{-(x_{ij} / \theta_i)^{\alpha_i}} - 1 \right\}}; \end{aligned}$$

$i = 1, 2, \dots, p,$

$$\begin{aligned} \frac{\partial \ell}{\partial \alpha_i} = & -\frac{n}{\alpha_i} - n \ln \theta_i + \sum_{j=1}^n \ln x_{ij} \\ & - \sum_{j=1}^n \left\{ \left(x_{ij} / \theta_i \right)^{\alpha_i} \ln \left(x_{ij} / \theta_i \right) \right\} - 2 (\lambda_i + \lambda_{p+1}) \\ & \sum_{j=1}^n \frac{\left(x_{ij} / \theta_i \right)^{\alpha_i} \ln \left(x_{ij} / \theta_i \right) e^{-(x_{ij} / \theta_i)^{\alpha_i}}}{1 + \sum_{i=1}^p (\lambda_i + \lambda_{p+1}) \left\{ 2e^{-(x_{ij} / \theta_i)^{\alpha_i}} - 1 \right\}}; \end{aligned}$$

$i = 1, 2, \dots, p,$

$$\begin{aligned} \frac{\partial \ell}{\partial \lambda_i} = & \sum_{j=1}^n \frac{2e^{-(x_{ij} / \theta_i)^{\alpha_i}} - 1}{1 + \sum_{i=1}^p (\lambda_i + \lambda_{p+1}) \left\{ 2e^{-(x_{ij} / \theta_i)^{\alpha_i}} - 1 \right\}}; \end{aligned}$$

$i = 1, 2, \dots, p,$

and

$$\frac{\partial \ell}{\partial \lambda_{p+1}} = \sum_{j=1}^n \frac{2 \left(\sum_{i=1}^p e^{-(x_{ij} / \theta_i)^{\alpha_i}} - 1 \right)}{1 + \sum_{i=1}^p (\lambda_i + \lambda_{p+1}) \left\{ 2e^{-(x_{ij} / \theta_i)^{\alpha_i}} - 1 \right\}}.$$

The maximum likelihood estimators of unknown parameters are obtained by equating the above $(3p+1)$ derivatives to zero and numerically solving the resulting $(3p+1)$ equations in $(3p+1)$ unknowns.

Real data applications

In this sub-section, real data applications of the *MTW* distribution are given. The real data applications are done by using daily *COVID-19* data of the World for three recent dates; November 20–22, 2020. The data can be accessed at www.worldometer.com. Since the data on daily *COVID-19* cases represents counts, we have used the logarithmic transformation of the data to make it continuous. We have carried out the data analysis on overall data and data split with respect to the median of the log of daily cases. We have divided the transformed daily *COVID-19* cases of the World into two groups; one below the median of the log of daily cases and one above. The summary statistics for the overall data and two groups are given in Table 1.

The correlation coefficients between different variables for the whole data and the two subsets are given in Table 2.

From Table 2 we can see that the variables have high pairwise correlation. Also all the correlations are significant at 1%. Infact the correlation coefficients are significant at 0.1%. These correlation coefficients indicate that the variables are jointly dependent upon each other and hence they should be modelled by using some trivariate distribution.

We have modelled these three data sets by using three trivariate distributions. The distributions that we have fitted include the trivariate transmuted Weibull (*TrTW*) distribution, obtained by using $p = 3$ in (6), the FGM trivariate Weibull (*FGMTW*) distribution obtained by using the Weibull distribution in Gumble copula and a trivariate the Weibull distribution, the HS trivariate Weibull (*HSTW*) distribution, introduced by Hanif Shahbaz et al. (2012).

The density functions of *FGMTW* and *HSTW* distributions are, respectively

Table 1: Summary statistics of the data

Data	Date	<i>n</i>	Min	Mean	<i>Q</i> ₁	Median	<i>Q</i> ₃	Skew	Max
Whole	20-11(<i>X</i> ₁)	144	0.000	6.021	4.100	6.276	7.963	-0.242	12.186
	21-11(<i>X</i> ₂)	144	0.000	6.086	4.131	6.470	7.864	-0.168	12.090
	22-11(<i>X</i> ₃)	144	0.000	5.918	3.965	6.163	7.643	-0.309	11.869
Below Median	20-11(<i>Y</i> ₁)	72	0.000	3.907	2.901	4.057	5.443	-0.448	6.219
	21-11(<i>Y</i> ₂)	72	0.000	4.077	3.032	4.119	5.421	-0.319	6.465
	22-11(<i>Y</i> ₃)	72	0.000	3.883	2.785	3.940	5.324	-0.607	6.071
Above Median	20-11(<i>Z</i> ₁)	72	6.333	8.134	7.231	7.972	8.771	0.766	12.186
	21-11(<i>Z</i> ₂)	72	6.475	8.096	7.158	7.869	8.781	0.894	12.090
	22-11(<i>Z</i> ₃)	72	6.256	7.952	7.021	7.655	8.583	0.798	11.869

Table 2: Correlation coefficient between various variables

Whole data			Below median			Above median		
<i>r</i> _{<i>X</i>₁<i>X</i>₂}	<i>r</i> _{<i>X</i>₁<i>X</i>₃}	<i>r</i> _{<i>X</i>₂<i>X</i>₃}	<i>r</i> _{<i>Y</i>₁<i>Y</i>₂}	<i>r</i> _{<i>Y</i>₁<i>Y</i>₃}	<i>r</i> _{<i>Y</i>₂<i>Y</i>₃}	<i>r</i> _{<i>Z</i>₁<i>Z</i>₂}	<i>r</i> _{<i>Z</i>₁<i>Z</i>₃}	<i>r</i> _{<i>Z</i>₂<i>Z</i>₃}
0.9845	0.9763	0.9834	0.7603	0.9173	0.7377	0.6995	0.9514	0.6605
<i>p</i> <0.01	<i>p</i> <0.01	<i>p</i> <0.01	<i>p</i> <0.01	<i>p</i> <0.01	<i>p</i> <0.01	<i>p</i> <0.01	<i>p</i> <0.01	<i>p</i> <0.01

$$f_{FGMTW}(x_1, x_2, x_3) = \frac{\alpha_1 \alpha_2 \alpha_3 x_1^{\alpha_1 - 1} x_2^{\alpha_2 - 1} x_3^{\alpha_3 - 1}}{\theta_1^{\alpha_1} \theta_2^{\alpha_2} \theta_3^{\alpha_3}} \left[1 + \lambda_1 \left\{ 1 - 2e^{-(x_1/\theta_1)^{\alpha_1}} \right\} \left\{ 1 - 2e^{-(x_2/\theta_2)^{\alpha_2}} \right\} \left\{ 1 - 2e^{-(x_3/\theta_3)^{\alpha_3}} \right\} \right] \dots(33)$$

and

$$f_{HSTW}(x_1, x_2, x_3) = \frac{\alpha_1 \alpha_2 \alpha_3 x_1^{3\alpha_1 - 1} x_2^{2\alpha_2 - 1} x_3^{\alpha_3 - 1}}{\theta_1^{3\alpha_1} \theta_2^{2\alpha_2} \theta_3^{\alpha_3}} \exp \left[- \left(\frac{x_1}{\theta_1} \right)^{\alpha_1} \left\{ 1 + \left(\frac{x_2}{\theta_2} \right)^{\alpha_2} + \left(\frac{x_2}{\theta_2} \right)^{\alpha_2} \left(\frac{x_3}{\theta_3} \right)^{\alpha_3} \right\} \right] \dots(34)$$

where $(x_1, x_2, x_3) > 0$ and all the parameters are positive for both of the distributions, except $\lambda_1 \in [-1, 1]$.

Table 3: Fitted distributions for the whole COVID-19 data

Parameters	Distributions		
	TrTW	FGMTW	HSTW
θ	7.1940	0.0001	6.0392
θ_2	6.0676	4.12 x 10 ⁻⁷	7.1671
θ_3	7.0621	0.0002	7.9643
α_1	2.7534	0.4576	0.9725
α_2	2.4721	0.4584	1.3277
α_3	2.7776	0.4572	2.1416
λ_1	0.3773	0.1171	
λ_2	-0.6227		
λ_3	0.3773		
λ_4	-0.0705		
Log-likelihood	-986.8249	-1814.5921	-1288.9752
<i>AIC</i>	1993.6498	3643.1842	2589.9504
<i>BIC</i>	2023.3479	3663.9729	2607.7693

We have fitted these distributions on three data sets by computing the maximum likelihood estimates of the unknown parameters. The maximum likelihood estimates of unknown parameters are computed by using the *R* package “maxLik” introduced by Henningsen & Toomet (2011). The performance of the distributions are assessed

by computing the Akaike’s information criterion (*AIC*) and the Bayesian information criterion (*BIC*). The results of these analyses are given in Tables 3–5. Table 3 contains results for the whole data, Table 4 has results for data below median cases and Table 5 contains results for data above median cases.

Table 4: Fitted distributions for the daily COVID–19 data below the median

Parameters	Distributions		
	TrTW	FGMTW	HSTW
θ_1	4.6627	0.0006	12.1665
θ_2	4.0476	1.53×10^{-7}	20.5443
θ_3	4.6437	0.0006	5.6202
α_1	2.9923	0.4432	14.5263
α_2	2.6842	0.4448	18.7934
α_3	2.9506	0.4428	19.4948
λ_1	0.3654	0.1144	
λ_2	-0.6344		
λ_3	0.3655		
λ_4	-0.1069		
Log-likelihood	-391.6393	-1651.8421	-790.0924
<i>AIC</i>	803.2786	3317.6842	1592.1848
<i>BIC</i>	826.0453	3333.6209	1605.8448

Table 5: Fitted distributions for the daily COVID–19 data above the median

Parameters	Distributions		
	TrTW	FGMTW	HSTW
θ_1	8.4667	3.55×10^{-7}	8.1952
θ_2	9.1262	7.77×10^{-7}	7.2235
θ_3	8.2789	0.0002	9.2567
α_1	6.1104	0.4633	12.2257
α_2	7.3003	0.4632	10.5287
α_3	6.0972	0.4627	11.6772
λ_1	-0.3147	0.1176	
λ_2	0.6852		
λ_3	-0.3147		
λ_4	0.0464		
Log-likelihood	-359.3084	-1584.8859	-663.42
<i>AIC</i>	738.6168	3183.7718	1338.8400
<i>BIC</i>	761.3835	3199.7085	1352.5000

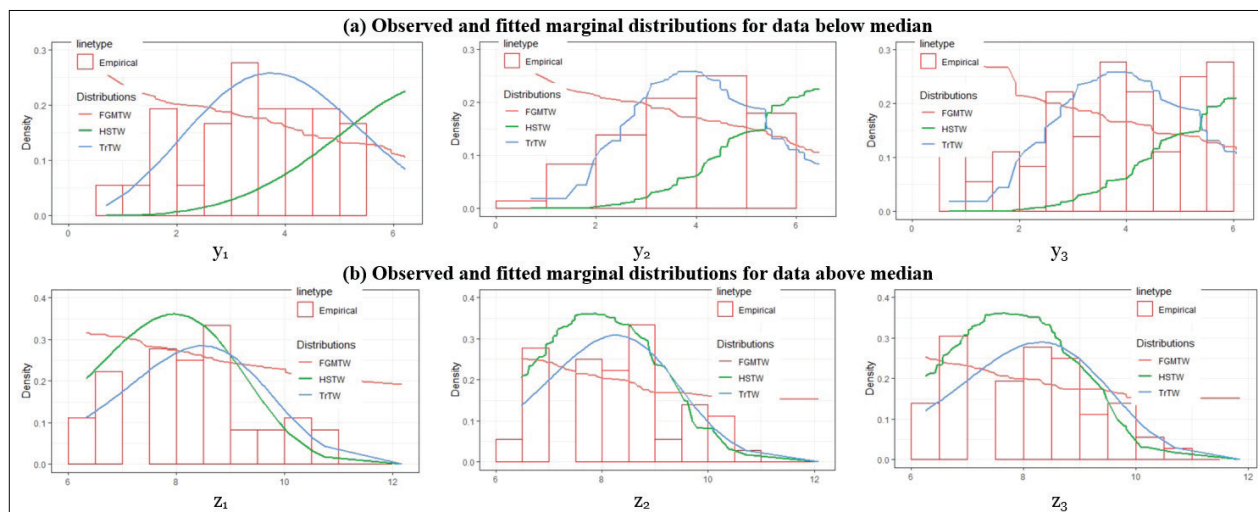


Figure 1: Observed and fitted marginal distributions for data below median (a) and above median (b)

It can be easily seen that the *AIC* and *BIC* values of the proposed trivariate transmuted Weibull distributions for the whole data and two sub data sets are smallest indicating that the trivariate transmuted Weibull distribution is the best fit for logarithms of the daily COVID-19 cases.

The plot of observed and fitted marginal distributions for data below median (Panel-a) and above median (Panel-b) are given in Figure 1, below. The plots of observed data and fitted marginal distributions also indicates that the trivariate transmuted Weibull distribution is the most suitable distribution for capturing behaviour of the data. Also, this distribution is the most appropriate for capturing tail behaviour.

CONCLUSION

In this paper, we have proposed a new multivariate transmuted family of distributions. Some properties of the proposed family have been studied. We have also obtained expressions for the maximum likelihood estimation of the parameters of the family of distributions. The proposed multivariate family provides the transmuted family of distributions, proposed by Shaw and Buckley (2007), and the bivariate transmuted family of distributions, proposed by Darwish *et al.* (2020), as special case. The proposed multivariate family has been studied for parent Weibull distribution giving rise to the multivariate transmuted Weibull (*MTW*) distribution. Some properties of the proposed *MTW* distribution alongside the maximum likelihood estimation of the parameters has been discussed. We have applied the *MTW* distribution on daily COVID-19 cases of the world. We have seen that the proposed *MTW* turned out to be the best fit for modeling of the data used. The multivariate transmuted family of distributions can be further explored for any baseline distributions.

Conflicts of interest

The authors declare no conflict of interest regarding the publication of this paper.

REFERENCES

- Afify A., Yousof H. & Nadarajah S. (2017). The beta transmuted-H family for lifetime data. *Statistics and its Interface* **10**: 505–520.
DOI: <https://doi.org/10.4310/SII.2017.v10.n3.a13>
- Afify A.Z., Cardeiro G.M., Yousof H.M., Alzaatreh A. & Nofal Z.M. (2016). The Kumaraswamy transmuted-G family of distributions: Properties and applications. *Journal of Data Science* **14**: 245–270.
DOI: [https://doi.org/10.6339/JDS.201604_14\(2\).0004](https://doi.org/10.6339/JDS.201604_14(2).0004)
- Alizadeh M., Merovci F. & Hamedani G.G. (2017). Generalized transmuted family of distributions: Properties and applications. *Hacetatepe Journal of Mathematics and Statistics* **46**: 645–667.
DOI: <https://doi.org/10.15672/HJMS.201610915478>
- Alzaatreh A., Lee C. & Famoye F. (2013). A new method for generating families of continuous distributions. *Metron* **71**: 63–79.
DOI: <https://doi.org/10.1007/s40300-013-0007-y>
- Arslan O. (2004). Family of multivariate generalized t distributions. *Journal of Multivariate Analysis* **89**: 329–337.
DOI: <https://doi.org/10.1016/j.jmva.2003.09.008>
- Barreto-Souza W. & Lemonte A.J. (2013). Bivariate Kumaraswamy distribution: Properties and a new method to generate bivariate classes. *American Journal of Theoretical and Applied Statistics* **47**: 1321–1342.
DOI: <https://doi.org/10.1080/02331888.2012.694446>
- Cambanis S. (1977). Some properties and generalizations of multivariate Eyrard-Gumbel-Morgenstern distributions. *Journal of Multivariate Analysis* **7**: 551–559.
DOI: [https://doi.org/10.1016/0047-259X\(77\)90066-5](https://doi.org/10.1016/0047-259X(77)90066-5)
- Darwish J.A., Al turk L.I. & Shahbaz M.Q. (2021). The bivariate transmuted family of distributions: Theory and applications. *Computer Systems Science and Engineering* **36**: 83–100.
DOI: <https://doi.org/10.32604/csse.2021.014764>
- Gomez E., Gomez-Villegas M.A. & Marin J.M. (1998). A multivariate generalization of the power exponential family of distributions. *Communications in Statistics: Theory and Methods* **27**: 589–600.
DOI: <https://doi.org/10.1080/03610929808832115>
- Gumbel E.J. (1960). Multivariate distributions with given margins and analytical examples. *Bulletin de l'Institut International de Statistique* **37**: 363–373.
- Hanif Shahbaz S., Shahbaz M.Q., Rafiq A. & Acu A.M. (2012). On trivariate pseudo Weibull distribution. *Acta Universitatis Apulensis* **31**: 241–247.
- Henningesen A. & Toomet O. (2011). maxLik: A package for maximum likelihood estimation in R. *Computational Statistics* **26**: 443–458.
DOI: <https://doi.org/10.1007/s00180-010-0217-1>
- Holland P.V. & Wang Y.J. (1987). Dependence function for continuous bivariate densities. *Communications in Statistics: Theory and Methods* **16**: 863–876.
DOI: <https://doi.org/10.1080/03610928708829408>
- Jayakumar K. & Babu M.G. (2017). T-transmuted X family of distributions. *Statistica* **LXXVII**: 251–276.
- Khan M.S., King R. & Hudson I.L. (2017). Transmuted Weibull distribution: properties and estimation. *Communications in Statistics: Theory and Methods* **11**: 5394–5418.
DOI: <https://doi.org/10.1080/03610926.2015.1100744>
- Nofal Z.M., Afify A.Z., Yousof H.M. & Cordeiro G.M. (2016). The generalized transmuted-G family of distributions. *Communications in Statistics: Theory and Methods* **46**: 4119–4136.
DOI: <https://doi.org/10.1080/03610926.2015.1078478>
- Rahman M.M., Al-Zahrani B., Hanif Shahbaz S. & Shahbaz

- M.Q. (2020). Transmuted distributions: a review. *Pakistan Journal of Statistics and Operation Research* **16**: 83–94.
DOI: <https://doi.org/10.18187/pjsor.v16i1.3217>
- Sankaran P.G., Nair N.U. & John P. (2014). A family of bivariate Pareto distributions. *Statistica* **LXXIV**: 199–215.
- Sarabia J.M., Prieto F. & Jorda V. (2014). Bivariate beta-generated distributions with applications to well-being data. *Journal of Statistical Distributions and Applications* **1**: Article number 15.
DOI: <https://doi.org/10.1186/2195-5832-1-15>
- Schmid F. & Schmidt R. (2007). Multivariate extensions of Spearman's rho and related statistics. *Statistics and Probability Letters* **77**: 407–416.
DOI: <https://doi.org/10.1016/j.spl.2006.08.007>
- Shaw W.T. & Buckley I.R.C. (2007). The alchemy of probability distributions: Beyond Gram-Charlier expansions, and a skew-kurtotic-normal distribution from a rank transmutation map. *UCL discovery repository*.
- Taylor M.D. (2016). Multivariate measures of concordance for copulas and their marginal. *Dependence Modeling* **4**: 224–236.
DOI: <https://doi.org/10.1515/demo-2016-0013>

RESEARCH ARTICLE

Polymer science and technology

Synthesis of polyethylene glycol-grafted graphite and effect of its loading on properties of natural rubber composites

WDM Sampath^{1,2*}, CAN Fernando¹ and DG Edirisinghe²

¹ Department of Nano Science Technology, Faculty of Technology, Wayamba University of Sri Lanka, Kuliyapitiya 60200, Sri Lanka.

² Rubber Technology and Development Department, Rubber Research Institute of Sri Lanka, Telawala Road, Ratmalana 10390, Sri Lanka.

Submitted: 24 January 2022; Revised: 01 June 2022; Accepted: 24 June 2022

Abstract: Modified graphite has attracted considerable interest over recent years due to its surface functionality and better dispersibility with polymeric materials. Incorporation of a small quantity of modified graphite filler into polymer can create novel composites with improved properties. In this study, polyethylene glycol (PEG) was grafted onto the graphite surface in the presence of maleic anhydride (MAH). The PEG-grafted graphite (PEG-g-Graphite) was characterized via Fourier Transform infrared spectroscopy (FTIR), X-ray diffraction spectroscopy (XRD), thermogravimetric analysis (TGA), and scanning electron microscopy (SEM), and the analysis proved that PEG was successfully grafted onto the graphite surface. Subsequently, natural rubber (NR) composites were prepared by varying the PEG-g-Graphite loading from 0 phr (parts per hundred rubber) to 10 phr at 2 phr intervals. The 10 phr PEG-g-Graphite filled NR composite showed an increment in scorch time and cure time in comparison to the NR composite prepared without PEG-g-Graphite (control). Further, heat resistance of the PEG-g-Graphite/NR composites prepared with 8 and 10 phr loadings of PEG-g-Graphite was at a high level. Due to sheet resistance, values of the 10 phr loading of PEG-g-Graphite and the control composites were 2×10^5 and 3.9×10^7 ohms/square, respectively. The NR composite prepared with 10 phr loading of PEG-g-Graphite could be suitable for high electrical conductive polymeric applications.

Keywords: Graphite, natural rubber composites, polyethylene glycol, polyethylene glycol-grafted graphite.

INTRODUCTION

Graphite is a well-known filler material used in the rubber industry, and it is a naturally abundant, relatively low cost, and lightweight material when compared to other carbon allotropes (Mokhena *et al.*, 2018). It is reported as the best conductive filler for its excellent conductive properties. Additionally, it has good mechanical properties and disperses well in a polymer matrix (Rus *et al.*, 2016). Polymer/graphite composites are widely used for different applications such as sensors, memory material, and energy storage, due to their excellent electrical and thermal conductivity (Zhao *et al.*, 2015). Polymer/graphite composites have been used in many applications including structural and aerospace materials, and sporting goods (Mokhena *et al.*, 2018). A study conducted by Shih *et al.* (2010) revealed that graphite incorporated with polydimethylsiloxane (PDMS) shows the highest temperature sensitivity and higher thermal stability than the composites containing conventional carbon-based fillers. Moreover, graphite has been incorporated to polyurethane, silicone rubber, and epoxy resins to prepare composite materials to be used in the preparation of electrodes for different industrial applications (Calixto *et al.*, 2007). A composite prepared with polypropylene (PP) and graphite showed a significant improvement

* Corresponding author (wikcramage@yahoo.com;  <https://orcid.org/0000-0002-6481-7189>)



This article is published under the Creative Commons CC-BY-ND License (<http://creativecommons.org/licenses/by-nd/4.0/>). This license permits use, distribution and reproduction, commercial and non-commercial, provided that the original work is properly cited and is not changed in anyway.

of the surface tension with increasing graphite content, and the composite was applied to adhesives in fuel cell applications (Rzeczkowski *et al.*, 2019).

Graphite consists of carbon atoms trigonally bound to each other by covalent bonds, forming hexagonal rings. Each carbon is sp^2 -hybridized with three of the four valence electrons used to form bonds to each of the three attached carbon atoms (Mokhena *et al.*, 2018; Sampath *et al.*, 2021). The fourth electron resonates freely within the graphene layer, and generates van der Waals forces acting between adjacent graphene layers (Mokhena *et al.*, 2018). Several graphite modification methods have been carried out to improve its dispersion in different polymeric materials. In this study, graphite is modified by grafting polyethylene glycol (PEG) to enhance the performance of the final composite, and further it was noted that unmodified graphite disperses poorly in the polymer matrix. PEG is nontoxic, biocompatible, and heat resistant, and could be used as a dispersant and a toughening agent (Huang *et al.*, 2019). The characteristic behaviour of PEG seems to be due to the crucial balance of the hydrophobic forces exerted by the ethylene units ($-CH_2-CH_2-$) with the hydrophilic interactions of the oxygen atoms present in the oxirane units and in the terminal groups (Zohuri, 2012). The thermal stability and processability of bamboo fibre (BF)/polylactic acid (PLA) composites have been developed with high molecular weight PEG (Long *et al.*, 2019). Other than that, some polymer composites have been prepared by mixing different filler materials including metallic materials with graphite to generate different properties (Saraswati *et al.*, 2020; Kitisavetjit *et al.*, 2021).

Carbon nanotube (CNT) and graphite hybrid fillers have been used as reinforcing fillers in NR vulcanizates (Kitisavetjit *et al.*, 2021) and the wettability of the CNT and graphite was assessed to elucidate filler dispersion in the NR matrix. NR composites prepared with 3 phr of CNT and 30 phr graphite have shown superior properties in terms of cure characteristics, mechanical properties and conductivity (Kitisavetjit *et al.*, 2021). In another study, metal-graphene-filled hybrid polyamide composites have been developed and, combination of the two different fillers increased the mechanical properties up to 120% compared to the metal reinforced composites (Rad *et al.*, 2019). In addition, the functionality of graphene (GNP) has been increased by grafting NH_2 -poly(methyl methacrylate) (PMMA), and 2 wt. % of NH_2 -PMMA-GNPs in PMMA were found to increase the elastic modulus, strength, and strain at break (Vallés *et al.*, 2020).

Titanate base coupling agents have been utilized for modification of the graphite surface (Meng, 2012) and polymer composites have been prepared using capric acid (CA), myristic acid (MA) and poly-methyl methacrylate (PMMA) by varying titanate coated graphite powder loadings from 2–15% (w/w). The results indicated that the graphite/CA-MA/PMMA composites maintained good thermal storage performance, while the thermal expansibility became weaker (Meng, 2012). Most of the previous studies stated that graphite and modified graphite have been utilized to enhance the thermal and electrical performance of polymeric materials. No studies have been conducted regarding modified graphite incorporated NR composites and their performance. The main goal of this study is to enhance the physico-mechanical, thermal, electrical and rheological properties of NR composites using surface functionalized graphite obtained by grafting PEG on micro scale graphite powder.

MATERIALS AND METHODS

Materials

RSS-2 with a Plasticity Retention Index of 64 was supplied by the Rubber Research Institute of Sri Lanka. PEG with a number-average molecular weight of 4000 g mol^{-1} was purchased from the local market. Maleic anhydride (MAH) was used as the grafting material and was obtained from Morex Lanka (Pvt.) Ltd., Sri Lanka. Graphite with a mean particle size of 14 micron was used as conductive filler and was obtained from Bogala Graphite Lanka Plc., Sri Lanka. N,N -dimethylformamide (DMF) and all rubber compounding ingredients were purchased from local suppliers.

Synthesis of PEG-g-graphite

Figure 1 shows the fabrication procedure of PEG-g-Graphite. Graphite (5 g) was added to DMF (20 mL) to form a stable graphite / DMF suspension via ultrasonication (20kHz / 500W) for 30 min. The graphite / DMF mixture was then heated with an excess of MAH (10 g) at $100\text{ }^\circ\text{C}$ for 24 h under dry nitrogen. After the reaction, 10 g of PEG was added based on a 1:1 PEG: MAH ratio. The mixture was reacted at $80\text{ }^\circ\text{C}$ for 48 h through continuous mechanical stirring and poured into a beaker containing 98% ethanol. Then, the product obtained was filtered and washed several times to remove free PEG and MAH at low pressure. The final product was dried at $50\text{ }^\circ\text{C}$ in a vacuum oven (Huang *et al.*, 2019).

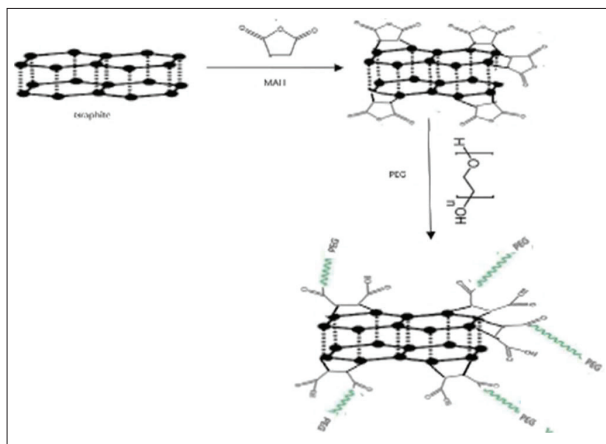


Figure 1: Schematic diagram of the PEG-g-graphite synthesis

Preparation of PEG-g-Graphite/NR composites

A series of NR composites was formulated by varying the PEG-g-Graphite loading from 2 phr to 10 phr at 2 phr intervals. The NR composite prepared without PEG-g-Graphite was considered as the control. The formulation of the composites is given in Table 1.

Table 1: Formulation of the PEG-g-Graphite / NR composites

Ingredient	Function	Phr
Natural rubber (RSS-2)	Rubber	100
ZnO	Inorganic activator	5.0
Stearic acid	Organic co-activator	2.0
TMQ	Antioxidant	1.0
PEG-g-Graphite	Conductive filler	0,2,4,6,8,10
ZDC	Accelerator	1.5
Sulphur	Vulcanizing agent	2.0

Table 2: Mixing cycle of the PEG-g-Graphite/NR composites

Total time, min	Ingredient
0	Added NR
1	Added Zinc oxide + Stearic acid + TMQ
2	Added PEG-g-Graphite
5	Added ZDC
6	Added Sulphur
14	Dumped the compound

The composites were prepared by melt mixing using a Brabender Plasticorder operated at room temperature, at a rotor speed of 60 rpm. The total mixing time was kept constant at 10 min. The mixing cycle used in the preparation of NR composites is given in Table 2. The composites were compressed in an electrically heated hydraulic press machine at 150 °C under a pressure of 0.35 MPa to produce 2 mm thick sheets. Test specimens were cut from these sheets according to the required standards.

Characterization

X-ray diffraction (XRD) analysis was conducted using an X-ray diffractometer (UltimaIV, Japan) to confirm the crystallographic nature of graphite and PEG-g-Graphite materials. The PEG-g-Graphite and graphite materials were scanned in continuous mode by varying the scanning angle from 0.50 to 90.0 degrees at a scanning speed of 3 degrees per minute in 2θ (degrees). Further, chemical structures of graphite and PEG-g-Graphite were characterized using a Nicolet 380 FTIR spectrometer. Spectra were recorded in the range of 400–3500 cm^{-1} operated at 4 cm^{-1} resolution. The surface morphology of graphite, PEG-g-Graphite and tensile fracture surfaces of PEG-g-Graphite/NR composites were examined by Scanning Electron microscopy (SEM) using a ZEISS EVO LS 15 Microscope. The specimens were sputter coated with a thin layer of gold to avoid electrostatic charging during examination. The thermal stability of the two materials was investigated through thermogravimetric analysis (TGA) (TGA 400, Perkin Elmer) at a heating rate of 10 °C / min from room temperature to 600°C in a nitrogen atmosphere.

Cure characteristics

Cure characteristics of PEG-g-Graphite/NR composites, such as minimum torque (ML), maximum torque (MH), scorch time (T_{s2}), optimum cure time (T_{90}), cure rate index (CRI), and extent of cure or delta cure (MH-ML), were obtained by a Dynamic Rubber Process Analyzer (D-RPA 3000- MonTech, Germany) at 150 °C.

Physico-mechanical properties

Tensile properties and tear strength of PEG-g-Graphite/NR composites were determined using Instron tensile testing machine according to BS ISO 37:2017 and BS ISO 34-1:2015, respectively. Dumb-bell shaped tensile test specimens and angle shaped tear test specimens were used. The cross-head speed was maintained at 500 mm/min. The hardness of the composites was

determined using Digi Test hardness tester according to BS ISO 48-4:2018. The resilience of the composites was measured by a Wallace Lupke pendulum in accordance with ISO 4662: 2017.

Ageing properties

Accelerated ageing of the composites was carried out at 70 °C for 72 hours in an air circulating oven. Tensile properties were evaluated after ageing, and percentage retention of these properties was calculated according to equation 1.

$$\text{Retention of tensile strength (\%)} = \frac{\text{Tensile strength after ageing}}{\text{Tensile strength before ageing}} \times 100 \quad \dots(1)$$

Sheet resistance

Sheet resistance of PEG-g-Graphite/NR composites was assessed using a four-probe electrical conductivity meter (Jandel RM 3000). The specimens were cut into 10 mm × 10 mm square-shaped pieces of 1 mm thickness.

RESULTS AND DISCUSSION

Characterization of graphite and PEG-g-Graphite

Figure 2 shows the comparison of FTIR spectra between graphite and PEG-g-Graphite. After the MAH and PEG reaction, a wide broad peak has appeared at 3340 cm⁻¹ corresponding to the stretching vibration of O-H groups (Rawn & Ouellette, 2018). Further, asymmetrical and symmetrical stretching vibrations of C-H bonds are assigned at 2935 and 2915 cm⁻¹; these belong to the PEG molecular chain (Huang et al., 2019). In addition, the

narrow peak at 1028 cm⁻¹ is attributed to the stretching vibration of C-O-C bond in the ester groups of PEG-g-Graphite owing to the reaction of the hydroxyl group with MAH (Xu et al., 2015). Hence, FTIR results suggest that PEG molecules are chemically grafted to the graphite through the esterification reaction with the MAH coupling agent.

XRD patterns of graphite and PEG-g-Graphite are shown in Figure 3. Graphite powder shows a characteristic peak at 2θ = 26.6° (Volanti et al., 2015). When PEG is grafted to graphite, the graphitic peak shifts to 2θ = 26.73°. In addition, two extra narrow peaks have appeared at 2θ = 23.65° and 2θ = 31.36° due to grafting PEG via the MAH (Barron et al., 2003). In addition, graphite shows two other very low peaks at 2θ = 44.65° and 2θ = 54.67°. However, these peaks are shifted to 2θ = 44.08° and 2θ = 54.54°, respectively due to incorporation of PEG.

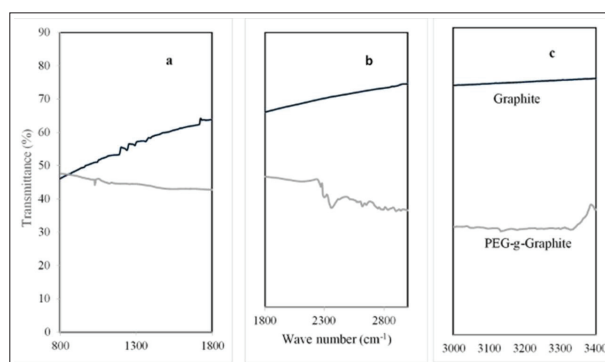


Figure 2: FTIR spectra of Graphite and PEG-g-Graphite for different regions/s
a) 800 to 1800 cm⁻¹; b) 2000 to 3000 cm⁻¹; c) 3000 to 3400 cm⁻¹

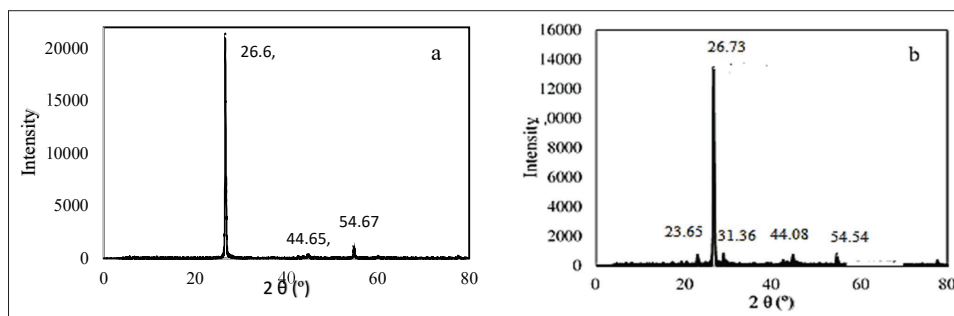


Figure 3: XRD diffractogram of (a) Graphite (b) PEG- g-Graphite

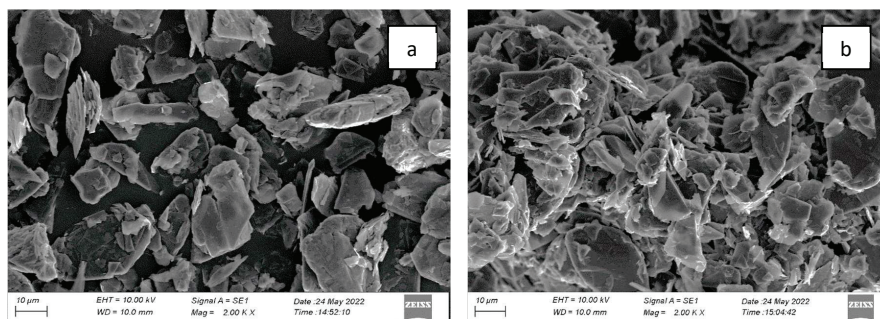


Figure 4: SEM images of surface of (a) graphite and (b) PEG-g-graphite

The surface morphologies of the graphite and PEG-g-Graphite were studied using SEM as shown in Figure 4. As seen in this figure, graphite [Figure 4(a)] looks like a thin “petal” flake with a typical lamella structure (Esmacili *et al.*, 2020) in which graphene layers are not distinguishable. Further, the graphite surface has not shown good adhesion among the graphite particles. However, in PEG-g-Graphite [Figure 4(b)], the dispersibility and homogeneity of the graphite surface have been improved. Furthermore, the free volume of the PEG-g-Graphite is less than that of the graphite due to improved surface adhesion among the graphite particles via the PEG.

The PEG-g-Graphite sample was assessed via TGA (Figure 5) for confirmation of success of grafting. Based on the results, graphite exhibited no significant weight loss up to 600 °C. However, two weight loss stages are observed in PEG-g-Graphite after its modification. The primary mass loss of the grafted samples is indicated in the temperature range 120 – 205 °C, which

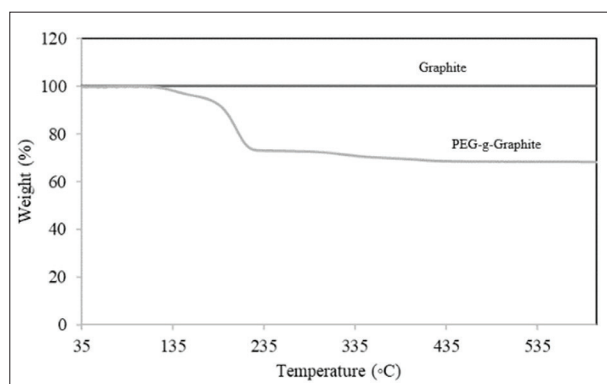


Figure 5: TGA curves of graphite and PEG-g-graphite

is assigned to the degradation of the moiety deriving from the grafted MAH molecules (Samadaei *et al.*, 2016). The major weight loss of grafted sample occurs at the temperature range approximately between 205–400 °C, which originates from the grafted PEG chain (Kou *et al.*, 2019).

Cure characteristics of PEG-g-Graphite/NR composites

Minimum torque (ML) is an indication of stock viscosity and processability of rubber composites (Ismail *et al.*, 2002). Maximum torque (MH) is an indication of the state of cure, whereas delta cure (MH-ML) is an indication of cross-link density of rubber composites (Surya *et al.*, 2018). Table 3 shows that addition of 2 phr of PEG-g-Graphite has increased ML and MH of the composite in comparison to the control. Accordingly, delta cure has also increased with the addition of 2 phr of PEG-g-Graphite. All the composites prepared with PEG-g-Graphite show higher ML and MH than the control. Furthermore, when the PEG-g-Graphite loading is increased beyond 4 phr, ML of PEG-g-Graphite/NR composites has decreased, due to the effect of increased wettability and low density of graphite-based materials (Kitisavetjit *et al.*, 2021). The addition of 2 phr PEG-g-Graphite has increased MH and (MH-ML) torque of the PEG-g-Graphite/NR composite in comparison to the control, while the literature indicates an improvement of reinforcing efficiency, crosslink density and better filler dispersion on NR matrix (Surya *et al.*, 2018; Kitisavetjit *et al.*, 2021).

In addition, the increase in the PEG-g-Graphite loading has increased scorch time and cure time of NR composites (Table 3). Scorch time, which indicates processing safety, ranges from 0.61 min to 0.83 min in the composites. The control composite has shown the

lowest scorch time and cure time due to poor viscosity of the material (Ismail *et al.*, 2002). Further, it is reported in literature that the cross-link density and thermal conductivity of graphite filled rubber compounds increase with the increase of graphite percentage (Somaweera *et al.*, 2021). However, composites prepared with PEG-g-Graphite have shown a low cure time at 150 °C since

graphite has a higher possibility to form agglomerates in the NR matrix at a low loading level (Sumita *et al.*, 1991). Additionally, Matthew *et al.* (2019) found that PEG could act as an activator in NR composites. This could be another reason for the low values of scorch and cure times shown by all PEG-g-Graphite filled NR composites.

Table 3: Cure characteristics of PEG-g-Graphite/NR composites

Property	PEG-g-graphite loading					
	0 Phr	2 Phr	4 Phr	6 Phr	8 Phr	10 Phr
Minimum torque, ML (dNm)	0.39	0.66	0.66	0.56	0.43	0.61
Maximum torque, MH (dNm)	6.79	7.92	7.51	6.84	6.80	7.02
Scorch time, T_{S_2} (Min)	0.61	0.71	0.74	0.81	0.83	0.81
Cure time, T_{90} (Min)	1.55	1.63	1.61	1.66	1.67	1.77
Cure rate index, CRI (Min ⁻¹)	106.3	108.6	114.9	117.6	119.0	104.2
Delta cure ((MH-ML) torque) (dNm)	6.60	7.26	6.85	6.28	6.35	6.41

The increase in cure time with the increase of filler loading, a known effect in rubber vulcanization due to restriction of cross-link formation, has been reported in the literature (Shanmugaraj *et al.*, 2019). The composite prepared with 10 phr loading of PEG-g-Graphite showed about a 14% increase in cure time compared to the control. CRI indicates the rate of crosslink formation of a sample. An 8.5–12% increase in CRI has been observed for the composites prepared with 4-8 phr PEG-g-Graphite in comparison to the control, probably due to enhancement of filler-rubber interaction as reported in the literature (Sumita *et al.*, 1991). However, 10 phr of PEG-g-Graphite filled composite exhibits a lower CRI than the control. This can be a result of the high increase in cure time shown by the 10 phr PEG-g-Graphite composite compared to the control (Hassan *et al.*, 2012).

Moreover, cure characteristics depend upon filler properties such as the nature of the filler, surface area, surface reactivity, aspect ratio, and particle size (Shanmugaraj *et al.*, 2019). As stated earlier, graphite particles are chemically inert and do not react with the rubber matrix, and hence, air voids could be formed around the graphite particles (Shanmugaraj *et al.*, 2019). This could be a reason for cure characteristics not showing a large variation with the increase of PEG-g-Graphite loading.

Physico-mechanical properties of PEG-g-Graphite/NR composites

Stress-strain curves provide an extremely important graphical measure of mechanical properties of a material such as modulus, tensile strength and elongation at break. These parameters are highly important to explain the elastic behaviour of a material. Figure 6 shows the stress-strain behaviour of NR composites with and without PEG-g-Graphite. The composite prepared with 10 phr loading of PEG-g-Graphite shows higher stress-strain properties compared to the other PEG-g-Graphite filled composites and the control. Generally, toughness of rubber composites increases with filler loading (Bokobza, 2017). Hence, 10 phr PEG-g-Graphite loaded composite shows the highest toughness, which is indicated by the highest area under the stress-strain curve. In addition, the area under this curve represents the elastic potential energy of a polymeric material (Sampath *et al.*, 2019a; 2019b). Hence, the composite prepared with 10 phr loading of PEG-g-Graphite shows a higher elastic potential energy per unit volume ($4873.5 \times 10^6 \text{ Jm}^{-3}$) than the other composites.

The variation of hardness of NR composites with PEG-g-Graphite loading is shown in Figure 7. The hardness of all six composites is observed in the range

40–45 IRHD. The hardness of all the composites prepared with PEG-g-Graphite is higher than that of the control. The hardness of a polymeric material is a measure of its stiffness (Edirisinghe & Freakley, 2003). The composite

prepared with 10 phr loading of PEG-g-Graphite shows the highest hardness and this can be attributed to the highest toughness indicated earlier by the area under the stress-strain curve.

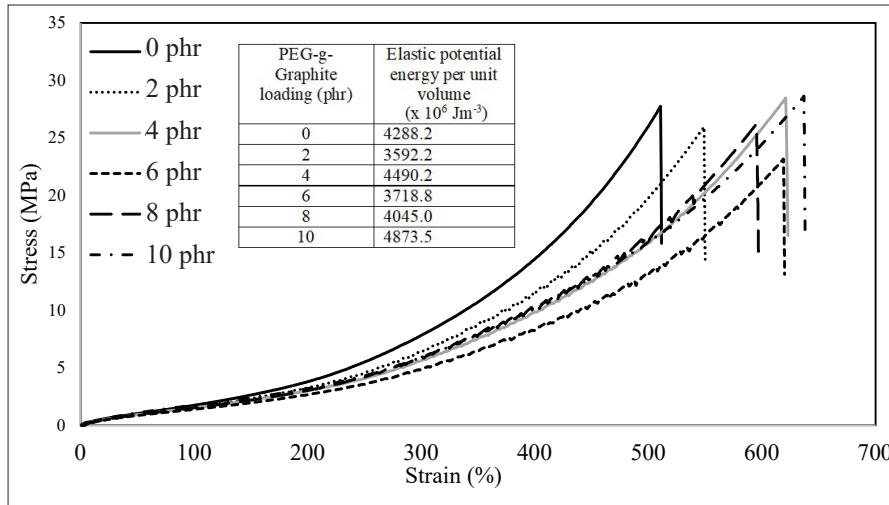


Figure 6: Stress-strain properties of PEG-g-Graphite/NR composites

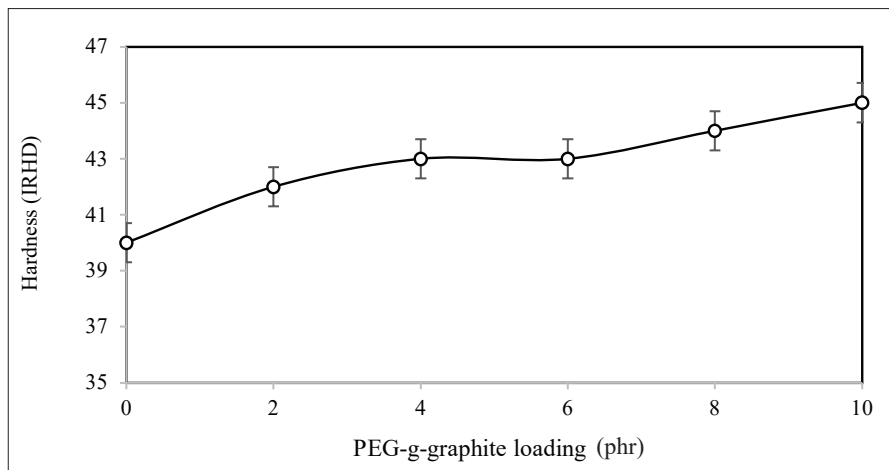


Figure 7: Hardness of PEG-g-Graphite / NR composites

Tensile strength and modulus at 300% elongation of the NR composites vary according to a cyclic pattern with the increase of PEG-g-Graphite loading, as shown in Figures 8 and 9, respectively. This behaviour can be attributed to the combined effect of the plasticizing action of graphite (Imiela *et al.*, 2019) and the agglomeration of graphite-

based materials at low loading levels (Kitisavetjit *et al.*, 2021). The composite prepared with 2 phr loading of PEG-g-Graphite shows the highest modulus at 300% elongation, and this can be attributed to the highest crosslink density, as indicated by the (MH-ML) torque values (Table 3).

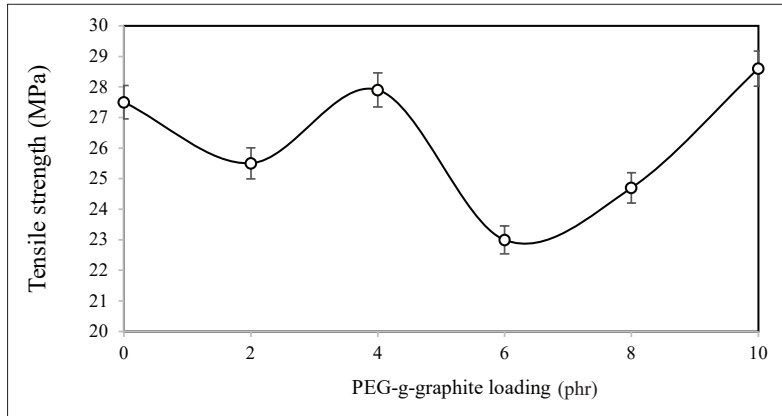


Figure 8: Tensile strength of PEG-g-Graphite / NR composites

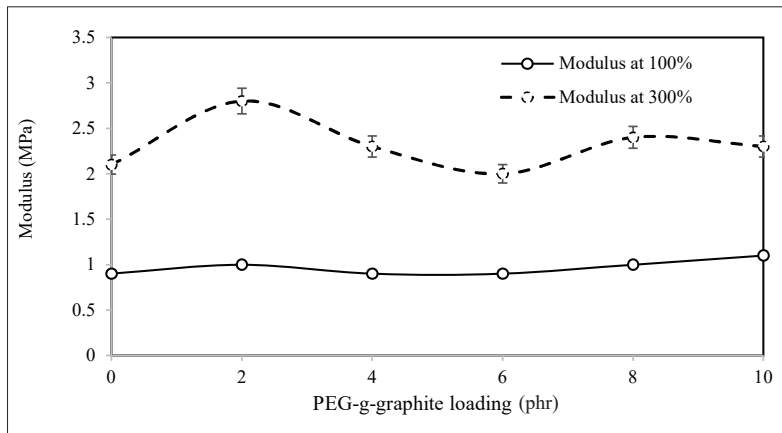


Figure 9: Modulus at 100% and 300% elongations of PEG-g-Graphite/NR composites

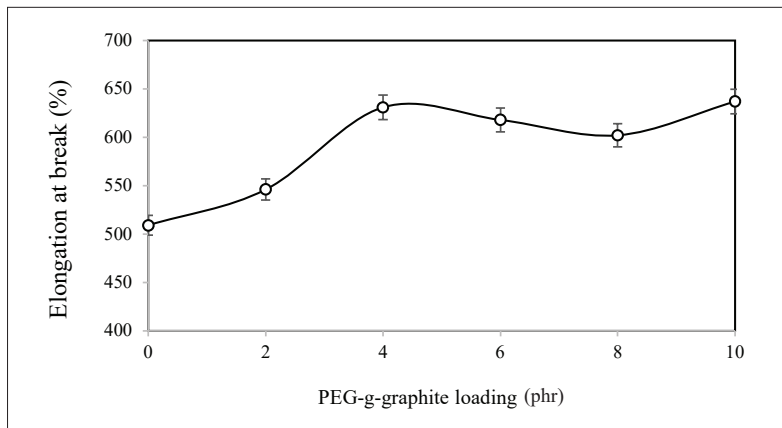


Figure 10: Elongation at break of PEG-g-Graphite/NR composites

All the composites exhibit similar tangents at 100% elongation (Figure 6) and hence modulus at 100% elongation of NR composites has not shown a significant variation with the increase of PEG-g-Graphite loading (Figure 9).

Elongation at break of the composites has also varied in a cyclic pattern with the increase of PEG-g-Graphite loading (Figure 10); however an increasing trend is observed. Elongation at break of PEG-g-Graphite based composites is higher than that of the control due to the presence of long-chain organic PEG molecules, which encourage compatibility with the NR matrix leading to improved dispersion (Maiti *et al.*, 2017). In addition, PEG is a strong bio-compatible polymeric material (Huang *et al.*, 2019) and hence forms chemical linkages between the NR phase and graphite surface effectively. The higher elongation at break shown by the NR composite prepared

with 10 phr loading of PEG-g-Graphite compared to other NR composites indicates better adhesion between NR and PEG-g-Graphite material in the former composite. Huang *et al.* (2019) reported a similar observation in regard to elongation at break of PEG-g-Graphene filled poly (lactic acid) nanocomposites.

The resistance to initiate and propagate a crack is measured by tear strength. Similar to tensile strength, tear strength also varies according to a cyclic pattern with the increase of PEG-g-Graphite loading (Figure 11). Variation in tear strength could be considerably affected by the change from crystallinity in the morphology of the interface. The tear strength of most of the NR composites prepared with PEG-g-Graphite is higher than that of the control and may be due to existence of a strong interface between the NR matrix and PEG-g-Graphite due to improved adhesion between the two materials.

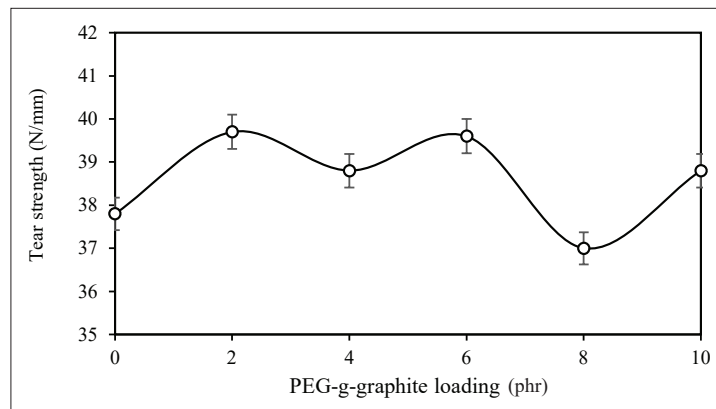


Figure 11: Tear strength of PEG-g-Graphite/NR composites

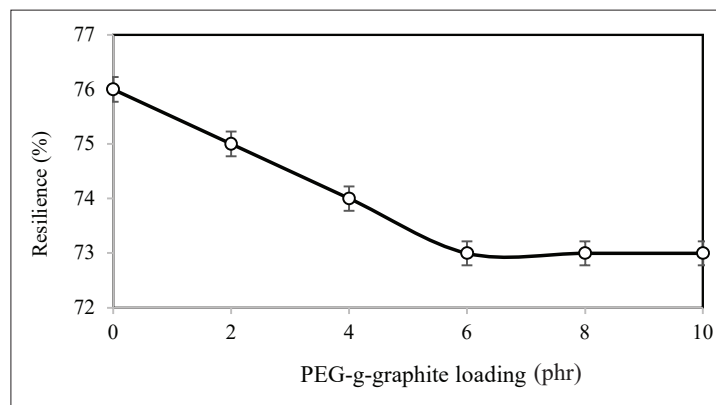


Figure 12: Resilience of PEG-g-Graphite / NR composites

The resilience of a polymeric material emphasizes the flexibility and elastic behaviour of a material. The control composite has indicated the highest resilience due to the absence of PEG-g-Graphite as the filler material (Figure 12). However, there is no marked difference in resilience between the PEG-g-Graphite composites and the control. Generally, resilience decreases with the increase in hardness and hence the resilience results are in agreement with the hardness results. Further, it can be stated that higher PEG-g-Graphite loadings in NR composites lead to an increase in the ability to transform mechanical energy into heat, thus decreasing the rebound resilience.

Tensile properties of PEG-g-Graphite / NR composites after ageing

Table 4 shows the tensile properties, after ageing of the control, and the other NR composites prepared with different PEG-g-Graphite loadings. The composites prepared with PEG-g-Graphite loadings of 8 phr and 10 phr have shown higher retention of tensile properties, and hence exhibit higher resistance to thermal

degradation. The control and NR composites prepared with PEG-g-Graphite loadings of 2 phr and 4 phr indicate poor resistance to thermal degradation. In other words, during ageing, low loadings of PEG-g-Graphite are not sufficient to retain the strong interactions formed with the NR matrix. In addition, PEG is a polymeric material with a low melting point and hence, low loadings of PEG-g-Graphite would not be sufficient to provide better adhesion between PEG and NR. A conventional sulphur vulcanizing system was used in this study. Matthews *et al.* (2019) reported that initial polysulphide crosslinks formed from the conventional sulphur vulcanizing system react further to form weak mono-, di-, and cyclic sulphide bonds during vulcanization via the dissociation, recombination, and rearrangement of the sulphur linkages. Therefore, the initial polysulphidic crosslinks formed are thermally unstable and hence undergo homolytic scission of the sulphur bonds and thermal decomposition and desulphuration, leading to weaker bonds. Deterioration of tensile properties of the NR composites observed with ageing at low loadings of PEG-g-Graphite is a result of the above-mentioned phenomena.

Table 4: Retention of tensile properties of PEG-g-Graphite / NR composites after ageing

Property	PEG-g-Graphite loading (phr)					
	0	2	4	6	8	10
Retention of tensile strength (%)	12.18	14.51	16.77	58.39	91.54	83.92
Retention of elongation at break (%)	57.37	52.21	55.47	76.54	87.71	86.97

Table 5: Sheet resistance of PEG-g-Graphite/NR composites

Property	PEG-g-Graphite loading (phr)					
	0	2	4	6	8	10
Sheet resistance ($\times 10^5$) (ohms/square)	3879.58	2.10	2.08	2.03	2.00	2.00

Sheet resistance of PEG-g-Graphite / NR composites

Sheet resistance of PEG-g-Graphite filled NR composites varies from 3.88×10^8 to 2×10^5 ohms/ square as shown in Table 5. The sheet resistance of a material is directly proportional to its resistivity. The composites prepared with PEG-g-

Graphite have shown lower sheet resistance than the control. Hence, PEG-g-Graphite composites exhibit better electrical conductivity. Further, the electrical conductivity of polymeric materials depends on many factors such as particle shape of filler, polymer–filler interaction, nature of particle–particle boundary and influence of preparation conditions on the volume

distribution of conductive particles (Wu & McLachlan, 1997; Gonon & Boudefel, 2006). Hence, it is evident that PEG forms a strong interaction between NR and graphite. In addition, sheet resistance of PEG-g-Graphite composites has not shown a significant variation as it varies from 2×10^5 only to 2.1×10^5 ohms/square. It is to be noted that the sheet resistance of 10 phr PEG-g-Graphite loaded NR composite has decreased by 99.9% from that of control. The interaction between PEG-g-Graphite and NR has produced a unique material

with enhanced electrical properties. Moreover, with the increase in PEG-g-Graphite loading, electrical conductive networks gradually form and penetrate into the insulating NR matrix. The literature reports that MAH and PEG molecular chains occupy a certain space, allowing graphite to overcome its attraction and disperse well (Huang *et al.*, 2019). Hence, electrical conductivity has slightly increased with the increase of PEG-g-Graphite loading.

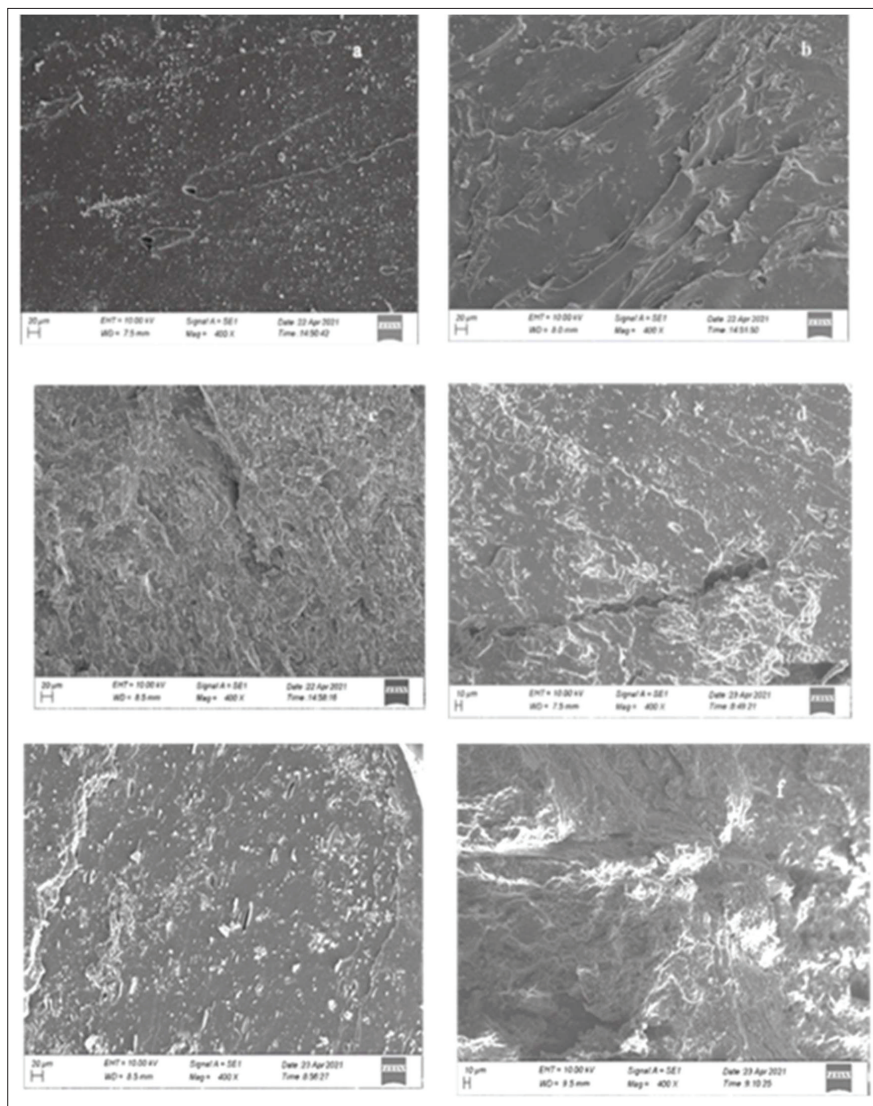


Figure 13: SEM images of tensile fracture surfaces of composites prepared with different PEG-g-Graphite loadings: (a) 0 phr (b) 2 phr (c) 4 phr (d) 6 phr (e) 8 phr and (f) 10 phr

Morphology of PEG-g-Graphite / NR composites

The micrographs of the composites obtained via SEM are shown in Figure 13. As observed from Figure 13a, the fracture surface of the control (without PEG-g-Graphite) is smooth and planar. Further, it could be designated as a brittle fracture surface as it exhibits a low elongation at break according to Figure 10. On the other hand, the NR composites prepared with PEG-g-Graphite indicate an elastic nature, and also, this indication has been confirmed by the results of elongation at break of the composites. Furthermore, the NR composites prepared with 2, 4, and 6 phr loadings of PEG-g-Graphite have shown a weak interface of fracture surface and hence indicate poor surface adhesion [Figure 13(b-d)]. However, composites prepared with 8 and 10 phr loadings of PEG-g-Graphite show better surface adhesion [Figure 13(e-f)] as it homogeneously disperses in the NR matrix and this has led to an improvement in properties.

CONCLUSIONS

PEG-g-Graphite was synthesized successfully using MAH as coupling agent. Transformation of graphite to PEG-g-Graphite was confirmed by FTIR, XRD, and TGA techniques and SEM analysis. Scorch and cure times increased with the increase of PEG-g-Graphite loading. The 10 phr PEG-g-Graphite filled NR composite showed an increase in scorch time and cure time by 33% and 14%, respectively, in comparison to the NR composite prepared without PEG-g-Graphite (control). Also, the former composite (with 10 phr PEG-g-Graphite) showed an enhancement in elongation at break and hardness compared to the latter composite (control). Ageing resistance of the PEG-g-Graphite/NR composites prepared with 8 and 10 phr loadings of PEG-g-Graphite was at a high level. Further, most of the physico-mechanical properties of PEG-g-Graphite/NR composites are at a level acceptable for super elastic rubber-based applications. The PEG-g-Graphite filled NR composites showed a remarkable improvement in electrical conductivity when compared to the control. The NR composite prepared with 10 phr loading of PEG-g-Graphite could be suitable for high electrical conductive polymeric applications.

Acknowledgements

The author wishes to thank the Rubber Research Institute of Sri Lanka, Bogala Graphite Lanka Plc. and Morex Lanka (Pvt.) Ltd., for supplying the raw materials for the study.

REFERENCES

- Barron M.K., Young T.J., Johnston K.P. & Williams R.O. (2003). Investigation of processing parameters of spray freezing into liquid to prepare polyethylene glycol polymeric particles for drug delivery. *Aaps Pharmscitech* **4**(2): 1–13. DOI: <http://doi.org/10.1208/pt040212>
- Bokobza L. (2017). Mechanical and electrical properties of elastomer nanocomposites based on different carbon nanomaterials. *C-Journal of Carbon Research* **3**(2): 10. DOI: <https://doi.org/10.3390/c3020010>
- Calixto C.M.F., Mendes R.K., Oliveira A.C.D., Ramos L.A., Cervini P. & Cavalheiro É.T.G. (2007). Development of graphite-polymer composites as electrode materials. *Materials Research* **10**: 109–114. DOI: <https://doi.org/10.1590/S1516-14392007000200003>
- Edirisinghe D. & Freakley P.K. (2003). Effect of varied carbon black distribution on the morphology and properties of blends of natural and nitrile rubber. *Journal of the Rubber Research Institute of Sri Lanka* **86**: 58. DOI: <https://doi.org/10.4038/jrrisl.v86i0.1807>
- Esmacili Y., Zarrabi A., Mirahmadi-Zare S.Z. & Bidram E. (2020). Hierarchical multifunctional graphene oxide cancer nanotheranostics agent for synchronous switchable fluorescence imaging and chemical therapy. *Microchimica Acta* **187**(10): 1–15. DOI: <https://doi.org/10.1007/s00604-020-04490-6>
- Gonon P. & Boudefel A. (2006). Electrical properties of epoxy/silver nanocomposites. *Journal of Applied Physics* **99**(2): 024308. DOI: <https://doi.org/10.1063/1.2163978>
- Hassan H.H., Ateia E., Darwish N.A., Halim S.F. & Abd El-Aziz A.K. (2012). Effect of filler concentration on the physico-mechanical properties of super abrasion furnace black and silica loaded styrene butadiene rubber. *Materials and Design* **34**: 533–540. DOI: <https://doi.org/10.1016/j.matdes.2011.05.005>
- Huang K., Yu H., Xie M., Liu S. & Wu F. (2019). Effects of poly (ethylene glycol)-grafted graphene on the electrical properties of poly (lactic acid) nanocomposites. *RSC Advances* **9**(19): 10599–10605. DOI: <https://doi.org/10.1039/C9RA01060B>
- Ismail H., Nordin R. & Noor A.M. (2002). Cure characteristics, tensile properties and swelling behaviour of recycled rubber powder-filled natural rubber compounds. *Polymer Testing* **21**(5): 565–569. DOI: [https://doi.org/10.1016/S0142-9418\(01\)00125-8](https://doi.org/10.1016/S0142-9418(01)00125-8)
- Imiela M., Anyszka R., Bieliński D.M., Masłowski M., Pędzich Z., Ziabka M., Rybiński P. & Syrek B. (2019). Effect of graphite and common rubber plasticizers on properties and performance of ceramizable styrene-butadiene rubber-based composites. *Journal of Thermal Analysis and Calorimetry* **138**(4): 2409–2417. DOI: <https://doi.org/10.1007/s10973-019-08339-w>
- Kitisavetjitt W., Nakaramontri Y., Pichaiyut S., Wisunthorn S., Nakason C. & Kiatkamjornwong S. (2021). Influences of carbon nanotubes and graphite hybrid filler on properties

- of natural rubber nanocomposites. *Polymer Testing* **93**: 106981.
DOI: <https://doi.org/10.1016/j.polymertesting.2020.106981>
- Kou Y., Wang S., Luo J., Sun K., Zhang J., Tan Z. & Shi Q. (2019). Thermal analysis and heat capacity study of polyethylene glycol (PEG) phase change materials for thermal energy storage applications. *The Journal of Chemical Thermodynamics* **128**: 259–274.
DOI: <https://doi.org/10.1016/j.jct.2018.08.031>
- Lai W.C., Liao W.B. & Lin T.T. (2004). The effect of end groups of PEG on the crystallization behaviors of binary crystalline polymer blends PEG/PLLA. *Polymer* **45**(9): 3073–3080.
DOI: <https://doi.org/10.1016/j.polymer.2004.03.003>
- Long H., Wu Z., Dong Q., Shen Y., Zhou W., Luo Y., Zhang C. & Dong X. (2019). Effect of polyethylene glycol on mechanical properties of bamboo fiber reinforced polylactic acid composites. *Journal of Applied Polymer Science* **136**(26): 47709.
DOI: <https://doi.org/10.1002/app.47709>
- Maiti M., Basak G.C., Srivastava V.K. & Jasra R.V. (2017). Influence of synthesized nano-ZnO on cure and physico-mechanical properties of SBR/BR blends. *International Journal of Industrial Chemistry* **8**(3): 273–283.
DOI: <https://doi.org/10.1007/s40090-016-0107-7>
- Matthew C., Emmanuel O. & Lawrence E. (2019). Effects of polyethylene glycol as alternative activator in a bamboo fibre filled natural rubber composite. *Global Scientific Journal* **7**(5): 296–310.
- Meng D. (2012). Effects of modified graphite on thermal properties of modified graphite/CA-MA/PMMA composite for latent heat thermal energy storage. *Advanced Materials Research* **562**: 401–404.
DOI: <https://doi.org/10.4028/www.scientific.net/AMR.562-564.401>
- Mokhena T.C., Mochane M.J., Sefadi J.S., Motloung S.V. & Andala D.M. (2018). Thermal conductivity of graphite-based polymer composites. In: *Impact of Thermal Conductivity on Energy Technologies* (ed. A. Shahzad), pp. 181. IntechOpen Limited, London, UK.
DOI: <https://doi.org/10.5772/intechopen.75676>
- Rad S.D., Islam A. & Alnasser A. (2019). Development of metal-graphene-filled hybrid composites: Characterization of mechanical, thermal, and electrical properties. *Journal of Composite Materials* **53**(24): 3363–3376.
DOI: <https://doi.org/10.1177/0021998318812928>
- Rawn J.D. & Ouellette R.J. (2018). *Organic Chemistry: Structure, Mechanism, Synthesis*. Academic Press, 2nd edition, pp. 1033. Elsevier Science, Netherlands.
- Rus A.Z.M., Abdullah N.M. & Abdullah M.F.L. (2016). Mechanical behavior of ultra violet (UV) curable renewable polymer/graphite (PG). *Indian Journal of Science and Technology* **9**(48): 1–4.
DOI: <https://doi.org/10.17485/ijst/2016/v9i48/102157>
- Rzeczkowski P., Krause B. & Pötschke P. (2019). Characterization of highly filled PP/graphite composites for adhesive joining in fuel cell applications. *Polymers* **11**(3): 462.
DOI: <https://doi.org/10.3390/polym11030462>
- Samadaei F., Salami-Kalajahi M. & Roghani-Mamaqani H. (2016). Radical coupling of maleic anhydride onto graphite to fabricate oxidized graphene nanolayers. *Bulletin of Materials Science* **39**(1): 229–234.
DOI: <https://doi.org/10.1007/s12034-015-1135-1>
- Sampath W.D.M., Egodage S.M. & Edirisinghe D.G. (2019a). Effect of an organotitanate coupling agent on properties of calcium carbonate filled low-density polyethylene and natural rubber composites. *Journal of the National Science Foundation of Sri Lanka* **47**(1): 17–27.
DOI: <http://doi.org/10.4038/jnsfsr.v47i1.8923>
- Sampath W.D.M., Egodage S.M. & Edirisinghe D.G. (2019b). Effect of peroxide loading on properties of natural rubber and low-density polyethylene composites. *Journal of Physical Science* **30**(3).
DOI: <https://doi.org/10.21315/jps2019.30.3.4>
- Sampath W.D.M., Fernando C.A.N. & Edirisinghe D.G. (2021). Review on carbon black and graphite derivatives-based natural rubber composites. *Advances in Technology* **1**(1): 101–126.
DOI: <https://doi.org/10.31357/ait.v1i1.4857>
- Saraswati T.E., Maharani D. & Widiyandari H. (2020). Copper oxide-based carbonaceous nanocomposites: Electrochemical synthesis and characterization. *AIP Conference Proceedings* **2243**(1): 020024.
DOI: <https://doi.org/10.1063/5.0001626>
- Shih W.P., Tsao L.C., Lee C.W., Cheng M.Y., Chang C., Yang Y.J. & Fan K.C. (2010). Flexible temperature sensor array based on a graphite-polydimethylsiloxane composite. *Sensors* **10**(4): 3597–3610.
DOI: <https://doi.org/10.3390/s100403597>
- Shanmugaraj A.M., Kumar K.T., Sundari G.S., Kumar E.S., Ashwini A., Ramya M., Varsha P., Kalavani R., Raghu S. & Ryu S.H. (2019). Study on the effect of silica-graphite filler on the rheometric, mechanical, and abrasion loss properties of styrene-butadiene rubber vulcanizates. *Journal of Elastomers and Plastics* **51**(4): 359–378.
DOI: <https://doi.org/10.1177/0095244318787560>
- Somaweera D., Abeygunawardane G.A., Weragoda S. & Ranatunga S. (2021). Effect of vein graphite powder on mechanical, curing, and thermal properties of solid tire vulcanizate. *Materials Today: Proceedings* **59**: 316–323.
DOI: <https://doi.org/10.1016/j.matpr.2021.11.181>
- Sumita M., Sakata K., Asai S., Miyasaka K. & Nakagawa H. (1991). Dispersion of fillers and the electrical conductivity of polymer blends filled with carbon black. *Polymer Bulletin* **25**(2): 265–271.
DOI: <https://doi.org/10.1007/BF00310802>
- Surya I., Hayemasae N. & Ginting M. (2018). Cure characteristics, crosslink density and degree of filler dispersion of kaolin-filled natural rubber compounds in the presence of alkanolamide. *IOP Conference Series. Materials Science and Engineering* **343**(1): 012009.
DOI: <https://doi.org/10.1088/1757-899X/343/1/012009>

- Vallés C., Papageorgiou D.G., Lin F., Li Z., Spencer B.F., Young R.J. & Kinloch I.A. (2020). PMMA-grafted graphene nanoplatelets to reinforce the mechanical and thermal properties of PMMA composites. *Carbon* **157**: 750–760.
DOI: <https://doi.org/10.1016/j.carbon.2019.10.075>
- Volanti D.P., Felix A.A., Suman P.H., Longo E., Varela J.A. & Orlandi M.O. (2015). Monitoring a CuO gas sensor at work: an advanced in situ X-ray absorption spectroscopy study. *Physical Chemistry Chemical Physics* **17**(28): 18761–18767.
DOI: <https://doi.org/10.1039/c5cp02150b>
- Wu J. & McLachlan D.S. (1997). Percolation exponents and thresholds obtained from the nearly ideal continuum percolation system graphite-boron nitride. *Physical Review B* **56**(3): 1236.
DOI: <https://doi.org/10.1103/PhysRevB.56.1236>
- Xu J.Z., Zhang Z.J., Xu H., Chen J.B., Ran R. & Li Z.M. (2015). Highly enhanced crystallization kinetics of poly (l-lactic acid) by poly (ethylene glycol) grafted graphene oxide simultaneously as heterogeneous nucleation agent and chain mobility promoter. *Macromolecules* **48**(14): 4891–4900.
DOI: <https://doi.org/10.1021/acs.macromol.5b00462>
- Zhao L.M., Feng X., Mi X.J., Li Y.F., Xie H.F. & Yin X.Q. (2015). Mechanical reinforcement and shape memory effect of graphite nanoplatelet-reinforced epoxy composites. *Journal of Intelligent Material Systems and Structures* **26**(12): 1491–1497.
DOI: <https://doi.org/10.1177/1045389X14544142>
- Zohuri G. (2012). *Polymer Science: A Comprehensive Reference*, 1st edition, pp. 7760. Elsevier Science, Netherlands.

RESEARCH ARTICLE

Renewable energy

Analysis of instantaneous, daily and monthly statistics 2017-2021 of rooftop solar energy

JR Lucas*

Department of Electrical, Electronic and Telecommunication Engineering, Faculty of Engineering, General Sir John Kotelawala Defence University, Ratmalana, Sri Lanka.

Submitted: 17 February 2022; Revised: 15 July 2022; Accepted: 26 August 2022

Abstract: Solar photovoltaic systems are used in rooftops of buildings, especially to supply excess electricity to the grid. Analysis of the data from a site in Sri Lanka shows that, while the variation of the energy supplied during a given month is somewhat constant, large variations may occur from day to day, even within a given week. Further, dependent on the month, fluctuations from instant to instant could follow a typical sunny day sinusoid or on the other extreme fluctuate heavily. Since good statistics are not routinely available, many studies on solar electricity dispatch do not take these variations into account. Thus, supply authorities have to plan generation schedules without a knowledge of the likelihood of such variations. This paper analyses the power output of a 4.16 kWp domestic solar rooftop system, to allow the findings of fluctuations of solar energy output patterns to be used in system studies. The study shows that for a fixed rooftop installation, the maximum daily solar energy production can decrease to around 83% in months where the solar panel direction is adversely affected by the declination angle. It also shows that 80% of the maximum daily energy available in a given month can be assured 50% of the time in the worst-case scenario, while a day can produce just 3% of the maximum energy. It is also found that in the best month, near capacity production can be assured 90% of the time, where the sky is clear and the panel is ideally oriented.

Keywords: Fluctuation statistics, photovoltaic systems, rooftop solar, solar intermittency, solar power generation.

INTRODUCTION

With the world moving towards environmentally friendly sources of energy, harnessing rooftop solar electricity has become prudent (Atluri *et al.*, 2018; www.adb.org, 2021). Thus, many rooftop solar photovoltaic (PV) installations are coming up in both industrial and domestic sites. However, there is little information available to the solar electricity producers on the probable solar electricity that can be extracted. They are thus at the mercy of the solar system vendors who paint a glorified picture. A site (latitude 6.83°N) in Mount Lavinia, Sri Lanka has been selected to study this global phenomenon. To optimise solar electricity generation, rooftop installations in the northern hemisphere should preferably be facing South with a tilt angle of the PV panels corresponding to the latitude for the site of around 7°N.

The instantaneous and daily electricity produced would vary due to cloud cover (Lucas, 2021), while monthly variations occur due to the position of the earth relative to the sun (www.lankanrailblazer.wordpress.com, 2019; Vidanapathirana *et al.*, 2021) or to monthly weather variations. The decrease in the solar electricity output, other than due to the position of the sun, are the

*jrohanlucas@yahoo.com;  <https://orcid.org/0000-0001-7215-0815>



This article is published under the Creative Commons CC-BY-ND License (<http://creativecommons.org/licenses/by-nd/4.0/>). This license permits use, distribution and reproduction, commercial and non-commercial, provided that the original work is properly cited and is not changed in anyway.

temperature, clearness of sky, rainfall, number of wet days, and wind speed (Wickramarathna *et al.*, 2011; www.weatherspark.com, 2016). This paper provides a multitude of fluctuation statistics for both the electricity supply authority and the solar electricity producer.

MATERIALS AND METHODS

In the present study, the radiation falling on the solar panel is first analysed starting from the global irradiation and the location of the site. Considering a site where the panels have a fixed orientation with respect to solar irradiation, the monthly variation of solar insolation is determined considering also the declination angle and the probable cloud cover. Daily solar output curves during a 4-year period from 2017 to 2021 have been considered for a domestic rooftop. Analysis is carried out on a monthly basis by considering the energy output in a number of bands. A particular site in Mount Lavinia Sri Lanka has been selected to illustrate the determination of assurance of solar energy production from the site. Variation of solar energy output with panel temperature is taken into account. The results of the analysis are presented in graphical form, and statistics obtained based on the probable energy output.

RESULTS AND DISCUSSION

Analysis of radiation falling on solar panel

The total extra-terrestrial radiation resulting in the solar irradiance at the top of the Earth's atmosphere is around 1361 W/m^2 (Tukiainen & Gaisma.com, 2021). However, based on the clearness of the sky (Tukiainen & Gaisma.com, 2021) or transparency of the atmosphere, the maximum direct beam irradiance reaching the earth's surface is around 1050 W/m^2 (Coddington, 2016). Thus, the maximum irradiance on the horizontal Earth's surface, which would occur in a cloudless sky when the Sun is at its zenith, is around 1120 W/m^2 including diffused radiation.

The direction of the sun's rays which fall on the Earth depends on the latitude of the site. Further, as the day progresses, the path of the radiation to ground level changes, with maximum at mid-day. Thus, near the equator, the Sun's beams can be considered to reach the Earth's surface from 6 am to 6 pm. However, diffused sunlight would still reach the earth's surface at night-time. It can be said that some part of the Earth's surface receives direct sunlight 24 hours of the day. The Earth, being a near sphere with radius R would have a surface area of $4\pi R^2$, and a horizontal projected area of πR^2 .

This means that a maximum of one-fourth of the direct sunlight falling would be captured perpendicular to the horizontal area on the Earth. Thus, the theoretical maximum energy that could be harvested from a given site would be one-fourth of 1.361×24 or $8.17 \text{ kWh/m}^2/\text{day}$, including any diffused radiation. At present, commercial solar panels can have a maximum efficiency of around 20% under standard test conditions, while 18.6% is more typical in currently installed sites (Lucas, 2021) and will be used in the present analysis. This yields a peak realizable solar electricity generation of 0.253 kWp or $1.52 \text{ kWh/m}^2/\text{day}$.

If the solar radiation (www.newport.com, 2021) falling on a solar panel is considered, there would be the direct beam, with a component normal to the panel, and diffused radiation from the top of the atmosphere and from clouds within the atmosphere, as seen from Figure 1. As the sun appears to move from East to West due to the rotation of the Earth, maximum electricity is produced near mid-day when the direct beam would be near normal to the solar panel. However, the temperature of the solar cells of the panel would also be highest at this time.

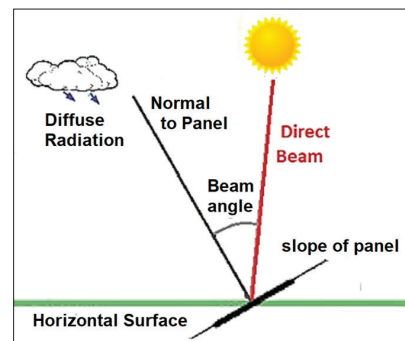


Figure 1: Composition of irradiance

It is known that on a hot sunny day, the cell temperature can rise to more than 30°C above ambient temperature. If efficient monocrystalline solar cells are considered, they have a solar panel efficiency of 18.6% and a negative temperature coefficient of $0.4\%/^\circ\text{C}$ (www.solaredge.com).

A rise in cell temperature of 30°C would cause a drop of 12% in power output, giving an effective solar panel efficiency of 16.4%. Since most electricity from the solar panel is produced near mid-day when the solar panel is hot, with a relatively clear sky, electrical energy output from the panel would be around $1.34 \text{ kWh/m}^2/\text{day}$. A typical monocrystalline solar panel of size $1 \text{ m} \times 1.65 \text{ m}$

can be expected to yield 1.34×1.65 or 2.21 kWh per panel per clear day.

Monthly variation of solar insolation

Figure 2 shows the seasonal variation of the declination angle between $\pm 23.45^\circ$ due to the tilt of the Earth on its rotating axis and the elliptical path of the Earth around the sun.

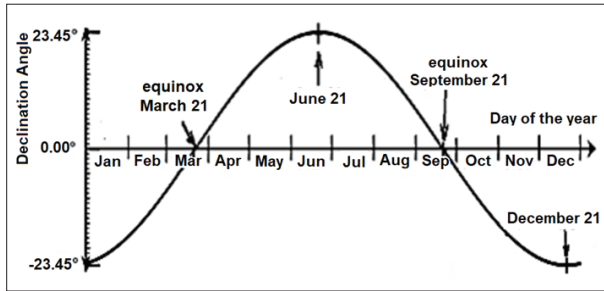


Figure 2: Monthly variation of the declination angle

The clearness of the sky, defined in terms of the percentage of time the sky is covered by clouds (Sanusi & Ojo, 2015) is usually categorized in 20% steps as clear, mostly clear, partly cloudy, mostly cloudy and overcast conditions and need to be considered to make a realistic prediction. Further, Lucas (2021) presents the probability of yielding a given solar energy on a monthly basis. Battery storage could be used to enhance the usability of solar panels and somewhat mitigate the effects of fluctuations (Nayanathara *et al.*, 2019; Lucas *et al.*, 2020).

Site in Mount Lavinia, Sri Lanka

Although the findings of the study are of general nature, analysis has been conducted with solar data of a domestic rooftop site in Mount Lavinia, Sri Lanka (Figure 3). The site has 12 monocrystalline solar panels installed, with each panel being of size 1.65×1.0 m. The vendor’s stated capacity for the site is 4.16 kWp. Based on a typical 80% efficiency on rated capacity, when the solar panel is hot, this site can be considered to generate a maximum peak of around 0.8×4.16 or 3.328 kW near noon on a clear day, with an expected maximum yield of around 12×2.21 or 26.5 kWh/day. However, the actual daily solar electricity production will depend on both clearness of the sky as well as on seasonal variations, in addition to the variation of sunlight from sunrise to sunset.



Figure 3: Orientation of solar panels on roof

Solar output measurements are available online for the site on the SolarEdge monitoring portal provided by the manufacturer of the panels every 15 min although monitored continuously. Records are available from the inception for the solar system at the Mount Lavinia site, from mid July 2017. Thus, for analysis purposes, the four-year period from August 2017 to July 2021 has been considered.

The solar irradiance curve at the surface of the Earth is usually considered ideal, similar to part of a parabola as in Figure 4. Since the inverted parabola shown has a mean value equal to two-thirds, which can be easily obtained from integration, the energy in kWh works out to 8 times the peak value in kW, with the base duration from 6am to 6pm. Thus, quite often the solar curve is considered to be of duration 8 h at peak value giving the same energy. However, the ideal parabolic shape is rarely seen in practice.

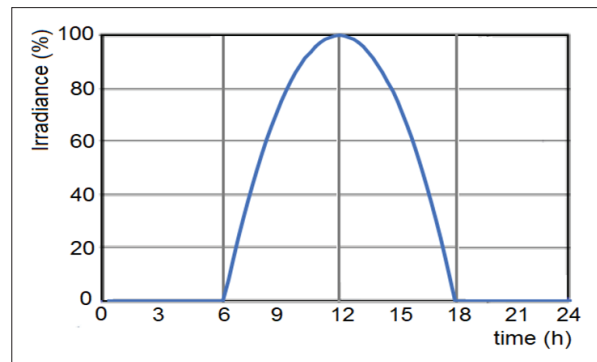


Figure 4: Daily solar irradiance

At the site considered, almost ideal conditions, although rare, were recorded on 1st February 2018 and shown in Figure 5 with a peak power of 3.332 kW and energy of 26.27 kWh. These values correspond very well with the theoretically anticipated values of 3.328 kW and 26.5 kWh/day. The shape also compares well with the expected parabolic shape also inscribed in Figure 5 for comparison.

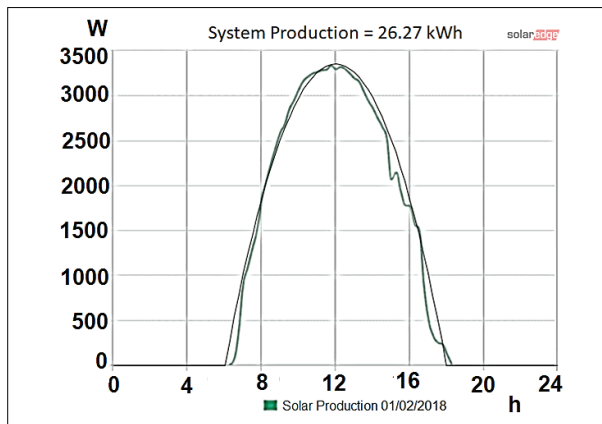


Figure 5: Peak solar energy day 1st February 2018

Clear blue skies have been commonly observed at the site during daytime in January and February, but near ideal days do not occur every day of week. At the site, the best week observed, during the four-year period evaluated for solar production, occurred from 3rd to 9th January 2019 of which the best four consecutive days are shown overlapped in Figure 6.

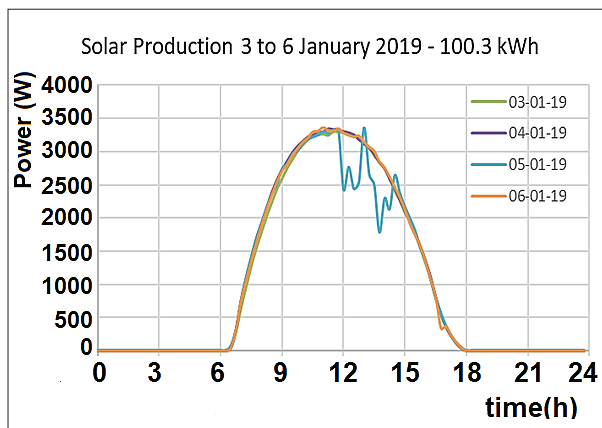


Figure 6: Solar output during a good period

It is seen that during this period, the peak power is virtually the same at around 3.3 kW each day, but the energy produced varied slightly from 24.4 to 25.5 kWh from day to day, with a mean of 25.1 kWh. While the total production for this period was 100 kWh, that for the week was 170 kWh.

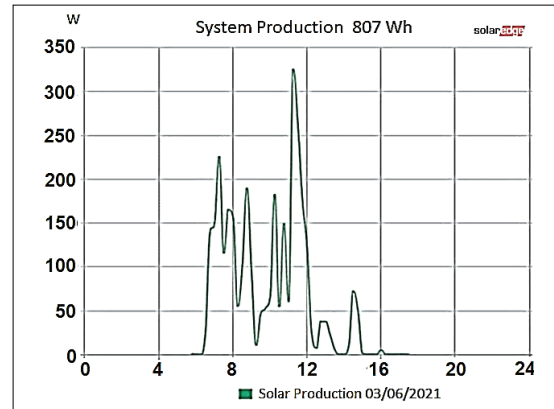


Figure 7: Minimum energy day

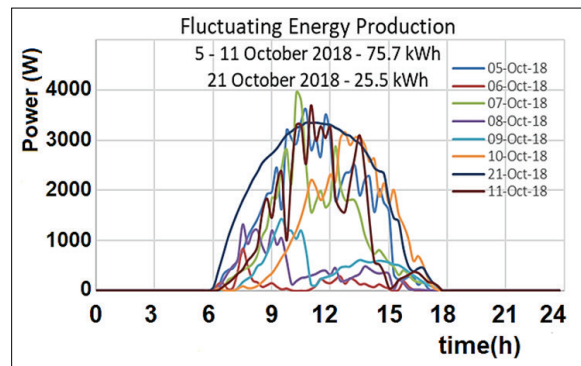


Figure 8: Solar output of a highly fluctuating week

The study has also found that certain months are relatively bad for the energy production, with the lowest recorded during the four-year period being on 3rd June 2021, just around one-tenth of maximum peak power, or 0.324 kW peak, and with the day's energy being just 0.807 kWh, or just 3% of the maximum energy produced, as shown in Figure 7. In particular, if the week of 5th to 11th October 2018 is considered, as shown in Figure 8, it can be seen that during this period the peak power varied drastically between 0.84 kW and 3.94 kW on adjacent days, 6th and 7th October. Correspondingly, the energy varied substantially from day to day during this week,

between 1.5 kWh and 18.5 kWh. For comparison, the best production day in the month that year, 21st October has been plotted alongside for comparison. It is seen that while the peak power was 3.35 kW, the energy produced that day was 25.5 kWh. Comparison also shows that the energy of the particular week is just 3 times that of the best day for the month.

Planning to cater for highly fluctuating weeks like these is a tremendous task, and it is important to know how often such weeks occur. Thus, this aspect is also addressed in this paper.

The solar monitoring portal also stores monthly solar output energy, as shown in Figure 9 for the four-year period considered. It is seen that while the solar output is somewhat constant for the same month in different years, it also shows a significant seasonal variation from month to month due to changes in declination angle (on the 21st of each month), as given in table 1, and seasonal weather, as expected.

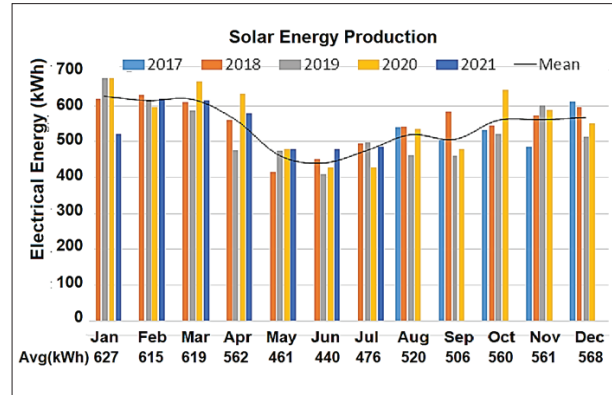


Figure 9: Monthly solar electricity production over a 4 year period

To obtain maximum solar electricity output, the solar panel needs to be rotated to face the sun throughout the year corresponding to the declination angle (Vidanapathirana *et al.*, 2021).

Table 1: Monthly declination angle

Jan	Feb	Mar	Apr	May	Jun	Jul	Aug	Sep	Oct	Nov	Dec
-20.1°	-11.2	0°	11.6°	20.1°	23.4°	20.4°	11.8°	0°	-11.8°	-20.4°	-23.3°

Table 2: Correction factor for declination

Month	δ	ϵ	$\text{Cos } \epsilon$	Max kWh	Observed max
Jan	-20.1°	0°	1	687	686.5
Feb	-11.2°	6°	0.994	683	631.5
Mar	0°	16°	0.961	660	667.3
Apr	11.6°	27°	0.891	612	555.9
May	20.1°	37°	0.799	549	455.3
Jun	23.4°	44°	0.719	494	427.6
Jul	20.4°	46°	0.695	477	472.5
Aug	11.8°	41°	0.755	519	519.7
Sep	0°	31°	0.857	589	506.4
Oct	-11.8°	21°	0.934	641	560.2
Nov	-20.4°	9°	0.988	678	561.5
Dec	-23.3°	2°	0.999	687	568

δ - Declination angle, ϵ - Correction angle

However, in a domestic solar installation, the panel is neither rotated to track the sun daily nor seasonally. The parabolic curve considered is based on the assumption that the panel is not rotated from sunrise to sunset, so that no correction needs to be made. However, depending on the direction the solar panel is installed to face, a correction for the maximum solar yield would need to be done. Based on the monthly solar output variation, it is likely that the particular solar system under investigation had been installed to give maximum output during January. Thus, the angles are corrected to be taken as reference, or give 0°, on 1st January, and correction factors are based on that, as given in Table 2. Considering, from observations over 4 years, that the maximum solar energy output practically obtainable in a month to be 687 kWh, maxima for all the months have been calculated based on the correction factor $\cos \epsilon$ and shown in Table 2.

The estimated monthly changes due to change in declination are compared with actual maxima in the corresponding month, over a 4-year period, and are shown in Figure 10. A very close match is seen.

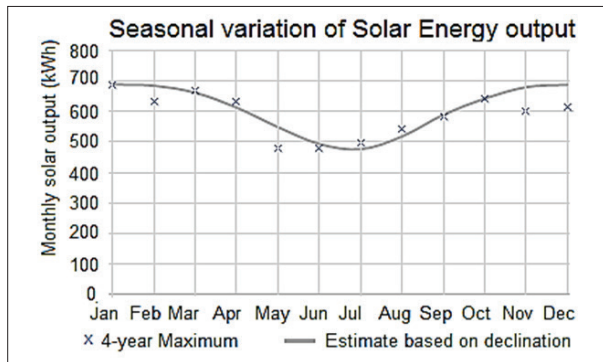


Figure 10: Comparison with seasonal variation

Figure 11 shows the variation of solar production for 22nd July 2018, a day with a very clear sky, as observed by the shape. However, the peak solar electric power produced, and the corresponding peak energy are 2.70 kW and 19.4 kWh respectively rather than the ideal 3.3 kW and 26 kWh.

Thus, the correction factor suggested in Table 2 has been selected as 19.4/26 or 0.75 and used to scale the maximum power output curve, which is drawn alongside in a dashed line. While the peak value of this scaled curve is lower at 2.50 kW the corresponding energy is 20.0 kWh which is slightly higher justifying the correction.

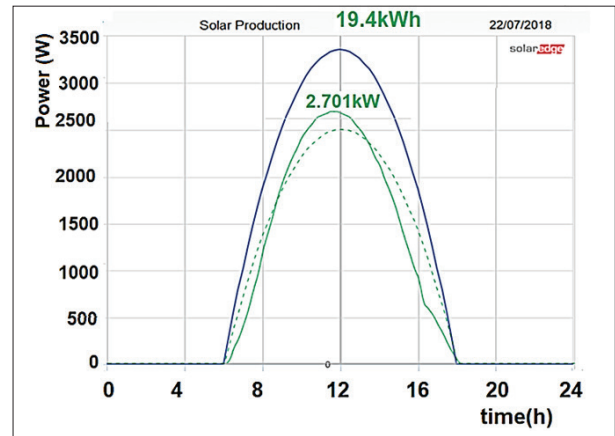


Figure 11: A near ideal day in July

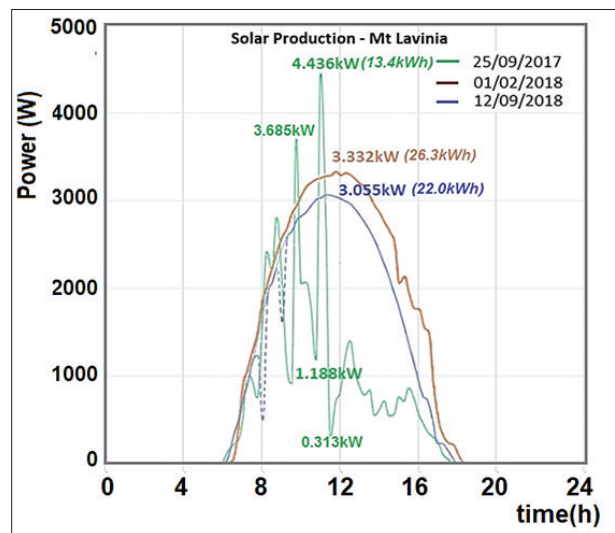


Figure 12: Analysis of solar output during fluctuations

Solar output fluctuations analysis

25th September 2017 has been found to be a day where the solar output power fluctuated a lot, going down to 0.313 kW while seemingly unexpectedly reaching even slightly higher than the stated capacity. to 4.436 kW moments later. Yordanov *et al.* (2012) have suggested that these bursts of energy are due to cloud reflections, but the author begs to differ as the conditions just prior to the dip have indicated a heavy dip, probably cooling the panel and increasing its efficiency. The output of 25th September has been compared in Figure 12 with that of the overall maximum energy day (01/02/2018) and

a maximum power day in September (12/09/2018) to take into account seasonal behaviour. On this particular peak day, 12th September, while the curve followed the expected parabolic shape, two minor dips are seen (shown dotted), but which did not change the basic shape during the time period investigated near noon.

It is seen from the figure that while, the peak power for a clear day achieved 3.332 kW with a daily energy of 26.27 kWh, the month of September never gave such high outputs for this site over the 4-year period considered. Thus, comparison only with the overall peak day was not considered prudent, and the best day ever in September (12/09/2018) was considered, where the peak power was nearly 10% lower at 3.055 kW.

It might be surprising to note that the peak power on a cloudy day like 25th September 2018, with 13.42 kWh/day, was in fact much higher at 4.436 kW, compared to what could have been expected, *i.e.*, 3.055 kW, for even a clear day. While it seems strange, detailed analysis gives the reason for this apparent discrepancy. Studying the curves of 25th September 2018 with those of 12th September shows that there are a number of points which are above the clear day curve. Examination of each of these points shows that each higher peak occurred just after a very low point just before that instant. For example, for the peak of 4.436 kW, the power stood at 1.188 kW moments before, and fell to around 0.313 kW moments later. This seems very strange at first sight, but it can be easily explained by considering the movement of clouds above the solar panel. Yordanov *et al.* (2012) have studied these bursts with probably 1 min data steps which showed many such bursts, but which did not show the energy fluctuations which became prominent with the integrated step of 15 min in Figure 12.

A solar panel of capacity 4.16 kWp under standard conditions would probably normally operate at around 30°C higher than the ambient temperature at mid-day. However, the temperature would fall to near ambient during cloud cover. Thus, soon after a cold session for the solar cell, when the sun suddenly appears, the solar panel efficiency is high due to the much lower temperature, giving a value very close to the nominal value of 4.16 kWp.

A sample of solar output patterns

Near ideal clear sky days, like Figure 5 or even Figure 11, are rare and do not occur even on one or two days of the month, even in clear sky months like January and February. In the months of May and June, it was not

possible to even find a single clear sky day during the 4 years under investigation.

A collection of the days with the highest energy production for each month is compared and shown in Figure 13. The individual months are not identified in Figure 13, but could be identified, if necessary, by the observed peak values given in Table 2. The intention here is to show that if the solar panel is not rotated periodically, even the solar radiation falling on the panel cannot be fully captured, and thus the particular month is of no significance in this graph.

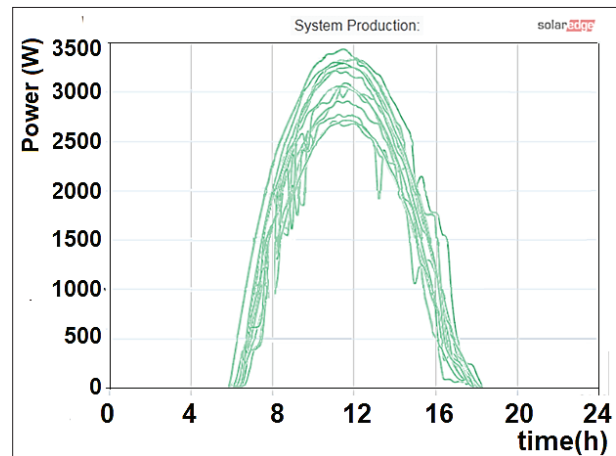


Figure 13: Near clear sky days in different months

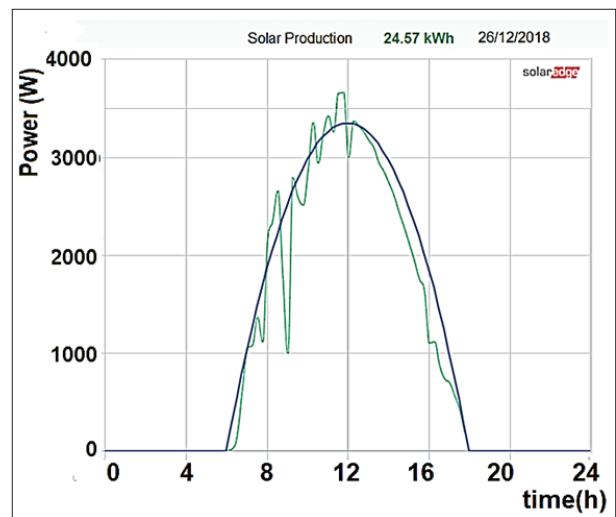


Figure 14: Minor fluctuations on good clear day

Since one of the solutions to mitigate the effects of fluctuations economically is the choice of optimum battery capacity, samples of partially cloudy, cloudy and overcast days are shown to give an insight on what sort of samples need to be put into the analysis basket for good validation or research studies. They are placed together with an ideal parabolic curve for comparison in each case.

Figure 14 shows minor fluctuations in solar power output caused by minor cloud movements on 26th December 2018. However, almost the maximum realisable energy is obtained (24.57 kWh).

On 9th February 2018, shown in Figure 15, partial clouds occurred in the morning (up to about 10 am), the normal peak was achieved slightly earlier, and the solar output dropped by 20% (21.38 kWh).

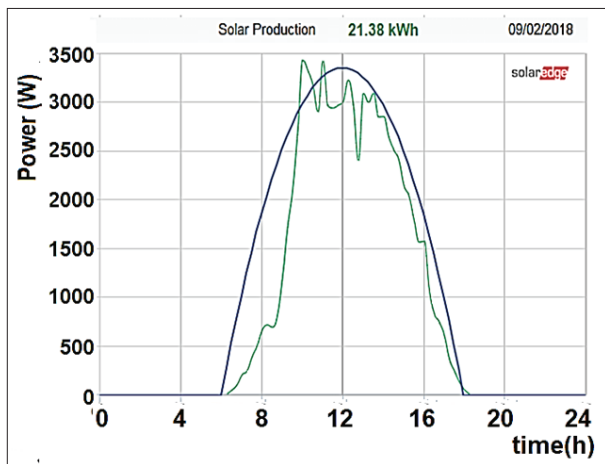


Figure 15: Solar output on a day with morning clouds

On 1st April 2018, a cloudy morning and the effect of declination angle have given rise to a 30% reduction of peak to around 3 kW and a reduction in the solar power output to 18.15 kWh as shown in Figure 16.

It is seen that it would have been a very cloudy morning with clearing of the sky thereafter.

Figure 17 shows the solar output on 10th October 2017, an overcast morning till about 11 am keeping the solar panels cool. A sudden clearing of the sky thereafter would have increased the efficacy of the panels giving a higher peak of 4 kW power output immediately thereafter.

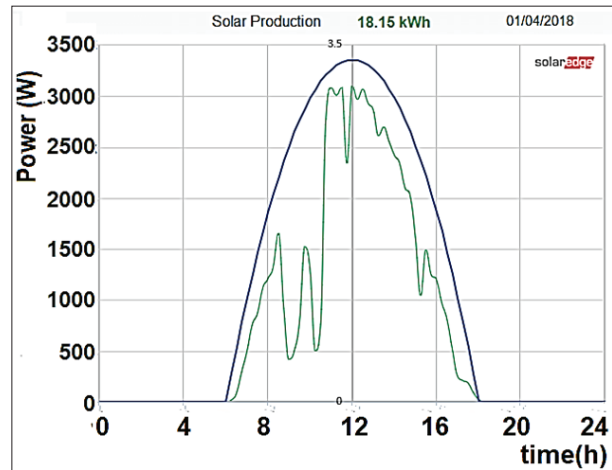


Figure 16: Solar output on a cloudy morning

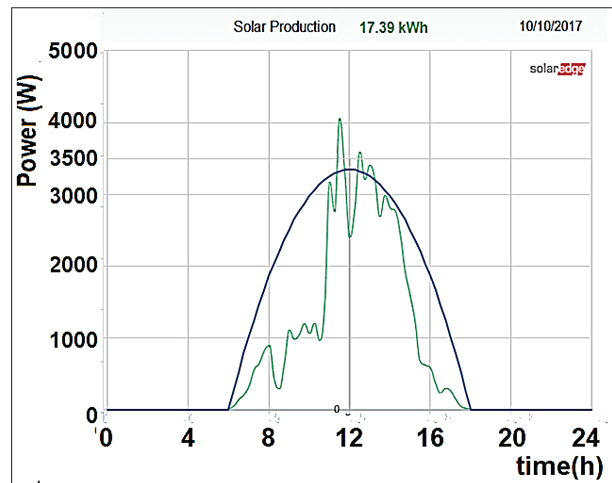


Figure 17: Solar output on an overcast morning

However, it is seen that while there is no reduction due to declination, there is still a near 35% reduction in the energy output (17.39 kWh).

17th March 2018 was a similar overcast morning, but with declination also affecting the solar power output and reducing it by nearly 45%. It can be seen from Figure 18 that in the evening the curve is nearly parabolic with the declination reduction factor.

The 25th September 2017 was a morning with a heavy movement of clouds and overcast conditions in the evening, as seen in Figure 19. It is seen that the alternate

cooling and strong sunlight has caused the peak power to go to 4.4 kW, even above the value at test conditions of 4.17 kW. However, the resulting solar output energy has been reduced by nearly 50% due to the overcast conditions in the evening.

Figure 20 on 9th October 2017 shows an unusual day with overcast conditions during mid-day. It is seen that while the morning and evening are relatively free of clouds, mid-day has been completely overcast with power output falling to nearly zero just before mid-day, giving a reduction of the energy of just over 55% (11.45 kWh).

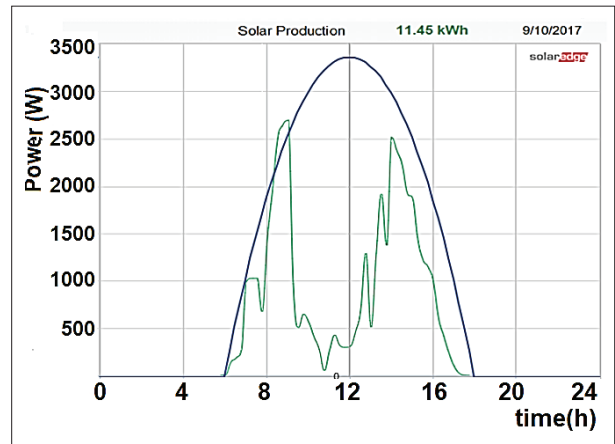


Figure 20: Solar output on an overcast mid-day

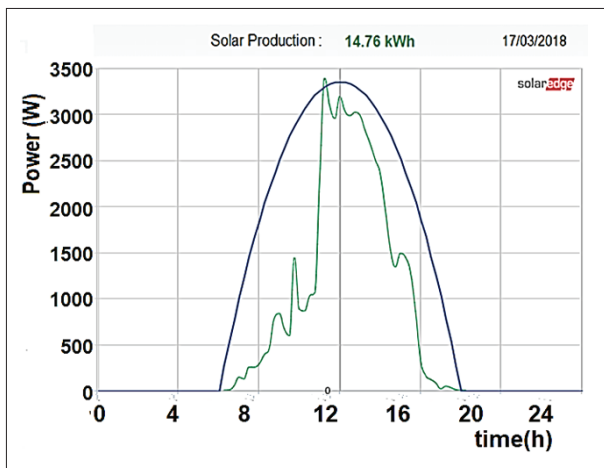


Figure 18: Solar output on an overcast morning in March

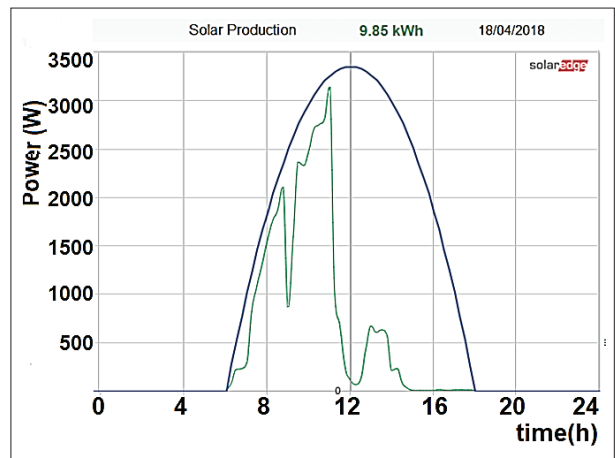


Figure 21: Solar output with a fully overcast evening

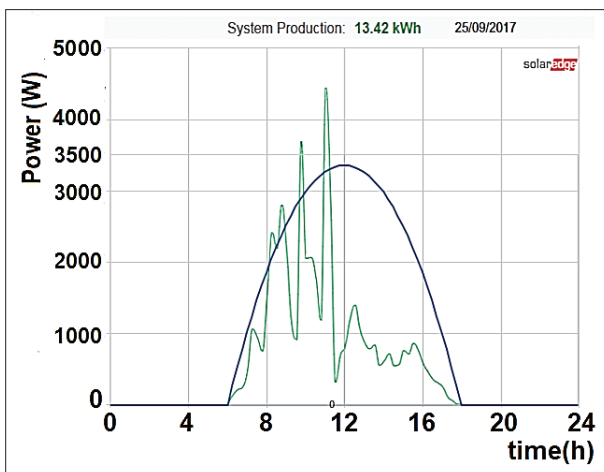


Figure 19: Solar output on a cloudy morning and overcast evening

Figure 21 shows a partially cloudy morning on 18th April 2018, with the power curve following quite closely the theoretical curve, and a fully overcast sky in the evening. It is seen that the energy has reduced by over 60% to 9.85 kWh due mainly to the evening overcast conditions, with power not exceeding 0.5 kW from around 11 pm onwards.

Figure 22 corresponds to the solar output on a fully overcast day, 3rd September 2017, with a slight clearing of the sky later in the evening, allowing the power to rise to near normal at 2.1 kW in the late afternoon and thereafter. It is seen that the energy reduction corresponds to over 70% (7.8 kWh).

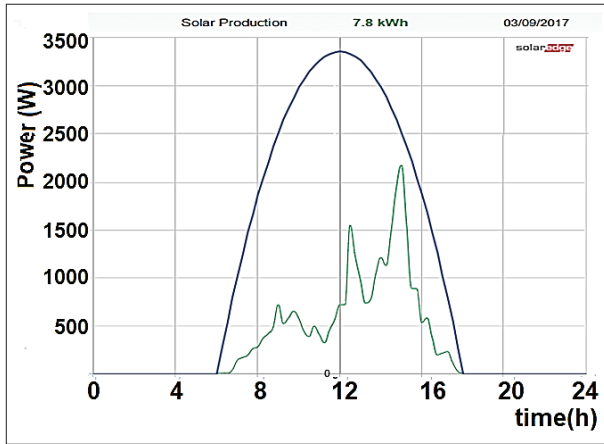


Figure 22: Solar output on an overcast day

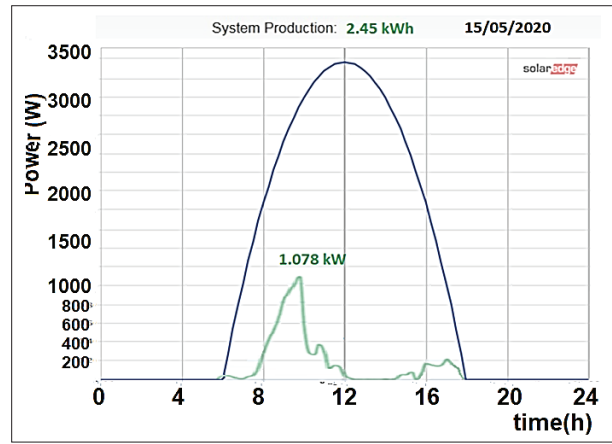


Figure 24: A very overcast day in May

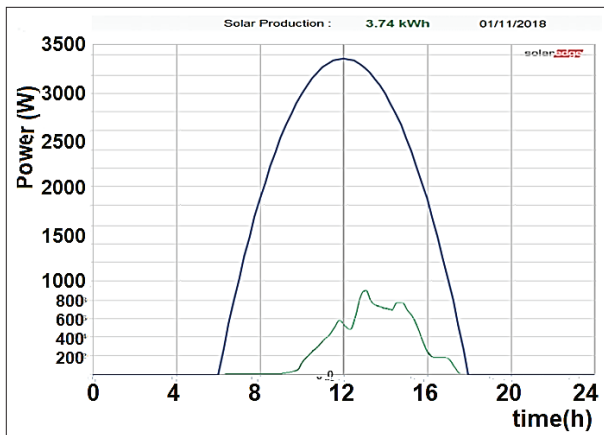


Figure 23: Very overcast day in November

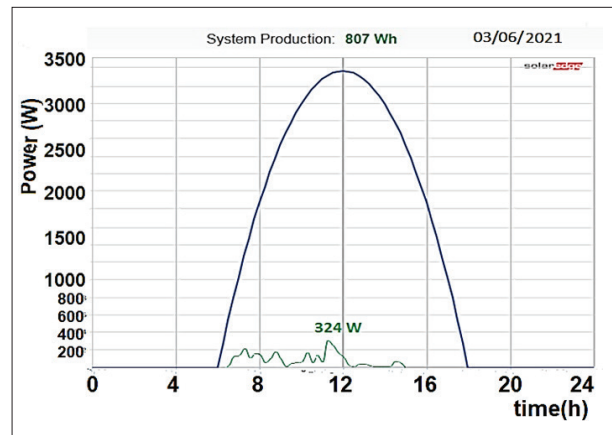


Figure 25: Lowest solar electricity producing day

Figure 23 shows a day with almost no sunlight throughout the day, with peak power around 0.8 kW or 25% of maximum achievable. The energy has also drastically reduced by 85% to 3.73 kWh.

Figure 24 shows a day with little sunlight in the morning and nothing after that (20 May 2020). The reduction in energy is 90% to 2.45 kWh with the peak power for the day just exceeding 1 kW. This day was however not the lowest energy producing day, which occurred on 3rd June 2021, as seen in Figure 25. This day had a peak solar output electric power of just 324 W (one-tenth normal peak) and an energy of 807 kWh, a huge reduction of 97%, with only 3.07% of maximum energy being generated on this day.

Categorization statistics of solar power

It is seen from the foregoing study that large fluctuations in both power and energy occur from season to season, day to day and hour to hour. Thus, statistics of the occurrence of varying levels of solar energy production would be very useful in planning and operating solar rooftop installations. Study of the energy production of the solar installation at the particular site considered, has shown, from both theoretical and practical considerations, that the maximum daily energy from the site is around 26.5 kWh. Thus, for statistical analysis, Categorization was done based on 2 kWh steps aligned at mid-value, for the 4-year period considered.

Figure 26 shows a summary of the probability of assurance of solar energy production at the site, plotted against assured energy. It is seen that in a good solar production month, like February for the site, over 20 kWh/day can

be assured to be produced on around 25 days, while on a bad solar energy producing month like June, one would find it difficult to assure even 15 kWh/day on the same number of days,

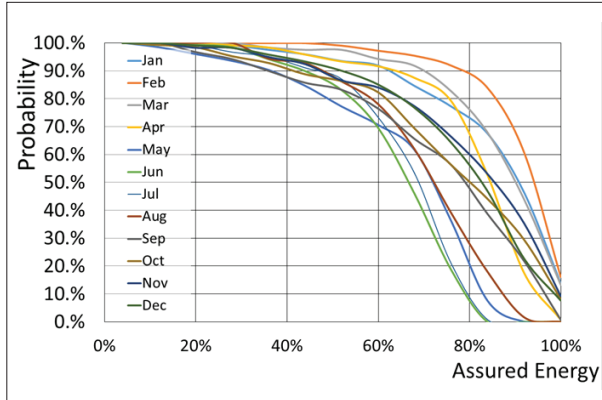


Figure 26: Probability of assurance of a solar energy production

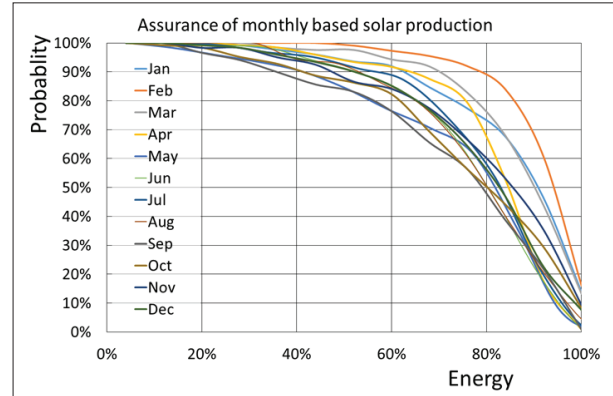


Figure 27: Assurance of a weighted monthly solar production

Table 3: Categorization of solar output days for the site

Category (kWh)	Average number of days in range												Total
	Jan	Feb	Mar	Apr	May	Jun	Jul	Aug	Sep	Oct	Nov	Dec	
1	0.0%	0.0%	0.0%	0.0%	1.6%	0.8%	0.0%	0.0%	0.0%	0.8%	0.0%	0.0%	0.3%
3	0.0%	0.0%	0.0%	0.0%	2.4%	0.0%	0.8%	0.0%	3.3%	0.8%	1.7%	0.8%	0.8%
5	0.8%	0.0%	0.0%	0.8%	2.4%	0.8%	2.4%	0.0%	2.5%	3.2%	0.0%	0.8%	1.2%
7	1.6%	0.0%	1.6%	0.8%	3.3%	4.3%	1.6%	5.6%	4.2%	2.4%	3.3%	2.5%	2.6%
9	1.6%	0.0%	0.8%	2.5%	5.7%	4.3%	4.0%	1.6%	4.2%	4.0%	2.5%	2.5%	2.8%
11	2.4%	0.9%	0.0%	2.5%	7.4%	6.8%	4.0%	6.6%	2.5%	2.4%	5.9%	3.3%	3.7%
13	1.6%	1.8%	3.3%	1.7%	6.6%	13.5%	14.0%	8.2%	6.8%	4.0%	2.5%	5.0%	5.7%
15	7.4%	1.8%	2.5%	4.2%	9.0%	24.0%	20.0%	16.0%	11.0%	13.0%	6.8%	8.4%	10.0%
17	7.4%	3.5%	9.1%	8.3%	25.0%	27.0%	32.0%	23.0%	9.3%	13.0%	11.0%	12.0%	15.0%
19	9.8%	8.1%	15.0%	27.0%	29.0%	19.0%	20.0%	21.0%	18.0%	12.0%	13.0%	18.0%	17.0%
21	21.0%	23.0%	24.0%	35.0%	7.4%	0.0%	0.8%	16.0%	17.0%	15.0%	18.0%	24.0%	17.0%
23	32.0%	45.0%	31.0%	17.0%	0.0%	0.0%	0.0%	1.6%	21.0%	21.0%	26.0%	15.0%	17.0%
25	14.0%	16.0%	13.0%	0.8%	0.0%	0.0%	0.0%	0.0%	0.8%	8.2%	9.3%	7.5%	5.8%

It is seen from Figure 27 that for the particular solar installation, trying to assure a monthly energy of even 25 kWh can never be achieved. Table 3 shows that for any month, while 90% of the maximum solar energy

production can be guaranteed on 62 days (17% of the days), 70% of the possible energy can be supplied on 219 (60% of the days). The days on which less than 10% of the possible energy can be supplied is less than 7 days

(2%). These results can be made use of to offer a partial capacity charge to rooftop solar producers for perhaps half the capacity, which can be guaranteed on 86.7% of the days or 317 days of the year. However, if we go month by month, a better guarantee can be made as seen from Figure 27. Columns 4 and 5 of Table 3 give the number of days in each category for two selected months, January 2019 and May 2019. For example, in January 2019, 15 kWh (60% of the maximum power) could be guaranteed 95% of the time with an average availability of 21.43 kWh. Similarly, on no day in May 2019 did the power exceed 19 kWh, and on 25 days (80% of the days) the power exceeded 55% of this capacity (10 kWh).

CONCLUSION

The paper has presented an analysis of solar output for solar photovoltaic systems, considering a 4.16 kWp monocrystalline rooftop solar system in Mount Lavinia, Sri Lanka. Fluctuation of actual power and energy have been observed over a four-year period from August 2017 to August 2021. It is seen that, not only is the generated power intermittent, with the peak for the day exceeding 4.5 kW on one occasion but going down to as low as 0.324 kW on a heavily overcast day, with variation of solar electric energy output per day from 0.807 kWh to 26.27 kWh. It was also observed that in a good month like January or February, daily output would be high, averaging 22 kWh/day, while on a month like May or June it could decrease to 13 kWh/day, sometimes varying drastically from day to day, even within a given week. A range of solar output patterns are analysed, and reasons for even higher power outputs during high fluctuations are explained. It is expected that the findings will be useful for those not having actual data, in analysing solar power systems. While this detailed analysis has been presented for a particular site, lessons to be learnt from this study are general. While the data presented is for a specific site in Mount Lavinia, cloud cover and other considerations would be perhaps very similar for a range of locations close to the site. Similar studies could be carried out for other sites to yield a map of solar energy assurances to permit partial capacity cost for solar installations.

Acknowledgement

Obtaining free access to the monitoring portal of the domestic solar rooftop installation of Ms Roshanthi Gunaratne is gratefully acknowledged.

REFERENCES

- Atluri K., Hananya S.M., & Navothna B. (2018). Performance of rooftop solar PV system with crystalline solar cells. *IEEE Xplore. 2018 National Power Engineering Conference (NPEC)*, 09–10 March, Madurai, India.
DOI: <http://doi.org/10.1109/NPEC.2018.8476721>
- Coddington O., Lean J.L., Pilewskie P., Snow M., & Lindholm D. (2016). A solar irradiance climate data record. *Bulletin of the American Meteorological Society* **97**(7): 1265–1282.
- Lucas J.R. (2021). What guarantee can be given for the electrical power output from a fixed rooftop solar installation? *SLEMA Journal* **24**(2): 7–13.
DOI: <http://doi.org/10.4038/slemaj.v24i2.30>
- Lucas J.R., Devanarayana O.C., Pathirana A.P.K.S., Fernando W.F.R.C., & Boteju P.S.C. (2020). Optimum battery capacity for a rooftop PV solar system. *IEEE Xplore. 2020 Moratuwa Engineering Research Conference (MERCOn)*, 28–30 July 2020, Moratuwa, Sri Lanka.
DOI: [10.1109/MERCOn50084.2020.9185275](https://doi.org/10.1109/MERCOn50084.2020.9185275)
- Nayanathara P.M.D., Perera H.S., Abeyrathne R., & Lucas J.R. (2019). Techno-economic solution for semi-dispatchable solar. Available at <http://ir.kdu.ac.lk/handle/345/2229>.
- Sanusi Y. & Ojo M. (2015). Evaluation of clearness index and diffuse ratio of some locations in Southwestern, Nigeria using solar radiation data. *IOSR Journal of Applied Physics* **7**: 45–51.
- Tukiainen M.T.J. & Gaisma.com (2021). Dehiwala-Mount Lavinia, Sri Lanka - Sunrise, sunset, dawn and dusk times for the whole year. Available at <https://www.gaisma.com/en/location/dehiwala-mount-lavinia.html>
- Vidanapathirana K., Kumarapeli K., Marasinghe M., Amarasinghe D., & Lucas J.R. (2021). Performance evaluation of a hybrid dual-axis solar tracking system. *IEEE Xplore. 2021 3rd International Conference on Electrical Engineering (EECon)*, 24–24 September, Colombo, Sri Lanka.
DOI: [10.1109/EECon52960.2021.9580961](https://doi.org/10.1109/EECon52960.2021.9580961)
- Wickramarathna M., Rifai G., Sellahannadi S., Gamage H., Hewage R., Wimalasiri R., & Abeyweera (2011). Off-grid development of sustainable energy resources for ecotourism facilities in Kalpitiya Peninsula Sri Lanka. *SLEMA Journal* **14**(1): 7–15.
- www.adb.org (2021). Solar power from the rooftops in Sri Lanka. Available at <https://www.adb.org/results/solar-power-rooftops-sri-lanka>
- www.lankanrailblazer.wordpress.com (2019). Sri Lankan Dream. How to design a Solar PV system (Estimation of net monthly insolation). Available at <https://lankanrailblazer.wordpress.com/2019/10/04/how-to-design-a-solar-pv-system-estimation-of-net-monthly-insolation/>
- www.newport.com. (2021). Introduction to Solar Radiation. Available at <https://www.newport.com/t/introduction-to-solar-radiation>
- www.solaredge.com. Solar Panel – 60 cell Monocrystalline

PERC Panel data sheet. Available at https://www.solaredge.com/sites/default/files/se_solar_module_monoperc_datasheet.pdf, Accessed 30 July 2021.

www.weatherspark.com (2016). Dehiwala-Mount Lavinia climate, weather by month, average temperature (Sri Lanka). Available at <https://weatherspark.com/y/109710/Average-Weather-in-Dehiwala-Mount-Lavinia-Sri-Lanka->

Year-Round

Yordanov G.H., Midtgård O.-M., Saetre T.O., Nielsen H.K., & Norum L.E. (2012). Overirradiance (cloud enhancement) events at high latitudes. *IEEE Xplore. 2012 IEEE 38th Photovoltaic Specialists Conference (PVSC) Part 2*, 03–08 June, Austin, USA.
DOI: 10.1109/PVSC-Vol2.2012.6656797

RESEARCH ARTICLE

Coastal erosion

Assessment of wave climate change and its impact on littoral drift along the Kalutara and Kalpitiya beaches in Sri Lanka

RSM Samarasekara*, MM Sahthy, AHMS Siriwardana and HPAM Siriwardana

Department of Civil Engineering, Faculty of Engineering, University of Sri Jayawardenepura, 41, Lumbini Avenue, Ratmalana, Sri Lanka.

Submitted: 07 December 2021; Revised: 01 July 2022; Accepted: 26 August 2022

Abstract: Natural and anthropogenic activities have accelerated the coastal erosion in Sri Lanka by threatening the economic developments and livelihoods in coastal zones. However, there is a limited number of studies on coastal erosion in Sri Lanka due to the lack of observed wave climate data around the island. This study identified the impact of wave climate changes on the littoral drift of seven selected locations in Sri Lanka. The reanalyzed wave climate data were used to estimate sediment transport rate in seven locations using empirical methods. The chronological volumetric changes of Kalutara and Kalpitiya beach volume were estimated, as those beaches experienced severe morphological changes during the above period. The relationship among the capacity of coastal sediment transportation of littoral drift, actual sediment accretion (and erosion), and shoreline management activities was critically discussed by collecting data from diverse sources to its fullest extent. The wave climate becomes rough on the western and southern coasts during the southwest monsoon and the eastern coast during the northeast monsoon. The average wave direction periodically changes on the southwest coast, and thus, the littoral drift occurs southwards at the Kalutara coast. The Kalpitiya areas were the main sediment accretion areas, but the Kalpitiya peninsula is slowly eroding with the recently intensified wave climate. Coastal erosion is an integrated effect of shoreline management, wave climate change, and reduction of river sediment supply. Therefore, coastal erosion should be studied with accurate numerical and physical model studies for the betterment of erosion management.

Keywords: Coastal erosion, Kalpitiya, Kalutara, littoral drift, wave climate.

INTRODUCTION

Coastal erosion occurs when waves and currents remove the sediments from the beach; thus, the beach becomes narrow and steep in elevation (Orme 2005). As a result of coastal erosion, we lose valuable land, which adversely affects the livelihoods of beach users (Dayananda 1992; Samaranyake 2007; Senevirathna *et al.* 2018). The capacity for sand transportation by littoral drift mainly depends on the wave climate (*i.e.*, significant wave height (H_s), peak wave period (T_p), and the angle (θ) of the direction of the incoming wave) (Kamphuis *et al.*, 1986; Bayram *et al.*, 2007; Ratnayakage *et al.*, 2020). A coast with predominant littoral drift is highly sensitive to wave climate and its changes. Wave climate changes are assessed worldwide (Ranasinghe, 2016), and it has been found that global climate change is directly contributing to shaping beaches worldwide (US EPA, 2021). The disappearance of sand splits, the narrowing of wide sandy beaches, and damage to existing coastal protection works are the most common impacts of wave climate changes. Those cases highlight the importance of the assessment of wave climate changes to mitigate their adverse effects. Kalutara is located in the western region of Sri Lanka and plays a vital role in attracting tourists through its Calido beach. As a result of the coastal erosion of Calido beach, livelihoods have been heavily affected in this area (Ampitiyawatta & Guo, 2010; Perera & Ranasinghe,

* Corresponding author (samarasekara@sjp.ac.lk;  <https://orcid.org/0000-0002-1555-1302>)



2021). Not only are the livelihoods of the residents in the Kalu river estuary affected, but they also face the issue of salinity intrusion along the river, thereby affecting the quality of raw water abstracted for water supplies (Ratnayake *et al.*, 2013). High-energy, steep, southwest monsoon waves lead to the reduction of beach breadth and flatten the intertidal shoreface (Ratnayake *et al.* 2019). In the recent past, approximately 0.8 billion Sri Lankan rupees have been invested in erosion management annually. Upstream erosion in the Kalu river estuary was measured as 4.88 m/yr; its downstream erosion is 0.83 m/yr, and sediment deposition occurs towards the north (Lakmali *et al.*, 2017).

Kalpitiya has massive sand dunes, which are presumed to be sediment-deposited areas. Lagoonal and estuarine deposits of the Holocene period are found in the Puttalam, Kalpitiya, and Dutch Bay areas. High rates of accretion and erosion are evident on the coasts of the Kalpitiya peninsula. It is important to understand wave climate change and erosion and accretion in those areas, which must be estimated by clearly differentiating the anthropogenic and natural erosion drivers to develop policies and strategies to conserve the coastal region.

Archived wave climate data is required to assess wave climate change. In the absence of such wave climate data, it is impossible to predict sediment transport rates in coastal areas. Moreover, there will not be sufficient data to develop policies on the conservation of the coastal environment and related economic strategies. However, such data is lacking in many developing countries (Stronkhorst *et al.*, 2018). Reanalyzed wind data can be used to predict the wave climate data using wave models such as WAVEWATCH III (Reguero *et al.*, 2012; Stopa & Cheung, 2014; Kalourazi *et al.*, 2021). With the aid of such reanalyzed data, the capacity of the littoral current can be estimated.

Sri Lanka is a country surrounded by 1,340 km of coastline; the coastal environment consists of rich biodiversity, which brings high environmental, economic, and social value to the island. Since the 1970s, coastal erosion has become a severe threat to the country in connection with the development of fishery, commercial harbours, logistics, and tourism-related industries (Samarasekara *et al.*, 2018). The coastal segment of 685 km extending from Kalpitiya to Yala loses about 175,000–285,000 m² of its coastal land each year (CCD, 1997). During annual monsoon seasons, erosion is very

severe in Kalutara and Kalpitiya. From south to north along the western coast, a strong longshore current is generated during these seasons due to monsoon waves (Dayananda, 1992). During the southwest monsoon, swell waves break and hit the southern and western coastlines. Thereby, the net annual sediment transportation rates are very high during monsoon seasons (Ansaf, 2011). The estimated longshore drift capacity from south to north is 1.1 million m³/year (Dayananda, 1992). However, the longshore drift capacity of recent years has not been estimated due to the lack of measured wave data.

Not only anthropogenic causes, such as coastal reclamation and management, but also natural causes, such as wave climate changes, could accelerate the coastal erosion in Sri Lanka. Though there are some recent studies that elaborate on the anthropogenic causes (Ratnayakage *et al.*, 2020; Gunasinghe *et al.*, 2021) that accelerate coastal erosion, there is a limited number of studies on natural causes in Sri Lanka. The lack of observed data is the main issue, and this research aims to fill that gap by estimating the capacity of littoral drift with the modelled wave climate data by using reanalyzed wind data. This study firstly estimates the littoral drift along the Sri Lankan coast and secondly evaluates the erosion and accretion rates in the Kalutara and Kalpitiya beaches. Thirdly, the estimated values of littoral drift along the western coast are compared with the Kalutara and Kalpitiya cases by differentiating the anthropogenic and natural drivers of erosion. This study emphasizes the patterns of erosion and accretion of sediments on the western coast of Sri Lanka by collecting data from diverse sources to their fullest extent.

MATERIALS AND METHODS

Study location

In this study, coastal cell segments were defined as shown on satellite images in Figure 1. Cells 1, 2, and 3 are on the Kalpitiya coast, and Cells 4 and 5 are on the Kalutara beach. Each cell is bounded by either a headland or breakwater of a fishery harbour or a river mouth. The boundary of cells 4 and 5 goes through the Kalu river mouth. The five points demarcated are the points and ocean depths where wave climate data and information have been extracted. The nearshore sediment transport rate is determined at each defined cell by considering the orientation of wave breaking.

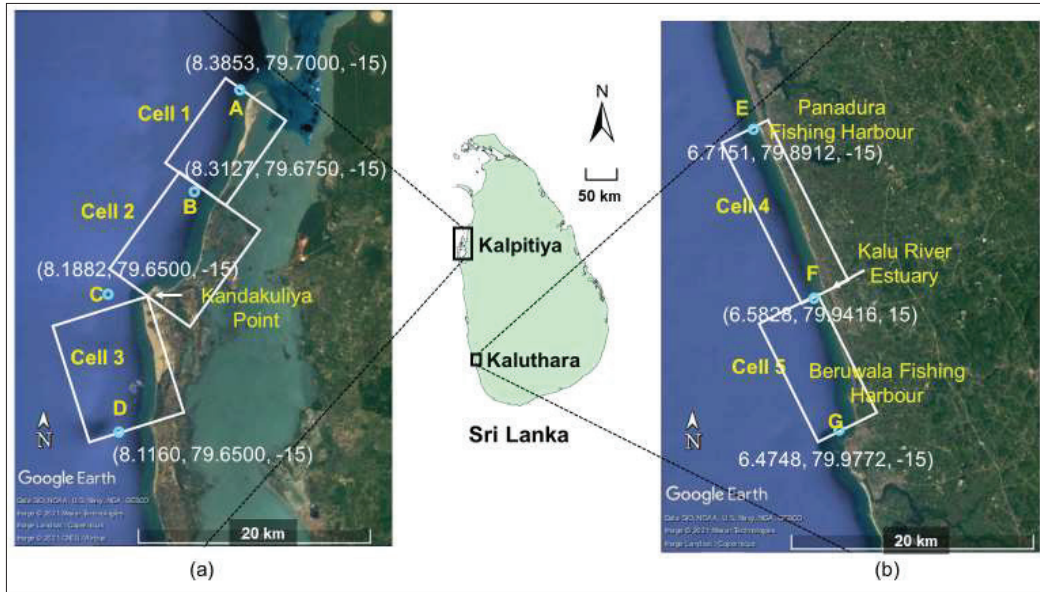


Figure 1: Locations of defined coastal cells and extracted points along the Kalutara and Kalpitiya coasts (Source: Google Earth, Data SIO, NOAA, US Navy, NGA, GEBCO)

Assessment of wave climate

In this study, the wave climate data from 1 January 2007 to 31 December 2017 were collected from a recently concluded study (Samarasekera, 2019) in netCDF format. The wave data were modelled from WAVEWATCH III (Tolman, 2009) using the reanalyzed wind data from NCEP/NCAR Reanalysis 1 (2000). The authors extracted daily time series of H_s , T_p , and θ in CSV format at the locations of nodes of study (Figure 1) by developing a Python Code. The depth of the sea at the nodes is approximately 15 m. The wave breaker line, shoreline orientation, and wave angle at the breaker line were observed from satellite images in respective years. When a satellite image is not available for a year, the wave angle values at the breaker line for the nearest year were assumed in this analysis. The capacity of coastal sediment transportation was estimated by using the CERC (Coastal Engineering Research Center) equation, as shown in equation 1 (Van Rijn, 2013).

$$Q_{t,Volume} = 0.0483(H_{s,br})^{2.5} \sin |2\theta_{br}| \dots(01)$$

where, θ_{br} = wave angle at breaker line (between wave crest line and coastline); $H_{(s,br)}$ = significant wave height (m) at breaker line, and $Q_{(t, Volume)}$ = longshore sediment transport rate (m^3/s).

Analysis of erosion and accretion

The west coast of Sri Lanka has experienced erosion and accretion since the 1970s (Bandara *et al.*, 1987; Fittschen *et al.*, 1992b). The transportation of sediment along the western coast occurs mainly due to the Southwest monsoon (Gunarathna *et al.*, 2011). These transported sands accumulate near the Kalpitiya area and generate sandy islands (Ratnayakage *et al.*, 2020). In this research, chronological changes in the shoreline of the Kalpitiya and Kaluthara areas were observed using satellite images in Google Earth Pro. The available clear satellite images of December 2004, October 2009, November 2011, October 2012, October 2013, February 2014, March 2015, March 2016, and March 2017 were chosen for analysis. The accreted (and eroded) shore areas were calculated relative to the shoreline of December 2004.

Firstly, the shoreline is demarcated using Google Maps. Thereafter, the demarcated shoreline files are inserted into ArcGIS. Each shoreline was split into equidistant segments. The split coordinates were extracted to Microsoft Excel. Afterwards, the reference line coordinates were calculated based on the shoreline. Successively the perpendicular distance was calculated from shoreline coordinates. Finally, the area was assessed using the above steps.

Different years of shorelines are denoted as $t = t_1, t_2, t_3, t_4, \dots, t_n$ and particular shoreline polylines are split into equal segments of approximately 1 m. The midpoint coordinate of each segment is obtained by using ESRI-ArcGIS in two decimal degrees. Particular coordinates are denoted as $i = i_1, i_2, i_3, i_4, \dots, i_n$. A reference line is considered, as shown in Figure 2. The term ‘Q’ is denoted as the coordinates of split points of a particular shoreline, the term ‘L’ is denoted as the perpendicular distance from a particular shoreline, the term ‘t’ is denoted as the day of shoreline, the term ‘u’ is denoted as points of split shoreline, and $Q_{t+1, u+3}$ is denoted as the coordinate of u+3 point at t+1 day shoreline.

A perpendicular line is drawn from a particular coordinate i to the reference line. The relative accreted (or eroded) area to day t is calculated by using equations 2 and 3.

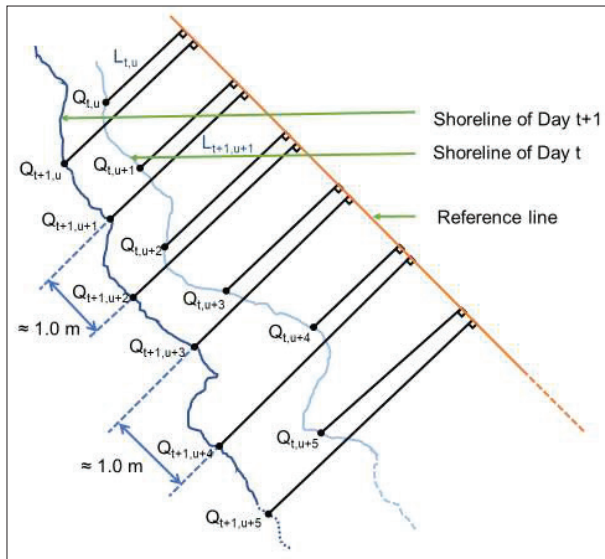


Figure 2: Schematic diagram of the shoreline (plan view) at time t_1, t_2 and reference line

$$L_{t,u} = \sqrt{\left(X_{t,u} - \frac{x_{t,u} + m y_{t,u} - m c}{m^2 + 1}\right)^2 + \left(y_{t,u} - \frac{m^2 y_{t,u} + m x_{t,u} + c}{m^2 + 1}\right)^2} \quad \dots(02)$$

$$A_{\Delta t, \Delta u} = \frac{(L_{t+1,u} - L_{t,u}) + (L_{t+1,u+1} - L_{t,u+1})}{2} \quad \dots(03)$$

$$V_{t+1, \Delta u} = \frac{1}{4} [(L_{t+1,u}^2 - L_{t,u}^2) \tan \phi_{t+1,u} + (L_{t+1,u+1}^2 - L_{t,u+1}^2) \tan \phi_{t,u+1} - (L_{t,u}^2 - L_{t,u}^2) \tan \phi_{t,u} - (L_{t,u+1}^2 - L_{t,u+1}^2) \tan \phi_{t,u}] \tan \phi_{t,u+1} \quad \dots(04)$$

The altitude between the shoreline and coastline ($\tan \phi \tan \phi$) is extracted for Kalutara from the literature (Gunasinghe et al., 2021). The altitude data between the shoreline and coastline is extracted from Google Earth Pro for Kalpitiya. It is assumed that the value of the beach slope uniformly changed throughout the considered periods. The beach volume change between two consecutive periods is calculated from the methodology provided by Ratnayakage et al. (2020). The coastline, which can be determined from L , is also obtained similarly to the shoreline. The beach volume change (V) between point u and $u+1$ was calculated from equation 4.

Overall methodology

Figure 3 shows key data and methodologies involved in the study. Firstly, the wave climate data at Kalutara and Kalpitiya were collected. Based on that, a study of the sediment transport rate in both locations was carried out. This was followed by the study of the chronological volumetric change of Kalutara and Kalpitiya beaches. Using the results so derived, a study was done on the relationship between the capacity of coastal sedimentation transportation and actual sediment transportation under the influence of wave climate change. Finally, the change in volume and area was assessed. After clearly observing the impact of shoreline management, a relationship between the capacity of coastal sedimentation transportation and actual sediment transportation was observed and discussed to identify the influence of wave climate change.

RESULTS AND DISCUSSION

Littoral drift along the Sri Lankan Coast

Sri Lanka experiences two monsoons and two inter-monsoon seasons. The littoral drift and its direction are mainly governed by the northeast monsoon

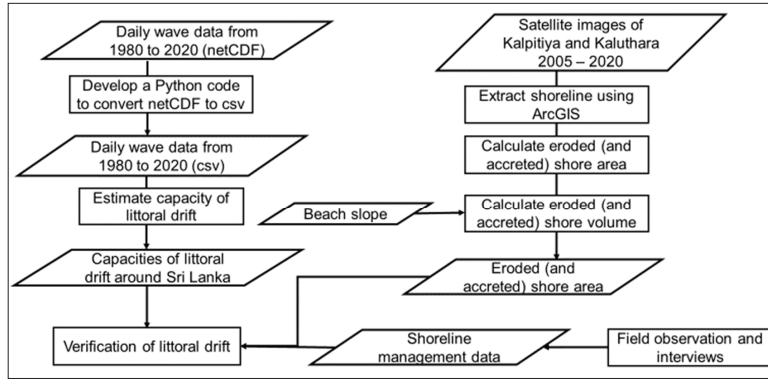


Figure 3: Key data and methodologies involved in the study

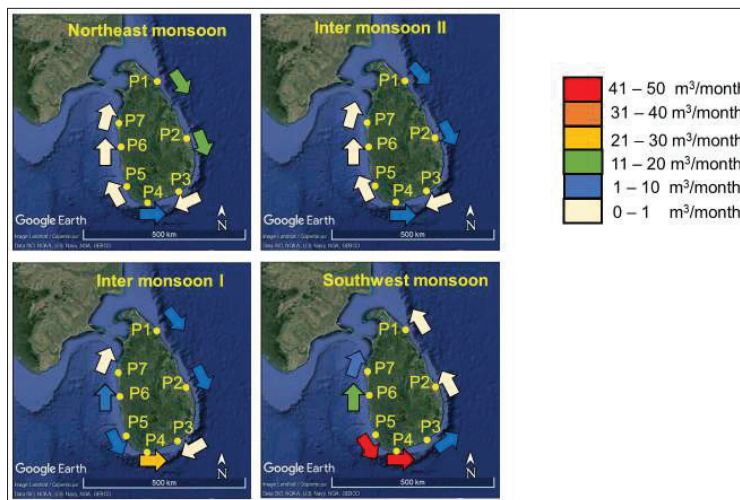


Figure 4: Monthly sediment transport potential values in northeast monsoon (December-February), inter-monsoon 1 (March-April), southwest monsoon (May-September), and inter-monsoon 2 (October-November) based on daily average littoral drift from 2007 to 2017

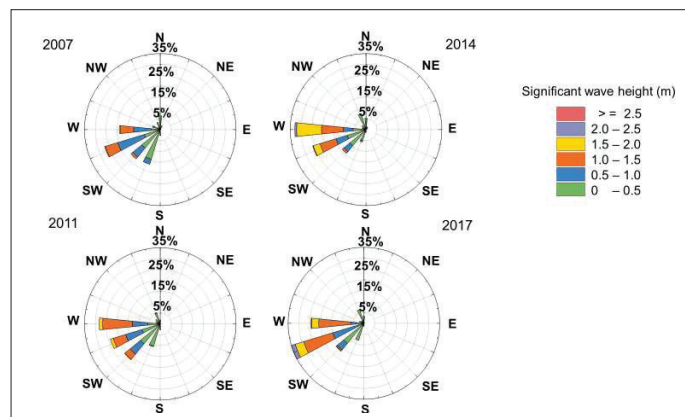


Figure 5: The wave rose diagrams at Kalutara in 2007, 2011, 2014, and 2017

(December-February), inter-monsoon 1 (March-April), southwest monsoon (May-September), and inter-monsoon 2 (October-November). Figure 4 shows monthly sediment transport potential values based on the daily average of littoral drift from 2007 to 2017. Sediment transport potential values are shown for 6 locations around the island during four seasons. Those locations are Mullaitivu (P1), Kattankudy (P2), Yala (P3), Dondra (P4), Kalutara (P5), Chilaw (P6), and Kalpitiya (P7). Sediment transportation on the eastern coast is predominant during the northeast monsoon, but sediment transportation on the western and southern coasts is predominant during the southwest monsoon.

The wave climate is slightly rough on the southern coast during inter-monsoon 1 as well. The wave climate during the southwest monsoon could transport more sediment compared to the wave climate during the northeast monsoon.

Figure 5 shows the wave rose diagrams at Kalutara in 2007, 2011, 2014, and 2017. It shows that the direction of littoral drift is quite a sensitive parameter as the direction of the wave front slightly changes from year to year. The shorelines are also changed due to major shore protection and development activities. Therefore, the direction of littoral drift from time to time changed southwards and northwards.

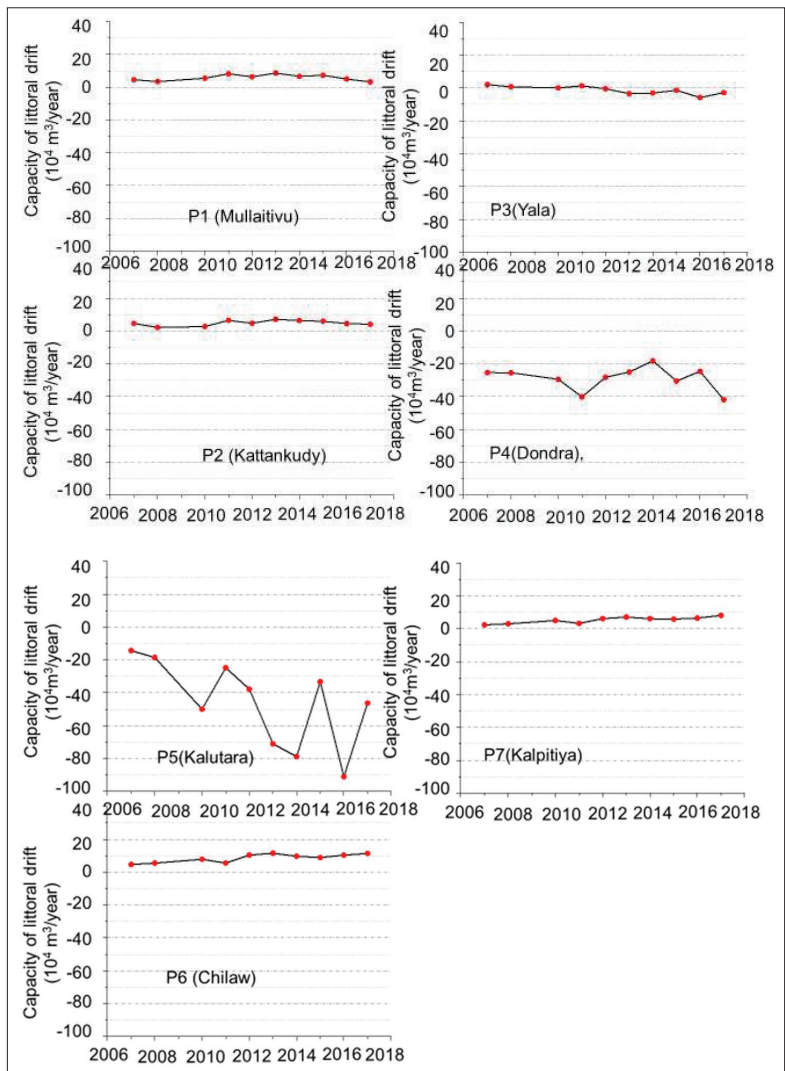


Figure 6: The annual average sediment transport potential of littoral drift at P1 (Mullaitivu), P2 (Kattankudy), P3 (Yala), P4 (Dondra), P5 (Kalutara), P6 (Chilaw), and P7 (Kalpitiya)

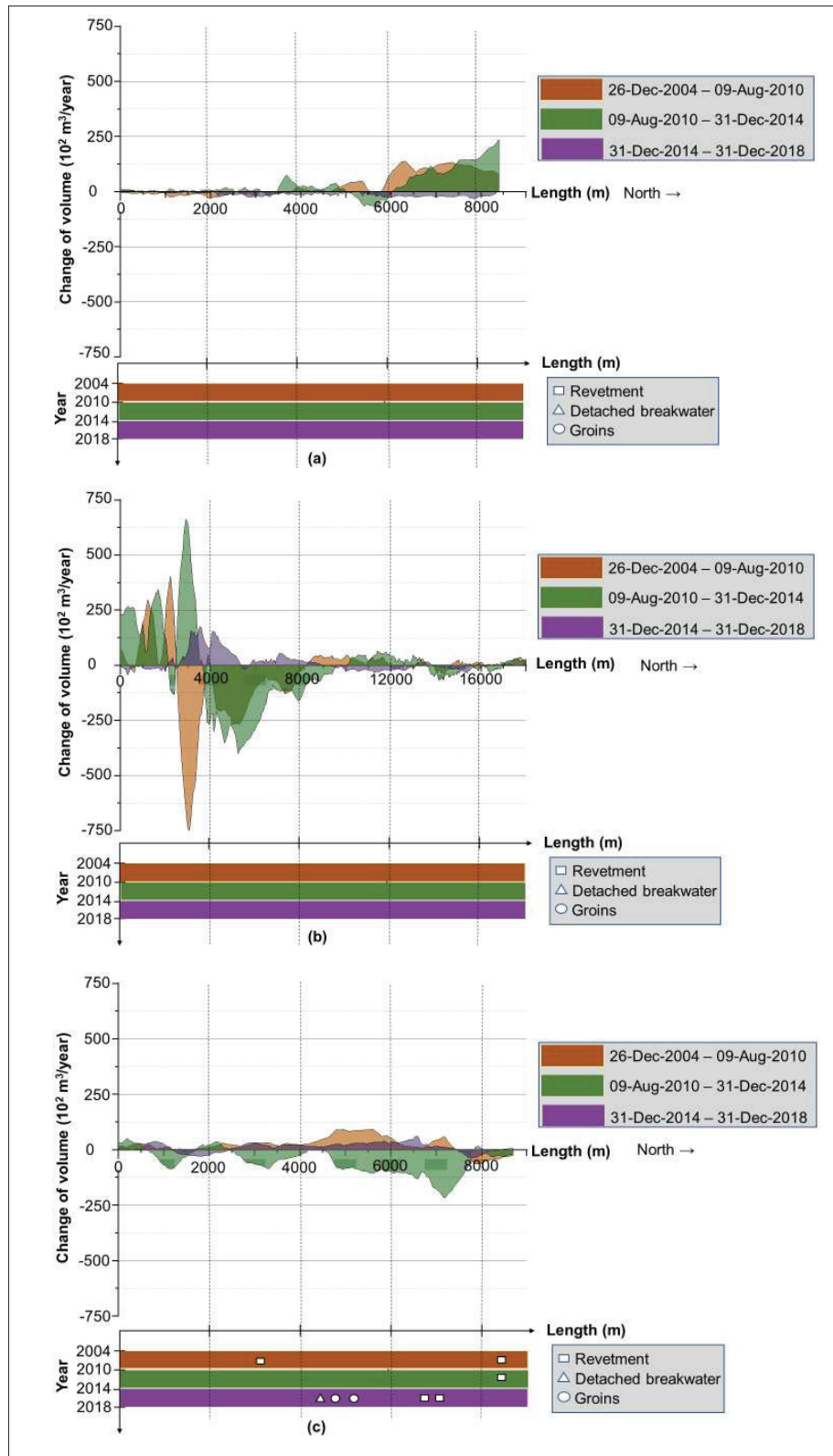


Figure 7: The beach volume accretion in sediment (a) cell - 1, (b) cell - 2 and (c) cell - 3 in Kalpitiya during 26 December 2004 - 31 December 2018

A couple of past researchers have studied the wave climate on the southwest coast, mainly the significant wave height relative to the wave direction (Sheffer & Frohle, 1991; Fittschen *et al.*, 1992a; Gunaratna *et al.* 2011). The sediment transportation direction of the southwest coast is considered as south to north by some researchers (Ansaf, 2011; Abeykoon *et al.*, 2021), but the results of this study show that the average littoral drift is from north to south during 2005 and 2017. It is evident that the littoral drift could have been periodically changed southwards and northwards because the sand spit which the Kalu river builds periodically moves southwards and northwards (Bandara *et al.*, 1987). Figure 6 shows the annual average sediment transport potential of littoral drift at the locations P1 to P7. The annual average littoral drift in Kalutara is predominately southwards during 2004.

Erosion and accretion rates in Kalpitiya and Kalutara

Figure 7 illustrates the beach accretion (and erosion) in each cell in different years. The shoreline volume change values are given in the order of 10^4 m^3 . The negative values refer to erosion, and the positive values refer to accretion. Figure 7 (a), (b), and (c) show the beach volume accretion in cells 1, 2, and 3 in Kalpitiya, respectively. The x-axis is

the linear distance of the beach, and the y-axis is the rate of beach accretion in the unit of m^3 per year. The shoreline management activities which took place are shown under the plot of beach accretion (and erosion).

The most northern area in cell 1 is an accreting area. Beach accreted in this area at a maximum rate of $25,000 \text{ m}^3/\text{year}$ during 2005 and 2014. The accreted beach slightly eroded during 2014 and 2018. Kaldakuliya point, which is the southern boundary of cell 2, is a sensitive area. Figure 8 shows satellite image photos of sediment accretion in the field of groynes on 11 March 2011, 29 August 2013, and 27 December 2019. It shows evidence of high sedimentation sensitivity in cell 2 (Kalpitiya peninsula). There are detached breakwaters and groynes which were constructed before 2004 in this area. Sediments accreted at the beach where the protection structures were constructed by eroding neighbouring beaches in the north because of the reduction in sediment in the northward littoral drift. Similar incidents are also observed in Marawila beach (Samarasekara *et al.*, 2018) and on coasts in Colombia (Rangel-Buitrago *et al.*, 2018). Many shore protection activities have taken place in cell 3, and they protected the beach, maintaining net accretion in cell 3 during 2014 and 2020.



Figure 8: Satellite image photos of sediment accretion in the field of groynes on (a) 11 March 2011, (b) 29 August 2013 and (c) 27 December 2019

Figure 9 (a) and (b) show the beach volume accretion in cells 4 and 5 in Kalutara, respectively. Cell 4 is bounded by Panadura harbour in the north and the Kalu river estuary in the south. Cell 4 is quite a stable coast and receives sediments from the Kalu River. A series of groynes were constructed in cell 4 during 2014 and 2018. Cell 5 is bounded by Beruwala harbour in the south and Kalu river

estuary in the north. Cell 4 experienced severe erosion, and detached breakwaters were constructed before 2004. However, the tombolos were not fully developed due to the Indian Ocean Tsunami in 2004. Figure 9 (b) shows that the left-hand sides were accreted, and the right-hand sides were eroded at tombolos in cell 4 during 2014 and 2018. It is evidence of the southward littoral drift.

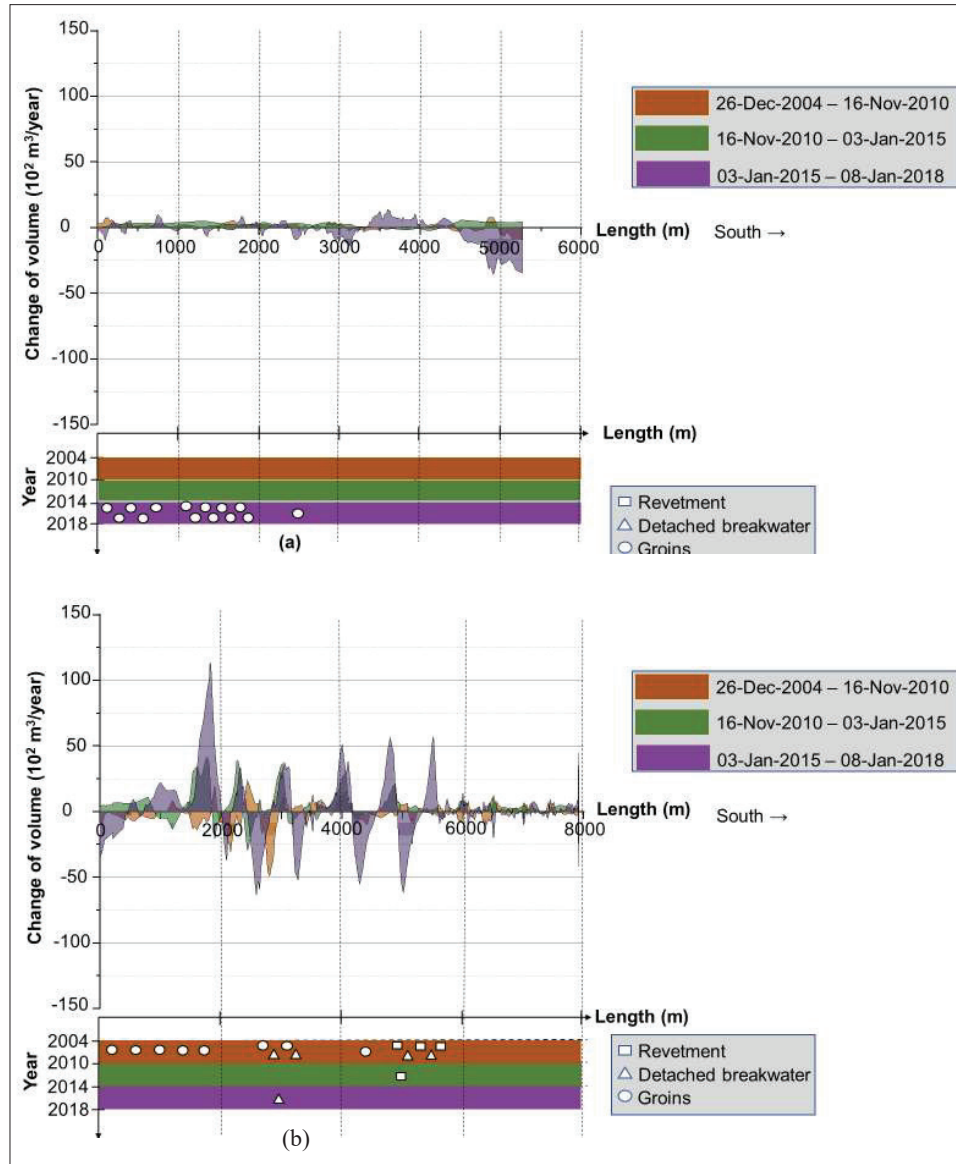


Figure 9: The beach volume accretion in sediment (a) cell - 4 and (b) cell - 5 in Kalutara during 26 December 2004 and 31 December 2018 (Source: Google Earth Pro, Maxar Technologies).

Impact on littoral drift at Kalpitiya and Kalutara

The capacity of the littoral drift at nodes, shore accretion (and erosion), and shoreline management strategies during (a) 26 December 2004 – 09 August 2010, (b) 09 August 2010 – 31 December 2014, (c) 31 December 2014 – 31 December 2018 are shown in Table 1. The capacity of littoral drift is in the unit

of m^3 per year. The length of cells is different in each cell; therefore, the beach volume was mentioned per unit length. Positive (+) values denote northward drift, and negative (-) values denote southward drift. Beach volume change along the shoreline is in the unit of m^3 per year per unit length. Positive (+) values denote beach accretion, and negative (-) values denote coastal erosion.

Table 1: Comparison of the capacity of littoral drift, the erosion accretion rate, and shoreline management activities have taken place in Kalpitiya (a) 26 December 2004–09 August 2010; (b) 09 August 2010–31 December 2014; (c) 31 December 2014–31 December 2018

Kalpitiya				
Node	The capacity of Littoral drift (10^4 m ³ /year)	Cell	Change of volume along the shoreline (10^6 m ³ /year/km)	Management activities which have taken place
26 December 2004–09 August 2010				
A	1.05	1	-0.08	-
B	2.98			
B	2.98	2	-1.32	6 Groynes are constructed
C	3.98			
C	3.98	3	0.75	1 Detached breakwater is constructed
D	4.33			
09 August 2010–31 December 2014				
A	1.66	1	1.26	-
B	4.34			
B	4.34	2	-0.43	-
C	6.38			
C	6.38	3	-2.64	2 Detached breakwaters are constructed
D	6.52			
31 December 2014–31 December 2018				
A	2.00	1	-0.91	-
B	4.87			
B	4.87	2	0.59	-
C	7.96			
C	7.96	3	0.47	2 Groynes and 2 detached breakwaters are constructed
D	7.81			

The capacity of littoral drift reduces towards the north along the Kalpitiya peninsula. An increase in the capacities can be observed in those cells. Therefore, erosion is predominant though the area is historically a beach accreting area. Two detached breakwaters were constructed at cell 3 during 09 August 2010 and 31 December 2014 and it caused sedimentation in subsequent years. Two detached breakwaters were constructed in cell 3 during 09 August 2010 and 31 December 2014. Two groynes and detached breakwaters were constructed in the same cell during 31 December 2014 and 31 December 2018 by resulting

sedimentation. The beach area was increased due to shoreline management activities in cell 3. The erosion (and accretion) is a result of the combined effect of the capacity of littoral drift, shoreline management, and the transported sediments from the south. The Kalpitiya peninsula is eroding at a slow pace with intensified wave climate.

Sediment transportation capacities of littoral drifts are also amplified in cells 5 and 6, as in the Kalutara beach area. The direction of littoral drift is from north to south. The capacity is comparatively low near the

Table 2: Comparison of the capacity of littoral drift, the erosion accretion rate, and shoreline management activities have taken place in Kalutara areas from (a) 26 December 2004 to 16 November 2010 (b) 16 November 2010 to 03 January 2015 (c) 03 January 2015 to 08 January 2018

Kalutara				
Node	The capacity of Littoral drift ($10^5 \text{ m}^3/\text{year}$)	Cell	Change of volume along the shoreline ($10^5 \text{ m}^3/\text{year}/\text{km}$)	Management Activities which have taken place
26 December 2004 to 16 November 2010				
E	-2.76	4	0.05	-
F	-0.78			
F	-0.78	5	-0.15	1 Groyne, 4 coves, 1 revetment (250 m), and 3 detached breakwaters are constructed
G	-2.42			
16 November 2010 to 03 January 2015				
E	-4.45	4	0.25	3 new groynes were constructed
F	-1.75			
F	-1.75	5	0.46	Tombolos are fully developed at built detached breakwaters.
G	-4.06			A new detached breakwater is constructed
03 January 2015 to 08 January 2018				
E	-6.23	4	-0.34	6 Groynes are constructed
F	-2.91			
F	-2.91	5	0.26	1 Groyne and 1 detached breakwater are constructed
G	-5.89			



Figure 10: Satellite images of a detached breakwater on 2 August 2005 and 1 January 2013 in cell 5 (Source: Google Earth Pro, Maxer Technologies)

river mouth. Cell 4 is an accreting area as the capacity of littoral drift reduces towards the south. However, cell 4 eroded with the intensified wave climate. Therefore, revetment and a field of groynes were constructed by CC&CRMD to protect the shoreline during 26 December 2004 and 16 November 2010. December 2004 is the date of the Indian Ocean Tsunami. Revetments, groynes, and detached breakwaters were constructed during 2004 and 2010; as a result, the shore was accreted during 16 November 2010 and 03 January 2015. Figure 10 shows a satellite image of the detached breakwater in cell 5, and vegetation is also full-grown in the evolved tombolo on 1 January 2013, where there was no beach on 2 August 2005. Another detached breakwater also constructed further sediment upstream and thus, further sediment accretion was observed during 03 January 2015 and 08 January 2018. The sediment accretion and erosion are more linked to shoreline management instead to wave climate change in Kalutara.

It was identified that the wave climate in the Indian Ocean has become severe in recent years (Gupta *et al.*, 2015; Nurfaida & Shimozono, 2019), and this study also confirms a wave of intensified climate change. This study also confirms that coastal erosion (and accretion) is linked with shoreline management activities as well. The current erosion management activities in Kalutara and Kalpitiya are successful in coast protection. Lack of sediment supply from rivers and streams is the main reason for coastal erosion on the western coast of Sri Lanka (CCD, 2003; Samarawikrama *et al.*, 2009; Wickramaarachchi, 2012; Samarasekara *et al.*, 2018); thus, both Kalpitiya and Kalutara also experience coastal erosion. Therefore, coastal erosion can only be controlled by combined protection using beach nourishment with hard structures such as detached breakwaters. Beach nourishment combined with hard structures has been successful in Sri Lanka (Ratnayake *et al.*, 2019; Ratnayakage *et al.*, 2020), Thailand (Saengsupavanich, 2013), and Italy (Pranzini, 2018).

CONCLUSION

The sediment transportation capacity of littoral drift was measured between 2007 and 2017. The wave climate becomes rough during the southwest monsoon period on the western and southern coasts and the northeast monsoon period on the eastern coast. As a result, the capacity of littoral drift on the southwest coast is the largest among all coasts. Those values are relatively small in the Yala and Kalpitiya areas, and thus those areas became major sediment accretion areas. However,

the Kalpitiya peninsula is slowly eroding with the intensified wave climate. The average wave direction periodically changes between west and west-south-west, and the littoral drift was predominantly southwards at the Kalutara coast from 2007 to 2017. Beaches in both Kalutara and Kalpitiya generally erode, but the beaches accrete where detached breakwaters are constructed as a shoreline protection measure. Beaches erode as an integrated effect of shoreline management, wave climate change, and reduction of river sediment supply. The reality of coastal erosion is more complex, and more studies are required to identify the causes of erosion and accretion based on hydraulic model studies and numerical estimation. However, this study provides an empirical framework to verify the results of numerical studies where there are no observed results. As a result of the erosion, the tourism-based and fishing communities would be heavily affected due to the loss of valuable beaches. Wave climate change-induced coastal erosion cannot be evident, and thus, a sufficient budget needs to be allocated to protect the shoreline of Sri Lanka.

Conflicts of interest

The authors disclose that they have no conflicts of interest concerning this article.

Acknowledgement

The authors acknowledge Mr HHADMN Hettiarachchi, Mr KWND Withanarachchi, Mr J. Kavinthan, and Mr RKDG Kaluarachchi for their scientific support.

REFERENCES

- Abeykoon L.C.K., Thilakarathne E.P.D.N., Abeygunawardana A.P., Warnasuriya T.W.S. & Egodaunya K.P.U.T. (2021). Are coastal protective hard structures still applicable with respect to shoreline changes in Sri Lanka? *ADBI Working Paper Series*. Available at <https://www.adb.org/sites/default/files/publication/692461/adbi-wp1240.pdf>, accessed 07 January 2021.
- Ampitiyawatta A.D. & Guo S. (2010). Precipitation trends in the Kalu Ganga Basin in Sri Lanka. *Journal of Agricultural Sciences* 4(1): 10.
DOI: <https://doi.org/10.4038/jas.v4i1.1641>.
- Ansaf K.M.M. (2011). Investigations on coastal sediment transport and shoreline behaviour. *MSc thesis*, University of Moratuwa, Moratuwa, Sri Lanka.
- Bandara M.C.M., Wikramagamage P. & Wilson W.M. (1987). *Coastal Changes of Negombo Lagoon Outfall and Kaluriver River Estuary*, pp. 24. Coast Conservation Department, Colombo, Sri Lanka.

- Bayram A., Larson M. & Hanson H. (2007). A new formula for the total longshore sediment transport rate. *Coastal Engineering* **54**(9): 700–710.
DOI: <https://doi.org/10.1016/j.coastaleng.2007.04.001>
- CCD (2003). Coastal Zone Management Plan Sri Lanka 2003. Colombo, Sri Lanka. Available at http://www.coastal.gov.lk/downloads/pdf/CZMP_English.pdf, accessed 07 January 2021.
- CCD (1997). Coastal Zone Management Plan Sri Lanka 1997 Colombo. Available at <https://www.crc.uri.edu/download/SLCZPlan97.pdf>, accessed 07 January 2021.
- Dayananda H.V. (1992). Shoreline Erosion in Sri Lanka's Coastal Areas, Colombo. Available at https://pdf.usaid.gov/pdf_docs/pnabs575.pdf, accessed 07 February 2021.
- Fittschen T., Perera J.A.S.C. & Scheffer H.J. (1992). *Sediment Transport Study for the Southwest Coast of Sri Lanka*. CCD-GTZ Conservation Project. Colombo, Sri Lanka.
- Gunaratna P.P., Ranasinghe D.P.L. & Sugandika T.A.N. (2011). Assessment of nearshore wave climate off the southern coast of Sri Lanka. *Engineer* **44**: 33–42.
DOI: <https://doi.org/10.4038/engineer.v44i2.7021>
- Gunasinghe G.P., Ruhunage L., Ratnayake N.P., Ratnayake A.S., Samaradivakara G.V.I. & Jayaratne R. (2021). Influence of manmade effects on geomorphology, bathymetry and coastal dynamics in a monsoon-affected river outlet in southwest coast of Sri Lanka. *Environmental Earth Sciences* **80**(7): 1–16.
DOI: <https://doi.org/10.1007/s12665-021-09555-0>
- Gupta N., Bhaskaran P.K. & Dash M.K. (2015). Recent trends in wind-wave climate for the Indian Ocean. *Current Science* **108**(12): 2191–2201.
- Kalourazi M.Y., Siadatmousavi S.M., Abbas Y.B. & Jose F. (2021). WAVEWATCH-III Source terms evaluation for optimizing hurricane wave modeling: a case study of hurricane Ivan. *Oceanologia* **63**(2): 194–213.
DOI: <https://doi.org/10.1016/j.oceano.2020.12.001>
- Kamphuis J.W., Davies M.H., Naim R.D. & Sayao O.J. (1986). Calculation of littoral sand transport rate. *Coastal Engineering* **10**(1): 1–21.
DOI: [https://doi.org/10.1016/0378-3839\(86\)90036-0](https://doi.org/10.1016/0378-3839(86)90036-0)
- Lakmal E.N., Deshapriya W.G.A., Jayawardene K.G.A.I., Raviranga R.M.P., Ratnayake N.P., Premasiri H.M.R. & Senanayake I.P. (2017). Long term coastal erosion and shoreline positions of Sri Lanka. *Journal of Survey in Fisheries Sciences* **3**(2): 1–6.
DOI: <https://doi.org/10.18331/sfs2017.3.2.1>
- NCEP/NCAR Reanalysis 1 (2000). The NOAA physical sciences laboratory (PSL). Available at <https://www.esrl.noaa.gov/psd/data/gridded/data.ncep.reanalysis.pressure.html>, accessed 05 August 2018.
- Nurfaida W. & Shimozono T. (2019). Intensifying swells and their impacts on the south coast of Java, Indonesia. *Coastal Engineering Journal* **61**(3): 267–277.
DOI: <https://doi.org/10.1080/21664250.2019.1595345>
- Orme A.R. (2005). Accretion and erosion waves on beaches. In: *Encyclopedia of Coastal Science* (ed. M.L. Schwartz). Encyclopedia of Earth Sciences Series. Springer Dordrecht, Germany.
DOI: <https://doi.org/10.1007/1-4020-3880-1>
- Perera K.R.L. & Ranasinghe D.P.L. (2021). An analysis of causes of coastal erosion in Calido Beach, Kalutara, West Coast of Sri Lanka. *KDU Journal of Multidisciplinary Studies* **3**(1): 69–79.
- Pranzini E. (2018). Shore protection in Italy: from hard to soft engineering and back. *Ocean and Coastal Management* **156**: 43–57.
DOI: <https://doi.org/10.1016/j.ocecoaman.2017.04.018>
- Ranasinghe R. (2016). Assessing climate change impacts on open sandy coasts: a review. *Earth-Science Reviews* **160**: 320–332.
DOI: <https://doi.org/10.1016/j.earscirev.2016.07.011>
- Rangel-Buitrago N., Williams A.T. & Anfuso G. (2018). Hard protection structures as a principal coastal erosion management strategy along the Caribbean Coast of Colombia. a chronicle of pitfalls. *Ocean and Coastal Management* **156**: 58–75.
DOI: <https://doi.org/10.1016/j.ocecoaman.2017.04.006>
- Ratnayakage S.M.S., Sasaki J., Suzuki T., Jayaratne R., Ranawaka R.A.S. & Pathmasiri S.D. (2020). On the status and mechanisms of coastal erosion in Marawila Beach, Sri Lanka. *Natural Hazards* **103**(1): 1261–1289.
DOI: <https://doi.org/10.1007/s11069-020-04034-4>
- Ratnayake N.P., Silva K.B.A. & Kumara I.G.I.K. (2013). Chloride contamination in construction aggregates due to periodic saline water intrusion: a case study in the Kaluganga river estuary, Sri Lanka. *Environmental Earth Sciences* **69**(8): 2529–2540.
DOI: <https://doi.org/10.1007/s12665-012-2077-1>
- Ratnayake N.P., Ratnayake A.M., Azoor R.M., Weththasinghe S.M., Seneviratne I.D.J., Senarathne N., Premasiri R. & Dushyantha N. (2019). Erosion processes driven by monsoon events after a beach nourishment and breakwater construction at Uswetakeiyawa Beach, Sri Lanka. *SN Applied Sciences* **1**(1): 52(2019).
DOI: <https://doi.org/10.1007/s42452-018-0050-7>
- Reguero B.G., Menéndez M., Méndez F.J., Mínguez R. & Losada I.J. (2012). A global ocean wave (GOW) calibrated reanalysis from 1948 onwards. *Coastal Engineering* **65**: 38–55.
DOI: <https://doi.org/10.1016/j.coastaleng.2012.03.003>
- Saengsupavanich C. (2013). Detached breakwaters: communities' preferences for sustainable coastal protection. *Journal of Environmental Management* **115**: 106–113.
DOI: <https://doi.org/10.1016/j.jenvman.2012.11.029>
- Samaranayake R.A.D.B. (2007). Pre-and post-tsunami coastal planning and land-use policies and issues in Sri Lanka, pp. 167–198. Available at <https://www.semanticscholar.org/paper/Pre-and-post-tsunami-coastal-planning-and-land-use-Samaranayake-Lanka/s/d52bd4b1132b4436544945cc1a9e3e2370390e20>, accessed 09 April 2021.
- Samarasekara R.S.M. (2019). Evaluation of coastal erosion processes and management in a developing country: a case study in Marawila Beach, Sri Lanka. *PhD thesis*, The

- University of Tokyo, Japan.
- Samarasekara R.S.M., Sasaki J., Jayaratne R., Suzuki T., Ranawaka R.A.S. & Pathmasiri S.D. (2018). Historical changes in the shoreline and management of Marawila Beach, Sri Lanka, from 1980 to 2017. *Ocean and Coastal Management* **165**: 370–384.
DOI: <https://doi.org/10.1016/j.ocecoaman.2018.09.012>
- Samarawikrama S.P., Costa W.A.J., Dissanayaka D.M.B. & Dulshan P.R.D. (2009). Coastal erosion management in Sri Lanka. *Undergraduate thesis*, University of Moratuwa, Moratuwa, Sri Lanka.
- Senevirathna E.M.T.K., Edirisooriya K.V.D., Uluwaduge S.P. & Wijerathna K.B.C.A. (2018). Analysis of causes and effects of coastal erosion and environmental degradation in southern coastal belt of Sri Lanka special reference to Unawatuna Coastal Area. *Procedia Engineering* **212**: 1010–1017.
DOI: <https://doi.org/10.1016/j.proeng.2018.01.130>
- Sheffer H.J. & Frohle P. (1991). Results of directional wave measurement off Galle. In: *Seminar on Causes of Coastal Erosion in Sri Lanka* (ed. H.J. Scheffer), pp. 75–97. Coast Conservation Department, Colombo, Sri Lanka.
- Stopa J.E. & Cheung K.F. (2014). Intercomparison of wind and wave data from the ECMWF reanalysis interim and the NCEP climate forecast system reanalysis. *Ocean Modelling* **75**: 65–83.
DOI: <https://doi.org/10.1016/j.ocemod.2013.12.006>
- Stronkhorst J., Alex L., Hendriksen G., Rangel-Buitrago N. & Appelquist R.S. (2018). Regional coastal erosion assessment based on global open access data: a case study for Colombia. *Journal of Coastal Conservation* **22**(4): 787–798.
DOI: <https://doi.org/10.1007/s11852-018-0609-x>
- Tolman H.L. (2009). User manual and system documentation of WAVEWATCH III TM Version 3.14. *Technical Note, MMAB Contribution 276*: 220.
- US EPA (2021). United States Environmental Protection Agency, Climate Impacts on Coastal Areas. Available at https://19january2017snapshot.epa.gov/climate-impacts/climate-impacts-coastal-areas_.html#:~:text=Climate%20change%20threatens%20coastal%20areas,disrupt%20coastal%20and%20marine%20ecosystems, accessed 09 April 2021.
- Van Rijn L.C. (2013). Simple general formulae for sand transport in rivers, estuaries and coastal waters. pp.1–16. Available at <https://www.leovanrijn-sediment.com/>, accessed 09 April 2021.
- Wickramaarachchi B. (2012). *Hazard Profiles of Sri Lanka* (ed. S. Piyasiri), pp. 25–45. Ministry of Disaster Management, Colombo, Sri Lanka.

RESEARCH ARTICLE

Computational chemistry

M-polynomial and topological indices for the anti-tuberculosis drugs

TP Jude¹, P Elango^{1*} and M. Koneswaran²

¹ Department of Mathematics, Faculty of Science, Eastern University of Sri Lanka, Vantharumoolai, Chenkalady, 30350 Sri Lanka.

² Department of Chemistry, Faculty of Science, Eastern University of Sri Lanka, Vantharumoolai, Chenkalady, 30350 Sri Lanka.

Submitted: 15 November 2021; Revised: 23 May 2022; Accepted: 22 July 2022

Abstract: Tuberculosis (TB) is one of the deadliest infectious diseases which is caused by the *Mycobacterium tuberculosis*. A group of first line anti-TB drugs namely isoniazid, rifampicin, pyrazinamide and ethambutol have been accepted for the treatment of drug susceptible tuberculosis. A topological index is a molecular structure descriptor which is a numerical value associated with chemical constitution for correlation of a chemical structure with its properties. The aim of this work is to investigate some degree-based topological indices for the above-mentioned anti-TB drugs using a polynomial approach. The molecular graphs of these anti-TB drugs structures were used to derive the M-Polynomials and then the derived formulas were used to calculate topological indices of the respective structures. This research could facilitate the design of new medicines against these pathogenic bacteria.

Keywords: Anti-TB drugs, M-polynomial, Randić index, topological indices, tuberculosis, Zagreb index.

INTRODUCTION

Tuberculosis (TB) is one of the deadliest infectious diseases, responsible for millions of deaths annually in the globe (Floyd *et al.*, 2018). The German Microbiologist, Robert Koch declared in 1882 that the TB is an airborne disease which caused by the rod shaped bacillus called *Mycobacterium tuberculosis* (MTB) (Cambau &

Drancourt, 2014). This bacterium usually affects the lungs leading to severe coughing, fever, and chest pains; however, it can affect other organs in the body (except nails and hair) as well (Comas & Gagneux, 2009). TB is an airborne infection, and these bacilli are expelled into the air in the form of tiny droplet when the infected patients coughs, sneezes, or laughs, and these droplets may remain suspended in the air for several hours (Keshavjee & Farmer, 2012). The infection process typically occurs after long and repeated exposure to infected individuals via inhalation of these droplets into the lungs (Feng *et al.*, 2020). According to the World Health Organisation (WHO), an untreated TB patient can infect 10–15 persons over the course of one year (WHO, 2002). Early diagnosis and effective treatment are the major challenges in controlling TB globally. A standard TB treatment regime has been recommended by the WHO, and active tuberculosis is treated with first line drugs which include isoniazid, rifampicin, pyrazinamide, and ethambutol for two months (British Thoracic Society, 1984). These anti TB drugs act as bactericidal or bacteriostatic agents against MTB by effecting inhibition of their cell wall, protein synthesis inhibition, nucleic acid inhibition or inhibition of the membrane energy metabolism. (Ma *et al.*, 2010; Favrot & Ronning 2012).

* Corresponding author (elangop@esn.ac.lk;  <https://orcid.org/0000-0002-7359-989X>)



This article is published under the Creative Commons CC-BY-ND License (<http://creativecommons.org/licenses/by-nd/4.0/>). This license permits use, distribution and reproduction, commercial and non-commercial, provided that the original work is properly cited and is not changed in anyway.

Synthesizing a drug molecule with desired properties is the key for targeting specific diseases (Gao *et al.*, 2016; Zheng *et al.*, 2019). Therefore, studying the properties of drug molecule is important in drug design. These properties of the compound could be interpreted by using well known topological indices in molecular graph theory or molecular topology.

Currently many researchers are focusing on calculating the topological indices for the chemical structures used in various applications to overcome the painstaking approach of computing a certain type of index of a specific category of graphs (Mobeen *et al.*, 2016; Zuo *et al.*, 2020). Furthermore, the role of topological indices in drug design research has been reported by various scientists (Rouvray, 1973; Estrada & Uriarte, 2001; Estrada *et al.*, 2003; Gálvez *et al.*, 2012; Zanni *et al.*, 2015). Therefore, the study of topological indices of essential first line anti-TB drugs namely isoniazid, rifampicin, pyrazinamide, and ethambutol is important to evaluate their properties.

A graph $G = G(V, E)$ with the vertex set $V = V(G)$ and the edge set $E = E(G)$ is said to be a connected if there is a connection between any pair of vertices in the graph. The number of edges which are connected to that fixed vertex is called the degree of a vertex, v , and is denoted by $d_v(G)$ or d_v .

A topological index is a numerical quantity which is derived mathematically in a direct and unambiguous manner from the structural graph of a molecule. The first topological index which is a distance based (non-degree based) index was introduced by Wiener in 1947 and defined by the following formula

$$W(G) = \sum_{\{u,v\} \subseteq V(G)} d_G(u, v).$$

where $d_G(u, v)$ is the shortest distance between the vertices u and v in the graph G . Degree-based topological indices are another type of topological indices. Nowadays, the degree-based topological indices play a prominent role in molecular graph theory.

The Randić index and the Zagreb index are the mostly studied types of degree-based topological indices in drug design (Gao *et al.*, 2013; Nilanjan De, 2018; Jude *et al.*, 2019; Jude *et al.*, 2020). The well-known Zagreb index which is the oldest degree-based topological index was introduced by Gutman and Trinajstić in 1972 during the analysis of the structure-dependency of total π -electron energy (Gutman & Trinajstić, 1972). The Zagreb index is presented in two different formats as the first Zagreb

index, $M_1(G)$, and the second Zagreb index, $M_2(G)$. The second modified Zagreb index, ${}^mM_2(G)$, was introduced by Hao in 2011 (Hao, 2011).

Another old degree-based topological index called the Randić index, $R(G)$, was introduced by Milan Randić in 1975 (Randić, 1975). Another format of the Randić index called the generalized Randić index, $R_\alpha(G)$, was introduced in 1998 by Bollobás and Erdős (1998) and Amic *et al.* (1998) independently (here α is an arbitrary real number). This has been studied extensively by both chemists and mathematicians (Hu *et al.*, 2005) and the mathematical properties have been discussed by (Caporossi *et al.*, 2005). When substituting $\alpha = -1/2$ in this formula, the (original) Randić index could be obtained.

There are many topological indices introduced and studied by mathematical chemists. The symmetric division degree index (or simply *sdd*-index), $SDD(G)$, was proposed by Vukičević (2010) as a remarkable predictor of total surface area of polychlorobiphenyls. The forgotten topological index, $F(G)$, was proposed by Furtula and Gutman in 2015, and is quite helpful for pharmaceutical and medical scientists to grasp the biological and chemical characteristics of new drugs (Gao *et al.*, 2016). The harmonic index, $H(G)$, was proposed by Fajtlowicz (1987) as another variant of the Randić index. The inverse sum index, $I(G)$, was proposed by Balaban (1982) and that is a significant predictor of the total surface area of octane isomers. The augmented Zagreb index, $A(G)$, was introduced by Furtula *et al.* (2010) for computing the heat of formation of alkanes.

The definition for the above-described degree-based topological indices are expressed by $D(G) = \sum_{uv \in E(G)} f(d_u, d_v)$, where the function $f(d_u, d_v)$ for each of the topological indices are given in the Table 1:

The topological indices could be calculated by direct calculation or by using the algebraic polynomials. For instance, the first derivative of the Hosoya polynomial (Hosoya, 1988) could be used to compute the Wiener index. For computing the degree-based topological indices, the M -polynomial, introduced by Deutsch and Klavžar in 2015, is used. For a graph $G = G(V, E)$, the M -polynomial is defined by

$$M(G) = \sum_{i \leq j} m_{ij}(G) x^i y^j,$$

where $m_{ij}(G)$, $i, j \geq 1$ is the number of edges $e = uv$ of G such that $\{d_u, d_v\} = \{i, j\}$, $u, v \in V(G)$.

Table 1: Description of some of the degree based topological indices.

Topological index	Notation	$f(d_u, d_v)$	Reference
First Zagreb index	$M_1(G)$	$d_u + d_v$	Gutman & Trinajstić, 1972
Second Zagreb index	$M_2(G)$	$d_u d_v$	Gutman & Trinajstić, 1972
Second modified Zagreb	${}^m M_2(G)$	$\frac{1}{d_u d_v}$	Hao, 2011
Generalized Randić index	$R_\alpha(G)$	$(d_u d_v)^\alpha$	Amic <i>et al.</i> , 1998; Bollobás & Erdős 1998
Randić index	$R_{-1/2}(G)$	$\frac{1}{\sqrt{d_u d_v}}$	Randić, 1975
Symmetric division deg index	$SDD(G)$	$\frac{d_u^2 + d_v^2}{d_u d_v}$	Vukicevic, 2010
Forgotten topological index	$F(G)$	$d_u^2 + d_v^2$	Furtula & Gutman, 2015
Harmonic index	$H(G)$	$\frac{2}{d_u + d_v}$	Fajtlowicz, 1987
Inverse sum indeg index	$I(G)$	$\frac{d_u d_v}{d_u + d_v}$	Balaban, 1982
Augmented Zagreb index	$A(G)$	$\left(\frac{d_u d_v}{d_u + d_v}\right)^3$	Furtula <i>et al.</i> , 2010

Table 2: The derivation of some degree-based topological indices from the M -polynomial (Deutsch & Klavzar, 2015).

Topological index	Notation	Derivation from $M(G)$
First Zagreb index	$M_1(G)$	$(D_x + D_y)(M(G)) _{x=y=1}$
Second Zagreb index	$M_2(G)$	$(D_x D_y)(M(G)) _{x=y=1}$
Second modified Zagreb	${}^m M_2(G)$	$(S_x S_y)(M(G)) _{x=y=1}$
Generalized Randić index	$R_\alpha(G)$	$(D_x^\alpha D_y^\alpha)(M(G)) _{x=y=1}$
Randić index	$R_{-1/2}(G)$	
Symmetric division deg index	$SDD(G)$	$(D_x S_y + S_x D_y)(M(G)) _{x=y=1}$
Forgotten topological index	$F(G)$	$(D_x^2 + D_y^2)(M(G)) _{x=y=1}$
Harmonic index	$H(G)$	$2S_x J(M(G)) _{x=y=1}$
Inverse sum indeg index	$I(G)$	$S_x J D_x D_y(M(G)) _{x=y=1}$
Augmented Zagreb index	$A(G)$	$S_x^3 Q_{-2} J D_x^3 D_y^3(M(G)) _{x=y=1}$

The topological indices described-above could be calculated using the respective derivation formula of the M -polynomial $M(G)$ given in the Table 2:

$$\text{Here } D_x(f(x,y)) = x \frac{\partial f(x,y)}{\partial x}, D_y(f(x,y)) = y \frac{\partial f(x,y)}{\partial y},$$

$$S_x(f(x,y)) = \int_0^x \frac{f(t,y)}{t} dt, \quad D_x^\alpha = \sum_i n_i^\alpha k_i x^{n_i} y^{m_i}$$

$$\text{here } D_x = \sum_i k_i x^{n_i} y^{m_i}, S_y(f(x,y)) = \int_0^y \frac{f(x,t)}{t} dt,$$

$$J(f(x,y)) = f(x,x), S_x J = S_x(f(x,x)) = \int_0^x \frac{f(t,t)}{t} dt,$$

$$\text{and } Q_\alpha(f(x,y)) = x^\alpha f(x,y).$$

In this study, we calculate some of the well-known degree based topological indices (expressed in the above table) using the M -polynomial for the first line anti-TB drugs, namely, isoniazid, rifampicin, pyrazinamide and ethambutol.

MATERIALS AND METHODS

In this paper, we considered four anti-TB drugs namely isoniazid, rifampicin, pyrazinamide and ethambutol and calculated their topological indices. The molecular graphs of these drug structures were used to derive the M -Polynomials, and then the derived formulas were used to calculate topological indices of the respective structures. The calculated topological indices are given in Table 2.

The edge sets were portioned by observing the molecular graph of a structure and find the M -Polynomial. We denote $E(i,j)$ be the set of edge partitions of the graph G , where $E(i,j) = \{uv \in E(G): d_u = i \text{ and } d_v = j\}$. In a molecular representation (in a molecular structure), a dashed line indicates that the bond is extending behind the plane of the drawing surface; a bold-wedged line indicates that the bond is protruding out from the plane of the drawing surface and a solid line indicates that the bond exists in the plane of the drawing surface. In molecular graph theory, all these bonds are considered as single edges for the calculation except a bond with Hydrogen. Furthermore, the multiple edges are treated as single edge in molecular graph theory. We calculated the topological indices using the derivation formula for the respective M -Polynomial. MATLAB is used to sketch $M(G)$.

RESULTS AND DISCUSSION

First, we considered the molecular graph of isoniazid (Figure 1).

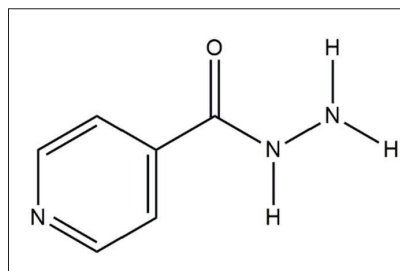


Figure 1: Molecular graph of isoniazid

Theorem 1: Let G be the molecular graph of isoniazid. Then the M -Polynomial of isoniazid is given by,

$$M(G) = xy^2 + xy^3 + 4x^2y^2 + 3x^2y^3 + x^3y^3.$$

Proof: Let G be the molecular graph of isoniazid which has 10 numbers of edges.

Let $E(i,j)$ be the set of edge partitions with the degree of end vertices i,j .

i.e., $E(i,j) = \{e = uv \in E(G): d_u = i \text{ and } d_v = j\}$. By observing the structure, we inferred four partitions of the edge set as follows:

$$E(1,2) = \{e = uv \in E(G): d_u = 1 \text{ and } d_v = 2\},$$

$$E(1,3) = \{e = uv \in E(G): d_u = 1 \text{ and } d_v = 3\},$$

$$E(2,2) = \{e = uv \in E(G): d_u = d_v = 2\} \quad E(2,3) = \{e = uv \in E(G): d_u = 2 \text{ and } d_v = 3\} \quad \text{and} \quad E(3,3) = \{e = uv \in E(G): d_u = 3 \text{ and } d_v = 3\},$$

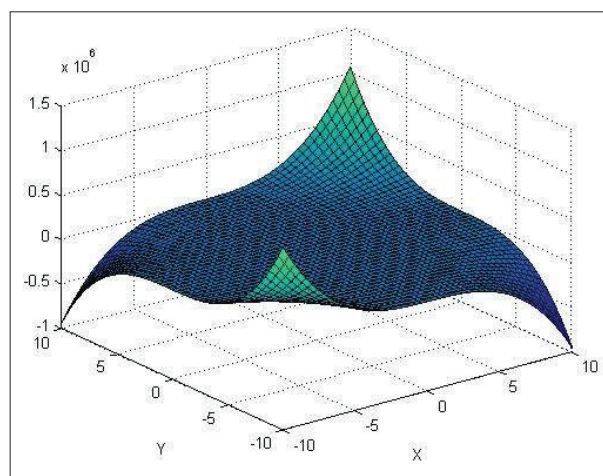


Figure 2: Plotting of M -polynomial for isoniazid

Also we get $|E(1,2)| = 1$, $|E(1,3)| = 1$, $|E(2,2)| = 4$, $|E(2,3)| = 3$ and Therefore, the M the M -polynomial of the molecular graph of isoniazid is

$$M(G) = xy^2 + xy^3 + 4x^2y^2 + 3x^2y^3 + x^3y^3.$$

Theorem 2: Let G be the molecular graph of isoniazid. Then, the first Zagreb index $M_1(G)$, second Zagreb index $M_2(G)$ second modified Zagreb index ${}^mM_2(G)$, generalized Randić index, $R_\alpha(G)$, Randić index $R_{-1/2}(G)$ (which is actually $R(G)$), symmetric division degree index $SDD(G)$, forgotten topological index $F(G)$, harmonic index $H(G)$, inverse sum index index $I(G)$, and the augmented Zagreb index $A(G)$ are given by

1. $M_1(G) = 44$.
2. $M_2(G) = 48$.
3. ${}^mM_2(G) = \frac{22}{9}$.
4. $R_\alpha(G) = 2^\alpha + 3^\alpha + 4(4)^\alpha + 3(6)^\alpha + (9)^\alpha$.
5. $R_{-1/2}(G) = \frac{1}{\sqrt{2}} + \frac{1}{\sqrt{3}} + \frac{3}{\sqrt{6}} + \frac{7}{3}$.
6. $SDD(G) = \frac{67}{3}$.
7. $F(G) = 104$.
8. $H(G) = \frac{141}{30}$.
9. $I(G) = \frac{631}{60}$.
10. $A(G) = \frac{5041}{64}$.

Proof: Let be the M -polynomial of the molecular graph of isoniazid. Then we get the following:

$$D_x(M(G)) = xy^2 + xy^3 + 8x^2y^2 + 6x^2y^3 + 3x^3y^3.$$

$$D_y(M(G)) = 2xy^2 + 3xy^3 + 8x^2y^2 + 9x^2y^3 + 3x^3y^3.$$

$$D_xD_y(M(G)) = 2xy^2 + 3xy^3 + 16x^2y^2 + 18x^2y^3 + 9x^3y^3.$$

$$S_x(M(G)) = xy^2 + xy^3 + 2x^2y^2 + \frac{3}{2}x^2y^3 + \frac{1}{3}x^3y^3.$$

$$S_y(M(G)) = \frac{1}{2}xy^2 + \frac{1}{3}xy^3 + 2x^2y^2 + x^2y^3 + \frac{1}{3}x^3y^3.$$

$$S_xS_y(M(G)) = \frac{1}{2}xy^2 + \frac{1}{3}xy^3 + x^2y^2 + \frac{1}{2}x^2y^3 + \frac{1}{9}x^3y^3.$$

$$D_x^\alpha(M(G)) = xy^2 + xy^3 + 4(2)^\alpha x^2y^2 + 3(2)^\alpha x^2y^3 + (3)^\alpha x^3y^3.$$

$$D_y^\alpha(M(G)) = 2^\alpha xy^2 + 3^\alpha xy^3 + 4(2)^\alpha x^2y^2 + 3(3)^\alpha x^2y^3 + (3)^\alpha x^3y^3.$$

$$D_x^\alpha D_y^\alpha(M(G)) = 2^\alpha xy^2 + 3^\alpha xy^3 + 4(4)^\alpha x^2y^2 + 3(6)^\alpha x^2y^3 + (9)^\alpha x^3y^3.$$

$$S_xD_y(M(G)) = 2xy^2 + 3xy^3 + 4x^2y^2 + \frac{9}{2}x^2y^3 + x^3y^3.$$

$$S_yD_x(M(G)) = \frac{1}{2}xy^2 + \frac{1}{3}xy^3 + 4x^2y^2 + 2x^2y^3 + x^3y^3.$$

$$J(M(G)) = x^3 + 5x^4 + 3x^5 + x^6.$$

$$S_xJ(M(G)) = \frac{1}{3}x^3 + \frac{5}{4}x^4 + \frac{3}{5}x^5 + \frac{1}{6}x^6.$$

$$JD_xD_y(M(G)) = 2x^3 + 19x^4 + 18x^5 + 9x^6.$$

$$S_xJD_xD_y(M(G)) = \frac{2}{3}x^3 + \frac{19}{4}x^4 + \frac{18}{5}x^5 + \frac{9}{6}x^6$$

$$D_x^3D_y^3(M(G)) = 8xy^2 + 27xy^3 + 256x^2y^2 + 648x^2y^3 + 729x^3y^3.$$

$$Q_{-2}JD_x^3D_y^3(M(G)) = 8x + 283x^2 + 648x^3 + 729x^4.$$

$$S_x^3Q_{-2}JD_x^3D_y^3(M(G)) = 8x + \frac{283}{8}x^2 + 24x^3 + \frac{729}{64}x^4.$$

By using the derived formulas of the M -polynomial, we find,

1. $M_1(G) = (D_x + D_y)(M(G))|_{x=y=1} = 44$.
2. $M_2(G) = D_xD_y(M(G))|_{x=y=1} = 48$.
3. $R_\alpha(G) = D_x^\alpha D_y^\alpha(M(G))|_{x=y=1} = 2^\alpha + 3^\alpha$
4. $R(G) = R_{-1/2}(G) = D_x^{-1/2}D_y^{-1/2}(M(G))|_{x=y=1} = \frac{1}{\sqrt{2}} + \frac{1}{\sqrt{3}} + \frac{3}{\sqrt{6}} + \frac{7}{3}$.
5. $SDD(G) = (S_xD_y + S_yD_x)|_{x=y=1} = \frac{67}{3}$.
6. $F(G) = (D_x^2 + D_y^2)(M(G))|_{x=y=1} = 104$.
7. $H(G) = 2S_yD_x(M(G))|_{x=y=1} = \frac{141}{30}$.
8. $I(G) = S_xJD_xD_y(M(G))|_{x=y=1} = \frac{631}{60}$.
9. $A(G) = S_x^3Q_{-2}JD_x^3D_y^3(M(G))|_{x=y=1} = \frac{5041}{64}$.

Now we considered the molecular graph of rifampicin (Figure 3).

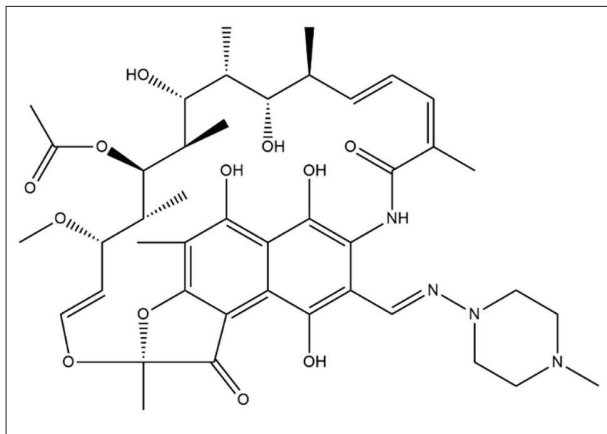


Figure 3: Molecular graph of rifampicin

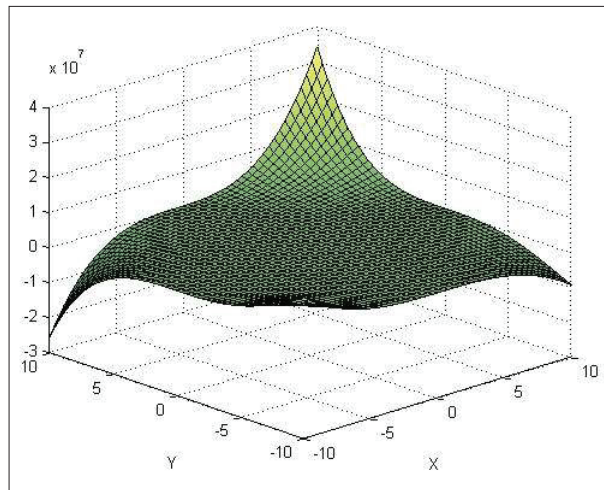


Figure 4: Plotting of M -polynomial for rifampicin

Theorem 3: Let G be the molecular graph of rifampicin. Then the M -Polynomial of rifampicin is given by,

$$M(G) = xy^2 + 16xy^3 + xy^4 + 5x^2y^2 + 17x^2y^3 + 2x^2y^4 + 20x^3y^3 + x^3y^4.$$

Proof: Let G be the molecular graph of rifampicin which has 63 numbers of edges.

By observing the structure, we inferred eight partitions of the edge set as follows:

$$E(1,2) = \{e = uv \in E(G) : d_u = 1 \text{ and } d_v = 2\},$$

$$E(1,3) = \{e = uv \in E(G) : d_u = 1 \text{ and } d_v = 3\},$$

$$E(1,4) = \{e = uv \in E(G) : d_u = 1 \text{ and } d_v = 4\},$$

$$E(2,2) = \{e = uv \in E(G) : d_u = d_v = 2\},$$

$$E(2,3) = \{e = uv \in E(G) : d_u = 2 \text{ and } d_v = 3\},$$

$$E(2,4) = \{e = uv \in E(G) : d_u = 2 \text{ and } d_v = 4\},$$

$$E(3,3) = \{e = uv \in E(G) : d_u = d_v = 3\}, \text{ and}$$

$$E(3,4) = \{e = uv \in E(G) : d_u = 3 \text{ and } d_v = 4\}.$$

Also we get $|E(1,2)| = 1$, $|E(1,3)| = 16$, $|E(1,4)| = 1$, $|E(2,2)| = 5$, $|E(2,3)| = 17$, $|E(2,4)| = 1$, and $|E(3,4)| = 1$.

Therefore, the M -polynomial of the structure of rifampicin is

$$M(G) = xy^2 + 16xy^3 + xy^4 + 5x^2y^2 + 17x^2y^3 + 2x^2y^4 + 20x^3y^3 + x^3y^4.$$

Theorem 4: Let G be the molecular graph of rifampicin. Then, the first Zagreb index $M_1(G)$, second Zagreb index $M_2(G)$, second modified Zagreb index ${}^mM_2(G)$, generalized Randić index, $R_\alpha(G)$, Randić index $R_{-1/2}(G)$ (which is actually $R(G)$), symmetric division degree index $SDD(G)$, forgotten topological index $F(G)$, harmonic index $H(G)$, inverse sum index $I(G)$, and the augmented Zagreb index are given by

1. $M_1(G) = 316$.
2. $M_2(G) = 384$.
3. ${}^mM_2(G) = \frac{229}{18}$.
4. $R_\alpha(G) = (2)^\alpha + 16(3)^\alpha + 6(4)^\alpha + 17(6)^\alpha + 2(8)^\alpha + 20(9)^\alpha + (12)^\alpha$.
5. $R(G) = \frac{2}{\sqrt{2}} + \frac{33}{2\sqrt{3}} + \frac{17}{\sqrt{6}} + \frac{29}{3}$.
6. $SDD(G) = 154$.
7. $F(G) = 868$.
8. $H(G) = \frac{647}{70}$.
9. $I(G) = \frac{7691}{105}$.
10. $A(G) = 102$.

Proof: Let $M(G)$ be the M -polynomial of the molecular graph of rifampicin. Then we get the following:

$$D_x(M(G)) = xy^2 + 16xy^3 + xy^4 + 10x^2y^2 + 34x^2y^3 + 4x^2y^4 + 60x^3y^3 + 3x^3y^4.$$

$$D_y(M(G)) = 2xy^2 + 48xy^3 + 4xy^4 + 10x^2y^2 + 51x^2y^3 + 8x^2y^4 + 60x^3y^3 + 4x^3y^4$$

$$D_xD_y(M(G)) = 2xy^2 + 48xy^3 + 4xy^4 + 20x^2y^2 + 102x^2y^3 + 16x^2y^4 + 180x^3y^3 + 12x^3y^4$$

$$S_x(M(G)) = xy^2 + 16xy^3 + xy^4 + \frac{5}{2}x^2y^2 + \frac{17}{2}x^2y^3 + x^2y^4 + \frac{20}{3}x^3y^3 + \frac{1}{3}x^3y^4.$$

$$S_y(M(G)) = \frac{1}{2}xy^2 + \frac{16}{3}xy^3 + \frac{1}{4}xy^4 + \frac{5}{2}x^2y^2 + \frac{17}{3}x^2y^3 + \frac{1}{2}x^2y^4 + \frac{20}{3}x^3y^3 + \frac{1}{4}x^3y^4.$$

$$S_xS_y(M(G)) = \frac{1}{2}xy^2 + \frac{16}{3}xy^3 + \frac{1}{4}xy^4 + \frac{5}{4}x^2y^2 + \frac{17}{6}x^2y^3 + \frac{1}{4}x^2y^4 + \frac{20}{9}x^3y^3 + \frac{1}{12}x^3y^4.$$

$$D_x^\alpha(M(G)) = xy^2 + 16xy^3 + xy^4 + 5(2)^\alpha x^2y^2 + 17(2)^\alpha x^2y^3 + 2(2)^\alpha x^2y^4 + 20(3)^\alpha x^3y^3 + (3)^\alpha x^3y^4.$$

$$D_y^\alpha(M(G)) = (2)^\alpha xy^2 + 16(3)^\alpha xy^3 + (4)^\alpha xy^4 + 5(2)^\alpha x^2y^2 + 17(3)^\alpha x^2y^3 + 2(4)^\alpha x^2y^4 + 20(3)^\alpha x^3y^3 + (4)^\alpha x^3y^4.$$

$$D_x^\alpha D_y^\alpha(M(G)) = (2)^\alpha xy^2 + 16(3)^\alpha xy^3 + (4)^\alpha xy^4 + 5(4)^\alpha x^2y^2 + 17(6)^\alpha x^2y^3 + 2(8)^\alpha x^2y^4 + 20(9)^\alpha x^3y^3 + (12)^\alpha x^3y^4.$$

$$S_xD_y(M(G)) = 2xy^2 + 48xy^3 + 4xy^4 + 5x^2y^2 + \frac{51}{2}x^2y^3 + 4x^2y^4 + 20x^3y^3 + \frac{4}{3}x^3y^4.$$

$$S_yD_x(M(G)) = \frac{1}{2}xy^2 + \frac{16}{3}xy^3 + \frac{1}{4}xy^4 + 5x^2y^2 + \frac{34}{3}x^2y^3 + x^2y^4 + 20x^3y^3 + \frac{3}{4}x^3y^4.$$

$$J(M(G)) = x^3 + 21x^4 + 18x^5 + 22x^6 + x^7.$$

$$S_xJ(M(G)) = \frac{1}{3}x^3 + \frac{21}{4}x^4 + \frac{18}{5}x^5 + \frac{11}{3}x^6 + \frac{1}{7}x^7.$$

$$JD_xD_y(M(G)) = 2x^3 + 68x^4 + 106x^5 + 196x^6 + 12x^7.$$

$$S_xJD_xD_y(M(G)) = \frac{2}{3}x^3 + 17x^4 + \frac{106}{5}x^5 + \frac{98}{3}x^6 + \frac{12}{7}x^7$$

$$D_x^3D_y^3(M(G)) = 8xy^2 + 432xy^3 + 64xy^4 + 320x^2y^2 + 3672x^2y^3 + 1024x^2y^4 + 14580x^3y^3 + 1728x^3y^4$$

$$JD_x^3D_y^3(M(G)) = 8x^3 + 752x^4 + 3736x^5 + 15604x^6 + 1728x^7.$$

$$Q_{-2}JD_x^3D_y^3(M(G)) = 8x + 752x^2 + 3736x^3 + 15604x^4 + 1728x^5.$$

$$S_x^3Q_{-2}JD_x^3D_y^3(M(G)) = 8x + \frac{752}{2^3}x^2 + \frac{3736}{3^3}x^3 + \frac{15604}{4^3}x^4 + \frac{1728}{5^3}x^5.$$

By using the derived formulas of the M -polynomial, we find,

1. $M_1(G) = (D_x + D_y)(M(G))|_{x=y=1} = 316.$
2. $M_2(G) = D_xD_y(M(G))|_{x=y=1} = 384.$
3. ${}^mM_2(G) = S_xS_y(M(G))|_{x=y=1} = \frac{229}{18}.$
4. $R_\alpha(G) = D_x^\alpha D_y^\alpha(M(G))|_{x=y=1} = (2)^\alpha + 16(3)^\alpha + 6(4)^\alpha + 17(6)^\alpha + 2(8)^\alpha + 20(9)^\alpha + (12)^\alpha.$
5. $R(G) = R_{-1/2}(G) = D_x^{-1/2}D_y^{-1/2}(M(G))|_{x=y=1} = \frac{2}{\sqrt{2}} + \frac{33}{2\sqrt{3}} + \frac{17}{\sqrt{6}} + \frac{29}{3}.$
6. $SDD(G) = (S_xD_y + S_yD_x)|_{x=y=1} = 154.$
7. $F(G) = (D_x^2 + D_y^2)(M(G))|_{x=y=1} = 868.$
8. $H(G) = 2S_yD_x(M(G))|_{x=y=1} = \frac{647}{70}.$
9. $I(G) = S_xJD_xD_y(M(G))|_{x=y=1} = \frac{7691}{105}.$
10. $A(G) = S_x^3Q_{-2}JD_x^3D_y^3(M(G))|_{x=y=1} = 102 + \frac{3736}{3^3} + \frac{15604}{4^3} + \frac{1728}{5^3}.$

Now we considered the molecular graph of pyrazinamide (Figure 5).

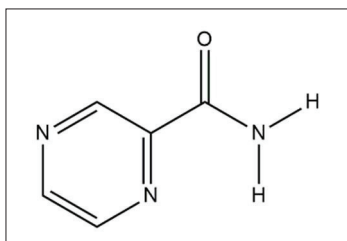


Figure 5: Molecular graph of pyrazinamide

Theorem 5: Let G be the molecular graph of pyrazinamide. Then the M -Polynomial of pyrazinamide is given by,

$$M(G) = 2xy^3 + 4x^2y^2 + 2x^2y^3 + x^3y^3.$$

Proof: Let be the molecular graph of pyrazinamide which has 9 numbers of edges.

By observing the structure, we inferred four partitions of the edge set as follows:

$$E(1,3) = \{e = uv \in E(G) : d_u = 1 \text{ and } d_v = 3\},$$

$$E(2,2) = \{e = uv \in E(G) : d_u = d_v = 2\},$$

$$E(2,3) = \{e = uv \in E(G) : d_u = 2 \text{ and } d_v = 3\},$$

$$\text{and } E(3,3) = \{e = uv \in E(G) : d_u = d_v = 3\}.$$

Also we get, $|E(1,3)| = 2$, $|E(2,2)| = 4$, $|E(2,3)| = 2$ and $|E(3,3)| = 1$.

Therefore, the M -polynomial of the molecular graph of pyrazinamide is

$$M(G) = 2xy^3 + 4x^2y^2 + 2x^2y^3 + x^3y^3.$$

Theorem 6: Let G be the molecular graph of pyrazinamide. Then, the first Zagreb index $M_1(G)$, second Zagreb index $M_2(G)$, second modified Zagreb index ${}^mM_2(G)$, generalized Randić index, $R_\alpha(G)$, Randić index $R_{-1/2}(G)$ (which is actually $R(G)$), symmetric division degree index $SDD(G)$, forgotten topological index $F(G)$, harmonic index $H(G)$, inverse sum index $I(G)$, and the augmented Zagreb index $A(G)$ are given by

$$1. \quad M_1(G) = 40.$$

$$2. \quad M_2(G) = 43.$$

$$3. \quad {}^mM_2(G) = \frac{19}{9}.$$

$$4. \quad R_\alpha(G) = 2(3)^\alpha + 4(4)^\alpha + 2(6)^\alpha + (9)^\alpha.$$

$$5. \quad R(G) = \frac{2}{\sqrt{3}} + \frac{2}{\sqrt{6}} + \frac{7}{3}.$$

$$6. \quad SDD(G) = 21.$$

$$7. \quad F(G) = 96.$$

$$8. \quad H(G) = \frac{62}{15}.$$

$$9. \quad I(G) = \frac{47}{5}.$$

$$10. \quad A(G) = \frac{310}{2^3} + \frac{432}{3^3} + \frac{729}{4^3} = \frac{4233}{64}.$$

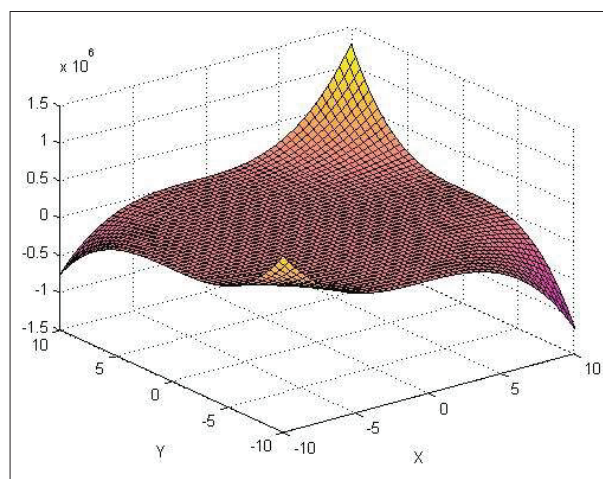


Figure 6: Plotting of M -polynomial for pyrazinamide

Proof: Let $M(G)$ be the M -polynomial of the molecular graph of pyrazinamide. Then we get the following:

$$D_x(M(G)) = 2xy^3 + 8x^2y^2 + 4x^2y^3 + 3x^3y^3.$$

$$D_y(M(G)) = 6xy^3 + 8x^2y^2 + 6x^2y^3 + 3x^3y^3.$$

$$D_x D_y(M(G)) = 6xy^3 + 16x^2y^2 + 12x^2y^3 + 9x^3y^3.$$

$$S_x(M(G)) = 2xy^3 + 2x^2y^2 + x^2y^3 + \frac{1}{3}x^3y^3.$$

$$S_y(M(G)) = \frac{2}{3}xy^3 + 2x^2y^2 + \frac{2}{3}x^2y^3 + \frac{1}{3}x^3y^3.$$

$$S_x S_y(M(G)) = \frac{2}{3}xy^3 + x^2y^2 + \frac{1}{3}x^2y^3 + \frac{1}{9}x^3y^3.$$

$$D_x^\alpha(M(G)) = 2(3)^\alpha xy^3 + 4(2)^\alpha x^2y^2 + 2(2)^\alpha x^2y^3 + (3)^\alpha x^3y^3.$$

$$D_y^\alpha(M(G)) = 2(3)^\alpha xy^3 + 4(2)^\alpha x^2y^2 + 2(3)^\alpha x^2y^3 + (3)^\alpha x^3y^3.$$

$$D_x^\alpha D_y^\alpha(M(G)) = 2(3)^\alpha xy^3 + 4(4)^\alpha x^2y^2 + 2(6)^\alpha x^2y^3 + (9)^\alpha x^3y^3$$

$$S_x D_y(M(G)) = 6xy^3 + 4x^2y^2 + 3x^2y^3 + x^3y^3.$$

$$S_y D_x(M(G)) = \frac{2}{3}xy^3 + 4x^2y^2 + \frac{4}{3}x^2y^3 + x^3y^3.$$

$$J(M(G)) = 6x^4 + 2x^5 + x^6.$$

$$S_x J(M(G)) = \frac{6}{4}x^4 + \frac{2}{5}x^5 + \frac{1}{6}x^6.$$

$$J D_x D_y(M(G)) = 22x^4 + 12x^5 + 9x^6.$$

$$S_x J D_x D_y(M(G)) = \frac{11}{2}x^4 + \frac{12}{5}x^5 + \frac{3}{2}x^6.$$

$$D_x^3 D_y^3(M(G)) = 54xy^3 + 32x^2y^2 + 54x^2y^3$$

$$J D_x^3 D_y^3(M(G)) = 310x^4 + 432x^5 + 729x^6.$$

$$Q_{-2} J D_x^3 D_y^3(M(G)) = 310x^2 + 432x^3 + 729x^4.$$

$$S_x^3 Q_{-2} J D_x^3 D_y^3(M(G)) = \frac{310}{2^3}x^2 + \frac{432}{3^3}x^3 + \frac{729}{4^3}x^4.$$

By using the derived formulas of the M -polynomial, we find,

1. $M_1(G) = (D_x + D_y)(M(G))|_{x=y=1} = 40.$
2. $M_2(G) = D_x D_y(M(G))|_{x=y=1} = 43.$
3. $mM_2(G) = S_x S_y(M(G))|_{x=y=1} = \frac{19}{9}.$
4. $R_\alpha(G) = D_x^\alpha D_y^\alpha(M(G))|_{x=y=1} = 2(3)^\alpha + 4(4)^\alpha + 2(6)^\alpha + (9)^\alpha.$
5. $R(G) = R_{-1/2}(G) = D_x^{-1/2} D_y^{-1/2}(M(G))|_{x=y=1} = \frac{2}{\sqrt{3}} + \frac{2}{\sqrt{6}} + \frac{7}{3}.$
6. $SDD(G) = (S_x D_y + S_y D_x)|_{x=y=1} = 21.$

$$7. F(G) = (D_x^2 + D_y^2)(M(G))|_{x=y=1} = 96.$$

$$8. H(G) = 2S_y D_x(M(G))|_{x=y=1} = \frac{62}{15}.$$

$$9. I(G) = S_x J D_x D_y(M(G))|_{x=y=1} = \frac{47}{5}.$$

$$10. A(G) = S_x^3 Q_{-2} J D_x^3 D_y^3(M(G))|_{x=y=1} = \frac{310}{2^3} + \frac{432}{3^3} + \frac{729}{4^3} = \frac{4233}{64}.$$

Finally, we considered the molecular graph of ethambutol (Figure 7).

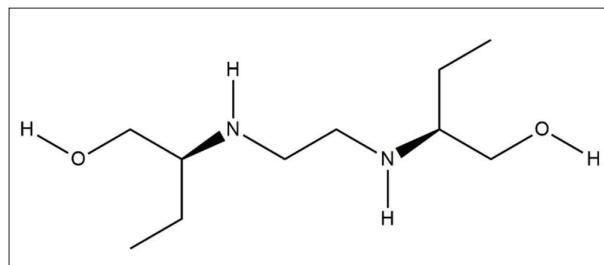


Figure 7: Molecular graph of ethambutol

Theorem 7: Let G be the molecular graph of Ethambutol. Then the M -Polynomial of isoniazid is given by,

$$M(G) = 4xy^2 + 3x^2y^2 + 6x^2y^3.$$

Proof: Let be the molecular graph of ethambutol which has 13 numbers of edges.

Let $E(i, j)$ be the set of edge partitions with the degree of end vertices i, j .

i.e., $E(i, j) = \{e = uv \in E(G) : d_u = i \text{ and } d_v = j\}$. By observing the structure, we inferred three partitions of the edge set as follows:

$$E(1,2) = \{e = uv \in E(G) : d_u = 1 \text{ and } d_v = 2\},$$

$$E(2,2) = \{e = uv \in E(G) : d_u = d_v = 2\}, \quad \text{and}$$

$$E(2,3) = \{e = uv \in E(G) : d_u = 2 \text{ and } d_v = 3\}.$$

Also, we get $|E(1,2)| = 4$, $|E(2,2)| = 3$, and $|E(2,3)| = 6$.

Therefore, the M -polynomial of the molecular graph of ethambutol is

$$M(G) = 4xy^2 + 3x^2y^2 + 6x^2y^3.$$

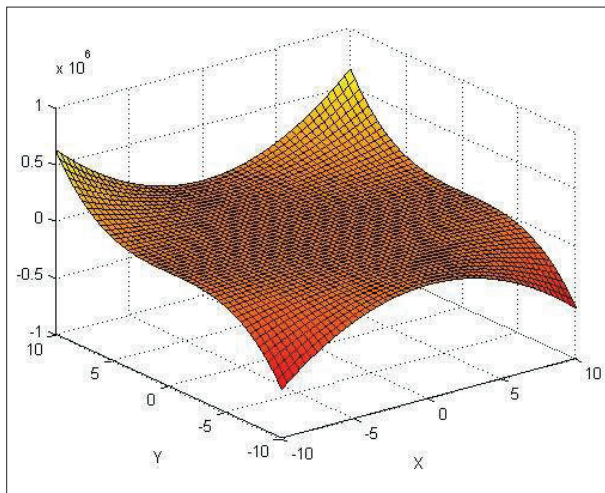


Figure 8: Plotting of M -polynomial for ethambutol

Theorem 8: Let G be the molecular graph of ethambutol. Then, the first Zagreb index $M_1(G)$, second Zagreb index $M_2(G)$ second modified Zagreb index ${}^mM_2(G)$, generalized Randić index, $R_\alpha(G)$, Randić index $R_{-1/2}(G)$ (which is actually $R(G)$), symmetric division degree index $SDD(G)$, forgotten topological index $F(G)$, harmonic index $H(G)$, inverse sum index $I(G)$, and the augmented Zagreb index $A(G)$ are given by

1. $M_1(G) = 54$.
2. $M_2(G) = 56$.
3. ${}^mM_2(G) = \frac{15}{4}$.
4. $R_\alpha(G) = 4(2)^\alpha + 3(4)^\alpha + 6(6)^\alpha$.
5. $R_{-1/2}(G) = 2\sqrt{2} + \sqrt{6} + \frac{3}{2}$.
6. $SDD(G) = 29$.
7. $F(G) = 122$.
8. $H(G) = \frac{197}{30}$.
9. $I(G) = \frac{193}{15}$.
10. $A(G) = 104$.

Proof: Let $M(G)$ be the M -polynomial of the molecular graph of ethambutol. Then we get the following:

$$D_x(M(G)) = 4xy^2 + 6x^2y^2 + 12x^2y^3.$$

$$D_y(M(G)) = 8xy^2 + 6x^2y^2 + 18x^2y^3.$$

$$D_xD_y(M(G)) = 8xy^2 + 12x^2y^2 + 36x^2y^3.$$

$$S_x(M(G)) = 4xy^2 + \frac{3}{2}x^2y^2 + 3x^2y^3.$$

$$S_y(M(G)) = 2xy^2 + \frac{3}{2}x^2y^2 + 2x^2y^3.$$

$$S_xS_y(M(G)) = 2xy^2 + \frac{3}{4}x^2y^2 + x^2y^3.$$

$$D_x^\alpha(M(G)) = 4xy^2 + 3(2)^\alpha x^2y^2 + 6(2)^\alpha x^2y^3.$$

$$D_y^\alpha(M(G)) = 4(2)^\alpha xy^2 + 3(2)^\alpha x^2y^2 + 6(3)^\alpha x^2y^3.$$

$$S_xD_y(M(G)) = 8xy^2 + 3x^2y^2 + 9x^2y^3.$$

$$D_x^\alpha D_y^\alpha(M(G)) = 4(2)^\alpha xy^2 + 3(4)^\alpha x^2y^2 + 6(6)^\alpha x^2y^3$$

$$S_yD_x(M(G)) = 2xy^2 + 3x^2y^2 + 4x^2y^3.$$

$$J(M(G)) = 4x^3 + 3x^4 + 6x^5.$$

$$S_xJ(M(G)) = \frac{4}{3}x^3 + \frac{3}{4}x^4 + \frac{6}{5}x^5.$$

$$JD_xD_y(M(G)) = 8x^3 + 12x^4 + 36x^5.$$

$$S_xJD_xD_y(M(G)) = \frac{8}{3}x^3 + 3x^4 + \frac{36}{5}x^5.$$

$$D_x^3D_y^3(M(G)) = 32xy^2 + 192x^2y^2 + 1296x^2y^3.$$

$$JD_x^3D_y^3(M(G)) = 32x^3 + 192x^4 + 1296x^5.$$

$$Q_{-2}JD_x^3D_y^3(M(G)) = 32x + 192x^2 + 1296x^3.$$

$$S_x^3Q_{-2}JD_x^3D_y^3(M(G)) = 32x + 24x^2 + 48x^3.$$

By using the derived formulas of the M -polynomial, we find,

$$1. \quad M_1(G) = (D_x + D_y)(M(G))|_{x=y=1} = 54.$$

$$2. \quad M_2(G) = D_xD_y(M(G))|_{x=y=1} = 56.$$

$$3. \quad {}^mM_2(G) = S_xS_y(M(G))|_{x=y=1} = \frac{15}{4}.$$

$$4. \quad R_\alpha(G) = D_x^\alpha D_y^\alpha(M(G))|_{x=y=1} = 4(2)^\alpha + 3(4)^\alpha + 6(6)^\alpha.$$

$$5. \quad R(G) = R_{-1/2}(G) = D_x^{-1/2}D_y^{-1/2}(M(G))|_{x=y=1} \\ = 2\sqrt{2} + \sqrt{6} + \frac{3}{2}.$$

$$6. \quad SDD(G) = (S_xD_y + S_yD_x)|_{x=y=1} = 29.$$

7. $F(G) = (D_x^2 + D_y^2)(M(G))|_{x=y=1} = 122.$
8. $H(G) = 2S_y D_x(M(G))|_{x=y=1} = \frac{197}{30}.$
9. $I(G) = S_x J D_x D_y(M(G))|_{x=y=1} = \frac{193}{15}.$
10. $A(G) = S_x^3 Q_{-2} J D_x^3 D_y^3(M(G))|_{x=y=1} = 104.$

CONCLUSION

This research is focused on calculating some degree-based topological indices for the anti TB drugs namely isoniazid, rifampicin, pyrazinamide and ethambutol. M -polynomial for these molecular structures was derived using the molecular graphs of these drugs molecules and the topological indices were calculated using the derived formulas of the M -polynomial. These finding could be useful to design and develop new drug molecules against this deadly disease.

Conflict of interest

There are no conflicts of interest.

REFERENCES

- Amić D., Bešlo D., Lučić B., Nikolić S. & Trinajstić N. (1998). The vertex-connectivity index revisited. *Journal of Chemical Information and Computer Sciences* **38**: 819–822.
DOI: <https://doi.org/10.1021/ci980039b>
- Balaban A.T. (1982). Highly discriminating distance based numerical descriptor. *Chemical Physics Letters* **89**: 399–404.
DOI: [https://doi.org/10.1016/0009-2614\(82\)80009-2](https://doi.org/10.1016/0009-2614(82)80009-2)
- Bollobás B. & Erdős P. (1998). Graphs of extremal weights. *Ars Combinatoria* **50**: 225–233.
- British Thoracic Society (1984). A controlled trial of 6 months' chemotherapy in pulmonary tuberculosis Final report: Results during the 36 months after the end of chemotherapy and beyond. *British Journal of Diseases of the Chest* **78**: 330.
DOI: [https://doi.org/10.1016/0007-0971\(84\)90165-7](https://doi.org/10.1016/0007-0971(84)90165-7)
- Cambau E. & Drancourt M. (2014). Steps towards the discovery of *Mycobacterium tuberculosis* by Robert Koch, 1882. *Clinical Microbiology and Infection* **20**: 196–201.
DOI: <https://doi.org/10.1111/1469-0691.12555>
- Caporossi G., Gutman I., Hansen P. & Pavlović L. (2003). Brief communication: graphs with maximum connectivity index. *Computational Biology and Chemistry* **27**: 85–90.
DOI: [https://doi.org/10.1016/S0097-8485\(02\)00016-5](https://doi.org/10.1016/S0097-8485(02)00016-5)
- Comas I. & Gagneux S. (2009). The past and future of tuberculosis research. *PLoS Pathogens* **5**: e1000600.
DOI: <https://doi.org/10.1371/journal.ppat.1000600>
- Deutsch E. & Klavzar S. (2015). M -polynomial and degree-based topological indices. *Iranian Journal of Mathematical Chemistry* **6**: 93–102.
DOI: <https://doi.org/10.22052/ijmc.2020.224280.1492>
- Estrada E., Patlewicz G. & Uriarte E. (2003). From molecular graphs to drugs. a review on the use of topological indices in drug design and discovery. *Indian Journal of Chemistry Section A* **42**: 1315–1329.
- Estrada E. & Uriarte E. (2001). Recent advances on the role of topological indices in drug discovery research. *Current Medicinal Chemistry* **8**: 1573–1588.
- Fajtlowicz S. (1987). On conjectures of graffiti II. *Congressus numerantium* **60**: 189–197.
- Favrot L. & Ronning D.R. (2012). Targeting the mycobacterial envelope for tuberculosis drug development. *Expert Review of Anti-infective Therapy* **10**: 1023–1036.
DOI: <https://doi.org/10.1586/eri.12.91>
- Feng Z., Castillo-Chavez C. & Capurro A.F. (2000). A model for tuberculosis with exogenous reinfection. *Theoretical Population Biology* **57**: 235–247.
DOI: <https://doi.org/10.1006/tpbi.2000.1451>
- Floyd K., Glaziou P., Zumla A. & Raviglione M. (2018). The global tuberculosis epidemic and progress in care, prevention, and research: an overview in year 3 of the End TB era. *The Lancet Respiratory Medicine* **6**: 299–314.
DOI: [https://doi.org/10.1016/S2213-2600\(18\)30057-2](https://doi.org/10.1016/S2213-2600(18)30057-2)
- Furtula B., Graovac A. & Vukičević D. (2010). Augmented Zagreb index. *Journal of Mathematical Chemistry* **48**: 370–380.
DOI: <https://doi.org/10.1007/s10910-010-9677-3>
- Furtula B. & Gutman I. (2015). A forgotten topological Index. *Journal of Mathematical Chemistry* **53**: 1184–1190.
DOI: <https://doi.org/10.1007/s10910-015-0480-z>
- Gálvez J., Gálvez-Llompert M. & García-Domenech R. (2012). Molecular topology as a novel approach for drug discovery. *Expert Opinion on Drug Discovery* **7**: 133–153.
DOI: <https://doi.org/10.1517/17460441.2012.652083>
- Gao W., Muzaffar B. & Nazeer W. (2017). K-Banhatti and K-hyper Banhatti indices of dominating David Derived network. *Open Journal of Mathematical Analysis* **1**: 13–24.
DOI: <https://doi.org/10.30538/psrp-oma2017.0002>
- Gao W., Siddiqui M.K., Imran M., Jamil M.K. & Farahani M.R. (2016). Forgotten topological index of chemical structure in drugs. *Saudi Pharmaceutical Journal* **24**: 258–264.
DOI: <https://doi.org/10.1016/j.jsps.2016.04.012>
- Gao W., Wang W. & Farahani M.R. (2016). Topological indices study of molecular structure in anticancer drugs. *Journal of Chemistry* **2016**: 1–8.
DOI: <https://doi.org/10.1155/2016/3216327>
- Gutman I. & Trinajstić N. (1972). Graph theory and molecular orbitals total f-electron energy of alternant hydrocarbons. *Chemical Physics Letters* **77**: 535–538.
DOI: [https://doi.org/10.1016/0009-2614\(72\)85099-1](https://doi.org/10.1016/0009-2614(72)85099-1)
- Hao J. (2011). Theorems about Zagreb indices and modified Zagreb indices. *MATCH Communications in Mathematical and in Computer Chemistry* **65**: 659–670.

- Hosoya H. (1988). On some counting polynomials in chemistry. *Discrete Applied Mathematics* **19**: 239–257.
DOI: [https://doi.org/10.1016/0166-218X\(88\)90017-0](https://doi.org/10.1016/0166-218X(88)90017-0)
- Hu Y., Li X., Shi Y., Xu T. & Gutman I. (2005). On molecular graphs with smallest and greatest zeroth-order general Randić index. *MATCH Communications in Mathematical and in Computer Chemistry* **54**: 425–434.
- Jude T.P., Panchadcharam E. & Masilamani K. (2019). Computation of Zagreb and Randić indices of two biodegradable dendrimers used in cancer therapy. *Ceylon Journal of Science* **48**: 359–366.
DOI: <http://doi.org/10.4038/cjs.v48i4.7677>
- Jude T.P., Panchadcharam E. & Masilamani K. (2020). Computing Zagreb and Randić indices of PEG-cored dendrimers used for drug and gene delivery. *Journal of Chemistry* **2020**: 1–7.
DOI: <https://doi.org/10.1155/2020/2821510>
- Keshavjee S. & Farmer P.E. (2012). Tuberculosis, drug resistance, and the history of modern medicine. *The New England Journal of Medicine* **367**: 931–936.
DOI: <https://doi.org/10.1056/NEJMra1205429>
- Ma Z., Lienhardt C., McIlleron H., Nunn A.J. & Wang X. (2010). Global tuberculosis drug development pipeline: the need and the reality. *Lancet* **375**: 2100–2009.
DOI: [https://doi.org/10.1016/S0140-6736\(10\)60359-9](https://doi.org/10.1016/S0140-6736(10)60359-9)
- Mobeen M., Nazeer W., Rafique S. & Kang S. (2016). M-polynomial and related topological indices of nanostar dendrimers. *Symmetry* **8**: 97–108.
DOI: <https://doi.org/10.3390/sym8090097>
- Nilanjan De. (2018). Computing reformulated first Zagreb index of some chemical graphs as an application of generalized hierarchical product of graphs. *Open Journal of Mathematical Sciences* **2**: 338–350.
DOI: <https://doi.org/10.30538/oms2018.0039>
- Randić M. (1974). On Characterization of molecular branching. *Journal of the American Chemical Society* **97**: 6609–6615.
DOI: <https://doi.org/10.1021/ja00856a001>
- Rouvray D.H. (1973). The search for useful topological indices in chemistry: Topological indices promise to have far-reaching applications in fields as diverse as bonding theory, cancer research, and drug design. *American Scientist* **61**: 729–735.
DOI: <https://www.jstor.org/stable/27844077>
- Vukicevic D. (2010). Bond additive modeling 2 mathematical properties of max-min Rodeg index. *Croatica Chemica Acta* **54**: 261–273.
- Wiener H. (1947). Structural determination of paraffin boiling points. *Journal of the American Chemical Society* **69**: 17–20.
DOI: <https://doi.org/10.1021/ja01193a005>
- World Health Organization. (2002). WHO Tuberculosis e Fact Sheet. Available at <https://www.who.int/news-room/fact-sheets/detail/tuberculosis>
- Zanni R., Galvez-Llompart M., García-Domenech R. & Galvez J. (2015). Latest advances in molecular topology applications for drug discovery. *Expert Opinion on Drug Discovery* **10**: 945–957.
DOI: <https://doi.org/10.1517/17460441.2015.1062751>
- Zheng L., Wang Y. & Gao W. (2019). topological indices of hyaluronic acid-paclitaxel conjugates' molecular structure in cancer treatment. *Open Chemistry* **17**: 81–87.
DOI: <https://doi.org/10.1515/chem-2019-0009>
- Zuo M.X., Liu J-B, Iqbal H., Ali K. & Rizvi S.T.R. (2020). Topological indices of certain transformed chemical structures. *Journal of Chemistry* **2020**: 3045646.
DOI: <https://doi.org/10.1155/2020/3045646>

RESEARCH ARTICLE

Corrosion

Developing a model to predict the propagation of sulphide stress corrosion of steel used for petroleum pipelines

A Manimendra^{1*}, I De Silva¹ and R Jayasundara²

¹ Department of Materials Science and Engineering, Faculty of Engineering, University of Moratuwa, Sri Lanka.

² Department of Mathematics, Faculty of Engineering, University of Moratuwa, Sri Lanka.

Submitted: 17 June 2021; Revised: 05 August 2022; Accepted: 26 August 2022

Abstract: Sulphide stress corrosion (SSC) is an abundant type of corrosion in petroleum refineries. Steel pipes in petroleum refineries are influenced by the synergistic effect of tensile stress/pressure and high H₂S concentrations in different environments. This paper focuses on the prediction of the propagation of depth of SSC in API 5L Grade B steel as a function of pH value, applied load, and time duration. The model has been established based on the experimental values of the depth of SSC under different predetermined test environmental conditions kept within the pH value of 2.7–3.5, an applied load of 400–800 N, and a time duration of 15–45 days. Further, the model was validated by another data set obtained for the depth of corrosion within the same aforementioned ranges of parameters. All the laboratory experiments were conducted in accordance with ANSI/NACE TM0177-2016 standard test methods. In addition, this paper discusses the microstructural observations of specimens kept under the aforementioned test environmental conditions. The scanning electron microscope (SEM) images of cross-sections of corroded specimens showed that crack initiation occurred after 15 days under all different test environmental conditions. Further, crack propagation occurred transversely, developing branches through the cross section until 30 days of time duration and the behaviour of the propagation of the crack was completely changed at 45 days of time duration.

Keywords: API 5L grade B steel, depth of corrosion, mackinawite, sulphide stress corrosion, sulphur.

INTRODUCTION

Corrosion is one of the main phenomena considered in engineering design because most of the failures in power

plants, infrastructure constructions, and machinery occur due to the effect of corrosion (Foroulis, 1996; European Commission, 2013). Sulphide stress corrosion (SSC) predominantly occurs in petroleum power plants due to the synergistic effect of pressure/tensile force exerted on components and their corrosive environment containing H₂S. Petroleum pipelines can be identified as one of those components that are severely attacked by sulphide stress corrosion as they are exposed to extreme pressure conditions with high H₂S concentrations (Gosette, 2007; Pieris *et al.*, 2020).

Sulphide stress corrosion must be carefully controlled as it causes failures without a prior warning. Techniques such as non-destructive testing (NDT), SEM image analysis, optical techniques, and electrochemical techniques are applied to time-based inspection routines to track the sulphide stress corrosion. They indicate only the extent to which the corrosion has propagated. If the corrosion mechanism behaves in an unexpected way in between two inspections, there is a possibility of failure in pipelines, which would have an adverse impact on the industry. Therefore, the petroleum industry focuses on developing mathematical and statistical prediction models to get accurate predictions for the propagation of sulphide stress corrosion.

Even though prediction models have been developed over the past fifteen years to predict the propagation of SSC, some of them are not very accurate (Traidia, 2018). The rest of the models make accurate predictions under

* Corresponding author (akeshmanimendra@gmail.com);  <https://orcid.org/0000-0002-4684-6621>)



This article is published under the Creative Commons CC-BY-ND License (<http://creativecommons.org/licenses/by-nd/4.0/>). This license permits use, distribution and reproduction, commercial and non-commercial, provided that the original work is properly cited and is not changed in anyway.

certain conditions. It can be seen that the results predicted by the model developed by Asmara *et al.* (2013) deviated significantly from the experimental values when the time period was increased beyond 800 hours. Some of the models predict accurate results when they are predicting corrosion behaviour at low H₂S concentrations (Sun & Nestic, 2007), while some of the other models predict accurate results at high H₂S concentrations (Asmara *et al.*, 2013). SSC-based research has been conducted for the materials which are used to manufacture oil country tubular goods (OCTG). Some of the common materials that have been used for sulphide stress corrosion-based experiments are API 5L grade B steel, AISI 4137H steel, AISI 1018 carbon steel, 20# steel, X65 pipeline steel, FV520B steel etc. (Asahi *et al.*, 1994; Smith *et al.*, 2002; Sun & Nestic, 2007; Liao *et al.*, 2012; Zheng *et al.*, 2014). All these metals used in OCTG are mild steel types. The present study focuses on predicting the propagation of sulphide stress corrosion of API 5L grade B steel that is used for manufacturing the pipes used in the refinery system of the Ceylon Petroleum Corporation. Furthermore, there is a possibility of applying this developed model to a part of this refinery system to ensure the functionality and accuracy of the model in a real working environment.

MATERIALS AND METHODS

Materials

API 5L Grade B steel samples, procured from Ceylon Petroleum Corporation in the form of a seamless pipe of 1 m in length, 11 mm in thickness and 168 mm in diameter, were used for the experiments. The chemical composition (Table 1) of the sample was verified by spark emission spectroscopy (Model: Ametek-spectrocheck). The maximum allowed weight fractions are given as per the API 5L 45th edition of the specification for line pipes (American Petroleum Institute, 2003).

Table 1: Chemical composition of API 5L grade B steel

Element	Mass fraction (%)	Max allowed weight fraction (%)
Fe	98.600	Not specified
C	0.201	0.28
Si	0.292	Not specified
Mn	0.470	1.20
P	0.029	0.03
S	0.007	0.03
Cr	0.059	0.50
Ni	0.103	0.50
Al	0.043	Not specified

Experimental setup – Test conditions in the corrosive vessel

Fabrication of the test vessel and specimens

Fabrication of the test vessel and test specimens were carried out in accordance with the ANSI/NACE TM0177-2016 standard test method. The test vessel was made out of 5 mm thick acrylic sheets, and the chamber was sealed by applying silica glue (Figure 1). The test vessel was tested for leaks with N₂ gas at 1.5 atm. The total volume of the test vessel was 2856 cm³, while the volume of the test solution was 2000 cm³ (70.0 % of the volume of the test vessel). The test specimen was prepared using the CNC machining technique since the specimens can be machined without overheating and cold working. The final surface finish was achieved through mechanical polishing that was done using 0.25 μm grit papers. The dimensions of the test specimen are shown in Figure 2.

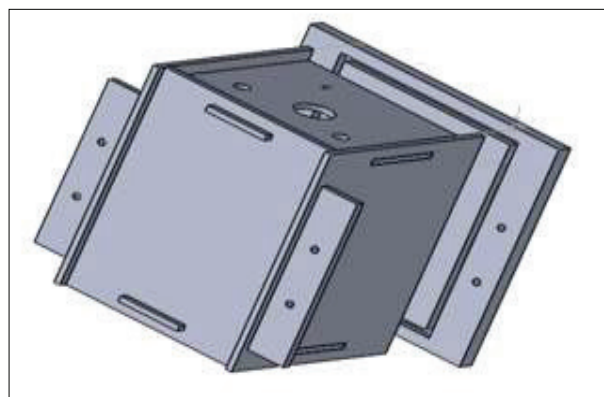


Figure 1: Designed model of the test vessel

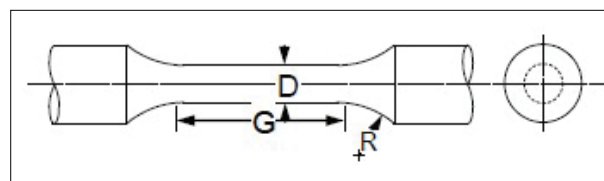


Figure 2: Dimensions of the test specimen
G = 55.00 mm, D = 6.72 mm, R = 1.00 mm

The sample holder was made out of mild steel, and it was fully coated with an epoxy coating to mitigate the influence of galvanic corrosion. The final experimental setup is shown in Figure 3.

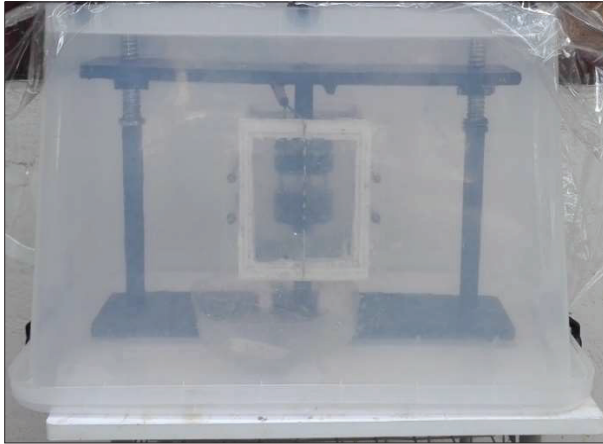


Figure 3: Experimental setup

Test conditions

The specimens were kept under 18 different test conditions/environments, which were predetermined by varying the applied load to the test specimen, the pH value of the H₂S solution, and time duration, as shown in Table 2. Three specimens were tested for each set of conditions. Temperature and pressure were maintained at 24 ± 3 °C and 1 atm, respectively.

Table 2: Test environmental conditions

No	Applied load (N)	pH value	Time duration (days)
1	400	2.7	15
2	600	2.7	15
3	800	2.7	15
4	400	3.5	15
5	600	3.5	15
6	800	3.5	15
7	400	2.7	30
8	600	2.7	30
9	800	2.7	30
10	400	3.5	30
11	600	3.5	30
12	800	3.5	30
13	400	2.7	45
14	600	2.7	45
15	800	2.7	45
16	400	3.5	45
17	600	3.5	45
18	800	3.5	45

The loads were applied to the specimen as a constant load in accordance with the Method A – standard tensile test mentioned in the ANSI/NACE TM0177-2016 standard test method (NACE International Standard, 2005). Test solutions A and B mentioned in the standard (NACE International Standard, 2005) were prepared to maintain the pH value at 2.7 and 3.5, respectively.

Determination of depth of corrosion by SEM observations

The specimens corroded under the 18 test conditions were prepared for SEM observations. Observations were performed by the SEM [Model: SEM- ZEISS EVO18-Research] under BSD mode with a 100 µA current. The magnification was determined based on the crack length. At the end of the specified time duration, each specimen was taken out of the test vessel and washed with DI water. Each test specimen was slashed transversely by using a low-speed precision cutting machine at three different places to obtain three different cross-sections (Figure 4).

Three different segments of each cross-section were observed by SEM, and the maximum depth of corrosion for each segment was identified. The depth of corrosion for a selected cross-section (d) was obtained by calculating the average value of three maximum depths of corrosion (Figure 4).

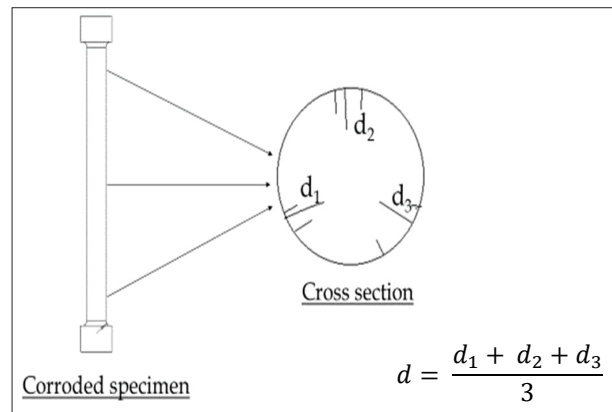


Figure 4: Three transverse cuts of a specimen and obtaining average depth of corrosion

Since there had been three cross-sections obtained for one specimen, the depth of sulphide stress corrosion of a selected specimen was obtained by calculating the average value of the depth of corrosion of each cross-section. Following that, the depth of sulphide stress

corrosion of the API 5L Grade B steel for a specific test condition was obtained by calculating the average of depth of corrosions of three specimens which were corroded under this specific test condition.

SEM/EDAX analysis of SSC cracks

The SCC cracks were further analysed using SEM/EDAX elemental line profiles. The distribution of sulphur within the crack surface was investigated using this technique.

Development of the statistical model

The statistical model was developed using experimental data to predict the depth of corrosion of the sulphide stress corrosion as a function of the time duration, pH value of the solution, and applied load. At the development stage of the model, a linear relationship, normality of responses, little or no multi-collinearity, no autocorrelation and homoscedasticity were assumed (Statics Solution, 2016). The depth of corrosion was considered the dependent variable of the model, while the time duration, pH value, and applied load were considered independent variables. Multiple linear regression analysis was selected over nonlinear regression analysis, as the model becomes simpler to use.

Validation of the model assumptions

- Multiple linear regression needs the relationship between the independent and dependent variables to be linear. Therefore, the outliers were also checked since multiple linear regression is sensitive to outlier effects. Scatter plots were prepared for the testing of linearity. As the dependent variable was not linearly related to some independent variables, a nonlinear transformation was carried out.
- As the multiple linear regression analysis requires residuals to be normal, this assumption was checked with a histogram and a *p-p* plot.
- Multi-collinearity was checked against four key criteria mentioned below.
 - Correlation matrix – when computing the matrix of Pearson's Bivariate Correlation among all independent variables, the correlation coefficients need to be smaller than 1.
 - Tolerance – the tolerance measures the influence of one independent variable on all the other independent variables. Tolerance is defined as $T = 1 - R^2$ for these first-step regression analyses. With $T < 0.1$, there might be multi-collinearity in the data, and with $T < 0.01$, there certainly is.

- Variance Inflation Factor (VIF) – the variance inflation factor of the linear regression is defined as $VIF = 1/T$. Similarly, with $VIF > 10$, there is an indication for multi-collinearity to be present.
 - Condition Index – the condition index was calculated using a factor analysis of the independent variables. Values of 10–30 indicate a mediocre multi-collinearity in the regression variables, and values > 30 indicate strong multi-collinearity
- Multiple linear regression analysis requires that there is little or no autocorrelation in the data. Autocorrelation occurs when the residuals are not independent of each other. The Durbin-Watson test was carried out to check the autocorrelation.
 - Another assumption of multiple linear regression analysis is homoscedasticity. The scatter plot was used to check homoscedasticity.

RESULTS AND DISCUSSION

Implementation of the model

The developed statistical model predicts the depth of sulphide stress corrosion in terms of time duration, pH value, and applied load, as expressed in the following formula.

$$DoC = -5.035e^{pH} - \frac{95455.143}{Applied\ Load} + 4.333 \times 10^{-6} \times Time^{4.45} + 400.140 \quad \dots(1)$$

Where,

DoC = the depth of sulphide stress corrosion in micrometres

Applied Load = the applied load on the test specimen in N

Time = the time duration in days that the specimen has been exposed to test environment

pH = average pH value of the test solution

The implemented empirical formula was subjected to a series of statistical tests to confirm if it satisfies the initial assumptions made.

Figure 5, Figure 6, and Table 3 stand for the normality test of the model. The histogram (Figure 5) shows a normal bell curve shape indicating that all standardized residuals are normally distributed in the model. The *p-p* plot (Figure 6) indicates that the expected cumulative probability vs observed cumulative probability plot lies along the normal line. The linear behaviour of the model

was further confirmed by Shapiro Wilk p values, which are shown in Table 3. It can be seen that the p values obtained for standardized residuals and unstandardized residuals are equal to each other. Further, based on the null hypothesis of H_0 – depth of corrosion is normally distributed in the population, and the alternative hypothesis of H_1 – depth of corrosion is not normally distributed in the population, at 5% significance level, since the asymptotic significance is greater than 5%, the null hypothesis is not rejected, and it can be concluded that the dependent variable is normally distributed in the population.

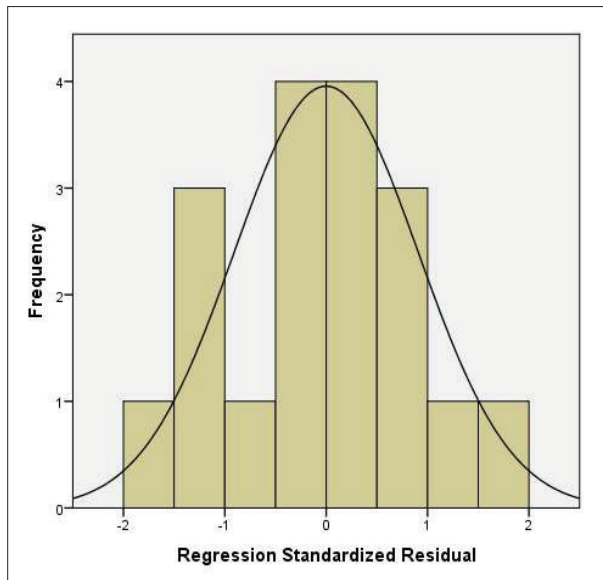


Figure 5: Histogram of frequency vs regression standardized residual

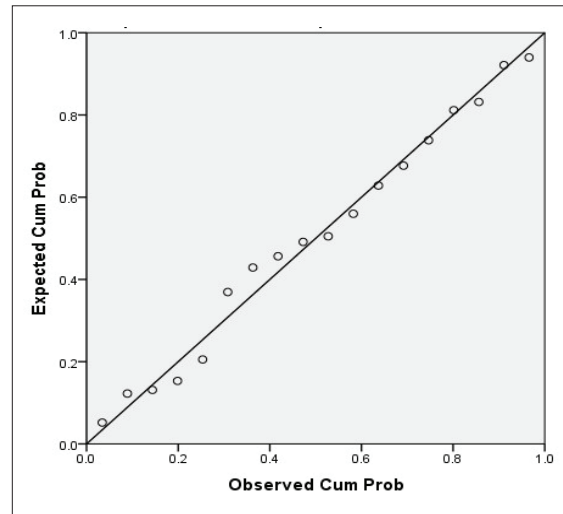


Figure 6: Normal P - P plot of regression standardized residuals

Table 3: Test of normality

	Shapiro-Wilk		
	Statistic	df	sig
Unstandardized residual	0.974	18	0.867
Standardized residual	0.974	18	0.867

Table 4: Pearson’s correlation matrix

Variable	Depth of sulphide stress corrosion	e^{pH}	Time ^{4.45}	1/Load
Depth of sulphide stress corrosion	1.000	-0.487	0.455	-0.526
e^{pH}	-0.487	1.000	0.000	0.000
Time ^{4.45}	0.455	0.000	1.000	0.000
1/Load	-0.526	0.000	0.000	1.000

Table 4 shows the Pearson’s bivariate correlation matrix for the dependent variables and independent variables. It can be seen that all correlation coefficients are less than 0.08 other than the coefficient between time 0.455 and the depth of sulphide stress corrosion (Table 4).

Therefore, it can be considered that the multi-collinearity in data is negligible. Variance inflation factor (VIF), tolerance, and condition index were tested for the multi-collinearity diagnostics, and tolerance values (Table 5) for all dimensions are 1 ($\gg 0.1$). It proves again that

the multi-collinearity in data is negligible. Furthermore, VIF values and condition index values that were obtained for model dimensions indicate that they are less than 10 (Table 5). Therefore, these values provide evidence that no multi-collinearity is found in the data.

Table 5: Collinearity diagnostic tables

Model dimensions	Tolerance	VIF	Condition index
Constant	1.000	1.000	1.000
e ^{pH}	1.000	1.000	2.661
1/Applied Load	1.000	1.000	5.690
Time ^{4.45}	1.000	1.000	10.353

The autocorrelation was tested by the Durbin-Watson test, and the statistic says the value is 1.343. This indicates that the residuals are not linearly autocorrelated. Hence autocorrelation in the data is negligible.

The homoscedasticity of data was tested using scatter plots of standardized residuals vs standardized predicted values (Figure 7) and standardized residuals vs unstandardized predicted values (Figure 8). Both the scatter plots are rectangular enough to conclude the homoscedasticity in the data.

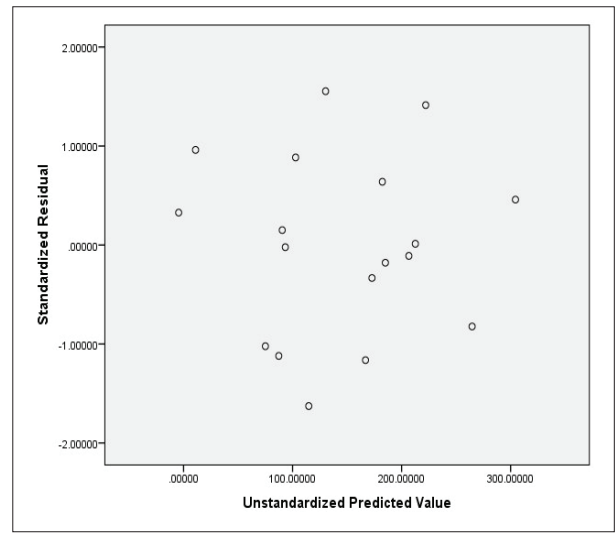
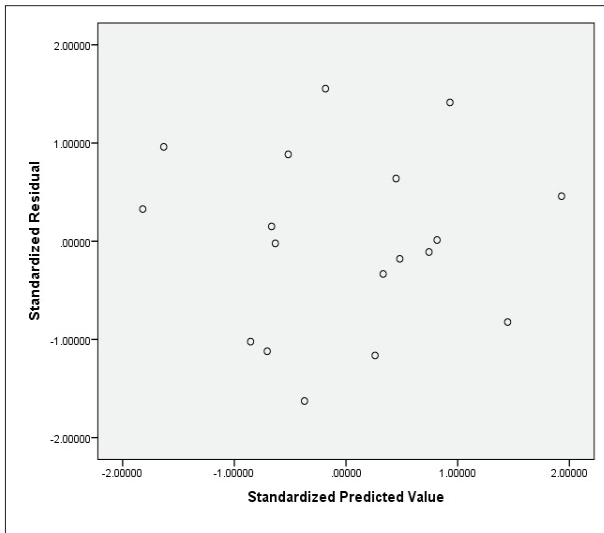


Figure 7: Scatter plot of standardized residuals vs standardized predicted values

Figure 8: Scatter plot of standardized residuals vs unstandardized predicted values

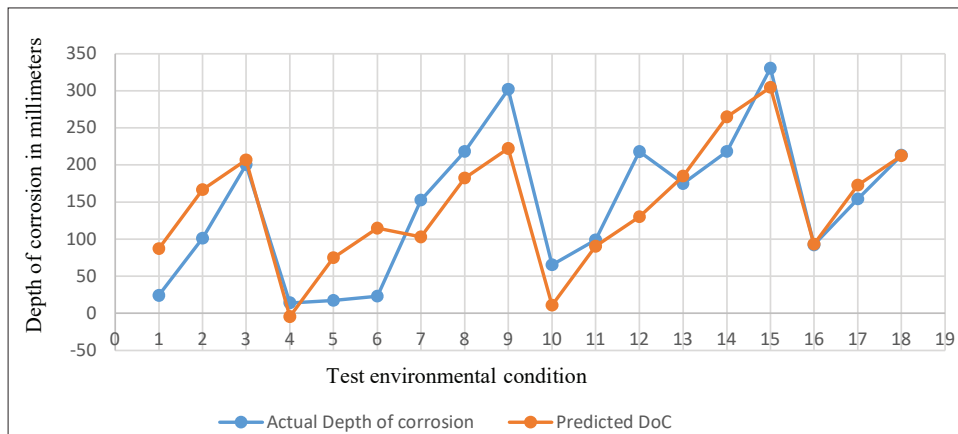


Figure 9: The comparison of model predicted values and experimental values of depth of sulphide stress corrosion at 27 °C and 1 atm under different test environmental conditions

Validation of the model based on the predetermined test environmental conditions

Model predictions were compared with the experimental values that were used to develop the model, as shown in Figure 9. The test environmental conditions given by Figure 9 correspond to the test environmental conditions defined in Table 2. The range of parameters considered are such that pH values vary between 2.7 and 3.5, applied loads vary between 400 N, 600 N, and 800 N, and time durations vary between 15 days, 30 days, and 45 days. All the depths of corrosions were between 24 μm and 214 μm.

It can be seen in Figure 9 that the depth of sulphide stress corrosion varies with the test environmental conditions in a manner similar to the behaviour of a wave. The variation of experimental values of depth of corrosion under different test environments agrees well with the values predicted by the model. It can be seen that the model successfully captures the upward and downward trends of the depth of sulphide stress corrosion with time duration, applied load, and pH value. From test environmental conditions 1 to 3, there can be seen an increase in the depth of corrosion. But the test environmental condition 4 shows a sudden reduction of the depth of sulphide stress corrosion. Again, an increase in the depth of sulphide stress corrosion can be observed from test conditions 4 to 6. If one set of depths of corrosion values which are monotonically increased, is identified as one cluster, three clusters can be seen up to the test environmental condition 10. Every cluster includes three depths of corrosion values obtained under the applied loads of 400 N, 600 N, and 800N each. However, the pH values and the time durations were constant within a certain cluster.

This behaviour is no longer obeyed from the 10th test environmental condition onwards. According to the previous pattern, test environmental condition 13 should have a smaller depth of corrosion value compared to the value shown at test environmental condition 12. Instead, the depth of corrosion values is monotonically increased from test environmental conditions 10 to 15. However, a reduction in the depth of corrosion at the 13th environmental condition was observed in the experimental depths of corrosion. The test environmental conditions 10 to 15 differ from test environmental conditions 1 to 10 mainly by time duration. The usual cluster pattern behaviour starts to be disobeyed at the 13th environmental condition when the time duration is 45 days. The cluster pattern behaviour occurring from the 15th test environmental condition onwards cannot be

predicted properly, as experiments were continued only up to the 18th test environmental condition.

However, the errors occurred at (pH = 2.5, load = 400 N, Time = 15 days), (pH = 3.5, load = 400 N, Time = 15 days), (pH = 3.5, Load = 600 N, Time = 15 days) and (pH = 3.5, Load = 800 N, Time = 15 days) reflected an outlying nature. Accordingly, the average percentage error calculated disregarding the outlying points was -7.65%. Thus, the model was considered for predictions after model validation was done using five more experimental data values.

Validation of the model based on the random test environmental conditions

Model predictions were further compared with experimental results obtained under random test environmental conditions. The test environmental conditions were maintained within the two extremes of pH = 3.5, Applied load = 400 N, Time duration = 15 days and pH value = 2.7, Applied load = 800 N, Time duration = 45 days. Figure 10 shows the comparison between model prediction values and the experimental results obtained under random test environmental conditions. Table 6 shows the corresponding test environmental conditions, maintained at a temperature of 24 ± 4 °C and a pressure of 1 atm. It can be observed that the trend line of the predicted depth of corrosion values is in reasonable agreement with the trend line of the experimental depth of corrosion values. The average percentage error for the predicted depth of corrosion was -0.131% for the five test environmental conditions.

Table 6: Test environmental conditions given by numbers in Figure 14

No	pH	Applied load (N)	Time (days)
1	2.9	750	18
2	3.0	500	20
3	2.8	700	32
4	3.3	650	38
5	3.5	550	42

Limitation of the model

Although the model predicted values follow the upward and downward trends of experimental trend lines (Figure 9 and Figure 10), it can be seen that the model is predicting the lower depth of corrosion values under

some of the test environmental conditions, especially when the time duration approaches 30 days. Figure 9 shows that all the predicted depth of corrosion values from test environmental conditions 7 to 12 are less compared to the experimental depth of corrosion values. A similar trend is observed in Figure 10 as well.

The minimum depth of corrosion value, which was detected at the test environmental condition number 4 mentioned in Table 6, has a pH value of 3.5, applied

load of 400 N and time duration of 15 days. However, this test environmental condition gives a minus value for the predicted depth of sulphide stress corrosion. However, the model starts showing a positive value for the depth of corrosion when the applied load reaches 408 N or higher values when the pH value is 3.5 and the time duration is 15 days. Therefore, the model gives an acceptable positive depth of corrosion values if the test environmental conditions are maintained under the following parameter ranges shown in Table 7.

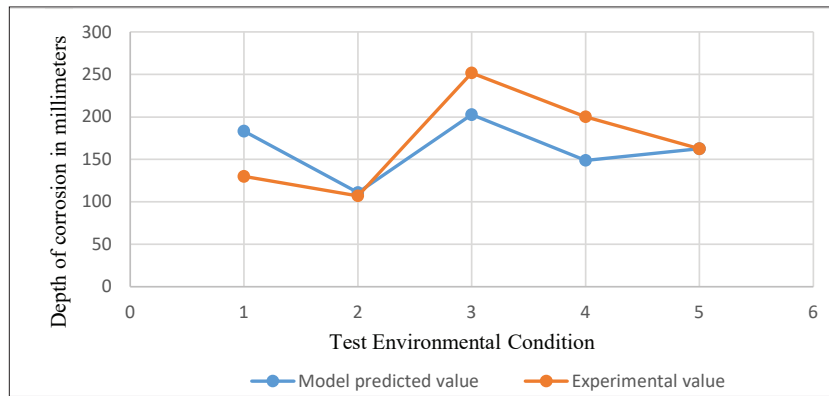


Figure 10: comparison between model prediction values and the experimental results

Table 7: Parameter ranges defined for the model at temperature 27 °C and pressure 1 atm

Parameter	Minimum value	Maximum value
Applied load	408 N	800 N
pH value	2.7	3.5
Time duration	15 days	45 days

of cracks under all the aforementioned 18 sets of conditions occurs after an incubation period of 15 days, irrespective of the pH value and applied load.

Interpretation of behaviour of SSC by SEM/EDAX analysis

Experimental results indicated that the time period is the controlling factor in the initiation of cracks. Figure 11 shows the SEM image of a cross-section of the steel sample, which does not show crack initiation on the 14th day under test conditions of pH value 3.5 and applied load 600 N. According to Figure 12, it is obvious that the crack was initiated after 15 days under the same conditions. Therefore, at the primary stage, based on the experimental results, it was concluded that the initiation

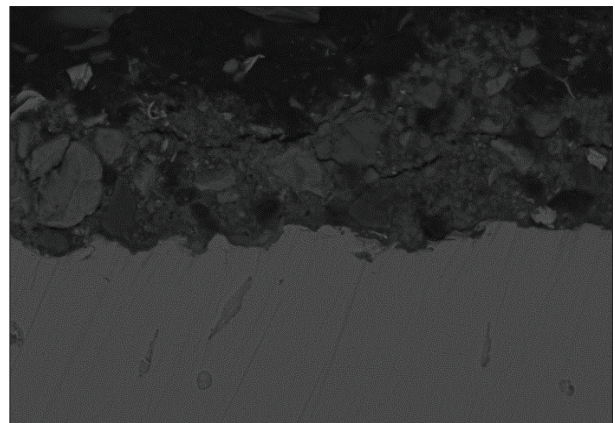


Figure 11: SEM image of the cross section of a specimen under the test conditions of pH value = 3.5, load = 600 N, time duration = 14 days

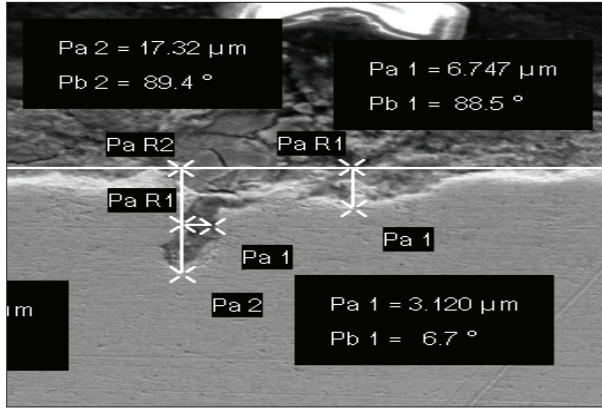


Figure 12: Sulphide stress crack initiation under the test conditions of pH value = 3.5, load = 600 N, time duration = 15 days

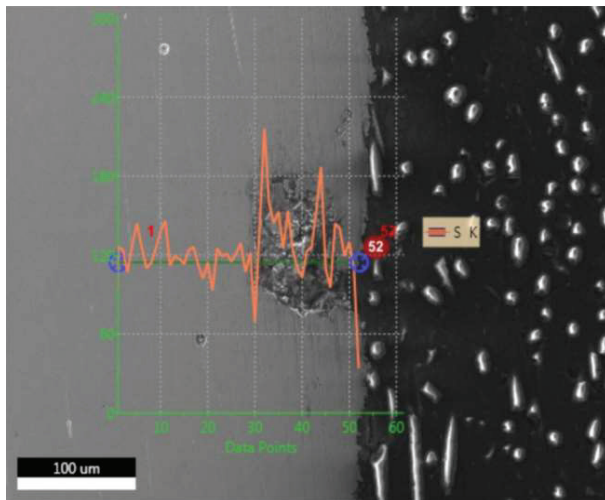


Figure 13: Elemental profile plot of the cross section of a specimen under the test conditions of pH value = 2.5, Load = 600 N, Time duration = 15 days

The initiation and propagation of sulphide stress cracks were investigated by SEM/EDAX analysis. The sulphur distribution along the crack was observed by SEM/EDAX elemental line profile, as shown in Fig 13, which clearly shows the higher content of sulphur associated with the crack relative to the other portions of the base metal. Therefore, these cracks can be identified as sulphide stress cracks.

The initiation of a sulphide stress crack occurs if there are surface discontinuities or surface pits (Ziaei *et al.*, 2013). The formation of pits is a result of ruptures in the surface of mackinawite layers where the mackinawite

is the predominant iron sulphide polymorph present in the corrosion product in the sour environment. Once the mackinawite layers reach a certain thickness, they rupture, leading to the formation of pits. These pits get filled with mackinawite with time (Smith, 2015). Later these pits grow into cracks (Smith, 2015). Once the initiation occurs, the crack starts to propagate transversely inwards to the core of the steel. The crack penetrates the steel, making branches similar to a growth of a taproot, as shown in Figure 14.

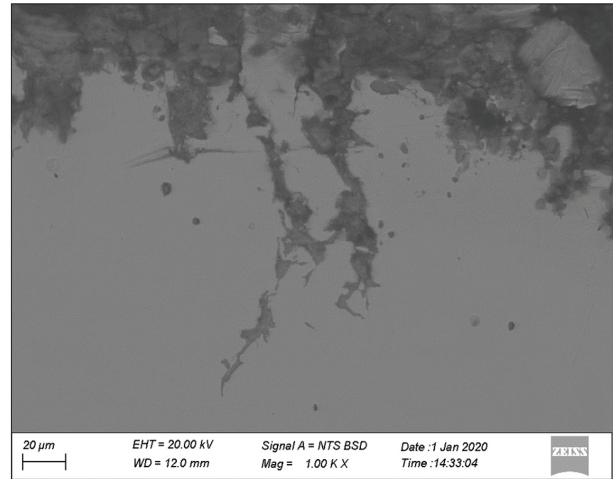


Figure 14: SEM image of the cross section of a specimen under the test conditions of pH value = 2.5, applied load = 400 N and time duration = 20 days

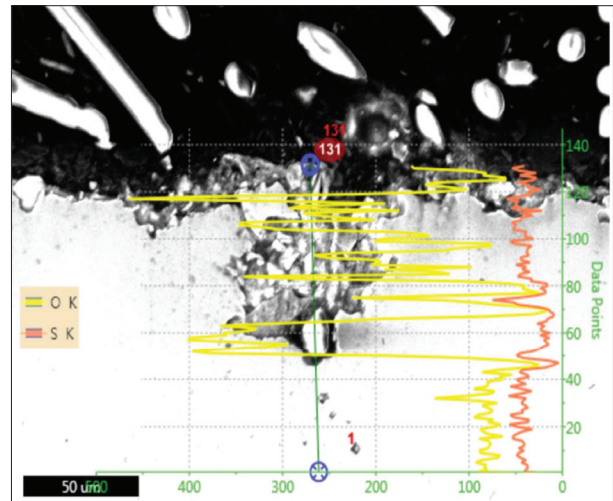


Figure 15: Elemental profile plot of the cross section of a specimen under the test conditions of pH value = 3.5, load = 600 N, time duration = 30 days

The SEM-EDAX elemental line profiles obtained for corroded samples in 30 days showed an interesting behaviour in the distribution of sulphur content throughout the crack. A sulphur-enriched area which was closer to the middle of the crack length, was observed (Figure 15). The formation of the sulphur-enriched area, specifically closer to the middle of the crack length relative to the crack initiation and tip areas, can be described based on the mechanism of the propagation of sulphide stress cracks.

In the sour environment, at high H_2S concentrations, mackinawite is the predominant component over iron carbonate in the corrosion layer. At low H_2S concentrations, both iron carbonate and mackinawite may be present in the corrosion product (Sun *et al.*, 2008). Under both conditions, mackinawite forms very rapidly on the surface as a very thin, tightly adherent film (Smith, 2015). Mackinawite is formed through the direct heterogeneous reaction between S^{2-} and Fe^{2+} (Smith *et al.*, 2002; Sun & Nesic, 2007; Cancio *et al.*, 2012; Asmara *et al.*, 2013). Once the mackinawite film is formed, it starts a reverse reaction to dissolve the formed mackinawite layers (Smith, 2015). If the formation rate of mackinawite is greater than the dissolution rate, the mackinawite layer begins to grow, covering the whole base metal. The continuous formation of the mackinawite layer causes multiple ruptures to form, and these ruptures act as pathways that allow the solution access to the mackinawite-based metal interface for continued corrosion via a tortuous path (Sun & Nesic., 2007; Cancio *et al.*, 2012).

Mackinawite is an electron conductor (Pearce *et al.*, 2006). The metal surface, which is underneath the mackinawite layer, dissolves, forming Fe^{2+} . The electrons removed from iron atoms are conducted through the mackinawite layer resulting cathodic reduction of hydrogen on the interlayer of mackinawite and the bulk solution. When the lattice parameters of the mackinawite crystal structure (Figure 16) are considered, the c dimension of the mackinawite crystal lattice is much larger than the a – b dimension (5.03 Å vs 3.67 Å). It forms an almost sheet-like structure. Because of this sheet-like structure, mackinawite can absorb divalent metallic cations into the lattice, as shown in Figure 17. Rather than substituting the cations for Fe^{2+} in the mackinawite structure, the adsorbed cations are moved between the “sheets” of iron sulphide (Zhao *et al.*, 2005). Therefore, Fe^{2+} ions, which are formed at the anodic sites on the metal surface, should be able to migrate away from the metal surface towards the film-electrolyte boundary by moving along this path.

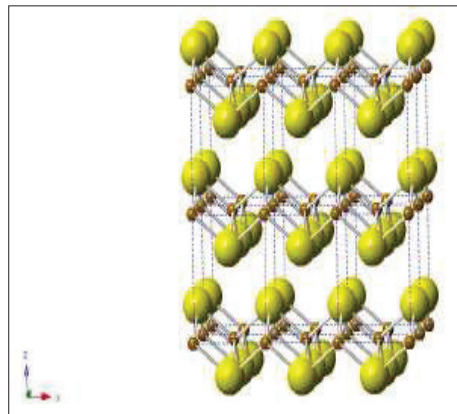


Figure 16: Mackinawite crystal structure

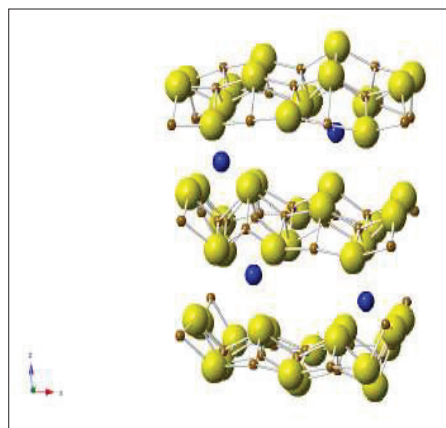


Figure 17: Mackinawite structure with additional cations (shown in blue color spheres) intercalated in the structure.

Fe^{2+} ions, which are formed on the metal surface, can find the film electrolyte along the ruptured pathways and within the interlayer of mackinawite - bulk solution. The Fe^{2+} ions which are diffusing out through the ruptured pathway can form FeS only along these ruptured pathways, and the Fe^{2+} ions which are moving along the planes of the mackinawite can form FeS once they meet a sudden ruptured pathway or once they meet the interlayer of bulk solution and the top surface of the mackinawite. When a cross-section of a crack is selected, much less mackinawite should be formed closer to the crack tip, and more mackinawite should be formed closer to the crack initiation point. Therefore, it can be expected that the ruptures along the crack length should be increased from crack initiation to crack tip. Similarly, the pathways

for the solution to enter the crack should be increased from crack initiation to crack tip. Therefore, when Fe^{2+} ions move upwards along the mackinawite sheets, there is a higher possibility of meeting more pathways of solution closer to the middle of the crack. Once they meet solution pathways, FeS is formed through direct heterogeneous reactions. Hence, the FeS -rich area can be seen closer to the middle of the crack (Figure 15).

CONCLUSION

The depth of sulphide stress corrosion of API 5L Grade B corresponding to the specific combination of pH value (2.7–3.5), applied load/pressure (400 N–800 N), and time duration (15 to 45 days) under ambient temperature and atmospheric pressure can be predicted using the developed model.

The results for the corrosion depths can be obtained through the model under the standard test conditions as per the ANSI/NACE TM0177-2016 standard test method.

Out of the aforementioned three major factors, it was found that the time duration is the leading factor that influences the crack initiation and propagation behaviour of sulphide stress corrosion.

Although the developed model successfully follows the experimental results, it underestimates the depth of sulphide stress corrosion when the time duration gets values closer to 30 days.

The propagation behaviour of sulphide stress corrosion can clearly be explained using SEM-EDAX elemental line profiles obtained for different directions of the propagated cracks. The observation of the formation of a sulphur-enriched area which was closer to the middle of the crack length, can be explained by relating the downward movement of the H_2S solution along the ruptured pathways formed in the cracks and the upward movement of Fe^{2+} ions along the mackinawite sheets. Hence it can be concluded that the mackinawite formed as a corrosion product plays a dominant role in the propagation of sulphide stress corrosion.

Acknowledgement

The authors would like to express sincere appreciation to the Ceylon Petroleum Corporation for providing API 5L Grade B steel samples to conduct experiments. They also wish to thank the Senate Research Council (SRC) grant of the University of Moratuwa for providing financial

assistance for the research project. The academic and non-academic staff of the Department of Materials Science and Engineering, University of Moratuwa are also acknowledged for their support in conducting laboratory experiments.

REFERENCES

- American Petroleum Institute (2003). *Specification for Line Pipe*. American Petroleum Institute Washington DC, USA.
- Asahi H., Ueno M. & Yonezawa T. (1994). Prediction of sulfide stress cracking in high-strength tubulars. *Corrosion* **50**(7): 537–545.
DOI: <https://doi.org/10.5006/1.3294355>
- Asmara Y.P., Juliawati A., Sulaiman A. & Jamiluddin (2013). Mechanistic model of stress corrosion cracking (SCC) of carbon steel in acidic solution with presence of H_2S . *International Conference on Mechanical Engineering Research (ICMER2013)*, Bukit Gambang Resort City, Kuantan, Pahang, Malaysia.
DOI: <https://doi.org/10.1088/1757-899X/50/1/012072>
- Cancio M.J., Latino M.L. & Perez T.E. (2012). Corrosion and hydrogen insertion in Uns G41300 steels in brine acid solutions saturated with hydrogen sulfide. *Corrosion 2012*. NACE-2012-1426, Salt Lake City, Utah.
- European Commission (2013). *Corrosion-Related Accidents in Petroleum Refineries*. Publications Office of the European Union, Luxembourg.
- Foroulis Z.A. (1996). The mechanism of refinery corrosion by sour water condensates. *Anti-Corrosion Methods and Materials* **29**(3): 4–14.
DOI: <https://doi.org/10.1108/eb007188>
- Gossett J. (2007). Detecting sulfide stress cracking and applying NACE MR0175. *Today's Refinery* **80921**: 1–14.
- Liao K., Yao Q., Wu X. & Jia W.A. (2012). Numerical corrosion rate prediction method for direct assessment of wet gas gathering pipelines internal corrosion. *Energies* **5**(10): 3892–3907.
DOI: <https://doi.org/10.3390/en5103892>
- NACE international standard (2005). *Standard Test Method Laboratory Testing of Metals For Resistance to Sulfide Stress Cracking and Stress Corrosion Cracking in H_2S Environments*. Houston, Texas, USA.
- Pearce C.I., Patrick R.A.D. & David J.V. (2006). Electrical and magnetic properties of sulfides. *Reviews in Mineralogy and Geochemistry* **61**: 127–180.
DOI: <https://doi.org/10.2138/rmg.2006.61.3>
- Peiris M.D.H.C., Perera W.L. & De Silva G.I.P. (2020). Study of the effect of sulphide stress corrosion on the load bearing capability of API 5L Grade B steel used in petroleum pipelines. *Engineer: Journal of the Institution of Engineers* **53**(2): 13–21.
DOI: <https://doi.org/10.4038/engineer.v53i2.7408>
- Smith S.N., Jorge L. & Pacheco (2002). Predicting corrosion in slightly sour environment. *Corrosion 2002*, Denver, Colorado, USA.
- Smith S.N. (2015). Current understanding of corrosion

- mechanisms due to H₂S in oil and gas production environments. *NACE - International Corrosion Conference Series*. Woodlands, Texas, USA.
- Statistics Solution (2016). Available at <http://www.statisticssolutions.com>. Accessed 2020.
- Sun W. & Nescic S. (2007). A mechanistic model of H₂S corrosion of mild steel. *Corrosion 2007 Conference and Expo*, Athens, Ohio, USA.
- Sun W., Nescic S. & Papavinasam S. (2008). Kinetics of corrosion layer formation, Part 2 – iron sulfide and mixed iron sulfide/carbonate layers *Corrosion* **7**(64): 586–599. DOI: <https://doi.org/10.5006/1.3278494>
- Traidia A., Chatzidouros E. & Jouiad M. (2018). Review of hydrogen-assisted cracking models for application to service lifetime prediction and challenges in the oil and gas industry. *De Gruyter* **36**(4): 323–347. DOI: <https://doi.org/10.1515/corrrev-2017-0079>
- Zhao J.M., Wei Z., Zuo Y. & Zhao X.H. (2005). Effects of some ions on ion-selectivity of ferrous sulfide film. *Journal of Applied Electrochemistry*. **35**: 267–271. DOI: <https://doi.org/10.1007/s10800-004-6704-8>
- Zheng Y., Ning J., Brown B. & Nescic S. (2014). Electrochemical model of mild steel corrosion in a mixed h₂s/co₂ aqueous environment. *Corrosion* **3901**: 1–20.
- Ziaei S.M.R., Kokabi A.H. & Nasr-Esfehani M. (2013). Sulfide stress corrosion cracking and hydrogen induced cracking of A216-WCC wellhead flow control valve body. *Case Studies in Engineering Failure Analysis* **1**(3): 223–234. DOI: <https://doi.org/10.1016/j.csefa.2013.08.001>

RESEARCH ARTICLE

Physical oceanography

Anomalous propagation pathway of the Sri Lanka Dome in summer 2014

G Pathirana^{1,2*}, G Chen², D Wang², MK Abeyratne³ and T Priyadarshana⁴

¹ Department of Oceanography and Marine Geology, Faculty of Fisheries and Marine Sciences & Technology, University of Ruhuna, Wellamadama, Matara, Sri Lanka.

² South China Sea Institute of Oceanology, Guangzhou, China.

³ Department of Mathematics, Faculty of Science, University of Ruhuna, Wellamadama, Matara, Sri Lanka.

⁴ Department of Limnology and Water Technology, Faculty of Fisheries and Marine Sciences & Technology, University of Ruhuna, Wellamadama, Matara, Sri Lanka.


Submitted: 28 July 2021; Revised: 17 July 2022; Accepted: 26 August 2022

Abstract: During the southwest monsoon, a cold dome referred to as the Sri Lanka Dome (SLD) appears east of Sri Lanka in response to the cyclonic curl in the local wind field. In general, SLD forms around May/June and decays during September. However, satellite altimetry data revealed an anomalous propagation pattern of the SLD with a lifetime of more than six months in the southwestern region of the Bay of Bengal (BoB) during 2014. This study is carried out to explain the plausible forcing factors which produced this anomalous event using satellite altimetry, surface currents, and wind data. Previous studies have shown that in general, the SLD propagates westward and then northward from its initial centre. In 2014, the SLD first appeared east of Sri Lanka around 6.5–7.5° N, 83–84° E and propagated eastward/northeastward from its initial centre (7.1018° N, 83.7111° E) with forcing from wind-stress and the Summer Monsoon Current (SMC). During early August it started to propagate westward until mid-October with the support of westward geostrophic flow and upwelling Rossby waves, noted between 10–12° N latitudes. Then the western boundary currents (WBC) in the BoB further facilitated the trajectory of the SLD and guided it towards the Arabian Sea (AS), where it disappeared in late December 2014, south of India (4.5474° N, 78.0223° E). Thus, we show that the stronger winds and SMC existed during 2014 in the BoB, guided the SLD eastward/northeastward compared to its general trajectory, and that allowed the SLD to undergo the forcing from westward geostrophic flow, upwelling Rossby waves and WBC.

Keywords: Rossby waves, Sri Lanka Dome, summer monsoon current, western boundary currents, wind-stress.

INTRODUCTION

The Bay of Bengal (BoB) is a unique oceanic basin due to seasonally reversing currents associated with the Asian Monsoon (Schott & McCreary, 2001; Jinadasa *et al.*, 2020) and forced remotely by seasonal winds in the equatorial Indian ocean (Han & Webster, 2002), propagating waves (Poterma *et al.*, 1991; Yu *et al.*, 1991) and freshwater discharges (Harenduprakash & Mitra, 1988; Thadathil *et al.*, 2002). The upper circulation in the BoB is characterized by a cyclonic flow during November and an anti-cyclonic gyre during most of the months (Somayajulu *et al.*, 2003). Previous studies have revealed the presence of the eastward flowing Southwest Monsoon Current (SMC) during summer (June – September) and westward flowing Northeast Monsoon Current (NMC) during winter (December – February) in the BoB (Schott *et al.*, 1994; Vinayachandran & Yamagata, 1998; Jensen, 2001). Vinayachandran *et al.* (1999) pointed out the intrusion of the SMC into the BoB with a mean seasonal transport during May – September. The East Indian Coastal Current (EICC), which flows along the western boundary of the BoB reverses its direction twice a year as a response to the local and remote alongshore winds (McCreary *et al.*, 1993; Shankar *et al.*, 1996). EICC flows poleward during February – September with a strong peak during March – April and starts to reverse its direction with the onset of

* Corresponding author (upgpathirana@fish.ruh.ac.lk;  <https://orcid.org/0000-0002-4670-579X>)



This article is published under the Creative Commons CC-BY-ND License (<http://creativecommons.org/licenses/by-nd/4.0/>). This license permits use, distribution and reproduction, commercial and non-commercial, provided that the original work is properly cited and is not changed in anyway.

post-summer monsoon (October) and flows equatorward until February with a strong peak in November (Shetye *et al.*, 1993; Eigenheer & Quadfasel, 2000).

Mesoscale eddies, which could transport heat, salt, and nutrient-rich waters are an important phenomenon in the world's oceans (Dong *et al.*, 2014). Energetic deep ocean eddies are capable of transporting water that wraps around it (Cherion & Brink, 2016). Previous studies were carried out on the existence of mesoscale eddies and their importance in the BoB based on observations (Cheng *et al.*, 2013; Patnaik *et al.*, 2014) and model simulations (Chen *et al.*, 2012). Cui *et al.* (2016) showed that the mesoscale eddies are prominent in the western region of the BoB, and Chen *et al.* (2012) concluded that baroclinic instability at the interface of two opposing boundary currents supports eddy generation in the western BoB. The presence of the SMC, strong positive wind stress curl, and the Ekman pumping associated with the curl are considered as the dominant processes that contribute to the formation of cyclonic eddies (CEs) to the east of Sri Lanka (the southwestern region of the BoB) (Dandapat & Chakraborty, 2016). Based on theoretical and observational analyses, Dong *et al.* (2014) suggested that CE and anticyclonic eddies (ACEs) propagate westward and move pole-ward and equatorward, owing to the β of the Earth's rotation (i.e. β represents the meridional gradient of the Coriolis parameter at a fixed latitude). In addition, Chen *et al.* (2012), showed that the eddy propagation south of 10° N in the BoB is westward at first and then northwestward with velocities of 2.0 – 11.0 cm/s.

The Sri Lanka Dome (SLD) is an upwelling dome that forms in a region of strong wind stress curl within

the SMC system (Vinayachandran & Yamagata, 1998; Cullen & Shroyer, 2019). In general, the SLD appears in May, matures in July, and decays around September (Burns *et al.*, 2017). The presence of the SMC, strong positive wind stress curl, and Ekman pumping associated with the curl are considered to be the dominant processes which contribute to the formation of the SLD east of Sri Lanka (Burns *et al.*, 2017). In general, the cyclonic and anti-cyclonic eddies formed in the southwestern region of the BoB propagate westward from the initial centre. However, in 2014, satellite altimetry data revealed an anomalous propagation pattern of the SLD, with a lifetime of more than six months in the southwestern region of the BoB, east of Sri Lanka. Therefore, this study is carried out to explain the plausible forcing factors which produced this anomalous event using satellite altimetry, surface currents, and wind data.

MATERIALS AND METHODS

The anomalous trajectory of the SLD during 2014 and the forcing mechanisms are examined utilizing gridded sea level anomaly (SLA) data from Physical Oceanography Active Archive Data Centre (PODAAC), wind-stress data from the Advanced Scatterometer (ASCAT), ocean surface currents data from Ocean Surface Current Analysis Real-time (OSCAR) and drifter observations. The drifter observation was conducted under the ASIRI program by National Aquatic Resources Research and Development Agency (NARA) of Sri Lanka collaboratively with Scripps Institution of Oceanography (SIO), USA (Wijesekera *et al.*, 2016). Details of the utilized datasets are given in Table 1.

Table 1: Summary of the datasets used in the study

Parameter	Source	Resolution	Time period
SLA (m)	https://podaac.jpl.nasa.gov/	$1/6^\circ \times 1/6^\circ$ (5-day)	1993 – 2018
ASCAT wind-stress (pa)	http://apdrc.soest.hawaii.edu/	$0.25^\circ \times 0.25^\circ$ (monthly)	2008 – 2017
OSCAR currents (m/s)	http://apdrc.soest.hawaii.edu/	$1/3^\circ \times 1/3^\circ$ (5-day)	2005 – 2015

Further, we estimate the geostrophic currents based on the equations given in Yu *et al.* (2014).

$$u = -\frac{g}{f} \frac{\partial h}{\partial y} \quad \dots(1)$$

$$v = \frac{g}{f} \frac{\partial h}{\partial x} \quad \dots(2)$$

In which, u and v are the zonal and meridional components of the geostrophic velocities, g is the

gravitational constant, f is the Coriolis parameter ($f = 2\Omega\sin\varphi$, where φ is the latitude) and h is the sea surface height.

Eddy detection and tracking procedure

Aside from the observed trajectory of the SLD through SSHA, we have estimated the trajectory of the SLD using the winding-angle method (Chen *et al.*, 2012). Considering the SLD as a cyclonic eddy with a cold-water upwelling region, the winding-angle method is used as the eddy identification procedure in this study (Sadarjoen & Post, 2000; Chaigneau *et al.*, 2008; Chen *et al.*, 2012). OSCAR currents and SSHA data are interpolated to a resolution of $1/4^\circ \times 1/4^\circ$ to facilitate the analysis. Then an algorithm specifically developed for the BoB region by Chen *et al.* (2012) is used to track eddies in the region.

Initially, possible anti-cyclonic eddy (cyclonic eddy) centres were identified through searching for local SSHA maxima (minima) in a moving window of $4^\circ \times 4^\circ$ grid points (Chen *et al.*, 2012; Dong *et al.*, 2014). Then streamlines were computed for each possible eddy centre, following the trajectories of virtual particles release in the geostrophic current field. The closed streamlines are then selected by computing the winding angle, and clustered into different eddies. The detailed description of the eddy tracking procedure is explained by Chen *et al.* (2012). Then using the detected eddy information, eddy centre location, time, eddy polarity, eddy size, and

eddy movement velocity are calculated. The eddy kinetic energy (EKE) was computed following Chen *et al.* (2012) (equation 3).

$$EKE = \frac{1}{2} (u'^2 + v'^2) \quad \dots(3)$$

RESULTS AND DISCUSSION

SLD climatology

The monthly climatology of sea level anomalies (SLA) is presented in Figure 1. In agreement with previous studies (Vinayachandran & Yamagata, 1998), a negative SLA appears east of Sri Lanka in June, which has been referred as the SLD. The mechanism of formation and propagation of the SLD has been verified by Burns *et al.* (2017), and their study confirms the importance of strong cyclonic curl in wind stress which starts in May and continues up to October, facilitating the SLD. The SLD decays during September in response to the downwelling Rossby waves that reach the SLD region (Vinayachandran & Yamagata, 1998). The westward propagating Rossby waves push the thermocline down and prevents cold water upwelling to the surface, and act as a negative feedback for sustaining SLD during September (Vinayachandran & Yamagata, 1998). Even though the mechanism for the formation and decay of the SLD is well-known (Burns *et al.*, 2017), the anomalous propagation pathway of the SLD identified in 2014 raised the importance of understanding the responsible forcing factors.

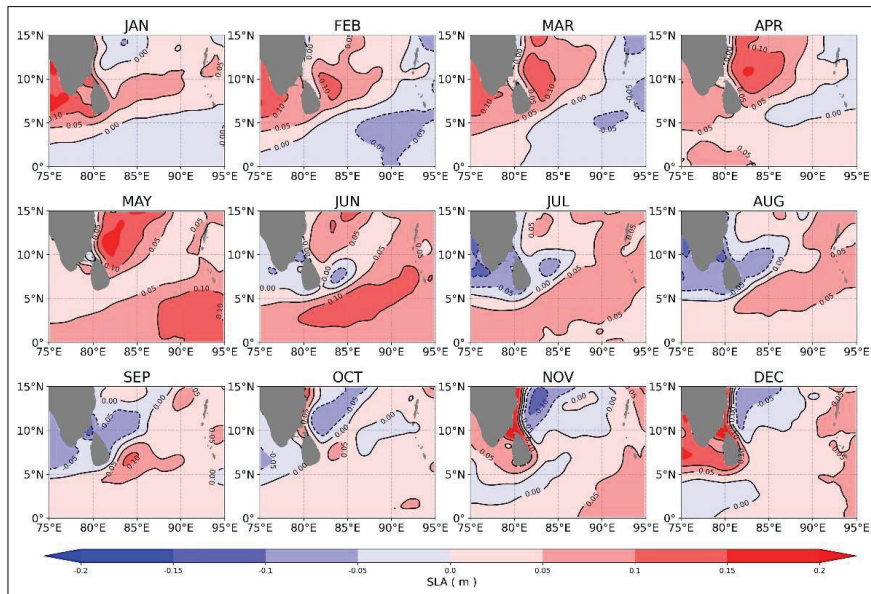


Figure 1: Monthly climatology of sea level anomalies in the southwestern Bay of Bengal

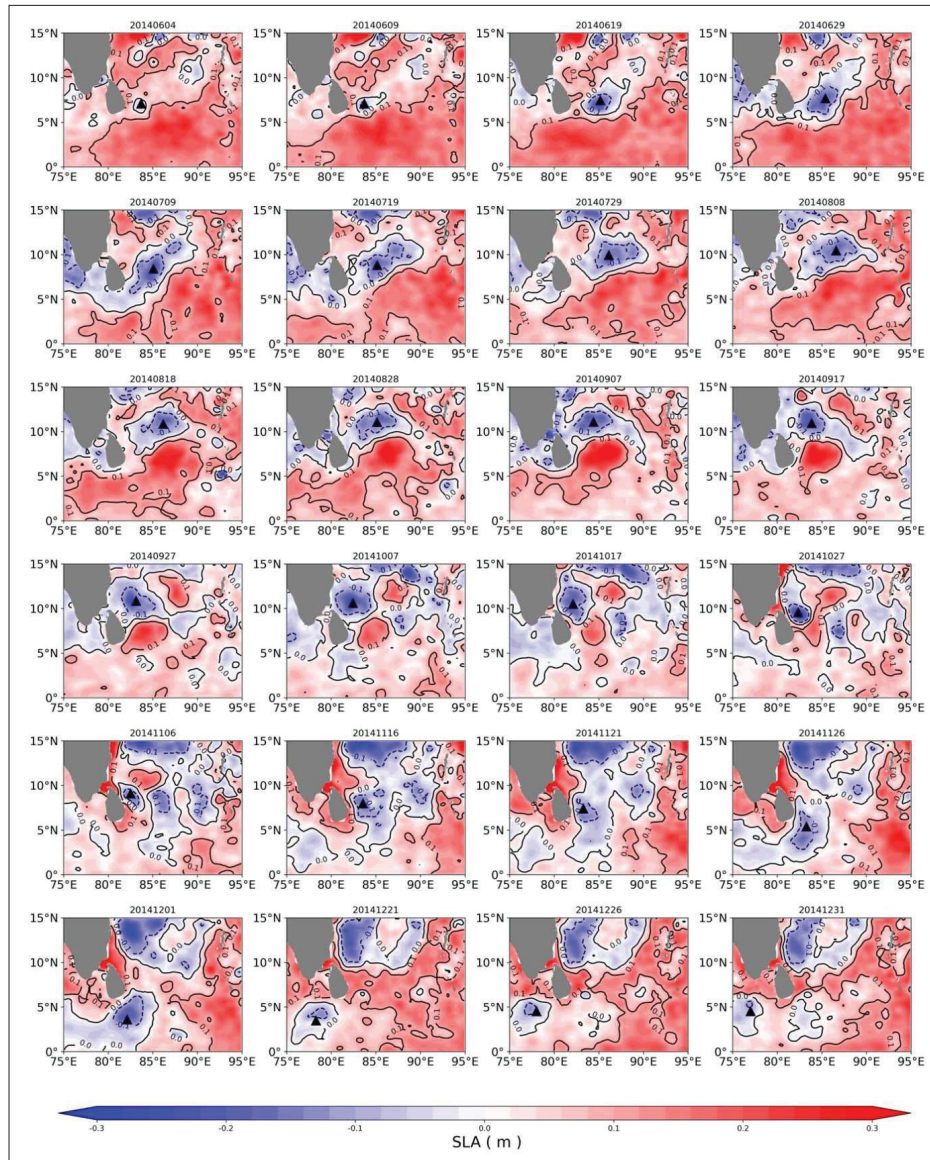


Figure 2: Snapshots of sea level anomalies from June 2014 to December 2014 in the southwestern Bay of Bengal. The centre of the anomalous Sri Lanka Dome (SLD) (tracked using winding-angle method) is marked with a black triangle in each time-step.

Trajectory of SLD during 2014

Time series (1995 - 2015) of SLAs have been examined to identify the propagation pathways of CEs and ACEs in the BoB region. The presence of a negative sea level anomaly east of Sri Lanka, referred to as the SLD, was observed during 2014 with an exceptional lifetime of nearly six months. This observed anomalous feature

during 2014 follows a different propagation trajectory compared to the general pattern described in earlier studies (Burns *et al.*, 2017). The snapshots of SLAs from June to December in 2014 is presented in Figure 2 to illustrate the propagation pathway of the SLD. Using the winding-angle method with SLA and OSCAR currents, the anomalous propagation of the SLD has been tracked and the results are presented in Figure 3.

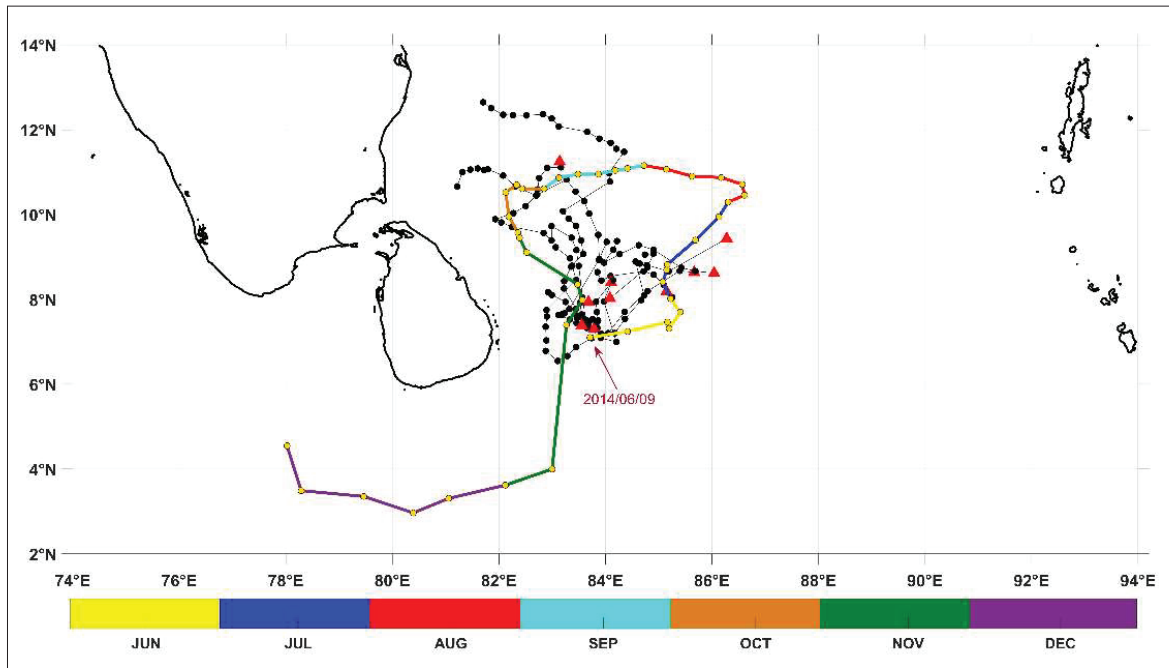


Figure 3: Anomalous propagation pathway of the Sri Lanka Dome (SLD) in 2014. Yellow circles illustrate the anomalous trajectory of the SLD observed in 2014, and the associated colour lines indicate the calendar months. The arrow denotes the initial centre of the anomalous SLD. Black circles indicate the general trajectories of the SLD in selected years. The red triangles denote the initial centre of the SLD in each year.

Based on the SLA observations, the SLD first appeared east of Sri Lanka around $6.5\text{--}7.5^\circ\text{N}$, $83\text{--}84^\circ\text{E}$ in early June and propagated eastward from its initial centre (7.1018°N , 83.7111°E) until the end of June. Then it turned north/northeastward and continued until the end of July. During early August it started to propagate westward until mid-October. From mid-October, it propagated equatorward along the eastern and southern coast of Sri Lanka and disappeared in the Arabian Sea in late December 2014, south of India (4.5474°N , 78.0223°E). Thus, the data revealed the existence of the SLD with a lifetime of more than six months during 2014, and its anomalous propagation pathway. As the eddies which form in the southwestern region of the BoB generally propagate westward, the observed anomalous feature highlighted the importance of influence from other forcing factors in the BoB on eddy formation and propagation. Therefore, to decipher the anomalous propagation of the SLD and the forcing mechanisms, monthly wind stress and curl, surface currents, geostrophic currents, Rossby wave forcing, and kinetic energy has been examined from June – December 2014 in the region.

Forcing mechanism

Wind-stress and SMC

With the onset of the summer monsoon (June), wind stress over the BoB is directed northeastward and it is sustained until the end of the summer monsoon (August). Relaxation of winds over the bay is identical during the post-summer monsoon (October – November). A strong positive wind stress curl is a prominent feature which appears east of Sri Lanka and points out the Ekman divergence in the region. The presence of positive wind stress curl associated with Ekman divergence supports the formation of cyclonic eddies in the region (Burns *et al.*, 2017). Relatively strong surface wind stress directed northeastward is observed during May-June in 2014, which weakens with the progress of the season (Figure 4). The SMC triggered by the seasonal winds starts to flow into the BoB from the Arabian Sea south of Sri Lanka with the onset of the summer monsoon (Figure 4). The SMC strengthens with the progression of the summer monsoon and weakens during the

post-summer period. Results revealed that the SMC was stronger during July 2014 and occupied a larger area in the southwestern BoB.

As the strong wind-stress curl and SMC are well-known initial forcing factors for the SLD (Cullen & Shroyer, 2019), we show the monthly anomalies of wind-stress (Figure 5a) and surface currents (Figure 5b) to explain the initial forcing that facilitated the SLD in

2014. The results indicate the presence of an eastward wind stress and surface currents in the southern BoB during June 2014, which has further strengthened towards the east/northeast during July 2014. Based on the quasi-geostrophic theory, Chen *et al.* (2012) reported that eddies on a β -plane should propagate westward. However, the anomalous trajectory of the SLD, observed in 2014, indicated an eastward/northeastward propagation. Therefore, here we suggest that the existence of weaker

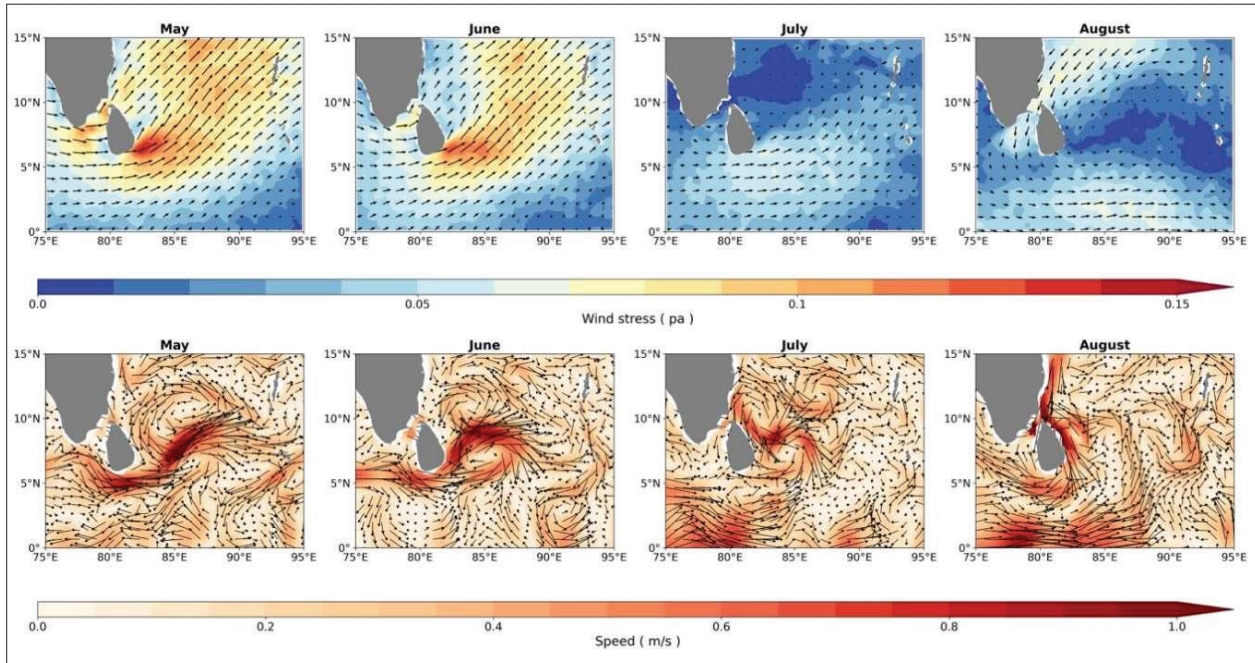


Figure 4: Monthly average wind-stress (upper panel) and surface currents (lower panel) in the Bay of Bengal during May – August 2014.

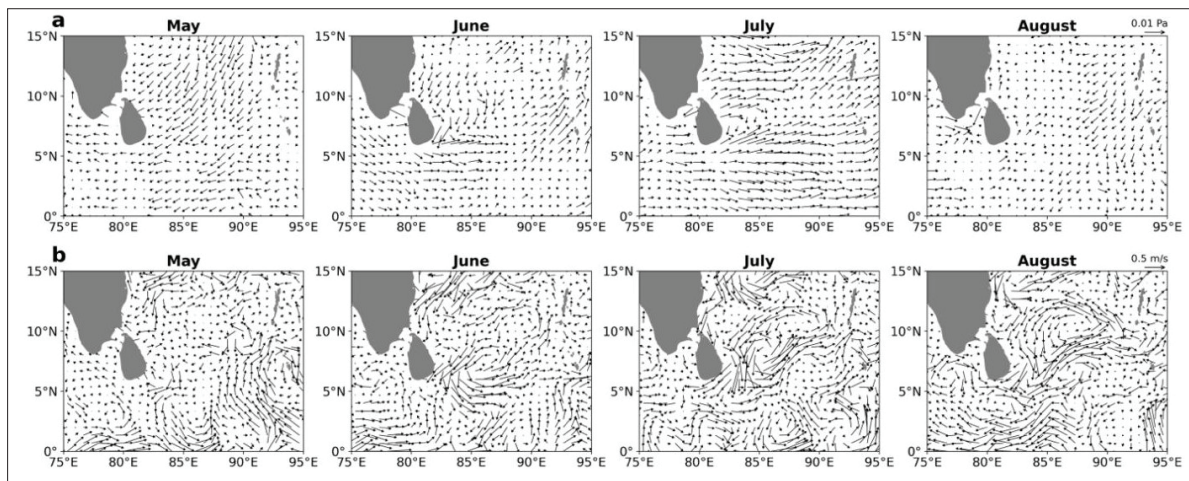


Figure 5: Anomalies of wind-stress (a), and surface currents (b) in the Bay of Bengal during May–August 2014.

upwelling Rossby waves in the 6–8° N latitudinal band (Figure 6a) and the presence of strong eastward winds and SMC during June–July 2014 may have facilitated the eastward/northeastward propagation of the SLD. The

eastward/northeastward propagation may have allowed the SLD to undergo the forcing of upwelling Rossby waves and the western boundary currents during August to December in 2014.

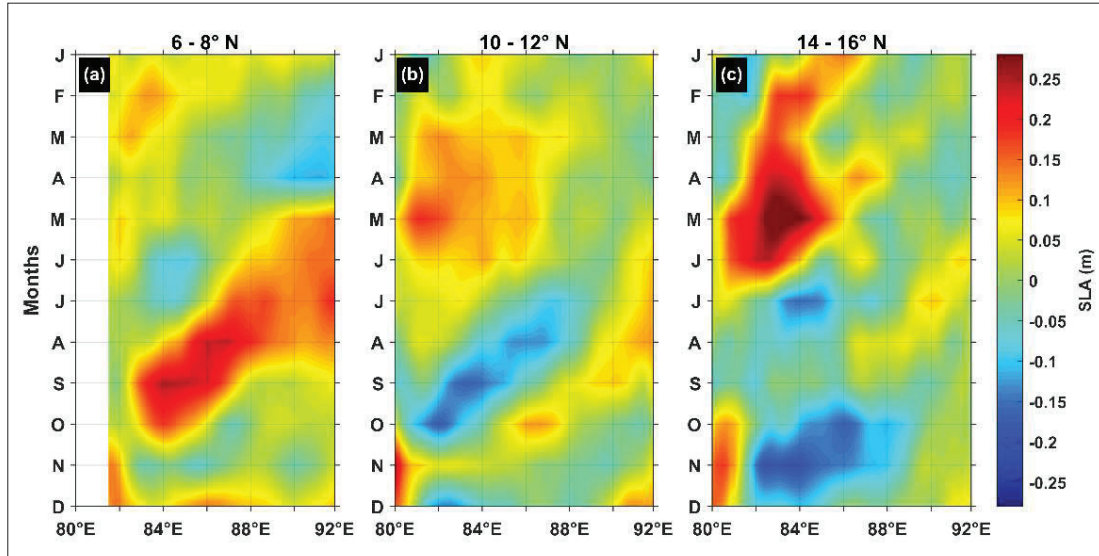


Figure 6: Hövmoller diagram (time versus longitude) of monthly average sea level anomalies (a) 6–8° N, 80–92° E; (b) 10–12° N, 80–92° E, and (c) 14–16° N, 80–92° E, during 2014.

Rosby waves

The Kelvin and Rossby waves are important dynamic features of the ocean, as they are capable of transferring wind energy in the basin due to their non-dispersive character (Kumar *et al.*, 2000; Rao *et al.*, 2013). Chelton *et al.* (2007) reported that in the oceans, westward propagating eddies and Rossby waves are intrinsically related to each other and sometimes it is difficult to differentiate these two phenomena. A Hövmoller diagram for the BoB at three different latitudinal bands (6–8° N, 10–12° N, 14–16° N) shows the westward propagation of positive and negative of SLAs during the study period implying the existence of westward propagating Rossby waves (Figure 6). The existence of downwelling Rossby waves is thought to inhibit the CEs, while upwelling Rossby waves facilitate the CEs in the ocean. However, the observed Rossby waves were weaker in the 6–8° N latitudinal band and hence had less influence on the propagation of the SLD in 2014 (Figure 6a). Further, a negative SLA signal was observed between 10–12° N latitudes during June–October 2014 which propagated westward in the BoB (Figure 6b). This is in agreement

with earlier findings (Kumar *et al.*, 2000), that reported the movement of low SLAs from the eastern boundary in March and ended up in the western boundary during October, along the 12° N latitude in the BoB. Therefore, the upper ocean variability of the BoB, to a larger extent is controlled by the westward propagating Rossby waves. Also, Chen *et al.* (2012) have pointed out that, in the central BoB (10° N–15° N) eddies tend to move quasiwestward with velocities of 2.0–11.0 cm/s. Thus, in agreement with the earlier findings, the SLD after crossing the 10° N latitude turned and propagated westward until mid-October with the forcing of upwelling Rossby waves. Further, it has been identified that the northeastward propagating SLD merged with another westward propagating CE around 10° N latitude in mid-July 2014, and the combination propagated westward until mid-October (Figure 2). Generally, the SLD does not undergo forcing from westward propagating waves during the late summer monsoon, as it decays at the western boundary of the BoB. However, the initial eastward propagation has allowed the SLD to undergo the forcing of upwelling Rossby waves in the region.

Western boundary currents (WBC)

With the onset of the post-summer monsoon, winds over the BoB weaken and reverse direction towards southwest. The seasonally reversing East Indian Coastal Current (EICC) starts to flow equatorward along the western boundary of the BoB as a response to the seasonally reversing winds during October. The seasonal changes in the western boundary currents of the BoB are evident in the SVP drifter observations (Jinadasa *et al.*, 2020) and they are presented in Figure 7. During mid-October,

the westward propagating SLD interacts with the equatorward flowing EICC at the northeast of Sri Lanka (Figure 2) and starts to flow equatorward (Figure 3). The SLD is located about 100 km away from the east coast of Sri Lanka during late October, it interacts with the WBC of the BoB, and it is evident in the surface current observations (Figure 7). In general, the SLD does not prevail till post-summer monsoon to undergo the forcing of the WBC. Thus, with the forcing of WBC the SLD propagated along the east coast of Sri Lanka towards AS during late October – December, in 2014.

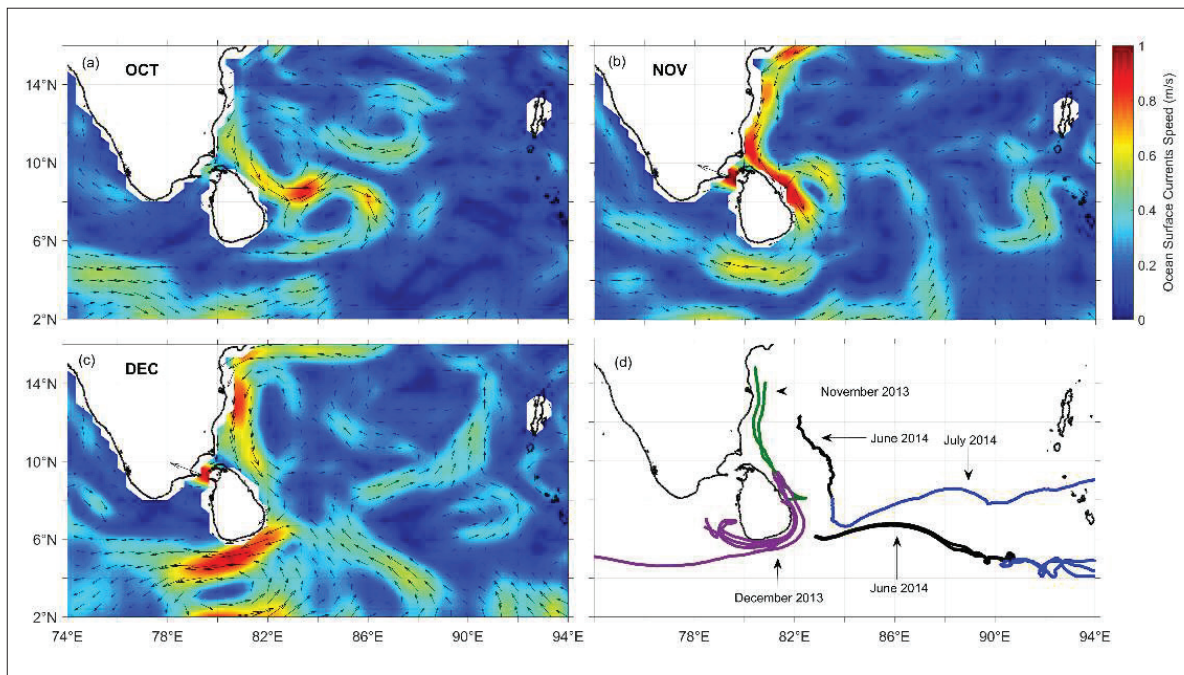


Figure 7: Surface currents in the southwestern Bay of Bengal, (a) October, (b) November, and (c) December 2014. And (d) surface currents estimated from SVP drifter trajectories in the southwestern region of the Bay of Bengal during 2013-2014.

Variability of eddy properties

The variability of eddy kinetic energy (EKE), eddy radius, and eddy velocity of the anomalous SLD have been examined and the results are presented in Figure 8. From mid-June to mid-October 2014 EKE remained in between 0 – 0.05 cm^2s^{-2} and peaked to a maximum of 0.25 cm^2s^{-2} in early November. From late-October to mid-December the EKE was comparatively high and varied between 0.05 and 0.25 cm^2s^{-2} . Further, the calculated eddy velocity along the trajectory clearly indicates that it was increasing during November – December and

peaked to a maximum of 8.76 cm/s in end of November 2014 (Figure 8). The identified peaks in EKE and eddy velocity during late-October to mid-December clearly emphasize the influence of the WBC on the anomalous SLD. Rao *et al.* (2013), pointed out that the kinetic energy is higher along the coastally trapped waves during December-January, and in January the energy is much higher (10,000 cm^2s^{-2}) in the western BoB. Using 17 years (Oct. 1992 to Oct. 2009) of altimetry data, Chen *et al.* (2012) have explained the mean eddy properties and their temporal and spatial variations in the BoB. Further, they pointed out that the total eddy energy

observed at the western boundary is higher than in the east, while the baroclinic and barotropic conversions are both active at the western boundary but the former is stronger. The growth of the perturbation through baroclinic instability is more important to the formation and existence of eddies in the west, hence strong EICC should be the key factor. This could be the reason that the detected SLD has a higher EKE and velocity after reaching the western boundary of the BoB. Further it highlights that the forcing from the boundary current on the SLD is higher compared to that of forcing from

westward propagating Rossby waves and seasonal winds. The eddy radius varies in between about 75 and 400 km and the maximum radius, ~ 375 km, is observed during mid-August. Merging with another eddy during this period and the weakening of external forcing may be one of the reasons for the noted increase in the radius (Figure 2). Theoretically when an eddy is more energetic, the radius remains small. It is evident in Figure 8, and it clearly indicates that, during November, the radius of the anomalous CE is reducing when the EKE reaches a maximum.

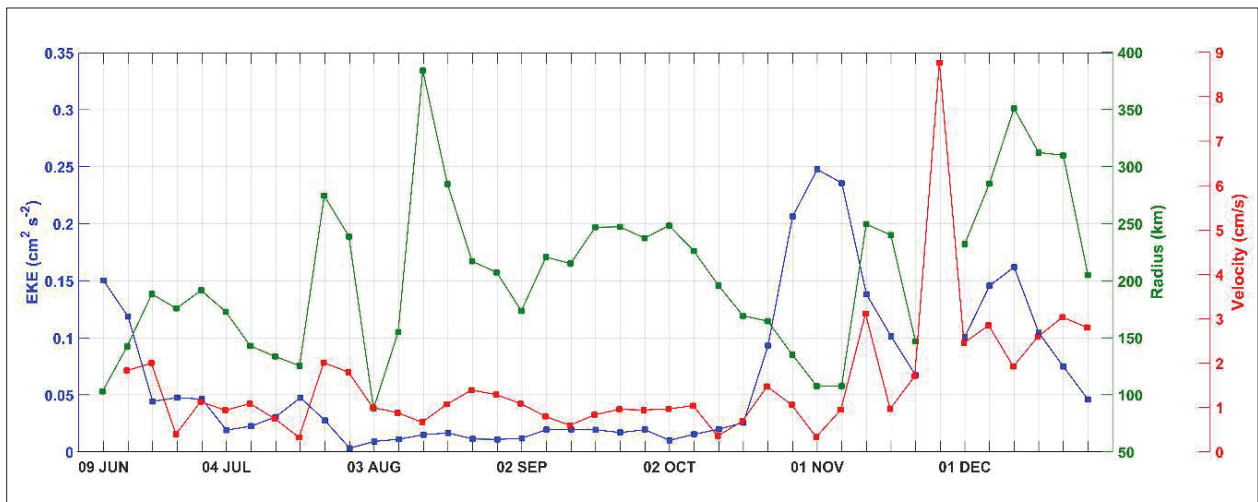


Figure 8: Variability of EKE, eddy radius and velocity along the trajectory of the Sri Lanka Dome (SLD) during 2014.

CONCLUSION

The SLD is a feature that appears off the east of Sri Lanka during May-September. The formation of the SLD seems to be linked with the strong cyclonic curl in wind stress and SMC, while the decay is linked with the westward propagating downwelling Rossby waves in the region. However, an anomalous propagation pathway of the SLD has been identified during 2014, and this study is carried out to understand the influencing factors behind this anomalous propagation. The trajectory, radius, EKE, and velocity of the SLD are identified using the winding-angle method with SLA and OSCAR currents. The SLD propagated eastward/northeastward from its initial centre with the forcing of strong wind and SMC which dominates over the westward propagating Rossby waves during June – July 2014. After crossing the 10° N latitude, the SLD tended to propagate westward until

mid-October, with the forcing of Rossby waves. Finally, the SLD was carried towards the AS along the east coast of Sri Lanka by the WBC that exists in the BoB. The detected SLD existed for a longer time in the ocean while propagating over longer distances compared to its behaviour in the previous years. The initial eastward shift facilitated by the SMC may have supported the observed anomalous trajectory of the SLD. As the processes involved in SLD are conceived to influence the formation and frequency of monsoon depressions in the northern BoB (Burns *et al.*, 2017), further studies are recommended to understand inter-annual variability of the dome dynamics.

Acknowledgements

This work is supported by the National Key R&D program of China (2017YFC1405103), the Major

State Research Development Program of China (2016YFC1402603), XDA 20060502, NSFC (grants 41822602 and 41521005), XDA (grant 11010102), Guangzhou Science and Technology Foundation (201804010133), State Key Laboratory of Tropical Oceanography SCSIO (LTOZZ1702), and the Youth Innovation Promotion Association of CAS (2017397). The encouragement and the facilities provided by the China-Sri Lanka Joint Centre for Education and Research (CSL-CER) are gratefully acknowledged.

Data availability

All the information related to the data sources used in this study can be accessed using the links provided in the text.

REFERENCES

- Burns J.M., Subrahmanyam B. & Murty V.S.N. (2017). On the dynamics of the Sri Lanka Dome in the Bay of Bengal. *Journal of Geophysical Research: Oceans* **122**: 7737–7750. DOI: <https://doi.org/10.1002/2017JC012986>
- Chaigneau A., Gizolme A. & Grados C. (2008). Mesoscale eddies off Peru in altimeter records: identification algorithms and eddy spatio-temporal patterns. *Progress in Oceanography* **79**(2–4): 106–119. DOI: <https://doi.org/10.1016/j.pocean.2008.10.013>
- Chelton D.B., Schlax M.G., Samelson R.M. & De Szoeke R.A. (2007). Global observations of large oceanic eddies. *Geophysical Research Letters* **34**. DOI: <https://doi.org/10.1029/2007GL030812>
- Chen G., Wang D. & Hou Y. (2012). The features and interannual variability mechanism of mesoscale eddies in the Bay of Bengal. *Continental Shelf Research* **47**: 178–185. DOI: <https://doi.org/10.1016/j.csr.2012.07.011>
- Cheng X., Xie S.-P., McCreary J.P., Qi Y. & Du Y. (2013). Intraseasonal variability of sea surface height in the Bay of Bengal. *Journal of Geophysical Research* **118**: 816–830. DOI: <https://doi.org/10.1002/jgrc.20075>
- Cherion D.A. & Brink K.H. (2016). Offshore transport of shelf water by deep-ocean eddies. *Journal of Physical Oceanography* **46**: 3599–3621. DOI: <https://doi.org/10.1175/JPO-D-16-0085.1>
- Cui W., Yang J. & Ma Y. (2016). A statistical analysis of mesoscale eddies in the Bay of Bengal from 22-year altimetry data. *Acta Oceanologica Sinica* **35**(11): 16–27. DOI: <https://doi.org/10.1007/s13131-016-0945-3>
- Cullen K.E. & Shroyer E.L. (2019). Seasonality and interannual variability of the Sri Lanka dome. *Deep Sea Research Part II* **168**: 104642. DOI: <https://doi.org/10.1016/j.dsr2.2019.104642>
- Dandapat S. & Chakraborty A. (2016). Mesoscale Eddies in the Western Bay of Bengal as observed from satellite altimetry in 1993–2014: statistical characteristics, variability and three-dimensional properties. *IEEE Journal of Selected Topics in Applied Earth Observations and Remote Sensing* **9**(11): 5044–5054. DOI: <https://doi.org/10.1109/JSTARS.2016.2585179>
- Dong C., McWilliams J.C., Liu Y. & Chen D. (2014). Global heat and salt transports by eddy movement. *Nature Communications* **5**. DOI: <https://doi.org/10.1038/ncomms4294>
- Eigenheer A. & Quadfasel D. (2000). Seasonal variability of the Bay of Bengal circulation inferred from TOPEX/Poseidon altimetry. *Journal of Geophysical Research* **105**(C2): 3243–3252. DOI: <https://doi.org/10.1029/1999JC900921>
- Han W. & Webster P.J. (2002). Forcing mechanisms of sea level interannual variability in the Bay of Bengal. *Journal of Physical Oceanography* **32**: 216–239. DOI: [https://doi.org/10.1175/1520-0485\(2002\)032<0216:FMOCLI>2.0.CO;2](https://doi.org/10.1175/1520-0485(2002)032<0216:FMOCLI>2.0.CO;2)
- Harenduprakash L.L. & Mitra A.K. (1988). Vertical turbulent mass flux below the sea surface and air-sea interaction: monsoon region of the Indian ocean. *Deep Sea Research* **143**(8): 423–1451. DOI: [https://doi.org/10.1016/0198-0149\(88\)90014-3](https://doi.org/10.1016/0198-0149(88)90014-3)
- Jensen T.G. (2001). Arabian Sea and Bay of Bengal exchange of salt and tracers in an ocean model. *Geophysical Research Letters* **28**(20): 3967–3970. DOI: <https://doi.org/10.1029/2001GL013422>
- Jinadasa S.U.P., Pathirana G., Ranasinghe P.N., Centurioni L. & Hormann V. (2020). Monsoonal impact on circulation pathways in the Indian Ocean. *Acta Oceanologica Sinica* **39**: 103–112. DOI: <https://doi.org/10.1007/s13131-020-1557-5>
- Kumar S.P., Unnikrishnan A.S. & Muraleedharan P.M. (2000). Signatures of Kelvin and Rossby wave propagation in the northern Indian Ocean from TOPEX/POSEIDON Altimeter. *PORSEC Proceeding*, volume 1, Goa, India, pp. 276–279.
- McCreary J.P., Kundu P.K. & Molinari R.L. (1993). A numerical investigation of dynamics, thermodynamics, and mixed layer processes in the Indian Ocean. *Progress in Oceanography* **31**(3): 181–224. DOI: [https://doi.org/10.1016/0079-6611\(93\)90002-U](https://doi.org/10.1016/0079-6611(93)90002-U)
- Patnaik K.V.K.R.K., Maneesha K., Sadhuram Y., Prasad K.V.S.R., Ramana Murty T.V. & Brahmananda Rao V. (2014). East India coastal current induced eddies and their interaction with tropical storms over Bay of Bengal. *Journal of Operational Oceanography* **7**(1): 58–68. DOI: <https://doi.org/10.1080/1755876X.2014.11020153>
- Poterma J.T., Luther M.E. & O'Brien J.J. (1991). The seasonal circulation of the upper ocean in the Bay of Bengal. *Journal of Geophysical Research* **96**(C7): 12667–12683. DOI: <https://doi.org/10.1029/91JC01045>
- Rao A.R., Rao G.N. & Kumar P.V.H. (2013). Propagating waves and their influence on eddy field variability in the northeastern Arabian Sea and northern Bay of Bengal. *International Journal of Remote Sensing* **35**(14): 5467–5478. DOI: <https://doi.org/10.1080/01431161.2014.926418>

- Sadarjoen A. & Post F. (2000). Detection, quantification, and tracking of vortices using streamline geometry. *Computers and Graphics* **24**(3): 333–341.
DOI: [https://doi.org/10.1016/S0097-8493\(00\)00029-7](https://doi.org/10.1016/S0097-8493(00)00029-7).
- Schott F.A. & McCreary J.P. (2001). The monsoon circulation of the Indian Ocean. *Progress in Oceanography* **51**: 1 – 123.
DOI: [https://doi.org/10.1016/S0079-6611\(01\)00083-0](https://doi.org/10.1016/S0079-6611(01)00083-0).
- Schott F., Reppin J., Fischer J. & Quadfasel D. (1994). Currents and transports of the monsoon current south of Sri Lanka. *Journal of Geophysical Research: Oceans* **99**(C12): 25127–25141.
DOI: <https://doi.org/10.1029/94JC02216>.
- Shankar D., McCreary J.P., Han W. & Shetye S.R. (1996). Dynamics of the east India coastal current: analytic solutions forced by interior Ekman pumping and local alongshore winds. *Journal of Geophysical Research* **101**(C6): 13975–13991.
DOI: <https://doi.org/10.1029/96JC00559>.
- Shetye S.R., Gouveia A.D., Shenoi S.S.C., Sundar D., Michael G.S. & Nampoothiri G. (1993). The western boundary current of the seasonal subtropical gyre in the Bay of Bengal. *Journal of Geophysical Research* **98**(C1): 945 – 954.
DOI: <https://doi.org/10.1029/92JC02070>.
- Somayajulu Y.K., Murty V.S.N. & Sarma Y.V.B. (2003). Seasonal and inter-annual variability of surface circulation in the Bay of Bengal from TOPEX/Poseidon altimetry. *Deep Sea Research II* **50**(5): 867–880.
DOI: [https://doi.org/10.1016/S0967-0645\(02\)00610-0](https://doi.org/10.1016/S0967-0645(02)00610-0).
- Thadathil P., Gopalakrishna V.V, Muraleedharan P.M., Reddy G.V, Araligidat N. & Shenoy S. (2002). Surface layer temperature inversion in the Bay of Bengal. *Deep Sea Research I* **49**: 1801–1818.
DOI: [https://doi.org/10.1016/S0967-0637\(02\)00044-4](https://doi.org/10.1016/S0967-0637(02)00044-4).
- Vinayachandran P.N., Masumoto Y., Mikawa T. & Yamagata T. (1999). Intrusion of the southwest monsoon current into the Bay of Bengal. *Journal of Geophysical Research: Oceans* **104**(C5): 11077–11085.
DOI: <https://doi.org/10.1029/1999JC900035>.
- Vinayachandran P.N. & Yamagata T. (1998). Monsoon response of the sea around Sri Lanka: Generation of thermal domes and anticyclonic vortices. *Journal of Physical Oceanography* **28**: 1946–1960.
DOI: [https://doi.org/10.1175/1520-0485\(1998\)028<1946:MRO TSA>2.0.CO;2](https://doi.org/10.1175/1520-0485(1998)028<1946:MRO TSA>2.0.CO;2).
- Wijesekera H.W. et al. (2016). ASIRI: An Ocean-Atmosphere Initiative for Bay of Bengal. *American Meteorological Society* **97**: 1859–1884.
DOI: <https://doi.org/10.1175/BAMS-D-14-00197.1>.
- Yu L., O'Brien J.J. & Yang J. (1991). On the remote forcing of the circulation in the Bay of Bengal. *Journal of Geophysical Research* **96**(C11): 20449–20454.
DOI: <https://doi.org/10.1029/91JC02424>.
- Yu Y., Wang L., Zheng Q. & Li Z. (2014). Geostrophic current estimation using altimetric cross-track method in northwest Pacific. *Earth and Environmental Science* **17**: 012105.
DOI: <https://doi.org/10.1088/1755-1315/17/1/012105>.

RESEARCH ARTICLE

Astrophysics

Simulation of coloured particles radiation spectra from black holes

CNT Wijewardhana* and KAILW Gamalath

Department of Physics, Faculty of Science, University of Colombo, Colombo 3, Sri Lanka.

Submitted: 19 July 2021; Revised: 22 July 2022; Accepted: 23 September 2022

Abstract: This work investigates the spectra of coloured particles radiated from Schwarzschild black holes and Kerr black holes as their mass decrease from $\sim 10^{13}$ g to Planck mass. The emission rate formulas in terms of black hole mass, temperature, entropy, and spin are derived. The variation of spectra with time, and black hole parameters such as mass, temperature, entropy, and spin are obtained and discussed. During the last stages of black hole evaporation, black hole loses its mass at a drastic rate. When the orders of magnitude of particles were disregarded, the spectrum of quarks and gluons emitted from the 10^{13} g black hole over 3171 millennia was emitted from the 10^8 g black hole within 2.5×10^{-4} s. It only took 3.5×10^{-25} s for a Schwarzschild black hole to reduce its mass from 10.00 g to 2.55×10^{-5} g. As the black hole reaches the end of its lifetime, the emission rates of the high energetic particles gradually recede and reach the limit of zero as Planck mass is reached. By the time the black hole begins to emit coloured particles its temperature is $\sim 10^{12}$ K, but when it reaches the Planck mass its temperature has reached closer to the Planck temperature. As Planck mass is reached, the entropy of the black hole gradually decreases and gets very close to zero.

Keywords: Black hole entropy, black hole mass, black hole spin, black hole temperature, coloured particles, Hawking radiation.


INTRODUCTION

Hawking's discovery of particle emission by black holes (BHs) led to many further investigations (Carr, 1976; Page, 1976a; 1976b; 1977; MacGibbon & Webber, 1990). One of the earliest works in astrophysics on the theory

of BH evaporation via particle emission was by Page and Hawking (1976), who examined the possibilities of detecting gamma rays produced by the evaporation of primordial black holes (PBHs). They predicted the gamma-ray spectra produced by PBHs and suggested that the best prospect for detecting a PBH would be to look for hard gamma rays that are expected in the final stages of the evaporation of the BH. Carr (1976) investigated how small PBHs could have contributed to the background density of gravitons, electrons, neutrinos, nucleons, and photons in the universe. He also predicted the spectrum of gravitons, electrons, and neutrinos which should result from PBH evaporations.

Page (1976a) calculated the emission rates for the known massless particles from a nonrotating, uncharged BH. He also estimated that a PBH would decay away within the present age of the universe if and only if its initial mass were less than $(5 \pm 1) \times 10^{14}$ g. In a subsequent paper (1976b), Page extended the calculations of the first paper to a rotating BH and the resultant evolution of the BH. He showed that angular momentum is given off a few times quicker than energy and thus, a swiftly spinning BH spins down to a nearly nonrotating state prior to giving up most of its mass.

A calculation done for the colour charge by Perry (1977) showed that a BH conserves colour and any fluctuation in the radiation process that generates a coloured BH will immediately be countered by the BH losing its colour in much the same way as a charged BH would lose its charge in the case of electromagnetism.

* Corresponding author (chamathka.wijewardhana@stonybrook.edu;  <https://orcid.org/0000-0002-4499-8568>)



This article is published under the Creative Commons CC-BY-ND License (<http://creativecommons.org/licenses/by-nd/4.0/>). This license permits use, distribution and reproduction, commercial and non-commercial, provided that the original work is properly cited and is not changed in anyway.

Thus, the BH will remain neutral concerning colour guaranteeing a colourless final state for the emission products.

The first calculation of BH emission considering the particle decays and emission of quarks and gluons from BHs was done by MacGibbon and Webber. They assumed that quarks and gluons would be emitted by the BH above the Quark Gluon Deconfinement (QGD) temperature ($\sim 150\text{--}200$ MeV) and the emitted quarks and gluons fragment into hadrons, which further decay into neutrinos, electrons, photons, etc., and found (1990) that owing to the tremendous rise in the degrees of freedom for quarks and gluons, and the huge number of final particles produced by the decay of each coloured particle, the quark and gluon emission dominates the evaporation of BHs beyond the QGD temperature ($\sim 150\text{--}200$ MeV). They also showed that the emitted quarks and gluons are similar to those produced in e^+e^- collider events and therefore must decay in the same way into final colourless hadronic states.

A group theoretical approach was used by Kofoed (2015) to study the emission of coloured particles from sufficiently hot BHs. He performed the calculations using the bird track notation, a pictorial representation of SU(N) tensor calculations and compared quantum chromodynamics (QCD) to quantum electrodynamics. During more recent times Ukwatta *et al.* (2016) have investigated the emission of coloured particles from BHs approaching the end of their lifetimes and calculated the energy dependent PBH burst light curves in the GeV/TeV energy range.

The objective of this work is to derive emission rate formulas in terms of BH parameters such as mass, temperature, entropy, and spin and investigate the variation of primary spectra of coloured particles from Schwarzschild black holes (SBHs) and Kerr black holes (KBHs) of masses between $\sim 10^{13}$ g and Planck mass ($\sim 10^5$ g) with time, mass, temperature, entropy, and spin. SBHs are non-rotating, uncharged BHs, and KBHs are rotating, uncharged BHs. More detailed definitions of SBHs and KBHs and their basic properties are presented in Methodology under Theoretical Formulation. We restrict the analysis to BHs of masses below $\sim 10^{13}$ g because these are the only BHs that emit coloured particles. Furthermore, the classical description used in our analysis breaks down when the BH mass approaches Planck mass. All formulas used are in Planck units where $\hbar = c = k_B = G = 1$ (\hbar = reduced Planck constant, c = speed of light in vacuum, k_B = Boltzmann constant, G = gravitational constant), unless stated otherwise.

The available C code BlackHawk (Arbey & Auffinger, 2019; 2021) at <https://blackhawk.hepforge.org> was used to calculate the emission rates. The study of emission of coloured particles is important because coloured particles are being emitted more dominantly than other types of particles from the BHs of the considered mass range. And BHs of the considered mass range are the ones which can produce any observable bursts of Hawking radiation.

MATERIALS AND METHODS

Theoretical formulation

Schwarzschild black holes

Schwarzschild black holes (SBHs) are spherically symmetric, nonrotating, uncharged BHs which are described by the Schwarzschild metric in Schwarzschild coordinates (t, r, θ, ϕ) ,

$$ds^2 = \left(1 - \frac{r_H}{r}\right) dt^2 - \left(1 - \frac{r_H}{r}\right)^{-1} dr^2 - r^2(d\theta^2 + \sin^2\theta d\phi^2) \quad \dots(1)$$

r_H is the Schwarzschild radius of the BH defined by,

$$r_H = 2M \quad \dots(2)$$

where M is the BH mass. Given that the spacetime is asymptotically flat, the boundary in spacetime between events that can communicate with distant observers and events that cannot, is called the event horizon. The area of the event horizon of a SBH is,

$$A = 4\pi r_H^2 \quad \dots(3)$$

Hawking's area theorem (Hawking, 1971) says that the area of a BH cannot decrease under any process. This is the second law of BH mechanics. This is evocative of the second law of thermodynamics which states that the entropy of a closed system cannot decrease under any process. Bekenstein proposed that a BH has an entropy which is a finite multiple of its area. Later the Bekenstein-Hawking formula for the entropy of a BH was given as,

$$S_{BH} = \frac{1}{4}A = \pi r_H^2 \quad \dots(4)$$

Hawking showed that the event horizon of any stationary BH must be a Killing horizon for some vector field. For every Killing horizon, there is an associated quantity called the surface gravity (Carroll, 2019). The

surface gravity of a SBH is,

$$\kappa = \frac{1}{4M} \quad \dots(5)$$

The zeroth law of BH mechanics states that the surface gravity of a stationary BH is constant over its event horizon and the third law of BH mechanics states that it cannot be reduced to zero by any finite sequence of operations (Bardeen *et al.*, 1973).

Hawking showed (1975) that the gravitational fields of SBHs create particles from their event horizons and emit them to infinity as if they were hot bodies with temperature T , given by,

$$T = \frac{\kappa}{2\pi} \quad \dots(6)$$

Using the definition of gravity given in equation (5) the temperature of the BH can be defined in terms of BH mass as,

$$T = \frac{1}{8\pi M} \quad \dots(7)$$

A BH with angular velocity Ω and electric potential Φ emits particles with total energy between Q and $Q+dQ$ at a rate (MacGibbon & Webber, 1990),

$$d\dot{N} = \frac{\Gamma_s dQ}{2\pi\hbar} \left[\exp\left(\frac{Q - n\hbar\Omega - q\Phi}{\hbar\kappa/2\pi c}\right) - (-1)^{2s} \right]^{-1} \quad \dots(8)$$

Where Γ_s are the graybody factors for the particle species which are dependent on energy of the emitted particles, Q , and the mass of the BH, M . They have to be calculated numerically. Rewriting the equation using Planck units where $\hbar = c = 1$,

$$\frac{d^2N}{dQdt} = \frac{\Gamma_s}{2\pi} \left[\exp\left(\frac{Q - n\Omega - q\Phi}{\kappa/2\pi}\right) - (-1)^{2s} \right]^{-1} \quad \dots(9)$$

For a SBH, $\Omega = \Phi = 0$. Hence, equation (9) reduces to,

$$\frac{d^2N}{dQdt} = \frac{\Gamma_s}{2\pi} \left[\exp\left(\frac{Q}{\kappa/2\pi}\right) - (-1)^{2s} \right]^{-1} \quad \dots(10)$$

Taking into consideration all the degrees of freedom of a particle species, the emission rate formula can be written as,

$$\frac{d^2N}{dQdt} = \frac{\Gamma_s}{2\pi} \left[\exp\left(\frac{Q}{\kappa/2\pi}\right) - (-1)^{2s} \right]^{-1} \cdot n_{dof} \quad \dots(11)$$

Here n_{dof} is the number of degrees of freedom of the particle species such as electric charge, colour, etc.

and s is particle spin. Equation (5) gives the relationship between the surface gravity, κ and the mass of the BH, M . Using equation (5) particle emission rates can be written in terms of the energy of the emitted particles, Q and the mass of the BH, M as,

$$\frac{d^2N}{dQdt} = \frac{\Gamma_s}{2\pi} \left[\exp(8\pi MQ) - (-1)^{2s} \right]^{-1} \cdot n_{dof} \quad \dots(12)$$

Equation (7) gives the relationship between the surface gravity, κ and the temperature of the BH, T . It can be used to modify the equation (12) to write the emission rate formulas in terms of the energy of the emitted particles, Q and the temperature of the BH, T as,

$$\frac{d^2N}{dQdt} = \frac{\Gamma_s}{2\pi} \left[\exp\left(\frac{Q}{T}\right) - (-1)^{2s} \right]^{-1} \cdot n_{dof} \quad \dots(13)$$

Equation (11) can also be modified to be written in terms of the energy of the emitted particles, Q and the entropy of the BH, S_{BH} by using equations (2), (4) and (5). It can be given as,

$$\frac{d^2N}{dQdt} = \frac{\Gamma_s}{2\pi} \left[\exp(4Q\sqrt{\pi S_{BH}}) - (-1)^{2s} \right]^{-1} \cdot n_{dof} \quad \dots(14)$$

The mass of the Hawking evaporating SBH as a function of time can be written in the form of a differential equation (Arbey & Auffinger, 2019),

$$\frac{dM}{dt} = -\frac{f(M)}{M^2} \quad \dots(15)$$

$f(M)$ is the Page factor which accounts for all directly radiated particle species by a BH of mass M and their quantum degrees of freedom. When the BH evaporates the value of M is decreased by a quantity equal to the total mass-energy of the radiated particles. By conservation of energy,

$$\frac{dM}{dt} = -\sum_i \int_0^{+\infty} \frac{d^2N_i}{dQdt} Q dt \quad \dots(16)$$

where the summation over i is over all the directly emitted species. Thus, the Page factor can be obtained as,

$$f(M) = -M^2 \frac{dM}{dt} = M^2 \int_0^{+\infty} \sum_i \frac{\Gamma_s(Q, M)}{2\pi} \left[\exp\left(\frac{Q}{\kappa/2\pi}\right) - (-1)^{2s} \right]^{-1} \cdot n_{dof} Q dQ \quad \dots(17)$$

For SBHs the mass decay gets faster with time, as the temperature gets higher as the mass decreases.

Kerr black holes

Kerr black holes (KBHs) are an expansion of SBHs. They are uncharged but rotating and thus, have a nonzero spin. They are described by the Kerr metric which can be given in Boyer-Lindquist coordinates as,

$$ds^2 = (dt - a \sin^2 \theta d\phi)^2 \frac{\Delta}{\Sigma} - \left(\frac{dr^2}{\Delta} + d\theta^2 \right) \Sigma - [(r^2 + a^2)d\phi - a dt]^2 \frac{\sin^2 \theta}{\Sigma} \quad \dots(18)$$

where the coordinates r, θ, ϕ are standard oblate spheroidal coordinates. Here Σ and Δ are defined as,

$$\begin{aligned} \Sigma(r) &= r^2 + a^2 \cos^2 \theta \\ \Delta(r) &= r^2 - 2Mr + a^2 \end{aligned} \quad \dots(19)$$

and a is the BH spin defined by,

$$a = \frac{J}{M} \quad \dots(20)$$

where J is the angular momentum of the BH. The reduced spin parameter can be defined as,

$$a^* = \frac{a}{M} \in [0, 1] \quad \dots(21)$$

When $a^* = 1$, the BH is maximally rotating. Kerr geometry has an inner and an outer horizon located at,

$$r_{\pm} = M \pm \sqrt{M^2 - a^2} \quad \dots(22)$$

where $a \rightarrow 0$, KBH simplifies to a SBH. The area of the event horizon of KBH located at r_+ can be given as (Page, 2005),

$$A = 4\pi(r_+^2 + a^2) \quad \dots(23)$$

The Bekenstein-Hawking entropy of the rotating BH is thus defined as (Ibunghochouba Singh *et al.*, 2014),

$$S_{BH} = \frac{1}{4}A = \pi(r_+^2 + a^2) \quad \dots(24)$$

The surface gravity of Kerr solution is defined as (Page, 2005),

$$\kappa = \frac{4\pi(r_+ - M)}{A} \quad \dots(25)$$

The temperature of a rotating KBH is given by (Arbey & Auffinger, 2019),

$$T = \frac{1}{2\pi} \left(\frac{r_+ - M}{r_+^2 + a^2} \right) \quad \dots(26)$$

The particle emission rates from a KBH can be derived from equation (9). For a KBH electric potential, $\Phi = 0$, and it has an angular velocity at the horizon defined by,

$$\Omega = \frac{a^*}{2r_+} \quad \dots(27)$$

Thus, for a KBH equation (9) reduces to,

$$\frac{d^2N}{dQdt} = \frac{\Gamma_s}{2\pi} \left[\exp\left(\frac{Q - m\Omega}{\kappa/2\pi}\right) - (-1)^{2s} \right]^{-1} \quad \dots(28)$$

In this case the graybody factors are dependent on the energy of the emitted particles, Q , the mass of the BH, M , and the reduced spin parameter, a^* . Taking into account all the degrees of freedom of a particle species, the emission rate formula is,

$$\frac{d^2N}{dQdt} = \frac{\Gamma_s}{2\pi} \left[\exp\left(\frac{Q - m\Omega}{\kappa/2\pi}\right) - (-1)^{2s} \right]^{-1} \cdot n_{dof} \quad \dots(29)$$

Similar to the derivation done for a SBH, the emission rate formula can be written in terms of the temperature of the KBH using equations (23), (25), and (26). It can be given as,

$$\frac{d^2N}{dQdt} = \frac{\Gamma_s}{2\pi} \left[\exp\left(\frac{Q - m\Omega}{T}\right) - (-1)^{2s} \right]^{-1} \cdot n_{dof} \quad \dots(30)$$

Similarly, emission rate formulas can be written in terms of the mass of the BH M , entropy S_{BH} , and reduced spin parameter a^* as,

$$\frac{d^2N}{dQdt} = \frac{\Gamma_s}{2\pi} \left[\exp\left(\frac{2S_{BH}(Q - m\Omega)}{M\sqrt{1 - a^*}}\right) - (-1)^{2s} \right]^{-1} \cdot n_{dof} \quad \dots(31)$$

In KBHs both mass M and angular momentum J evolve with time. A rotating BH is more likely to emit particles with high angular momentum, and with a projection m of that angular momentum aligned with the BH spin. Hence, the angular momentum of the BH will be gradually extracted. The Page factor for a KBH is,

$$f(M, a^*) = -M^2 \frac{dM}{dt} = M^2 \int_0^{+\infty} \sum_i \frac{\Gamma_s(Q, M, a^*)}{2\pi} \left[\exp\left(\frac{Q - m\Omega}{\kappa/2\pi}\right) - (-1)^{2s} \right]^{-1} \cdot n_{dof} Q dQ \quad \dots(32)$$

The differential equation describing the evolution of BH angular momentum is,

$$\begin{aligned}
 g(M, a^*) &= -\frac{M}{a^*} \frac{dJ}{dt} \\
 &= -\frac{M}{a^*} \int_0^{+\infty} \sum_i \sum_{dof} \frac{m\Gamma_s(Q, M, a^*)}{2\pi} \\
 &\quad \left[\exp\left(\frac{Q - m\Omega}{\kappa/2\pi}\right) - (-1)^{2s} \right]^{-1} \cdot n_{dof} dQ \quad \dots(33)
 \end{aligned}$$

After obtaining $f(M, a^*)$ and $g(M, a^*)$, the evolution of a^* can be obtained as,

$$\begin{aligned}
 \frac{da^*}{dt} &= \frac{d(J/M^2)}{dt} = \frac{1}{M^2} \frac{dJ}{dt} - 2 \frac{J}{M^3} \frac{dM}{dt} \\
 &= a^* \frac{2f(M, a^*) - g(M, a^*)}{M^3} \quad \dots(34)
 \end{aligned}$$

Simulation

First the emission rate formulas in terms of black hole mass, temperature, entropy, and spin were derived for both Schwarzschild and Kerr BHs. Then the public C code BlackHawk (Arbey & Auffinger, 2019; 2021) was used to calculate the particle emission rates. Then separate Python scripts were written to simulate the variation of the emission rates of different particle species

with time and different BH parameters. BHs radiate coloured particles once their temperatures exceed QGD temperature (~200 MeV). In this paper, all BHs radiating coloured particles are categorized into three categories based on their mass and temperature. (i) BHs beginning to emit coloured particles, (ii) Intermediate BHs emitting coloured particles, and (iii) BHs reaching the end of their lifetime.

For BHs beginning to emit coloured particles, BHs of mass ~10¹³ g were simulated. For intermediate BHs emitting coloured particles, BHs of mass ~10⁸-10¹¹ g were simulated. For a BH reaching the end of its lifetime, a BH of mass 10 g decaying away down to Planck’s mass ~2.18 × 10⁻⁵ g was simulated. When simulating KBHs, the spin of the BH was given as 0.9999 to simulate the maximally rotating BHs.

To obtain the primary spectra, one million elementary particle energies were simulated. In the simulation, the minimum and maximum energies a directly emitted elementary particle was allowed to have were 10⁻⁷ GeV and 10²¹ GeV, respectively. However, this range was modified according to the mass of the BH. Variation of total primary spectra and spectra of coloured particles with time, variation of spectra of coloured particles with BH mass, the temperature, with BH entropy and with BH spin plots were generated for the investigation.

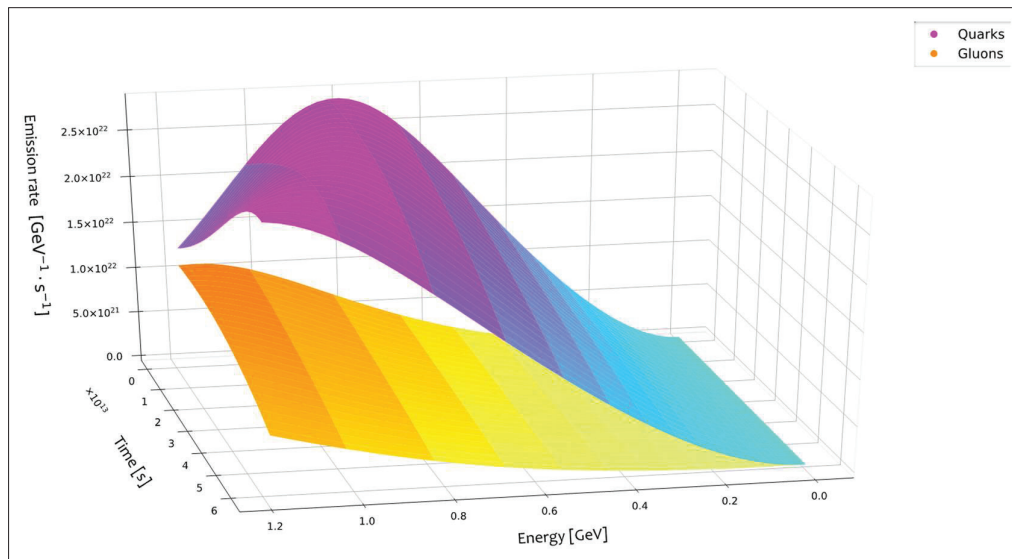


Figure 1: Variation of quark and gluon spectra from a SBH beginning to emit coloured particles with time. Mass of the BH is dropped from 5.29 × 10¹³ to 3.53 × 10¹³ g

RESULTS AND DISCUSSION

Variation of spectra with time

Schwarzschild black holes

Figure 1 presents the variation of primary spectra with time from a BH as the mass of the BH is dropped from 5.29×10^{13} to 3.53×10^{13} g within 6×10^{13} s. In the process, the temperature of the BH is increased from 200 to 300 MeV. Quarks, neutrinos, e^\pm , μ^\pm , gluons, and photons are the only primary particle species that are being emitted. Results of instantaneous primary spectra also show that these are the only types of particles that are being emitted from a SBH of this temperature (Wijewardhana & Gamalath, 2021). Figure 1 shows that the emission of quarks dominates the spectrum when they begin to radiate. This provides proof for the fact that the emission of coloured particles dominates the BH evaporation spectrum above the QGD temperature. In Figure 1, it can be seen how the peak of the quark spectrum is reached at energies lower than the peak of the gluon spectrum. When the mass of the black hole drops further, its temperature increases and surpasses the rest mass energies of the more massive particle species such as W^\pm , Z^0 and Higgs bosons. The emission of those particles becomes significant when the mass of the black

hole has reached down to $\sim 10^{11}$ g and the temperature has increased to ~ 50 GeV.

Figure 2 denotes the coloured spectrum from a BH of mass 1.06×10^8 g for about 2.5×10^{-4} s. This BH mass is about half of the mass of a BH which is just hot enough to radiate coloured particles. All primary particle species, quarks, neutrinos, e^\pm , μ^\pm , gluons, photons, Higgs bosons, W^\pm and Z^0 are being emitted from the BH at this temperature. The emission of quarks far exceeds the emission of all other primary particles. The plot is drawn considering only a single quark flavour. When all twelve quark flavours are considered, the emission of quarks must dominate the primary spectrum from a BH radiating at this temperature. One striking feature is that, if the orders of magnitude of the energy axis are disregarded, Figure 2 which shows the coloured spectrum for 2.5×10^{-4} s is remarkably similar to the coloured spectrum shown in Figure 1, which is plotted for 6×10^{14} s. Hence, we can conclude that the spectrum of quarks and gluons that may be emitted from the 10^{13} g BH over 3171 millennia, will be emitted from the 10^8 g BH within 2.5×10^{-4} s. However, the energies of emitted particles will be hugely different. Energies of emitted quarks and gluons from the 10^8 g BH will be several orders of magnitude greater than the energies of quarks and gluons emitted from the 10^{13} g BH.

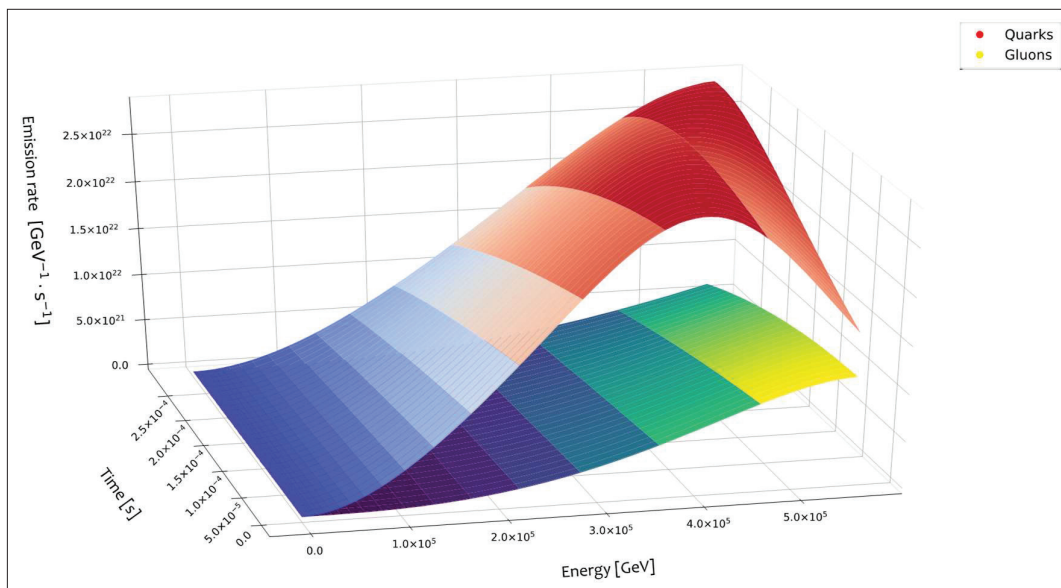


Figure 2: Variation of quark and gluon spectra from an intermediate SBH emitting coloured particles with time. BH mass is 1.06×10^8 g. Note that the energy axis is flipped compared to Figure 1

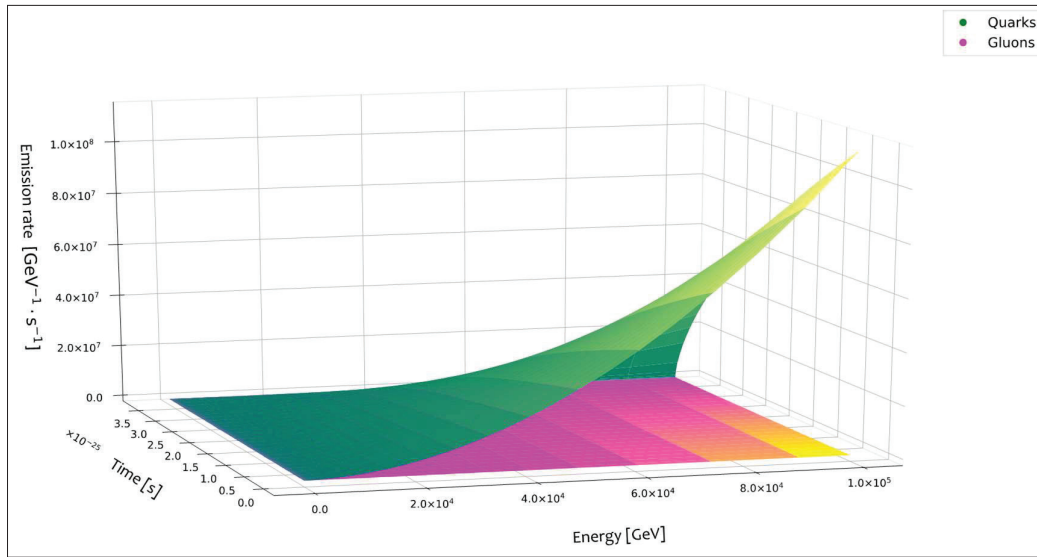


Figure 3: Variation of quark and gluon spectra with time from SBH reaching its end. BH mass is dropped to Planck mass from 10 g

Figure 3 presents the variation of quark and gluon spectra when the BH mass reaches down to Planck mass from 10 g. In Figure 3, time begins when the mass of the BH has dropped to 10 g and time counts-up till the BH mass reaches down to Planck mass. As can be seen from Figure 3, this only takes 3.5×10^{-25} s for the BH to reduce its mass from 10.00 g to 2.55×10^{-5} g. Hence, during the last stages of BH evaporation, it loses its mass at a drastic rate. When comparing with the rates of mass loss from the SBH as seen from the previous two cases, BH beginning to emit coloured particles and the intermediate BH emitting coloured particles, it can be concluded that these results agree with the fact that BHs lose mass at an ever-increasing rate. In Figure 3 also, quark emission dominates over gluon emission. It can be seen that, when comparing quark and gluon spectra, the emission of quarks at high energies far exceeds the emission of gluons at high energies.

It is observable that, with respect to both quarks and gluons, the emission rates of particles with exceedingly small energies are close to zero throughout the entire course of time considered. The highest overall emission rate is observed at the beginning of the considered timespan. This is because from the timespan considered, this is the time at which the BH possesses the most mass and energy. At this time BH emits highly energetic particles having energies of the order of 10^5 GeV the most. As time increases, even the emission rates of the highly energetic particles gradually recede and reach the limit of

zero as Planck mass is reached. The emission rates of low energy particles are comparatively low throughout the entire timespan considered. However, after a long time has passed and the BH has reached its end, the emission rates of all particles of all energies reach the limit of zero. This is because when the BH has reached its end it has an exceedingly small total energy remaining. The spectra of quarks and gluons when plotted separately look similar to each other. However, when examining the emission rates there are striking differences in the orders of magnitude. Even though when compared together, the spectrum of gluons look flattened out in comparison as seen in Figure 3, the spectra of both quarks and gluons look similar to each other in their corresponding scales. This shows that when the last moments of the BH are reached, quark emission would dominate over gluon emission. Ukwatta *et al.* (2016) have also obtained this domination of quark emission over gluon emission at higher energies.

Kerr black holes

Figure 4 is plotted for a KBH with the same initial mass considered for the SBH beginning to radiate coloured particles. In Figure 4, the BH mass is reduced from 5.29×10^{13} to 4.85×10^{13} g. The BH had a spin of 0.99 when its mass was 5.29×10^{13} g and throughout the entire timespan depicted in Figure 4, its spin has receded down only to 0.90. If the BH were maximally rotating when it reached QGD temperature, its primary spectrum would be this.

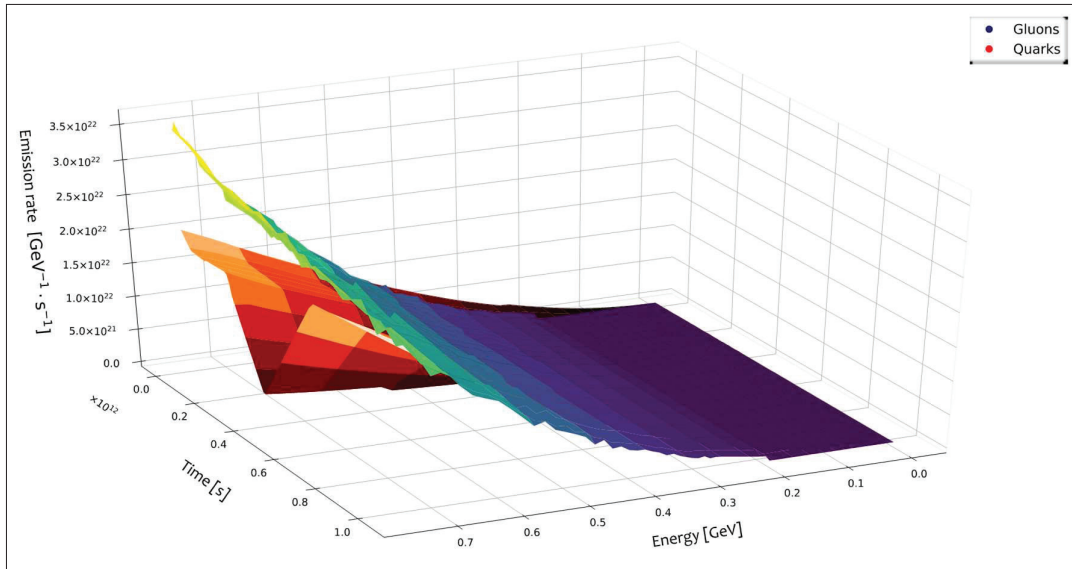


Figure 4: Variation of quark and gluon spectra from a maximally rotating KBH beginning to emit coloured particles with time

All quarks, gluons neutrinos, e^\pm , μ^\pm , and photons are emitted. The emission of μ^\pm resulted in the same curve as e^\pm . τ^\pm was not emitted in the plotted energy range as their rest mass is $1.78 \text{ GeV}/c^2$. Because of larger variations than in the case of the SBH, only a time span of $1 \times 10^{12} \text{ s}$ is considered in Figure 4. From Figure 4, it is clear that in this considered energy range, the emission of quarks dominates over the emission of other denoted

particle species. Figure 4 shows the emission spectra of quarks and gluons from a BH which starts its mass with $5.29 \times 10^{13} \text{ g}$ and emits particles for $1 \times 10^{12} \text{ s}$. In the considered range of energies, between 0.0 GeV and 0.7 GeV , the gluon emission rate dominates over the quark emission rate. It was apparent that the emission of gluons dominates the primary spectrum in the considered energy range.

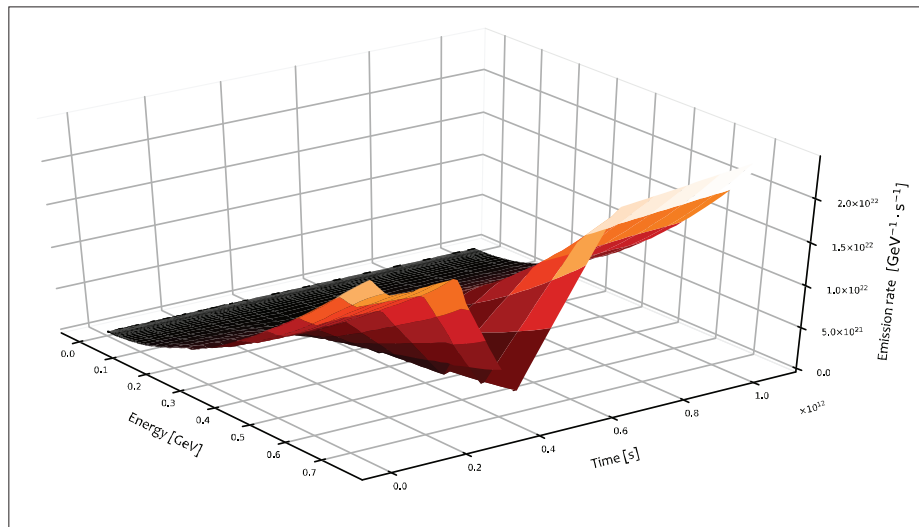


Figure 4(a): Variation of quark spectrum from a maximally rotating KBH beginning to emit coloured particles with time

Figure 4(a) shows the quark spectrum from KBH which starts emission with 5.29×10^{13} g and continues to emit particles for 1×10^{12} s. When comparing this quark spectrum from the KBH with the quark spectrum from the SBH, this dip seen in Figure 4(a) is a notable feature of the KBH spectrum. Figure 4(b) shows the gluon emission spectrum from KBH, which starts its mass with 5.29×10^{13} g and emits particles for 1×10^{12} s. When comparing with the smooth curve observed for the SBH, it can be seen that KBH has many irregularities in the gluon spectrum. These irregularities can be observed in instantaneous spectra as well (Wijewardhana &

Gamalath, 2021). Another notable feature that can be observed in Figure 4(b) is that during the entire time span considered, the emission rate of gluons with energies below 0.2 GeV is zero. This is because the temperature above which the gluons can exist as free particles is the QGD temperature, 0.2 GeV. This was observed in the instantaneous spectra as well (Wijewardhana & Gamalath, 2021). In Figure 4(a) and 4(b), variations of quark and gluon spectra are plotted for a shorter time period of 1×10^{12} s. The variation of the spectra for a longer time period of 3.62×10^{13} s are given in Figure 4(c) and 4(d).

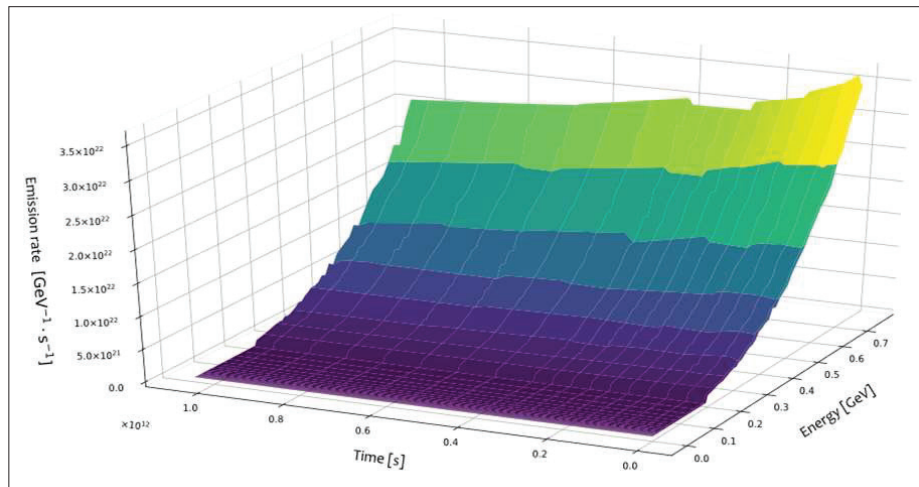


Figure 4(b): Variation of quark spectrum from a maximally rotating KBH beginning to emit coloured particles with time

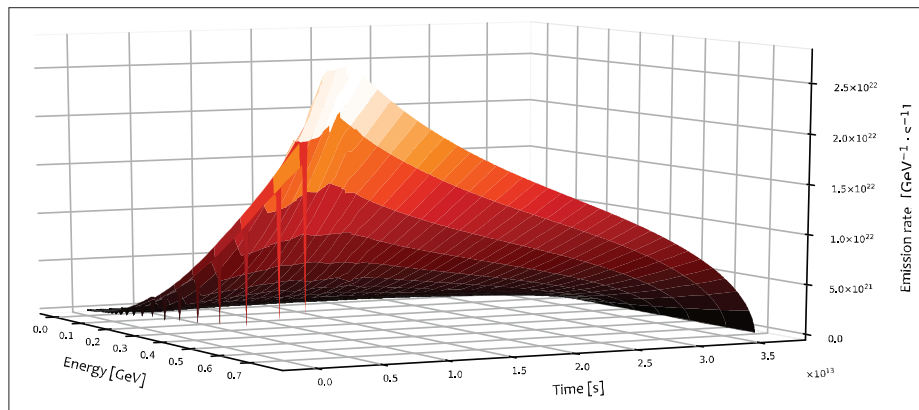


Figure 4(c): Variation of quark spectrum from a maximally rotating KBH beginning to emit coloured particles with time for an extended time span

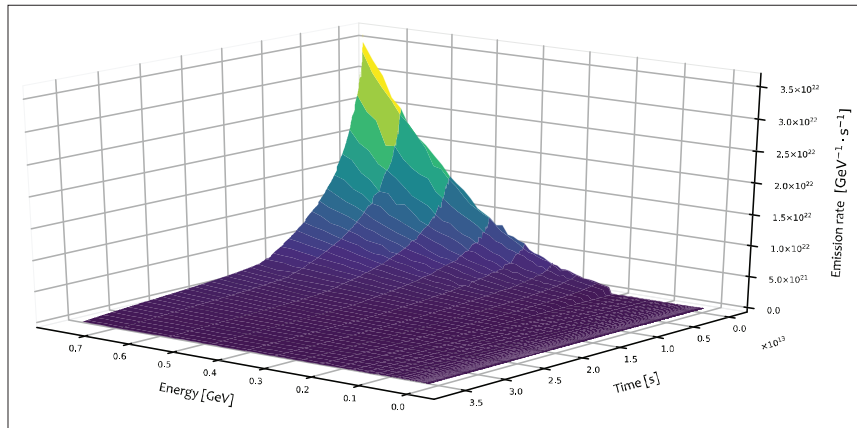


Figure 4(d): Variation of gluon spectrum from a maximally rotating KBH beginning to emit coloured particles with time for an extended time span

In Figure 7(c) plotted for an extended time period, it can be seen that there are many dips in the quark spectrum close to zero in the time axis. The dip seen in Figure 4(a) is corresponding to these minute dips observed in Figure 4(c). In fact, the spectra of KBHs have many fluctuations and variations like these.

The quark and gluon spectra presented respectively in Figure 4(c) and Figure 4(d) are plotted for the same range of energy and time. The resultant quark and gluon spectra are quite different from each other.

The variation of spectra of coloured particles is presented in Figure 5. Figure 5 shows the variation of

quark and gluon spectra of a KBH of mass 1.06×10^8 g with time for 1.7×10^{-6} s. The range of time represented in the figure of the KBH is two orders of magnitude less than the range of time represented in the figure of the SBH. But the variations in spectra of the KBH are drastically large. In contrast to the SBH, the KBH emits gluons at higher rates than quarks in the energy range considered.

Figure 6 shows the variation of quark and gluon spectra of a BH with time when the BH mass reaches down to Planck mass, and a non-rotating state from a 10 g maximally rotating state. In Figure 6, the gluon spectrum looks flattened out in comparison to the quark

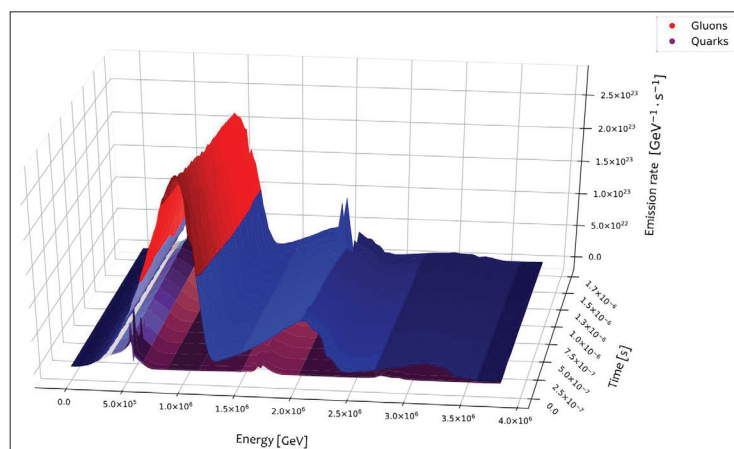


Figure 5: Variation of quark and gluon spectra from an intermediate maximally rotating KBH emitting coloured particles with time

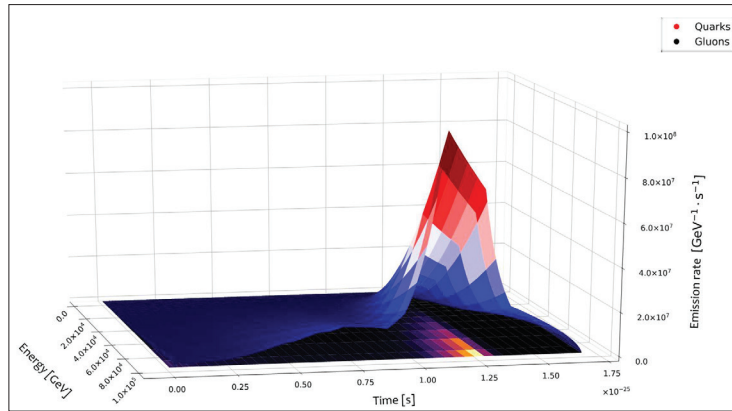


Figure 6: Variation of quark and gluon spectra with time from maximally rotating KBH reaching its end

spectrum. It can be noted that the emission rates of both quarks and gluons have been reduced from the usually observed order of magnitude 10^{22} .

Variation of spectra with black hole mass

Schwarzschild black holes

Figure 7 shows the variation of the spectra of quarks and gluons with the mass of the BH as the mass of the BH is reduced from 5.29×10^{13} to 3.53×10^{13} g. This

is the same range of masses that the BH depicted in Figure 1 has. It can be observed that as the mass of the BH is decreased, the peak of the quark spectrum shifts towards higher energies. That the gluon emission rate is zero below 0.199 GeV can also be observed. This is because gluons cannot exist as free particles below the QGD temperature which is 0.2 GeV. The shapes of the surfaces are a bit similar to those observed in Figure 1. This is because the mass of the BH is a function of time. Similar to Figure 1, in Figure 7 also the quark emission dominates over gluon emission.

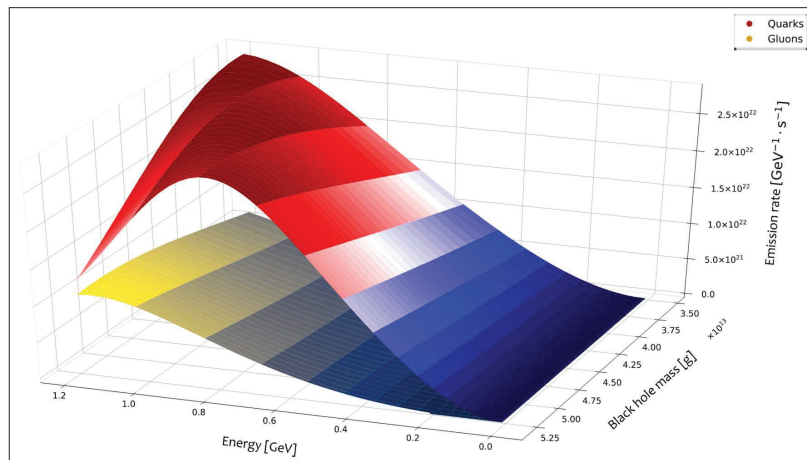


Figure 7: Variation of quark and gluon spectra from a SBH beginning to emit coloured particles with BH mass

Figure 8 shows the quark and gluon spectrum from a BH with a mass of 1.06×10^8 g, which starts emitting particles, and shows how the spectra vary as the BH

gradually loses mass and reaches the Planck mass. As the mass of the SBH was reduced from 10 g to Planck mass, the resultant spectrum looked similar to Figure 3.

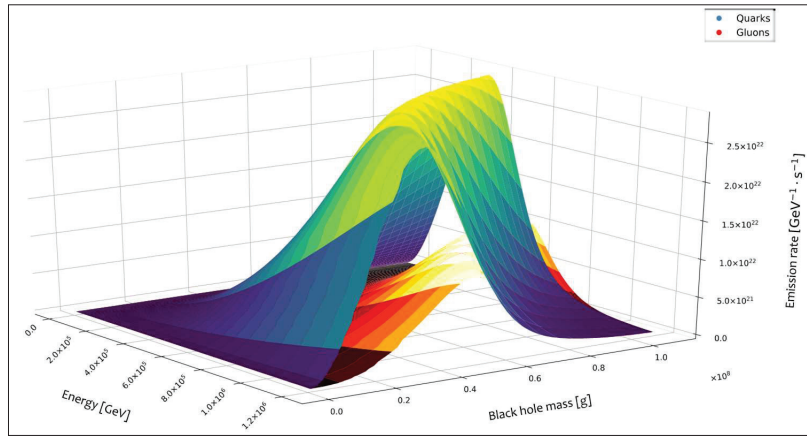


Figure 8: Variation of quark and gluon spectra from an intermediate SBH emitting coloured particles with BH mass

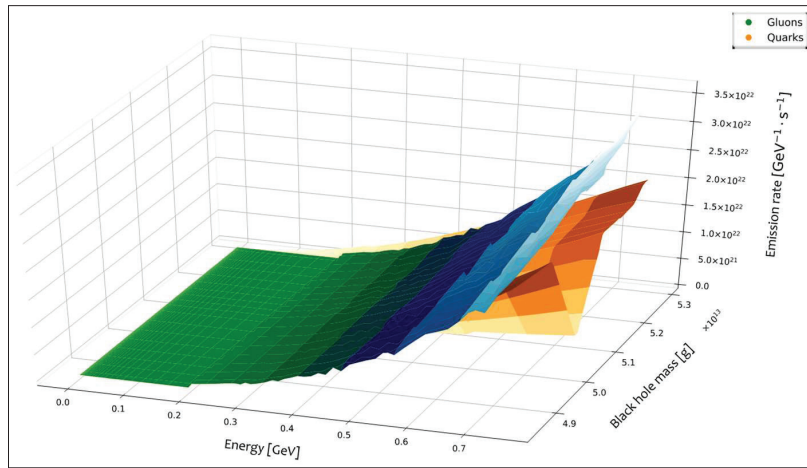


Figure 9: Variation of quark and gluon spectra from a maximally rotating KBH beginning to emit coloured particles with BH mass

Kerr black holes

Figure 9 shows the variation of the spectra of quarks and gluons with the mass of the BH as the mass of the BH is reduced from 5.29×10^{13} to 4.85×10^{13} g, which is less than the range of masses of the BH depicted in Figure 7. This is because the variation in quark and gluon spectra is higher when the mass of the BH is larger and therefore the high mass area was plotted for better comprehensibility. In the range of energies considered in Figure 9, the emission of gluons is more dominant than the emission of quarks.

Figure 10 shows the variation of quark and gluon

spectra of a BH of initial mass 1.06×10^8 g with BH mass as the BH mass is reduced down to 0.75×10^8 g. Unlike the case the of SBH, KBH has many fluctuations in the spectra. Hence, the variation of spectra in a small range of BH mass is denoted. In this considered range of energies, emission of quarks is dominant when the BH mass is comparatively small in the range of BH mass considered, and emission of gluons is dominant when the BH mass is comparatively large. It can be seen that the spectrum of gluons does not have many fluctuations as in the spectrum of quarks in the mass range considered. Even in instantaneous spectra, it was seen that in some energies, one of quark or gluon spectra varied smoothly while the other had many fluctuations.

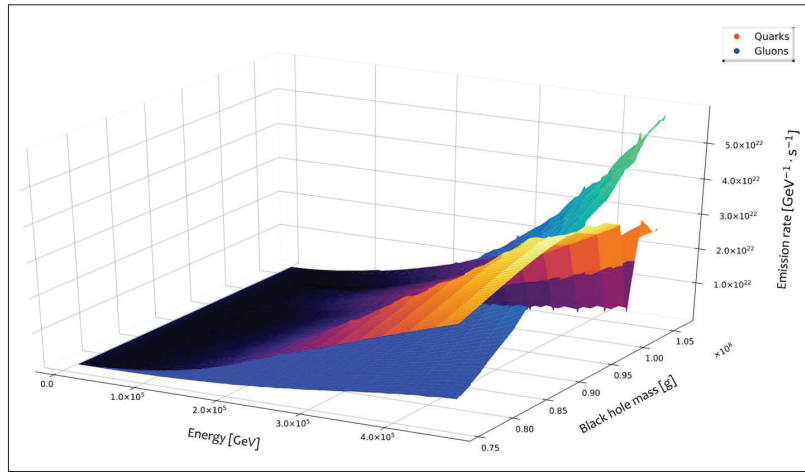


Figure 10: Variation of quark and gluon spectra from an intermediate maximally rotating KBH emitting coloured particles with BH mass

When the BH’s mass is reduced from 10 g to Planck mass it was observed that the variations of spectra with BH mass were similar to the variation of spectra with time presented in Figure 6.

Variation of spectra with temperature

Schwarzschild black hole

Figure 11 shows the variation of quark and gluon spectra of a BH with temperature in Kelvins. When the temperature varies between 2.423×10^{12} and 3.5×10^{12} K as given in the figure, the variation in energy units is between

200 and 300 MeV. Thus, it is a BH that has just started to exceed the QGD temperature and beginning to emit quarks and gluons. Hence, the minimum temperature, in Kelvins, of a SBH emitting coloured particles would be $\sim 10^{12}$ K.

Figure 12 shows the variation of quark and gluon spectra with the temperature of the BH. In energy units, the temperature of this BH is 100 TeV. The graph is plotted for the energies with maximum emission rates. It can be seen that the quark emission exceeds the gluon emission at peak emission rates.

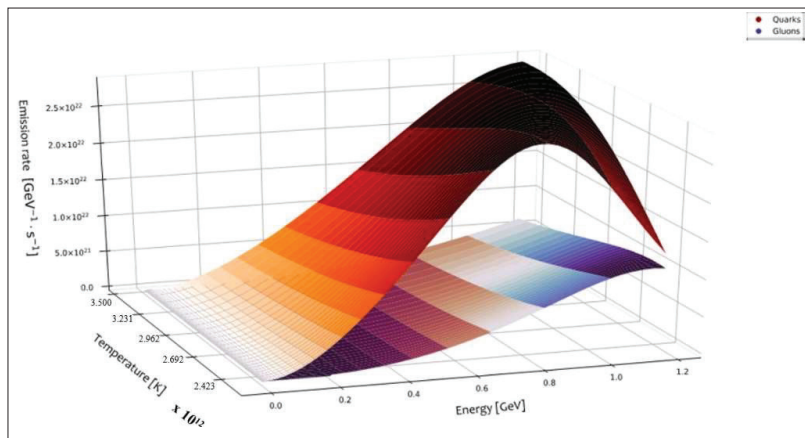


Figure 11: Variation of quark and gluon spectra from a SBH beginning to emit coloured particles with the temperature

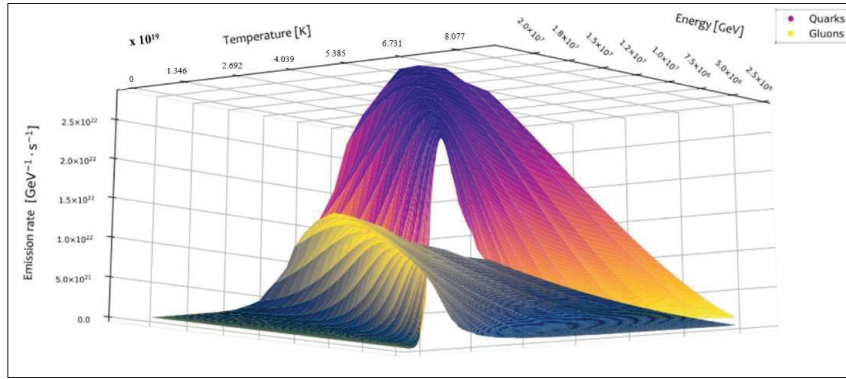


Figure 12: Variation of quark and gluon spectra from an intermediate SBH emitting coloured particles with the temperature

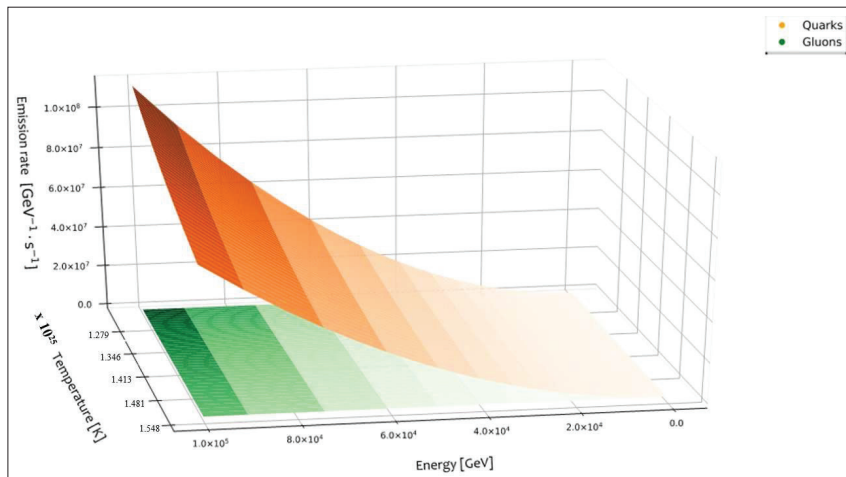


Figure 13: Variation of quark and gluon spectra from SBH reaching its end with the temperature

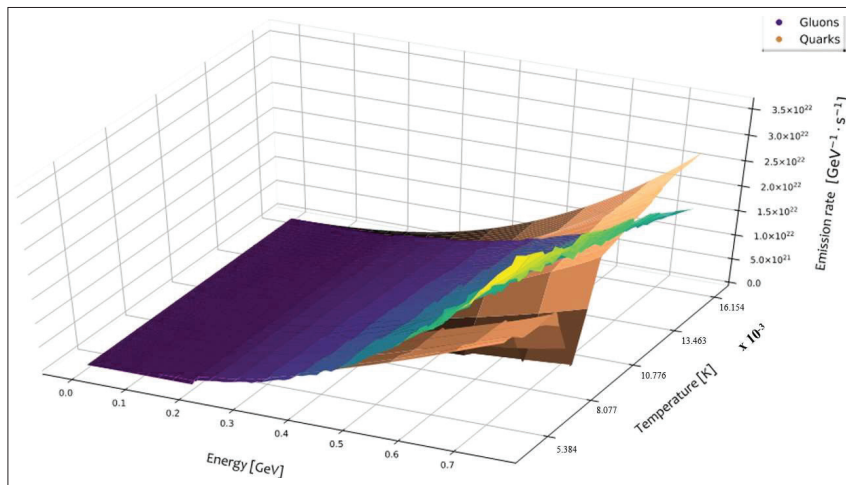


Figure 14: Variation of quark and gluon spectra from a maximally rotating KBH beginning to emit coloured particles with the temperature

Figure 13 shows the variation of quark and gluon spectra with the temperature of a BH as the BH reaches Planck mass. One notable feature is that now the temperature of the BH has reached $\sim 10^{25}$ K, which is considerably closer to Planck mass when compared with a BH, which is just hot enough to radiate coloured particles.

Kerr Black Holes

Figure 14 gives the variation of quark and gluon spectra from a maximally rotating KBH with temperature. In the Kelvin scale, temperature varies between 5.384×10^{-3} and 16.154×10^{-3} K. When comparing Figure 13 and Figure 14, there is a striking difference in the orders of magnitudes of temperature scales. A rotating KBH appears to be colder than a SBH of the same mass. However, the range of temperatures considered in Figure 14 is also exceedingly small. This is because the

large variations in spectra at lower temperatures of KBH make the spectra in the same range incomprehensible.

Variation of spectra with black hole entropy

Schwarzschild black hole

Figure 15 shows the variation of quark and gluon spectra with the entropy of BHs as the BH entropy varies between 1.50×10^{28} to 3.50×10^{28} cal. K^{-1} . As Figure 15 denotes a BH that started emitting particles with a mass that corresponds to a temperature that is just hot enough to radiate coloured particles, it can be observed from this graph that a SBH emitting coloured particles would have a minimum entropy of $\sim 1.50 \times 10^{28}$ cal. K^{-1} . Figure 15 shows the variation of quark and gluon spectra until the BH entropy reaches 3.50×10^{28} cal. K^{-1} .

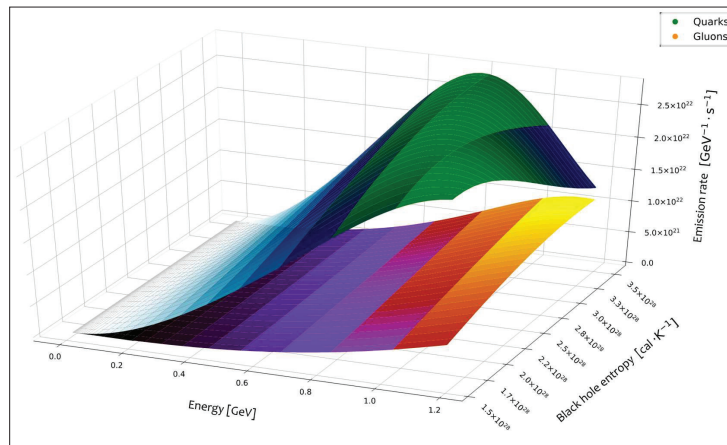


Figure 15: Variation of quark and gluon spectra from a SBH beginning to emit coloured particles with BH entropy

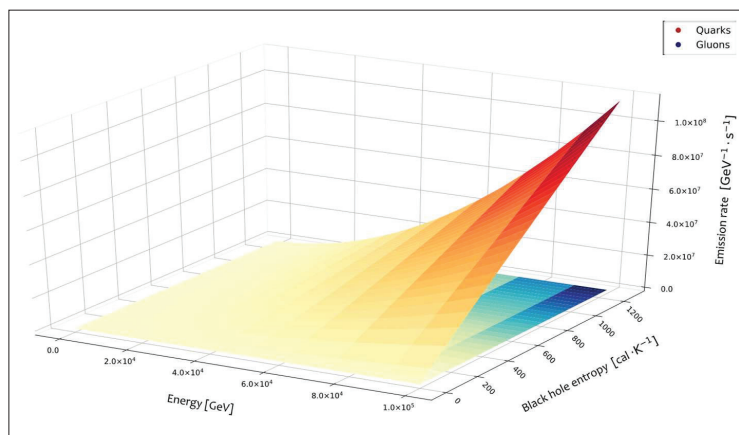


Figure 16: Variation of quark and gluon spectra from SBH reaching its end with BH entropy

When the quark and gluon emission from a SBH of mass of about 10^8 g was considered, it was observed that such a SBH would possess an entropy of the order of 10^{16} cal. K^{-1} .

Figure 16 shows the variation of quark and gluon spectra with the entropy of the BH when the BH reaches Planck mass from 10 g of mass. When the BH's mass is about 10 g, it possesses an entropy of about 1256.64 cal. K^{-1} . As Planck mass is reached, the entropy of the BH gradually decreases and gets very close to zero. Correspondingly, quark and gluon emission rates also gradually decrease and reach the limit of zero.

Kerr black holes

Figure 17 shows the variation of quark and gluon spectra with the entropy of the BH as the BH entropy varies between 2.00×10^{28} to 2.12×10^{28} cal. K^{-1} . Both Figure 15 and Figure 17 are plotted for a BH of initial mass 5.29×10^{13} g. The starting entropy values of plots imply that a maximally rotating KBH would have greater entropy than an SBH with the same mass.

Moreover, it was observed that that the entropy of a maximally rotating KBH having a mass of about 10^8 g is of the order of 10^{16} cal. K^{-1} . The emission of gluons dominated over the emission of quarks.

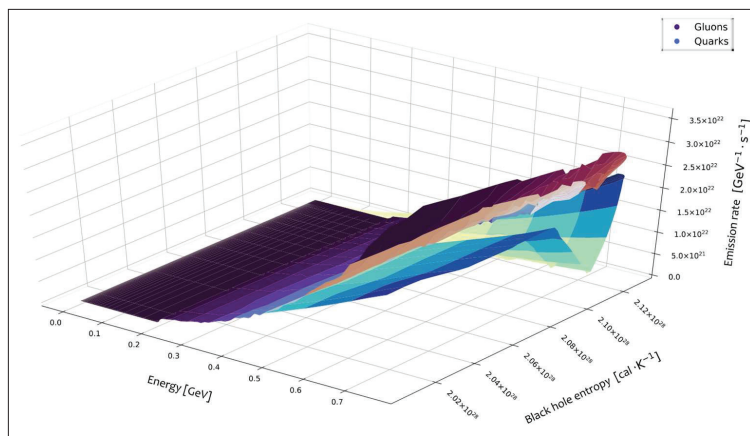


Figure 17: Variation of quark and gluon spectra from a maximally rotating KBH beginning to emit coloured particles with BH entropy

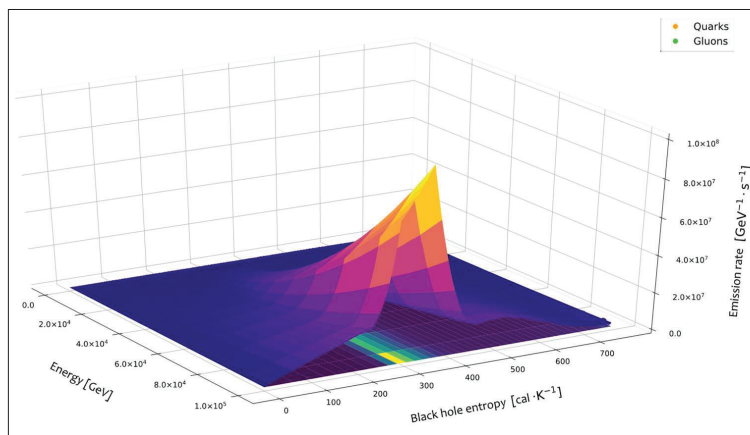


Figure 18: Variation of quark and gluon spectra from maximally rotating KBH reaching its end with BH entropy

Figure 18 shows the variation of quark and gluon spectra with the entropy of BH when the KBH reaches Planck mass from 10 g of mass. By inspecting the ranges of entropy values, it can be noted that when the BH reaches Planck mass, an SBH possesses more entropy than a KBH.

Variation of spectra with black hole spin

Kerr black hole

Figure 19 shows the variation of quark and gluon spectra with spin, of a BH with an initial mass of 5.29×10^{13} g,

which loses its spin through the course of its lifetime before its mass is reduced down to Planck mass. Hence it is a plot that shows how the quark and gluon spectra vary as a rotating KBH that emits coloured particles loses its spin.

Figure 20 shows the variation of quark and gluon spectra with time for a BH that was maximally rotating when its mass was 10 g and gradually lose its spin as the BH evaporates and finally reaches Planck mass. It can be observed that the emission rates of coloured particles are comparatively higher for lower BH spins.

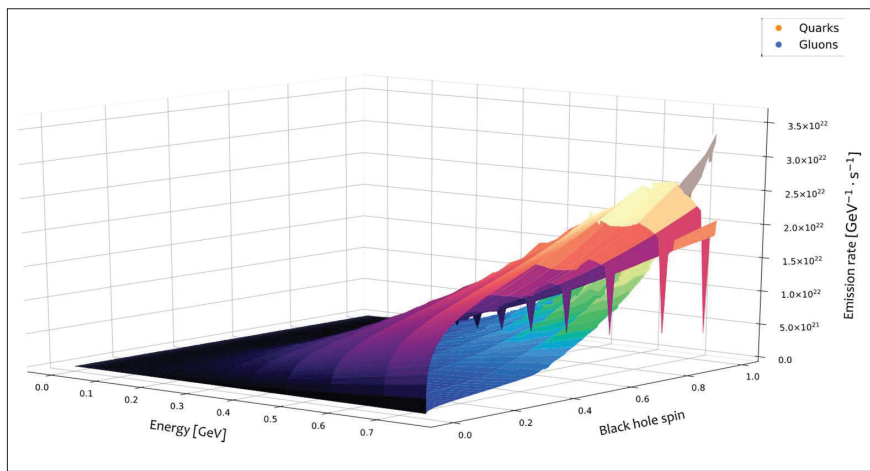


Figure 19: Variation of quark and gluon spectra from a maximally rotating KBH beginning to emit coloured particles with BH spin

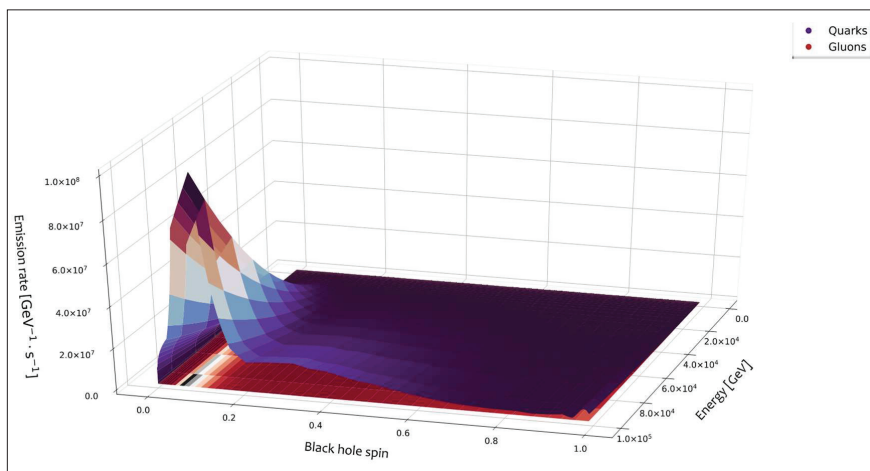


Figure 20: Variation of quark and gluon spectra from rotating KBH reaching its end with BH spin

CONCLUSIONS

The emission rate formulas in terms of black hole mass, temperature, entropy, and spin were derived and the Hawking spectra of coloured particles radiating from BHs of different masses, temperatures, entropies, and spin were investigated. Only BHs of mass $\sim 10^{13}$ g or less are capable of radiating coloured particles. Emission of particles from BHs of mass ranging from $\sim 10^{13}$ g to Planck mass, 2.18×10^{-5} g was investigated focusing mainly on the emission of coloured particles. Even though it is tempting to know what the spectrum would be like as the BH reaches the zero mass limit, the classical laws break down at Planck mass. Therefore, Planck mass is the lower limit of BH mass that can be investigated. Quarks, neutrinos, e^\pm , μ^\pm , gluons, and photons are the only primary particle species that are being emitted from a BH of mass $\sim 10^{13}$ g. Results show that, when the orders of magnitude of particles are disregarded, the spectrum of quarks and gluons that may be emitted from the 10^{13} g BH over 3171 millennia will be emitted from the 10^8 g BH within 2.5×10^{-4} s. It was also observed it only takes 3.5×10^{-25} s for a SBH to reduce its mass from 10.00 g to 2.55×10^{-5} g. Hence, during the last stages of BH evaporation, it loses its mass at a drastic rate. As the BH reaches the end of its lifetime, the emission rates of the highly energetic particles gradually recede and reach the limit of zero as Planck mass is reached. It was noted that, by the time the BH begins to emit coloured particles its temperature is $\sim 10^{12}$ K, but when it reaches the Planck's mass its temperature has reached $\sim 10^{25}$ K. That is much closer to the Planck temperature which is $\sim 10^{32}$ K, than the BH's original temperature. From the results, a rotating KBH appears to be colder than an SBH of the same mass. Moreover, results imply that a maximally rotating KBH has a greater entropy than an SBH with the same mass. As Planck mass is reached, the entropy of the BH gradually decreases and gets very close to zero.

REFERENCES

- Arbey A. & Auffinger J. (2019). BlackHawk: a public code for calculating the Hawking evaporation spectra of any black hole distribution. *The European Physical Journal C* **79**(08): 693.
DOI: <https://doi.org/10.1140/epjc/s10052-019-7161-1>
- Arbey A. & Auffinger J. (2021). Physics beyond the standard model with BlackHawk v2.0. *The European Physical Journal C* **81**(10): 910.
DOI: <https://doi.org/10.1140/epjc/s10052-021-09702-8>
- Bardeen J., Carter B. & Hawking S. (1973). The four laws of black hole mechanics. *Communications in Mathematical Physics* **31**(02): 161–170.
DOI: <https://doi.org/10.1007/bf01645742>
- Carr B. (1976). Some cosmological consequences of primordial black-hole evaporations. *The Astrophysical Journal* **206**: 8.
DOI: <https://doi.org/10.1086/154351>
- Carroll S. (2019). *Spacetime and Geometry*, pp. 238–272. Cambridge University Press, Cambridge, UK.
- Hawking S. (1971). Gravitationally collapsed objects of very low mass. *Monthly Notices of the Royal Astronomical Society* **152**(01): 75–78.
DOI: <https://doi.org/10.1093/mnras/152.1.75>
- Hawking S. (1975). Particle creation by black holes. *Communications in Mathematical Physics* **43**(03): 199–220.
DOI: <https://doi.org/10.1007/bf02345020>
- Ibunghochouba Singh T., Ablu Meitei I. & Yugindro Singh K. (2014). Hawking radiation and entropy of Kerr-Newman black hole. *Astrophysics And Space Science* **352**(02): 737–741.
DOI: <https://doi.org/10.1007/s10509-014-1927-6>
- Kofoed E. (2015) A black hole radiating colour charged particles. *BSc thesis*, Lund University, Lund, Sweden.
- MacGibbon J., Carr B. & Page D. (2008). Do evaporating black holes form photospheres?. *Physical Review D* **78**(06): 064043.
DOI: <https://doi.org/10.1103/physrevd.78.064043>
- MacGibbon J. & Webber B. (1990). Quark- and gluon-jet emission from primordial black holes: The instantaneous spectra. *Physical Review D* **41**(10): 3052–3079.
DOI: <https://doi.org/10.1103/physrevd.41.3052>
- Page D. (1976a). Particle emission rates from a black hole: Massless particles from an uncharged, nonrotating hole. *Physical Review D* **13**(02): 198–206.
DOI: <https://doi.org/10.1103/physrevd.13.198>
- Page D. (1976b). Particle emission rates from a black hole. II. Massless particles from a rotating hole. *Physical Review D* **14**(12): 3260–3273.
DOI: <https://doi.org/10.1103/physrevd.14.3260>
- Page D. (1977). Particle emission rates from a black hole. III. Charged leptons from a nonrotating hole. *Physical Review D* **16**(08): 2402–2411.
DOI: <https://doi.org/10.1103/physrevd.16.2402>
- Page D. (2005). Hawking radiation and black hole thermodynamics. *New Journal of Physics* **7**: 203.
DOI: <https://doi.org/10.1088/1367-2630/7/1/203>
- Page D. & Hawking S. (1976). Gamma rays from primordial black holes. *The Astrophysical Journal* **206**: 1–7.
DOI: <https://doi.org/10.1086/154350>
- Perry M. (1977). Black holes are coloured. *Physics Letters B* **71**(01): 234–236.
DOI: [https://doi.org/10.1016/0370-2693\(77\)90786-9](https://doi.org/10.1016/0370-2693(77)90786-9)
- Ukwatta T., Stump D., Linnemann J., MacGibbon J., Marinelli S., Yapici T. & Tollefson K. (2016). Primordial Black Holes: Observational characteristics of the final evaporation. *Astroparticle Physics* **80**: 90–114.
DOI: <https://doi.org/10.1016/j.astropartphys.2016.03.007>
- Wijewardhana C.N.T. & Wijewardana Gamalath K.A.I.L. (2021). Simulation of primary spectra of particle radiation from black holes. *World Scientific News* **158**: 105–129.

RESEARCH ARTICLE

Agricultural systems

Designing a closed-loop information flow model in bridging the market information gap among agriculture stakeholders in Sri Lanka

TB Mallikaarachchi^{1*}, G Samaraweera¹, A Walisadeera², L De Silva³ and S Munasinghe²

¹ Department of Agricultural Economics and Agribusiness, Faculty of Agriculture, University of Ruhuna, Kamburupitiya 81100, Sri Lanka.

² Department of Computer Science, Faculty of Science, University of Ruhuna, Wellamadama, Matara, 81000, Sri Lanka.

³ University of Colombo School of Computing, UCSC Building Complex, 35 Reid Ave, Colombo 00700, Sri Lanka.

Submitted: 18 February 2021; Revised: 23 August 2021; Accepted: 27 August 2021

Abstract: The stakeholders in the agriculture domain need agricultural information and relevant knowledge to make informed decisions at various stages of the crop life cycle. Coordination failures among the stakeholders in the agriculture sector result in the inability to provide accurate, timely, and actionable information. As a result, the agriculture sector faces several challenges, such as oversupply, undersupply and crop wastage. The existing digital agriculture eco-system can gather data produced by different stakeholders more frequently and accurately. However, the data collected from various stakeholders should be analyzed and forecasted to deliver the required knowledge to make more informed and appropriate decisions. This study was carried out to propose a ‘Closed-loop information flow model’ to provide forecasted demand and supply to create better coordination among stakeholders. Different prototypes were designed to deliver forecasted demand and supply information for major stakeholders in the agriculture sector. Initially, farmers, input suppliers, and logistic suppliers were selected in this study to expand to other stakeholders in the future. The prediction model was developed and evaluated according to stakeholder requirements by analyzing the actual and predicted data. The existing ‘Govi-Nena’ mobile-based farmer application was refined to provide supply and demand information for farmers. Separate web dashboards were designed to deliver the required information to other stakeholders such as input suppliers and logistic suppliers. Designed prototypes will be evaluated with the stakeholders for further improvements. The proposed Closed-loop information flow model for forecasted demand and supply will bridge the market information gap among stakeholders.

Thus, it will reduce the coordination failures in the Sri Lankan agriculture sector while increasing transparency in making informed decisions.

Keywords: Closed-loop market information flow model, demand and supply modeling, UI/UX designing.

INTRODUCTION

Stakeholders involved in the agriculture domain need agricultural information and relevant knowledge to make informed decisions. Accurate agriculture information on market prices, seasonal weather, input supplies such as seeds, fertilizers, pesticides, machinery, and forecasted supply and demand are essential to make informed decisions at various stages of the crop production life cycle to achieve maximum potential productivity of each crop (De Silva *et al.*, 2012; Sachin *et al.*, 2020).

The current information flow within the agriculture domain resembles an open-loop system, creating difficulties in controlling information flow in the agriculture domain in Sri Lanka (Ginige, 2018). An open-loop information flow model is a control system where the system’s output depends on the input. Still, the input or the controller is independent of the system’s output. Hence, though the information is produced, there is no proper coordination among the stakeholders in an open-

* Corresponding author (thanuja@agri.ruh.ac.lk;  <https://orcid.org/0000-0003-3707-6044>)



loop information system. As a result, stakeholders do not effectively access accurate and timely information; hence, they face several challenges. For example, at present, a common problem for Sri Lankan farmers is not being able to sell their harvest due to oversupply that occurs due to not getting the planned harvest and not being aware of market demand and supply in the planning stage (De Silva *et al.*, 2012; Ginige, 2018). Therefore, market demand and supply production predictions are essential for farmers and other stakeholders in the agriculture sector.

Developing a closed-loop information flow model to deliver accurate information and maintain better coordination among stakeholders is necessary for improving the agriculture domain in Sri Lanka. To that end, the 'Govi-Nena' project (www.govinena.lk) was initiated to create a digital knowledge agriculture ecosystem to close up the open-loop information flow model for better coordination. The digital agriculture ecosystem can gather data more frequently and accurately, combined with external sources (De Silva *et al.*, 2014; Ginige *et al.*, 2016). Data generated by the stakeholders can be further analyzed and forecasted to make more informed and appropriate decisions. The stakeholders can efficiently use this information with greater transparency and accuracy through a closed-loop (De Silva *et al.*, 2012; Giovanni *et al.*, 2013; Ginige, 2018) information flow model to produce actionable information.

Producing accurate information on agriculture market demand and supply is vital. Therefore, this study was carried out to propose a Closed-loop Information Flow Model (CIFM) to generate and deliver forecasted demand and supply information. The prototypes were designed to disseminate the information generated through the CIFM model among the main stakeholders in the agriculture domain.

The design of the CIFM model was influenced by the sustainable and closed-loop supply chain management research carried out in the literature. Over time, oversupply and undersupply may occur within the agriculture supply chain management due to inaccurate information on agriculture production. In addition, the lack of accurate information on service requirements, quantity, and quality of required services and products is another major cause within the agriculture supply chain (Mahaliyanaarachchi, 2003; Luthra, 2018; Sachin *et al.*, 2020). Furthermore, in Sri Lanka, past studies have identified that oversupply and undersupply occurred in three major phases (Input supply stage, Production stage,

Logistic supply stage) within the agriculture supply chain management (Basnayake, 2019; Sachin *et al.*, 2020).

The concept of agriculture supply chain management is a relatively recent idea in agribusiness management literature that originated to reduce agriculture wastage in the agriculture product life cycle (Bhagat *et al.*, 2011). However, the efficiency of such supply chain management systems can be increased by creating better networks and strong inter-relationships among all stakeholders, including input suppliers, producers, processors, traders, retailers, and consumers (Bhagat *et al.*, 2011; Ackerman & Pantel, 2017).

Various types of opened-loop and closed-loop supply chain models have been proposed to manage the entire process of producing products and services in many different product manufacturing domains. The closed-loop supply chain concept is well defined for product manufacturing, where products are generally returnable after use (Amin *et al.*, 2020). Closed-loop supply chain models have been used in such domains as a sustainable solution for preventing wastage while increasing productivity (Almató *et al.*, 1999; Boin & Bertram, 2005; Barros *et al.*, 2009; Abraham, 2011).

Returning used products is the significant difference between closed-loop and open-loop supply chain models (Ene & Öztürk, 2014; Ozceylan, 2016). The open-loop supply chain is a system whose constituent parts include material suppliers, production facilities, distribution services and customers linked together by the feed-forward flow of materials and feedback flow of information (Stevens, 1989; Ene & Öztürk, 2014; Ozceylan, 2016). However, in an open-loop supply chain, material or information does not flow back from the customer (Debo *et al.*, 2004).

The existing agriculture supply chain models resemble open-loop supply chain models due to the nature of the products. Inefficiencies and product wastage are common factors if there is no proper coordination among the stakeholders within an open-loop supply chain (Cheraghalipour *et al.*, 2018; Kamble *et al.*, 2020). It is evident from other domains that introducing a closed-loop supply chain model can reduce the loopholes in an open-loop supply chain model (Cheraghalipour *et al.*, 2018; Mosallanezhad, 2021). Such studies have shown that closed-loop supply chain models can effectively manage the domain stakeholders, thereby increasing efficiency and reducing wastage (Cheraghalipour *et al.*, 2018; Zhao *et al.*, 2018; Amirhossein *et al.*, 2021).

Furthermore, studies conducted by Yuanjie (2017) and Zeballos (2014) stated the possibility of sharing the risk of uncertainty among the stakeholder within a closed-loop supply chain (Jabarzadeh *et al.*, 2020; Salehi-Amiri *et al.*, 2021). This can reduce the risk caused due to product uncertainty to a certain extent.

Designing a closed-loop supply chain model for the agriculture domain is a challenging task. Very few closed-loop supply chain models have been introduced in the agriculture domain. The research work carried out by Banasik and his colleagues (2017) demonstrated the possibility of designing a closed-loop supply chain in industrial mushroom production. They explored alternative recycling technologies to quantify trade-offs between economic and environmental indicators in mushroom production (Banasik *et al.*, 2017). In addition, Cheraghalipour *et al.* (2018) proposed a Citrus closed-loop supply chain tool to minimize operational costs while maximizing responsiveness to customer demand. In this study, they have looked into the issue of spoiled fruits. Hence a returned product model was proposed to convert these into organic fertilizer and shipped as compost to customers (Iqbal, 2021). A similar study conducted by Mosallanezhad (2021) developed a mathematical tool to achieve cost savings in the seafood supply chain.

However, it is essential to identify different means and ways of designing closed-loop supply models other than the traditional concept in domains such as agriculture. We argue that by holistically providing and maintaining actionable information, an agriculture supply chain can be converted into a closed-loop scenario while reducing waste. There are hardly any modeling approaches in the literature on closed-loop agriculture supply chains using closed-loop information flow modeling concepts, particularly in the Sri Lankan context.

However, identifying and providing essential information is insufficient to achieve a sustainable closed-loop information flow model. A sustainable closed-loop information flow model should demonstrate continuous coordination, monitoring, analysis, and evaluation of the relevant information (Boulaalam *et al.*, 2013, Yang, 2015; Zhou *et al.*, 2018). With the rapid development of Information and Communication Technology (ICT), data and information can be effectively generated, stored, analyzed, and disseminated to support stakeholders in the agriculture sector. Thereby, this technology can be used to achieve a closed-loop information flow model to improve agricultural productivity and sustainability (Zhang *et al.*, 2016).

In this regard, supply and demand predictions play an essential role in an agriculture supply chain for stakeholders to make informed decisions. Visibility of this type of actionable information will empower the farmers and other stakeholders in the agriculture domain to take suitable corrective measures on their production while minimizing oversupply or undersupply in the agriculture sector, thereby reducing waste. Therefore, a closed-loop information flow model was designed to disseminate the actionable information while balancing the demand and supply to ensure sustainability.

MATERIALS AND METHODS

This study mainly focuses on potato cultivation in Sri Lanka due to its high economic importance. Potato growers, the main stakeholder in the supply chain, face many issues and challenges. The main challenge is the lack of information and visibility of the supply and demand. However, not only the farmers but also the stakeholders within the supply chain, including Input suppliers, Logistic Suppliers, Exporters, and Policymakers (Struik, 2006; Ortiz *et al.*, 2013; Beumer & Edelenbosch, 2019), even face issues due to the lack of information at the time of decision making. Hence, targeting the selected stakeholders in Sri Lankan potato cultivation, a closed-loop supply chain model was designed to increase visibility by providing real-time information to reduce wastage.

Design Science Research (DSR) methodology was used in this research study to design the proposed innovative artifact (model). As shown in Supplementary Figure 1, DSR consists of three major cycles (Hevner, 2007). The relevance cycle initiates DSR by providing the research requirements as inputs and defining acceptance criteria for the research results. Then the rigor cycle provides the existing knowledge to the research project to ensure its innovation. The design cycle refines the research activities and iterates more rapidly between the construction of an artifact, its evaluation, and subsequent feedback to further refine the design.

Major stakeholders involved in potato cultivation were identified through iterating the relevance cycle. As aforementioned, through surveys and existing literature, four major categories of stakeholders in the agriculture domain were identified: Farmers, Input Suppliers, Logistic Service Suppliers, and Policymakers. Exporters were excluded in the proposed model as no exports of raw potatoes were done to other countries (Agriculture and Environment Statistics Division, 2018).

The current demand and supply information requirements for each stakeholder to engage in the supply chain were further investigated via questionnaires and interviews. In addition, the current ways of obtaining predicted and real-time demand and supply information by the identified stakeholders to make decisions in providing services were also investigated. The studies revealed that predicted and real-time information was not shared adequately among these stakeholders. Moreover, they were making decisions based on rough measurements, and there was no proper coordination among the stakeholders to communicate this type of actionable information.

Farmers are not properly aware of the current production or market price to engage in potato cultivation. There were situations where overproduction or undersupply of potatoes is being reported in the market from time to time. On the other end, there were times when the government imported potatoes, creating an unprofitable marketplace for local potato farmers. To reduce this situation, farmers and the relevant stakeholders need information on the national consumption and the quantities of the production. Policymakers can also develop applicable policies in such circumstances to reduce the issues faced by the potato farmers.

The input suppliers provide seeds, fertilizer, pesticides, equipment, etc., that are locally produced or imported. Due to the difficulty in predicting the supply and demand, there were times when the input suppliers could not meet the demand and were defeated by their competitors. Almost all input suppliers currently predict the input requirement based on experience and informal measures.

The logistic service providers find it challenging to provide their services optimally due to the inability to predict the required services and quantities to be delivered. As a result, there were times when the product got wasted. Logistic suppliers can also save costs if they know the need beforehand and plan.

As per the findings, supply and demand information requirements for input suppliers, farmers (producers), and logistics suppliers are summarized in Table 1 below. Next, we iterated through the design cycle to design a CIFM to provide forecasted demand and supply to the relevant stakeholders. The proposed model was integrated with the existing 'Govi-Nena' mobile application. Based on the findings, the model was designed to cater to the supply and demand information needed at three levels: Farmer, Input Supplier, and Logistic Supplier.

The three main levels were considered in designing the proposed closed-loop information flow model to forecast stakeholders' demand and supply requirements based on the product quantities. The overall architecture of the proposed closed-loop information flow model is discussed in the next section.

The closed-loop information flow model (CIFM)

The closed-loop information flow architecture of CIFM model includes three (3) end-user levels and five (5) sub-modules to deliver the service requirement information required by the relevant stakeholders, as illustrated in Figure 1.

Table 1: Demand and supply information needs of the relevant stakeholders

Stakeholder	Information Needs
Farmers	Growing risk Market demand Market price Price predictions Price fluctuations
Input Suppliers	Predicted aggregated Input requirement for next year/season Predicted aggregated input requirement according to the District/ DS Division/ GN division / Agro-ecological Region. Crop production statistics
Logistic Suppliers	Predicted logistic requirement for next year/season Predicted aggregated logistic requirement according to the District/ DS Division/ GN division / Agro-ecological Region Crop production statistics

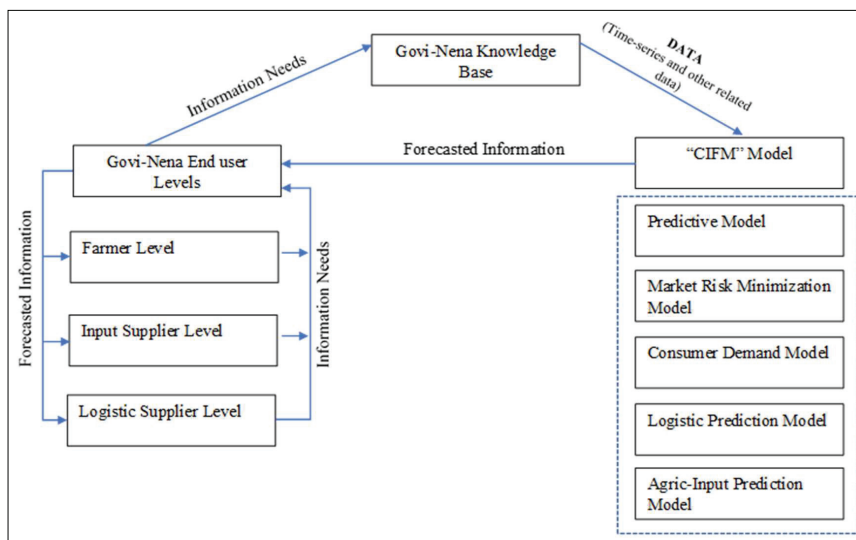


Figure 1: Closed-loop Information Flow Model (CIFM) architecture

Govi-Nena knowledge base

Govi nena Knowledgebase is containing two parts, one is crop ontology and the other one is a database that was developed to store market data which collects through users, and government domains. Through that database, CIFM model can get relavent data to forecast the market information.

Predictive model in CIFM

Crop forecasts are vital between the time of planting and harvesting. The past scholars used several techniques ranging from simple predictive techniques to advanced machine learning to predict crop yield. Forecasting methods can also vary from subjective to more objective ways. The subjective prediction methods are based on stakeholders’ intentions or the forecaster’s or other experts’ opinions or intentions. The objective methods use a more statistical approach, including univariate to multivariate/associative techniques.

In crop yield prediction, different factors directly impact the accuracy of the forecast due to its dynamic nature. In that regard, the changing conditions concerning soil, weather, etc., play a significant role in predicting yield accurately. However, limitations in the availability of such data might cause considerable uncertainty in the large area yield forecasting models, especially when using multivariate/associative models (Russell & Van Gardingen, 1997; Hoogenboom, 2000). Hansen and Jones, (2000) revealed that it is unclear how these

uncertainties transmit through the non-linear behavior of crop yield models and the aggregation errors that may creep in when aggregating crop yields to more significant regions. Moreover, several research studies were carried out to understand the effects of uncertainty in weather and other relevant factors on crop yield.

The crop yield modeling was focused on local-scale models to assess uncertainty in yield management (Bouman, 1994), condition of the soil (Launay & Guérif, 2003), and weather components that affect crop yield (Soltani *et al.*, 2004; Fodor & Kovacs, 2005). However, the existing studies revealed that the accuracy was reduced primarily due to uncertainties in soil conditions and/or weather components. In addition, the local scale representation makes the results less representative of the regional-scale crop yield forecast.

Hence, in this study, we selected the district as a regional unit, i.e., forecasting crop yield over large areas to minimize the effect on prediction due to the unavailability or reliability of variables such as soil and weather conditions. Therefore, we used the univariate multi-step time series forecasting method based on the neural network in this study. In addition, the effect on variants was minimized by predicting specific selected districts/areas and seasons. Badulla and Nuwara Eliya districts were selected for this study because these are the major potato cultivating districts in Sri Lanka. In 2019, Potato harvest of 71759MT (3935Ha) and 28743MT (1422Ha), was produced in Badulla and Nuwara Eliya districts, respectively (Department of

Census and Statistics, 2019). According to past scholars, Multi-Layer Perceptron Neural Network (MLP), Convolutional Neural Networks (CNN) and Long-Short Term Memory (LSTM) are used as multi-step univariate forecasting methods to make predictions (Ruß *et al.*, 2008; Nevavuori *et al.*, 2019; Schwalbert *et al.*, 2020; Tedesco-Oliveira *et al.*, 2020). Therefore, MLP, CNN, and LSTM techniques were used in this study. The measures of Mean Absolute Percentage Error (MAPE) and Normalized Root Mean Squared Error (NRMSE) were calculated and used in method comparison to select the best fit multi-step univariate forecasting method from the MLP, CNN, and LSTM neural networks. A time-

series data set of the potato production for 1998–2019, covering both cultivation seasons, Yala and Maha, was obtained for Nuwara Eliya and Badulla districts from the Department of Census and Statistics to train and validate the univariate forecasting methods.

The predictive model in the proposed CIFM includes three (3) sub-processes. It uses real-time, time-series data generated due to the current usage of the ‘Govi-Nena’ mobile application. Supplementary Figure 2 illustrates the flow processes of the predictive model, and Table 2 lists the input, output, and outcome that will be fed at the next stage of the model.

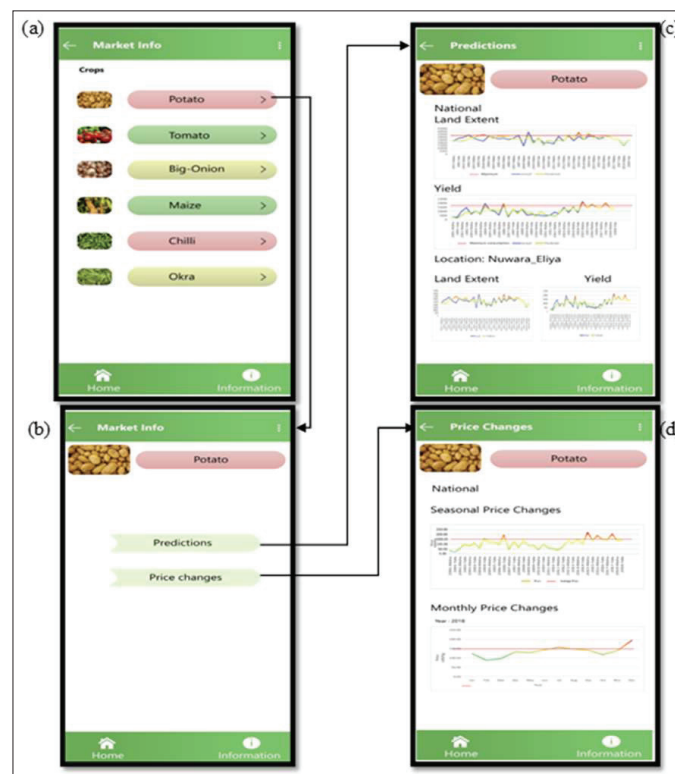


Figure 2: Market information UIs in farmer app

Table 2: Data requirement of the predictive model flow processes

	Input	Output	Outcome
Predictive model	Step 1 The past seasonal growing land extent in Ha (area-wise)	Predicted area-wise growing land extent for next two seasons	Used in the Agric-Input prediction Model
	Step 2 The past seasonal harvest yield (area-wise)	Predicted area-wise harvested yield for next two seasons	Used in the Logistics prediction Model
	Step 3 Per capita consumption (area-wise)	Predicted per capita consumption (area-wise)	Used in the Consumer and Demand Prediction Model

According to table 2, area-wise growing land extent for next two seasons was forecasted using a selected multi-step univariate forecasting method using past seasonal growing extent (Ha). Then, the area-wise past seasonal harvest yield is used to predict area-wise harvested yield for the next two seasons with a selected multi-step univariate forecasting

method. As the final step in the predictive model, area-wise per capita consumption was forecasted with the selected multi-step univariate forecasting method. Then the output was sent back to the Govinena knowledge base to be used as Inputs in the respective model mentioned under the Outcome in Table 2.

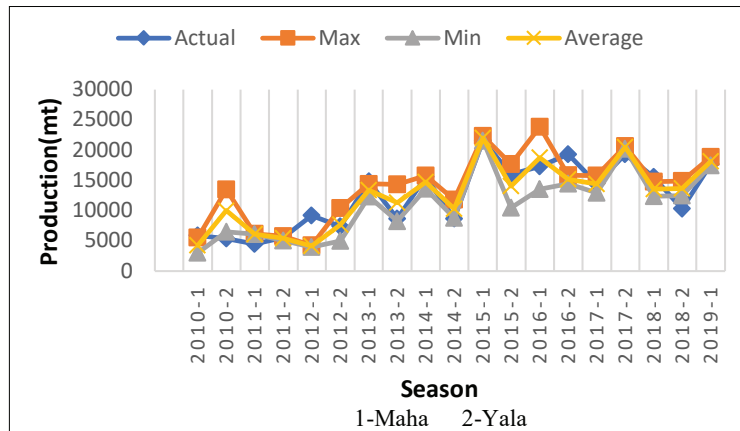


Figure 3: Maximum (max), minimum (min) and average seasonal potato production predicted by using LSTM neural network

Table 3: Consumer demand prediction model flow processes data requirements

	Input	Output	Outcome
Farmer market risk minimization model	Step 1 Predicted area wise harvested yield for next two seasons	Predicted area wise harvested yield for next two seasons	Used to make decisions in risk management
	Step 2 Real-time cultivation Ha (area wise) Average Yield per Ha	Average predicted yield per season	Used to identify market risk
	Step 3 The output of consumer demand prediction model Average predicted yield per season	Farmer’s risk level (high/moderate/good to grow)	Used to select the best crop to grow by minimizing the risk

Table 4: Farmer market risk minimization model flow processes data requirements

	Input	Output	Outcome
Farmer market risk minimization model	Step 1 Predicted area wise harvested yield for next two seasons	Predicted area wise harvested yield for next two seasons	Used to make decisions in risk management
	Step 2 Real-time cultivation Ha (area wise) Average Yield per Ha	Average predicted yield per season	Used to identify market risk
	Step 3 The output of consumer demand prediction model Average predicted yield per season	Farmer’s risk level (high/moderate/good to grow)	Used to select the best crop to grow by minimizing the risk

Consumer demand model in CIFM

The average consumption per person within a population is referred to as per capita consumption. Hence, predicted per capita consumption for the next two seasons, i.e., the output from the ‘Predictive Model’ and the area-wise average population, is used to calculate the area-wise consumption for the next two seasons. Table 3 shows the input, output, and model to which the output is fed at the next stage. Supplementary Figure 3 illustrates the flow processes of the Consumer Demand Prediction model. The output of this model was used as an input for the ‘Risk Minimization Model’ and the ‘Logistic Prediction Model’.

Farmer market risk minimization model in CIFM

The main aim of this model is to provide actionable information six months before sowing seeds to assist farmers in minimizing the risk of oversupply or undersupply. First, the predicted area-wise harvested yield for the next two seasons is re-organized from the Predictive Model. Next, the derived information is provided to the farmer via the ‘Govi-Nena’ mobile application. Then, Real-time cultivation land extent (area wise) derived through the ‘Govi-Nena’ mobile application and the Average Yield per Hectar, derived through the time series data, are used to predict the Average yield per season. Finally, the output derived from Step 2 and output derived from the Consumer Demand model indicate the market risk level, as illustrated in Table 4.

A color-coding mechanism is used to indicate the risk level based on predictions on the farmers’ market risk level of the selected crop, as illustrated in Supplementary Figure 4. As such, the red color indicates the high

market risk of growing the particular crop. Yellow color represents the ‘Moderate’ risk level, and hence farmers may opt for cultivating the relevant crop but with medium risk. The green color represents the ‘Lowest’ market risk level. The risk of producing the selected crop is minimal at that stage, and thus, farmers may choose to grow with minimum market risk.

Agric-input prediction model in CIFM

The two inputs for the ‘Agric-Input Prediction Model’ are the predicted area-wise growing land extent for the next two seasons and the average input (fertilizer & agrochemicals/ seeds/ machinery/ labour) requirement per Hectar (Table 5). This calculates the input required for the next two seasons based on the input type. Supplementary Figure 5 illustrates the ‘Agric-Input Prediction Model’ flow processes for input suppliers.

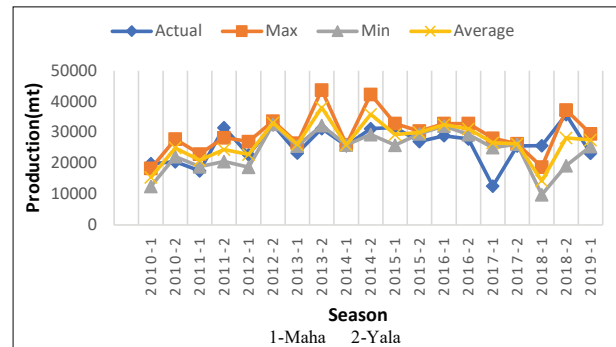


Figure 4: Maximum (max), minimum (min) and average seasonal potato production predicted by using LSTM neural network

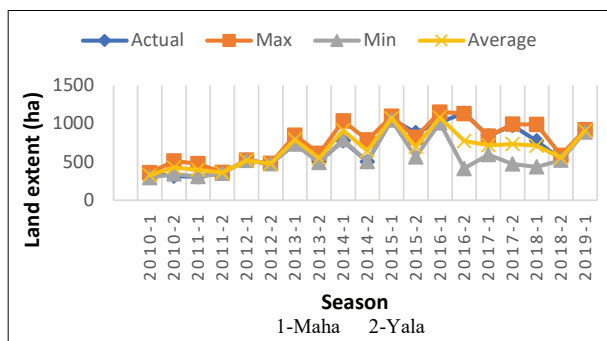


Figure 5: Maximum (max), minimum (min) and average seasonal potato cultivation extent predicted by using LSTM neural network

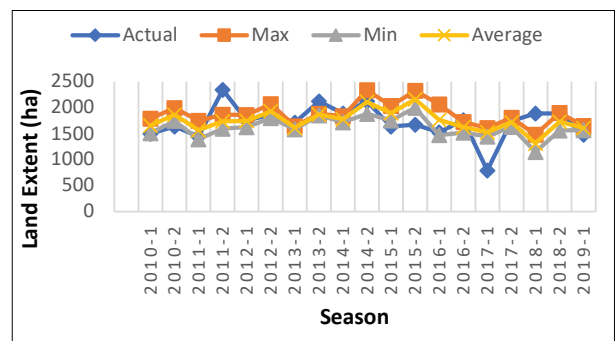


Figure 6: Maximum (max), minimum (min) and average seasonal potato cultivation extent predicted by using LSTM neural network

Logistic prediction model in CIFM

The ‘Logistic Prediction Model’ uses the output from the ‘Consumer demand prediction model’ and the predicted area-wise harvested yield for the next two seasons to predict the logistics requirement, as illustrated in

Supplementary Figure 6. The logistic service providers require this information to plan and manage their services at their earliest and provide a better service for farmers. The derived data is re-organized to provide a better purview of the current trend. Table 6 lists the ‘Logistic Prediction Model’ flow processes data requirement.

Table 5: Data requirements for the input demand prediction model

	Input	Output	Outcome
Agric-Input prediction model	Predicted area-wise growing land extent for next two seasons	Predicted area-wise input requirement for the next two seasons	Used to plan and manage the agric-input requirements
	Input (fertilizer & agrochemicals/ seeds/ machinery/ labour) requirement per Ha		

Table 6: Data requirements for logistic demand prediction model

	Input	Output	Outcome
Logistic prediction model	Output Predictive Model	Predicted area wise harvested yield for next two seasons	Predicted area wise transport and storage requirement for next two seasons
		Output of consumer demand prediction model	Used to plan and manage the logistics requirement

Designing the user interfaces

User Interfaces were designed to deliver the predicted outcomes on demand and supply derived from the proposed ‘Closed-loop Information Flow Model,’ iterating through the design cycle of DSR. In addition, the existing ‘Govi-Nena’ mobile farmer application was studied and refined to provide the predicted demand and supply information for farmers. The UI/UX design theories (Heimgärtner *et al.*, 2017; Canziba 2018; Yu *et al.*, 2020) were used to design the relevant interfaces.

Separate web dashboards were designed for other stakeholders, such as input suppliers and logistic suppliers, to deliver the required information through the ‘Closed-loop Information Flow Model.’ The designed prototypes will be evaluated with the stakeholders for further improvements.

Farmer mobile user interface: colour coding system for risk identification

The existing ‘Govi-Nena’ Farmer mobile application was refined to provide the predicted supply and demand information for farmers. When farmers are selecting the

crops, awareness concerning the market risk is essential for better decision-making. The output derived from the predictive model was mapped to the proposed color schema (Giovanni *et al.*, 2012) for the ‘Govi-Nena’ farmer application to minimize their market risk.

In the ‘Govi-Nena’ mobile application, as shown in Supplementary Figure 7 (a), farmers can go to the ‘My Crops’ section to add crops to their farms. In that stage, the farmers can see that the market risk will be highlighted using a color schema based on the results derived from the prediction model based on listed crops based. and the agro-ecological zones [Supplementary Figure 7 (b)],

The crops with a higher market saturation are denoted using red color. This color will inform the users that growing such crops may be risky due to the over-supply at the market level. The yellow color code was then used to show that the crop is in the intermediate level of market saturation; therefore, farmers can grow that crop at their own risk. The green color indicated that the crop had no market risk at that time. Therefore, farmers are encouraged to grow such crops to avoid crop wastage due to oversupply.

Moreover, the crop section in Supplementary Figure 7 (a) provides access to market information by clicking the market info icon to make an accurate decision during their cultivation. Looking at the color schema and these statistics, farmers can decide what to grow in which

quantities and add the decided crops as they wish to the ‘Short List’ section [Supplementary Figure 7 (c)]. After farmers add their first selected crops to the shortlist, they can decide the growing extent and add the shortlist to the final grow list.

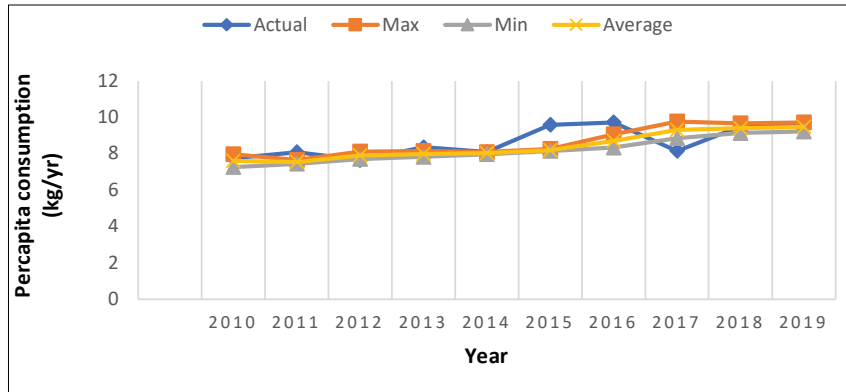


Figure 7: Maximum (max), minimum (min) and average per capita potato consumption predicted by using CNN neural network

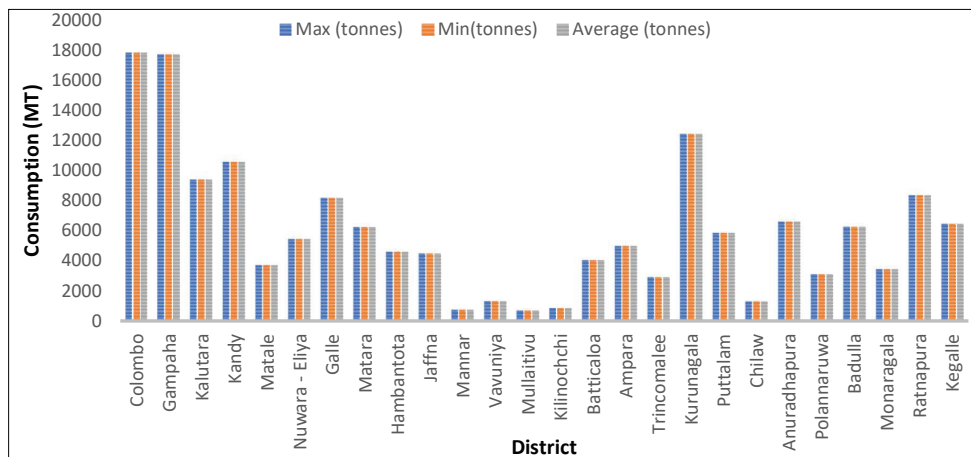


Figure 8: Maximum (max), minimum (min) and average area-wise potato consumption

Farmer mobile user interfaces: interface designs for delivering market information

Farmers can access the ‘Market Info’ section to get an idea about all available crops grown in their area [Figure 2(a)]. The ‘market info’ section will allow

farmers to access market information related to the selected crops. For example, when a farmer chooses a crop, a farmer can view the predicted crop cultivation statistics per season. In addition, monthly and seasonal price changes will be shown to the user, as illustrated in Figure 2 (b, c, and d).

Input supplier user interfaces: interface designs of the input suppliers dashboard

The prototype design of the input suppliers' dashboard is designed to visualize information on area-wise input requirements for crop cultivation, expected growing extent, and expected production for the next season. As shown in Supplementary Figure 8(a), the 'Market Summary' tab on the home page summarizes the current crop extent grown by the farmers. Moreover, users can get access to the input requirements details directly by clicking the 'icons' (Seeds & seedlings, Agrochemicals, Agromachinery, and Labours) in the 'input requirement' section, as shown in Supplementary Figure 8 (a). Users can select the crop in the input requirement section to view the predicted or real-time input requirement data.

Moreover, users can access the predicted crop data for the next two seasons by clicking on each crop's predicted tab, as shown in Supplementary Figure 8 (b). After accessing the predicted section [Supplementary Figure 8 (c)], users can select the district to obtain aggregated predicted input requirements for the next two seasons. In addition, users can obtain information on predicted growth extent and yield according to the selected area. Moreover, users can also access real-time input requirements by clicking the 'real-time' tab in each crop [Supplementary Figure 8 (b)]. Thereafter, farmers can access the real-time information interface, as shown in Supplementary Figure 8 (d). According to Supplementary Figure 8 (d), users can select the district to get aggregated real-time information. After selecting the district, users will gain the ability to access real-time seasonal input requirements. Moreover, users also can get information about real-time changes in the growing extent and real-time production [Supplementary Figure 8 (d)].

Logistic supplier user interface: interface designs of the logistic suppliers dashboard

As illustrated in Supplementary Figure 9, the prototype was designed to deliver area-wise seasonal requirements on farmers' harvested yield's transport and storage needs. During the field interviews, the logistic suppliers informed that they need next season's expected growing extent and expected production to better coordinate and manage their activities. Hence, to fulfill this requirement, expected national real-time growing extent and expected production statistics are added to their dashboard.

In addition, the logistic suppliers can access the predicted and real-time logistic requirements by clicking

the 'predicted' or 'real-time' tab in each crop, as shown in Supplementary Figure 9 (a). After accessing the predicted section, users must select the district to obtain logistic information, as shown in Supplementary Figure 9 (b). After that, users can access transport and storage requirements according to the selected district for the next two seasons. Moreover, in this section, users also can get information about the predicted growth extent and production according to the district chosen for the next two seasons.

Furthermore, users can access the Real-time information by clicking the 'Real-time' tab in the 'Logistic Requirement Section,' as shown in Supplementary Figure 9 (a). After accessing the Real-time section, users need to select a district in which they are willing to get Real-time logistic information [Supplementary Figure 9 (b)]. Thereafter, users can get information on Real-time transport and logistic requirement according to the selected district. In addition, users can access the information on real-time changes in growing extent and production according to the chosen area, as shown in Supplementary Figure 9 (b).

RESULTS AND DISCUSSION

Predictive model

The predictive model was trained for potato cultivation based on the derived dataset.

Predictions of area-wise potato production

Three models were developed by using MLP, CNN, and LSTM. The models were trained and validated using the data from the Nuwara Eliya district's seasonal potato production. Maximum, minimum, and average seasonal potato production was predicted through MLP and CNN models for the Nuwara Eliya district, which are shown in Supplementary Figures 10, 11, and the LSTM model in Figure 3. The expected production results were analyzed against the actual seasonal potato production.

The model developed using MLP showed the highest (23.21%) mean absolute percentage of error compared to the CNN (23.08%) and the LSTM (19.68%). However, when considering the NRMSE, MLP showed a lower (0.226) value than the CNN model (0.229). The LSTM model has shown the lowest NRMSE value of 0.118 among all three models (Supplementary Table 1).

All pre-trained MLP, CNN, and LSTM neural network models for Nuwara Eliya were fine-tuned to

make the potato production predictions for Badulla District. The models were compared using the NRMSE and MAPE. Actual seasonal potato production and predicted maximum, minimum, and average seasonal potato production using MLP and CNN models for the Badulla district were illustrated in Supplementary Figures 12 and 13 and the LSTM model in Figure 4.

Comparing the forecast accuracy by using the measures mentioned in Supplementary Table 2, CNN showed the highest (22.82%) mean absolute percentage of error (MAPE) when compared to the MLP (20.50%) and the LSTM (19.87%). Moreover, when considering NRMSE, CNN has shown a higher NRMSE (0.248) value than MLP (0.243). However, LSTM has demonstrated the lowest NRMSE value of 0.219 among the models. Therefore, the LSTM model showing high accuracy level than other methods. LSTM was used to predict seasonal potato production, and the results are shown in Supplementary Table 3.

Prediction of the area-wise land extent of potato cultivation

The same procedure mentioned above was carried out to predict the land extent for potato cultivation in Nuwara Eliya and Badulla District. Maximum, minimum, and average seasonal potato cultivation land extent were predicted through MLP and CNN models for Nuwara Eliya district as shown in Supplementary Figures 14, 15 and LSTM models in Figure 5. The predicted seasonal potato cultivation land extent was analyzed against the actual seasonal potato cultivation land extent.

The MLP showed the highest (19.40%) mean absolute percentage of error compared to the CNN (17.96%) and the LSTM (13.11%). However, when considering the NRMSE, MLP showed a higher (0.265) value than the CNN model (0.201). On the other hand, the LSTM model has shown the lowest NRMSE value of 0.188 among all three models (Supplementary Table 4).

Pre-trained MLP, CNN, and LSTM models for the Nuwara Eliya dataset were fine-tuned to make the potato production predictions for Badulla District. The models were compared by using the NRMSE and MAPE. Actual seasonal potato cultivation land extent and predicted maximum, minimum and average seasonal potato cultivation land extent results of MLP and CNN models for the Badulla district were illustrated in Supplementary Figures 16, 17, and LSTM model in Figure 6.

As a result, the CNN has shown the highest (20.04%) mean absolute percentage of error (MAPE) when compared to the MLP (17.37%) and the LSTM (15.62%). Moreover, when considering NRMSE, the CNN showed a higher NRMSE (0.231) value than MLP (0.206). However, the model developed using LSTM showed the lowest NRMSE value of 0.180 compared to other models (Supplementary Table 5). Therefore, LSTM was used to predict the land extent of seasonal potato production, and the results are shown in Supplementary Table 6.

Prediction of per capita potato consumption

Maximum, minimum, and average national per capita potato consumption was predicted using MLP and CNN models for Nuwara Eliya district as shown in Supplementary Figures 18, 19, and LSTM model in Figure 7. The predicted national per capita potato consumption results were analyzed against the actual national per capita potato consumption, as illustrated in the graphs.

Comparing forecasting models, the LSTM showed the highest (3.93%) mean absolute percentage of error compared to the MLP (3.60%) and the CNN (3.10%). However, when considering the NRMSE, LSTM showed a higher (0.105) value than MLP (0.094). On the other hand, CNN has shown the lowest NRMSE value of 0.090 compared to other models (Supplementary Table 7). Hence, CNN was used to predict the per capita potato consumption and the results derived are listed in Supplementary Table 8.

Consumer demand prediction model

The output from the 'Predictive Model' and the national average population were used to calculate predicted per capita consumption for the next two seasons, and it is illustrated in Supplementary Figure 20. The area-wise average population was used to calculate the area-wise potato consumption as illustrated in Figure 8.

Agric-input model

Prediction of area wise fertilizer requirement

The predicted seasonal potato cultivation land extent and the average fertilizer requirement per hectare were used to predict the area-wise potato fertilizer requirement. Urea, Triple Super Phosphate (TSP), and Muriate of Potash (MOP) are the three major potato fertilizers used in potato cultivation. The fertilizer usage requirement

of Urea, TSP, and MOP for the Nuwara Eliya district were illustrated in Supplementary Figures 21, 22, and 23, respectively. Similarly, the Badulla district's Urea, TSP, and MOP requirement fertilizer requirement were calculated and depicted in Supplementary Figures 21, 22 and 23, respectively.

Prediction of area-wise seed potato requirement

The seed potato requirement was calculated using the predicted seasonal potato cultivation land extent and average seed potato requirement per hectare. The estimated seasonal seed potato requirement for Nuwara Eliya and Badulla district was graphed in Supplementary Figures 24 and 25.

Prediction of area-wise labour requirement

The predicted land extent of the seasonal potato cultivation and the required number of labor hours per hectare were used to calculate the average number of labor hours needed for potato cultivation. Supplementary Figures 26 and 27 depict the labor requirement for Nuwara Eliya and Badulla districts, respectively.

Logistic model

The output from the consumer demand prediction model and the predicted area-wise harvested yield for the next two seasons was used in the 'Logistic Model' to provide re-organized predicted logistic requirements. Supplementary Table 9 shows the expected potato production in metric tons (MT) in different districts in Sri Lanka, while Supplementary Table 10 represents the area-wise potato consumption. Having this information beforehand in an organized manner, the logistic suppliers can plan and effectively manage their services.

Discussion

The study concludes that the proposed 'Closed-loop information flow model' for providing the forecasted demand and supply information for stakeholders will reduce wastage while bridging the information gap. The proposed model will reduce coordination failures and increase transparency among the stakeholders in the agriculture sector of Sri Lanka. The existing 'Govi-Nena' mobile farmer application was refined and improved to provide supply and demand information for farmers. Separate web dashboards designed for other stakeholders, such as input and logistic suppliers, will deliver the required information more effectively and efficiently.

Comparing MLP, CNN, and LSTM multi-step univariate forecasting methods, the LSTM method shows the lowest value of mean absolute percentage error and normalized root mean square error than CNN and MLP method. Therefore, the LSTM multi-step univariate forecasting method can forecast demand and supply values.

CONCLUSION

The stakeholders in the agriculture domain need agricultural information and relevant knowledge to make informed decisions at various stages of the crop life cycle. However, coordination failures among the stakeholders in the agriculture sector result in the inability to provide accurate, timely, and actionable information. As a result, the agriculture sector faces several challenges, such as oversupply, undersupply and crop wastage. According to the preliminary surveys, the stakeholders mentioned the possibility of minimizing the over-supply to reduce waste and minimize the undersupply situations at the market level if they have access to supply and demand data beforehand. Moreover, managing coordination to reduce waste is essential for an agriculture supply chain. We have designed a closed-loop supply chain model to reduce waste by providing supply and demand information for relevant stakeholders. Many product manufacturing organizations argue that closed-loop supply chain models can be used to coordinate the supply chain better, reducing waste. However, the same cannot be applied to manage agriculture supply chains due to the nature of the products and the dynamic nature of the information shared by the stakeholders. To that end, the proposed model resembles a closed-loop information flow model for the agriculture supply chain.

The closed-loop information flow model receives user inputs, feedback, suggestions, and requirements through the 'Govi-Nena' mobile application. The CIFM derives real-time and past time-series data from the 'Govi-Nena' Knowledgebase to make necessary predictions required by the proposed prediction models. The predicted data will be sent back to the 'Govi-Nena' Knowledgebase for further processing. The processed data will be distributed to the corresponding end-users through the designed user interfaces based on their need.

In return, user actions will be restored in the 'Govi-Nena' Knowledgebase for further processing (Supplementary Figure 28). The proposed model will only provide information for the stakeholders to make their own decisions. The accuracy level of the proposed model will be provided, and hence it will aid the

stakeholders when making their decisions at minimum risk. Though the usability of the proposed user interfaces was evaluated during the initial field studies, complete validation of the proposed model is yet to be carried out. The accuracy of the proposed model was limited due to the lack of available data for predictions. However, we claim that the required data for predictions will be available when users start using the model through the ‘Govi-Nena’ mobile app. The challenge faced in designing the proposed solution due to the lack of technology awareness among the stakeholders was achieved through designing user-friendly interfaces. Based on the user survey, it was evident that most stakeholders were willing to use this digital agricultural model to fulfill their information needs.

Future work

The designed prototypes will be evaluated further using the stakeholders for further improvements.

Acknowledgement

This research was supported by the Accelerating Higher Education Expansion and Development (AHEAD) Operation of the Ministry of Higher Education, funded by the World Bank. The authors express their profound gratitude to the Peradeniya Socio-Economic and Planning Center officials in the Department of Agriculture, Uva Provincial Department of Agriculture, Agriculture Research and Development Centre - Seetha Eliya. Furthermore, we would like to express our sincere gratitude for the wholehearted support from the Agriculture Instructors and Farmers in Badulla, Nuwara Eliya, and Jaffna districts.

REFERENCES

- Abraham N. (2011). The apparel aftermarket in India – a case study focusing on reverse logistics. *Journal of Fashion Marketing and Management* **15**(2): 211–227.
DOI: <https://doi.org/10.1108/13612021111132645>
- Almató M., Sanmartí E., Espuña A. & Puigjaner L. (1999). Economic optimization of the water reuse network in batch process industries. *Computers and Chemical Engineering* **23**: S153–S156.
DOI: [https://doi.org/10.1016/S0098-1354\(99\)80038-6](https://doi.org/10.1016/S0098-1354(99)80038-6)
- Amin S.H., Zhang G. & Eldali M.N. (2020). A review of closed-loop supply chain models. *Journal of Data Information and Management* **2**: 279–307.
DOI: <https://doi.org/10.1007/s42488-020-00034-y>
- Ashby A., Leat M. & Hudson-Smith M. (2012). Making connections: a review of supply chain management and sustainability literature. *Supply Chain Management* **17**(5): 497–516.
- Banasik A., Kanellopoulos A., Claassen G.D.H., Bloemhof-Ruwaard J.M., Jack G.A.J. & van der Vorst (2017). Closing loops in agricultural supply chains using multi-objective optimization: A case study of an industrial mushroom supply chain. *International Journal of Production Economics* **183**(B): 409–420.
DOI: <https://doi.org/10.1016/j.ijpe.2016.08.012>
- Barros M.C., Bello P.M., Bao M. & Torrado J.J. (2009). From waste to commodity: transforming shells into high purity calcium carbonate. *Journal of Cleaner Production* **17**(3): 400–407.
DOI: <https://doi.org/10.1016/j.jclepro.2008.08.013>
- Basnayake B.M.A.L. & Rajapakse C. (2019). A Blockchain-based decentralized system to ensure the transparency of organic food supply chain. *Proceedings of the 2019 International Research Conference on Smart Computing and Systems Engineering (SCSE)*, 28–28 March, Colombo, Sri Lanka, pp. 103–107.
DOI: <https://doi.org/10.23919/SCSE.2019.8842690>
- Beumer K. & Edelenbosch R. (2019). Hybrid potato breeding: A framework for mapping contested socio-technical futures. *Futures* **109**: 227–239.
DOI: <https://doi.org/10.1016/j.futures.2019.01.004>
- Boin U.M.J. & Bertram M. (2005). Melting standardized aluminum scrap: A mass balance model for Europe. *JOM* **57**: 26–33
DOI: <https://doi.org/10.1007/s11837-005-0164-4>
- Canziba E. (2018). *Hands-On UX Design for Developers: Design, Prototype, and Implement Compelling User Experiences from Scratch*. pp. 7–291. Packt Publishing Ltd., Birmingham, UK.
- Cheraghalipour A., Paydar M.M. & Hajiaghaci-Keshteli M. (2018). A bi-objective optimization for citrus closed-loop supply chain using Pareto-based algorithms. *Applied Soft Computing* **69**: 33–59.
DOI: <https://doi.org/10.1016/j.asoc.2018.04.022>
- De Silva L.N.C., Goonetillake J.S., Wikramanayake G.N. & Ginige A. (2012). Towards using ICT to enhance flow of information to aid farmer sustainability in Sri Lanka, *Proceedings of the 23rd Australasian Conference on Information Systems (ACIS)*, Geelong, Australia, pp 1–10.
- Debo L.G., Savaskan R.C. & Wassenhove L.N.V. (2004). Coordination in closed-loop supply chains. In: *Reverse Logistics* (eds. R. Dekker, M. Fleischmann, K. Inderfurth & L.N. Van Wassenhove), pp 295–311. Springer, Berlin, Germany.
DOI: https://doi.org/10.1007/978-3-540-24803-3_12
- Department of Census and Statistics (2018). *Estimated Extent and Production of Potato (Solanum tuberosum)*. Agriculture and Environment Statistics Division, Department of Census and Statistics, Colombo, Sri Lanka.
- Ene S. & Öztürk N. (2014). Open loop reverse supply chain network design. *Procedia - Social and Behavioral Sciences* **109**: 1110–1115.
DOI: <https://doi.org/10.1016/j.sbspro.2013.12.596>
- Fodor N. & Kovács G.J. (2005). Sensitivity of crop models to the inaccuracy of meteorological observations. *Physics and Chemistry of the Earth* **30**(1–3): 53–57.
DOI: <https://doi.org/10.1016/j.pce.2004.08.020>

- Ginige A. (2018). Systems Engineering approach to smart computing: From farmer empowerment to achieving sustainable development goals. In: *International Conference on Smart Computing and Systems Engineering*. Department of Industrial Management, Faculty of Science, University of Kelaniya, Sri Lanka.
- Giovanni D.P., Romano M., Sebillo M., Tortora G., Vitiello G., Ginige T., De Silva L., Goonethilaka J., Wikramanayake G. & Ginige A. (2012). User centered scenario based approach for developing mobile interfaces for Social Life Networks. *Proceedings of the 1st International Workshop on Usability and Accessibility Focused Requirements Engineering (UsARE)*, 4 June. Zurich, Switzerland, pp. 18–24. DOI: <https://doi.org/10.1109/UsARE.2012.6226785>
- Giovanni D.P., Romano M., Sebillo M., Tortora G., Vitiello G., Ginige T., De Silva L., Goonethilaka J., Wikramanayake G. & Ginige A. (2013). Building social life networks through mobile interfaces: the case study of Sri Lanka farmers. In: *Organizational Change and Information Systems. Lecture Notes in Information Systems and Organisation* (ed. P. Spagnoletti), volume 2. Springer, Berlin, Germany. DOI: https://doi.org/10.1007/978-3-642-37228-5_39
- Hansen J.W. & Jones J.W. (2000). Scaling-up crop models for climate variability applications. *Agricultural Systems* **65**(1): 43–72. DOI: [https://doi.org/10.1016/S0308-521X\(00\)00025-1](https://doi.org/10.1016/S0308-521X(00)00025-1)
- Heimgärtner R., Solanki A. & Windl H. (2017). Cultural user experience in the car—toward a standardized systematic intercultural agile automotive UI/UX design process. In: *Automotive User Interfaces. Human–Computer Interaction Series* (eds. G. Meixner & C. Müller), Springer, Cham, Switzerland. DOI: https://doi.org/10.1007/978-3-319-49448-7_6
- Hevner A.R. (2007). A three cycle view of design science research. *Scandinavian Journal of Information Systems* **19**(2): 86–92.
- Hoogenboom G. (2000). Contribution of agrometeorology to the simulation of crop production and its applications. *Agricultural and Forest Meteorology* **103**(1–2): 137–157. DOI: [https://doi.org/10.1016/S0168-1923\(00\)00108-8](https://doi.org/10.1016/S0168-1923(00)00108-8)
- Iqbal M.W. & Kang Y. (2021). Waste-to-energy supply chain management with energy feasibility condition. *Journal of Cleaner Production* **291**: 125231. DOI: <https://doi.org/10.1016/j.jclepro.2020.125231>
- Jabarzadeh Y., Yamchi H.R., Kumar V. & Ghaffarinasab N. (2020). A multi-objective mixed-integer linear model for sustainable fruit closed-loop supply chain network. *Management of Environmental Quality* **31**(5): 1351–1373. DOI: <https://doi.org/10.1108/MEQ-12-2019-0276>
- Kamble S.S., Gunasekaran A. & Gawankar S.A. (2020). Achieving sustainable performance in a data-driven agriculture supply chain: A review for research and applications. *International Journal of Production Economics* **219**: 179–194. DOI: <https://doi.org/10.1016/j.ijpe.2019.05.022>
- Launay M. & Guérif M. (2003). Ability for a model to predict crop production variability at the regional scale: an evaluation for sugar beet. *Agronomie* **23**(2): 135–146. DOI: <https://doi.org/10.1051/agro:2002078>
- Luthra S., Mangla S.K., Garg D. & Kumar A. (2018) Internet of Things (IoT) in agriculture supply chain management: A developing country perspective. In: *Emerging Markets from a Multidisciplinary Perspective. Advances in Theory and Practice of Emerging Markets*. Springer, Cham, Switzerland, pp. 209–220. DOI: https://doi.org/10.1007/978-3-319-75013-2_16
- Mahaliyanarachchi R.P. (2003). Market-information systems for the up-country vegetable farmers and marketers in Sri Lanka. *The Journal of Agricultural Education and Extension* **9**(1): 11–20. DOI: <https://doi.org/10.1080/13892240385300041>
- Mosallanezhad B., Hajiaghaci-Keshteli M. & Triki C. (2021). Shrimp closed-loop supply chain network design. *Soft Computing* **25**: 7399–7422. DOI: <https://doi.org/10.1007/s00500-021-05698-1>
- Nevavuori P., Narra N. & Lipping T. (2019). Crop yield prediction with deep convolutional neural networks. *Computers and Electronics in Agriculture* **163**: 104859. DOI: <https://doi.org/10.1016/j.compag.2019.104859>
- Ortiz O. et al. (14 authors) (2013). Insights into potato innovation systems in Bolivia, Ethiopia, Peru and Uganda. *Agricultural Systems* **114**: 73–83. DOI: <https://doi.org/10.1016/j.agsy.2012.08.007>
- Ozceylan E. (2016). Simultaneous optimization of closed- and open-loop supply chain networks with common components. *Journal of Manufacturing Systems* **41**: 143–156. DOI: <https://doi.org/10.1016/j.jmsy.2016.08.008>
- Ruß G., Kruse R., Schneider M. & Wagner P. (2008). Data mining with neural networks for wheat yield prediction. in: advances in data mining. medical applications, e-commerce, marketing, and theoretical aspects. In: *Industrial Conference on Data Mining 2008* (ed. P. Perner), volume 5077. Springer, Berlin, Germany. DOI: https://doi.org/10.1007/978-3-540-70720-2_4
- Russell G. & Van Gardingen P.R. (1997). Problems with using models to predict regional crop production. In: *Scaling Up: from Cell to Landscape* (eds. P.R.V. Gardingen, M. Foody & P. Curran), pp. 273–294. Cambridge University Press, Cambridge, UK.
- Salehi-Amiri A., Zahedi A., Akbapour N. & Hajiaghaci-Keshteli M. (2021). Designing a sustainable closed-loop supply chain network for walnut industry. *Renewable and Sustainable Energy Reviews* **141**: 110821. DOI: <https://doi.org/10.1016/j.rser.2021.110821>
- Schwalbert R.A., Amado T., Corassa G., Pott L.P., Prasad P.V. & Ciampitti I.A. (2020). Satellite-based soybean yield forecast: Integrating machine learning and weather data for improving crop yield prediction in southern Brazil. *Agricultural and Forest Meteorology* **284**: 107886. DOI: <https://doi.org/10.1016/j.agrformet.2019.107886>
- Soltani A., Meinke H. & de Voil P. (2004). Assessing linear interpolation to generate daily radiation and temperature data for use in crop simulations. *European Journal of Agronomy* **21**(2): 133–148. DOI: [https://doi.org/10.1016/S1161-0301\(03\)00044-3](https://doi.org/10.1016/S1161-0301(03)00044-3)

- Stevens G.C. (1989). Integrating the supply chain. *International Journal of Physical Distribution and Materials Management* **19**(8): 3–8.
DOI: <https://doi.org/10.1108/EUM00000000000329>
- Struik P.C. (2006). Trends in agricultural science with special reference to research and development in the potato sector. *Potato Research* **49**: 5–18.
DOI: <https://doi.org/10.1007/s11540-006-9000-7>
- Tedesco-Oliveira D., Da Silva R.P., Maldonado Jr W. & Zerbatto C. (2020). Convolutional neural networks in predicting cotton yield from images of commercial fields. *Computers and Electronics in Agriculture* **171**: 105307.
DOI: <https://doi.org/10.1016/j.compag.2020.105307>
- Yu F., Ruel L., Tyler R., Xu Q., Cui H., Karanasios S., Nguyen B.X., Keilbach A. & Mostafa J. (2020). Innovative UX methods for information access based on interdisciplinary approaches: practical lessons from academia and industry. *Data and Information Management* **4**(1): 74–80.
DOI: <https://doi.org/10.2478/dim-2020-0004>
- Yuanjie H. (2017). Supply risk sharing in a closed-loop supply chain. *International Journal of Production Economics* **183**: 39–52.
DOI: <http://dx.doi.org/10.1016/j.ijpe.2016.10.012>
- Zeballos L.J., Méndez C.A., Barbosa-Povoa A.P. & Novais A.Q. (2014). Multi-period design and planning of closed-loop supply chains with uncertain supply and demand. *Computers and Chemical Engineering* **66**: 151–164.
DOI: <https://doi.org/10.1016/j.compchemeng.2014.02.027>
- Zhang Y., Wang L. & Duan Y. (2016). Agricultural information dissemination using ICTs: A review and analysis of information dissemination models in China. *Information Processing in Agriculture* **3**(1): 17–29.
DOI: <https://doi.org/10.1016/j.inpa.2015.11.002>
- Zhao R., Liu Y., Zhang Z., Guo S., Tseng M.-L. & Wu K.-J. (2018). Enhancing eco-efficiency of agro-products' closed-loop supply chain under the belt and road initiatives: a system dynamics approach. *Sustainability* **10**(3): 668.
DOI: <https://doi.org/10.3390/su10030668>

List of Referees - Volume 50 (2022)

Prof. Charmalie Abayasekera Dept. of Botany Univ. of Peradeniya	Dr Ravimal Bandara Dept. of Computer Science Univ. of Sri Jayewardenepura	Prof. A Deepananda Dept. of Fisheries & Aquaculture Univ. of Ruhuna
Prof. AM Abeysekera Univ. of Sri Jayewardenepura	Prof. Chalinda Beneragama Dept. of Crop Science Univ. of Peradeniya	Prof. Nelum Deshapriya Dept. of Botany Univ. of Sri Jayewardenepura
Dr WKSAM Abeysekera Dept. of Agricultural Technology Univ. of Colombo	Dr Muhammad Bilal Univ. of Veterinary & Animal Sciences Pakistan	Prof. Eleonora Desnica Dept. for Production Engineering Univ. of Novi Sad, Serbia
Dr Sumith Abeysiriwardene CIC Agribusiness Pelwehera, Dambulla	Dr Mangala Bopagoda Dept. of Pathology Univ. of Kelaniya	Prof. Saman Dharmakeerthi Dept. of Soil Science Univ. of Peradeniya
Dr Hemalika Abeysundara Dept. of Statistics & Computer Science Univ. of Peradeniya	Prof. Upali Chandrasekara Dept. of Zoology & Environmental Management Univ. of Kelaniya	Prof. Gihan Dias Dept. of Computer Science & Engineering Univ. of Moratuwa
Prof. W Abeywickreme Dept. of Para Clinical Sciences General Sir John Kotelawala Defence University	Prof. SDM Chinthaka Dept. of Chemistry Univ. of Sri Jayewardenepura	Prof. MAKL Dissanayake National Institute of Fundamental Studies, Kandy
Dr AMMN Adikaram Dept. of Physical Science South Eastern Univ. of Sri Lanka	Dr DDGL Dahanayake Dept. of Zoology The Open Univ. of Sri Lanka	Prof. Jayanthi Edirisinghe Dept. of Zoology Univ. of Peradeniya
Dr Senaka Amarakeerthi Dept. of Information & Communication Technology Univ. of Sri Jayewardenepura	Prof. NDK Dayawansa Dept. of Agricultural Engineering Univ. of Peradeniya	Prof. JB Ekanayake Dept. of Electrical & Electronic Engineering Univ. of Peradeniya
Prof. Padma Amarasinghe Dept. of Chemical & Process Engineering Univ. of Moratuwa	Dr Kaushika De Silva Dept. of Mathematics Univ. of Sri Jayewardenepura	Prof. UPK Epa Dept. of Zoology & Environmental Management Univ. of Kelaniya
Prof. US Amarasinghe Dept. of Zoology & Environmental Management Univ. of Kelaniya	Prof. KM Nalin De Silva Dept. of Chemistry Univ. of Colombo	Dr BPW Fernando Dept. of Mathematics Univ. of Sri Jayewardenepura
Dr Yannis Assael Google DeepMind, UK	Dr LIN de Silva Dept. of Civil Engineering Univ. of Moratuwa	Dr Eustace Y Fernando Dept. of Biological Sciences Rajarata Univ. of Sri Lanka
Dr AMRG Athapaththu Dept. of Civil Engineering Univ. of Peradeniya	Prof. Mangala CS de Silva Dept. of Zoology Univ. of Ruhuna	Dr PLN Fernando Dept. of Civil Engineering Univ. of Moratuwa
Prof. Bandunee Athapaththu Dept. of Civil Engineering The Open Univ. of Sri Lanka	Prof. MPKSK De Silva Dept. of Zoology Univ. of Ruhuna	Dr T Nilanthi Fernando National Engineering Research & Development Centre (NERD)
Dr Sarangi Athukorala Dept. of Botany Univ. of Peradeniya	Prof. Priyanka de Silva Dept. of Zoology Univ. of Peradeniya	Dr Naleen Ganegoda Dept. of Mathematics Univ. of Sri Jayewardenepura
Prof. Renuka Attanayake Dept. of Plant & Molecular Biology Univ. of Kelaniya	Prof. Ranjith Premalal de Silva Univ. of vocational Technology Ratmalana	Dr DR Gimhani Dept. of Biotechnology Wayamba Univ. of Sri Lanka
Dr Dilum Bandara Dept. of Computer Science & Engineering, Univ. of Moratuwa	Prof. Sudhira de Silva Dept. of Civil & Environment Engineering, Univ. of Ruhuna	Prof. KB Gunaherath The Open Univ. of Sri Lanka

- Prof. MHJP Gunarathna
Dept. of Agricultural Engineering & Soil Science
Rajarata Univ. of Sri Lanka
- Dr Duleeka Gunaratne
Dept. of Chemical & Process Engineering
Univ. of Moratuwa
- Dr Banuri Gunasekera
Dept. of Immunology & Molecular Medicine
Univ. of Sri Jayewardenepura
- Dr Thilini Gunasekera
Dept. of Polymer Science
Univ. of Sri Jayewardenepura
- Dr Sameera R Gunatilake
Institute of Chemistry Ceylon
- Prof. Sampath Hemakumara
Dept. of Geography
Univ. of Ruhuna
- Dr HMLNK Herath
Dept. of Computer Science
Kandy Regional Center
The Open Univ. of Sri Lanka
- Prof. HMVR Herath
Dept. of Electrical & Electronic Engineering
Univ. of Peradeniya
- Dr Manjula Hettiarachchi
Nuclear Medicine Unit
Univ. of Ruhuna
- Prof. Sanath Hettiarachchi
Dept. of Biological Science
Rajarata Univ. of Sri Lanka
- Prof. Ruwani Hewawasam
Dept. of Biochemistry
Univ. of Ruhuna
- Prof. OA Ileperuma
Dept. of Chemistry
Univ. of Peradeniya
- Prof. Leslie Jayasekera
Dept. of Mathematics
Univ. of Ruhuna
- Dr Chathuri Jayasinghe
Dept. of Statistics
Univ. of Sri Jayewardenepura
- Prof. CVL Jayasinghe
Dept. of Food Science & Technology
Wayamba Univ. of Sri Lanka
- Prof. Lalith Jayasinghe
National Institute of Fundamental Studies,
Kandy
- Dr Susanthi Jayasinghe
Dept. of Chemistry
Univ. of Peradeniya
- Dr Himali Jayasinghearachchi
General Sir John Kotelawala Defence University
- Prof. Thusitha Jayasooriya
7/21, Second Lane, Nawala
Rajagiriya
- Dr Yashika Jayathunga
Dept. of Mathematics
Univ. of Colombo
- Dr Daham Jayawardana
Dept. of Forestry & Environmental Science
Univ. of Sri Jayewardenepura
- Prof. BPA Jayaweera
Faculty of Livestock, Fisheries & Nutrition
Wayamba Univ. of Sri Lanka
- Prof. Mahesh Jayaweera
Dept. of Civil Engineering
Univ. of Moratuwa
- Mr Priyantha Jinadasa
Dept. of Marine Engineering
Ocean Univ. of Sri Lanka
- Dr HK Kadupitiya
Natural Resource Management Center
Dept. of Agriculture
- Prof. Shahid Kamal
Univ. of Faisalabad
Pakistan
- Dr Achala Kamaladasa
Dept. of Immunology & Molecular Medicine
Univ. of Sri Jayewardenepura
- Dr Chandima Kamaral
Univ. of Southern Queensland
Australia
- Dr Makan Karegar
Institute of Geodesy & Geoinformation
Univ. of Bonn, Germany
- Dr IU Kariyawasam
Dept. of Botany
Univ. of Sri Jayewardenepura
- Dr PAK Karunananda
Dept. of Civil Engineering
The Open Univ. of Sri Lanka
- Prof. Laleen Karunanayake
Dept. of Chemistry
Univ. of Sri Jayewardenepura
- Prof. Inoka Karunaratne
Dept. of Zoology
Univ. of Peradeniya
- Prof. Nedra Karunaratne
Dept. of Chemistry
Univ. of Peradeniya
- Prof. HS Kaththirarachchi
Dept. of Plant Sciences
Univ. of Colombo
- Dr MN Kaumal
Dept. of Chemistry
Univ. of Colombo
- Dr Manjit Kaur
Gwangju Institute of Science & Technology
South Korea
- Dr B Prabhu Kavin
Sri Ramachandra Institute of Higher Education & Research, India
- Prof. Peter E Kloeden
Univ. of Tubingen
Germany
- Prof. KAS Kodikara
Dept. of Botany
Univ. of Ruhuna
- Dr K Komathiraj
Dept. of Mathematical Sciences
South Eastern Univ. of Sri Lanka
- Dr Achintha I. Kondarage
Dept. of Electrical and Information Engineering
University of Ruhuna
- Prof. Enoka Kudavidanage
Dept. of Natural Resources
Sabaragamuwa Univ. of Sri Lanka
- Prof. Sunil Kulatunga
Dept. of Radiography/Radiotherapy
Univ. of Peradeniya
- Prof. KL Wasantha Kumara
Dept. of Plant Pathology
Univ. of Ruhuna
- Dr WGCW Kumara
Dept. of Computer Science & Engineering
South Eastern Univ. of Sri Lanka
- Dr Chandana Kurukulasuriya
Dept. of Civil Engineering
Univ. of Peradeniya
- Prof. Yury Kuznetsov
Orel State Agrarian University
Russia
- Prof. WDG Lakmini
Dept. of Crop Science
Univ. of Ruhuna
- Dr G.H. Jayantha Lanel
Dept. of Mathematics
Univ. of Sri Jayewardenepura
- Dr Rukshani Liyanaarachchi
Dept. of Electronic & Telecommunication Engineering
Univ. of Moratuwa

- Prof. Kalana Maduwage
Dept. of Biochemistry
Univ. of Peradeniya
- Prof. Dhammika Magana-Arachchi
National Institute of Fundamental Studies,
Kandy
- Prof. KRR Mahanama
Dept. of Chemistry
Univ. of Colombo
- Prof. Mohd Razali Mahmud
Faculty of Built Environment & Surveying
University Technology Malaysia
- Prof. Pathmalal M. Manage
Dept. of Zoology
Univ. of Sri Jayewardenepura
- Prof. Jagath Manatunge
Dept. of Civil Engineering
Univ. of Moratuwa
- Dr Amani Mannakkara
Dept. of Agricultural Biology
Univ. of Ruhuna
- Prof. G Mikunthan
Dept. of Agricultural Biology
Univ. of Jaffna
- Dr Wajira U Mirihanage
School of Materials
The Univ. of Manchester, UK
- Dr Krishna Kumar Mohbey
Dept. of Computer Science
Central Univ. of Rajasthan
India
- Prof. AM Muzathik
Dept. of Mechanical Engineering
South Eastern Univ. of Sri Lanka
- Prof. Mayuri Napagoda
Dept. of Biochemistry
Univ. of Ruhuna
- Prof. M Narayana
Dept. of Chemical & Process Engineering
Univ. of Moratuwa
- Prof. SB Navarathne
Dept. of Food Science & Technology
Univ. of Sri Jayewardenepura
- Dr L Nugaliyadda
Dept. of Agricultural Biology
Univ. of Ruhuna
- Dr Hanieh Panahi
Dept. of Mathematics & Statistics
Islamic Azad University, Iran
- Prof. Priyani Paranagama
Dept. of Chemistry
Univ. of Kelaniya
- Prof. Asoka Pathiratne
Dept. of Zoology & Environmental
Management
Univ. of Kelaniya
- Prof. Sriyani Peiris
Sri Lanka Institute of Information
Technology (SLIIT)
- Dr Serhat Peker
Dept. of Management & Information
Systems
Bakircay University, Turkey
- Dr BBP Perera
Arecibo Observatory
Puerto Rico
- Prof. Inoka C Perera
Dept. of Zoology & Environment Sciences
Univ. of Colombo
- Prof. Jennifer Perera
Dept. of Medical Microbiology &
Immunology
Univ. of Colombo
- Prof. Priyan Perera
Dept. of Forestry & Environmental Science
Univ. of Sri Jayewardenepura
- Ms Rashindrie Perera
Dept. of Mechanical Engineering
The Univ. of Melbourne, Australia
- Prof. SACN Perera
Dept. of Agricultural Biology
Univ. of Peradeniya
- Ms Deshani Poddenige
Dept. of Mechanical Engineering
The Univ. of Melbourne, Australia
- Prof. Rohitha Prasantha
Dept. of Food Science
Univ. of Peradeniya
- Dr Nadeej Priyankara
Dept. of Civil Engineering
Univ. of Ruhuna
- Prof. Namal Priyantha
Dept. of Chemistry
Univ. of Peradeniya
- Prof. Nimal Punyasiri
Institute of Biochemistry, Molecular Biology
and Biotechnology
- Dr Milan Radenković
Dept. of Production Engineering
The Academy of Applied Studies Šumadija,
Serbia
- Dr RPNP Rajapakse
Dept. of Food Science
Univ. of Peradeniya
- Dr N Ramaruban
Dept. of Mathematics & Statistics
Univ. of Jaffna
- Prof. Manjula Ranagalage
Dept. of Environmental Management
Rajarata Univ. of Sri Lanka
- Mr Nisal Ranasinghe
Dept. of Mechanical Engineering
The Univ. of Melbourne, Australia
- Dr Surangika Ranathunga
Dept. of Computer Science & Engineering
Univ. of Moratuwa
- Prof. NP Ranathunge
Dept. of Agricultural Biology
Univ. of Ruhuna
- Prof. AL Ranawake
Dept. of Agricultural Biology
Univ. of Ruhuna
- Prof. KKDS Ranaweera
Dept. of Food Science & Technology
Univ. of Sri Jayewardenepura
- Dr Ruwan Ranaweera
Dept. of Electrical & Electronic Engineering
Univ. of Peradeniya
- Prof. Anura Ratnayake
Dept. of Agricultural Engineering
Univ. of Arkansas, USA
- Dr K Raveenthiran
Lanka Hydraulic Institute Ltd.
Moratuwa
- Prof. P Ravirajan
Dept. of Physics
Univ. of Jaffna
- Prof. Upali Samarajeewa
Dept. of Food Science & Technology
Univ. of Peradeniya
- Dr Jayantha Senanayake
Rice Research & Development Institute
Batalagoda
- Dr Tharindu Senapathi
Dept. of Chemistry
Univ. of Sri Jayewardenepura
- Prof. Athula Senaratne
Dept. of Geology
Univ. of Peradeniya
- Prof. Rohini Seneviratne
Dept. of Paraclinical Sciences
General Sir John Kotelawala Defence
University
- Prof. Sampath Seneviratne
Dept. of Zoology & Environment Sciences
Univ. of Colombo

Dr Samir Shrestha
Dept. of Mathematics
Kathmandu University, Nepal

Dr Nirmala D. Sirisena
Dept. of Anatomy
Univ. of Colombo

Dr Harsha Sooriyaarachchi
Dept. of Civil & Environment Engineering
Univ. of Ruhuna

Prof. Roshini Sooriyarachchi
Dept. of Statistics
Univ. of Colombo

Dr LKT Srimal
Dept. of Mechanical & Manufacturing
Engineering
Univ. of Ruhuna

Prof. KAS Susantha
Dept. of Engineering Mathematics
Univ. of Peradeniya

Prof. WL Sumathipala
Rajamahavihara Road
Pitakotte

Prof. DA Tantrigoda
Univ. of Sri Jayewardenepura

Dr Jitendra V Tembhumne
Indian Institute of Information Technology
Nagpur, India

Dr Mayuri Thammitiyagodage
Medical Research Institute
Colombo 08

Dr UGIGK Udagedara
Dept. of Mathematics
Univ. of Peradeniya

Dr Ruwan Udayanga
Dept. of Electronic & Telecommunication
Engineering
Univ. of Moratuwa

Prof. RJM Uduporuwa
Dept. of Geography & Environmental
Management
Sabaragamuwa Univ. of Sri Lanka

Prof. KP Vidanapathirana
Dept. of Electronics
Wayamba Univ. of Sri Lanka

Prof. Shantha Walpalage
Dept. of Chemical & Process Engineering
Univ. of Moratuwa

Prof. BC Walpola
Dept. of Soil Science
Univ. of Ruhuna

Dr SK Wasala
Department of Agriculture
Peradeniya

Prof. WAP Weerakkody
Dept. of Crop Science
Univ. of Peradeniya

Dr Laksiri Weerasinghe
Dept. of Chemistry
Univ. of Sri Jayewardenepura

Dr Ruwan Weerasinghe
Univ. of Colombo School of Computing

Prof. Rohan Weerasooriya
National Institute of Fundamental Studies,
Kandy

Prof. HCE Wegiriya
Dept. of Zoology
Univ. of Ruhuna

Prof. Jayantha Welihinda
Institute of Chemistry Ceylon

Dr Sampath Weragoda
Dept. of Materials Science & Engineering
Univ. of Moratuwa

Dr HM Wijekoon Banda
Ceylon Electricity Board

Dr Udaya Wijenayake
Dept. of Computer Engineering
Univ. of Sri Jayewardenepura

Prof. Mayuri R Wijesinghe
Dept. of Zoology & Environment Sciences
Univ. of Colombo

Prof. Priyanga Wijesinghe
Dept. of Botany
Univ. of Peradeniya

Prof. JJ Wijetunge
Dept. of Civil Engineering
Univ. of Ruhuna

Prof. LCR Wijewardhana
Univ. of Cincinnati
USA

Prof. Dimuthu Wijeyaratne
Dept. of Zoology & Environmental
Management
Univ. of Kelaniya

Dr Shanthi Wilson
10A, 1/1, Skelton Road
Colombo - 05

Prof. GDSP Wimalaratne
Univ. of Colombo School of Computing

Prof. Deepthi Yakandawala
Dept. of Botany
Univ. of Peradeniya

Abayasekara CL *see* Rangama BNLD *et al.* (2022)

Abbas N *see* Rasheed H *et al.* (2022)

Abeyratne MK *see* Pathirana G *et al.* (2022)

Abey Siri HASN, Wanigasuriya JKP, Suresh TS, Beneragama DH & Manage PM - Effect of cylindrospermopsin on the hepatotoxicity in wistar rats **50**: 595-605 (2022)

Abey Sundara SP *see* Shashiprabha HED *et al.* (2022)

Abo-Elfadl MT *see* Gamal-Eldeen AM *et al.* (2022)

Alakus K *see* Dündler E *et al.* (2022)

Ali MRK *see* Gamal-Eldeen AM *et al.* (2022)

Al-Turk LI *see* Darwish JA *et al.* (2022)

Amarasinghe US, Pushpalatha KBC & Wijenayake WMHK - New paradigm for inland fisheries development in Sri Lanka: a transdisciplinary approach for addressing food and nutritional security **50**: 177-194 (2022)

Andrew MS *see* Gamage TS *et al.* (2022)

Ariyaratna HACK *see* Shashiprabha HED *et al.* (2022)

Ariyasinghe M *see* Dampage U & Ariyasinghe M (2022)

Aslam F *see* Yousaf K *et al.* (2022)

Attygalla E *see* Ilangarathna G *et al.* (2022)

Balqees K *see* Yousaf K *et al.* (2022)

Bandara JMSJ *see* Jayasooriya NK *et al.* (2022)

Bandarathilake HMDP, Palamakumbura GWRMR & Maithripala DHS - A coupled system of stochastic differential equations for probabilistic wind speed modelling **50**: 613-623 (2022)

Bashir R *see* Yousaf K *et al.* (2022)

Basnayake S *see* Gamage TD *et al.* (2022)

Beneragama DH *see* Abey Siri HASN *et al.* (2022)

Borosova R *see* Tennakoon TMSG *et al.* (2022)

Cannata M *see* Warusavitharana E *et al.* (2022)

Cengiz MA *see* Dündler E *et al.* (2022)

Ch'ng Y-K *see* Nisar H *et al.* (2022)

Chandrajith R & Diyabalanage S - Geo-environmental assessment of geochemistry of groundwater and associated human health risks in the dry zone terrain of Sri Lanka **50**: 213-229 (2022)

Chandramali DVP *see* Ranawceera NI *et al.* (2022)

Chandranimal D *see* Perera SJ *et al.* (2022)

Chandrasekara A *see* Gnanarathna KADC *et al.* (2022)

Chen G *see* Pathirana G *et al.* (2022)

Cooray AT *see* Koliyabandara PA *et al.* (2022)

Dampage U & Ariyasinghe M - Novel nebulizer design with adaptive flow regulation **50**: 101-109 (2022)

- Dar IS *see* Rasheed H *et al.* (2022)
- Darwish JA, Al-Turk LI & Shahbaz MQ - A new multivariate transmuted family of distributions: theory and application for modelling of daily world COVID-19 cases **50**: 771-784 (2022)
- de Silva AP *see* Yao CY & de Silva AP (2022)
- De Silva I *see* Manimendra A *et al.* (2022)
- De Silva L *see* Mallikaarachchi TB *et al.* (2022)
- De Silva S *see* Ranasinghe K & De Silva S (2022)
- De Silva T *see* Tennakoon TMSG *et al.* (2022)
- de Silva V & Eeswara JP - Induction of somatic embryogenesis from leaf explants of *Exacum trinervium* (L.) Druce (Binara) **50**: 27-33 (2022)
- de Vos A *see* Pattiaratchi CB *et al.* (2022)
- Dharmapala RMAU, Satharasinghe DM, Silva SPI & Jeyasugithan J - Determination of safe zone of the mandible for implant and bone harvesting (using CBCT) of mandible in a group of Sri Lankan subjects **50**: 65-72 (2022)
- Dharmaratne HRW *see* Haniffa HM *et al.* (2022)
- Dharmaratne S *see* Ilangarathna G *et al.* (2022)
- Dihovicni D, Mišćević M, Kovačević NR & Kreculj D - Implementation of a fuzzy logic approach for a smart production system **50**: 695-703 (2022)
- Dissanayake CSB & Wijesooriya UD - On the construction of unitaries representing minimal inner toral polynomials **50**: 607-611 (2022)
- Diyabalanage S *see* Chandrajith R & Diyabalanage S (2022)
- Dolatabadian A *see* Fernando WGD & Dolatabadian A (2022)
- Dünder E, Zaman T, Cengiz MA & Alakus K - Implementation of adaptive lasso regression based on multiple Theil-Sen Estimators using differential evolution algorithm with heavy tailed errors **50**: 395-404 (2022)
- Edirisinghe DG *see* Sampath WDM *et al.* (2022)
- Ediriweera A *see* Perera SJ *et al.* (2022)
- Ediriweera S, Jayarathna PB, Samarasinghe R & Lucas R - Fractal characteristics of creeping discharges propagating on nano-epoxy composite insulators immersed in coconut oil **50**: 663-673 (2022)
- Ediriweera S, Jayarathna PB, Samarasinghe R & Lucas R - Investigation of oil level and type of solid insulator on creeping discharges propagating under an AC electric field **50**: 725-732 (2022)
- Edwards S *see* Tennakoon TMSG *et al.* (2022)
- Eeswara JP *see* de Silva V & Eeswara JP (2022)
- Ekanayake J *see* Ilangarathna G *et al.* (2022)
- Ekanayake P *see* Ilangarathna G *et al.* (2022)
- Ekanayake P, Panahatipola O & Jayasinghe J - Development of wind energy prediction models using statistical, machine learning and hybrid techniques: a case study **50**: 489-502 (2022)
- Ekanayake SY *see* Ilangarathna G *et al.* (2022)
- Ekaratne K *see* Perera SJ *et al.* (2022)
- Elango P *see* Jude TP *et al.* (2022)
- El-Daly SM *see* Gamal-Eldeen AM *et al.* (2022)
- Escudie R *see* Wickramaarachchi AL *et al.* (2022)

Fahmy CA *see* Gamal-Eldeen AM *et al.* (2022)

Fernando CAN *see* Sampath WDM *et al.* (2022)

Fernando GVAR *see* Walpita SC *et al.* (2022)

Fernando IPS *see* Jayawardena TU *et al.* (2022)

Fernando S *see* Ranasinghe N *et al.* (2022)

Fernando TSP *see* Ranasinghe RPTI *et al.* (2022)

Fernando WGD & Dolatabadian A - Microbiome: diversity, distribution, and potential role in sustainable crop production **50**: 231-250 (2022)

Gamage P *see* Premarathna WAAS *et al.* (2022)

Gamage TD, Sonnadara U, Jayasinghe S & Basnayake S - Forecasting the track and the intensity of the cyclone Burevi using WRF **50**: 675-684 (2022)

Gamage TS, Mutucumarana RK & Andrew MS - Influence of different bone meal particle size induced calcium specific appetite on performance and egg quality parameters of layer chickens **50**: 745-754 (2022)

Gamalath KAIL *see* Wijewardhana CNT & Gamalath KAIL (2022)

Gamal-Eldeen AM, Raafat BM, Fahmy CA, Abo-Elfadl MT, El-Daly SM & Ali MRK - Effect of PEGylated gold nanorods on the circulating vascular endothelial growth factor, platelet-derived growth factor, and miR-29a in CD-1 mice **50**: 467-475 (2022)

Ganapathy S *see* Ramasamy-Rajeswari A *et al.* (2022)

Gnanarathna KADC, Jayasumama MTLK, Weragama KWDP, Gunasekara DCS, Weerasingha WVVR, Chandrasekara A & Prasanna PHP - Physicochemical and sensory attributes of inulin incorporated set yoghurt prepared using cow and buffalo milk **50**: 651-661 (2022)

Gnanavelrajah N *see* Kirisan A *et al.* (2022)

Godaliyaddha R *see* Ilangarathna G *et al.* (2022)

Goonatilake de AS *see* Perera SJ *et al.* (2022)

Gordon DM *see* Rangama BNLD *et al.* (2022)

Gunaratna N *see* Tennakoon TMSG *et al.* (2022)

Gunasekara DCS *see* Gnanarathna KADC *et al.* (2022)

Gunasekera N *see* Tennakoon TMSG *et al.* (2022)

Gupta S *see* Sabir S *et al.* (2022)

Halgamuge S *see* Ranasinghe N *et al.* (2022)

Hameed PN *see* Ranasinghe N *et al.* (2022)

Hanci F - Application of Benford's law in agricultural production statistics **50**: 387-393 (2022)

Hanif M, Khattak MK, Ul Haq I, Uddin R & Ullah K - A novel approach for energy and exergy analysis of a flat plate solar collector with energy storage **50**: 151-160 (2022)

Haniffa HM, Dharmaratne HRW & Mohommad MY - Bioactive cyclo-(S-Pro-R-Leu) from *Aspergillus flavus*, the marine endophytic fungus from brown alga, *Dictyota kunthii* **50**: 717-721 (2022)

Hansika KAS, Kodikara KAS, Wijeweera AA, Senanayake G & Jayatissa LP - Vegetative and reproductive phenology of *Cinnamomum verum* J. Presl grown in intermediate climatic zone of Sri Lanka **50**: 87-99 (2022)

Herath D *see* Ranasinghe N *et al.* (2022)

Herath HMT *see* Ranaweera NI *et al.* (2022)

Herath S *see* Tennakoon TMSG *et al.* (2022)

Herath V *see* Ilangarathna G *et al.* (2022)

Idroos FS *see* Wijerathne RS *et al.* (2022)

Ilangarathna G, Weligampola H, Ranasinghe Y, Attygalla E, Godaliyaddha R, Herath V, Ekanayake P, Ekanayake SY, Pinnawela M, Dharmaratne S, Tilakaratne G & Ekanayake J - Artificial intelligence framework for threat assessment and containment for covid-19 and future epidemics while mitigating the socioeconomic impact to women, children, and underprivileged groups **50**: 251-262 (2022)

Iqbal MCM *see* Karunarathna HG MK *et al.* (2022)

Jayarathna PB *see* Ediriweera S *et al.* (2022)

Jayarathna PB *see* Ediriweera S *et al.* (2022)

Jayasinghe J *see* Ekanayake P *et al.* (2022)

Jayasinghe JASC *see* Premarathna WAAS *et al.* (2022)

Jayasinghe JASC *see* Thevega T *et al.* (2022)

Jayasinghe S *see* Gamage TD *et al.* (2022)

Jayasooriya NK, Perera HLK & Bandara JMSJ - Increasing the effectiveness of T-junctions with an innovative geometrical and phasing arrangement **50**: 73-86 (2022)

Jayasumama MTLK *see* Gnanarathna KADC *et al.* (2022)

Jayasundara R *see* Manimendra A *et al.* (2022)

Jayatissa LP *see* Hansika KAS *et al.* (2022)

Jayawardena TU, Fernando IPS, Nagahawatta DP, Wang L, Yang HW, Oh JY, Sanjeeva KKA & Jeon Y - Sonication-assisted water extract of *Dendronephthya gigantea* exhibits anti-fine dust effects; attenuation of MAPK phosphorylation in macrophages **50**: 151-160 (2022)

Jeon Y *see* Jayawardena TU *et al.* (2022)

Jeon YJ *see* Samarakoon KW *et al.* (2022)

Jeyasugiththan J *see* Dharmapala RMAU *et al.* (2022)

JR Lucas - Analysis of instantaneous, daily and monthly statistics 2017-2021 of rooftop solar energy **50**: 799-811 (2022)

Jude TP, Elango P & Koneswaran M - M-polynomial and topological indices for the anti-tuberculosis drugs **50**: 827-838 (2022)

Kannan A *see* Ramasamy-Rajeswari A *et al.* (2022)

Karunarathna HG MK, Medagama K, Wijesundara S & Iqbal MCM - Micropropagation of *Stevia rebaudiana* (Bertoni) Bertoni using nutrient water of *Cocos nucifera* var. *aurantiaca* (King coconut) as a natural growth enhancer **50**: 3-12 (2022)

Karunaratne SHPP & Surendran SN - Mosquito control: A review on the past, present and future strategies **50**: 277-292 (2022)

Khattak MK *see* Hanif M *et al.* (2022)

Kirisan A, Gnanavelrajah N & Ratnayake RR - Screening of potential aerobic denitrifying bacteria for nitrate removal from water **50**: 639-649 (2022)

Ko JY *see* Samarakoon KW *et al.* (2022)

Kodikara KAS *see* Hansika KAS *et al.* (2022)

Koliyabandara PA, Cooray AT, Liyanage S & Siriwardhana C - Characterization of landfill leachate at the Karadiyana open dumpsite, Sri Lanka, and assessment of water pollution in its vicinity **50**: 111-124 (2022)

Koneswaran M *see* Jude TP *et al.* (2022)

Kovačević NR *see* Dihovcni D *et al.* (2022)

Kreculj D *see* Dihovcni D *et al.* (2022)

Kulothungan K *see* Ramasamy-Rajeswari A *et al.* (2022)

LBD Suriyagoda - Rice production in nutrient-limited soils: Strategies for improving crop productivity and land sustainability **50**: 521-539 (2022)

Lee JH *see* Samarakoon KW *et al.* (2022)

Liyanage GY, Weerasekera MM & Manage PM - Screening and quantitative analysis of antibiotic resistance genes in hospital and aquaculture effluent in Sri Lanka as an emerging environmental contaminant **50**: 361-370 (2022)

Liyanage S *see* Koliyabandara PA *et al.* (2022)

Lucas R *see* Ediriweera S *et al.* (2022)

Lucas R *see* Ediriweera S *et al.* (2022)

Mahanama PKS *see* Warusavitharana E *et al.* (2022)

Maithripala DHS *see* Bandarathilake HMDP *et al.* (2022)

Malepathirana T *see* Ranasinghe N *et al.* (2022)

Mallikaarachchi TB, Samaraweera G, Walisadeera A, De Silva L & Munasinghe S - Designing a closed-loop information flow model in bridging the market information gap among agriculture stakeholders in Sri Lanka **50**: 881-896 (2022)

Manage PM *see* Abeysiri HASN *et al.* (2022)

Manage PM *see* Liyanage GY *et al.* (2022)

Manage PM *see* Wijerathne RS *et al.* (2022)

Manimendra A, De Silva I & Jayasundara R - Developing a model to predict the propagation of sulphide stress corrosion of steel used for petroleum pipelines **50**: 839-850 (2022)

Masakorala K *see* Wijesooriya MM *et al.* (2022)

Medagama K *see* Karunarathna HG MK *et al.* (2022)

Miščević M *see* Dihovicni D *et al.* (2022)

Mohammad MY *see* Haniffa HM *et al.* (2022)

Munasinghe S *see* Mallikaarachchi TB *et al.* (2022)

Munir N *see* Yousaf K *et al.* (2022)

Mutucumarana RK *see* Gamage TS *et al.* (2022)

Nagahawatta DP *see* Jayawardena TU *et al.* (2022)

Nanayakkara DKK *see* Raheem S & Nanayakkara DKK (2022)

Narayana M *see* Wickramaarachchi AL *et al.* (2022)

Naz S *see* Yousaf K *et al.* (2022)

Niranjan M *see* Ranasinghe N *et al.* (2022)

Nisar H, Ch'ng Y-K & Yeap KH - Non invasive automated approach for eczema lesions segmentation using colour space normalization **50**: 705-716 (2022)

Oh JY *see* Jayawardena TU *et al.* (2022)

Padumadasa C *see* Tennakoon TMSG *et al.* (2022)

Palamakumbura GWRMR *see* Bandarathilake HMDP *et al.* (2022)

Panahatipola O *see* Ekanayake P *et al.* (2022)

- Pathirana G & Priyadarshani K - Tropical cyclones in the Arabian Sea and the Bay of Bengal: comparison of environmental factors **50**: 53-64 (2022)
- Pathirana G, Chen G, Wang D, Abeyratne MK & Priyadarshana T - Anomalous propagation pathway of the Sri Lanka Dome in summer 2014 **50**: 851-861 (2022)
- Pattiaratchi CB, Wijeratne EMS & de Vos A - Ocean circulation around Sri Lanka **50**: 293-302 (2022)
- Peiris JSM - COVID-19 pandemic: lessons for global health security **50**: 315-320 (2022)
- Perera HLK *see* Jayasooriya NK *et al.* (2022)
- Perera LV *see* Perera SJ *et al.* (2022)
- Perera SJ, Perera WPN, Goonatilake de AS, Ekaratne K, Wijesinghe D, Perera LV, Chandranimal D & Ediriveera A - Assessment of marine turtle nesting habitats from Tangalle to the Kumbukkan Oya estuary in south-eastern Sri Lanka **50**: 755-769 (2022)
- Perera WPN *see* Perera SJ *et al.* (2022)
- Pinnawela M *see* Ilangarathna G *et al.* (2022)
- Pitipanaarachchi RC *see* Ranaweera NI *et al.* (2022)
- Prasanna PHP *see* Gnanarathna KADC *et al.* (2022)
- Premarathna WAAS, Jayasinghe JASC, Senanayake CD, Wijesundara KK & Gamage P - Failure prediction of solid resilient tyres due to kerb impact: A finite element modelling approach **50**: 625-637 (2022)
- Premarathne KSD *see* Sewwandi M *et al.* (2022)
- Priyadarshana T *see* Pathirana G *et al.* (2022)
- Priyadarshani K *see* Pathirana G & Priyadarshani K (2022)
- Pushpalatha KBC *see* Amarasinghe US *et al.* (2022)
- Raafat BM *see* Gamal-Eldeen AM *et al.* (2022)
- Raheem S & Nanayakkara DKK - Comparison of radioactive iodine therapy outcome and the duration of pretreatment discontinuation of carbimazole among hyperthyroid patients: a prospective study **50**: 417-423 (2022)
- Rajapakse RMG - Nanotechnology in sustainable value addition to Sri Lankan minerals **50**: 303-314 (2022)
- Rajapaksha AU *see* Sewwandi M *et al.* (2022)
- Ramanan A *see* Ranasinghe N *et al.* (2022)
- Ramasamy-Rajeswari A, Ganapathy S, Kulothungan K & Kannan A - Fuzzy based congestion detection and control algorithm for energy efficient wireless sensor network (WSN) **50**: 563-576 (2022)
- Ranasinghe K & De Silva S - Combined use of non-destructive tests, visual inspection and service life prediction to ensure the reliability of reinforced concrete water tanks **50**: 371-386 (2022)
- Ranasinghe N, Ramanan A, Fernando S, Hameed PN, Herath D, Malepathirana T, Suganthan P, Niranjana M & Halgamuge S - Interpretability and accessibility of machine learning in selected food processing, agriculture and health applications **50**: 263-276 (2022)
- Ranasinghe RPTI, Fernando TSP & Wijesinghe MR - Effects of dietary lead exposure on the call of Japanese quail (*Coturnix japonica*) hatchlings **50**: 477-487 (2022)
- Ranasinghe Y *see* Ilangarathna G *et al.* (2022)
- Ranaweera NI, Pitipanaarachchi RC, Herath HMT & Chandramali DVP - Development of vacuum-dried powder and drinking yoghurt from sour sop fruit (*Annona muricata* L.) and evaluation of their physico-chemical and functional properties **50**: 489-502 (2022)
- Rangama BNLD, Abayasekara CL & Gordon DM - Predominance of phylogenetic group B2 among commensal *Escherichia coli* in humans from Kandy District, Sri Lanka **50**: 137-150 (2022)
- Rasheed H, Dar IS, Saqib M, Abbas N & Suhail M - The odd modified Burr-III exponential distribution: properties, estimation and application **50**: 425-439 (2022)

Rathnasiri PG *see* Wickramaarachchi AL *et al.* (2022)

Ratnaweera P *see* Walpita SC *et al.* (2022)

Ratnayake R *see* Warusavitharana E *et al.* (2022)

Ratnayake RR *see* Kirisan A *et al.* (2022)

Sabir S, Sanaullah A & Gupta S - Estimation of mean considering the joint influence of measurement errors and non-response in two-phase sampling designs **50**: 13-25 (2022)

Sahthy MM *see* Samarasekara RSM *et al.* (2022)

Samarakoon KW, Ko JY, Lee JH & Jeon YJ - Anti-inflammatory activity of nonyl 8-acetoxy-6-methyloctanoate, isolated from the cultured marine diatom, *Phaeodactylum tricornutum*: mediated via suppression of inflammatory mediators in LPS-stimulated RAW 264.7 macrophages **50**: 685-693 (2022)

Samarasekara RSM, Sahthy MM, Siriwardana AHMS & Siriwardana HPAM - Assessment of wave climate change and its impact on littoral drift along the Kalutara and Kalpitiya beaches in Sri Lanka **50**: 813-826 (2022)

Samarasinghe R *see* Ediriweera S *et al.* (2022)

Samarasinghe R *see* Ediriweera S *et al.* (2022)

Samaraweera G *see* Mallikaarachchi TB *et al.* (2022)

Sampath WDM, Fernando CAN & Edirisinghe DG - Synthesis of polyethylene glycol-grafted graphite and effect of its loading on properties of natural rubber composites **50**: 785-798 (2022)

Sanaullah A *see* Sabir S *et al.* (2022)

Sanjeewa KKA *see* Jayawardena TU *et al.* (2022)

Saqib M *see* Rasheed H *et al.* (2022)

Satharasinghe DM *see* Dharmapala RMAU *et al.* (2022)

Senanayake CD *see* Premarathna WAAS *et al.* (2022)

Senanayake G *see* Hansika KAS *et al.* (2022)

Sewwandi M, Premarathne KSD, Wijesekara H, Rajapaksha AU, Soysa S & Vithanage M - Vector transport of microplastics bound potentially toxic elements (PTEs) in water systems **50**: 331-344 (2022)

Shahbaz MQ *see* Darwish JA *et al.* (2022)

Shashiprabha HED, Abeyundara SP & Ariyaratna HACK - Meta-QTL analysis identified stable quantitative trait loci (QTLs) and associated resistance gene analogues in rice **50**: 35-51 (2022)

Silva SPI *see* Dharmapala RMAU *et al.* (2022)

Siriwardana AHMS *see* Samarasekara RSM *et al.* (2022)

Siriwardana HPAM *see* Samarasekara RSM *et al.* (2022)

Siriwardhana C *see* Koliyabandara PA *et al.* (2022)

Sonnadara U *see* Gamage TD *et al.* (2022)

Soysa S *see* Sewwandi M *et al.* (2022)

Strigaro D *see* Warusavitharana E *et al.* (2022)

Sudantha BH *see* Warusavitharana E *et al.* (2022)

Suganthan P *see* Ranasinghe N *et al.* (2022)

Suhail M *see* Rasheed H *et al.* (2022)

Suraweera C *see* Tennakoon TMSG *et al.* (2022)

Surendran SN *see* Karunaratne SHPP & Surendran SN (2022)

Suresh TS *see* Abeysiri HASN *et al.* (2022)

Susantha KAS *see* Thevega T *et al.* (2022)

Tennakoon TMSG, Borosova R, Suraweera C, Herath S, De Silva T, Padumadasa C, Weerasena J, Gunaratna N, Gunasekera N, Edwards S & Wijesundara S - First record of *Thottea duchartrei* Sivar., A. Babu & Balach. (Aristolochiaceae) in Sri Lanka **50**: 441-452 (2022)

Thevega T, Jayasinghe JASC & Susantha KAS - Seismic performance of stiffened steel box column with different corner stiffener arrangements: a numerical approach **50**: 453-466 (2022)

Thiagalingam S - The road to precision cancer therapy – history and strategies **50**: 321-330 (2022)

Tilakaratne G *see* Ilangarathna G *et al.* (2022)

Torrijos M *see* Wickramaarachchi AL *et al.* (2022)

U Samarajeewa - Heavy metals and food safety in Sri Lanka: A review **50**: 541-562 (2022)

Uddin R *see* Hanif M *et al.* (2022)

Ul Haq I *see* Hanif M *et al.* (2022)

Ullah K *see* Hanif M *et al.* (2022)

Vithanage M *see* Sewwandi M *et al.* (2022)

Walakulu Gamage SS *see* Wijesooriya MM *et al.* (2022)

Walisadeera A *see* Mallikaarachchi TB *et al.* (2022)

Walpita SC, Ratnaweera P & Fernando GVAR - Stability analysis of a partially saturated layered soil formation associated with shallow landslides **50**: 405-415 (2022)

Wang D *see* Pathirana G *et al.* (2022)

Wang L *see* Jayawardena TU *et al.* (2022)

Wanigasuriya JKP *see* Abeysiri HASN *et al.* (2022)

Warusavitharana E, Mahanama PKS, Cannata M, Ratnayake R, Sudantha BH & Strigaro D - Evaluating the potential of an open sensor network to support reservoir pre-release decision making **50**: 577-587 (2022)

Weerasekera MM *see* Liyanage GY *et al.* (2022)

Weerasena J *see* Tennakoon TMSG *et al.* (2022)

Weerasingha WVVR *see* Gnanarathna KADC *et al.* (2022)

Weligampola H *see* Ilangarathna G *et al.* (2022)

Weragama KWDP *see* Gnanarathna KADC *et al.* (2022)

Wickramaarachchi AL, Rathnasiri PG, Torrijos M, Escudie R & Narayana M - Optimization of high solids batch anaerobic co-digestion of lignocellulosic biomass and cow dung under mesophilic temperature conditions **50**: 125-136 (2022)

Widana Gamage SMK *see* Wijesooriya MM *et al.* (2022)

Wijenayake WMHK *see* Amarasinghe US *et al.* (2022)

Wijerathne RS, Manage PM & Idroos FS - Poly- β -hydroxybutyrate (PHB) production potential of naturally existing cyanobacterial blooms **50**: 733-743 (2022)

Wijeratne EMS *see* Pattiaratchi CB *et al.* (2022)

Wijesekara H *see* Sewwandi M *et al.* (2022)

Wijesinghe D *see* Perera SJ *et al.* (2022)

Wijesinghe MR *see* Ranasinghe RPTI *et al.* (2022)

Wijesooriya MM, Masakorala K, Widana Gamage SMK & Walakulu Gamage SS - An approach to develop bioremediation by isolation and characterization of microorganisms from soil contaminated with used lubricating oil **50**: 347-360 (2022)

Wijesooriya UD *see* Dissanayake CSB & Wijesooriya UD (2022)

Wijesundara KK *see* Premarathna WAAS *et al.* (2022)

Wijesundara S *see* Karunarathna HGMK *et al.* (2022)

Wijesundara S *see* Tennakoon TMSG *et al.* (2022)

Wijewardhana CNT & Gamalath KAIL - Simulation of coloured particles radiation spectra from black holes **50**: 863-880 (2022)

Wijeweera AA *see* Hansika KAS *et al.* (2022)

Yang HW *see* Jayawardena TU *et al.* (2022)

Yao CY & de Silva AP - Molecular logic-based computation and fluorescent sensors: The story so far **50**: 195-211 (2022)

Yeap KH *see* Nisar H *et al.* (2022)

Yousaf K, Bashir R, Balqees K, Naz S, Munir N & Aslam F - High prevalence of glaucoma-associated CYP1B1 mutation (p.G61E) in primary congenital and open angle glaucoma patients in Pakistan **50**: 589-594 (2022)

Zaman T *see* Dündar E *et al.* (2022)

SUBJECT INDEX 2022

1-D infiltration

Stability analysis of a partially saturated layered soil formation associated with shallow landslides (Walpita SC, Ratnaweera P & Fernando GWR) **50**: 405-415 (2022)

4ONSE

Evaluating the potential of an open sensor network to support reservoir pre-release decision making (Warusavitharana E, Mahanama PKS, Cannata M, Ratnayake R, Sudantha BH & Strigaro D) **50**: 577-587 (2022)

Acclimatization

Micropropagation of *Stevia rebaudiana* (Bertoni) Bertoni using nutrient water of *Cocos nucifera* var. *aurantiaca* (King coconut) as a natural growth enhancer (Karunarathna HGMK, Medagama K, Wijesundara S & Iqbal MCM) **50**: 3-12 (2022)

Adaptive lasso

Implementation of adaptive lasso regression based on multiple Theil-Sen Estimators using differential evolution algorithm with heavy tailed errors (Dünder E, Zaman T, Cengiz MA & Alakus K) **50**: 395-404 (2022)

Aggressive environments

Combined use of non-destructive tests, visual inspection and service life prediction to ensure the reliability of reinforced concrete water tanks (Ranasinghe K & De Silva S) **50**: 371-386 (2022)

Agriculture

Application of Benford's law in agricultural production statistics (Hanci F) **50**: 387-393 (2022)

Angiogenesis

Effect of PEGylated gold nanorods on the circulating vascular endothelial growth factor, platelet-derived growth factor, and miR-29a in CD-1 mice (Gamal-Eldeen AM, Raafat BM, Fahmy CA, Abo-Elfadl MT, El-Daly SM & Ali MRK) **50**: 467-475 (2022)

Annual cycle

Vegetative and reproductive phenology of *Cinnamomum verum* J. Presl grown in intermediate climatic zone of Sri Lanka (Hansika KAS, Kodikara KAS, Wijeweera AA, Senanayake G & Jayatissa LP) **50**: 87-99 (2022)

Antibiotic-resistant genes

Screening and quantitative analysis of antibiotic resistance genes in hospital and aquaculture effluent in Sri Lanka as an emerging environmental contaminant (Liyanage GY, Weerasekera MM & Manage PM) **50**: 361-370 (2022)

Anti-fine dust

Sonication-assisted water extract of *Dendronephthya gigantea* exhibits anti-fine dust effects; attenuation of MAPK phosphorylation in macrophages (Jayawardena TU, Fernando IPS, Nagahawatta DP, Wang L, Yang HW, Oh JY, Sanjeeva KKA & Jeon Y) **50**: 151-160 (2022)

Anti-inflammatory activity

Anti-inflammatory activity of nonyl 8-acetoxy-6-methyloctanoate, isolated from the cultured marine diatom, *Phaeodactylum tricorutum*: mediated via suppression of inflammatory mediators in LPS-stimulated RAW 264.7 macrophages (Samarakoon KW, Ko JY, Lee JH & YJ Jeon YJ) **50**: 685-693 (2022)

Antioxidant potential

Development of vacuum-dried powder and drinking yoghurt from soursop fruit (*Annona muricata* L.) and evaluation of their physico-chemical and functional properties (Ranaweera NI, Pitipanaarachchi RC, Herath HMT & Chandramali DVP) **50**: 489-502 (2022)

Anti-TB drugs

M-polynomial and topological indices for the anti-tuberculosis drugs (Jude TP, Elango P & Koneswaran M) **50**: 827-838 (2022)

Apatite

Nanotechnology in sustainable value addition to Sri Lankan minerals (Rajapakse RMG) **50**: 303-314 (2022)

API 5L grade B steel

Developing a model to predict the propagation of sulphide stress corrosion of steel used for petroleum pipelines (Manimendra A, De Silva I & Jayasundara R) **50**: 839-850 (2022)

Arabian Sea

Tropical cyclones in the Arabian Sea and the Bay of Bengal: comparison of environmental factors (Pathirana G & Priyadarshani K) **50**: 53-64 (2022)

Arsenic

Geo-environmental assessment of geochemistry of groundwater and associated human health risks in the dry zone terrain of Sri Lanka (Chandrajith R & Diyabalanage S) **50**: 213-229 (2022)

Arsenic

Heavy metals and food safety in Sri Lanka: A review (Samarajeewa U) **50**: 541-562 (2022)

Artificial intelligence

Implementation of a fuzzy logic approach for a smart production System (Dihovicni D, Mišćević M, Kovačević NR & Kreculj D) **50**: 695-703 (2022)

Artificial intelligence (AI)

The road to precision cancer therapy – history and strategies (Thiagalasingam S) **50**: 321-330 (2022)

Artificial intelligence

Artificial intelligence framework for threat assessment and containment for covid-19 and future epidemics while mitigating the socioeconomic impact to women, children, and underprivileged groups (Ilangarathna G, Weligampola H, Ranasinghe Y, Attygalla E, Godaliyaddha R, Herath V, Ekanayake P, Ekanayake SY, Pinnawela M, Dharmaratne S, Tilakaratne G & Ekanayake J) **50**: 251-262 (2022)

Aspergillus flavus

Bioactive cyclo-(S-Pro-R-Leu) from *Aspergillus flavus*, the marine endophytic fungus from brown alga, *Dictyota kunthi* (Haniiffa HM, Dharmaratne HRW & Mohommad MY) **50**: 717-721 (2022)

Aspergillus fumigatus

An approach to develop bioremediation by isolation and characterization of microorganisms from soil contaminated with used lubricating oil (Wijesooriya MM, Masakorala K, Widana Gamage SMK & Walakulu Gamage SS) **50**: 347-360 (2022)

Atopic dermatitis

Non invasive automated approach for eczema lesions segmentation using colour space normalization (Nisar H, Ch'ng Y-K & Yeap KH) **50**: 705-716 (2022)

Autocorrelation function

A coupled system of stochastic differential equations for probabilistic wind speed modelling (Bandarathilake HMDP, Palamakumbura GWRMR & Maithripala DHS) **50**: 613-623 (2022)

Automation

Implementation of a fuzzy logic approach for a smart production System (Dihovicni D, Mišćević M, Kovačević NR & Kreculj D) **50**: 695-703 (2022)

Auxiliary variable

Estimation of mean considering the joint influence of measurement errors and non-response in two-phase sampling designs (Sabir S, Sanaullah A & Gupta S) **50**: 13-25 (2022)

Bay of Bengal

Tropical cyclones in the Arabian Sea and the Bay of Bengal: comparison of environmental factors (Pathirana G & Priyadarshani K) **50**: 53-64 (2022)

Beira Lake

Poly-β-hydroxybutyrate (PHB) production potential of naturally existing cyanobacterial blooms (Wijerathne RS, Manage PM, & Idroos FS) **50**: 733-743 (2022)

Bifidobacterium

Physicochemical and sensory attributes of inulin incorporated set yoghurt prepared using cow and buffalo milk (Gnanarathna KADC, Jayasumama MTLK, Weragama KWDP, Gunasekara DCS, Weerasingha WVVR, Chandrasekara A & Prasanna PHP) **50**: 651-661 (2022)

Binara

Induction of somatic embryogenesis from leaf explants of *Exacum trinervium* (L.) Druce (Binara) (de Silva V & Eeswara JP) **50**: 27-33 (2022)

Biodegradable plastics

Poly-β-hydroxybutyrate (PHB) production potential of naturally existing cyanobacterial blooms (Wijerathne RS, Manage PM, & Idroos FS) **50**: 733-743 (2022)

Biodegradation

An approach to develop bioremediation by isolation and characterization of microorganisms from soil contaminated with used lubricating oil (Wijesooriya MM, Masakorala K, Widana Gamage SMK & Walakulu Gamage SS) **50**: 347-360 (2022)

Biodiversity

First record of *Thottea duchartrei* Sivar., A. Babu & Balach. (Aristolochiaceae) in Sri Lanka (Tennakoon TMSG, Borosova R, Suraweera C, Herath S, De Silva T, Padumadasa C, Weerasena J, Gunaratna N, Gunasekera N, Edwards S & Wijesundara S) **50**: 441-452 (2022)

Biological control

Mosquito control: A review on the past, present and future strategies (Karunaratne SHPP & Surendran SN) **50**: 277-292 (2022)

Biological sustainability

New paradigm for inland fisheries development in Sri Lanka: a transdisciplinary approach for addressing food and nutritional security (Amarasinghe US, Pushpalatha KBC & Wijenayake WMHK) **50**: 177-194 (2022)

BioMercator

Meta-QTL analysis identified stable quantitative trait loci (QTLs) and associated resistance gene analogues in rice (Shashiprabha HED, Abeysundara SP & Ariyaratna HACK) **50**: 35-51 (2022)

Bioremediation

Screening of potential aerobic denitrifying bacteria for nitrate removal from water (Kirisan A, Gnanavelrajah N & Ratnayake RR) **50**: 639-649 (2022)

Birds

Effects of dietary lead exposure on the call of Japanese quail (*Coturnix japonica*) hatchlings (Ranasinghe RPTI, Fernando TSP & Wijesinghe MR) **50**: 477-487 (2022)

bla TEM

Screening and quantitative analysis of antibiotic resistance genes in hospital and aquaculture effluent in Sri Lanka as an emerging environmental contaminant (Liyanage GY, Weerasekera MM & Manage PM) **50**: 361-370 (2022)

Black hole entropy

Simulation of coloured particles radiation spectra from black holes (Wijewardhana CNT & Gamalath KAILW) **50**: 863-880 (2022)

Black hole mass

Simulation of coloured particles radiation spectra from black holes (Wijewardhana CNT & Gamalath KAILW) **50**: 863-880 (2022)

Black hole spin

Simulation of coloured particles radiation spectra from black holes (Wijewardhana CNT & Gamalath KAILW) **50**: 863-880 (2022)

Black hole temperature

Simulation of coloured particles radiation spectra from black holes (Wijewardhana CNT & Gamalath KAILW) **50**: 863-880 (2022)

Block matrices

On the construction of unitaries representing minimal inner toral polynomials (Dissanayake CSB & Wijesooriya UD) **50**: 607-611 (2022)

Blood electrolyte analyzer

Molecular logic-based computation and fluorescent sensors: The story so far (Yao CY & de Silva AP) **50**: 195-211 (2022) Fluorescent PET sensing/switching Molecular logic-based computation and fluorescent sensors: The story so far (Yao CY & de Silva AP) **50**: 195-211 (2022)

Blue revolution

New paradigm for inland fisheries development in Sri Lanka: a transdisciplinary approach for addressing food and nutritional security (Amarasinghe US, Pushpalatha KBC & Wijenayake WMHK) **50**: 177-194 (2022)

Bone meal

Influence of different bone meal particle size induced calcium specific appetite on performance and egg quality parameters of layer chickens (Gamage TS, Mutucumarana RK & Andrew MS) **50**: 745-754 (2022)

Buffalo milk

Physicochemical and sensory attributes of inulin incorporated set yoghurt prepared using cow and buffalo milk (Gnanarathna KADC, Jayasumama MTLK, Weragama KWDP, Gunasekara DCS, Weerasingha WVVR, Chandrasekara A & Prasanna PHP) **50**: 651-661 (2022)

Cadmium

Heavy metals and food safety in Sri Lanka: A review (Samarajeewa U) **50**: 541-562 (2022)

Calcium

Influence of different bone meal particle size induced calcium specific appetite on performance and egg quality parameters of layer chickens (Gamage TS, Mutucumarana RK & Andrew MS) **50**: 745-754 (2022)

Calls

Effects of dietary lead exposure on the call of Japanese quail (*Coturnix japonica*) hatchlings (Ranasinghe RPTI, Fernando TSP & Wijesinghe MR) **50**: 477-487 (2022)

Carbimazole

Comparison of radioactive iodine therapy outcome and the duration of pretreatment discontinuation of carbimazole among hyperthyroid patients: a prospective study (Raheem S & Nanayakkara DKK) **50**: 417-423 (2022)

CBCT

Determination of safe zone of the mandible for implant and bone harvesting (using CBCT) of mandible in a group of Sri Lankan subjects (Dharmapala RMAU, Satharasinghe DM, Silva SPI & Jeyasugiththan J) **50**: 65-72 (2022)

Chloride induced corrosion

Combined use of non-destructive tests, visual inspection and service life prediction to ensure the reliability of reinforced concrete water tanks (Ranasinghe K & De Silva S) **50**: 371-386 (2022)

Cinnamomum verum

Vegetative and reproductive phenology of *Cinnamomum verum* J. Presl grown in intermediate climatic zone of Sri Lanka (Hansika KAS, Kodikara KAS, Wijeweera AA, Senanayake G & Jayatissa LP) **50**: 87-99 (2022)

CKDu

Geo-environmental assessment of geochemistry of groundwater and associated human health risks in the dry zone terrain of Sri Lanka (Chandrajith R & Diyabalanage S) **50**: 213-229 (2022)

Closed-loop market information flow model

Designing a closed-loop information flow model in bridging the market information gap among agriculture stakeholders in Sri Lanka (Mallikaarachchi TB, Samaraweera G, Walisadeera A, De Silva L & Munasinghe S) **50**: 881-896 (2022)

Coastal erosion

Assessment of wave climate change and its impact on littoral drift along the Kalutara and Kalpitiya beaches in Sri Lanka (Samarasekara RSM, Sahthy MM, Siriwardana AHMS & Siriwardana HPAM) **50**: 813-826 (2022)

Coconut oil

Fractal characteristics of creeping discharges propagating on nano-epoxy composite insulators immersed in coconut oil (Ediriweera S, Jayarathna PB, Samarasinghe R & Lucas R) **50**: 663-673 (2022)

Coconut oil

Investigation of oil level and type of solid insulator on creeping discharges propagating under an AC electric field (Ediriweera S, Jayarathna PB, Samarasinghe R & Lucas R) **50**: 725-732 (2022)

Coconut water

Micropropagation of *Stevia rebaudiana* (Bertoni) Bertoni using nutrient water of *Cocos nucifera* var. *aurantiaca* (King coconut) as a natural growth enhancer (Karunarathna HGMK, Medagama K, Wijesundara S & Iqbal MCM) **50**: 3-12 (2022)

Coloured particles

Simulation of coloured particles radiation spectra from black holes (Wijewardhana CNT & Gamalath KAILW) **50**: 863-880 (2022)

Commensal

Predominance of phylogenetic group B2 among commensal *Escherichia coli* in humans from Kandy District, Sri Lanka (Rangama BNLD, Abayasekara CL and Gordon DM) **50**: 137-150 (2022)

Computational algorithms

The road to precision cancer therapy – history and strategies (Thiagalingam S) **50**: 321-330 (2022)

Condition assessment

Combined use of non-destructive tests, visual inspection and service life prediction to ensure the reliability of reinforced concrete water tanks (Ranasinghe K & De Silva S) **50**: 371-386 (2022)

Cone beam computed

Determination of safe zone of the mandible for implant and bone harvesting (using CBCT) of mandible in a group of Sri Lankan subjects (Dharmapala RMAU, Satharasinghe DM, Silva SPI & Jeyasugiththan J) **50**: 65-72 (2022)

Congestion detection

Fuzzy based congestion detection and control algorithm for energy efficient wireless sensor network (WSN) (Ramasamy-Rajeswari A, Ganapathy S, Kulothungan K & Kannan A) **50**: 563-576 (2022)

Contamination

Screening of potential aerobic denitrifying bacteria for nitrate removal from water (Kirisan A, Gnanavelrajah N & Ratnayake RR) **50**: 639-649 (2022)

Control

Fuzzy based congestion detection and control algorithm for energy efficient wireless sensor network (WSN) (Ramasamy-Rajeswari A, Ganapathy S, Kulothungan K & Kannan A) **50**: 563-576 (2022)

Correlation

Development of wind energy prediction models using statistical, machine learning and hybrid techniques: a case study (Ekanayake P, Panahatipola O & Jayasinghe J) **50**: 503-517 (2022)

COVID-19

Artificial intelligence framework for threat assessment and containment for covid-19 and future epidemics while mitigating the socioeconomic impact to women, children, and underprivileged groups (Ilangarathna G, Weligampola H, Ranasinghe Y, Attygalla E, Godaliyaddha R, Herath V, Ekanayake P, Ekanayake SY, Pinnawela M, Dharmaratne S, Tilakaratne G & Ekanayake J) **50**: 251-262 (2022)

Creeping discharges

Fractal characteristics of creeping discharges propagating on nano-epoxy composite insulators immersed in coconut oil (Ediriweera S, Jayarathna PB, Samarasinghe R & Lucas R) **50**: 663-673 (2022)

Crop improvement

Microbiome: diversity, distribution, and potential role in sustainable crop production (Fernando WGD & Dolatabadian A) **50**: 231-250 (2022)

Cultured marine diatom

Anti-inflammatory activity of nonyl 8-acetoxy-6-methyloctanoate, isolated from the cultured marine diatom, *Phaeodactylum tricorutum*: mediated via suppression of inflammatory mediators in LPS-stimulated RAW 264.7 macrophages (Samarakoon KW, Ko JY, Lee JH & YJ Jeon YJ) **50**: 685-693 (2022)

Cyanobacteria

Poly- β -hydroxybutyrate (PHB) production potential of naturally existing cyanobacterial blooms (Wijerathne RS, Manage PM, & Idroos FS) **50**: 733-743 (2022)

Cyclic analysis

Seismic performance of stiffened steel box column with different corner stiffener arrangements: a numerical approach (Thevega T, Jayasinghe JASC & Susantha KAS) **50**: 453-466 (2022)

Cyclo- (S-Pro-R-Leu)

Bioactive cyclo-(S-Pro-R-Leu) from *Aspergillus flavus*, the marine endophytic fungus from brown alga, *Dictyota kunthi* (Haniffa HM, Dharmaratne HRW & Mohommad MY) **50**: 717-721 (2022)

Cylindrospermopsin (CYN)

Effect of cylindrospermopsin on the hepatotoxicity in wistar rats (Abeyisiri HASN, Wanigasuriya JKP, Suresh TS, Beneragama DH & Manage PM) **50**: 595-605 (2022)

Deduru Oya basin

Evaluating the potential of an open sensor network to support reservoir pre-release decision making (Warusavitharana E, Mahanama PKS, Cannata M, Ratnayake R, Sudantha BH & Strigaro D) **50**: 577-587 (2022)

Delay reduction

Increasing the effectiveness of T-junctions with an innovative geometrical and phasing arrangement (Jayasooriya NK, Perera HLK and Bandara JMSJ) **50**: 73-86 (2022)

Demand and supply modeling

Designing a closed-loop information flow model in bridging the market information gap among agriculture stakeholders in Sri Lanka (Mallikaarachchi TB, Samaraweera G, Walisadeera A, De Silva L & Munasinghe S) **50**: 881-896 (2022)

Dendronephthya gigantea

Sonication-assisted water extract of *Dendronephthya gigantea* exhibits anti-fine dust effects; attenuation of MAPK phosphorylation in macrophages (Jayawardena TU, Fernando IPS, Nagahawatta DP, Wang L, Yang HW, Oh JY, Sanjeeva KKA & Jeon Y) **50**: 151-160 (2022)

Dental fluorosis

Geo-environmental assessment of geochemistry of groundwater and associated human health risks in the dry zone terrain of Sri Lanka (Chandrajith R & Diyabalanage S) **50**: 213-229 (2022)

Dependence functions

A new multivariate transmuted family of distributions: theory and application for modelling of daily world COVID-19 cases (Darwish JA, Al-Turk LI & Shahbaz MQ) **50**: 771-784 (2022)

Depth of corrosion

Developing a model to predict the propagation of sulphide stress corrosion of steel used for petroleum pipelines (Manimendra A, De Silva I & Jayasundara R) **50**: 839-850 (2022)

Dictyota kunthi

Bioactive cyclo-(S-Pro-R-Leu) from *Aspergillus flavus*, the marine endophytic fungus from brown alga, *Dictyota kunthi* (Haniffa HM, Dharmaratne HRW & Mohommad MY) **50**: 717-721 (2022)

Discharge length

Investigation of oil level and type of solid insulator on creeping discharges propagating under an AC electric field (Ediriweera S, Jayarathna PB, Samarasinghe R & Lucas R) **50**: 725-732 (2022)

Disease detection in agriculture

Interpretability and accessibility of machine learning in selected food processing, agriculture and health applications (Ranasinghe N, Ramanan A, Fernando S, Hameed PN, Herath D, Malepathirana T, Suganthan P, Niranjan M & Halgamuge S) **50**: 263-276 (2022)

Distinguished varieties

On the construction of unitaries representing minimal inner toral polynomials (Dissanayake CSB & Wijesooriya UD) **50**: 607-611 (2022)

DNA barcodes

First record of *Thottea duchartrei* Sivar., A. Babu & Balach. (Aristolochiaceae) in Sri Lanka (Tennakoon TMSG, Borosova R, Suraweera C, Herath S, De Silva T, Padumadasa C, Weerasena J, Gunaratna N, Gunasekera N, Edwards S & Wijesundara S) **50**: 441-452 (2022)

Drinking yoghurt

Development of vacuum-dried powder and drinking yoghurt from soursop fruit (*Annona muricata* L.) and evaluation of their physico-chemical and functional properties (Ranaweera NI, Pitipanaarachchi RC, Herath HMT & Chandramali DVP) **50**: 489-502 (2022)

Drug repositioning

Interpretability and accessibility of machine learning in selected food processing, agriculture and health applications (Ranasinghe N, Ramanan A, Fernando S, Hameed PN, Herath D, Malepathirana T, Suganthan P, Niranjan M & Halgamuge S) **50**: 263-276 (2022)

Ductility

Seismic performance of stiffened steel box column with different corner stiffener arrangements: a numerical approach (Thevega T, Jayasinghe JASC & Susantha KAS) **50**: 453-466 (2022)

Ecotoxicity

Vector transport of microplastics bound potentially toxic elements (PTEs) in water systems (Sewwandi M, Premarathne KSD, Wijesekara H, Rajapaksha AU, Soysa S & Vithanage M) **50**: 331-344 (2022)

Efficiency

A novel approach for energy and exergy analysis of a flat plate solar collector with energy storage (Hanif M, Khattak MK, Ul Haq I, Uddin R & Ullah K) **50**: 161-172 (2022)

Egg quality

Influence of different bone meal particle size induced calcium specific appetite on performance and egg quality parameters of layer chickens (Gamage TS, Mutucumarana RK & Andrew MS) **50**: 745-754 (2022)

Egg shell

Influence of different bone meal particle size induced calcium specific appetite on performance and egg quality parameters of layer chickens (Gamage TS, Mutucumarana RK & Andrew MS) **50**: 745-754 (2022)

Electric field

Investigation of oil level and type of solid insulator on creeping discharges propagating under an AC electric field (Ediriweera S, Jayarathna PB, Samarasinghe R & Lucas R) **50**: 725-732 (2022)

Electrodynamic motion

Investigation of oil level and type of solid insulator on creeping discharges propagating under an AC electric field (Ediriweera S, Jayarathna PB, Samarasinghe R & Lucas R) **50**: 725-732 (2022)

Energy

Fuzzy based congestion detection and control algorithm for energy efficient wireless sensor network (WSN) (Ramasamy-Rajeswari A, Ganapathy S, Kulothungan K & Kannan A) **50**: 563-576 (2022)

Energy storage

A novel approach for energy and exergy analysis of a flat plate solar collector with energy storage (Hanif M, Khattak MK, Ul Haq I, Uddin R & Ullah K) **50**: 161-172 (2022)

ENSO

Tropical cyclones in the Arabian Sea and the Bay of Bengal: comparison of environmental factors (Pathirana G & Priyadarshani K) **50**: 53-64 (2022)

Escherichia coli

Predominance of phylogenetic group B2 among commensal *Escherichia coli* in humans from Kandy District, Sri Lanka (Rangama BNLD, Abayasekara CL and Gordon DM) **50**: 137-150 (2022)

Exacum trinervium

Induction of somatic embryogenesis from leaf explants of *Exacum trinervium* (L.) Druce (Binara) (de Silva V & Eeswara JP) **50**: 27-33 (2022)

Excess fluoride

Geo-environmental assessment of geochemistry of groundwater and associated human health risks in the dry zone terrain of Sri Lanka (Chandrajith R & Diyabalanage S) **50**: 213-229 (2022)

Exergy

A novel approach for energy and exergy analysis of a flat plate solar collector with energy storage (Hanif M, Khattak MK, Ul Haq I, Uddin R & Ullah K) **50**: 161-172 (2022)

Exponential distribution

The odd modified Burr-III exponential distribution: properties, estimation and application (Rasheed H, Dar IS, M Saqib M, Abbas N & Suhail M) **50**: 425-439 (2022)

Exponential estimator

Estimation of mean considering the joint influence of measurement errors and non-response in two-phase sampling designs (Sabir S, Sanullah A & Gupta S) **50**: 13-25 (2022)

Fatty alcohol esters

Anti-inflammatory activity of nonyl 8-acetoxy-6-methyloctanoate, isolated from the cultured marine diatom, *Phaeodactylum tricoratum*: mediated via suppression of inflammatory mediators in LPS-stimulated RAW 264.7 macrophages (Samarakoon KW, Ko JY, Lee JH & YJ Jeon YJ) **50**: 685-693 (2022)

Feldspar

Nanotechnology in sustainable value addition to Sri Lankan minerals (Rajapakse RMG) **50**: 303-314 (2022)

Final discharge length

Fractal characteristics of creeping discharges propagating on nano-epoxy composite insulators immersed in coconut oil (Ediriweera S, Jayarathna PB, Samarasinghe R & Lucas R) **50**: 663-673 (2022)

Flat plate

A novel approach for energy and exergy analysis of a flat plate solar collector with energy storage (Hanif M, Khattak MK, Ul Haq I, Uddin R & Ullah K) **50**: 161-172 (2022)

Flora of Sri Lanka

First record of *Thottea duchartrei* Sivar., A. Babu & Balach. (Aristolochiaceae) in Sri Lanka (Tennakoon TMSG, Borosova R, Suraweera C, Herath S, De Silva T, Padumadasa C, Weerasena J, Gunaratna N, Gunasekera N, Edwards S & Wijesundara S) **50**: 441-452 (2022)

Fluctuation statistics

Analysis of instantaneous, daily and monthly statistics 2017-2021 of rooftop solar energy (Lucas JR) **50**: 799-811 (2022)

Food

Application of Benford's law in agricultural production statistics (Hanci F) **50**: 387-393 (2022)

Food chain

Heavy metals and food safety in Sri Lanka: A review (Samarajeewa U) **50**: 541-562 (2022)

Food processing

Interpretability and accessibility of machine learning in selected food processing, agriculture and health applications (Ranasinghe N, Ramanan A, Fernando S, Hameed PN, Herath D, Malepathirana T, Suganthan P, Niranjana M & Halgamuge S) **50**: 263-276 (2022)

Fractals

Fractal characteristics of creeping discharges propagating on nano-epoxy composite insulators immersed in coconut oil (Ediriweera S, Jayarathna PB, Samarasinghe R & Lucas R) **50**: 663-673 (2022)

Free choice

Influence of different bone meal particle size induced calcium specific appetite on performance and egg quality parameters of layer chickens (Gamage TS, Mutucumarana RK & Andrew MS) **50**: 745-754 (2022)

Functional properties

Development of vacuum-dried powder and drinking yoghurt from soursop fruit (*Annona muricata* L.) and evaluation of their physico-chemical and functional properties (Ranaweera NI, Pitipanaarachchi RC, Herath HMT & Chandramali DVP) **50**: 489-502 (2022)

Fuzzy inference system

Fuzzy based congestion detection and control algorithm for energy efficient wireless sensor network (WSN) (Ramasamy-Rajeswari A, Ganapathy S, Kulothungan K & Kannan A) **50**: 563-576 (2022)

Fuzzy logic

Implementation of a fuzzy logic approach for a smart production System (Dihovcni D, Mišević M, Kovačević NR & Kreculj D) **50**: 695-703 (2022)

GenBank

First record of *Thottea duchartrei* Sivar., A. Babu & Balach. (Aristolochiaceae) in Sri Lanka (Tennakoon TMSG, Borosova R, Suraweera C, Herath S, De Silva T, Padumadasa C, Weerasena J, Gunaratna N, Gunasekera N, Edwards S & Wijesundara S) **50**: 441-452 (2022)

Gender

Effect of PEGylated gold nanorods on the circulating vascular endothelial growth factor, platelet-derived growth factor, and miR-29a in CD-1 mice (Gamal-Eldeen AM, Raafat BM, Fahmy CA, Abo-Elfadl MT, El-Daly SM & Ali MRK) **50**: 467-475 (2022)

Genome

The road to precision cancer therapy – history and strategies (Thiagalingam S) **50**: 321-330 (2022)

Genomics

Microbiome: diversity, distribution, and potential role in sustainable crop production (Fernando WGD & Dolatabadian A) **50**: 231-250 (2022)

Gold nanorods

Effect of PEGylated gold nanorods on the circulating vascular endothelial growth factor, platelet-derived growth factor, and miR-29a in CD-1 mice (Gamal-Eldeen AM, Raafat BM, Fahmy CA, Abo-Elfadl MT, El-Daly SM & Ali MRK) **50**: 467-475 (2022)

Gramene

Meta-QTL analysis identified stable quantitative trait loci (QTLs) and associated resistance gene analogues in rice (Shashiprabha HED, Abeyundara SP & Ariyaratna HACK) **50**: 35-51 (2022)

Graphite

Synthesis of polyethylene glycol-grafted graphite and effect of its loading on properties of natural rubber composites (Sampath WDM, Fernando CAN & Edirisinghe DG) **50**: 785-798 (2022)

Graphite

Nanotechnology in sustainable value addition to Sri Lankan minerals (Rajapakse RMG) **50**: 303-314 (2022)

Groundwater pollution

Characterization of landfill leachate at the Karadiyana open dumpsite, Sri Lanka, and assessment of water pollution in its vicinity (Koliyabandara PA, Cooray AT, Liyanage S & Siriwardhana C) **50**: 111-124 (2022)

Groundwater

Screening of potential aerobic denitrifying bacteria for nitrate removal from water (Kirisan A, Gnanavelrajah N & Ratnayake RR) **50**: 639-649 (2022)

Habitat suitability

Assessment of marine turtle nesting habitats from Tangalle to the Kumbukkan Oya estuary in south-eastern Sri Lanka (Perera SJ, Perera WPN, Goonatilake S de A, Ekaratne K, Wijesinghe D, Perera LV, Chandranimal D & Ediriweera A) **50**: 755-769 (2022)

Hawking radiation

Simulation of coloured particles radiation spectra from black holes (Wijewardhana CNT & Gamalath KAILW) **50**: 863-880 (2022)

Heavy metals

Effects of dietary lead exposure on the call of Japanese quail (*Coturnix japonica*) hatchlings (Ranasinghe RPTI, Fernando TSP & Wijesinghe MR) **50**: 477-487 (2022)

Heavy metals

Vector transport of microplastics bound potentially toxic elements (PTEs) in water systems (Sewwandi M, Premarathne KSD, Wijesekara H, Rajapaksha AU, Soysa S & Vithanage M) **50**: 331-344 (2022)

Heavy-tailed errors

Implementation of adaptive lasso regression based on multiple Theil-Sen Estimators using differential evolution algorithm with heavy tailed errors (Dünder E, Zaman T, Cengiz MA & Alakus K) **50**: 395-404 (2022)

Hepatotoxicity

Effect of cylindrospermopsin on the hepatotoxicity in wistar rats (Abeyisiri HASN, Wanigasuriya JKP, Suresh TS, Beneragama DH & Manage PM) **50**: 595-605 (2022)

High solids anaerobic co-digestion

Optimization of high solids batch anaerobic co-digestion of lignocellulosic biomass and cow dung under mesophilic temperature conditions (Wickramaarachchi AL, Rathnasiri PG, Torrijos M, Renaud Escudie & Narayana M) **50**: 125-136 (2022)

Histopathology

Effect of cylindrospermopsin on the hepatotoxicity in wistar rats (Abeyisiri HASN, Wanigasuriya JKP, Suresh TS, Beneragama DH & Manage PM) **50**: 595-605 (2022)

Hyper-elastic models

Failure prediction of solid resilient tyres due to kerb impact: A finite element modelling approach (Premarathna WAAS, Jayasinghe JASC, Senanayake CD, Wijesundara KK & Gamage P) **50**: 625-637 (2022)

Hyperthyroidism

Comparison of radioactive iodine therapy outcome and the duration of pretreatment discontinuation of carbimazole among hyperthyroid patients: a prospective study (Raheem S & Nanayakkara DKK) **50**: 417-423 (2022)

Ilmenite

Nanotechnology in sustainable value addition to Sri Lankan minerals (Rajapakse RMG) **50**: 303-314 (2022)

Impact simulations

Failure prediction of solid resilient tyres due to kerb impact: A finite element modelling approach (Premarathna WAAS, Jayasinghe JASC, Senanayake CD, Wijesundara KK & Gamage P) **50**: 625-637 (2022)

Industrial computer systems

Implementation of a fuzzy logic approach for a smart production System (Dihovicni D, Mišćević M, Kovačević NR & Kreculj D) **50**: 695-703 (2022)

Industry 4.0.

Implementation of a fuzzy logic approach for a smart production System (Dihovicni D, Mišćević M, Kovačević NR & Kreculj D) **50**: 695-703 (2022)

Inflammation

Sonication-assisted water extract of *Dendronephthya gigantea* exhibits anti-fine dust effects; attenuation of MAPK phosphorylation in macrophages (Jayawardena TU, Fernando IPS, Nagahawatta DP, Wang L, Yang HW, Oh JY, Sanjeeva KKA & Jeon Y) **50**: 151-160 (2022)

Inhalation therapy

Novel nebulizer design with adaptive flow regulation (Dampage U & Ariyasinghe M) **50**: 101-109 (2022) Jet nebulizer Novel nebulizer design with adaptive flow regulation (Dampage U & Ariyasinghe M) **50**: 101-109 (2022)

Inland fisheries enhancement

New paradigm for inland fisheries development in Sri Lanka: a transdisciplinary approach for addressing food and nutritional security (Amarasinghe US, Pushpalatha KBC & Wijenayake WMHK) **50**: 177-194 (2022)

Inner toral polynomials

On the construction of unitaries representing minimal inner toral polynomials (Dissanayake CSB & Wijesooriya UD) **50**: 607-611 (2022)

Innovative signal phasing

Increasing the effectiveness of T-junctions with an innovative geometrical and phasing arrangement (Jayasooriya NK, Perera HLK and Bandara JMSJ) **50**: 73-86 (2022)

Insect growth regulators

Mosquito control: A review on the past, present and future strategies (Karunaratne SHPP & Surendran SN) **50**: 277-292 (2022)

Insecticides

Mosquito control: A review on the past, present and future strategies (Karunaratne SHPP & Surendran SN) **50**: 277-292 (2022)

Interpretation of neural networks

Interpretability and accessibility of machine learning in selected food processing, agriculture and health applications (Ranasinghe N, Ramanan A, Fernando S, Hameed PN, Herath D, Malepathirana T, Suganthan P, Niranjan M & Halgamuge S) **50**: 263-276 (2022)

Intra ocular pressure

High prevalence of glaucoma-associated CYP1B1 mutation (p.G61E) in primary congenital and open angle glaucoma patients in Pakistan (Yousaf K, Bashir R, Balqees K, Naz S, Munir N & Aslam F) **50**: 589-594 (2022)

Inulin

Physicochemical and sensory attributes of inulin incorporated set yoghurt prepared using cow and buffalo milk (Gnanarathna KADC, Jayasumama MTLK, Weragama KWDP, Gunasekara DCS, Weerasingha WVVR, Chandrasekara A & Prasanna PHP) **50**: 651-661 (2022)

IOD

Tropical cyclones in the Arabian Sea and the Bay of Bengal: comparison of environmental factors (Pathirana G & Priyadarshani K) **50**: 53-64 (2022)

Island-mass effect

Ocean circulation around Sri Lanka (Pattiaratchi CB, Wijeratne EMS & de Vos A) **50**: 293-302 (2022)

Isolates

Screening of potential aerobic denitrifying bacteria for nitrate removal from water (Kirisan A, Gnanavelrajah N & Ratnayake RR) **50**: 639-649 (2022)

Junction capacity improvement

Increasing the effectiveness of T-junctions with an innovative geometrical and phasing arrangement (Jayasooriya NK, Perera HLK and Bandara JMSJ) **50**: 73-86 (2022)

Juvenile open angle glaucoma

High prevalence of glaucoma-associated CYP1B1 mutation (p.G61E) in primary congenital and open angle glaucoma patients in Pakistan (Yousaf K, Bashir R, Balqees K, Naz S, Munir N & Aslam F) **50**: 589-594 (2022)

Kalpitiya

Assessment of wave climate change and its impact on littoral drift along the Kalutara and Kalpitiya beaches in Sri Lanka (Samarasekara RSM, Sahthy MM, Siriwardana AHMS & Siriwardana HPAM) **50**: 813-826 (2022)

Kalutara

Assessment of wave climate change and its impact on littoral drift along the Kalutara and Kalpitiya beaches in Sri Lanka (Samarasekara RSM, Sahthy MM, Siriwardana AHMS & Siriwardana HPAM) **50**: 813-826 (2022)

Karadiyana open dumpsite

Characterization of landfill leachate at the Karadiyana open dumpsite, Sri Lanka, and assessment of water pollution in its vicinity (Koliyabandara PA, Cooray AT, Liyanage S & Siriwardhana C) **50**: 111-124 (2022)

K-means segmentation

Non invasive automated approach for eczema lesions segmentation using colour space normalization (Nisar H, Ch'ng Y-K & Yeap KH) **50**: 705-716 (2022)

Lactobacillus

Physicochemical and sensory attributes of inulin incorporated set yoghurt prepared using cow and buffalo milk (Gnanarathna KADC, Jayasumama MTLK, Weragama KWDP, Gunasekara DCS, Weerasingha WVVR, Chandrasekara A & Prasanna PHP) **50**: 651-661 (2022)

Landfill leachate

Characterization of landfill leachate at the Karadiyana open dumpsite, Sri Lanka, and assessment of water pollution in its vicinity (Koliyabandara PA, Cooray AT, Liyanage S & Siriwardhana C) **50**: 111-124 (2022)

Latent transforming growth factor-beta protein 2

High prevalence of glaucoma-associated CYP1B1 mutation (p.G61E) in primary congenital and open angle glaucoma patients in Pakistan (Yousaf K, Bashir R, Balqees K, Naz S, Munir N & Aslam F) **50**: 589-594 (2022)

Layered soil

Stability analysis of a partially saturated layered soil formation associated with shallow landslides (Walpita SC, Ratnaweera P & Fernando GVAR) **50**: 405-415 (2022)

Leachate pollution index

Characterization of landfill leachate at the Karadiyana open dumpsite, Sri Lanka, and assessment of water pollution in its vicinity (Koliyabandara PA, Cooray AT, Liyanage S & Siriwardhana C) **50**: 111-124 (2022)

Leachate recirculation

Optimization of high solids batch anaerobic co-digestion of lignocellulosic biomass and cow dung under mesophilic temperature conditions (Wickramaarachchi AL, Rathnasiri PG, Torrijos M, Renaud Escudie & Narayana M) **50**: 125-136 (2022)

Lead

Heavy metals and food safety in Sri Lanka: A review (Samarajeewa U) **50**: 541-562 (2022)

Lignocellulosic biomass

Optimization of high solids batch anaerobic co-digestion of lignocellulosic biomass and cow dung under mesophilic temperature conditions (Wickramaarachchi AL, Rathnasiri PG, Torrijos M, Renaud Escudie & Narayana M) **50**: 125-136 (2022)

Littoral drift

Assessment of wave climate change and its impact on littoral drift along the Kalutara and Kalpitiya beaches in Sri Lanka (Samarasekara RSM, Sathya MM, Siriwardana AHMS & Siriwardana HPAM) **50**: 813-826 (2022)

Mackinawite

Developing a model to predict the propagation of sulphide stress corrosion of steel used for petroleum pipelines (Manimendra A, De Silva I & Jayasundara R) **50**: 839-850 (2022)

Macrophages MAPK

Sonication-assisted water extract of *Dendronephthya gigantea* exhibits anti-fine dust effects; attenuation of MAPK phosphorylation in macrophages (Jayawardena TU, Fernando IPS, Nagahawatta DP, Wang L, Yang HW, Oh JY, Sanjeeva KKA & Jeon Y) **50**: 151-160 (2022)

Mandibular canal

Determination of safe zone of the mandible for implant and bone harvesting (using CBCT) of mandible in a group of Sri Lankan subjects (Dharmapala RMAU, Satharasinghe DM, Silva SPI & Jeyasugiththan J) **50**: 65-72 (2022)

Marine endophytes

Bioactive cyclo-(*S*-Pro-*R*-Leu) from *Aspergillus flavus*, the marine endophytic fungus from brown alga, *Dictyota kunthi* (Haniffa HM, Dharmaratne HRW & Mohommed MY) **50**: 717-721 (2022)

Marine turtles

Assessment of marine turtle nesting habitats from Tangalle to the Kumbukkan Oya estuary in south-eastern Sri Lanka (Perera SJ, Perera WPN, Goonatilake S de A, Ekaratne K, Wijesinghe D, Perera LV, Chandranimal D & Ediriweera A) **50**: 755-769 (2022)

MaxEnt

Assessment of marine turtle nesting habitats from Tangalle to the Kumbukkan Oya estuary in south-eastern Sri Lanka (Perera SJ, Perera WPN, Goonatilake S de A, Ekaratne K, Wijesinghe D, Perera LV, Chandranimal D & Ediriweera A) **50**: 755-769 (2022)

Maximum likelihood estimation

The odd modified Burr-III exponential distribution: properties, estimation and application (Rasheed H, Dar IS, M Saqib M, Abbas N & Suhail M) **50**: 425-439 (2022)

Maximum likelihood estimation

A new multivariate transmuted family of distributions: theory and application for modelling of daily world COVID-19 cases (Darwish JA, Al-Turk LI & Shahbaz MQ) **50**: 771-784 (2022)

Mean square error

Estimation of mean considering the joint influence of measurement errors and non-response in two-phase sampling designs (Sabir S, Sanaulah A & Gupta S) **50**: 13-25 (2022)

Measurement error

Estimation of mean considering the joint influence of measurement errors and non-response in two-phase sampling designs (Sabir S, Sanaulah A & Gupta S) **50**: 13-25 (2022)

Medical geology

Geo-environmental assessment of geochemistry of groundwater and associated human health risks in the dry zone terrain of Sri Lanka (Chandrajith R & Diyabalanage S) **50**: 213-229 (2022)

Mental foramen

Determination of safe zone of the mandible for implant and bone harvesting (using CBCT) of mandible in a group of Sri Lankan subjects (Dharmapala RMAU, Satharasinghe DM, Silva SPI & Jeyasugiththan J) **50**: 65-72 (2022)

Mercury

Heavy metals and food safety in Sri Lanka: A review (Samarajeewa U) **50**: 541-562 (2022)

Mesophilic

Optimization of high solids batch anaerobic co-digestion of lignocellulosic biomass and cow dung under mesophilic temperature conditions (Wickramaarachchi AL, Rathnasiri PG, Torrijos M, Renaud Escudie & Narayana M) **50**: 125-136 (2022)

Metagenomics

Interpretability and accessibility of machine learning in selected food processing, agriculture and health applications (Ranasinghe N, Ramanan A, Fernando S, Hameed PN, Herath D, Malepathirana T, Suganthan P, Niranjana M & Halgamuge S) **50**: 263-276 (2022)

Metal pollution index

Characterization of landfill leachate at the Karadiyana open dumpsite, Sri Lanka, and assessment of water pollution in its vicinity (Koliyabandara PA, Cooray AT, Liyanage S & Siriwardhana C) **50**: 111-124 (2022)

Meta-QTLs

Meta-QTL analysis identified stable quantitative trait loci (QTLs) and associated resistance gene analogues in rice (Shashiprabha HED, Abeyundara SP & Ariyaratna HACK) **50**: 35-51 (2022)

Microbiome

Microbiome: diversity, distribution, and potential role in sustainable crop production (Fernando WGD & Dolatabadian A) **50**: 231-250 (2022)
Pathogen Microbiome: diversity, distribution, and potential role in sustainable crop production (Fernando WGD & Dolatabadian A) **50**: 231-250 (2022)

Microplastics

Vector transport of microplastics bound potentially toxic elements (PTEs) in water systems (Sewwandi M, Premarathne KSD, Wijesekara H, Rajapaksha AU, Soysa S & Vithanage M) **50**: 331-344 (2022)

MiR-29a-3p

Effect of PEGylated gold nanorods on the circulating vascular endothelial growth factor, platelet-derived growth factor, and miR-29a in CD-1 mice (Gamal-Eldeen AM, Raafat BM, Fahmy CA, Abo-Elfadl MT, El-Daly SM & Ali MRK) **50**: 467-475 (2022)

Modified Burr-III distribution

The odd modified Burr-III exponential distribution: properties, estimation and application (Rasheed H, Dar IS, M Saqib M, Abbas N & Suhail M) **50**: 425-439 (2022)

Molecular logic-based computation

Molecular logic-based computation and fluorescent sensors: The story so far (Yao CY & de Silva AP) **50**: 195-211 (2022)
Photoinduced electron transfer Molecular logic-based computation and fluorescent sensors: The story so far (Yao CY & de Silva AP) **50**: 195-211 (2022)

Monsoon

Ocean circulation around Sri Lanka (Pattiaratchi CB, Wijeratne EMS & de Vos A) **50**: 293-302 (2022)

Mosquito control

Mosquito control: A review on the past, present and future strategies (Karunaratne SHPP & Surendran SN) **50**: 277-292 (2022)

Mosquito-borne diseases

Mosquito control: A review on the past, present and future strategies (Karunaratne SHPP & Surendran SN) **50**: 277-292 (2022)

M-polynomial

M-polynomial and topological indices for the anti-tuberculosis drugs (Jude TP, Elango P & Koneswaran M) **50**: 827-838 (2022)

Multi-modular molecular network (MMM)

The road to precision cancer therapy – history and strategies (Thiagalingam S) **50**: 321-330 (2022)

Multivariate T-X family of distributions

A new multivariate transmuted family of distributions: theory and application for modelling of daily world COVID-19 cases (Darwish JA, Al-Turk LI & Shahbaz MQ) **50**: 771-784 (2022)

Nanotechnology

Fractal characteristics of creeping discharges propagating on nano-epoxy composite insulators immersed in coconut oil (Ediriweera S, Jayarathna PB, Samarasinghe R & Lucas R) **50**: 663-673 (2022)

Natural resources

Nanotechnology in sustainable value addition to Sri Lankan minerals (Rajapakse RMG) **50**: 303-314 (2022)

Natural rubber composites

Synthesis of polyethylene glycol-grafted graphite and effect of its loading on properties of natural rubber composites (Sampath WDM, Fernando CAN & Edirisinghe DG) **50**: 785-798 (2022)

Nesting habitats

Assessment of marine turtle nesting habitats from Tangalle to the Kumbukkan Oya estuary in south-eastern Sri Lanka (Perera SJ, Perera WPN, Goonatilake S de A, Ekaratne K, Wijesinghe D, Perera LV, Chandranimal D & Ediriweera A) **50**: 755-769 (2022)

Network lifetime

Fuzzy based congestion detection and control algorithm for energy efficient wireless sensor network (WSN) (Ramasamy-Rajeswari A, Ganapathy S, Kulothungan K & Kannan A) **50**: 563-576 (2022)

Neural networks

Development of wind energy prediction models using statistical, machine learning and hybrid techniques: a case study (Ekanayake P, Panahatipola O & Jayasinghe J) **50**: 503-517 (2022)

Nitrate

Screening of potential aerobic denitrifying bacteria for nitrate removal from water (Kirisan A, Gnanavelrajah N & Ratnayake RR) **50**: 639-649 (2022)

Nodal segments

Micropropagation of *Stevia rebaudiana* (Bertoni) Bertoni using nutrient water of *Cocos nucifera* var. *aurantiaca* (King coconut) as a natural growth enhancer (Karunarathna HGMK, Medagama K, Wijesundara S & Iqbal MCM) **50**: 3-12 (2022)

Non linear finite element model

Failure prediction of solid resilient tyres due to kerb impact: A finite element modelling approach (Premarathna WAAS, Jayasinghe JASC, Senanayake CD, Wijesundara KK & Gamage P) **50**: 625-637 (2022)

Non-destructive test

Combined use of non-destructive tests, visual inspection and service life prediction to ensure the reliability of reinforced concrete water tanks (Ranasinghe K & De Silva S) **50**: 371-386 (2022)

Non-linear finite element analysis

Seismic performance of stiffened steel box column with different corner stiffener arrangements: a numerical approach (Thevega T, Jayasinghe JASC & Susantha KAS) **50**: 453-466 (2022)

North Indian Ocean

Forecasting the track and the intensity of the cyclone Burevi using WRF (Gamage TD, Sonnadara U, Jayasinghe S & Basnayake S) **50**: 675-684 (2022)

Numerical solutions

Stability analysis of a partially saturated layered soil formation associated with shallow landslides (Walpita SC, Ratnaweera P & Fernando GVAR) **50**: 405-415 (2022)

Nutrition

Application of Benford's law in agricultural production statistics (Hanci F) **50**: 387-393 (2022)

Oil Height

Investigation of oil level and type of solid insulator on creeping discharges propagating under an AC electric field (Ediriweera S, Jayarathna PB, Samarasinghe R & Lucas R) **50**: 725-732 (2022)

Oncogenes

The road to precision cancer therapy – history and strategies (Thiagalingam S) **50**: 321-330 (2022)

Open-source technologies

Evaluating the potential of an open sensor network to support reservoir pre-release decision making (Warusavitharana E, Mahanama PKS, Cannata M, Ratnayake R, Sudantha BH & Strigaro D) **50**: 577-587 (2022)

Order statistics

The odd modified Burr-III exponential distribution: properties, estimation and application (Rasheed H, Dar IS, M Saqib M, Abbas N & Suhail M) **50: 425-439 (2022)**

Organic

Rice production in nutrient-limited soils: Strategies for improving crop productivity and land sustainability (Suriyagoda LBD) **50: 521-539 (2022)**

Partially saturated soil

Stability analysis of a partially saturated layered soil formation associated with shallow landslides (Walpita SC, Ratnaweera P & Fernando GWARD) **50: 405-415 (2022)**

Particle size

Influence of different bone meal particle size induced calcium specific appetite on performance and egg quality parameters of layer chickens (Gamage TS, Mutucumarana RK & Andrew MS) **50: 745-754 (2022)**

Partition coefficient

Vector transport of microplastics bound potentially toxic elements (PTEs) in water systems (Sewwandi M, Premarathne KSD, Wijesekara H, Rajapaksha AU, Soysa S & Vithanage M) **50: 331-344 (2022)**

PCR

Predominance of phylogenetic group B2 among commensal *Escherichia coli* in humans from Kandy District, Sri Lanka (Rangama BNLD, Abayasekara CL and Gordon DM) **50: 137-150 (2022)**

Peelability

Vegetative and reproductive phenology of *Cinnamomum verum* J. Presl grown in intermediate climatic zone of Sri Lanka (Hansika KAS, Kodikara KAS, Wijeweera AA, Senanayake G & Jayatissa LP) **50: 87-99 (2022)**

Penicillin

Screening and quantitative analysis of antibiotic resistance genes in hospital and aquaculture effluent in Sri Lanka as an emerging environmental contaminant (Liyanage GY, Weerasekera MM & Manage PM) **50: 361-370 (2022)**

Phaeodactylum tricornutum

Anti-inflammatory activity of nonyl 8-acetoxy-6-methyloctanoate, isolated from the cultured marine diatom, *Phaeodactylum tricornutum*: mediated via suppression of inflammatory mediators in LPS-stimulated RAW 264.7 macrophages (Samarakoon KW, Ko JY, Lee JH & YJ Jeon YJ) **50: 685-693 (2022)**

Phenology

Vegetative and reproductive phenology of *Cinnamomum verum* J. Presl grown in intermediate climatic zone of Sri Lanka (Hansika KAS, Kodikara KAS, Wijeweera AA, Senanayake G & Jayatissa LP) **50: 87-99 (2022)**

Photovoltaic systems

Analysis of instantaneous, daily and monthly statistics 2017-2021 of rooftop solar energy (Lucas JR) **50: 799-811 (2022)**

Phylogenetic groups

Predominance of phylogenetic group B2 among commensal *Escherichia coli* in humans from Kandy District, Sri Lanka (Rangama BNLD, Abayasekara CL and Gordon DM) **50: 137-150 (2022)**

Pollution

Effects of dietary lead exposure on the call of Japanese quail (*Coturnix japonica*) hatchlings (Ranasinghe RPTI, Fernando TSP & Wijesinghe MR) **50: 477-487 (2022)**

Polyethylene glycol

Synthesis of polyethylene glycol-grafted graphite and effect of its loading on properties of natural rubber composites (Sampath WDM, Fernando CAN & Edirisinghe DG) **50: 785-798 (2022)**

Polyethylene glycol-grafted graphite

Synthesis of polyethylene glycol-grafted graphite and effect of its loading on properties of natural rubber composites (Sampath WDM, Fernando CAN & Edirisinghe DG) **50: 785-798 (2022)**

Polyhydroxyalkanoates (PHAs)

Poly- β -hydroxybutyrate (PHB) production potential of naturally existing cyanobacterial blooms (Wijerathne RS, Manage PM, & Idroos FS) **50: 733-743 (2022)**

Poly- β -hydroxybutyrate (PHB)

Poly- β -hydroxybutyrate (PHB) production potential of naturally existing cyanobacterial blooms (Wijerathne RS, Manage PM, & Idroos FS) **50: 733-743 (2022)**

Precision cancer therapy

The road to precision cancer therapy – history and strategies (Thiagalingam S) **50: 321-330 (2022)**

Pressure head

Stability analysis of a partially saturated layered soil formation associated with shallow landslides (Walpita SC, Ratnaweera P & Fernando GVAR) **50**: 405-415 (2022)

PRGdb

Meta-QTL analysis identified stable quantitative trait loci (QTLs) and associated resistance gene analogues in rice (Shashiprabha HED, Abeyundara SP & Ariyaratna HACK) **50**: 35-51 (2022)

Primary congenital glaucoma

High prevalence of glaucoma-associated CYP1B1 mutation (p.G61E) in primary congenital and open angle glaucoma patients in Pakistan (Yousaf K, Bashir R, Balqees K, Naz S, Munir N & Aslam F) **50**: 589-594 (2022)

Probabilistic modelling

A coupled system of stochastic differential equations for probabilistic wind speed modelling (Bandarathilake HMDP, Palamakumbura GWRMR & Maithripala DHS) **50**: 613-623 (2022)

Probiotic

Physicochemical and sensory attributes of inulin incorporated set yoghurt prepared using cow and buffalo milk (Gnanarathna KADC, Jayasumama MTLK, Weragama KWDP, Gunasekara DCS, Weerasingha WVVR, Chandrasekara A & Prasanna PHP) **50**: 651-661 (2022)

Production

Application of Benford's law in agricultural production statistics (Hanci F) **50**: 387-393 (2022)

Productivity

Rice production in nutrient-limited soils: Strategies for improving crop productivity and land sustainability (Suriyagoda LBD) **50**: 521-539 (2022)

Propagation

Fractal characteristics of creeping discharges propagating on nano-epoxy composite insulators immersed in coconut oil (Ediriweera S, Jayarathna PB, Samarasinghe R & Lucas R) **50**: 663-673 (2022)

Propagation

Investigation of oil level and type of solid insulator on creeping discharges propagating under an AC electric field (Ediriweera S, Jayarathna PB, Samarasinghe R & Lucas R) **50**: 725-732 (2022)

Proportional integral derivative controller

Novel nebulizer design with adaptive flow regulation (Dampage U & Ariyasinghe M) **50**: 101-109 (2022)

Pseudomonas aeruginosa

An approach to develop bioremediation by isolation and characterization of microorganisms from soil contaminated with used lubricating oil (Wijesooriya MM, Masakorala K, Widana Gamage SMK & Walakulu Gamage SS) **50**: 347-360 (2022)

Quartz

Nanotechnology in sustainable value addition to Sri Lankan minerals (Rajapakse RMG) **50**: 303-314 (2022)

Radioactive iodine

Comparison of radioactive iodine therapy outcome and the duration of pretreatment discontinuation of carbimazole among hyperthyroid patients: a prospective study (Raheem S & Nanayakkara DKK) **50**: 417-423 (2022)

Randić index

M-polynomial and topological indices for the anti-tuberculosis drugs (Jude TP, Elango P & Koneswaran M) **50**: 827-838 (2022)

Ratio estimator

Estimation of mean considering the joint influence of measurement errors and non-response in two-phase sampling designs (Sabir S, Sanullah A & Gupta S) **50**: 13-25 (2022)

RAW 264.7 cells

Anti-inflammatory activity of nonyl 8-acetoxy-6-methyloctanoate, isolated from the cultured marine diatom, *Phaeodactylum tricorutum*: mediated via suppression of inflammatory mediators in LPS-stimulated RAW 264.7 macrophages (Samarakoon KW, Ko JY, Lee JH & YJ Jeon YJ) **50**: 685-693 (2022)

Regression analysis

Development of wind energy prediction models using statistical, machine learning and hybrid techniques: a case study (Ekanayake P, Panahatipola O & Jayasinghe J) **50**: 503-517 (2022)

Regression estimator

Estimation of mean considering the joint influence of measurement errors and non-response in two-phase sampling designs (Sabir S, Sanullah A & Gupta S) **50**: 13-25 (2022)

Reservoir pre-release

Evaluating the potential of an open sensor network to support reservoir pre-release decision making (Warusavitharana E, Mahanama PKS, Cannata M, Ratnayake R, Sudantha BH & Strigaro D) **50**: 577-587 (2022)

Resistance genes

Meta-QTL analysis identified stable quantitative trait loci (QTLs) and associated resistance gene analogues in rice (Shashiprabha HED, Abeyesundara SP & Ariyaratna HACK) **50**: 35-51 (2022)

Rice Genome Annotation Project

Meta-QTL analysis identified stable quantitative trait loci (QTLs) and associated resistance gene analogues in rice (Shashiprabha HED, Abeyesundara SP & Ariyaratna HACK) **50**: 35-51 (2022)

Rooftop solar

Analysis of instantaneous, daily and monthly statistics 2017-2021 of rooftop solar energy (Lucas JR) **50**: 799-811 (2022)

Rooting

Micropropagation of *Stevia rebaudiana* (Bertoni) Bertoni using nutrient water of *Cocos nucifera* var. *aurantiaca* (King coconut) as a natural growth enhancer (Karunarathna HGMK, Medagama K, Wijesundara S & Iqbal MCM) **50**: 3-12 (2022)

Rosby waves

Anomalous propagation pathway of the Sri Lanka Dome in summer 2014 (Pathirana G, Chen G, Wang D, Abeyratne MK & Priyadarshana T) **50**: 851-861 (2022)

Routes of administration

Effect of PEGylated gold nanorods on the circulating vascular endothelial growth factor, platelet-derived growth factor, and miR-29a in CD-1 mice (Gamal-Eldeen AM, Raafat BM, Fahmy CA, Abo-Elfadl MT, El-Daly SM & Ali MRK) **50**: 467-475 (2022)

RT-qPCR

Sonication-assisted water extract of *Dendronephthya gigantea* exhibits anti-fine dust effects; attenuation of MAPK phosphorylation in macrophages (Jayawardena TU, Fernando IPS, Nagahawatta DP, Wang L, Yang HW, Oh JY, Sanjeeva KKA & Jeon Y) **50**: 151-160 (2022)

Selection modes

Non invasive automated approach for eczema lesions pigmentation using colour space normalization (Nisar H, Ch'ng Y-K & Yeap KH) **50**: 705-716 (2022)

Service life prediction

Combined use of non-destructive tests, visual inspection and service life prediction to ensure the reliability of reinforced concrete water tanks (Ranasinghe K & De Silva S) **50**: 371-386 (2022)

Shallow landslides

Stability analysis of a partially saturated layered soil formation associated with shallow landslides (Walpita SC, Ratnaweera P & Fernando GWR) **50**: 405-415 (2022)

Shooting

Micropropagation of *Stevia rebaudiana* (Bertoni) Bertoni using nutrient water of *Cocos nucifera* var. *aurantiaca* (King coconut) as a natural growth enhancer (Karunarathna HGMK, Medagama K, Wijesundara S & Iqbal MCM) **50**: 3-12 (2022)

Skin lesions

Non invasive automated approach for eczema lesions pigmentation using colour space normalization (Nisar H, Ch'ng Y-K & Yeap KH) **50**: 705-716 (2022)

Smoothing techniques

A coupled system of stochastic differential equations for probabilistic wind speed modelling (Bandarathilake HMDP, Palamakumbura GWRMR & Maithripala DHS) **50**: 613-623 (2022)

Socio-economic impacts

Artificial intelligence framework for threat assessment and containment for covid-19 and future epidemics while mitigating the socioeconomic impact to women, children, and underprivileged groups (Ilangarathna G, Weligampola H, Ranasinghe Y, Attygalla E, Godaliyaddha R, Herath V, Ekanayake P, Ekanayake SY, Pinnawela M, Dharmaratne S, Tilakaratne G & Ekanayake J) **50**: 251-262 (2022)

Socioeconomics

New paradigm for inland fisheries development in Sri Lanka: a transdisciplinary approach for addressing food and nutritional security (Amarasinghe US, Pushpalatha KBC & Wijenayake WMHK) **50**: 177-194 (2022)

Soil fertility

Rice production in nutrient-limited soils: Strategies for improving crop productivity and land sustainability (Suriyagoda LBD) **50**: 521-539 (2022)

Solar collector

A novel approach for energy and exergy analysis of a flat plate solar collector with energy storage (Hanif M, Khattak MK, Ul Haq I, Uddin R & Ullah K) **50**: 161-172 (2022)

Solar energy

A novel approach for energy and exergy analysis of a flat plate solar collector with energy storage (Hanif M, Khattak MK, Ul Haq I, Uddin R & Ullah K) **50**: 161-172 (2022)

Solar intermittency

Analysis of instantaneous, daily and monthly statistics 2017-2021 of rooftop solar energy (Lucas JR) **50**: 799-811 (2022)

Solar power generation

Analysis of instantaneous, daily and monthly statistics 2017-2021 of rooftop solar energy (Lucas JR) **50**: 799-811 (2022)

Solid resilient tyres

Failure prediction of solid resilient tyres due to kerb impact: A finite element modelling approach (Premarathna WAAS, Jayasinghe JASC, Senanayake CD, Wijesundara KK & Gamage P) **50**: 625-637 (2022)

Somatic embryogenesis

Induction of somatic embryogenesis from leaf explants of *Exacum trinervium* (L.) Druce (Binara) (de Silva V & Eeswara JP) **50**: 27-33 (2022)

Soursop fruit

Development of vacuum-dried powder and drinking yoghurt from soursop fruit (*Annona muricata* L.) and evaluation of their physico-chemical and functional properties (Ranaweera NI, Pitipanaarachchi RC, Herath HMT & Chandramali DVP) **50**: 489-502 (2022)

Southern Sri Lanka

Assessment of marine turtle nesting habitats from Tangalle to the Kumbukkan Oya estuary in south-eastern Sri Lanka (Perera SJ, Perera WPN, Goonatilake S de A, Ekaratne K, Wijesinghe D, Perera LV, Chandranimal D & Ediriweera A) **50**: 755-769 (2022)

Species-specific

An approach to develop bioremediation by isolation and characterization of microorganisms from soil contaminated with used lubricating oil (Wijesooriya MM, Masakorala K, Widana Gamage SMK & Walakulu Gamage SS) **50**: 347-360 (2022)

Sri Lanka

Ocean circulation around Sri Lanka (Pattiaratchi CB, Wijeratne EMS & de Vos A) **50**: 293-302 (2022)

Sri Lanka Dome

Anomalous propagation pathway of the Sri Lanka Dome in summer 2014 (Pathirana G, Chen G, Wang D, Abeyratne MK & Priyadarshana T) **50**: 851-861 (2022)

ST

Predominance of phylogenetic group B2 among commensal *Escherichia coli* in humans from Kandy District, Sri Lanka (Rangama BNL, Abayasekara CL and Gordon DM) **50**: 137-150 (2022)

Statistics

Application of Benford's law in agricultural production statistics (Hanci F) **50**: 387-393 (2022)

Steel column

Seismic performance of stiffened steel box column with different corner stiffener arrangements: a numerical approach (Thevega T, Jayasinghe JASC & Susantha KAS) **50**: 453-466 (2022)

Stevia rebaudiana

Micropropagation of *Stevia rebaudiana* (Bertoni) Bertoni using nutrient water of *Cocos nucifera* var. *aurantiaca* (King coconut) as a natural growth enhancer (Karunarathna HGMK, Medagama K, Wijesundara S & Iqbal MCM) **50**: 3-12 (2022)

Stiffener arrangements

Seismic performance of stiffened steel box column with different corner stiffener arrangements: a numerical approach (Thevega T, Jayasinghe JASC & Susantha KAS) **50**: 453-466 (2022)

Stochastic differential equation

A coupled system of stochastic differential equations for probabilistic wind speed modelling (Bandarathilake HMDP, Palamakumbura GWRMR & Maithripala DHS) **50**: 613-623 (2022)

Strength

Seismic performance of stiffened steel box column with different corner stiffener arrangements: a numerical approach (Thevega T, Jayasinghe JASC & Susantha KAS) **50**: 453-466 (2022)

Sulphide stress corrosion

Developing a model to predict the propagation of sulphide stress corrosion of steel used for petroleum pipelines (Manimendra A, De Silva I & Jayasundara R) **50**: 839-850 (2022)

Sulphur

Developing a model to predict the propagation of sulphide stress corrosion of steel used for petroleum pipelines (Manimendra A, De Silva I & Jayasundara R) **50**: 839-850 (2022)

Summer monsoon current

Anomalous propagation pathway of the Sri Lanka Dome in summer 2014 (Pathirana G, Chen G, Wang D, Abeyratne MK & Priyadarshana T) **50**: 851-861 (2022)

Surface circulation

Ocean circulation around Sri Lanka (Pattiaratchi CB, Wijeratne EMS & de Vos A) **50**: 293-302 (2022)

Sustainability

Rice production in nutrient-limited soils: Strategies for improving crop productivity and land sustainability (Suriyagoda LBD) **50**: 521-539 (2022)

Sustainable agriculture

Microbiome: diversity, distribution, and potential role in sustainable crop production (Fernando WGD & Dolatabadian A) **50**: 231-250 (2022)

Targeted cancer therapy

The road to precision cancer therapy – history and strategies (Thiagalingam S) **50**: 321-330 (2022)

Tet A

Screening and quantitative analysis of antibiotic resistance genes in hospital and aquaculture effluent in Sri Lanka as an emerging environmental contaminant (Liyanage GY, Weerasekera MM & Manage PM) **50**: 361-370 (2022)

Tet M

Screening and quantitative analysis of antibiotic resistance genes in hospital and aquaculture effluent in Sri Lanka as an emerging environmental contaminant (Liyanage GY, Weerasekera MM & Manage PM) **50**: 361-370 (2022)

Tetracycline

Screening and quantitative analysis of antibiotic resistance genes in hospital and aquaculture effluent in Sri Lanka as an emerging environmental contaminant (Liyanage GY, Weerasekera MM & Manage PM) **50**: 361-370 (2022)

Theil-Sen estimators

Implementation of adaptive lasso regression based on multiple Theil-Sen Estimators using differential evolution algorithm with heavy tailed errors (Dünder E, Zaman T, Cengiz MA & Alakus K) **50**: 395-404 (2022)

Thottea

First record of *Thottea duchartrei* Sivar., A. Babu & Balach. (Aristolochiaceae) in Sri Lanka (Tennakoon TMSG, Borosova R, Suraweera C, Herath S, De Silva T, Padumadasa C, Weerasena J, Gunaratna N, Gunasekera N, Edwards S & Wijesundara S) **50**: 441-452 (2022)

Time series analysis

Development of wind energy prediction models using statistical, machine learning and hybrid techniques: a case study (Ekanayake P, Panahatipola O & Jayasinghe J) **50**: 503-517 (2022)

Tomography

Determination of safe zone of the mandible for implant and bone harvesting (using CBCT) of mandible in a group of Sri Lankan subjects (Dharmapala RMAU, Satharasinghe DM, Silva SPI & Jeyasinghthan J) **50**: 65-72 (2022)

Topological indices

M-polynomial and topological indices for the anti-tuberculosis drugs (Jude TP, Elango P & Koneswaran M) **50**: 827-838 (2022)

Total microbial activity

An approach to develop bioremediation by isolation and characterization of microorganisms from soil contaminated with used lubricating oil (Wijesooriya MM, Masakorala K, Widana Gamage SMK & Walakulu Gamage SS) **50**: 347-360 (2022)

Toxicity

Effects of dietary lead exposure on the call of Japanese quail (*Coturnix japonica*) hatchlings (Ranasinghe RPTI, Fernando TSP & Wijesinghe MR) **50**: 477-487 (2022)

Track forecast

Forecasting the track and the intensity of the cyclone Burevi using WRF (Gamage TD, Sonnadara U, Jayasinghe S & Basnayake S) **50**: 675-684 (2022)

Traffic management

Increasing the effectiveness of T-junctions with an innovative geometrical and phasing arrangement (Jayasooriya NK, Perera HLK and Bandara JMSJ) **50**: 73-86 (2022)

Traffic signal design

Increasing the effectiveness of T-junctions with an innovative geometrical and phasing arrangement (Jayasooriya NK, Perera HLK and Bandara JMSJ) **50**: 73-86 (2022)

Transgenic mosquitoes

Mosquito control: A review on the past, present and future strategies (Karunaratne SHPP & Surendran SN) **50**: 277-292 (2022)

Transmuted distributions

A new multivariate transmuted family of distributions: theory and application for modelling of daily world COVID-19 cases (Darwish JA, Al-Turk LI & Shahbaz MQ) **50**: 771-784 (2022)

Treatments

Screening of potential aerobic denitrifying bacteria for nitrate removal from water (Kirisan A, Gnanavelrajah N & Ratnayake RR) **50**: 639-649 (2022)

Tropical cyclone

Forecasting the track and the intensity of the cyclone Burevi using WRF (Gamage TD, Sonnadara U, Jayasinghe S & Basnayake S) **50**: 675-684 (2022)

Tropical cyclones

Tropical cyclones in the Arabian Sea and the Bay of Bengal: comparison of environmental factors (Pathirana G & Priyadarshani K) **50**: 53-64 (2022)

Tropical reservoirs

New paradigm for inland fisheries development in Sri Lanka: a transdisciplinary approach for addressing food and nutritional security (Amarasinghe US, Pushpalatha KBC & Wijenayake WMHK) **50**: 177-194 (2022)

Tuberculosis

M-polynomial and topological indices for the anti-tuberculosis drugs (Jude TP, Elango P & Koneswaran M) **50**: 827-838 (2022)

Tumour suppressor genes

The road to precision cancer therapy – history and strategies (Thiagalingam S) **50**: 321-330 (2022)

Turtle nesting hotspots

Assessment of marine turtle nesting habitats from Tangalle to the Kumbukkan Oya estuary in south-eastern Sri Lanka (Perera SJ, Perera WPN, Goonatilake S de A, Ekaratne K, Wijesinghe D, Perera LV, Chandranimal D & Ediriweera A) **50**: 755-769 (2022)

UI/UX designing

Designing a closed-loop information flow model in bridging the market information gap among agriculture stakeholders in Sri Lanka (Mallikaarachchi TB, Samaraweera G, Walisadeera A, De Silva L & Munasinghe S) **50**: 881-896 (2022)

Unitary matrices

On the construction of unitaries representing minimal inner toral polynomials (Dissanayake CSB & Wijesooriya UD) **50**: 607-611 (2022)

Upwelling

Ocean circulation around Sri Lanka (Pattiaratchi CB, Wijeratne EMS & de Vos A) **50**: 293-302 (2022)

Used lubricating oil

An approach to develop bioremediation by isolation and characterization of microorganisms from soil contaminated with used lubricating oil (Wijesooriya MM, Masakorala K, Widana Gamage SMK & Walakulu Gamage SS) **50**: 347-360 (2022)

Vacuum-dried powder

Development of vacuum-dried powder and drinking yoghurt from soursop fruit (*Annona muricata* L.) and evaluation of their physico-chemical and functional properties (Ranaweera NI, Pitipanaarachchi RC, Herath HMT & Chandramali DVP) **50**: 489-502 (2022)

VEGF and PDGF

Effect of PEGylated gold nanorods on the circulating vascular endothelial growth factor, platelet-derived growth factor, and miR-29a in CD-1 mice (Gamal-Eldeen AM, Raafat BM, Fahmy CA, Abo-Elfadl MT, El-Daly SM & Ali MRK) **50**: 467-475 (2022)

VISSIM

Increasing the effectiveness of T-junctions with an innovative geometrical and phasing arrangement (Jayasooriya NK, Perera HLK and Bandara JMSJ) **50**: 73-86 (2022)

Visual inspections

Combined use of non-destructive tests, visual inspection and service life prediction to ensure the reliability of reinforced concrete water tanks (Ranasinghe K & De Silva S) **50**: 371-386 (2022)

Water hardness

Geo-environmental assessment of geochemistry of groundwater and associated human health risks in the dry zone terrain of Sri Lanka (Chandrajith R & Diyabalanage S) **50**: 213-229 (2022)

Wave climate

Assessment of wave climate change and its impact on littoral drift along the Kalutara and Kalpitiya beaches in Sri Lanka (Samarasekara RSM, Sahthy MM, Siriwardana AHMS & Siriwardana HPAM) **50**: 813-826 (2022)

Weibull distribution

A new multivariate transmuted family of distributions: theory and application for modelling of daily world COVID-19 cases (Darwish JA, Al-Turk LI & Shahbaz MQ) **50**: 771-784 (2022)

Weight vector selection

Implementation of adaptive lasso regression based on multiple Theil-Sen Estimators using differential evolution algorithm with heavy tailed errors (Dünder E, Zaman T, Cengiz MA & Alakus K) **50**: 395-404 (2022)

Western boundary currents

Anomalous propagation pathway of the Sri Lanka Dome in summer 2014 (Pathirana G, Chen G, Wang D, Abeyratne MK & Priyadarshana T) **50**: 851-861 (2022)

White noise

A coupled system of stochastic differential equations for probabilistic wind speed modelling (Bandarathilake HMDP, Palamakumbura GWRMR & Maithripala DHS) **50**: 613-623 (2022)

Wind energy

Development of wind energy prediction models using statistical, machine learning and hybrid techniques: a case study (Ekanayake P, Panahatipola O & Jayasinghe J) **50**: 503-517 (2022)

Wind-stress

Anomalous propagation pathway of the Sri Lanka Dome in summer 2014 (Pathirana G, Chen G, Wang D, Abeyratne MK & Priyadarshana T) **50**: 851-861 (2022)

Wistar rats

Effect of cylindrospermopsin on the hepatotoxicity in wistar rats (Abeyisiri HASN, Wanigasuriya JKP, Suresh TS, Beneragama DH & Manage PM) **50**: 595-605 (2022)

WRF-ARW

Forecasting the track and the intensity of the cyclone Burevi using WRF (Gamage TD, Sonnadara U, Jayasinghe S & Basnayake S) **50**: 675-684 (2022)

WSN

Fuzzy based congestion detection and control algorithm for energy efficient wireless sensor network (WSN) (Ramasamy-Rajeswari A, Ganapathy S, Kulothungan K & Kannan A) **50**: 563-576 (2022)

Yoghurt

Physicochemical and sensory attributes of inulin incorporated set yoghurt prepared using cow and buffalo milk (Gnanarathna KADC, Jayasumama MTLK, Weragama KWDP, Gunasekara DCS, Weerasingha WVVR, Chandrasekara A & Prasanna PHP) **50**: 651-661 (2022)

Zagreb index

M-polynomial and topological indices for the anti-tuberculosis drugs (Jude TP, Elango P & Koneswaran M) **50**: 827-838 (2022)

β -glucuronidase

Bioactive cyclo-(S-Pro-R-Leu) from *Aspergillus flavus*, the marine endophytic fungus from brown alga, *Dictyota kunthi* (Haniffa HM, Dharmaratne HRW & Mohommad MY) **50**: 717-721 (2022)

GUIDANCE TO CONTRIBUTORS

Scope

The Journal of the National Science Foundation of Sri Lanka publishes the results of research in all aspects of Science and Technology. It is open for publication of Research Articles, Reviews, Research Communications and Correspondence.

IT related and other non-empirical articles

The JNSF is a journal primarily devoted to natural sciences. It also considers for publication significant and novel contributions from formal sciences. Authors of emerging sub-disciplines of Computing and related areas such as Machine Learning, Artificial Intelligence and Data Sciences are requested to carefully adhere to the following guidelines when submitting manuscripts for this journal.

- Clear formulation of outcome-oriented **Research Objective/s** for targeted knowledge (sub)domain/s or (sub)discipline/s.
- Selection and comprehensive summarization of **appropriate Research Method/s** adopted to achieve the stated Research Objective/s.
- Reporting a sound (**Empirical**) **Evaluation** of the research finding/s thereby arguing reliability, validity, and generalizability of research claim/s.

Categories of manuscripts

Research Articles: Research Articles are papers that present complete descriptions of original research. Research Articles should include an Abstract, Keywords, Introduction, Methodology, Results and Discussion, Conclusion and Recommendations where relevant. References should be prepared according to the “Guidelines for the preparation of manuscripts”. Maximum length of the article should be limited to 25 pages with a word count of 10,000 including references, figures and tables. Any articles above this limit will be returned.

Reviews: Reviews are critical presentations on selected topics of Science or Technology. They should be well focused and organized and avoid general “textbook” style. As reviews are intended to be critical presentations on selected topics, reviewers need to have had substantial leadership in research supported by a publication track record in the areas covered by the review. A person/s wishing to submit a Review Article should obtain prior approval from the Editorial Board by submitting a concise summary of the intended article, along with a list of the author’s publications in the related area (jnsf@nsf.gov.lk). Maximum length of the article should be limited to 40 pages with a word count of 12,000 including references, figures and tables. Any articles above this limit will be returned.

Research Communications: Research Communications are intended to communicate important new findings in a specific area of limited scope that are worthy of rapid dissemination among the scientific community. Authors are required to provide a statement justifying the suitability of the submission for a Research Communication. The article should include an Abstract, Keywords, Introduction, Methodology, Results & Discussion, Conclusion and References. Maximum length of the article should be limited to 10 pages with a word count of 2,500 including references, figures and tables. Any articles above this limit will be returned.

Correspondence: Correspondence will be accepted regarding one or more articles in the preceding four issues of the Journal, as well as Letters to the Editor. Articles covering important scientific events or any other news of interest to scientists, reviews of books of scientific nature, articles presenting views on issues related to science and scientific activity will also be considered. Publication will be made at the discretion of the Editor-in-Chief. Maximum length of the article should be limited to 05 pages with a word count of 1,500 including references, figures and tables. Any articles above this limit will be returned.

SUBMISSION OF MANUSCRIPT

Authors submitting articles to the JNSF should first create an account in the Sri Lanka Journals Online System (<https://jnsfsl.sljol.info/>). All manuscripts in MS Word format must be electronically submitted to the journal’s online platform at <https://jnsfsl.sljol.info/submit/start/>. Submissions *via* emails are not encouraged. Please make sure that no author information is mentioned in the article submitted. The names and details of affiliations of all authors and contact information of the corresponding author must be fed into the system during the online submission process. Authors (at least the corresponding author) are required to provide their personal, validated ORCID ID (by obtaining an ORCID ID from <https://orcid.org/>) when submitting the manuscript. No change to the authors or order of authors will be accepted after the submission. All those who have made significant contributions should be listed as co-authors. The corresponding author should ensure that all contributing co-authors are included in the author list and have approved the final version of the paper and have agreed to its submission for publication.

All submissions should be in English. If the manuscript conforms to the guidelines specified, the date received will be the date that the manuscript was submitted to the online system.

Submissions are accepted for processing on the understanding that they will be reviewed and that they have not been submitted for publication elsewhere (including publication as a full paper or extended abstract as a part of Conference Proceedings). The JNSF does not accept manuscripts that have already been submitted to pre-print servers.

Suggesting potential reviewers by authors

The authors may suggest up to three names of referees when submitting their manuscript, in the Cover Letter space provided at the bottom of the page in the first stage of online submission. Referees should not be from the institution where the work was carried out and should not have been co-authors in previous publications. The address, institutional affiliation and e-mail of the suggested referees should be supplied. Please note that the JNSF is not bound to select all or any of the suggested referees for sending the manuscript for reviewing

Authorship

All authors designated as authors should be eligible for authorship. Those who have made a substantial contribution to the concept or design of the work; or acquisition, analysis or interpretation of data are recognized as Authors.

The corresponding author should be prompt and ensure adherence to timelines when responding to requests, queries and recommendation of reviewers conveyed by or on behalf of the Editor-in Chief and Editorial Board.

Supplementary materials

Any experimental data necessary to evaluate the claims made in the paper but not included in the paper should be provided as supplementary materials. Supplementary materials will be sent to the reviewers and published online with the manuscript if accepted. The supplementary materials should conform to Journal guidelines and should be uploaded as separate files. Authors should number Supplementary Tables and Figures as, for example, 'Supplementary Table S1'. Refer to each piece of supplementary material at the appropriate point(s) in the main article. Supplementary Materials may include description of the materials and methods, controls, or tabulated data presented in Tables or Figures, and programming codes.

Peer review

The manuscripts submitted to the JNSF will initially be screened by the Editorial Board and, if suitable, will be referred to at least two subject experts in the relevant field. The peer-review process of the JNSF is double-blind.

When revision of a manuscript has been requested, the revised manuscript should be submitted on or before the stated deadline. If the revised manuscript is not received on time, the manuscript will not be processed further. The authors' response to the comments of referees should be tabulated with the comment, response and the line number/s for reference. The decision of the Editorial Board shall be final.

Accepted papers are subject to editing. The date of acceptance will be the date when the Editorial Board has decided it to be acceptable for publication.

Article publication fee and complementary copies

A publication fee of US\$ 150 will be levied for each manuscript other than where the corresponding author is affiliated to a Sri Lankan Institute, to cover the publication cost.

A complimentary copy of the Journal issue carrying the respective article will be supplied to each of the authors.

Authors' declaration

When an article is accepted for publication, the authors are required to submit the Authors' Declaration signed by all the authors.

Copyright

Articles in JNSF are published under the Creative Commons License CC-BY-ND. This license permits use, distribution and reproduction of articles for commercial and non-commercial purposes, provided that the original work is properly cited and is not changed in anyway. The copyright of the article is with the National Science Foundation of Sri Lanka. Therefore, authors are requested to check with institution's copyright and publication policy before submitting an article to the JNSF. Authors secure the right to reproduce any material that has already been published or copyrighted elsewhere. When an article is accepted for publication, the authors are required to submit the Transfer of Copyright document signed by all the authors.

Post-publication corrections

The Editorial Board reserves the right to take action on publishing an erratum or corrigendum. If serious errors are identified in a published article, the Journal may consider a retraction or publishing a correction.

STRUCTURE OF MANUSCRIPT

Manuscript

The manuscript should be free of errors and prepared in single column, using double-spaced text of Times New Roman 12 font throughout with line numbers, leaving at least 2 cm margins on both sides, and liberal spacing at the top and bottom of each page. Pages should be numbered consecutively.-

a. Style

The paper should be written clearly and concisely. The style of writing should conform to scholarly writing. Slang, jargon, unauthorized abbreviations, abbreviated phrasings should not be used. In general, the impersonal form should be used. Poor usage of language will result in rejection of the manuscript during initial screening.

b. Layout

Manuscripts other than review articles should be generally organized as follows: Title, Abstract, Keywords, Introduction, Methodology, Results and Discussion, Conclusions and Recommendations (where relevant), Acknowledgements and References. Pages should be arranged in the following order:

Title page should include the title of manuscript, and no author information should be mentioned in the title page. If a major part of the research has been published as an abstract in conference proceedings, it should be cited as a footnote on the title page. Authors must also indicate the **general and specific research area** of the manuscript in the title page. In order to highlight the significance of the manuscript, authors are required to provide the following highlights in brief. (1) Why was this study conducted? (2) What are the new findings? (3) Possible applications of the findings. Please limit your answers to 25-30 words for each.

Title: Should accurately and concisely reflect the contents of the article.

Running title: Should be a shortened title (limited to a maximum of 50 characters) that could be printed at the top of every other page of the Journal article.

Abstract: Should be between 200 - 250 words for full length articles and written as a single paragraph. It should not contain any references and should be able to stand on its own. It should outline objectives and methodology together with important results and conclusions. A Review Article should carry a summary of not more than 300 words.

Keywords: Include a maximum of six keywords, which may include the names of organisms (common or scientific), methods or other important words or phrases relevant to the study.

Introduction: This should state the reasons for performing the work with a brief review of related research studies in the context of the work described in the paper. Objectives of the study should be clearly stated.

Materials and Methods: This section should give the details of how you conducted your study. New methods may be described in detail with an indication of their limitations. Established methods can be mentioned with appropriate references. Sufficient details should be included to allow direct repetition of the work by others. Where human subjects are involved, they should be referred to by numbers or fictitious names. A paper reporting the results of investigations on human subjects or on animals must include a statement to the effect that the relevant national or other administrative and ethical guidelines have been adhered to, and a copy of the ethical clearance certificate should be submitted. Methods of statistical analyses used should be mentioned where relevant.

Results and Discussion: Results: the results should be concisely and logically presented. Repetition of the same results in figures, tables or text should be avoided.

Discussion: data essential for the conclusions emerging from the study should be discussed. Long, rambling discussions should be avoided. The discussion should deal with the interpretation of results. It should logically relate new findings to earlier ones. Unqualified statements and conclusions not completely supported by data should be avoided.

Molecular sequence data, such as gene or rDNA sequences, genome sequences, metagenomic sequences etc. must be deposited in a public molecular sequence repository, such as GenBank, that is part of the International Nucleotide Sequence Database Collaboration (INSDC). The accession numbers obtained must be cited in the text, Table or on Figures of phylogenetic trees of the manuscript.

Conclusion: The conclusion should be brief, highlight the outcomes of the study and should be aligned with the objectives of the study. It should not contain references.

Conflict of interest statement: All authors should include a statement on conflict of interest disclosing any financial or other substantive conflicts of interest that may be construed to influence the results or interpretation of their research. All sources of financial support for the project should be disclosed.

Acknowledgement: Should be brief and made for specific scientific, financial and technical assistance only. If a significant part of the research was performed in an institution other than in those indicated by the authors' affiliations given in the title page, this fact should be acknowledged. All those who have made substantial contribution to the research but do not qualify to be authors should be acknowledged.

References :

All research work of other authors, when used or referred to or cited, should be correctly acknowledged in the text and in the References.

Citing references in the text:

- References to the literature must be indicated in the text and tables as per the Author-Year System, by the author's last name and year, in parenthesis (i.e. Able, 1997) or (Able & Thompson, 1998).
- Citation to work by more than two authors should be abbreviated with the use of *et al.* (i.e. Able *et al.*, 1997).
- Multiple publications by the same first author in the same year should be coded by letters, (i.e. Thompson, 1991a; b).
- Multiple citations should be made in chronological order and separated by a semi-colon, (i.e. Zimmerman *et al.*, 1986; Able *et al.*, 1997).
- Reference to unpublished work, work in preparation or work under review should be cited in italics as (*unpublished data*) or, with the author's initials and surname given; such works should not be included in the Reference section.
- Personal communications may be mentioned in the text with the date of communication as (*Personal communication*, 2 June 2000).

List of references:

- The list of References should be arranged in alphabetical order based on the last name of the first author.
- Names of all the authors should be given except when there are more than 10 authors. When there are more than 10 authors, only the name of the first author can be given followed by *et al.*
- All the initials of the author must be given after the last name and the year of publication should follow in parentheses.
- This should be followed by the full title of the referred publication.
- When journal articles are listed, the journal name should be given in full and in italics and followed by the volume number in bold type, issue number in parentheses and then the inclusive pages.
- Where there are several publications by the same author(s) and published in the same year they should be differentiated by adding a lower-case letter after the year. When books are listed, the order should be: author(s), year, book title, volume number, edition, pagination/ inclusive pages, publisher and place of publication. The book title should be in italics. When sections of a book are listed, the order should be: author(s) of chapter, year, title of the section, title of the book, edition, inclusive pages, publisher and place of publication.
- Digital object identifiers (DOIs) should be included for all references where available.
- References should only be cited as 'in press' if the paper has been accepted for publication.

Examples of correct forms of references are given below.

Journal Articles

Boutin C. & Harper J.L. (1991). A comparative study of the population dynamics of five species of *Veronica* in natural habitats. *Journal of Ecology* 79(01): 199 – 221.
DOI: <https://doi.org/10.2307/2260793>

Books

Burnham K.P. & Anderson D.R. (2002). *Model Selection and Multimodal Inference*, 2nd edition, pp. 488. Springer Science and Business Media, Inc., New York, USA.

Book Chapters

Hinrichsen R.A. & Holmes E.E. (2009). Using multivariate state-space models to study spatial structure and dynamics. In: *Spatial Ecology* (eds. R.S. Cantrell, C. Cosner & S. Ruan), pp. 145 – 166. CRC/ Chapman Hall, Florida, USA.
DOI: <https://doi.org/10.1201/9781420059861.ch8>

Edited Books

Kimatl H., Amorim L., Rezende J.A.M., Bergamin Filho A. & Camargo L.E.A. (eds.) (2005). *Manual de Fitopatologia*, volume 2. Doenças das Plantas Cultivadas, 4th edition. Ceres, São Paulo, Brazil.

Conference Papers

Weaver D. (2002). Implementation of a learning management system using an integrated approach to professional development. In: Winds of change in the sea of learning. *Proceedings of the 19th Annual Conference of the Australasian Society for Computers in Learning and Tertiary Education (ASCILITE)* (eds. A. Williamson, C. Gunn, A. Young & T. Clear), volume 2, Auckland, New Zealand, 8-11 December. Unitec Institute of Technology, Auckland, New Zealand, pp. 711-720.

Agency Publications

U.S. Census Bureau (2009). *World Population: 1950 – 2050*. U.S. Census Bureau, Washington DC, USA.

Department of Health (2008). *Health Inequalities: Progress and Next Step* (pdf). Department of Health, London, UK. Available at http://PublicationsPolicyAndGuidance/DH_08_5307, Accessed 9 June 2008.

Other

Robinson L.J. (2003) Spatial scale and depletion models of farmland birds in a fragmented landscape. *PhD thesis*, University of Reading, Reading, UK.

Efford M.G. (2008). Density 4.3: software for spatially explicit capture-recapture. Available at <http://www.otago.ac.nz/density>, Accessed 15 March 2009.

Abbreviations and Symbols: Unless common, these should be defined when first used, and not included in the abstract. The SI System of units should be used wherever possible. If measurements were made in units other than SI, the data should be reported in the same units followed by SI units in brackets, e.g. 5290 ft (1610 m).

Formulae and Equations: Equations should be typewritten and quadruple spaced. They should be started on the left margin and the number placed in parentheses to the right of the equation.

Nomenclature: Scientific names of plants and animals should be printed in italics. In the first citation, genus, species and authority must be given. e.g. *Borassus flabellifer* Linn. In latter citations, the generic name may be abbreviated, for example, *B. flabellifer* L.

Tables and figures: Tables and Figures should be clear and intelligible and kept to a minimum, and should not repeat data available elsewhere in the paper. Any reproduction of illustrations, tabulations, pictures etc. in the manuscript should be acknowledged.

Tables: Tables should be numbered consecutively with Arabic numerals and placed at the appropriate position in the manuscript. If a Table must be continued, a second sheet should be used and all the headings repeated. The number of columns or rows in each Table should be minimized. Each Table should have a title, which makes its general meaning clear, without reference to the text. All Table columns should have explanatory headings. Units of measurement, if any, should be indicated in parentheses in the heading of each column. Vertical lines should not be used and horizontal lines should be used only in the heading and at the bottom of the table. Footnotes to Tables should be placed directly below the Table and should be indicated by superscript lower case italic letters (^a, ^b, ^c, etc.).

Figures: All illustrations are considered as figures, and each graph, drawing or photograph should be numbered consecutively with Arabic numerals and placed at the appropriate position in the manuscript. Any lettering to appear on the illustrations should be of a suitable size for reproduction and uniform lettering should be used in all the Figures of the manuscript. Scanned figures or photographs should be of high quality (**300 dpi**), to fit the proportions of the printed page (12 × 17 cm). Each figure should carry a legend so that the general meaning of the figure can be understood without reference to the text. Where magnifications are used, they should be stated.

Units of measurement

Length: km, m, mm, µm, nm

Area: ha, km², m²

Capacity: kL, L, mL, µL

Volume: km³, m³, cm³

Mass: t, kg, g, mg, µg

Time: year(s), month(s), wk(s),
d(s), h, min, s

Concentration: M, mM, N, %, g/L, mg/L, ppm

Temperature: °C, K

Gravity: x g

Molecular weight: mol wt

Others: Radio-isotopes: 32P

Radiation dose: Bq

Oxidation-reduction potential: rH

Hydrogen ion concentration: pH